NBS SPECIAL PUBLICATION 596

U.S. DEPARTMENT OF COMMERCE / National Bureau of Standards

Ultrasonic Materials Characterization

NATIONAL BUREAU OF STANDARDS

The National Bureau of Standards[1] was established by an act of Congress on March 3, 1901. The Bureau's overall goal is to strengthen and advance the Nation's science and technology and facilitate their effective application for public benefit. To this end, the Bureau conducts research and provides: (1) a basis for the Nation's physical measurement system, (2) scientific and technological services for industry and government, (3) a technical basis for equity in trade, and (4) technical services to promote public safety. The Bureau's technical work is performed by the National Measurement Laboratory, the National Engineering Laboratory, and the Institute for Computer Sciences and Technology.

THE NATIONAL MEASUREMENT LABORATORY provides the national system of physical and chemical and materials measurement; coordinates the system with measurement systems of other nations and furnishes essential services leading to accurate and uniform physical and chemical measurement throughout the Nation's scientific community, industry, and commerce; conducts materials research leading to improved methods of measurement, standards, and data on the properties of materials needed by industry, commerce, educational institutions, and Government; provides advisory and research services to other Government agencies; develops, produces, and distributes Standard Reference Materials; and provides calibration services. The Laboratory consists of the following centers:

Absolute Physical Quantities[2] — Radiation Research — Thermodynamics and Molecular Science — Analytical Chemistry — Materials Science.

THE NATIONAL ENGINEERING LABORATORY provides technology and technical services to the public and private sectors to address national needs and to solve national problems; conducts research in engineering and applied science in support of these efforts; builds and maintains competence in the necessary disciplines required to carry out this research and technical service; develops engineering data and measurement capabilities; provides engineering measurement traceability services; develops test methods and proposes engineering standards and code changes; develops and proposes new engineering practices; and develops and improves mechanisms to transfer results of its research to the ultimate user. The Laboratory consists of the following centers:

Applied Mathematics — Electronics and Electrical Engineering[2] — Mechanical Engineering and Process Technology[2] — Building Technology — Fire Research — Consumer Product Technology — Field Methods.

THE INSTITUTE FOR COMPUTER SCIENCES AND TECHNOLOGY conducts research and provides scientific and technical services to aid Federal agencies in the selection, acquisition, application, and use of computer technology to improve effectiveness and economy in Government operations in accordance with Public Law 89-306 (40 U.S.C. 759), relevant Executive Orders, and other directives; carries out this mission by managing the Federal Information Processing Standards Program, developing Federal ADP standards guidelines, and managing Federal participation in ADP voluntary standardization activities; provides scientific and technological advisory services and assistance to Federal agencies; and provides the technical foundation for computer-related policies of the Federal Government. The Institute consists of the following centers:

Programming Science and Technology — Computer Systems Engineering.

[1] Headquarters and Laboratories at Gaithersburg, MD, unless otherwise noted; mailing address Washington, DC 20234.
[2] Some divisions within the center are located at Boulder, CO 80303.

Ultrasonic Materials Characterization

Proceedings of the First International Symposium on Ultrasonic Materials Characterization held at the National Bureau of Standards, Gaithersburg Md., June 7-9, 1978

Co-Editors:

Harold Berger
Melvin Linzer

National Measurement Laboratory
National Bureau of Standards
Washington, DC 20234

U.S. DEPARTMENT OF COMMERCE, Philip M. Klutznick, Secretary
Luther H. Hodges, Jr., Deputy Secretary
Jordan J. Baruch, Assistant Secretary for Productivity, Technology and Innovation
NATIONAL BUREAU OF STANDARDS, Ernest Ambler, Director

Issued November 1980

Library of Congress Catalog Card Number: 80-600148

National Bureau of Standards Special Publication 596
Nat. Bur. Stand. (U.S.), Spec. Publ. 596, 644 pages (Nov. 1980)
CODEN: XNBSAV

U.S. GOVERNMENT PRINTING OFFICE
WASHINGTON: 1980

For sale by the Superintendent of Documents, U.S. Government Printing Office, Washington, D.C. 20402
Price $11.00
(Add 25 percent for other than U.S. mailing)

FOREWORD

The First International Symposium of Ultrasonic Materials Characterization was held June 7-9, 1978, at the National Bureau of Standards in Gaithersburg, Md. The meeting, the first of its kind, was sponsored by the American Society of Nondestructive Testing, the Sonics and Ultrasonics Group of the Institute of Electrical and Electronic Engineers, the National Science Foundation, the Office of Naval Research, and NBS.

Harold Berger and Melvin Linzer, NBS, served as Co-Chairpersons of the Symposium Organizing Committee and as editors of this publication. Members of the Symposium Organizing Committee were George Alers, Science Center, Rockwell International; Graham Curtis, NDT Centre, Harwell; Robert E. Green, Jr., Johns Hopkins University; P. Höller, Institute für zerstorungsfreie Prufverfahren; Lawrence W. Kessler, Sonoscan, Inc.; Gordon S, Kino, Stanford University; Steven Serabian, University of Lowell; and H. Wüstenberg, Bundesanstalt für Materialprufung. Alers, Green, and Serabian served a liason function with the Sonics Committee of the ASNT Technical Council; and Richard S. Williams, Chairperson of the Sonics Committee, provided further information within ASNT.

All of the papers included in this volume were presented either in formal or poster sessions at the Symposium.

Acknowledgement is given to R. B. Johnson and his conference staff at NBS. The many colleagues who acted as reviewers for the technical papers in this volume are also acknowledged.

XII. LASER GENERATION AND DETECTION

INTRODUCTION

Nondestructive testing has traditionally involved a search for flaws in materials or structures; it has long been appreciated that cracks, voids, inclusions, and similar flaws can lead to failure. Obviously, once a flaw has been detected, it is natural to consider methods that will give more information. What is the size, type, location, or orientation of the flaw? This information is necessary if a realistic assessment of the influence of the flaw on performance is to be made. In addition, it is now more widely recognized that parameters such as hardness, grain size, bonding, and residual stress can also have a strong influence on material performance. The use of ultrasonic nondestructive testing to characterize a material in terms of both the properties and flaws which influence its performance is the subject of this volume.

The Symposium at which these papers were presented was the first to emphasize nondestructive characterization of materials by ultrasonic methods. The emphasis was placed on ultrasonic techniques because of their broad potential as characterization tools. The Symposium overlapped one day with the Third International Symposium on Ultrasonic Imaging and Tissue Characterization and thus provided a unique opportunity for researchers concerned with both medical and materials applications of ultrasonic characterization methods. There was effective interchange between these two groups of specialists.

The topics emphasized here are advanced techniques for ultrasonic characterization as well as ultrasonic measurements of material and defect parameters. In addition, closely related topics such as signal analysis, laser generation and detection, ultrasonic scattering, and calibration approaches are included.

It is the hope of the Symposium Organizing Committee that this record, outlining the current state-of-the-art of ultrasonic materials and defect characterization, will inspire new concepts to advance this important field.

Harold Berger and Melvin Linzer
Co-Editors and Symposium Chairpersons
National Bureau of Standards
Washington, DC

National Bureau of Standards Special Publication 596, Ultrasonic Materials Characterization, H. Berger and M. Linzer, eds., Proceedings of the First International Symposium on Ultrasonic Materials Characterization held at NBS, Gaithersburg, Md., June 7-9, 1978. Issued November, 1980.

DECTECTION AND ANALYSIS OF NEAR SURFACE-CRACKS BY ULTRASOUND

H. Wüstenberg, A. Erhard, and J. Kutzner

Bundesanstalt für Materialprüfung (BAM)
Unter den Eichen 87
D-1000 Berlin 45
W. Germany

The detection of near surface-cracks has been improved during the last few years by the use of transmitter receiver probes with inclined longitudinal waves and recently by the use of longitudinal creeping waves or shear horizontal waves. Another possibility for improved detection, especially on cladded surfaces, consists in the application of the well-known corner effect with shear and longitudinal waves and focusing probes. Examples of the application of creeping waves and focusing probes for crack detection are given. The influence of the probe parameters such as frequency, crystal size, and wedge angle for the creeping wave probe is mentioned; theoretical and experimental results for those influences are given. Focusing probes, acoustical holography and a scatter technique has been investigated for the analysis of detected cracks. The effectiveness and limitations of these techniques are discussed.

1. Introduction

The nondestructive inspection of surfaces, especially for cracks, can be done with a lot of well-established methods: for instance, magnetic particle testing, penetrant testing, eddy currents, and others. Among those methods, the ultrasonic technique, as a more or less volumetric inspection method, is not the method of choice. But in an increasing number of cases, especially in the nuclear industry, we are forced to use the ultrasonic technique due to its independence from electric and magnetic properties of the material and due to the possibility for automated use of this technique for automatic in-service inspections. In order to reach the performance of other competing methods, a number of typical limitations of the ultrasonic methods must be eliminated.

In figure 1 some of the physical, technical, and practical influences which must be regarded for ultrasonic methods are listed. As usual for all ultrasonic methods, especially for surface inspection techniques, we must differentiate between the detection of cracks and the analysis, e.g., concerning the depth extension. For detection, bulk waves and surface guided waves can be used. Bulk waves deliver very significant crack indications if the corner effect can be used, but a cracktip indication, due to a diffraction at the tip, can also be applied [1-3][1].

Surface guided waves often suffer from a low signal to noise ratio due to interfering indications from surface roughness, drop of liquids, drop of welding material, etc. This is especially true in the case for Rayleigh waves which only can be used under clinically clean conditions. Other guided waves such as shear horizontal waves or creeping longitudinal waves [4] only excite tangential movements at the surface and are therefore more independent of surface roughness and other sources of spurious indications.

Whereas the detection of cracks with the above mentioned ultrasonic techniques is in many cases possible with a useful signal-to-noise (S/N) ratio, it is often difficult to estimate the crack depth. For small cracks the use of differences in the delay path from surface guided waves and also from waves diffracted at the crack tip seems to be a possible method [2,5,6,11]. For crack depths greater than ~6 mm, the shadowing by the defect can

[1] Figures in brackets indicate the literature references at the end of this paper.

be used [7]. The potential of imaging techniques, like holography or the use of focused sou fields, will also be discussed. Special techniques for detection and for analysis include t use of focused sound fields and the use of transmitter receiver probes for inclined longi- tudinal waves [8], the use of the frequency spectrum [5], and acoustical holography.

	Detection	Analysis (e.g. crack depth)
Physical phenomenon	Bulkwaves (corner effect, crack tip diffraction)	Spectrum or delaytime Crack tip diffraction
	Guided waves (Rayleigh, creeping L-waves, S.H.)	Shadowing by cracks Imaging
Special Techniques	Focussed sound fields TR - probes	Frequency Analysis Holography Focussed fields
Practical limitations	Surface conditions Waviness, Roughness, Cladding, Access Coarse grained materials Geometry	

Figure 1. Near surface inspection by ultrasound.

The most common difficulties which reduce the S/N ratio for the detection of near surface cracks are the surface roughness and waviness and, especially in the nuclear field, the presence of a cladding. This contribution summarizes some results for those detection and analysis techniques from figure 1, on which some of the activities of our laboratory ar focused.

2. Detection Methods

2.1. Cladded surfaces

The use of bulk waves for the detection of cracks in a cladded area is limited by the structural noise from the interface and from the dentritic coarse grains of the austenitic cladding. In figure 2 we have compared several techniques for the detection of a 2 mm notc starting at the cladding surface. The echo-dynamic patterns from a probe movement parallel to the notch as well as the S/N ratio are compared for five techniques.

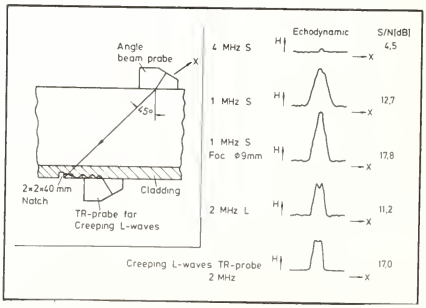

Figure 2. Surface crack detection influenced by a cladding.

It can be shown, that for coarse-grained materials, longitudinal waves will give in nearly all cases a remarkedly improved S/N ratio, if compared with shear waves of the same

wavelength [15]. However, using the corner effect, we must take into account mode conversion losses for the longitudinal waves; therefore, in our case, longitudinal waves do not deliver an improved S/N ratio. If bulk waves must be used, it seems that focused shear waves with a frequency as low as possible, e.g., 1 MHz, are a good choice. If the surface can be inspected from the cladding itself, transmitter receiver probes for inclined longitudinal waves have been proven as the most reliable alternative for inspection of the cladding volume, including the interface [8,9]. Signal-to-noise ratios in the range of 30 dB are obtained for a 2 mm diameter side-drilled hole. The transmitter receiver probe applied in figure 2 has been optimized for the generation of creeping longitudinal waves in order to increase the inspected area near the surface [4]. In this case the probe must be well designed to propagate longitudinal waves along the cladding surface.

2.2. Creeping longitudinal waves

If we excite longitudinal waves with an angle beam probe calculated for 90°, longitudinal waves propagate along the surface accompanied by a shear wave which is radiated from the surface under an angle in the range of 30° (fig. 3) [4]. At the surface, the longitudinal wave can only exist together with this radiated shear wave. Both form together a well-known head wave, which has been shown in Schlieren photos from ultrasonic waves propagating in glass blocks [10]. We have recorded the head waves also by electrodynamic pick-ups on a semicylindrical steel test block.

Figure 3 shows directivity patterns in the near and in the far field regions of a creeping wave probe measured with electrodynamic pick-ups. Even in the near field, the most important part of the energy is concentrated at an angle less than 76°, but a sufficiently large amount of energy remains at the surface for the creeping wave. In the far field, the creeping wave is nearly completely extinguished. This can be explained by the distance law in the right side of figure 3, which indicates that an echo indication produced by creeping waves decreases as $1/x^4$. This distance law can be calculated (as Lamb [12] has done) and is in good agreement with measurements. The very sharp decay with the distance requires the use of transmitter-receiver probes for the detection of surface cracks by creeping waves and limits the application to short distances between the probe and crack.

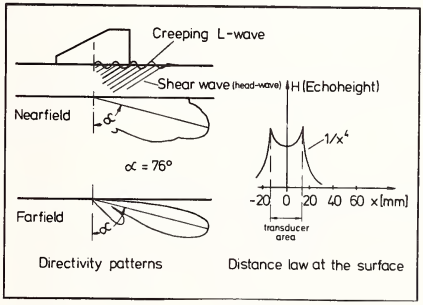

Figure 3. Directivity pattern and distance law for creeping-wave-probes.

In order to optimize probe construction, it is necessary to choose the right wedge angle and a membrane size as large as possible. In figure 4, we have traced the amplitude of the creeping wave depending on the wedge angle for two membrane sizes. For a large size, the radiated energy is more strongly concentrated in the creeping waves than for smaller sizes. The wedge angle for each transducer size should be the angle for the total reflection of the longitudinal wave.

Figure 5 shows the detection of artificial surface cracks of 1.5 mm and 2.5 mm depth with different inclinations. For the 1.5 mm crack, a S/N ratio in the range of 26 dB can be obtained. With 4 MHz, even 0.5 mm deep cracks have been detected with a 20 dB S/N ratio.

Another interesting application of creeping wave probes is shown in figure 6, where a filled weld is inspected in an area difficult to test with shear wave probes. The application of shear waves produces unclear indications whereas longitudinal waves excited by the creeping wave give significant indications for cracks.

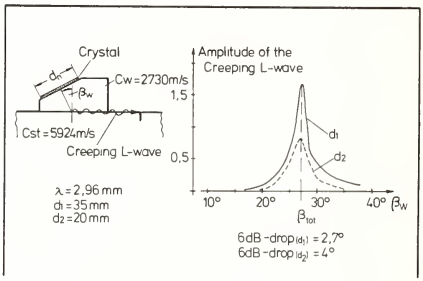

Figure 4. Influence of wedge angle and transducer size of the creeping wave amplitude.

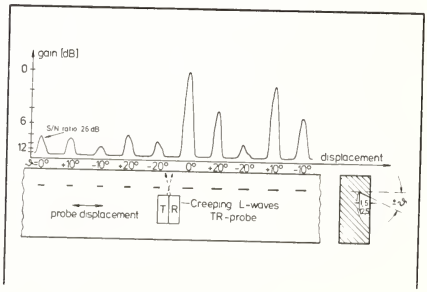

Figure 5. Echodynamic of inclined surface defects.

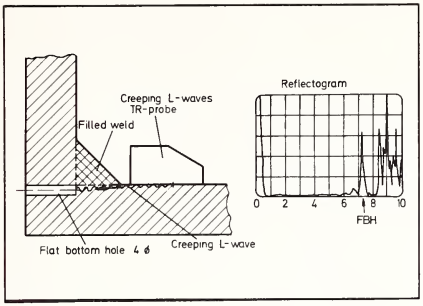

Figure 6. Creeping waves for the inspection of a filled weld.

2.3. Shear horizontal waves

Horizontally polarized shear waves propagating parallel to a surface also have only a tangential movement and allow a useful S/N ratio even at unsuitable surface conditions. But the excitation of shear horizontal waves up to now has been limited to electromagnetic probes with a suitable coil configuration. It seems basically possible to excite horizontal waves with a liquid coupling using a comb structure and intermediate creeping waves. But the energy transfer from creeping L-waves to SH-waves is rather poor. For practical applications, adequate electrodynamic probes are the only alternative.

3. Analysis of Detected Cracks

In our laboratories we have used three different techniques for the measurement of crack depths. These three techniques are linear acoustic: linear acoustic holography, focused sound fields, and shadowing of cracks by using forward scattering of longitudinal waves.

According to figure 7, for linear acoustic holography [13,14] along an aperture L, the real and imaginary part of an echo indication from a defect area is scanned. Based on the formula on figure 7 bottom, which corresponds to a Fresnel-approximation of a diffraction integral, distributions on circles around the middle point of aperture in the depth of the defect area can be reconstructed, as demonstrated in figure 7.

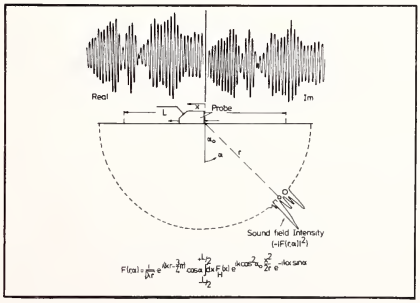

Figure 7. Numerical reconstructed holography.

Figure 8 shows the holographic scan of a crack with about 2.5 mm depth. Because of the corner effect, a single probe holography technique will record not only the defect itself, but also a mirror image of it. This is considered during the evaluation of the intensity distribution in figure 8. Furthermore, it should be considered, that each holographic reconstruction assumes a simple diffraction of waves at the object without mode conversion. If a very complicated conversion of the incoming wave into other modes must be considered (the corner effect is a typical example for such conversions), unreliable interpretations of reconstructed holograms are to be expected.

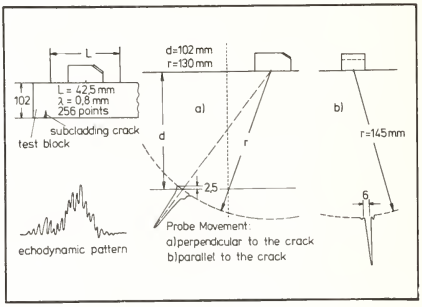

Figure 8. Holographic defect reconstruction of a small crack.

In figure 9 and 10 two different holographic techniques and the use of focused sound fields for analyzing crack depths are described and compared. The shadow technique in holography and the tandem technique for focusing probes seem to have good potential to eliminate some of the above mentioned difficulties.

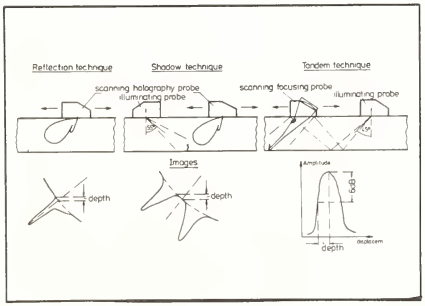

Figure 9. Crack sizing with imaging methods.

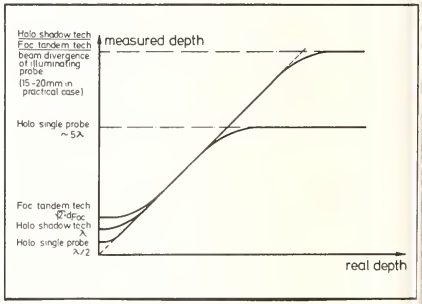

Figure 10. Accuracy of imaging techniques.

For scanning with the holographic probe or with the focusing probe, a fixed illuminating probe is used. Shadow techniques can also be applied with focusing probes. The images produced by such scanning procedures are presented on the bottom in figure 9.

The performance of the proposed arrangements for crack depth determination has been tested on notches with different depths, for cracks more of less perpendicular to the surface

Figure 10 shows some results. The measured depth is plotted as a function of the real depth. For small depths, the resolution power of the applied imaging technique represents a lower limit for the usable range. The upper limitation depends on the mode conversion for single probe holography and on the divergence of the illuminating sound field for the other two methods.

Single probe holography is limited to a range of 4 to 5 times the wavelength. Tandem-techniques (holography or focusing probes) or shadow techniques should use more divergent beams for deeper cracks. Only for the shadow techniques can we assume that figure 10 also applies to cracks with different orientations. This is also the case for the technique shown in figure 11.

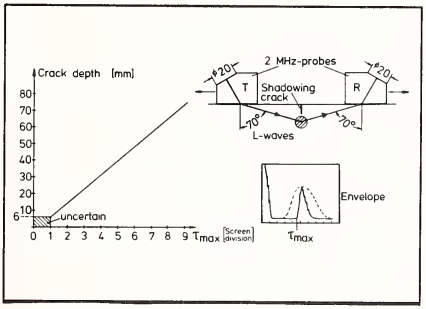

Figure 11. Crack size estimation by scattered waves.

The last figure (fig. 11), shows the forward scatter technique using the shadowing of cracks [7]. Usually we apply 70° - 72° longitudinal wave angle-probes in an arrangement shown on the right hand side in figure 11. A sharp indication from the cross-over of the transmitting and receiving beam can be obtained if no crack is shadowing this path. In the presence of a crack we must enlarge the distance between both probes and will obtain a maximum indication if the cross-over point is situated deeper than the crack tip. On the left-hand side in figure 11, the usable range of this technique is traced. For crack depths greater than 6 mm, we can expect an accuracy in the range of 1 mm.

4. Conclusions

The use of ultrasound to detect and to analyze cracks is possible with the same or even better performance than we normally expect for penetrant, magnetic particle or eddy current inspection. The analysis of detected indications can be accomplished by several techniques which must be chosen according to the expected crack depths and the required accuracy.

References

[1] Dijkstra, F. H., Flaw evaluation with particular reference to flaw size estimation, Report, Research and Development Dept., R.T.D., Rotterdam, Holland.

[2] Silk, M. G. and Lidington, B. H., Defect sizing using an ultrasonic time delay approach, British J. NDT, 17, 33-36 (1975).

[3] Wüstenberg, H., Kutzner, J., Schulz, E., and Erhard, A., Ultraschallanzeigen von Riβkanten, Conference and Exhibition on Nondestructive Testing by DGZfP, Mainz/Federal Republic of Germany (April 24-26th, 1978).

[4] Erhard, A., Wüstenberg, H., and Mundry, E., 90°-Longitudinal-wellen-Winkelprüfkopf zum Nachweis oberflächennaher Risse, Conference and Exhibition on Nondestructive Testing by DGZfP, Mainz/Federal Republic of Germany (April 24-26th, 1978).

[5] Morgan, L. L., The spectroscopic determination of surface topography using acoustic surface waves, Acustica, 30, 222-228 (1974).

[6] Flambard, C., Lambert, A., and Bouilly, G., Mesure nondestructive de l'étendue en profondeur des fissures débouchantes, Eighth World Conference on NDT, Cannes, France (Sept. 6-11, 1976).

[7] Böttcher, B., Schulz, E., and Wüstenberg, H., A new method for crack-depth determination in ultrasonic-materials-testing, Seventh International Conference on NDT, Warsaw, Poland, (June 4-8, 1973).

[8] Wüstenberg, H. and Schulz, E., Versuche zur Feststellung plattierungsnaher Reflexionsstellen an Reaktorteilen mit Ultraschall, Vortrag auf der Tagung, Zerstörungsfreie Materialprüfung der DGZfP, Saarbrücken, W. Germany (May 9-10, 1972).

[9] Wüstenberg, H., Kutzner, J., Mundry, E., Nabel, E., and Neumann, E., In-service inspection of nuclear power plant components. An opportunity to perfect ultrasonic nondestructive test methods, in Reliability of Nuclear Power Plants, pp. 603-614 IAEA-SM195/25 (International Atomic Energy Agency, Vienna, Austria, 1975).

[10] Slater, E. A., Baborovsky, V. M., and Marsh, D. M., Report 369A, TJ Research Laboratories Hinxton Hall, Hinxton, Saffron Walden Essex, U.K. (Oct. 3, 1974).

[11] Hall, K. G., Crack depth measurement in rail steel by Rayleigh waves aided by photoelastic visualisation, Non-destructive Testing, 121-126 (June, 1976).

[12] Lamb, H., On the propagation of tremors over the surface of an elastic solid, Philosophical Transactions, 203-A, 349 1-42 (1904).

[13] Kutzner, J. and Wüstenberg, H., Akustische Linienholographie, ein Hilfsmittel zur Fehleranzeigeninterpretation in der Ultraschallprüfung, Materialprüfung, 18, 189-194 (1976).

[14] Kutzner, J., Wüstenberg, H., and Mundry, E., Experience with flaw size estimation by ultrasonic holography with numerical reconstruction, Proceedings of the International Conference Nondestructive Evaluation in the Nuclear Industry, Salt Lake City, UT, U.S.A. (February 13-15, 1978)

[15] Wüstenberg, H., Just, T., Möhrle, W., and Kutzner, J., Zur Bedeutung fokussierender Prüfköpfe für die Ultraschallprüfung von Schweißnähten mit austenitischem Gefüge, Materialprüfung, 19, 246-251 (1977).

National Bureau of Standards Special Publication 596, Ultrasonic Materials Characterization, H. Berger and M. Linzer, eds., Proceedings of the First International Symposium on Ultrasonic Materials Characterization held at NBS, Gaithersburg, Md., June 7-9, 1978. Issued November, 1980.

DETERMINATION OF ORIENTATION AND SIZE OF BADLY ORIENTED DEFECTS BY MEANS OF FOCUSED PROBES

D. De Vadder and P. Azou

Ecole Centrale des Arts et Manufactures
Grande Voie des Vignes
92290 Chatenay-Malabry
FRANCE

and

R. Saglio

Commissariat à l'Energie Atomique
C.E.A. Centre d'Etudes Nucléaires de Saclay
Boîte Postale n°12
91190 Gif sur Yvette
FRANCE

The study of the diffraction of an ultrasonic wave by the edge of a defect, called the border effect, is still ongoing. Defect sizing by means of the border effect is considered. We show how the use of focused probes enables us to calculate both the size and orientation of quasi-plane defects. Experiments with flat bottomed holes have shown that we can characterize a defect, the size of which is equivalent to the 6 dB diameter of the focused beam.

1. Introduction

Since the publication of the first results of our research on the border effect [1][1], apers have been presented on the phenomenon and to apply it to defect sizing [2,3].

In this paper, we review those publications and our current research in order to point ut the gaps that still remain in the study of this phenomenon. We present the results of ur experiments of defect sizing using the border effect and explain why, in practice, best esults can be obtained when using focused probes.

2. The Border Effect: Description of the Phenomenon

The border effect may be defined as describing an echo coming from the edge of a de- ect, whose intensity is not explained by reflection laws (fig. 1). The reflector is ikened to a half-plane, its position in the ultrasonic field being characterized by angles and α, and distance e (fig. 2).

3. Study of the Parameters

In the case of longitudinal waves, we studied both theoretically and practically, the ariation of the echo as a function of e, θ, and α. Echoes are always referenced to the aximum echo coming back from an infinite plane reflector, perpendicular to the beam axis.

3.1. The e parameter

The distance parameter e has been studied using narrow ultrasonic beams. The maximum f the superintensity (border effect echo) occurs when e is zero, i.e., when the axis of the eam cut exactly the edge of the defect. When e is large, the whole pencil is intercepted

[1] Figures in brackets indicate the literature references at the end of this paper.

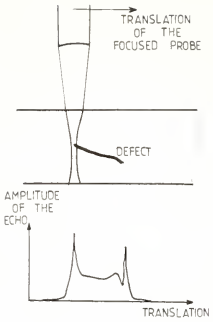

Figure 1. Variation of the amplitude of the echo, when obtaining the border effect.

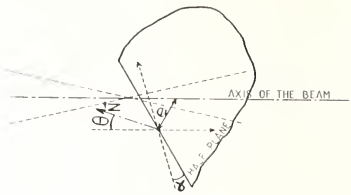

Figure 2. Position of the half-plane in the ultrasonic field.

by the defect and the decrease of the echo can be explained by an accurate diffraction calculation as well as by a simple calculation based on reflection laws [4]. For a 6 dB decrease of the echo, θ is given by[2]:

$$\tan \theta_{6\ dB} = \frac{1}{4} \frac{D}{F} \quad .$$

3.2. Superintensity: θ angle dependence

The amplitude of the superintensity is approximately dependent on the number N (fig. 3), where

$$N \cong \frac{F}{D} \tan \theta \quad .$$

This leads us to choose large transducers, and particularly focused ones in order to work in the nearfield.

3.3. Superintensity: α angle dependence

The echo decrease versus α is very rapid and the α angle for a 6 dB decrease is given by:

$$\tan \alpha_{6\ dB} = \frac{1}{4} \frac{D}{F} \quad .$$

Thus, both calculation and experiment lead to the choice of large focused probes. We can convey the above results in terms of ϕ (ϕ is the 6 dB diameter of the pencil) given by:

$$\phi = \lambda \frac{F}{D} \quad .$$

So

$$N = \frac{\phi}{\lambda} \tan \theta \quad ,$$

and

$$\tan \theta_{6\ dB} = \frac{\lambda}{\phi} \quad .$$

[2]When θ and α are real defect orientations, F, usually defined in water, is to be converted to its metal equivalent.

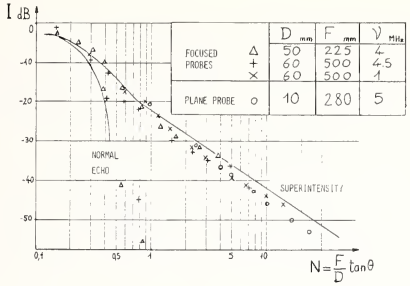

Figure 3. Decrease of normal echo and superintensity as a function of N.

The results presented by Wüstenberg and Kutzner [2] (whose text is not yet published as this is written) take into account longitudinal, shear, and surface waves created from incident longitudinal waves. It is shown that generally the border effect is more intense than explained above, but for some angles the superintensity can decrease strongly, and increase for larger θ. It is not clear that those calculations, made for a quasi-infinite field, are valid for a narrow field. Fortunately, it is possible to make focused pencils whose 6 dB diameter is as small as a few λ.

The phase of the echo signal changes rapidly as the beam propagates over the surface of an inclined flaw, but remains stationary when the pencil goes through the edge of the defect, where the superintensity occurs. This is in agreement with the theories of Young and Sommerfeld. They split the wave reflected by a half-plane into a plane wave according to reflection laws, and a cylindrical wave diffracted by the border.

Although still incomplete, our calculations have shown that, in order to get the most intense echo from the border effect, narrow ultrasonic beams from focused probes are necessary. Some other considerations lead us to the same choice.

3.4. Proportion of the ultrasonic pencil which is really useful

We have shown that, for the border effect, everything happens as if only a narrow part of the defect, along its edge, was actually reflecting. The more concentrated the energy of the ultrasonic field is, the larger the proportion of the total energy used for the border effect will be. Therefore, the echo will be more intense.

3.5. Similarity between the real and model defects

The real defect can be different from the model in two ways. Its periphery may not be a straight line. Its surface may not be a plane.

3.6. Curvature of the periphery

We have considered disk-like defects. Calculations of the diffraction of the wave by the defect have been made, while experiments have been performed; first in immersion with the extremities of cylinders, then with flat bottomed holes, as shown in figure 4.

The experiments have shown the appearance of the diffraction echo from one edge, then the other, for targets whose diameter was as small as the 6 dB diameter of the focal zone. Those results are better predicted by theory.

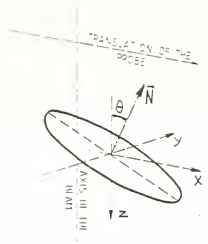

Figure 4. Translation of the probe over disk-like defect.

3.7. Inherent flatness of the plane surface

The irregularity of the surface must be compared to wavelength. It is the acoustic distance difference between possible ray paths that is important. It is usually assumed that the surface can be considered as plane if the maximum roughness does not exceed $\lambda/4$. Therefore, lowering the frequency is attractive, but by so doing, the divergence of the probe is increased. Using a focused probe, we can minimize this objection, because by using a strongly convergent lens, we can retain a narrow pencil while increasing the wave length.

4. Application to Determination of Dimensions and Orientation of Quasi-Plane Defects

Proegler [3] suggested the use of the border effect to determine the size of defects by measuring the difference of the round-trip transit time from the probe to one edge and to the other. This method, using a classical broadband transducer, makes the two characteristic echoes appear at the same time on the scope. As it has already been shown in Nabel and Neumann's work [5], and even in Otani and Jessel's [6] (and without mentioning the border effect at that time), the two edges of an inclined flaw send back similar echoes, but with opposite polarity. This permits the discrimination between two edges of the same defect or two isolated small defects. In this last case, the two echoes would not be different in polarity.

Except for this important discrimination, that method gives no more indication than methods using ultrasonic spectroscopy. The extent in depth of the defect is determined, but to characterize its size and orientation, at least two tests must be made, with two different orientations. This is not always possible or easy.

We propose using focused probes, to be able, by only one translation of the probe, to determine accurately the position along the three spatial directions of each edge of the defect intersected by the axis of the probe. The maximum superintensity occurs exactly when the axis of the probe intersects the edge. Even for small defects, only one border echo appears at the same time on the scope.

If d is the size of the defect to be determined and θ its orientation, the translation $\Delta\ell$ of the probe is

$$\Delta\ell = d \cdot \cos\theta \quad .$$

The difference in transit time Δt for the two occurrences of the border effect is:

$$\Delta t = 2\,\frac{d \cdot \sin\theta}{V} \quad .$$

The two measurements ($\Delta\ell$,Δt) permit one to calculate d and θ. That is very easy with the help of a pocket-size calculator, since d and θ are polar coordinates corresponding to V · $\Delta t/2$ and $\Delta\ell$ rectangular ones.

One advantage of this method is that there is no need for broad-band transducers, which have the disadvantage of poor efficiency. We obtain the two echoes of the two edges on two different oscillograms (figs. 8 and 10). This allows us to apply this method to bulky grain materials, for it is not necessary to send and receive an impulse containing high frequency components.

5. Results

Experiments carried out with the extremities of a cylinder and with flat bottomed holes have given results with surprising precision (figs. 5 to 10). Most valuable is to look for the smallest defect we are able to size with acceptable precision, and to compare this minimum defect size with the diameter of the focal zone. As can be seen from figures 8, 9 and 10, it has been possible to size disk-like defects the diameter of which are equivalent to the 6 dB diameter of the focal zone. Below this limit, precision decreases rapidly. For the largest defects, the precision is only dependent on the time-measuring instruments and mechanical rigidity of the equipment, used for probe translation and orientation.

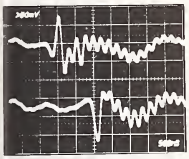

PROBE	F water mm	D mm	V MHz	Φ_{-6dB} mm	λ mm
	500	60	4.5	4.4	1.3

	d mm	θ °	$\Delta\ell$ mm	Δt µs	d mm	θ °
FLAT BOTTOMED HOLE	10	18	9.5 ± .2	1.1	9.8 10.0 10.1	19.1 18.8 18.5

Figure 5. Experimental results d > y.

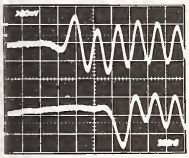

PROBE	F water mm	D mm	V MHz	Φ_{-6dB} mm	λ mm
	500	60	4.5	4.4	1.3

	d mm	θ °	$\Delta\ell$ mm	Δt µs	d mm	θ °
FLAT BOTTOMED HOLE	5	19	4.8 ± .2	.56	4.9 5.1 5.5	19.9 19.0 18.3

Figure 6. Experimental results d ∿ y.

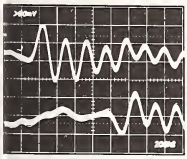

PROBE	F water mm	D mm	V MHz	Φ_{-6dB} mm	λ mm
	500	60	4.5	4.4	1.3

	d mm	θ °	$\Delta\ell$ mm	Δt µs	d mm	θ °
FLAT BOTTOMED HOLE	4	35	3.4 ± .2	.88	4.5 4.3 4.1	35.8 37.3 39.0

Figure 7. Experimental results d ∿ y.

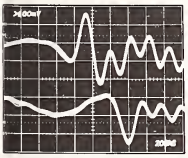

PROBE	F water mm	D mm	V MHz	Φ_{-6dB} mm	λ mm
	500	60	4.5	4.4	1.3

	d mm	θ °	$\Delta\ell$ mm	Δt µs	d mm	θ °
FLAT BOTTOMED HOLE	3	26	2.8 ± .4	.44	2.7 3.1 3.5	28.4 24.9 22.1

Figure 8. Experimental results d < y.

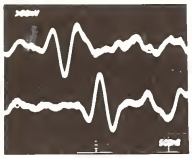

F	D	V	Φ_{-6dB}	λ
500	60	1	12,3	5,9

d	θ	Δl	Δt	d	θ
				9.3	18.2
10	18	9.5 ± 1.5	1	9.9	17.2
				10.6	16.4

Figure 9. Experimental results $d \sim \gamma$

F	D	V	Φ_{-6dB}	λ
2.5	50	1	1.7	1.5

d	θ	Δl	Δt	d	θ
				2.8	19.9
2	18	2.8 ± 1.2	3.2	2.9	18.0
				3.2	17.5

Figure 10. Experimental results $d \sim \gamma$

6. Conclusions

In the study of the border effect, many problems remain; these involve the whole study of the border effect for narrow pencils (taking into account longitudinal, shear, and surface waves), and the case of an incident shear wave. Nevertheless, we have shown that, for both theoretical and practical reasons, it is more probable to obtain the border effect when using focused probes. When echoes are diffracted from the edges of an inclined defect we are able to calculate its orientation and size quite simply and precisely.

This method seems to be particularly applicable to crack sizing and, therefore, to the survey of crack propagation, an important concern for in-service inspection.

References

[1] De Vadder, D., Azou, P., Bastien, P., and Saglio, R., Detection of plane, poorly oriented flaws using focused transducers, Eighth World Conference on Nondestructive Testing, paper 3H5, (Sept. 1976).

[2] Wüstenberg, H. and Kutzner, V., Ultrasound-indications of crack edges, European Conference on Nondestructive Testing, Mainz (W. Germany) (April 1978).

[3] Proegler, H., Ultrasonic delay measurement for the determination of the size of quasi-natural defect, European Conference on Nondestructive Testing, Mainz (W. Germany), (April 1978).

[4] Saglio, R., Better detection of large poorly oriented plane defects by ultrasonics, N.D.T. International, 9, (August 1976).

[5] Nabel, E., Neumann, E., Evaluation of flaw indications by ultrasonic pulse amplitude an phase spectroscopy, Eighth World Conference on Nondestructive Testing, paper 3H6, (Sept. 1976).

[6] Otani, Jessel, Directivité et réflectivité des ondes acoustiques pulsées, Journal de Physique, Colloque C6, supp. au N° 11-12, Tome 33, Nov., Déc. 1972, page 61.

National Bureau of Standards Special Publication 596, Ultrasonic Materials Characterization, H. Berger and M. Linzer, eds., Proceedings of the First International Symposium on Ultrasonic Materials Characterization held at NBS, Gaithersburg, Md., June 7-9, 1978. Issued November, 1980.

STRESS INTENSITY FACTOR MEASUREMENT OF SURFACE CRACKS[1]

M. T. Resch, B. T. Khuri-Yakub, G. S. Kino, and J. C. Shyne

Edward L. Ginzton Laboratory
Stanford University
Stanford, CA 94305

An acoustic technique for measuring the maximum stress intensity factor of a surface is described. Using glass samples, we have formed surface cracks, carried out the measurements with a surface acoustic wave probe, and predicted the fracture stress of the glass. For small enough cracks, the predicted fracture stress is less than 5 percent in error from the measured fracture stress.

1. Introduction

We describe in this paper an acoustic technique for a direct measurement of the maximum stress intensity factor of a surface crack. The results obtained predict very accurately the breaking strength of glass samples in which surface cracks had been formed.

In order to understand the principles of the measurement, consider first a sample with a flat elliptical shaped crack present in the interior. When a far field stress is applied with a component σ_{zz} normal to the face of the crack, the local stress σ in the plane of the crack will be of the form

$$\sigma = \frac{K_I(s)}{\sqrt{2\pi r}} = \frac{k_I(s)\sigma_{zz}}{\sqrt{2\pi r}} \quad , \tag{1}$$

where r is the distance along the normal from the crack edge and $K_I(s)$ is the stress intensity factor at a distance s along the crack edge. The crack will grow and hence a brittle sample will break at the point where the maximum value of $K_I(s)$ exceeds the fracture toughness K_{Ic} of the material.

It was shown by Budiansky and Rice [1][2] that by carrying out three measurements of the reflection coefficient of an acoustic wave with a wavelength much larger than the dimensions of the crack, the maximum value of the normalized stress intensity factor (SIF), $k_I(s)$ defined in eq. (1), could be determined. They showed that the measured normalized maximum SIF should vary by less than 10 percent for an elliptic crack where the ratio of major axis varies from 20 to 1 for cracks of the same area.

Our aim has been to check this theory experimentally. For this purpose we decided to work with surface cracks of a roughly semielliptical shape, for they are easier to produce. We assumed that the same type of theory would hold for surface cracks as for cracks in the bulk. We decided to carry out the experiments with a brittle material, glass, so that the critical maximum SIF could be checked by a simple fracture test. Finally, we modified the

[1]This work was supported by the NSF Materials Research Laboratory Program through the Center for Materials Research at Stanford University.
[2]Figures in brackets indicate the literature references at the end of this paper.

theory to make it appropriate for use with acoustic surface waves, and to simplify the experimental measurement technique as much as possible. This was done by supposing that the crack location and alignment could be found by a high frequency measurement or, in our case, by locating it by eye. Then, we showed a single measurement of the reflection coefficient of a surface acoustic wave incident normal to the surface of the crack is needed to evaluate the maximum value of the normalized SIF.

2. Theory of the Acoustic Measurement Technique

The reflection coefficients of a surface acoustic wave is given by the relation [2]

$$S_{11} = \frac{i\omega}{4} \int_{S_{crack}} \sigma_{zz} \Delta U_z \, dS \tag{2}$$

for the crack configuration in figure 1, where S_c is the crack area, σ_{zz} is the stress at $y = 0$ associated with an incident surface wave of unit power, and ΔU_z and σ_{zz} are identical to that for an applied static stress. The depth of the crack is much smaller than a wavelength. In this case σ_{zz} can be assumed to be uniform over the crack surface, and can be taken outside the integral. The stress σ_{zz} for unit incident power is [3]

$$(\sigma_{zz})^2 = \frac{16w}{\lambda_R Z} \frac{V_s^2}{V_R^2} \left[1 - \left(\frac{V_s}{V_\ell} \right)^2 \right]^2 \omega f_z \tag{3}$$

where w is the acoustic beam width, λ_R is the Rayleigh wavelength, V_R is the surface velocity, Z is the distance to the crack, V_s is the shear wave velocity, V_ℓ is the longitudinal wave velocity, ω is the radian frequency, ρ is the density, and f_z is a constant of value between 0 and 1 calculated by Auld [4] as a function of Poisson's ratio σ. The displacement jump integral is given by the relation [1,2].

$$\int \Delta U_z \, dS = \frac{1 - \sigma^2}{3E^2} \sigma_{zz} \frac{\pi^3}{8} k_{Imax}^6 \tag{4}$$

where E is the modulus of elasticity. By combining eqs. (2), (3) and (4) we obtain an expression for k_{Imax}:

$$K_{Imax} = \left[\frac{3}{2\pi^5} \frac{V_E^2}{V_s^2} \frac{\lambda_R^3 Z}{\omega f_z} \frac{|S_{11}|}{\left[1 - \left(\frac{V_s}{V_\ell} \right)^2 \right]^2} \right]^{1/6} \tag{5}$$

where V_E is the extensional wave velocity. We note that k_{Imax} is proportional to $|S_{11}|^{1/6}$. This is because k_I is proportional to the square root of the crack size while $|S_{11}|$ is proportional to the cube root of the crack size. Hence, a large experimental error in measuring $|S_{11}|$ results in a much smaller error in k_{Imax}. A plot of the calculated k_{Imax} versus $|S_{11}|$ for pyrex glass is shown in figure 2.

3. Specimen Preparation

Pyrex discs 3 mm thick by 7.6 cm in diameter in the annealed condition were prepared for fracture toughness testing by introducing small, semielliptical surface cracks in the

enter of each disc. These pre-cracks were made in a controlled way by applying a bending oment of approximately 2 Newton-meters to the disc, and on the side in tension, pressing a noop microhardness indenter quickly into the specimen with a force of 50-100 grams. This echnique produces roughly half penny shaped cracks with radii between 100 and 500 μm epending on the combinations of bending moment and force on the Knoop indenter. uch small cracks were required to limit the crack size to less than the acoustic wavelength, 9 mm. Additionally, these half penny shaped cracks may be coaxed to an extended semiellip- ical shape by applying additional bending moment to the disc after the initial crack s started.

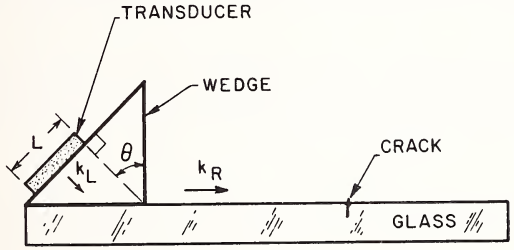

Figure 1. Schematic diagram of surface crack and test set-up.

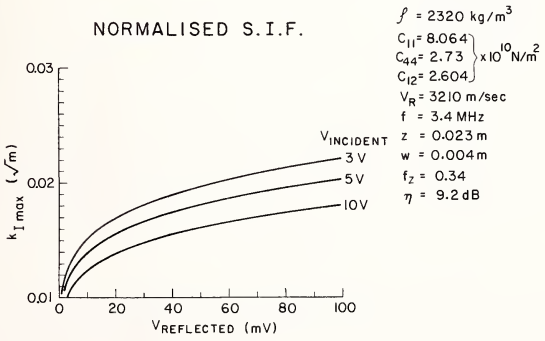

igure 2. Normalized SIF versus reflected voltage from the crack for different values of input voltage.

4. Fracture Toughness Testing

The strength of each disc in biaxial flexure was determined by the method of Wachtman, et al. [5]. This consists in supporting the specimen on three equally spaced balls concentric with the load, which is applied to the center of the specimen by a flat small diameter, flat end piston. The tensile stress in the disc is calculated from an equation derived by Kirstein and Woolley [6], and for our specimen geometry this equation reduces to:

$$S = c \frac{P}{d^2} \quad . \tag{6}$$

Here, P is the load required to fracture the disc, d is the thickness of the disc, and the constant c is a function of loading radius, specimen radius, piston radius, and Poisson's ratio ν for the material.

The discs were loaded to fracture at a loading rate of approximately 60 MPa per second using an MTS System 810 servohydraulic testing machine operated in stroke control mode. The loading rate was chosen to minimize possible slow crack growth effects [7]. To further insure against environmental influence (humidity), the specimens were pumped down in a vacuum for 1 hour prior to strength testing, and subjected to a stream of dry nitrogen gas for 3 minutes prior to, and during the flexure test.

Once the specimens were fractured, the geometry of the pre-cracks was studied by examining the fracture surface with a metallograph using reflected light and at a magnification of 50 - 100 X. The aspect ratio (a/c) of the semielliptical surface precracks could then be easily measured using an eyepiece with a properly graduated reticle. A typical crack is shown in figure 3.

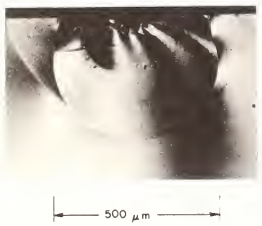

Figure 3. Picture of a typical crack visible on fracture surface.

The stress intensity factor for the pre-crack is evaluated by the method of Shaw and Kobayashi [8]. This analysis was chosen because it not only takes into account the proximity of the back surface to the precrack, but also allows for the presence of linearly varying stress field along the glass width. The expression for the maximum stress intensity is

$$K_I = \frac{M_B \sigma_B \sqrt{\pi a}}{E(k)} \quad , \tag{7}$$

where E(k) is an elliptic integral of the second kind, M_b is a magnification factor which takes into account the aspect ratio and the proximity of the crack depth to the neutral axis, σ_B is the maximum bending stress at the surface of the specimen, and a is the length of the semiminor axis (depth) of the pre-crack.

It should be noted that other forms for the evaluation of the stress intensity factor were tried, but eq. (2) yielded more consistent, and more conservative values of the fracture toughness, in good agreement with the results of Wiederhorn, on Pyrex glass fractured in a dry N_2 environment [9].

5. Fracture Toughness of Dry Pyrex Glass Determined in Biaxial Bend Tests

The ten samples tested gave a normally distributed set of fracture toughness measurement and the mean value of fracture toughness, K_{Ic}, at a confidence level of 90 percent is 0.76 ± 0.04 MPa $m^{1/2}$. This compares very well to Wiederhorn's experimental results of 0.75 ± 0.010 MPa $m^{1/2}$ for 6 pyrex specimens, 0.778 ± 0.011 MPa $m^{1/2}$ for 8 specimens [9].

6. Comparison of Acoustic and Mechanical Measurements

The experimental set-up for measuring the acoustic surface wave reflection coefficient $|S_{11}|$ is shown schematically in figure 1. A wide band, high efficiency wedge transducer [10], is used to excite and detect the surface acoustic waves. The transducer has a center frequency of 3.4 MHz, a bandwidth of 50 percent and a one way insertion loss of 9.2 dBs. Calibration of the transducers was carried out by measuring the transmission between a pair of transducers, as described in reference [10]. All measurements were taken in the far field of the transducer ($Z > w^2/\lambda_R$).

A set of acoustic measurements were taken with the front of the wedge a distance $Z = 2.3$ cm from the crack and with the acoustic surface wave normal to the crack surface. The measurements were taken in the bending jig, using a bending moment of approximately 2 Newton-meters to ensure the crack was open. A series of reflection measurements on 10 different cracks was made, and k_{Imax} calculated from eq. (5).

In figure 4 the acoustic prediction of σ_c is plotted against the mechanically measured value of σ_c for 10 specimens. A least squares regression of this data indicates a linear relationship between theoretical and experimental measurements with a slope of .85. We see that for larger, more irregular cracks, where the assumption of the theory that the diameter of the crack is less than 1/4 wavelength is not well satisfied, the error between theory and experiment increases. It is interesting to note that the effect of the ellipticity of some of the small surface pre-cracks appears not to affect the accuracy of the acoustic prediction of k_{Imax} to any appreciable degree. This confirms the predictions of Budiansky and Rice [1] that the effect, if any, should be less than 10 percent.

7. Conclusions

The acoustic wave reflection technique gives extremely accurate measurements of the maximum stress intensity factor of a surface crack, yielding a confident prediction of the fracture stress. The only restriction is that the wavelength of the acoustic wave should be approximately 10 times the depth of the pre-crack, and the acoustic wave must be incident in a direction approximately normal to the crack surface. Additionally, we have determined that the crack must be fully open, i.e., adjacent surfaces not touching, in order for an accurate acoustic measurement to be made of a surface pre-crack.

It is apparent that the original Budiansky-Rice [1] theory can be extended to deal with acoustic waves incident at an arbitrary angle to the crack, to deal with plane shear and antiplane shear stresses, by using the appropriate type of acoustic waves for probing the crack. It might also be expected that the method could be extended to measurements of fatigue cracks in metals.

The authors would like to thank A. G. Evans for suggesting the use of a Knoop hardness indenter to form the cracks and acknowledge the support of this work by NSF contract No. DMK-76-00726 through the Center of Materials Research at Stanford University.

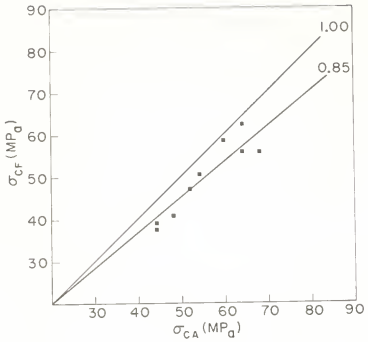

Figure 4. Actual fracture stress versus predicted fracture stress.

References

[1] Budiansky, B. and Rice, J. K., On the estimation of a crack fracture parameter by long wavelength scattering, preprint of a report for ARPA Materials Research Council (July 1977).

[2] Kino, G. S., The application of reciprocity theory to scattering of acoustic waves by flaws, J. Appl. Phys. (In press).

[3] Auld, B. A., General electrochemical reciprocity relations applied to the calculation of plastic wave scattering coefficients, submitted for publication to Wave Motion.

[4] Auld, B. A., Acoustic Fields and Waves in Solids, Vols. I and II (Wiley-Interscience, 1973).

[5] Wachtman, Jr., J. B., Capps, W., and Mandel J., Biaxial flexure tests of ceramic substrates, J. Matls., 7, 188-194 (1972).

[6] Kirstein, A. F. and Wooley, R. M., J. Res., National Bureau of Standards, JNBAA, 71C, 1-10 (1967).

[7] Evans, A. G. and Johnson, H., The fracture stress and its dependence on slow crack growth, J. Matls. Sci., 10, 214-222 (1975).

[8] Shah, R. C. and Kobayashi, A. S., On the surface flaw problem, The Surface Crack: Phys. Problems and Computational Solids, presented at Winter National Meeting of ASME, New York, N.Y., Nov. 26-30 (1972).

[9] Wiederhorn, S. M., Fracture surface energy of glass, J. Amer. Cer. Soc., 52, 99-105 (1969).

[10] Fraser, J. D., Khuri-Yakub, B. T., and Kino, G. S., The design of efficient broadband wedge transducers, Appl. Phys. Letters, 32, (1978).

National Bureau of Standards Special Publication 596, Ultrasonic Materials Characterization, H. Berger and M. Linzer, eds., Proceedings of the First International Symposium on Ultrasonic Materials Characterization held at NBS, Gaithersburg, Md., June 7-9, 1978. Issued November, 1980.

THE APPLICATION OF ADAPTIVE FILTERING TO DEFECT CHARACTERIZATION[1]

Y. Murakami, B. T. Khuri-Yakub, G. S. Kino,

Stanford University
Stanford, CA 94305

and

J. M. Richardson and A. G. Evans

Rockwell International
Science Center
Thousand Oaks, CA 91360

The inverse problem of defect characterization has typically been carried out by comparing backscattered or angular scattered power spectra to theoretical expectations in the frequency domain. Instead, we carry out such a comparison in the time domain where more insight can be gained as to the source and amplitude of the returning echoes. Working with defects in ceramics with pulse lengths of the order of 2 ns, the acoustic signals are digitized and fed into a computer. A Wiener filter is designed to match the transducer response, so the impulse response of the system approaches a delta function. The total bandwidth above the noise level of the transducer is being used instead of the 3 dB bandwidth, thus giving a great improvement in the depth resolution. We have carried out theoretical calculations on the response of defects in ceramics which indicate that different inclusions can be easily identified by this means. Experimental results on real defects are presented which demonstrate the power of such a technique for defect characterization.

1. Introduction

The problem of evaluating the type and size of a defect in a solid material by acoustic reflection techniques reduces to recognizing the "signature" of a flaw. Either pulse echo techniques can be employed, or scattering measurements as a function of frequency or angle can provide the required information.

In this paper, we describe pulse echo techniques and backscatter measurements as a function of frequency conducted on flaws in ceramics (Si_3N_4). The measurements are carried out in the 100 - 500 MHz frequency range, and the signals obtained are processed in a computer. We are concerned with comparing the reflected echo signals to theoretical calculations of scattering from flaws as a function of frequency. Alternatively, we are interested in the backscattered signal as a function of time due to an incident narrow acoustic base band pulse, which at least in theory has the form of a δ-function.

We describe in this paper how we have used adaptive filtering techniques to correct for the transducer response variation as a function of frequency and obtain very narrow pulses after processing. We correct not only for defects in the transducer characteristic itself, but also for distortion of the signals by the contacting system employed and by the attenuation in the sample varying with frequency. By this means we can use the corrected pulse to probe a flaw and the output signal obtained shows the true time domain response from the

[1]This work was supported by the Advanced Research Projects Agency through the United States Air Force, under Rockwell International subcontract RI 74-20773.

flaw, which can then be compared to theory. Experimental results obtained with real defects such as WC in Si_3N_4, and vacancies in Si_3N_4 are presented and used to predict the type and size of the defects.

2. Design of the Wiener Filter

The ultrasonic transducer used in our study is made by rf sputtering an 8 μm ZnO film on a sapphire buffer rod. The transducer has a center frequency of 300 MHz and is driven by 2 ns long electric pulse [1][2].

The received signal at the transducer is passed into a sampling oscilloscope which yields an output which is a slowed down version of the pulse. A Biomation analog-to-digital converter is used to sample the slowed down pulse and digitize it for insertion into a minicomputer. The computer is used to take fast Fourier transforms and correct the received signal.

The frequency response $S(\omega)$ of the transducer pulse is calculated by carrying out a 512 point Fast Fourier Transformation (FFT). The time and frequency response of our transducer a shown in figures 1(a) and 1(b), respectively. Ideally, we would like to correct the transducer response by constructing an inverse filter with a response $1/S(\omega)$. However, at frequencies where $S(\omega) \to 0$ the filter would not be realizable. Instead, we have designed a Wiener filter with a response

$$W(\omega) = \frac{S^*(\omega)}{S(\omega)S^*(\omega) + \Phi_N/\Phi_0} \quad , \tag{1}$$

where Φ_0, Φ_N are the power spectrum density of the signal and noise respectively, and Φ_N/Φ_0 corresponds to the signal-to-noise ratio. In the computation we set Φ_N/Φ_0 at an arbitrary but constant level, for simplicity.

From the formula (1), it is apparent that the total bandwidth above the arbitrary noise level of the transducer is being used instead of the 3 dB bandwidth; thus we can utilize the 10 dB or even 20 dB bandwidth of the transducer, and considerably improve the depth resolution by this technique. It will be noted that if $S(\omega)\, S^*(\omega) >> \Phi_N/\Phi_0$, $W(\omega) \to 1/S(\omega)$, i.e., the system behaves like an inverse filter. Whereas, when $S(\omega)\, S^*(\omega) << \Phi_N/\Phi_0$, $W(\omega) \to \Phi_0 S^*(\omega)/\Phi_N$ and the filter behaves like a correlation filter. This is the optimum choice for obtaining the maximum output peak pulse intensity in the presence of noise. The transfer function and the impulse response of the designed Wiener filter are shown in figure 1(c) and 1(d) respectively.

The output signal of the transducer pulse passed through this filter is calculated by multiplication in the frequency domain followed by the Inverse Fourier Transformation. As shown in figure 1(e) this output signal is uniform over a wide frequency range and is very close to a δ-function. Thus, we can effectively eliminate the defects in the transducer response, increase its effective bandwidth, and improve the impulse response and depth resolution by using a Wiener filter.

3. Defect Characterization by the Wiener Filter

In order to demonstrate this new technique, we have looked for defects in dense hot pressed silicon nitride and detected the backscattering from defects. The backscattered pulse from a defect is read into the digital computer using the same procedure already described. The frequency response of the signal is calculated by carrying out an FFT, and multiplied by the transfer function of the Wiener filter which has been designed previously Finally, by applying the Inverse Fourier Transformation, the output signal passing through the Wiener filter is obtained.

[2]Figures in brackets indicate the literature references at the end of this paper.

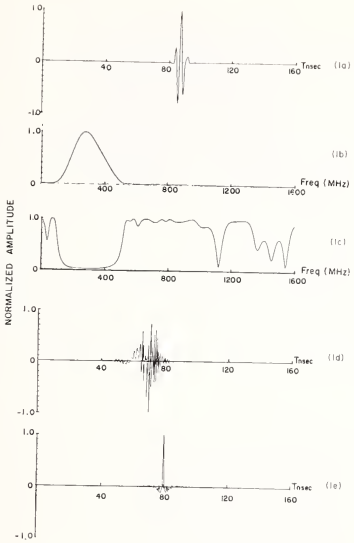

Figure 1. (a) Impulse response of ZnO/Al_2O_3 transducer, (b) frequency response of ZnO/Al_2O_3 transducer, (c) frequency response of Wiener filter, (d) impulse response of Wiener filter, and (e) Wiener filter output.

The time domain response from the defect is directly compared with the theoretical calculations, which enables us to decide whether the defect is a vacancy or an inclusion, and determine its size.

4. Experimental Results

The picture in figure 2 shows the reflected pulse from an unknown defect in a silicon nitride ceramic. The adaptive filter technique was applied to the reflected signal in order to evaluate this defect. The output signal passed through the filter is shown in figure 3(a) and 3(b), and its frequency and time domain response are compared with the theoretical response of typical inclusions shown in figures 3(c) and 3(d). It will be noted that the frequency responses of inclusions are very complicated. However, the time domain responses appear to be simpler in form.

First, a front surface specular reflection is observed. Later a weak signal is received from a vacancy due to waves passing around the spherical surface. On the other hand when an inclusion is present, a strong echo is usually observed from the back surface of the sphere which behaves as a spherical focusing lens. As seen from the normalized data in figure 3(d) this echo is usually not a simple pulse. However, in most materials, the first main pulse from the rear surface appears at a delay after the first pulse from the front surface, corresponding to the transit time through the sphere and back of a longitudinal wave in the medium of the inclusion.

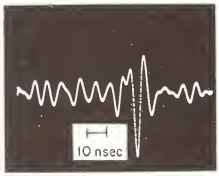

Figure 2. Backscattered signal from an unknown inclusion in Si_3N_4.

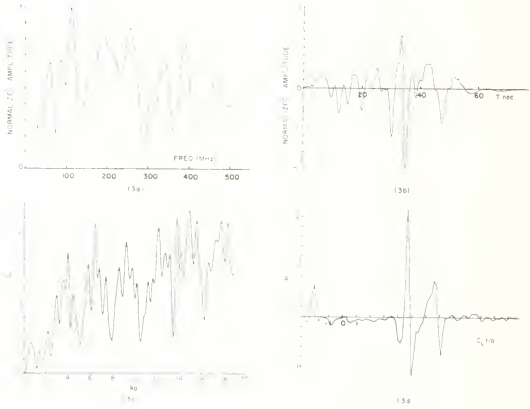

Figure 3. (a) Frequency response of defect in figure 2, (b) impulse response of defect in figure 2, (c) theoretical frequency response of a WC spherical inclusion in Si_3N_4, and (d) theoretical impulse response of a WC spherical inclusion in Si_3N_4.

Comparing figures 3(a), (b), (c), and (d), we concluded that the scattering from the unknown inclusion shown in figure 3(a) is equivalent to a WC sphere with a diameter of 90-130 μm. This result was obtained by measuring both the spacing of the nulls in the frequency domain, and the delay between the front and back surface echoes in the time domain.

The normalized amplitude of the front surface echo from a spherical surface can be sh to have the following dependence

$$S_{11} \propto \frac{a\Gamma}{Z^2} \quad ,$$

where a is the radius of the sphere, Γ is the reflection coefficient due to impedance mismatch, and Z is the distance from the transducer to the defect. By comparing the amplitude of the front surface echo to that of a hemispherical void drilled in the back of a piece of ceramic, we can make another estimate of the size of the bulk defects. In the case of the defect shown in figure 2, we calculate a diameter of 100 μm. This result is in agreement with the size estimate from the time and frequency domain analysis.

The silicon nitride sample has been lapped down to the defect. The defect was found out at exactly the same location where we predicted, and its size was measured to be 160 μm diameter compared to our estimated 90-130 μm diameter. However, the material within the defect has been analyzed by using x-ray spectroscopy, and turned out to be a two phase mixture of tungsten disilicide and silicon carbide. Interestingly enough in our experimental time domain results shown in figure 3(a) there are extra peaks in the response between the two main pulses expected in the theory; this appears to be associated with the two phase nature of the inclusion.

Figure 4(a) shows the reflected pulse from a void in a silicon nitride sample. By comparing to the theoretical scattering of figure 4(b), we see that only the specular reflection is observed. This we believe to be due to the fact that the inner surface of the void is rough, and a surface wave cannot propagate on it.

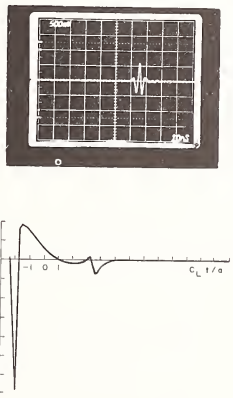

Figure 4. (a) Typical echo from a void in Si_3N_4, and (b) theoretical impulse response of a spherical void in Si_3N_4.

5. Conclusions

We note that our experimental measurement only gave a reasonable estimate of the size of the inclusion. But, there was some error because the material of the inclusion had a higher velocity than expected for tungsten carbide. Thus, we see that basically the technique determines the transit time of waves through the sample and the impedance mismatch at the sample. But other techniques such as low frequency angular scattering imaging measurements may be needed to supply one extra piece of information, the size or the density of the defect, to allow all its parameters to be evaluated accurately.

A major advantage of the present technique over x-ray methods is that it very easily determines if the inclusion is in contact with the surrounding medium. Other samples of tungsten carbide in silicon nitride showed up in microfocus x-ray measurements, but behaved like vacancies acoustically. When they were lapped down, the tungsten carbide was found to be supported from the surrounding medium only by a small fillet.

Finally, this high frequency technique appears to yield information on the uniformity of the inclusion. In one case where a two phase material was present, scattered signals from within the inclusion were clearly observed.

References

[1] Khuri-Yakub, B. T. and Kino, G. S., Acoustic pulse echo measurements at 200 MHz, Appl. Phys. Letters, 30, 78-80 (1977).

National Bureau of Standards Special Publication 596, Ultrasonic Materials Characterization, H. Berger and M. Linzer, eds., Proceedings of the First International Symposium on Ultrasonic Materials Characterization held at NBS, Gaithersburg, Md., June 7-9, 1978. Issued November, 1980.

SIZING OF CRACKS WITH SCATTERED ULTRASONIC WAVES

S. Golan

National Bureau of Standards
Washington, DC 20234

and

Israel Institute of Metals - Technion
Haifa, Israel

A method is described for calculating crack size from the time interval between the arrival of a surface compression reference beam and a beam scattered from the tip of the crack. The relationship between time delay and crack size has been established for various mode combinations of the transmitted and scattered beam. Optimum measuring conditions have been determined experimentally and cracks and slits between 5 and 17 mm long have been measured. Good agreement between direct and ultrasonic measurements has been found.

1. Introduction

With conventional ultrasonic techniques, flaw size is estimated by comparing its echo amplitude to the echo amplitudes of known reflectors, usually flat bottom or side-drilled holes. Unfortunately, the echo amplitude is strongly influenced by many factors other than size, such as flaw orientation, flaw topography, coupling efficiency, acoustic properties, and performance characteristic of the testing system. Consequently, a measurement of the comparative reflectivity is rather insensitive to flaw size. With all the limitations of this technique, it has been used by all standards for calibration of ultrasonic systems and for setting acceptability levels.

The limitation of this technique as a quantitative tool has provided the impetus for the development of techniques based on other phenomena of interaction between the acoustic field and the flaw. Two techniques based on scattering of beams from the periphery of flaws have been investigated; the spectrum analysis technique [1-4][1] and the time-delay technique [5-9].

The spectrum analysis method relates flaw size and orientation to the frequency spectrum formed by the interference of beam scattered from different points on the periphery of the flaw. This technique has not yet been developed into a practical field tool, as the relations between the spectrum and the complex characteristics of real flaws have not yet been adequately established.

The comparative reflectivity and the spectrum analysis methods are based on measurement of amplitudes, which are a function of many independent variables which are hard to control. Therefore, reproducibility of results is often very hard to obtain.

The time delay method is also based on the scattering phenomenum but instead of amplitude measurements this technique employs time delay measurements only; these can easily be measured with very high accuracy and are absolutely reproducible.

[1] Figures in brackets indicate the literature references at the end of this paper.

2. Crack Size - Time Delay Relationship

The time delay method is based on simple geometric relations between the depth of a point of scattering and the time delay caused by it. When an ultrasonic wave encounters a tip of a crack, beams of shear and compression modes are scattered in different directions (fig. 1). From the time interval between the arrival of a reference signal and a signal of a beam scattered from the tip of a crack, the depth of the tip can be computed.

Figure 2 shows the arrangement of the transducers and the triangle of diffraction formed by a transmitted, diffracted, and a surface compression beam. The signal from the surface beam is a very convenient reference point from which the time delay can be measured (fig. 3). A surface beam is propagated if

$$\alpha_c + \frac{\Theta}{2} \rightarrow \frac{\pi}{2} \tag{1}$$

where α_c is the Snell's angle of refraction and Θ the angle of divergence of the transmitted wave (fig. 4).

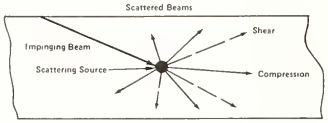

Figure 1. Scattering of ultrasonic beams from a small obstacle.

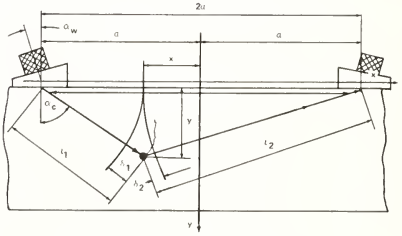

Figure 2. Triangle of diffraction.

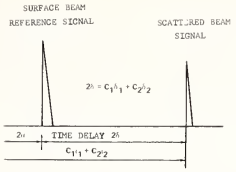

Figure 3. Screen pattern.

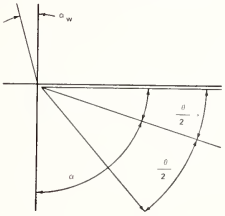

Figure 4. Condition for the formation of a surface beam.

This is achieved when α_w, the angle of the transducer wedge, is slightly smaller than the first critical angle which refracts into a surface compression beam. Using a plexiglas wedge, the critical wedge angle for steel is 27.6° and for aluminum 25.7°. By simple trigonometric calculations, the relationship between the depth of the flaw (y) and the time delay (δ) can be determined. Equation 2 shows this relationship in a normalized form for a constant distance (2a) between the transducers. (Capital letters denote nondimensional parameters.)

$$\left(C_2^2 - C_1^2\right) Y^2 + 4 \cos\alpha \left[C_1(\Delta+1) - C_2^2 (\sin\alpha)\right] Y - 4 \cos^2\alpha \left[(\Delta+1)^2 - C_2^2\right] = 0 \qquad (2)$$

α - Angle of Incident Beam

$C_1 C_2$ - Mode Coefficients

$C = 1$ - for a compression beam

$C = \frac{V_c}{V_s}$ - for a shear beam

V_s - Shear Wave Velocity

V_c - Compression Wave Velocity

$Y = \frac{y}{a}$ - Depth Of Source Of Diffraction; - Nondimensional

$W = \frac{w}{a}$ - Time Delay; - Nondimensional

Different combinations of the transmitted and diffracted beams can be used, e.g., the compression-compression (CC) combination, where the transmitted and diffracted beams are of the compression mode. Other possible combinations are the shear-compression (SC) combination or the (SS) combination. Rectangular (R), equalateral (E), and other diffraction triangles can be used.

For each arrangement a specific equation can be derived from the general equation. Some combinations and their equations are shown in figure 5.

CC-E $Y = \sqrt{(\lambda_{cc}+1)^2 - 1}$

CC-R $Y = (\lambda_{cc}+1) - \frac{1}{(\lambda_{cc}+1)}$

SS-E $Y = \frac{1}{C}\sqrt{(\lambda_{ss}+1)^2 - C^2}$

SS-R $Y = \frac{(\lambda_{ss}+1)}{C} - \frac{C}{(\lambda_{ss}+1)}$

SC $Y = \frac{2\cos\alpha}{C^2-1}\left[C(\lambda_{sc}+1) - \sin\alpha - \sqrt{\left[C(\lambda_{sc}+1) - \sin\alpha\right]^2 - (C^2-1)\left[(\lambda_{sc}+1)^2 - 1\right]}\right]$

SC-R $Y = \frac{2}{C^2-1}\left[C(\lambda_{sc}+1) - \sqrt{(C^2-1) + (\lambda_{sc}+1)^2}\right]$

Figure 5. Equations and schematical presentation of various arrays.

3. Optimum Testing Conditions

The intensity of a scattered beam is a function of angle and modes of the transmitted and diffracted beams. Usually the intensity of a diffracted beam is very low, but by choosing favorable angles and modes the intensity is sufficiently high to display a clear signal from which time delay can be measured and depth of flaw calculated.

To determine the favorable angle for the CC-E combination, amplitude measurements rsus relative position of the transducers were made on a specially designed goniometer. e goniometer is a disc with a radial slit cut to its center. Two series of measurements re made. In the first series, the angle β between the flaw and the transmitted beam s constant and the angle 2α between transmitted and diffracted beams varied. A second ries of measurements were made for a constant 2α and a variable β. Results are shown figures 6 and 7.

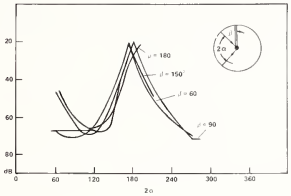

Figure 6. The amplitude of the diffracted signals as a function of 2α-the angle between the probes for a constant β-the angle between the slit and the incident beam.

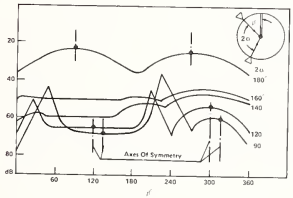

Figure 7. The amplitude of the diffracted signals as a function of β for constant 2α.

Two important conclusions can be drawn from the results:

1) The intensity approaches a maximum when 2α appraoches π;

2) For angles 2α close to π, the intensity is almost β-independent. This means that for a flat diffraction triangle, the intensity is very little influenced by the orientation of the flaw.

By employing flat diffraction triangles three advantages are achieved:

1) The intensity is highest;

2) A compression surface wave is propagated;

3) The tip of the crack will be detected and its depth determined independent of the crack orientation; hence, cracks open to the back surface and internal cracks might be detected and sized.

In practice there is a limit to how close 2α can approach π. When 2α approaches π, the distance between the transducers 2a tends to infinity and the time delay (2Δ) between the surface signal and the crack diffracted signal tends to zero. The attenuation due to distance will eliminate the appearance of a detectable signal and the time delay will become so small that even with a high resolution apparatus no time delay will be detected. It was determined experimentally that $70° < \alpha < 80°$ produces good results.

4. Results and Conclusions

Figures 8, 9 and 10 show results of measurement of depth of slits 5 to 17 mm deep obtained with a CC mode equilaterial triangle, SC mode and CC mode retangular triangle, respectively. The lines are the theoretical curves and the dots are measuring data.

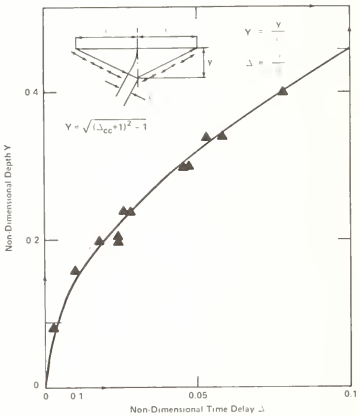

Figure 8. CC array. Equilateral triangle.

Very good agreement between the theoretical curve and the measurement was found. The accuracy was about 10 percent for 5 mm cracks and improved rapidly with size. For cracks larger than 10 mm the accuracy was 2 percent.

It seems that for small cracks the CC - arrangement is not the best choice, because of poor resolution and low intensity. The SS - arrangement with super-critical angles, n investigated, seems to be the right solution for smaller cracks.

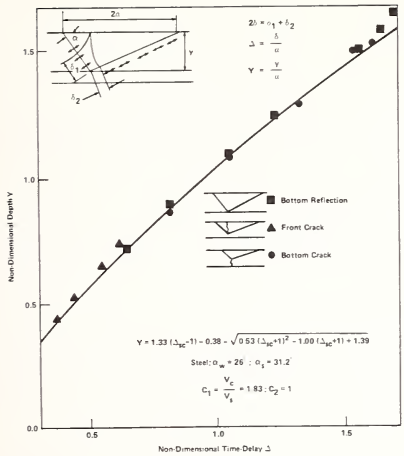

Figure 9. SC array.

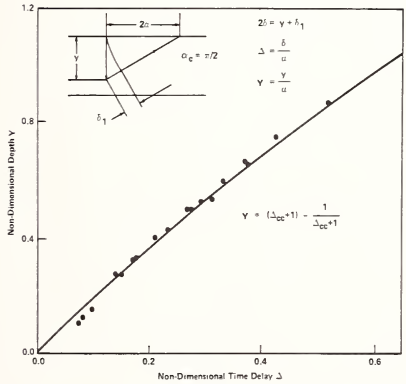

Figure 10. Rectangular CC array.

References

[1] Gericke, O. R., Determination of the geometry of hidden defects by ultrasonic pulse analysis testing, J. Acoust. Soc. Amer., 35, 351-56 (1963).

[2] Adler, L. and Lewis, D. K., Scattering of broadband ultrasonic pulse by discontinuities IEEE Trans. Sonics Ultrasonics, SU-23, 351-56 (1976).

[3] Adler, L., Cook, K. V., and Simpson, W. A., Ultrasonic frequency analysis in Research Techniques in Nondestructive Testing R. S. Sharpe, ed., Vol. III 1-49, (1976).

[4] Whaley, H. L. and Adler, L., Flaw characterization by ultrasonic frequency analysis, Materials Evaluation, 29, 182-92, (1971).

[5] Böttcher, B., Shulz, E., and Wustenberg, H., A new method of crack depth determination in ultrasonic materials testing, Proc. 7th Int. Conf. on NDT, Warsaw (1973).

[6] Silk, M. G. and Lidington, B. H., Defect sizing using ultrasonic time delay approach, Brit. J. NDT, 17, 33-38 (1975).

[7] Silk, M. G. and Lidington, B. H., An evaluation of single probe bulk wave time delay techniques in sizing cracks in steel, NDT International, 129-34 (1977).

[8] Silk, M. G., Sizing of cracks by ultrasonic means in Research Techniques in Nondestructive Testing R. S. Sharpe, ed., Vol. III, 51-99 (1976).

[9] Golan, S., Baruch, J., and Yaron, S., Sizing of cracks with time delay of scattered ultrasonic waves, Israel Institute of Metals - Technion, Internal Report 041-146, (1977).

lational Bureau of Standards Special Publication 596, Ultrasonic Materials Characterization, H. Berger and M. Linzer, eds., Proceedings of the First International Symposium on Ultrasonic Materials Characterization held at NBS, Gaithersburg, Md., June 7-9, 1978. Issued November, 1980.

MATERIALS CHARACTERIZATION

K. Goebbels

Fraunhofer-Gesellschaft
Institut für zerstörungsfreie Prüfverfahren
Universität, Geb. 37, 6600 Saarbrücken 11
Federal Republic of Germany

This section deals firstly with methods of analyzing structural parameters in metals by velocity and attenuation measurements of ultrasonic waves. Secondly, techniques are described to avoid and to correct for structural anomalies influencing ultrasonic propagation. This introduction presents a short review of the elastic and inelastic interactions between the ultrasonic energy and the structure. Velocity and attenuation are described quantitatively in terms of the propagation of ultrasonic waves.

For homogeneous materials, the velocity is simply related to the elastic constants. Attenuation, which is the sum of absorption and scattering losses, can be related to different structural parameters like grain size and heat treatment. For inhomogeneous materials where, for example, anisotropy, texture, residual stresses or secondary phases are present, wave propagation is influenced in a different manner. Phase variations in the untrasonic beam, the elastic constants of higher order, and multiple scattering effects affect the measured velocity and amplitude of ultrasonic signals. Therefore, measurements of velocity and attenuation with high accuracy make it possible to analyze structure and structural inhomogeneities quantitatively. From the point of view of nondestructive evaluation of defects, it is possible to improve the detectability of flaws in inhomogeneous materials, taking into account the special conditions of ultrasonic wave propagation.

1. Interactions Between Ultrasonic Waves and Material Microstructure

The elastic and inelastic interactions between ultrasonic waves and material microtructure bear quantitatively on the velocity and attenuation of the ultrasonic waves. hey are correlated with the different structural parameters (see table 1). For metals,

Table 1. Physical relations between structure and ultrasonic wave propagation.

VELOCITY v	ABSORPTION COEFFICIENT α_A	SCATTERING COEFFICIENT α_S
DENSITY ρ	DISLOCATION PARAMETERS	SIZE OF SCATTERER d
LAMÉ CONSTANTS λ, μ	MAGNETIC DOMAINS	WAVELENGTH λ_{US}
MURNAGHAN CONSTANTS l, m, n	THERMOELASTIC BEHAVIOUR	DENSITY ρ
STRAIN ϵ, STRESS σ		VELOCITY v
SCATTERING COEFFICIENT α_S		ELASTIC ANISOTROPY $H(c_{ij})$
		VARIATION IN ACOUSTIC IMPEDANCE AT GRAIN BOUNDARIES AND/OR PHASE BOUNDARIES: $\Delta\rho v$

and especially for steel, it is important to remember the relationship of wave velocity with elastic constants, density, and, for multiphasic systems, with scattering and multiple scattering. Secondly, the attenuation is the sum of absorption and scattering losses, and we have to consider as absorption processes in practical applications, the influences of dislocations and secondary phases, the interactions with the magnetic structure, and thermoelastic losses. Scattering in monophasic and multiphasic systems is correlated with velocity, density, elastic anisotropy, and grain size. Macroscopically, velocity and attenuation are influenced by structural anomalies like texture, lamellar tearing, anisotropy, residual stresses, and others (see table 2). Many reports in this volume are concerned with these anomalies. To measure some of these interactions by ultrasonic wave propagation or to avoid their sometimes negative influence on the wave propagation, we have to study them under idealized conditions by varying the different parameters:

1.) Velocity measurements with high accuracy (one part in 10^5 for the time-of-flight) allow us to study small variations in the materials structure.

2.) Absorption and scattering processes can be analyzed quantitatively especially for the ratio $d/\lambda \approx 1$, where λ is the ultrasonic wavelength and d is the linear extension of the structure parameter, which we wish to study (for example, the grain size).

In the following discussion, the different interactions are reviewed from a general point of view.

Table 2. Technological relations between structure and ultrasonic wave propagation.

VELOCITY v / ABSORPTION COEFFICIENT α_A	SCATTERING COEFFICIENT α_S
CHEMICAL COMPOSITION	CRYSTAL STRUCTURE
HEAT TREATMENT	GRAIN SIZE
RESIDUAL STRESSES	SIZE OF INCLUSIONS, SEGREGATIONS
FATIGUE	CONTENT OF SECONDARY PHASES
EMBRITTLEMENT	TEXTURE, ANISOTROPY
PLASTIC DEFORMATION	
TEXTURE, ANISOTROPY	
SECONDARY PHASES	

2. Velocity

The relations between the velocity of an ultrasonic wave and the elastic constants are well known. This is true especially for isotropic materials with the Lamé constants λ, μ, where Hooke's law is valid [1][1], and for the Murnaghan constants l, m, n in the non-linear region of elastic behaviour [2,3]. These relations predict small variations of the velocity if the structure is slightly changed, for example, by stress or strain. However, time-of-flight measurements are easily obtained to high accuracy by standard approaches, for example, with the pulse-overlap technique [4]. Also, oscilloscopes suited for time-delay measurements (like the HP 1743 A) enables one to resolve time-of-flight measurements with conventional ultrasonic equipment to one part in 10^5.

The absolute accuracy of a velocity measurement is only necessary for thickness determinations. Relative measurements at a fixed position can make full use of the resolution cited above. Therefore, structural anomalies like texture, anisotropy, residual

[1]Figures in brackets indicate the literature references at the end of this paper.

esses, plastic deformations, and others (see table 2) can be analyzed qualitatively and ntitatively.

Furthermore, the frequency dependence of the velocity is affected if the micro-ucture is drastically changed. This can be calculated [5] and has been observed [6,7] he case of two-phase systems. Current research and development work in this area has principal objectives: 1.) to study structure by time-of-flight measurements with opriate accuracy; 2.) to avoid the negative influence of these effects on the efficacy nondestructive evaluation of macroscopic defects by proper choice of transducers and/or surement techniques.

3. Absorption

More than ten processes are known to be responsible for energy loss in the propa-ng wave by absorption [5] (conversion of the ultrasonic energy into heat). However, he case of polycrystalline metals at room temperature with the ultrasonic frequency ween 1 and about 50 MHz, only three absorption effects are of importance:

1.) the interactions of the ultrasonic wave with the different dislocation parameters [8];

2.) the magnetoacoustic effect, especially in the case of steel;

3.) and thermoelastic losses [10], i.e., energy is carried between microscopic regions of compression (increasing temperature) and regions of dilatation (decreasing temperature).

Experience with several hundred samples of different types of steel shows a simple ar relation between absorption and frequency [11]. Macroscopically, the structural meters influencing the velocity of ultrasonic waves affect the absorption also. It is known that small changes in velocity and small variations in materials microstructure example, which are not resolved metallographically) are accompanied by drastic changes he absorption coefficient.

When scattering measurements [11] (see below) are used to separate absorption from tering quantitatively, it seems to be possible to further study the different absorp-processes.

4. Scattering

While absorption is present under every condition of ultrasonic wave propagation, tering, the other component of the attenuation, strongly depends on the ratio d/λ d above. For $d/\lambda \to 0$ and $d/\lambda \to \infty$ practically no microstructural scattering will be ted to a measurable extent (discussed in detail elsewhere [11]). But in the region

$$0.05 \lesssim d/\lambda \lesssim 0.5 \quad ,$$

scattering coefficient α_S contributes up to about 80 percent of the attenuation coef-ent α. For example, the grain size d_G influences strongly the measured value of α and enables us to correlate α with d_G and further to correlate α with material parameters, g the well-known Hall-Petch-equation [12]. One of the papers in this section goes greater detail regarding these interactions.

References

Krautkrämer, J. and Krautkrämer, H., Werkstoffprüfung mit Ultraschall, pp.584-585 (Berlin, Heidelberg, New York: Springer, 1975).

Murnaghan, F. D., Finite Deformation of an Elastic Solid, pp. 61-65 (New York, Wiley and Sons, 1951).

[3] Egle, D. M. and Bray, D. E., Measurement of acoustoelastic and third-order elastic constants for rail steel, J. Acoust. Soc. Amer., 60, 741 (1976).

[4] Chung, D. H., Silversmith, D. J., and Chick, B. B., A modified pulse-echo-overlap method for determining sound velocities and attenuation of solids, Rev. Sci. Instr., 40, 718 (1969).

[5] Truell, R., Elbaum, C., and Chick, B. B., Ultrasonic Methods in Solid State Physics, (Academic Press, New York, 1969).

[6] Latiff, R. H. and Fiore, N. F., Ultrasonic attenuation and velocity in two-phase microstructures, J. Acoust. Soc. Amer., 57, 1441 (1975).

[7] Goebbels, K., Kraus, S., and Zimmermann, W., Die Beurteilung inhomogener Gefüge mittels Ultraschall-Streuung, Berichtsband Vortragstagung Zerstörungsfreie Materialprüung, DGZfP, Mainz (1978).

[8] Bhatia, A. B, Ultrasonic Absorption (Clarendon Press, Oxford, 1967).

[9] Franz, H., Mechanische Dämpfung infolge magnetischer Vorgänge, Z. Metallkunde, 53, [27] (1962).

[10] Lücke, K., Ultrasonic attenuation caused by thermoelastic heat flow, J. Appl. Phys., 27, 1433 (1956).

[11] Goebbels, K. and Höller, P., Quantitative determination of grain size and detection of inhomogeneities in steel by ultrasonic backscattering measurements, this volume.

[12] Hall, E. O., Yield Point Phenomena in Metals and Alloys (Plenum Press, New York, 1970).

National Bureau of Standards Special Publication 596, Ultrasonic Materials Characterization, H. Berger and M. Linzer, eds., Proceedings of the First International Symposium on Ultrasonic Materials Characterization held at NBS, Gaithersburg, Md., June 7-9, 1978. Issued November, 1980.

QUANTITATIVE ULTRASONIC EVALUATION OF MECHANICAL PROPERTIES OF ENGINEERING MATERIALS

Alex Vary

National Aeronautics and Space Administration
Mail Stop 106-1
Lewis Research Center
Cleveland, OH 44135

Current progress in the application of ultrasonic techniques to nondestructive measurement of mechanical strength properties of engineering materials is reviewed. A hitherto dormant concept in nondestructive evaluation (NDE) is invoked: Even where conventional NDE techniques have shown that a part is free of overt defects, advanced NDE techniques should be available to confirm the material properties assumed in the part's design. There are many instances where metallic, composite, or ceramic parts may be free of critical defects while still being susceptible to failure under design loads due to inadequate or degraded mechanical strength. This must be considered in any failure prevention scheme that relies on fracture analysis. This review will discuss the availability of ultrasonic methods that can be applied to actual parts to assess their potential susceptibility to failure under design conditions. It will be shown that ultrasonic methods will yield measurements of elastic moduli, microstructure, hardness, fracture toughness, tensile strength, yield strength, and shear strength for a wide range of materials (including many types of metals, ceramics, and fiber composites). It will also be indicated that although most of these methods have been shown feasible in laboratory studies, more work is needed before they can be used on actual parts in processing, assembly, inspection, and maintenance lines.

1. Introduction

It is true that the most urgent problem in nondestructive evaluation (NDE) is usually that of flaw detection. Thus, the chief objective of ultrasonic NDE is the location and characterization of cracklike flaws and similar imperfections. However, the same ultrasonic waves that are used for flaw detection can also be used for indirectly measuring the inherent strengths of unflawed materials.

There is a growing consensus that the field of NDE encompasses a wider area than merely that of overt defect detection. Recent studies have shown that NDE methods can supplement and in some cases replace destructive methods for characterizing the properties of engineering materials. The need for nondestructive methods for determining engineering properties as well as actual flaw detection has been a theme in a number of previous papers [1-4][1].

In many instances the NDE approach offers distinct advantages. In conjunction with traditional destructive tests, nondestructive techniques can be used to reduce the cost of materials testing. Accelerated testing of new materials would benefit from NDE technology since there would be less need for large, specialized, or expensive test specimens. Moreover, once conventional nondestructive inspection has either detected or shown a particular part to be free of overt defects, advanced NDE can confirm the material properties assumed in the part's design. In this latter instance, NDE methods would verify material properties of an actual component rather than relying on tabulated values based on prior screening tests. Examples are the ultrasonic determination of bond strength in adhesive joints or fracture toughness of high strength structural components.

[1] Figures in brackets indicate the literature references at the end of this paper.

The chief purpose of this paper is to indicate recent advances in the application of ultrasonics to the nondestructive evaluation of material properties. A second purpose is to set forth a rationale for increased study and use of ultrasonics to characterize material properties. It will be seen that ultrasonic methods have demonstrated capabilities both for direct assessment of mechanical strength and for use in materials selection and development activities. The reviews given herein include brief accounts of recent and ongoing work at the NASA Lewis Research Center in the areas of ultrasonic evaluation of fiber composite strength and metal fracture toughness properties.

2. Background

A consideration of fracture prevention principles and an analysis of failure causes leads to the recognition of the vital role of NDE in assuring the reliability of high performance materials [5-7]. Table 1 lists material deficiencies that can reduce strength or performance. Table 2 lists material properties that can be evaluated nondestructively in efforts to reduce failure causes listed in table 1.

Table 1. Failure causes that generate the need for nondestructive evaluation of material properties.

Faulty processing
Wrong composition
Inclusions
Embrittling impurities
Wrong material properties
Casting defects
Segregations
Porosity
Faulty heat treatment
Faulty case hardening
Residual stress
Faulty surface treatment
Excessive grain growth
Deterioration
Microstructural changes from: local overheating, friction, grinding
Corrosion or chemical attack
Decarburization
Internal oxidation
Stress corrosion
Corrosion fatigue
Vibrational fatigue
Radiation damage
Excess deformation
Atmospheric contamination
Gas embrittlement

Table 2. Examples of material properties and characteristics that can be nondestructively evaluated.

Mechanical properties
Tensile modulus
Shear modulus
Tensile strength
Yield strength
Shear strength
Fracture toughness
Hardness
Metallurgical factors
Microstructure
Grain size
Phase composition
Porosity
Inclusions
Hardening depth
Residual stress
Heat treatment
Anisotropy

To appreciate the role of NDE in material properties determination, it is necessary to distinguish between two kinds of flaws: First, there are those overt flaws that can be individually detected and characterized (e.g., cracks in metals, delaminations in composites). Second, there are those flaws that are so numerous, microscopic, and dispersed that their presence is detected only in their effect on bulk properties (e.g., toughness, strength). Overt flaws or flaws of the first type are typically stress raisers and fracture nuclei. Dispersed flaws or flaws of the second type are those that predispose a material part to failure even under design conditions.

An example of the utility of ultrasonic NDE is provided by the requirements for determining and verifying the fracture toughness of high strength alloys [8-9]. The need for pid and inexpensive tests for determining fracture toughness has led to the investigation ultrasonic correlations with fracture toughness factors [10]. The correlations that have en developed indicate that purely ultrasonic methods can be used to verify a material's ane strain fracture toughness. In its present form, ultrasonic toughness testing is geared imarily to laboratory tests of small metal specimens. Were the method adapted for field plications, ultrasonic toughness testing could become an important inspection tool in adtion to the detection of voids and cracks in fracture-prone components.

In the past, material property characterization has been the province of those branches materials science that employ destructive test techniques or nondestructive tests on ghly specialized specimens. The relation of NDE to destructive testing (DT) and nondeructive testing (NDT) is illustrated in table 3. Given the perspective of table 3, NDE is en also a bridge between materials research and hardware inspection. Underlying sciences e also indicated for the major areas in table 3. Physical acoustics, the scientific basis r ultrasonic NDE and NDT, is pivotal in the measurement of the material properties given table 2. An overview and illustrative cases of practical applications of physical acoustics in ultrasonic NDE are given below.

Table 3. Relation of nondestructive evaluation to destructive testing and nondestructive testing.

<table>
<tr><td colspan="3">← Materials research →
← Hardware inspection →</td></tr>
<tr><td>Destructive testing</td><td>Nondestructive evaluation</td><td>Nondestructive testing</td></tr>
<tr><td colspan="2">Materials characterization, verification of properties, strength measurement, screening</td><td></td></tr>
<tr><td></td><td colspan="2">Flaw detection and characterization, process and fabrication control, preservice and inservice inspection</td></tr>
<tr><td colspan="3">Underlying sciences</td></tr>
<tr><td colspan="2">Solid state physics, dislocation theory, metallography</td><td>Physical acoustics, elastic wave theory, ultrasonics</td></tr>
</table>

3. Technology Overview

There are, of course, numerous techniques other than ultrasonics (e.g., radiometry, ldy current) that can be used for material properties evaluation [11]. Many of these e alternatives that can complement or corroborate ultrasonic measurements. A review of exting ultrasonic techniques shows that considerable advances have been made in the sophiscation of flaw detection and characterization methods [12-20]. In addition, there is an erging literature concerned with materials characterization through the ultrasonic assessnt of microstructure and elastic moduli. It will be clear presently that ultrasonic sigls recovered from material specimens can be a rich source of information relative to physal properties and material strength of engineering components. Table 4 summarizes the curnt capabilities of ultrasonics for properties and strength characterizations.

Progress in the use of ultrasonics for evaluation of material strength related properes may be categorized into three overlapping stages: (1) ultrasonic measurement of astic constants, (2) ultrasonic measurement of microstructure, and (3) ultrasonic measurent of mechanical strength. The last mentioned stage is the least developed and comprises e main focus of this report. The second stage will be discussed in relation to practical plications of ultrasonic attenuation theory. The first stage has usually involved physil acoustics applied to crystalline and atomic-scale phenomena. However, it will be evident at the moduli measured by ultrasonics (formed by the product of velocity squared and density) e related to elastic moduli and hence, strengths of polycrystalline and composite materials.

Table 4. Capabilities of ultrasonics for nondestructive evaluations of material properties.

Material property	Ultrasonic measurement	Applicable materials	References
Longitudinal modulus	Longitudinal velocity	Most engineering solids	2, 13, 21
Shear modulus	Transverse velocity	Most engineering solids	2, 13, 21
Grain size, microstructure	Attenuation, acoustic microscopy	Polycrystalline metals, ceramics	13, 20, 24, 26, 27
Porosity, void content	Velocity, attenuation	Fiber composites, ceramics	44, 48, 51
Hardness or hardness gradient	Velocity, velocity dispersion	Polycrystalline metals	28, 29, 30 31
Tensile strength	Velocity, stress wave attenuation	Brittle metals, ceramics, fiber composites	2, 13, 45, 46, 50
Yield strength	Frequency-dependent attenuation	Polycrystalline metals	33, 34
Fracture toughness	Frequency-dependent attenuation	Polycrystalline metals	33, 34
Bond shear strength	Resonance, spectrum analysis	Metal-metal adhesive bonds	37, 39, 40
Interlaminar shear strength	Attenuation, stress wave attenuation	Fiber composites	44, 47, 48

Physical acoustics generally encompasses the study of wave propagation and the interpretation of velocity and attenuation effects in solids [21-23]. Among the objectives of physical acoustics are the investigation of crystal imperfections, dislocation motions, internal friction, and elastic wave motions. The practical applications of physical acoustics involve the following ultrasonic measurements which are prominent in NDE: (1) velocity--involving the analysis of longitudinal, transverse, and surface waves, and frequency dispersion [12,14] (2) attenuation--involving the analysis of absorption, scatter, and frequency dispersion [12, 14,20], (3) resonance--involving the analysis of continuous wave interactions [13], (4) spectrum analysis--involving pattern analysis of frequency spectra [15-17], (5) acoustic emission --involving analysis of simulated or spontaneous signals emitted during strain or fracture [18], and (6) acoustic microscopy--involving direct imaging of microstructure, wave interferometry [12,19]. These six measurement methods form the basis of ultrasonic evaluation of physical properties and material strength. Most of the cases to be cited below involve recent efforts that illustrate feasibility rather than current practice.

4. Illustrative Cases

4.1. Elastic moduli

The earliest applications of ultrasonics to materials characterization involved the study of elastic constants, usually with specialized specimens such as single crystals. This work laid the foundations for ultrasonic characterization of polycrystalline, amorphous, and heterogeneous materials.

Physical acoustics theory indicates that the elastic behavior of solids can be determined by measurement of ultrasonic wave propagation. The measurement of longitudinal (v_ℓ) and transverse (v_t) velocities yield the longitudinal (L) and shear (G) moduli, respectively, where,

$$L = \rho v_\ell^2 \quad \text{and} \quad G = \rho v_\ell^2 \quad .$$

For linear elastic, isotropic solids these two moduli are sufficient to completely describe elastic behavior, given interconnecting relations with other moduli, e.g., bulk modulus, Young's modulus, Poisson's ratio [21]. These relations provide a basis for ultrasonic correlations with mechanical strength properties even for less ideal materials.

The magnitudes of elastic constants are related directly to the strengths of some groups of brittle materials, e.g., concrete, ceramics, cast iron. Because the elastic modulus may be determined on the basis of longitudinal velocity, ultrasonic measurements can form the basis for determination of the tensile strength of high-quality cast iron, for example [13]. To deduce the tensile strength in this case also requires the determination of Brinell hardness. Thus, by making two nondestructive measurements on a finished article, an important strength property can be verified.

4.2. Microstructure

There is a considerable literature built on the ultrasonic study of grain size in metals [13,20]. Some of this literature grew from the need to understand the effects of grains, boundaries, and inclusions on flaw detection. Detection of small, critical flaws in many metals is hampered by "grain noise". Thus, attenuation and velocity variations associated with grain size variations in various metals have been studied in conjunction with determining limitations on ultrasonic flaw detection. In the process, strong correlations were discovered among ultrasonic wave transmission and material microstructure variations due to hardening, annealing, quenching, and cold work.

Ultrasonic velocity and attenuation measurements have been conducted with the object of verifying microstructure [24-25]. The coarseness and quantity of graphite in lamellar cast iron, for example, has been found to influence the velocity of longitudinal waves [13]. Since the amounts and forms of graphite affect the tensile stregth of cast iron, velocity measurements can serve as a quality check for acceptance purposes.

Ultrasonic velocity and attenuation measurements can also provide quality checks for light metals such as aluminum, magnesium, titanium, and their alloys. The mechanical strengths of these materials are influenced by segregations, precipitates, impurities, dispersoids, alloy concentrations, and so forth, which can be assessed by ultrasonic methods [13].

Relative differences in microstructure of polycrystalline and amorphous solids can be determined by ultrasonic spectrum analysis [15]. The influence of grain size on frequency spectra has been demonstrated [16]. It is possible, for example, to ascertain the structural differences generated in carbon steels by different heat treatments by comparison with spectra obtained with reference samples. Heat treatments given to forged articles can be verified during the fabrication process. This capability meets a quality control requirement frequently expressed by steel processors.

Measurements of ultrasonic diffraction, dispersion, and scattering can contribute to material property assessment [17]. Some progress in this direction has been made by precise measurements of the frequency dependence of velocity and attenuation [14,25]. It appears that indirect determinations of grain size in polycrystalline metals are possible through the measurement of the scatter attenuation coefficients α_r and α_s, where

$$\alpha_r = D^3 f^4 S_r \quad \text{and} \quad \alpha_s = Df^2 S_s \quad .$$

The subscripts r and s pertain to Rayleigh and stochastic scattering, respectively, while D is grain diameter, f is frequency, and S is an experimentally determined scattering factor.

(Rayleigh scattering occurs when ultrasonic wavelength is >D and stochastic scattering when wavelength is <D, approximately.)

Acoustic microscopy affords advantages of direct microstructure imaging in the case of small articles. The technique visually reveals localized variations in the elastic properties of materials [19,27]. Therefore, microstructural features that govern sound propagation will appear in acoustic micrographs. The technique permits examination and characterization of microelastic variations, grain structure, and micro-inclusions. Both qualitative and quantitative assessments of a wide range of ultrasonically transparent articles are possible.

4.3. Hardness

The nondestructive measurement of hardness in metals is routinely accomplished chiefly by indentation test methods. Ultrasonic methods for hardness determination have been studied as a key to rapid, on-line product verification [28-29].

It has been found that ultrasonic velocity hardness measurements offer advantages over other methods in the rapid sorting of malleable cast iron [28]. The relationship between hardness and ultrasonic attenuation has also been demonstrated for some steels [29]. Direct correlations were found between Rockwell-C hardness and the attenuation coefficient.

In the previously cited cases ultrasonic hardness tests were applied to the examination of bulk microstructural changes due to variations in heat treatment, density, and so forth. Recent studies have focused on hardness gradients associated with surface treatments [30-31]. Ultrasonic surface waves are promising in the measurement of variations with depth of properties such as density, case hardening, mechanical deformation, and gas diffusion in metals. For example, hardness gradients in quench hardened steel have been shown to correlate with the frequency dependence of the velocity of ultrasonic surface waves [30].

4.4. Fracture toughness

The investigation of ultrasonic attenuation as a function of frequency has led to useful correlations with a variety of material properties [14,20]. The previous examples cited in Sections 4.2 and 4.3 emphasized nondestructive evaluations of material factors that are indirect indicators of strength. In the case of metals there have been some indications of the potentials of ultrasonic measurement of actual yield strength, impact strength, and fracture toughness [32-34].

There are strong incentives for ultrasonic toughness tests [8-9]. One of the major cost drivers in using fracture controlled materials in aircraft is the requirement to verify toughness levels of materials at receiving inspection and after any processing that may adversely affect fracture toughness. The major drawback of existing mechanical destructive tests for determining K_{Ic}, plane strain fracture toughness, is the high costs of machining and testing suitable specimens.

The feasibility of ultrasonic measurement of K_{Ic} has been demonstrated for two maraging steels and a titanium alloy [33]. Empirical correlations were found between ultrasonic attenuation factors and K_{Ic} and σ_y, the 0.2 percent yield strength, (fig. 1). The equation for figure 1 is,

$$K_{Ic}^2/\sigma_y = \psi(v_\ell\ \beta_\delta)^e$$

where v is velocity, β_δ is an ultrasonic attenuation factor, and ψ and e are experimental constants. In addition, figure 2 shows recent data that suggests a linear empirical relation of the form,

$$\sigma_y + AK_{Ik} + B\beta_1 = C$$

where β_1 is an ultrasonic attenuation factor and A, B, and C are experimental constants that depend on the material involved [33]. Given the previous equations, it appears that the

essential measurements for deducing fracture toughness and yield strength can be made by purely ultrasonic techniques once calibration curves have been established for a (polycrystalline) material [34].

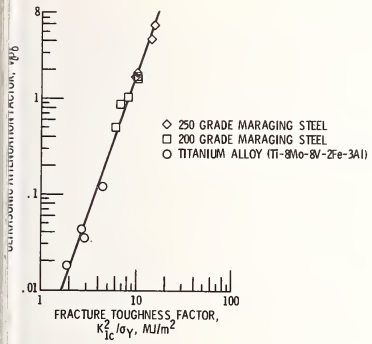

Figure 1. Correlation of ultrasonic and fracture toughness factors. The ultrasonic attenuation factor $v_t\beta_\delta$ is based on measurements of longitudinal velocity, v_t, and the slope of the attenuation versus frequency curve, β_δ. K_{Ic} and σ_y are the plane strain fracture toughness and 0.2 percent yield strength, respectively, as measured by destructive test methods (figure from ref. 33).

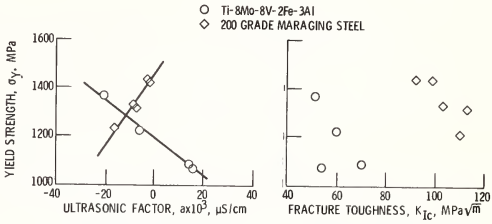

(a) YIELD STRENGTH VERSUS THE ULTRASONIC QUANTITY $a = (A/B)K_{Ic} + \beta_1$.

(b) CONVENTIONAL PLOT OF YIELD STRENGTH VERSUS FRACTURE TOUGHNESS.

Figure 2. Correlation of yield strength with fracture toughness via an ultrasonic factor. The ultrasonic quantity β_1 is determined by the slope of the attenuation versus frequency curve evaluated at unit attenuation. The quantities A and B are experimentally measured ultrasonic constants for a given material. K_{Ic} and σ_y are plane strain fracture toughness and 0.2 percent yield strength, respectively, as measured by destructive tests (figure from ref. 33).

4.5. Bond strength

The question of adhesive bond strength arises most frequently in aerospace structures which employ metal and composite laminated joints [35-36]. Ultrasonic resonance methods are widely used in assessing the integrity of metal-to-metal adhesive bonds [37]. The nondestructive estimation of bond shear strength is based on a formula that incorporates the resonance frequency, f, adhesive thickness, t, metal thickness, d, and elastic modulus, L_t, of the adhesive layer,

$$f = \frac{1}{2\pi}\sqrt{2L_t/\rho td} \quad .$$

The above equation is derived from the relation between velocity and longitudinal modulus given earlier: $L = \rho v_\ell^2$. Strength correlation obtained by resonance tests are, therefore, ultimately dependent on ultrasonic velocity velocity in the adhesive layer. Application of the resonance method requires the establishment of calibration curves for each individual joint configuration and adhesive system.

Improved methods are being sought to evaluate the actual strength of bond in layered structures [38-40]. The assessment of bond strength is currently being pursued by means of frequency spectrum analysis methods that are considerably more sophisticated than the previously mentioned resonance method. The resultant correlations of spectral patterns with bond strength are encouraging. Interconnecting relations between velocity and attenuation in adhesive materials are being studied in efforts to evolve purely ultrasonic methods for predicting adhesive bond strength [40].

4.6. Composite strength

Effective design and reliability assurance of composite materials depend on nondestructive methods for measuring mechanical properties before use and strength degradation during use. (In some fiber composites, for example, strength degradation can follow moisture absorption and matrix crazing.)

One approach for inferring strengths of fiber reinforced composites is that of velocity measurements to determine elastic moduli [41-42]. This approach is based on the familiar relations, $L = \rho v_\ell^2$, and $G = \rho v_t^2$. Another approach is that of measuring ultrasonic attenuation [43-44]. This latter approach is similar to that of ascertaining grain size in metals except that the emphasis usually is on determining microvoid content. Microvoids in fiber composites are known to be serious strength reducing factors.

Ultrasonic attenuation measurements afford a means of assessing microvoid content and hence (indirectly) material strength. The total attenuation coefficient, α_c, of a microvoid containing material is given by,

$$\alpha_c = \alpha_b + \alpha_v$$

where α_b is the attenuation coefficient under void-free conditions and α_v is the attenuation coefficient due to microvoids. (Both α_b and α_v may be frequency dependent.)

A problem peculiar to many fiber reinforced composites is the high degree of anisotropy due to fiber orientation. Ultrasonic methods for determining elastic constants must adapt to this situation. The effect of fiber orientation on elastic properties has been studied by use of special ultrasonic transducer arrangements [45-46]. The empirical equation,

$$\rho v_\theta^2 = \gamma L_\theta$$

was found to describe seven composite materials ranging from glass/epoxy to boron/aluminum [3]. The subscript θ refers to fiber angle in a series of laminate specimens. Velocity, v_θ, was measured in-plane, i.e., parallel to the major surfaces of the lamina. Good correlations were obtained between destructively measured tensile strength and the ultrasonic modulus, L_θ.

Correlations between ultrasonic attenuation and interlaminar shear strength (as measured by short beam shear tests) have also been demonstrated [44,47]. In these instances, the attenuation coefficient was determined by introducing pulsed ultrasound perpendicular to the major surfaces of the lamina. Increased attenuation corresponded to lower interlaminar shear strength.

An acoustic-ultrasonic method for fiber composite strength evaluation was reported recently [48-50]. The method differs from those described above in its use of simulated acoustic emissions which are introduced into the composite laminate specimens. The simulated acoustic emission signals are analyzed to determine a "stress wave factor", ε. The stress wave factor is a mixed function of attenuation, velocity, and resonance in the laminates. The method for measuring ε produces a numerical value that can rank specimen laminates according to strength. Correlations of ε with composite shear strength have been found for graphite/polyimide laminates. Using the stress wave factor in conjunction with velocity demonstrated the feasibility of purely ultrasonic methods for indirect measurement of the interlaminar shear strength of fiber composite laminates [48]. For example, τ, interlaminar shear strength, correlated with ε and v through,

$$\tau' = \zeta(v - a)/(b - \varepsilon)$$

where τ' is an estimator for τ and ζ, a, and b are experimentally determined constants for a particular composite material (fig. 3). (Both ε and v were, in this case, measured with waves propagating in-plane and perpendicular to the fibers which were unidirectional.)

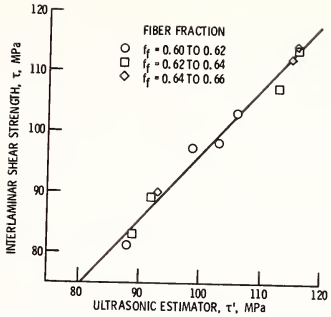

Figure 3. Correlation of interlaminar shear strength and ultrasonic shear strength estimator. The above calibration curve was developed for graphite/polyimide fiber composite laminates. The ultrasonic shear strength estimator, τ', is based on velocity and stress wave attenuation measurements. The interlaminar shear strength, τ, was obtained from short beam shear destructive tests (fig. from ref. [48]).

4.7. Ceramic strength

The ultrasonic evaluation of ceramic materials of current technological importance presents special demands. Silicon nitrides and carbides are examples of candidate materials for use in future high temperature engines. Micron-size voids and inclusions can constitute serious flaws in these ceramics. Advanced high frequency ultrasonic techniques are needed simply to detect flaws of this nature. On the other hand, these minute flaws may be distributed in large numbers throughout the bulk of a ceramic article and thus affect bulk properties that can be ultrasonically determined without the need to detect individual flaws.

The literature on ultrasonic evaluation of ceramic materials is dominated by studies of elastic wave propagation in fused silica, quartz, and other glasses [23]. Recent work on ultrasonic inspection of ceramics has generally dealt with microcrack detection and acoustic emission monitoring of crack growth. Some attempts have been made to apply ultrasonics to measure strength related properties of ceramics intermetallics [2,51]. There is a gap in NDE technology applicable to the evaluation of ceramic components. Ultrasonic methods for verification of the density and microstructure of sintered and reaction bonded ceramics await development. Measurement of ultrasonic moduli in conjunction with destructive tests are needed to confirm material properties in actual ceramic parts. Ultrasonic methods would be most useful for measuring elastic constants of ceramic and other brittle and semi-brittle materials (e.g., graphite) where other methods produce either poor or no results [2].

5. Additional Cases and Considerations

There are two major considerations that should guide the development of NDE technology for material strength evaluation: (1) verification and control of material strength properties in actual parts, and (2) investigation and characterization of factors governing material strength properties. The first consideration is a self-evident counterpart of material specification, reliability assurance, and inspection practices. The second consideration requires adoption of the view that NDE should be an integral part of materials testing practices.

In the usual conduct of destructive mechanical tests, specimens are inspected for dimensional conformity and overt flaws. However, little thought is given to the application of NDE methods to confirm the uniformity or quality of material specimens. Data scatter of over ±2 percent is often accepted as an inherent consequence of test procedures. The opportunity to reduce this scatter and to gain more information is available with the ultrasonic techniques cited previously in this paper. In particular, ultrasonic technology has demonstrated capabilities for direct assessment of strength related properties such as elastic moduli, microstructure, hardness, toughness, etc.

In addition to pretest material characterization or property prediction, ultrasonics has proven utility for in situ monitoring as, for example, during fracture toughness testing [52-53]. In situ applications of ultrasonics can afford continuous monitoring of materials undergoing thermal or mechanical processing [2]. For example, velocity measurements during sintering of ceramics can serve to follow the process of pore formation. Distinct velocity changes observed during the process of polymer hardening can be utilized for process control. Controlling the melting process and phase formation in metallurgy can be accomplished by monitoring changes in ultrasonic velocity and stopping the process at a critical stage.

A case for the addition of ultrasonic measurements to destructive test procedures is illustrated in figure 2. By comparing the plots therein, it is evident that the addition of an ultrasonically measured factor β_1 introduced considerably more coherence to the relation between fracture toughness and yield strength. Accordingly, it may be concluded that fracture toughness and yield strength are linked to ultrasonic stress wave propagation properties of polycrystalline materials. It appears that in addition to determining these material properties, ultrasonic measurements can be significant in indicating factors that govern toughness and strength [34].

The above examples suggest that ultrasonic interrogation of materials provides more than merely an assessment of static characteristics but provides an indication of dynamic response. That is, ultrasonic probing can apparently aid in studies of stress wave propagation factors that govern material response under static, quasi-static, and dynamic loading conditions [54-55]. It has been observed, for example, that polycrystalline, heterogeneous materials exhibit a distinct velocity dispersion (i.e., v as a function of f). From this it can be inferred that the elastic modulus will increase as velocity increases with frequency [2]. Knowledge of dynamic moduli would be of considerable importance in materials subjected to severe dynamic loads, e.g., composite fan blades.

The above-discussed factors ultimate converge to enhance material specification, reliability assurance, and inspection. The availability of NDE to ascertain yield strength, hardness, microstructure, etc., can become a prime element in assuring that a structure meets stringent strength specifications when necessary. NDE for material grading and reliability assurance would certainly generate cost and safety benefits that outweigh the cost of method development and adaptation.

6. Summary and Conclusion

Applications of ultrasonics to direct nondestructive evaluation (NDE) of material strength properties were reviewed. It was shown that probing with ultrasonic waves will yield measurements of elastic moduli, microstructure, hardness, toughness, tensile strength, and shear strength for a wide range of materials (including many types of metals, ceramics, and fiber composites). The review also indicated that: (1) reliability assurance should begin with NDE to verify material strength even in the absence of overt flaws particularly in critical high strength components, (2) failures caused by processing errors, inherent material deficiencies, or strength degradations in service can be reduced by application of advanced ultrasonic methods, (3) materials screening and accelerated testing of new materials would benefit from ultrasonic NDE technology since there would be less need for large, specialized, and expensive test specimens, and (4) improved quality control during thermal and mechanical processing can be accomplished by ultrasonic monitoring of microstructural changes.

In order to implement the above concepts, advanced technique development is required to assure the availability of ultrasonic methods and devices for strength evaluations of critical articles of high strength alloys, high temperature ceramics, and advanced fiber composites. Research reports on these topics are scarce. The greatest current need, therefore, is the development of theory and empirical correlations that will further establish and confirm ultrasonic capabilities for direct evaluation of material strengths. In particular, development of relationships based on solid state and physical acoustics theory would be of great benefit and would probably extend the usefulness of these techniques. Although some advanced ultrasonic methods have been created and shown feasible in laboratory studies, more work is needed before these methods can be used on actual parts in processing, assembly, inspection, and maintenance lines.

References

[1] Sharpe, R. S., Innovation and opportunity in NDT, British J. of Nondestructive Testing, 18, 98 (1976).

[2] Malecki, I., Application of ultrasonic physics in material technology, Archives of Acoustics, 2, 3 (1977).

[3] Zurbrick, J. R., Direct nondestructive prediction of engineering properties, Journal of Testing and Evaluation, 1, 13 (1973).

[4] McSkimin, H. J., in Proceedings of the Symposium on Physics and Nondestructive Testing, W. J. McGonnagle, ed., pp. 83-111, San Antonio, Texas, Southwest Research Institute, (1962).

[5] Application of Fracture Prevention Principles to Aircraft, National Materials Advisory Board, Washington, D.C., NMAB-302, (Feb. 1973).

[6] Grover, H., Sourcebook in Failure Analysis, pp. 31-39, American Society for Metals, Metals Park, OH (1974).

[7] Dolan, T. J., Sourcebook in Failure Analysis, pp. 31-39, American Society for Metals, Metals Park, OH, (1974).

[8] Rapid Inexpensive Tests for Determining Fracture Toughness, National Materials Advisory Board, Washington, D. C., NMAB-328 (1976).

[9] Berryman, R. G., Chesnutt, J. C., and Froes, F. H., A new cost-effective titanium alloy with high fracture toughness, Metal Progress, 112, 40 (1977).

[10] Vary, A., Ultrasonics takes on fracture toughness testing, Machine Design, 49, 145 (1977).

[11] Vary, A., Nondestructive Evaluation Technique Guide, NASA SP-3079 (1973).

[12] Silvus, H. S., Jr., Advanced Ultrasonic Testing Systems: A State-of-the-Art Survey, Southwest Research Institute, San Antonio, TX, NTIAC-77-1 (Sept. 1976).

[13] Krautkramer, J. and Krautkramer, H., Ultrasonic Testing of Materials, 2nd ed., (New York, Springer-Verlag, 1977).

[14] Papadakis, E. P., Physical Acoustics, Vol. XII, W. P. Mason and R. N. Thurston, eds., pp. 277-374 (1976) (New York, Academic Press).

[15] Gericke, O. R., Research Techniques in Nondestructive Testing, R. S. Sharpe, ed., pp. 31-61, London, (Academic Press, 1970).

[16] Canella, G. and Monti, F., Spectrum analysis: a new otol for quality control by ultrasonics, Nondestructive Testing International, 9, 187 (1976).

[17] Brown, A. F., Materials testing by ultrasonic spectroscopy, Ultrasonics, 11, 202 (1973).

[18] Liptai, R. G., Harris, D. O., Engle, R. B., and Tatro, C. A., Acoustic emission techniques in materials research, International J. of Nondestructive Testing, 3, 215 (1971).

[19] Kessler, L. W. and Yuhas, D. E., Structural perspective, Industrial Research, 20, 52 (1978).

[20] Rogers, E. H., A Report Guide to Ultrasonic Attenuation Literature, Army Materials Research Agency, Watertown, MA, AMRA-MS-65-09, Dec. 1965. (AD627565)

[21] Schreiber, E., Anderson, O. L., and Soga, N., Elastic Constants and their Measurement, (McGraw Hill, New York, 1973).

[22] Green, R. E., Jr., Ultrasonic Investigation of Mechanical Properties, (Academic Press, New York, 1972).

[23] Mason, W. P., Physical Acoustics and the Properties of Solids, (D. van Nostrand Co., Inc., New York, 1958).

[24] Papadakis, E. P., Revised grain-scattering formulas and tables, J. Acoust. Soc. Amer., 37, 703 (1965).

[25] Papadakis, E. P., Variation of ultrasonic grain-scattering factors with velocity, J. Acoust. Soc. Amer., 43, 876 (1968).

[26] Papadakis, E. P., Ultrasonic attenuation caused by scattering in polycrystalline metals, J. Acoust. Soc. Amer., 37, 711 (1965).

[27] Szilard, J. and Scrunton, G., 1974 Ultrasonic Symposium Proc., pp. 707-710, New York, IEEE, (1974).

[28] Tamburelli, C. and Quaroni, A., Ultrasonic velocity measurement to inspect malleable iron casting, Non-Destructive Testing, 8, 152 (1975).

[29] Roderick, R. L. and Truell, R., The measurement of ultrasonic attenuation in solids by the pulse technique and some results in steel, J. Appl. Phys., 23, 267 (1952).

[30] Tittmann, B. R. and Thompson, R. B., in Ninth Symposium on Nondestructive Evaluation, pp. 20-28, San Antonio, Texas, Southwest Research Institute, (1973).

[31] Tittmann, B. R., Alers, G. A., Thompson, R. B., and Young, R. A., in 1974 Ultrasonic Symposium Proc., pp. 561-564, New York, IEEE (1974).

[32] Papadakis, E. P., Ultrasonic attenuation in SAE 3140 and 4150 steel, J. Acoust. Soc. Amer., 32, 12, 1628 (1960).

[33] Vary, A., Correlations Among Ultrasonic Propagation Factors and Fracture Toughness Properties of Metallic Materials, NASA TM X-71889, 1976.

[34] Vary, A., Correlations Between Ultrasonic and Fracture Toughness Factors in Metallic Materials, NASA TM-73805, 1978.

[35] Forney, D. M., Jr., NDI in the United States Air Force, British J. of Nondestructive Testing, 19, 72 (1976).

[36] Schliekelmann, R. J., Nondestructive testing of adhesive bonded metal-to-metal joints, Nondestructive Testing, 5, 129 (1972).

[37] Van der Schee, E. J. and Bijlmer, P. F. A., Nondestructive Inspection Practices, E. Bolis, ed., pp.91-128, AGARD-AG-201, Brussels, North Atlantic Treaty Organization, (1975).

[38] Alers, G. A., in Proc. of the ARPA/AFML Review of Progress in Quantitative Nondestructive Evaluation, Air Force Materials Labs., pp. 52-58, AFML TR-44, (Sept. 1977).

[49] Buckley, M. J. and Raney, J. M., in Proc. of the ARPA/AFML Review of Progress in Quantitative Nondestructive Evaluations, Air Force Materials Lab., AFML TR-77-44, pp. 66-73 (Sep. 1977).

[50] Flynn, P. L., in Proc. of the ARPA/AFML Review of Progress in Quantitative Nondestructive Evaluation, Air Force Materials Lab., AFML TR-77-44, pp. 59-65, (Sep. 1977).

[51] Dean, G. D., and Lockett, F. J., in Analysis of Test Methods for High Modulus Fibers and Composites, pp. 326-346, ASTM STP-521, Philadelphia, ASTM, (1973).

[52] Martin, G., Metal and Ceramic Matrix Composites, eds., L. W. Davis and S. W. Bradstreet, pp. 133-173 (Cahners Publishing Co., Boston, 1970).

[53] Martin, G., Ultrasonic attenuation due to voids in fiber-reinforced plastics, Nondestructive Testing International, 9, 242, (1976).

[54] Stone, D. E. W. and Clarke, B., Ultrasonic attenuation as a measure of void content in carbon-fibre reinforced plastics, Nondestructive Testing, 8, 137 (1975).

[55] Hastings, C. H., Olster, E. F., and Lopilato, S. A., Development and Application of Nondestructive Methods for Predicting Mechanical Properties of Advanced Reinforced Nonmetallic Composites, Air Force Materials Lab., AFML TR-73-157 (May 1973).

[56] Schultz, A. W., The Development of Nondestructive Methods for the Quantitative Evaluation of Advanced Reinforced Plastic Composites, Air Force Materials Lab., AFML TR-70-20, (AD-875229) (Aug. 1970).

[57] Hayford, D. T., Hennecke, E. G. II., and Stinchcomb, W. W., The correlation of ultrasonic attenuation and shear strength in graphite/polyimide composites, J. Composite Materials, 11 (1977).

[58] Vary, A. and Bowles, K. J., Ultrasonic Evaluation of the Strength of Unidirectional Graphite/Polyimide Composites, NASA TM X -73646 (1977).

[59] Vary, A. and Bowles, K. J., Use of an Ultrasonic Acoustic Technique for Nondestructive Evaluation of Fiber Composite Strength, NASA TM-73813, (1978).

[60] Vary, A. and Lark, R. F., Correlations of Fiber Composite Tensile Strength with the Ultrasonic Stress Wave Factor, NASA TM-78846, (1978).

[61] Papadakis, E. P., Sonic and ultrasonic methods for nondestructive testing of catalytic converter substrates, Materials Evaluation, 34, 25 (1976).

[62] Tetelman, A. S. and Chow, R., in Acoustic Emission, ASTM STP-505, pp. 30-40, Philadelphia: ASTM, (1972).

[63] Klima, S. J., Fisher, D. M., and Buzzard, R. J., Monitoring crack extension in fracture toughness tests, J. Testing and Evaluation, 4, 397 (1976).

[64] Curran, D. R., Seaman, L., and Shockey, D. A., Dynamic failure in solids, Physics Today, 30, 46 (1977).

[65] Kolsky, H., Stress Waves in Solids, Dover Publishing Co. (New York, 1963).

ational Bureau of Standards Special Publication 596, Ultrasonic Materials Characterization,
. Berger and M. Linzer, eds., Proceedings of the First International Symposium on Ultrasonic
aterials Characterization held at NBS, Gaithersburg, Md., June 7-9, 1978. Issued
ovember, 1980.

SOME ULTRASONIC METHODS FOR CHARACTERIZING RESPONSE OF COMPOSITE MATERIALS

Edmund G. Henneke, II, Wayne W. Stinchcomb, and
Kenneth L. Reifsnider

Department of Engineering Science and Mechanics
Virginia Polytechnic Institute and State University
Blacksburg, VA 24061

A survey is given on the application of ultrasonics to material and damage characterization in several different composite material systems. The use of phase velocity measurements to determine the independent elastic constants of an orthotropic material is shown to be especially important in that this method yields values of the out-of-plane constants G_{23} and ν_{23} that are otherwise unobtainable by the usual tension test technique. Attenuation measurements and C-scans are found to be useful in the initial characterization of material quality. Perhaps of paramount importance and interest at the present time is the utility of ultrasonics for aiding in the identification of the initiation and progression of a characteristic damage state in graphite-epoxy laminates that ultimately grows to final failure.

1. Introduction

The application of nondestructive test methods to composite materials offers a vast mber of interesting, and necessary, research topics. With the increasing use of composite terials for the aerospace industry and the developing interest in the automotive industry, ong others, comes the immediate and future needs for well-founded NDT methods. These thods must be well-founded in the sense that the mechanics of the method itself, the chanics of the interaction of the technique with the material, and the mechanics of the terial behavior must be understood thoroughly. Ultrasonics, having played such a major le in the characterization of homogeneous materials, is an obvious choice for the study of mposite materials.

This work presents a short review of some ultrasonic NDT methods that have been applied various composite materials in our laboratories. These methods have been used to obtain ta for material characterization and for damage characterization. Materials have been aracterized by the ultrasonic determination of elastic constants and by comparing initial lues of ultrasonic attenuation with failure strengths. Damage characterization has oceeded by using real-time attenuation measurements to follow its initiation and ogression. In the latter instance, the ultrasonic technique has proven invaluable for taining data that was used to aid in the identification of the exact nature of first ilure in composite laminates and the subsequent development of a characteristic damage ate that precedes final failure. In the following sections the ultrasonic methods that ve proven useful in our laboratories will be discussed along with some of the more teresting findings.

2. Material Characterization

2.1. Determination of elastic constants

The complete description of stress and strain states in composite laminates requires the e of three-dimensional analysis. In any such analysis, the results can be no better than e material properties used, even assuming a correct theoretical model. Hashin [1][1]

developed a theoretical model for predicting macroscopic properties of fiber reinforced laminates given the isotropic properties of the matrix, the transversely isotropic properties of the fiber, and the fiber volume fraction. The transverse properties of a fiber such as graphite are difficult, if not impossible, to determine. Usually they are determined by using Hashin's model together with experimentally determined laminate stiffnesses for various volume fractions and extrapolating to a volume fraction of one. This procedure requires accurate values of laminate stiffnesses and, as shown in reference [2], ultrasonic velocity measurements offer the best approach to this determination.

In general, fiber reinforced composite materials are classified as orthotropic, having nine independent engineering constants. For some composites, particularly those having graphite fibers, the material may be assumed to be transversely isotropic; i.e., the plane perpendicular to the fibers is isotropic. In such cases, the number of independent engineering constants reduces to five. Letting the fiber direction be the "1" direction, the transverse direction in the plane of the lamina be the "2" direction, and the transverse direction out of the plane of the lamina be the "3" direction, the independent constants are E_{11}, $E_{22} = E_{33}$, $\nu_{12} = \nu_{13}$, ν_{23}, and $G_{12} = G_{13}$ where E_{ij}, ν_{ij}, and G_{ij} are Young's moduli, Poisson's ratios, and shear moduli, respectively. The shear modulus of the isotropic transverse plane is

$$G_{23} = \frac{E_{22}}{2(1+\nu_{23})} .$$

The in-plane elastic constants are frequently determined from data obtained during carefully controlled tensile tests with appropriately oriented rosette strain gages. However, out-of-plane properties (ν_{23} and G_{23}) cannot be determined from customary tensile test data. For convenience, it is often assumed that $\nu_{23} \approx \nu_{12}$ and $G_{23} \approx G_{12}$ in the numerical solution of stress analysis problems. Although these assumptions are quite common, they are not valid and introduce errors in the calculated intralaminar normal and shear stresses, in particular.

However, the elastic constants of a unidirectional composite can be determined by measuring the phase velocities of ultrasonic longitudinal and shear waves propagating through specimens at selected angles with respect to the lamina coordinates. The equations relating elastic stiffness components, C_{ij}, and wave phase velocities, c_{ij}, are presented in reference [2]. The engineering constants are calculated from the stiffness components using equations also give in reference [2].

The test specimens were machined from a 25.4 x 25.4 x 152.4 mm (1 in x 1 in x 6 in) block of unidirectional graphite epoxy. The size and orientation of each specimen were determined to ensure that the propagating wave did not reflect from unexpected boundaries by considering the deviation between the direction of the energy propagation (energy flux vector) and the wave normal. A Matec pulse generator with a 1-20 MHz rf plug-in was used along with Panametric transducers M110 and V156 to propagate 5 MHz longitudinal and shear waves respectively. A fused quartz delay block was bonded to the specimen using phenyl salicylate to provide sufficient time separation between the sending and receiving transducer waveforms on an oscilloscope screen so that accurate measurements could be made.

A wave phase velocity was determined by first measuring the time required for a group of stress waves to travel through the delay block and graphite-epoxy specimen. A second measurement was made to determine the time required for the same group of stress waves to travel through the delay block. The wave phase velocity was computed using the difference in time between the two received signals and the thickness of the specimen. At the same time, experimental checks were made on the deviation of the energy flux from the direction of the wave normal, and it was found that the angle of deviation was very close to that predicted from the usual homogeneous, anisotropic wave theory.

[1]Figures in brackets indicate the literature references at the end of this paper.

The values of G_{23} and ν_{23} calculated from the experimental wave velocity measurements e plotted in figures 1 and 2. These values lie between the upper and lower bound edictions from Hashin's equations [1] modified for transversely isotropic fiber properties. though the experimental value of ν_{23} falls within an acceptable range, the value obtained r ν_{23} is very sensitive to the accuracy to which the wave phase speeds can be measured. e experiments must be carried out very carefully to minimize errors in measurement. One of e most important uses of the engineering constants G_{23} and ν_{23} is in stress analysis of mposite laminates. Analytical values of interlaminar normal and shear stresses, which use delamination type failures, are sensitive to these properties. Interlaminar stresses mputed by assuming $\nu_{23} = \nu_{12}$ and $G_{23} = G_{12}$ are nonconservative and could result in early ilures when used in a design failure criterion.

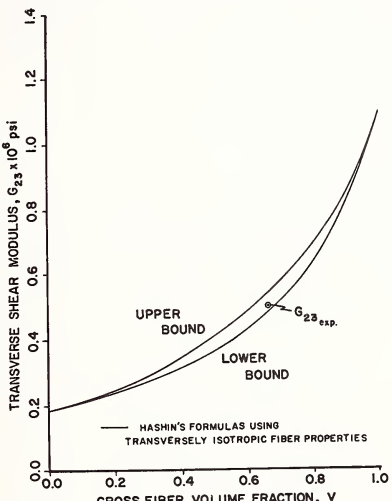

Figure 1. Transverse shear modulus, G_{23}, for AS-3501 graphite-epoxy.

2.2. Determination of material quality

Another need for the characterization of composite materials is a method for describing ie initial quality of the material in terms of an expected load carrying ability. One of ie research programs performed in our laboratory had as its major objective a parametric udy of the effect of fabrication variables upon the quality of unidirectional graphite- lyimide laminates. The laminates were tested by loading small, 6.4 mm x 12.70 mm, (1/4 in 1/2 in), fifteen plies thick, short beam shear specimens to failure [3]. In addition, trasonic attenuation measurements were performed on each specimen prior to testing in the ort beam test rig. The attenuation was measured by using a modified delay block technique d determining the amplitudes of two consecutive major echoes plus the amplitudes of echoes dded to the trailing edge of the major echo by multiple reflections inside the thin specimen. tails of the experimental technique and the analysis are give in reference [4].

The ultrasonic attenuation data were observed to correlate quite well with the observed ilure loads in each specimen (fig. 3). A higher initial value of attenuation typically s found in those specimens which failed at the lower loads. Since failure of the short am test specimens is controlled by the quality of the interlaminar bond and since the trasonic wave propagated perpendicularly to the laminate interfaces, the correlation is ysically meaningful.

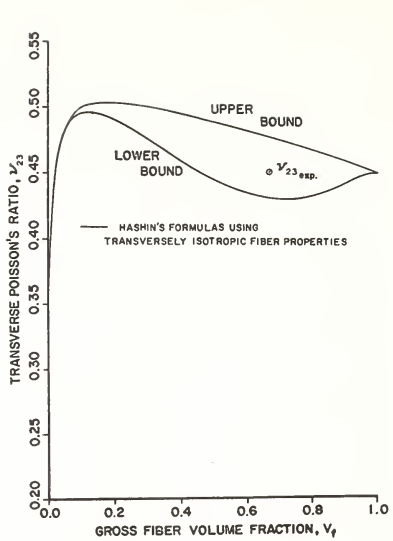

Figure 2. Transverse Poisson's ratio, ν_{23}, for AS-3501 graphite-epoxy.

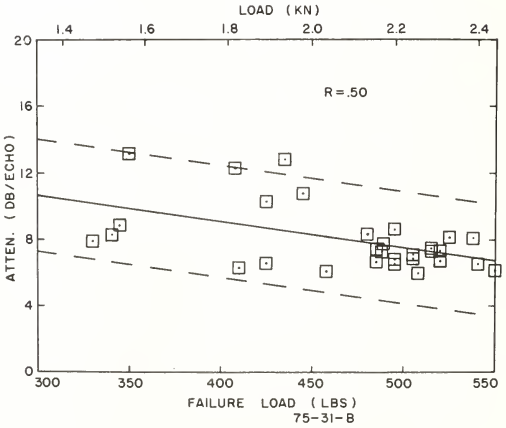

Figure 3. Attenuation versus failure load for graphite-polyimide, unidirectional laminate.

To complement the information obtained from the ultrasonic attenuation method, an ultrasonic C-scan was also taken of a graphite-panel before it was sectioned into the short beam shear specimens (fig. 4). In figure 4a, the dark regions represent an area of poorer quality material in the sense that a reduced amount of ultrasonic energy was able to propagate

ough the material. Attenuation measurements were taken by placing a 12.7 mm diameter nsducer in each of the regions marked 1-10 in figure 4a and by using the modified delay ck technique. The percentage of dark area obtained by the C-scan follows very closely h the value of the ultrasonic attenuation, as one would hope, since the data obtained by two methods should be similar. The attenuation technique has the advantage of giving an ediate quantitative parameter that might be correlated with other physical properties. this specimen the attenuation values again correlated closely with the observed failure engths of the short-beam test specimens.

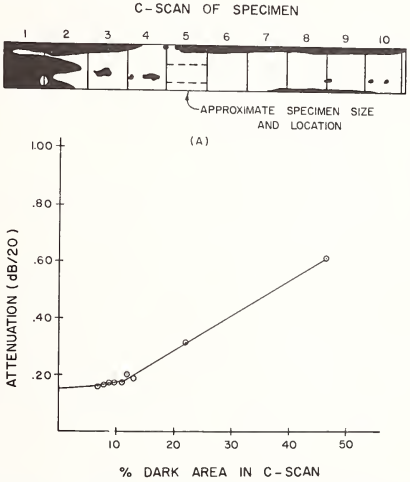

Figure 4. (a) Ultrasonic C-scan of graphite-polyimide specimen showing dark regions of poorer quality. (b) Average attenuation measured by pulse-echo method plotted versus the percentage of dark area found in each region on the C-scan.

Another test program was performed on a number of boron-aluminum composite laminates, $[\pm 45,0]_s$, that had a significant number of visible surface defects. These specimens were tially radiographed and C-scanned prior to testing in fatigue [5]. The results of this tial survey, (fig. 5), show some overlapping of inferior quality areas as determined by two techniques, but, for the most part, the two methods are supplementary. The speci- ıs were tested in fatigue to 100,000 cycles, a final C-scan was made, and their residual engths were determined by loading to failure. It was found that the amount of initial face damage could not be used to discriminate between "good" and "bad" laminates (except the case of gross damage where a flaw cut into many fibers). More interestingly, the ıal fracture surfaces of the boron-aluminum specimens always coincided with defects which e indicated in the initial or final C-scans. Most of these critical regions were regions ıt had grown during fatigue from initially indicated poor regions.

3. Damage Characterization

In addition to being able to categorize the initial quality of a composite material, it necessary to be able to characterize the initiation and progression of damage in these erials as a function of various load histories, particularly as this damage relates to ıer important parameters such as stiffness and strength. The development of damage in ıposite materials under cyclic loading, usually referred to as fatigue degradation, is a

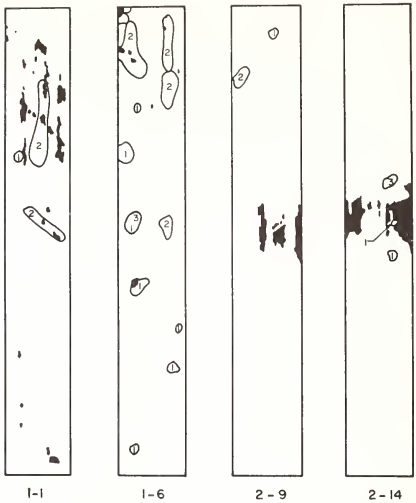

Figure 5. Initial x ray (lined areas) and C-scan (solid areas) comparisons.
Key: 1 - stray filament, 2 - misaligned filament, 3 - broken filament.

difficult process to monitor. While uniform homogeneous materials such as common metals usually develop a single dominant crack which propagates across the component to cause eventual failure, composite materials do not usually fail by such a relatively simple process. Rather, the constituant materials may fail individually in isolated localities, or separate from one another, or break up in some specific pattern depending upon the local distribution of stress and strength among the different phases of material. In fiberous composites, such as boron-epoxy (BEp) or graphite-epoxy (GEp) such failure events are referred to as fiber or matrix cracking, delamination, or debonding. The complex manner in which these damage components combine to cause specimen life, strength or stiffness reduction makes a choice of nondestructive test method to monitor damage development very difficult. Since no single physical or mechanical process completely characterizes damage, no single nondestructive test method is likely to be able to completely characterize fatigue degradation.

Several ultrasonic nondestructive test methods can be used, however, for general and specialized evaluation of damage development. In the general case it is desirable to have a method which is sensitive to the initiation of damage, i.e., a technique which is very sensitive to the threshold of damage development. For example, laminated composite materials have different levels of strength relative to the direction of a given applied load, a property called anisotropy. In particular, each layer or ply of the laminate will fail or degrade at a different stress level than its neighbor which has a different orientation of "strong" or "weak" directions, in general. However, the engineer must know when the first such damage just begins in the "weakest" ply at a load which he then identifies as the "first ply failure load". This requirement is very difficult to meet because the first damage usually consists of very small cracks or plastic flow of the matrix material in certain plies of the laminate buried inside numerous other undegraded plies, i.e., the damage is small in type and amount, and it is generally in the interior of the specimen or component.

In our laboratories at Virginia Tech a method has been originated for detecting this damage initiation which is very sensitive and quite reliable. Figure 6 shows an example of the output of that technique. The figure shows a plot of ultrasonic attenuation superposed on a stress-strain curve for quasi-static tensile loading of a GEp laminate having a stacking

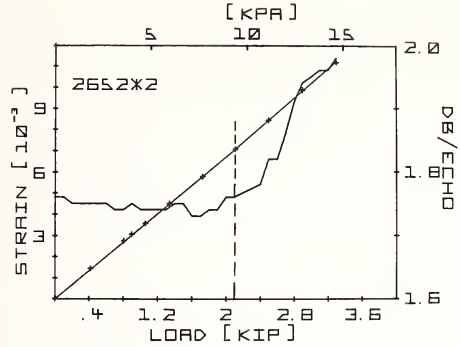

Figure 6. Correlation of ultrasonic attenuation with stress-strain response for a graphite-epoxy specimen with a $[0,\pm45,90]_s$ stacking sequence.

sequence of $[0,\pm45,90]_s$. The attenuation curve begins to change at a load of about 3.56 KN (800 lb). Microscopic examinations have shown that damage initiation begins at that load level. As loading continues the attenuation rises very sharply, showing the progress of degradation of the "weak" plies in a much more sensitive and precise way than any other NDT&E technique used by the present authors (or which they have seen reported). The unique aspect of this method is that the ultrasonic attenuation is due to diffraction of the incident ultrasonic beam by the microcracks that form in the "weak" plies. This diffraction is due to the general nature of the crack formation. In particular, it has been found that cracks form in a regularly spaced array determined by the mechanics of the stress redistribution between the plies as the cracks form [6]. The number of cracks, and therefore the array spacing depends upon the applied load level. As loads approaching the failure strength of the laminate are reached the crack spacing becomes essentially constant, i.e., no new cracks are formed beyond a "characteristic" spacing. These details are important to the mechanical response of the laminate.

The ultrasonic diffraction method is an excellent way to follow the development of these cracks. Figure 7 shows another ultrasonic attenuation vs. load plot for a GEp laminate with a $[0,\pm45,90]_s$ stacking sequence. The ultrasonic attenuation changes dramatically as cracks

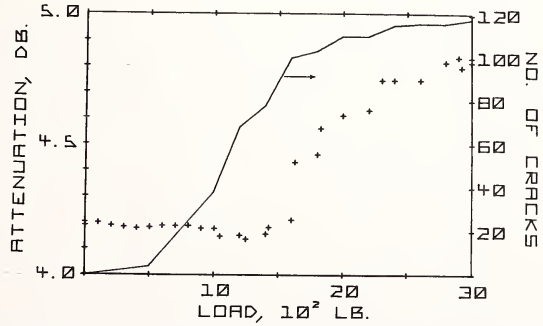

Figure 7. Correlation of ultrasonic attenuation and crack count with load for a graphite-epoxy specimen with a $[0,\pm45,90]_s$ stacking sequence.

develop between about 6.23 KN (1400 lb) and 13.3 KN (3000 lb) but levels off above and below that range. The crack count in the 90° plies of that laminate is also plotted in that figure. It can be seen that it has the same general shape. Of course, it is not necessary for the attenuation to increase or decrease monotonically in a diffraction situation as the diffraction grating (the cracks in this case) changes, as seen by an "observer" (receiving transducer) downstream from the diffraction event. The details of the present situation have been worked out by Hayford and Henneke [7]. In the present case the first change in attenuation is a decrease as the cracks begin to form, followed by a sharp increase with a greater number of cracks later on. The expected predicted behavior, using a simple diffraction model, is shown in figure 8 for several different crack openings, w. In the model used, the cracks were assumed to be rectangular screens equally spaced across the face of the transducer with widths that were in the range of experimentally observed crack openings.

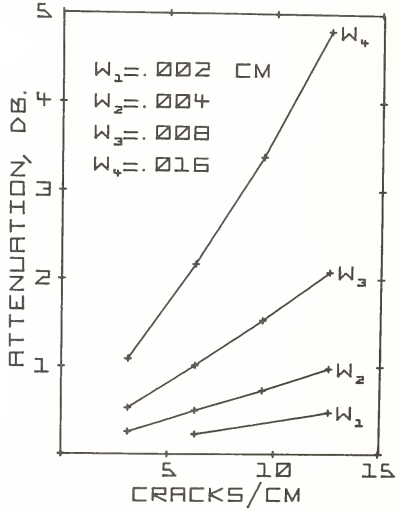

Figure 8. Theoretically predicted values of attenuation versus crack spacing for various crack openings, w.

It is also helpful to use other nondestructive test methods to assist in the interpretation of ultrasonic data. Figure 9 shows a correlation of acoustic emission rate and crack count with load level for a specimen technically identical to that shown in figure 8. It is again evident that cracking begins at a rather well defined load interval and that the rate of cracking (and the rate of acoustic emission) drops off as the higher loads are reached, assisting in our interpretation of the physical situation. The existence, and general nature, of the characteristic damage state mentioned earlier has been firmly established through the use of ultrasonic attenuation and acoustic emission along with replication and sectioning of these laminates following static and fatigue loading [6].

Another important use of ultrasonics for composite material damage characterization is the determination of elastic modulus values by the measurement of wave velocities as discussed in a previous section. Elastic modulus values are especially important in these materials for two reasons. First, damage such as microcracking of the matrix, delamination and fiber breakage is known to cause early and substantial stiffness change as it develops [8]. In contrast to metals, this stiffness change is manifested as a global (or macroscopic) variation in general, and is a monotonic indicator of the amount of damage present. It is also an excellent indicator of the type of damage present. Because the elastic modulus is a fourth order tensor which has four independent components in the plane of the laminate for an

thotropic material, the comparative changes in each of these four independent quantities n be used to discriminate various types of damage, i.e., the measurement technique is nsitive to damage mode as well as damage amount. This four-parameter stiffness measurement heme is under development in our laboratories.

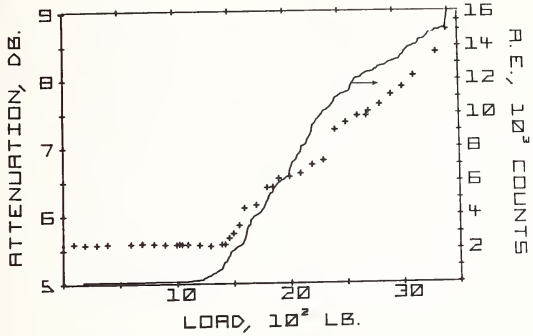

Figure 9. Correlation of ultrasonic attenuation and acoustic emission with load for a graphite epoxy specimen with a $[0,\pm45,90]_s$ stacking sequence.

Ultrasonic C-scan methods are well established and have been widely used in composite aterials. However, a particularly useful application of this technique in our laboratories as unusual. The need existed to follow the growth of an embedded flaw in connection with an nvestigation of the effect of constraint on flaw growth in composite laminates. The pecimens consisted of one or two plies with a center notch embedded between several outside lies, having different fiber orientations. The specimens were then loaded either statically r in fatigue and the growth of the flaw compared to the unconstrained behavior. Residual trengths and life were also compared. Particular attention was paid to the nature of the amage growth as a function of the type of embedded flaw and the type of constraining ayers. It was verified by destructive sectioning in some cases that the C-scan method could e used to follow the development of the internal defect, especially the growth of elamination regions. An example of this is shown in figure 10. That figure shows C-scan atterns at several different numbers of cycles of stress. The specimen was a 0° center-otched ply constrained by 90° plies and was cycled at 100 percent of the notched strength of he 0° ply unconstrained (unidirectional) laminate. The degree of damage is clearly elineated. Damage growth rates and damage modes were determined by this method. The echnique is especially helpful in following damage which is coupled together to form a amage zone, as opposed to scattered damage which is not coupled and does not relate to a ingle damage source such as a notch. The key to this last point is probably a result of the ensitivity of the method to delamination since cracks frequently combine to form a damage one by delamination between plies of the laminate.

4. Summary and Conclusions

Ultrasonic testing methods that have been well established over the years for pplication to metals and alloys cannot be immediately and directly applied to composite aterials. Because the latter are both heterogeneous and anisotropic, additional omplications arise in the mechanics of the interaction of the stress waves with the aterial. This fact leads to a variety of new problems for research that are both difficult nd interesting. The present report has attempted to survey several applications of ultra-onics to material and damage characterization in several different composite material ystems that have been used in our laboratory. The determination of phase velocity has been sed to determine the elastic constants needed to define the constitutive law for a nidirectional graphite-epoxy laminate. The two out-of-plane properties G_{23} and ν_{23}, which

are important in the analysis of interlaminar normal and shear stresses, cannot be measured by the standard tension tests. The values determined ultrasonically were within the upper and lower bounds predicted by Hashin's model [2].

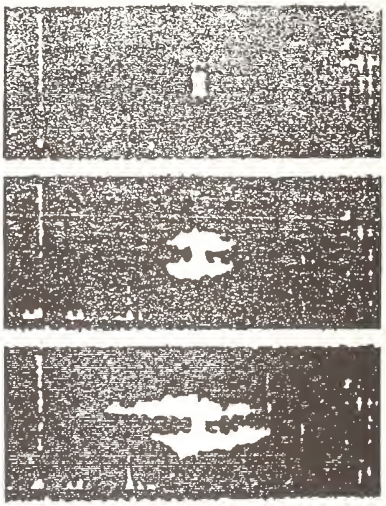

Figure 10. Development of an internal flaw as revealed by ultrasonic C-scan techniques.

Also, the initial state of the material was characterized ultrasonically by either of two techniques, a modified buffer rod, pulse-echo method and a C-scan. The attenuation of the stress waves as measured by the first method was found to correlate closely with the observed failure loads as measured by the short-beam shear test for graphite-polyimide specimens. The final fracture surface found after loading to failure previously fatigued boron-aluminum specimens always coincided with a region which had been delineated by the C-scan as being of poorer quality. The difficulty here is that not every region so delineated obviously grew into the final failure surface and it was not possible to predict a priori which region would do so.

The major utility of ultrasonics in our laboratory has been in the area of damage characterization. Since composite materials do not generally fail by the growth of a single crack in a self-similar fashion, the usual ultrasonic methods for flaw detection are not viable here. It has been found, however, that the pulse-echo method can be used, together with a diffraction model, to identify the load at which first damage occurs in the weakest plies in a laminate. Further, this method is very sensitive to the subsequent growth of this damage. Together with other NDT techniques such as replication, acoustic emission and thermography, ultrasonics has enabled us for the first time to identify a characteristic damage state in graphite-epoxy laminates that ultimately leads to final failure.

The work reported herein has been supported by a number of different projects under the guidance of three agencies. We hereby gratefully acknowledge their aid: the Air Force Materials Laboratory, NASA-Langley Research Center, and the National Science Foundation.

References

[1] Hashin, Z., Theory of Fiber Reinforced Materials, NASA CR-1974 (March 1972).

[2] Kriz, R. D. and Stinchcomb, W. W., Mechanical Properties for Thick Fiber Reinforced Composite Materials Having Transversely Isotropic Fibers, College of Engineering, Virginia Polytechnic Institute and State University, Report No. VPI-E-77-13 (May 1977).

[3] Stinchcomb, W. W., Henneke, E. G., and Price, H. L., Use of the short-beam shear test for quality control of graphite-polyimide laminates, in Reproducibility and Accuracy of Mechanical Tests, STP 626, American Society for Testing and Materials, pp. 96-109 (Phila., Pa. 1977).

[4] Hayford, D. T., Henneke, E. G., and Stinchcomb, W. W., The correlation of ultrasonic attenuation and shear strength in graphite-polyimide composites, J. Composite Materials, 11, 429-444 (1977).

[5] Knott, M. A., The Detection and Effect of Fabrication Damage in Boron Aluminum Composites, Master's Thesis, Department of Engineering Science and Mechanics, Virginia Polytechnic Institute and State University (September 1976).

[6] Reifsnider, K. L., Henneke, II, E. G., and Stinchcomb, W. W., Defect-Property Relationships in Composite Materials, AFML-TR-76-81, Part III, Wright Patterson AFB (May 1978).

[7] Hayford, D. T. and Henneke, II, E. G., A model for correlating damage and ultrasonic attenuation in composites, submitted for publication in the Proceedings of the 5th ASTM Conference on Composite Materials: Testing and Design, New Orleans (March 20-21, 1978).

[8] O'Brien, T. K. and Reifsnider, K. L., Fatigue damage, stiffness/strength comparisons for composite materials, J. Testing Evaluation, 5, 384-393 (1977).

National Bureau of Standards Special Publication 596, Ultrasonic Materials Characterization, H. Berger and M. Linzer, eds., Proceedings of the First International Symposium on Ultrasonic Materials Characterization held at NBS, Gaithersburg, Md., June 7-9, 1978. Issued November, 1980.

QUANTITATIVE DETERMINATION OF GRAIN SIZE AND DETECTION OF INHOMOGENEITIES IN STEEL BY ULTRASONIC BACKSCATTERING MEASUREMENTS

K. Goebbels and P. Höller

Fraunhofer-Gesellschaft
Institut für zerstörungsfreie Prüfverfahren
Universität, Geb. 37, D-6600 Saarbrücken 11
Federal Republic of Germany

Ultrasonic waves in steel are attenuated by absorption and scattering. Scattering from grain boundaries (elastic anisotropy) or phase boundaries (acoustic impedance) can be measured quantitatively. In backscattering experiments, scattering signals are detected and evaluated as a function of time-of-flight. For polycrystalline quasi-monophasic systems (where other phases are negligible because of their small dimensions and/or concentrations), the scattering coefficient can be calculated quantitatively. Several methods allow one to evaluate the mean grain size by backscattering measurements: 1) measurements with two frequencies, provided the frequency dependence of the absorption coefficient is known, 2) measurements of two samples with one frequency, provided the absorption coefficient is the same in the two samples and, 3) one measurement with a frequency high enough that multiple scattering is generated.

For different types of austenitic and ferritic steels with grain sizes between ASTM 1 and ASTM 10, results from more than 200 samples confirm the applicability of the grain size determination method. Regions of inhomogeneities in steel (inclusions, microcracks, welds) can be characterized in a simple way by backscattering measurements: scattering signals from these structures are superimposed on the scattering from the base material. Therefore, the extension and the grade of inhomogeneities can be described qualitatively. At the moment, it is not possible to determine the exact kind of anomalies present.

1. Introduction

Energy losses of ultrasonic waves propagating in steel are caused by absorption and scattering processes. By absorption, the elastic energy of the wave is changed into heat. Scattering causes vibrations of the grains, inclusions, etc., within the ultrasonic beam and the superposition of these vibrations is the scattered wave, going out in all directions. Therefore, backscattering can be measured in a simple way if the transmitting transducer is also acting as the receiver. Two features determine scattering: 1) the variation of acoustic impedance at grain boundaries or phase boundaries, and 2) the ratio d/λ between the linear dimension d of the scatterer (e.g., grain size, crack length, inclusion diameter) and the ultrasonic wavelength λ.

At grain boundaries, the elastic anisotropy of the single grain is responsible for the scattering process; at phase boundaries, there are variations in ultrasonic velocity and/or density. Mostly scattering is observed in the Rayleigh region ($d/\lambda \ll 1$) and in the stochastic region ($d/\lambda \approx 1$). Scattering goes to zero for $d/\lambda \to 0$ and for $d/\lambda \to \infty$ (where scattering changes into geometrical reflection). Therefore, this paper deals with the characterization of materials by backscattering measurements and the qualitative and quantitative evaluation of the scattering coefficient α_S.

2. Theoretical Background

For homogeneous materials the amplitude A(x) of an ultrasonic pulse shows an exponential decay [1][1] with increasing sound path x:

$$A(x) = A_o \, e^{-\alpha x} \quad ,$$

where beam diffraction is disregarded. A_o is the amplitude excited in the surface region at x = 0, and

$$\alpha = \alpha_A + \alpha_S$$

where α is the attenuation coefficient (sound pressure), and α_A is the absorption coefficient. In a similar manner the backscattering amplitude $A_S(x)$ is given by [2]

$$A_S(x) = A_o(\alpha_S \Delta)^{1/2} \, e^{-\alpha x} \qquad (1)$$

where Δ is the pulse length.

The scattering coefficient α_S can be calculated, e.g., for quasi-monophasic systems, where other phases are negligible with regard to their contribution to the measured scattering because of their small dimensions and/or small concentrations. For cubic crystallized materials and shear waves in the Rayleigh region this will be [3]

$$\alpha_S = S \, d^3 \, f^4 \; (mm^{-1})$$

with the frequency, f, and the scattering parameter, S:

$$S = \frac{6\pi^3}{375} \cdot \frac{1}{\rho^2} \cdot \frac{1}{v_s^3} \left(\frac{2}{v_1^5} + \frac{3}{v_s^5}\right) \cdot (c_{11} - c_{12} - 2c_{44})^2 \quad .$$

Here ρ is the density, v_1 and v_s are the velocities of longitudinal and shear waves and c_{11}, c_{12} and c_{44} are the elastic moduli of the single crystal materials.

For ferritic and austenitic steels, $S \approx 0.0131 \; (mm/\mu s)^{-4}$ and the mean grain size d can be calculated if α_S is known. The problem is to separate α_S from the product $A_o(\alpha_S \Delta)^{1/2}$ or the sum $\alpha_A + \alpha_S$. There are different ways to solve this problem [4-6]: 1) if the frequency dependence of α_A (e.g. $\alpha_A \sim f$) is known, then two backscattering measurements with two different frequencies f_1, f_2 allow one to calculate α_A and α_S separately (see fig. 1):

$$\alpha_1 = a f_1 + S d^3 f_1^4 \quad , \qquad \alpha_2 = a f_2 + S d^3 f_2^4 \quad ,$$

$$d = [(\alpha_2 - \alpha_1 f_2 / f_1)/(S f_2 \{ f_2^3 - f_1^3 \})]^{1/3} \quad .$$

2) If the absorption coefficient α_A can be assumed to be the same in two samples with different grain sizes d_1, d_2, then one backscattering measurement on each of the samples with one frequency leads to α_A and to the values for α_S (see fig. 2):

$$A_{S1}(0) = A_o \sqrt{\alpha_{S1} \Delta} \quad , \qquad A_{S2}(0) = A_o \sqrt{\alpha_{S2} \Delta} \quad ,$$

$$\alpha_1 = \alpha_A + S \, d_1^3 \, f^4 \quad , \qquad \alpha_2 = \alpha_A + S \, d_2^3 \, f^4 \quad ,$$

[1]Figures in brackets indicate the literature references at the end of this paper.

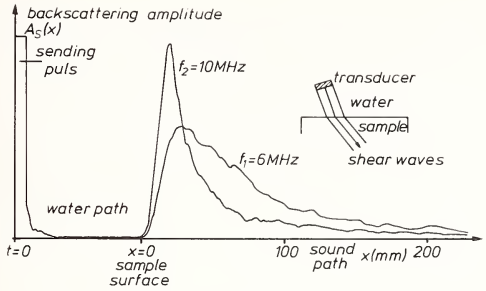

Figure 1. Backscattering amplitudes from austenitic steel for two different frequencies.

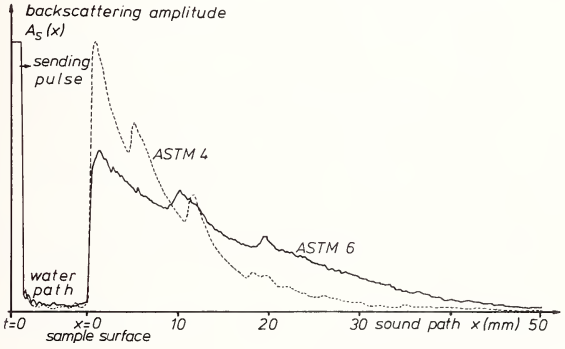

Figure 2. Backscattering amplitudes from two different ferritic steels (6 MHz, shear waves).

and therefore with i,j = 1,2:

$$d_i = [(\alpha_i - \alpha_j)/(Sf^4 \left\{1 - A_{Sj}^2(0)/A_{Si}^2(0)\right\})]^{1/3}$$

3) If the scattering coefficient is so great that multiple scattering is present (i.e. because of high frequency or grain size (see fig. 3), new scattering of the previous scattered ultrasound delivers a measurable additional amount of backscattering amplitude) then the backscattering amplitude $A_{SM}(x)$ is given by [6]

$$A_{SM}(x) = A_S(x) \cdot \left[1 + ce^{2\alpha_S x}\right]^{1/2}$$

where c is a constant but depends on α_S. In this case, by the transformation

$$\ln (A_{SM}^2(x)/A_S^2(x) - 1) = \ln c + 2\alpha_S x$$

one measurement with one frequency and with no assumptions concerning α_A allows one to calculate α_S and d.

For inhomogeneous materials, where the local structure is changed by inclusions, segregations, fields of microcracks, or welds, the coefficients α, α_A and especially α_S are functions of x and eq. (1) changes into

$$A_S(x) = A_0(\alpha_S(\tfrac{x}{2})\Delta^{1/2} \exp(-2\int_0^{x/2}\alpha(z)\,dz) \quad . \tag{2}$$

This is sketched in figure 4 with realistic values for α, α_A and α_S (6 MHz, shear waves, fine-grained steel).

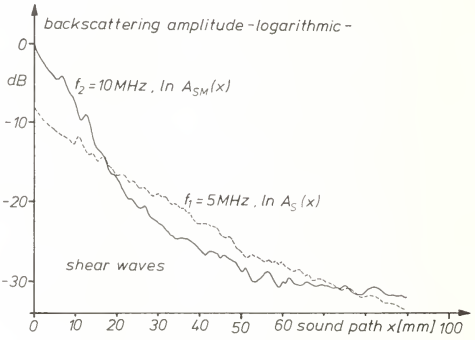

Figure 3. Semi-logarithmic plot of backscattering amplitudes from coarse grained austenitic steel (ASTM 3) with and without multiple scattering present.

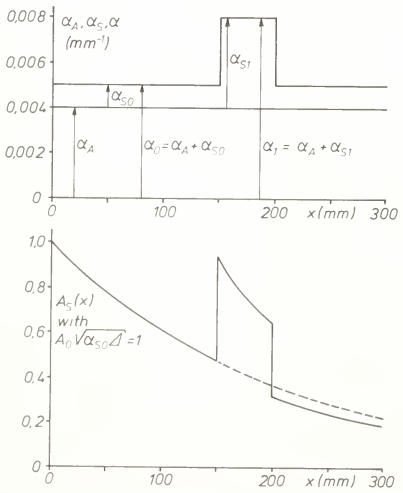

Figure 4. Schematic description of backscattering amplitude from a locally inhomogeneous structure.

3. Measurement Technique

Backscattering signal amplitudes lie about 40 to 60 dB (disregarding coarse grained ustenitic steels and welds) below usual ultrasonic signals like backwall echoes. Therefore, sensitive technique is needed for the quantitative detection of the scattering signals. igure 5 shows the block diagram of the equipment used. The high frequency burst is ampli- ied by a broad band power amplifier and a transmitting-receiving circuit protects the high ain receive amplifier (with a bandwidth of 3 MHz) against overload due to the transmitting ulse. The amplifier rectifies the scattering signal which is then digitized by an analog- o-digital-converter (ADC). The ADC is interfaced alternatively to a signal-averager (to sum selectable number of A-Scans by hardware) or directly to the computer memory (to do the ame by software). The backscattering measurement can be executed using either contact or mmersion technique. Surface condition of the material under test influences the result only ualitatively, but not quantitatively.

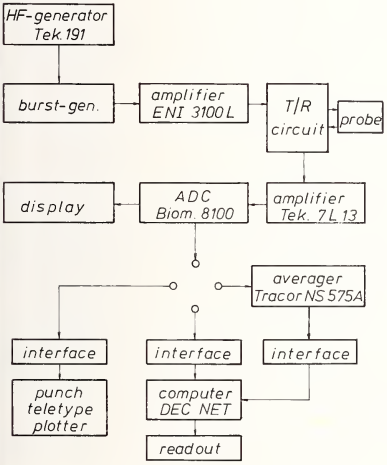

Figure 5. Block diagram of the equipment used for backscattering measurements.

4. Results

Shear wave backscattering measurements with frequencies from 4 to 20 MHz, on more than 200 samples of different types of ferritic and austenitic steels with grain sizes from ASTM 10 to 1, have confirmed the quantitative grain size determination by the methods described above. In figure 6 the comparison is made between the values determined by ultrasonics and by metallography for about 80 samples. The accuracy of the values d_{US} lies at ± 15 percent if the following condition is satisfied:

$$0.05 \lesssim d/\lambda \lesssim 0.5 \quad .$$

Grain sizes from ASTM 10 to 6 and 6 to 4 were analyzed with frequencies from 10 to 20, and 5 to 10 MHz respectively. For ASTM 4 to 1, the values d_{US} were obtained by the evaluation of the multiple scattering method with a frequency at about 6 MHz.

All the results confirm that, for steel, the grain size region examined and the frequencies used, the linear relationship between α_A and f holds good. The evaluation of the

absorption coefficient shows a mean value of $\alpha_A\lambda$ 0.007 where the single results scatter from 0.001 to 0.014. α_A seems to be correlated to the chemical composition of the steel but, as expected, not to the grain size.

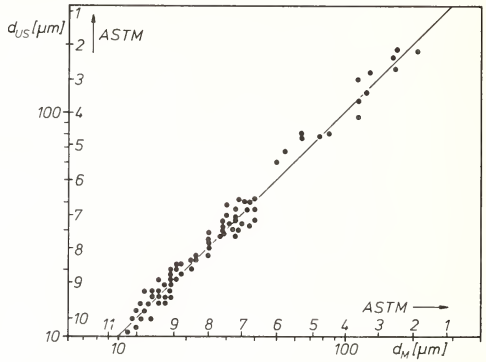

Figure 6. Comparison between grain-size determination by ultrasonics (d_{US}) and my metallography (d_M).

While homogeneous structures may be characterized by backscattering curves with an exponential decay (eq. (1) and figs. 1-3) this is not the case if inhomogeneities are present to a measurable extent (eq. (2), fig. 4). The exponential decay is locally superimposed by additional scattering indications from the inhomogeneities. Figure 7 shows three characteristic examples of structural anomalies detected by the backscattering measurement technique (shear waves, 6 MHz, 45°): 1) a small zone of pearlite segregations in the middle of a thin plate leads to a signal on the scattering curve between the surface and backwall. Because of the angle of incidence, beam spread and pulse length, the extension of some millimeters on the backscattering curve is higher than the metallographically analyzed zone width (0.5 mm). 2) Inclusions of MnS over a range of 50 mm in the middle of a reactor pressure vessel steel block (22 NiMoCr 3.7) with 220 mm thickness are well indicated by additional scattering signals. 3) In a similar way, fields of microcracks and cracks with lengths below 1 mm were found in the middle of an other test block (same steel) with 120 mm thickness. The extension of the region of inhomogeneities is also in agreement with the metallographic analysis.

These examples show that the detection of inhomogeneities by backscattering measurements is easy to obtain, but at the moment, there is no possibility to describe the kind of anomalies producing the additional scattering signals.

The oriented crystal growing process in ferritic and austenitic welds results in special scattering indications as shown in figure 8. The fusion line and the overlap of the passes lead to additional signals when high frequency ultrasonic waves (10 MHz, longitudinal waves in fig. 8) propagate through the weld. Figure 9 shows the application to a nozzle test piece with 210 mm thickness. Shear waves propagating under 45° from different points on the surface give a clear impression from the test piece: the plate material shows in the middle, inhomogeneities which can be well distinguished from a single defect in the fusion line.

5. Discussion

Measurements of backscattered ultrasonic waves, developed earlier [7], allow a quantitative grain size determination by different methods. The limits given here restrict application of these methods to quasi-monophasic and homogeneous systems where the grain size lies between ten and several hundred microns. For multiphasic, inhomogeneous materials and

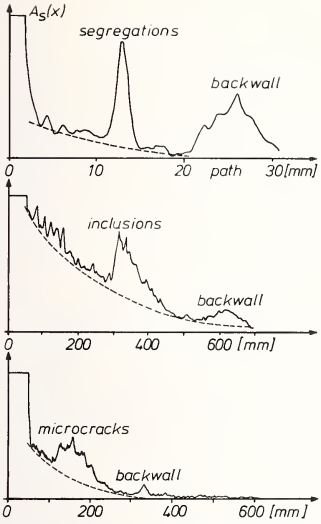

Figure 7. Backscattering amplitudes for different types of inhomogeneous steel structure.

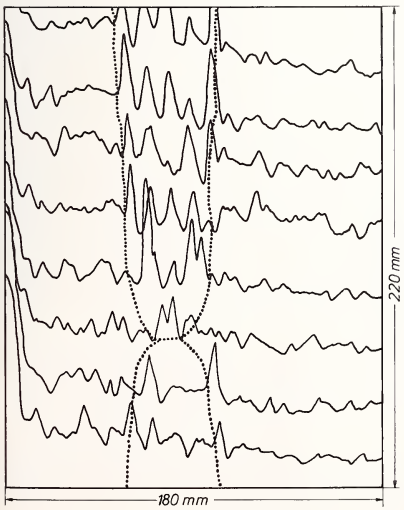

Figure 8. Backscattering amplitudes measured through a ferritic weld.

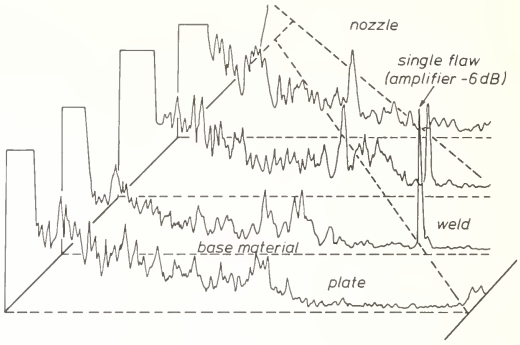

Figure 9. Backscattering amplitudes from a nozzle test block (6 MHz).

for grain sizes exceeding the limits cited, further research has to be done. The qualitative description of structural anomalies like welds, inclusions, microcracks, etc., seems to be of great advantage for the non-destructive characterization of material properties. But there is a need for further development work to distinguish between the different kinds of anomalies, especially for the structure around welds (base material, heat affected zone, fusion line, and weld). Needed are improvements in resolution and quantitative description.

The work described was executed with financial support of the Bundesministerium für Forschung und Technologie (reactor safety research program) and the European Community for Carbon and Steel. The authors wish to thank them for this support.

References

[1] Krautkrämer, J. and H. Werkstoffprüfung mit ultraschall (Springer Verlag, Berlin, West Germany, 1975).

[2] Fay, B., Theoretische betrachtungen zur ultraschallrückstreuung, Acustica, 28, 354 (1973).

[3] Bhatia, A. B. Ultrasonic Absorption (Clarendon, Oxford 1969).

[4] Goebbels, K., Gefügebeurteilung mittels ultraschall-streuung, Materialprüfung, 17, 231 (1975).

[5] Goebbels, K., Method of quantitatively determining the grain size of substances, United State Patent No. 4026 157 (May 31, 1977).

[6] Goebbels, K., Die messung des ultraschall-streukoeffizienten mit hilfe der mehrfach-streuung, Materialprüfung, 18, 86 (1976).

[7] Koppelmann, J., Härtetiefenmessung an stahlwalzen mit ultraschall, Materialprüfung, 9, 401 (1967).

National Bureau of Standards Special Publication 596, Ultrasonic Materials Characterization, H. Berger and M. Linzer, eds., Proceedings of the First International Symposium on Ultrasonic Materials Characterization held at NBS, Gaithersburg, Md., June 7-9, 1978. Issued November, 1980.

A PHASE INSENSITIVE TRANSDUCER-THEORY AND APPLICATION

Joseph S. Heyman, John H. Cantrell, Jr.,[1]
and John D. Whitcomb

NASA Langley Research Center
Laboratory for Ultrasonics
Mail Stop 499
Hampton, VA 23665

Materials characterization with ultrasonics is examined from the viewpoint of the receiving transducer. Signal artifacts are shown to exist for conventional phase-sensitive piezoelectric transducers. The signal artifacts are always present when differing phases (and/or frequencies) are present on any phase-sensitive receiver whose dimensions are greater than an acoustic wavelength. Use of a phase-insensitive ultrasonic receiver based on the acoustoelectric effect is shown to eliminate phase cancellation artifacts.

1. Introduction

Materials characterization with ultrasonics has advanced significantly during the last few years with the advent of high-speed electronics and signal processing. Phased array scanners and tomographic presentations are now practical with computerized systems. One element of the ultrasonic system which is relatively unchanged, however, is the receiving transducer. Conventional transducers are phase-sensitive piezoelectric devices which essentially convert the average acoustic pressure at their surfaces into an electrical signal. A new type of receiver based on the early work of Weinreich [1][2], Hutson and White [2], and Southgate [3] is being applied in the field of nondestructive evaluation (NDE) [4,5,6]. The device is an acoustoelectric transducer (AET), in contrast to piezoelectric devices (e.g., lead zirconate titanate transducers - PZT).

In this paper, we describe the problems encountered using phase-sensitive transducers to measure acoustic attenuation in the presence of spatially varying phase fronts. These problems are significantly reduced with the acoustoelectric transducer since it is insensitive to phase variations in the incident acoustic wave. The fundamental theory of operation of the transducer is described and an example of its application for attenuation measurements is presented and contrasted with conventional piezoelectric transducers. Through transmission "C" scan images of metals with machined flaws were obtained with the AET and are compared with similar scans obtained with conventional transducers. Fatigue damage in a composite specimen (graphite-epoxy) is examined with both AET and piezoelectric transducers. Following ultrasonic examination, the damage type and location were determined with x-ray pictures (enhanced with an opaque penetrant) and by microscopic examination of sections of the specimen.

2. Phase Superposition Effects

Conventional piezoelectric transducers generate an electrical output signal whose amplitude is proportional to the average surface pressure. For normal incidence of plane monochromatic waves, the electrical signal is dependent only on the acoustic amplitudes. However, for multifrequency or multiphase waves, the electrical signal is no longer related only to

[1]NRC Resident Research Associate
[2]Figures in brackets indicate the literature references at the end of this paper.

the amplitude of the incident acoustic waves. These effects can be severe at ultrasonic frequencies [7,8] and can result in total phase cancellation [9].

The nature of the problem is illustrated in figure 1, which represents two noninteracting acoustic waves at normal incidence to the transducer. For the case of "in-phase" incident waves, the superposition results in a large electrical signal (fig. 1a). Figure 1b shows the reduction in electrical signal due to a phase shift between the incident waves. A modulation of the electrical signal is shown (fig. 1c) to result from a frequency shift between the incident waves. In figure 1d, however, the constant electrical signal occurs with an ideal power detector for the three cases of incident waves considered here. Thus, acoustic attenuation measurements obtained with phase sensitive transducers depend not only on attenuation, but also on phase shifts resulting from material inhomogeneity and geometry. On the other hand, an ideal power detector measurement is determined only by absorption and scattering.

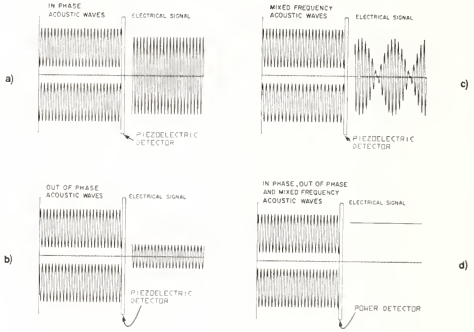

Figure 1. The electrical signal resulting from various acoustic waves incident on a piezoelectric detector and a power detector.

3. Acoustoelectric Transducer

A simple power detector for ultrasonics is a bolometer which measures temperature rise. The bolometer, however, has a very long time constant (seconds) and requires corrections for thermal diffusion and conduction. The inability of bolometers to perform with transient signals severely limits their usefulness.

An ultrasonic power detector compatible with transient signals ($\sim 10^{-6}$ s) has been developed. The device is based on the acoustoelectric effect occurring in piezoelectric semiconductors. The acoustoelectric transducer couples energy from the acoustic wave to free charge carriers in the semiconductor via the Hutson and White [2] absorption mechanism. The coupling mechanism depends on the ratio of the conductivity frequency, $\omega_c = \sigma/\varepsilon$, to the ultrasonic angular frequency, ω, where σ and ε are the material conductivity and dielectric permittivity, respectively. For an AET made from CdS, the absorption for longitudinal waves incident along the CdS crystalline "C" axis is:

$$\alpha = 3.5 \times 10^{-8}\, \omega \left(\frac{\omega_c/\omega}{1 + (\omega_c/\omega)^2} \right) \ (\mathrm{cm}^{-1}) \qquad (1)$$

The absorption of energy to the free charge carriers results in a phase-insensitive electrical signal predicted by the Weinreich relation [1]. The relation describes an acoustoelectric field:

$$E_{AE} = \frac{\Phi \mu \alpha}{v \sigma} \ , \qquad (2)$$

that accompanies absorption to free charge carriers. In eq. (2), Φ is the acoustic flux, μ is the free charge carrier mobility, and v is the velocity of sound. Physically, one may consider the AET signal as resulting from charge carrier "drag" - momentum transfer from the acoustic wave to the charge carriers.

The first use of the acoustoelectric effect for ultrasonics was reported by Southgate [3]. A theoretical analysis of the effects of multiple reflections and nonuniform carrier concentration and mobility is presented by Heyman [5]. The first AET devices used grade "A" CdS cut so as to admit longitudinal waves parallel to the "C" axis. Typically, the CdS AET geometry consists of a single crystal about 1.0 cm^2 in cross section by 0.1 to 1 cm in length (ℓ) (along the propagation axis) such that $\alpha\ell$ is large (typically 0.5).

Grade "A" CdS is photoconductive so that σ is easily varied with incident light to obtain the desired maximum material acoustic absorption from eq. (1). Electrodes applied to the "C" crystal faces then provide a signal containing both the piezoelectric RF voltage across the CdS as well as the acoustoelectric "DC" voltage through the CdS bulk. A new type of solid-state AET has been fabricated [10] which does not require photostimulation and, therefore, is immune to noise resulting from variations in light intensity. Details of the solid-state AET will be published when available. The phase-insensitive characteristics of the AET result in a directivity which rolls off at one tenth the rate of a similar sized piezoelectric transducer [6].

4. Application of the AET to metals

An important material parameter determined with ultrasonics is attenuation (absorption and scattering). Since the AET is insensitive to phase, it is ideal for determining attenuation in inhomogeneous material samples [6] or in biological samples [11]. An example of the errors that are possible using conventional transducers for measuring attenuation is shown in figure 2.

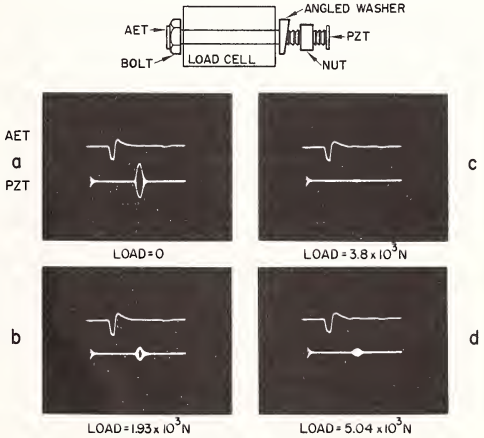

Figure 2. Comparative responses of the AET and PZT transducers to acoustic waves propagating in a nonuniformly loaded bolt. In each picture the upper and lower traces show the response of the AET and PZT transducers, respectively. (a) Zero load. (b) 1.93 x 10^3 N load. (c) 3.80 x 10^3 N load. (d) 5.04 x 10^3 N load.

The top part of figure 2 shows the test configuration for obtaining a stress gradient in a rod. Ultrasonic pulses are generated and the reflection measured by the PZT piezoelectric transducer. In addition, the pulses are measured by the AET transducer bonded

opposite to the PZT transducer. Figures 2a-d show the AET response (top) and the PZT response (bottom) as rod load is increased from 0 to 5 x 10^3 Newtons. Note in figure 2c that the PZT response has nearly nulled due to phase cancellation effects. The AET output remains virtually unchanged for all load levels.

Figure 3 shows the data for figure 2 plotted as an apparent change in attenuation vs load for the two transducers. The large change in attenuation seen by the PZT transducer is explained only by phase cancellation. The AET signal, however, is shown to be nearly constant. In fact, there is a slight decrease in attenuation with applied load followed by a slight increase. The AET response is entirely consistent with wave propagation in a cylindrical waveguide as calculated in reference [12].

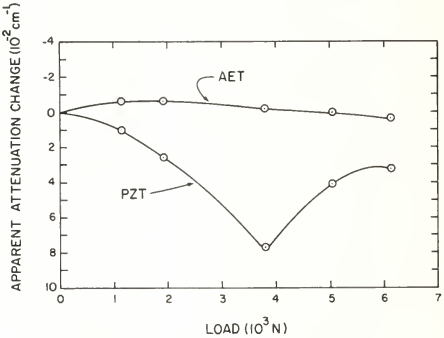

Figure 3. Graph of apparent attenuation change as a function of load for the test situation of figure 2.

Another application of the AET is in acoustical imaging. Most flaws have irregular geometry and hence present complicated phase fronts to the receiving transducer. A typical experimental arrangement is shown in figure 4. Here, plane acoustic waves are generated by an ultrasonic source and for simplicity, are shown being transmitted to a second transducer acting as a detector/receiver. The wave amplitude and phase is shown altered by the material under test. If the pair of transducers is scanned parallel to the material surface, the resulting changes in electrical signal from the receiver map out a spatial image of the material's acoustical properties.

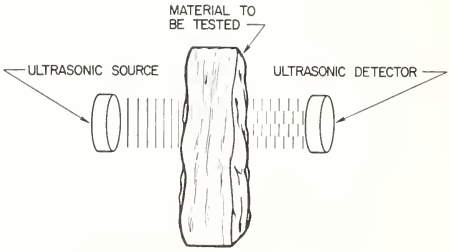

Figure 4. Typical C-scan test configuration.

An example of the acoustical imaging capabilities of the AET is shown in figure 5. The material tested consists of an aluminum plate 1.2 cm thick with engraved letters (NASA) ~0.03 cm deep and ~0.6 cm in height with an engraving line width of about 0.05 cm. Figure 5a

was obtained using a piezoelectric transducer receiver and figure 5b was obtained using an acoustoelectric transducer receiver (each ~1.2 cm diameter). Measurements were made at a frequency of 10 MHz. The phase distortion with the conventional transducer is quite noticeable and appears to show a residual stress field in the vicinity of the letters. The scan obtained with the AET shows a clear image of the letters because the AET is sensitive only to the change in scattered and absorbed sound.

Figure 5. Ultrasonic C-scans of phantom flaws milled into a metal plate. The lettering spells "NASA". (a) Scan using 1.3-cm diameter PZT piezoelectric transducer. (b) Scan using 1.1-cm diameter AET.

A similar imaging test is shown in figure 6. The sample consists of a brass plate 0.08 cm thick containing residual stresses. The residual stresses were produced by pressing a metal washer with a 2 cm hole against the brass plate. A hole (#80 drill ≈ 0.03 cm) was drilled half way through the plate in the region of residual stress. Figure 6a, obtained with a conventional transducer receiver, shows a stress field with perhaps a "hint" of the hole. However, figure 6b, obtained with the AET receiver, clearly shows both the stress field (strain-induced scattering) and the hole. Although it is difficult to image features of dimension less than an acoustic wavelength, especially in a highly strained region, the AET image is clear.

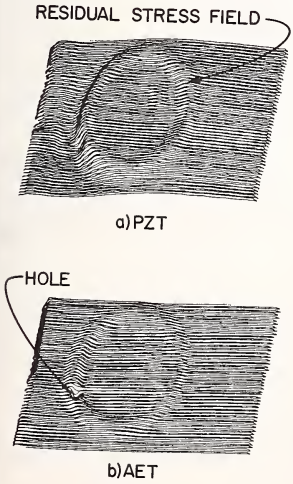

Figure 6. Ultrasonic C-scans of a phantom flaw in the residual stress field produced by imprinting a washer into a metal plate. The phantom flaw is a 0.03 cm hole drilled in the plate. (a) Scan using PZT transducer. (b) Scan using AET.

5. Application of the AET to Composites

The data reported in figures 2, 3, 5, and 6 result from carefully characterized, "machined in" defects in metals. In composites, however, real damage is more complicated. For example, fatigue damage propagation in composites consists of an expansion of a zone of degraded material, in contrast to the colinear crack growth exhibited by metals. Within this zone a complicated combination of fiber breakage, matrix cracking, fiber disbonding and other damage reduces the material strength or stiffness. The type and location of fatigue damage depends on such factors as material, geometry, fiber orientation, and loading.

Ultrasonic attenuation measurements made with the AET were found to be useful for locating fatigue damage in composites. For illustrative purposes a graphite/epoxy laminate with fiber directions of (90°/45°/-45°/0°/0°/-45°/45°/90°) was fatigue tested in tension. The specimen contained a circular hole to localize damage for ease of observation. Attenuation measurements made with a PZT transducer are shown in figure 7a, while measurements made with the AET are shown in figure 7b. The AET results are qualitatively clearer than the PZT results. Significant attenuation occurred around the hole at -45°, 0°, 135°, and 180° (with respect to the load direction).

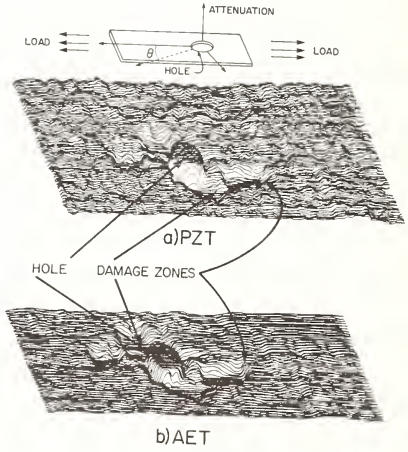

Figure 7. Ultrasonic C-scans of (90°/45°/-45°/0°/0!/-45°/45°/90°) graphite/epoxy specimen. (a) Scan using PZT transducer. (b) Scan using AET.

X radiography and light microscopy were used to ascertain the type and location of fatigue damage. Figure 8a shows a schematic of the specimen. The specimen was sectioned as shown and then examined with a metallograph. Micrographs of several sections are shown in figure 8b. Cracks developed between plies (interlaminar cracks) and through the thickness of the ply, as shown in the figure. The different distribution of cracking in the sections was due to the variation in stress state from point to point.

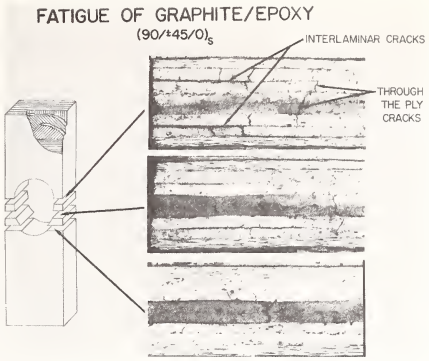

Figure 8. Microscopic fatigue damage in (90°/45°/-45°/0°/0°/-45°/45°/90°) graphite/epoxy specimen.

Figure 9 shows an x ray of the specimen. An opaque penetrant (tetrabromoethane) was pplied to accentuate the cracks. Interlaminar cracks appear as lightened regions; the hrough-the-ply cracks appear as light lines. Comparison of figures 7 and 9 reveals that the egion of high ultrasonic attenuation agrees with the region of interlaminar cracks. Through-he-ply cracking occurred outside the region of high attenuation. Thus, the measurements ere predominantly sensitive to interlaminar damage. The ultrasound technique was insensitive o the through-the-ply cracks because the cracks were parallel to the sound waves, thus the esolved area in the path of the wave was very small.

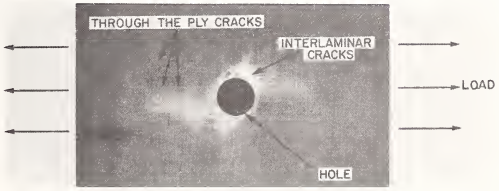

Figure 9. X ray of (90°/45°/-45°/0°/0°/-45°/45°/90°) graphite/epoxy (enhanced with opaque penetrant tetrabromoethane).

6. Summary

Use of conventional phase sensitive transducers is shown to produce anomalous data esulting from phase cancellation at the transducer. Under some circumstances the effect early causes complete signal cancellation. An acoustoelectric transducer is shown to be hase insensitive and thus gives more reliable attenuation measurements of inhomogeneous and eometrically irregular material.

References

[1] Weinreich, G., Ultrasonic attenuation by free carriers in germanium, Phys. Rev., 107, 317 (1957).

[2] Hutson, A. R. and White, D. L., Elastic wave propagation in piezoelectric semiconductors, J. Appl. Phys., 33, 40 (1962).

[3] Southgate, P. D., Use of a power-sensitive detector in pulse-attenuation measurements, J. Acoust. Soc. Amer., 39, 480 (1966).

[4] Heyman, J. S., Ultrasonic Coupling to Optically Generated Charge Carriers in CdS; Physical Phenomena and Applications, Ph.D. Thesis, Washington University (1975) (also NASA TMX-68732).

[5] Heyman, J. S., A phase insensitive acoustoelectric transducer, J. Acoust. Soc. Amer., 64, 243 (1978).

[6] Heyman, J. S. and Cantrell, Jr., J. H., Application of an ultrasonic phase insensitive receiver to material measurements, in IEEE 1977 Ultrasonic Symposium Proc. Cat. #77CH1264-1SU, pp. 124-128 (1977).

[7] Miller, J. G., Heyman, J. S., Weiss, A. N., and Yuhas, D. E., A power sensitive detector for echocardiography and other medical ultrasonic applications, presented at a meeting of the American Institute of Ultrasound in Medicine, (Seattle, WA, Oct. 8-10, 1974).

[8] Marcus, P. W. and Carstensen, E. L., Problems with absorption measurements of inhomogeneous solids, J. Acoust. Soc. Amer., 58, 1334-1335 (1975).

[9] Fuller, Jr., E. R., Granato, A. V., Holder, J., and Naimon, E. R., Ultrasonic studies of the properties of solids, in Methods of Experimental Physics, 11, R. V. Coleman, ed. (New York, Academic Press, 1974).

[10] Heyman, J. S., A solid state phase insensitive ultrasonic transducer, NASA Invention Disclosure LAR-12304-1 (Pending).

[11] Klepper, J. R., Brandenburger, G. H., Busse, L. J., and Miller, J. G., Phase cancellation, reflection, and refraction effects in quantitative ultrasonic attenuation tomography, IEEE Ultrasonic Symposium Proceedings, Cat. #77CH1264-1SU, pp. 182-188 (1977).

[12] Carome, E. F., Witting, J. M., and Fleury, P. A., Experimental study of diffraction and waveguide effects in ultrasonic attenuation measurement, J. Acous. Soc. Amer., 33, 1417 (1961).

National Bureau of Standards Special Publication 596, Ultrasonic Materials Characterization, H. Berger and M. Linzer, eds., Proceedings of the First International Symposium on Ultrasonic Materials Characterization held at NBS, Gaithersburg, Md., June 7-9, 1978. Issued November, 1980.

ULTRASONIC PREDICTION OF GRAIN SIZE, STRENGTH, AND TOUGHNESS IN PLAIN CARBON STEEL

R. Klinman, G. R. Webster, F. J. Marsh, and E. T. Stephenson

Homer Research Laboratories
Bethlehem Steel Corporation
Bethlehem, PA 18016

We propose to use the ultrasonic attenuation due to grain boundary scattering as proxy for grain size in the well-known Hall-Petch relations, which predict mechanical properties of steel. A laboratory experimental program was carried out on plain carbon steels to determine the range of applicability of the method, what information in addition to attenuation would be necessary, the effects of alloy and microstructure, and the accuracy of such predictions.

Our experimental program was based on standard metallurgical and mechanical test procedures and an ultrasonic pulse-echo immersion technique using broad-band pulses and spectral analysis to determine attenuation. The results of testing 46 plain carbon steel plates indicate that ultrasonic attenuation and chemical composition in combination serve to adequately predict some of the mechanical properties. Specifically, statistical analysis of our data shows that at the 95 percent confidence level the lower yield strength may be predicted to ±3.2 ksi (±22 MPa), the tensile strength to ±1.5 ksi (±10 MPa), and transition temperature to ±23 °F (±13 °K).

Although the experimental work was conducted under laboratory conditions, the results to date point to the possibility of developing an ultrasonic attenuation-based on-line method for predicting the mechanical properties of steel.

1. Introduction

Manufacturing requirements for the primary processing industries often include the need to specify the mechanical properties of material shipped to customers. In the steel industry, the classical and current method of obtaining the required information is to remove a representative sample from a portion of the production and analyze the sample through destructive laboratory tests. Limitations of this approach include the fact that less than 100 percent of the production is tested, delays in shipment, and the cost of sample preparation and mechanical testing. Nondestructive on-line measurement of the mechanical properties would alleviate these limitations.

The mechanical properties of primary interest in the steel industry relate to the response of steel at large stresses, i.e., yield and tensile strength. Since nondestructive tests stress a material at much lower levels, the logical deduction is that nondestructive tests cannot be used to directly measure mechanical properties. However, work has been reported [1-4][1] that relates the results of nondestructive examination of steels to their microstructure, which, in turn, relates to mechanical properties. This raises the possibility of using nondestructive tests to indirectly measure mechanical properties.

Review of the literature [1-5] on the problem of nondestructively predicting microstructural characteristics focused our attention on the possibility of incorporating the ultrasonic attenuation due to grain-boundary scattering into a technique for predicting the mechanical

[1]Figures in brackets indicate the literature references at the end of this paper.

properties of steel. The key relationships underlying this possibility may be summed up as follows: given the fact that ultrasonic attenuation is a function of mean grain size and that, in turn, grain size is a factor in determining mechanical properties, it should be possible to deduce information about certain mechanical properties of steel from an ultrasonic attenuation measurement.

Our overall program, aimed at ultimately developing a practical on-line technique based on ultrasonic attenuation measurement, includes determining the types of steels to which such a technique would be applicable, the effect of factors other than grain size (such as composition or phase present), the accuracy of such predictions in the laboratory, and an assessment of the feasibility of in-plant application of the technique.

The work to date, reported in the present paper, dealt with the laboratory preparation and testing of samples of plain carbon steel. Chemical, metallographic, mechanical, and ultrasonic tests were completed on a number of samples. The data were compared to those in published work. Finally, regression analysis was used to estimate the precision of the technique.

2. Review of Previous Studies

Many mechanical properties of steel are affected by grain size [6,7,8]. In particular, it has been shown that yield strength (YS) and impact transition temperature (TT) of ferritic-pearlitic steels obey the Hall-Petch relationships,

$$YS = Y_o + k_y\, d^{-1/2} \tag{1}$$

and

$$TT = T_o + k_T\, d^{-1/2} \tag{2}$$

where Y_o and T_o depend on composition and percent pearlite, k_y and k_T are constants, and d is the mean ferrite intercept (a measure of average grain diameter). Tensile strength (TS) obeys a similar relationship, but the relative influence of grain size is less and the influence of composition and pearlite is greater than in the case of yield strength or transition temperature. Elongation and reduction of area, two common measures of ducility, are known to be rather insensitive to grain size [9].

Since the paper of Roderick and Truell [1], describing the contribution of the grain-boundary scattering to the ultrasonic attentuation, there have been several studies elaborating on the subject. These studies cover both the theoretical prediction of the contribution of grain scattering to the ultrasonic attenuation in polycrystalline materials [3] and the experimental verification of the theory [2,4,10-12]. While quantitative agreement with the theory has not been outstanding, there is no question about the reality of the major trends. A significant portion of this work involved experiments on a wide variety of steels [5,10,13-17]. The primary conclusions of this prior work are that: (a) ultrasonic attenuation can be used to measure the mean ferrite grain diameter in a given type of steel, and (b) for this application measurement of attenuation should be made in the Rayleigh region, given by $\lambda > 2\pi d$, where λ is the ultrasonic wavelength. In the Rayleigh region, the ultrasonic attenuation due to grain-boundary scattering α_s varies as

$$\alpha_s = \alpha_o + k d^3 f^4, \tag{3}$$

where α_o is approximately constant for a given material and f is the ultrasonic frequency. While the majority of the previous work involved classical pulse-echo techniques of measuring the ultrasonic attenuation, or forward-scatter experiments, similar work has been reported based on backscatter measurements of the attenuation in the Rayleigh region [18-23]. Due to the extremely low level of the scattered ultrasonic signals, the difficulty in obtaining adequate precision, and therefore anticipated limitations for in-plant application, we have not pursued this approach.

The connection between the ultrasonic estimation of grain size and mechanical properties was mentioned by Aurich and Martin [5]. They presented data relating the ultrasonically predicted grain size of a small number of structural carbon steel samples to the yield stress ar

favorably compared this to the metallographically determined Hall-Petch relation for the steel. This work establishes the principle of the technique, but did not cover a sufficient range of steels to suit our purpose.

On the basis of indications in the above literature, we were cognizant of the need to design our experimental program not only to provide information on the possible relationship between ultrasonic attenuation and mechanical properties but also to determine to what degree the inherent difficulties of applying ultrasonic attenuation data to a variety of steels might be overcome by incorporating other types of information, in particular steel composition.

3. Experimental Procedure

Plain carbon steels were prepared under laboratory conditions to assure known and uniform metallurgical properties. In all, nine steel alloys were melted (table 1). The ingots were hot-rolled into 46 plates, each 3/4 in (19 mm) thick. These plates were normalized and then annealed according to table 2, which also lists the resulting range of grain size and size and percent pearlite. Each heat-treated plate was divided and machined into:

3 or 6 metallographic specimens
3 tensile test specimens, 0.505 in (12.5 mm) diameter
12 Charpy impact specimens, 0.394 in (10 mm) square cross section
1 chemical test specimen
1 ultrasonic test specimen, 2 in (5 cm) square by 0.70 in (1.78 cm) thick

Table 1. Composition of Alloys.

Alloy	Composition,[a] wt. % C	Mn	Si
A	0.06	0.32	0.01
B	0.15	0.35	0.00
C	0.15	1.09	0.00
D	0.24	0.33	0.00
E	0.25	1.09	0.00
F	0.05	0.01	0.26
G	0.15	0.01	0.22
H	0.26	0.01	0.21
I	0.38	0.05	0.36

[a]Aluminum, which was not added to any of the melts, was less than 0.005 percent in all alloys.

Metallographic measurements were made to determine the microstructural characteristics of the steel. The percent pearlite was determined on an image-analyzing microscope, and the mean ferrite intercept was manually determined by the Abrams circular intercept technique, ASTM E112-74.

Tensile tests were carried out in accordance with ASTM E8-77a. Charpy impact tests covered the full temperature-energy curve and were carried out in accordance with ASTM E23-72, although only the 15 ft-lb (20.2 J) transition temperature is discussed in this paper.

A spectral analysis technique similar to that described by Papadakis [24] was used to collect the ultrasonic attenuation data. Ultrasonic measurements were made in the water-immersion pulse-echo mode with the samples air-backed (fig. 1). A commercial wide-band unfocused immersion transducer was used. The pulser-receiver was a commercial wide-band unit with stepless-gate. The gated output of the pulser-receiver was connected to a spectrum analyzer, which displayed the frequency spectrum of the gated back-echo. The video output of the spectrum analyzer was processed by a peak detector and low-pass filter and connected to the Y-axis of an X-Y recorder. Simultaneously, the sweep sawtooth of the spectrum analyzer was used to drive the X-axis of the recorder. Data were obtained in the form of a graph of the logarithmic amplitude versus the frequency for each successive back-echo in a particular sample (fig. 2). The difference in amplitude between each of the first four successive back-echoes was measured at one particular frequency. These three differences were averaged and then divided by twice the sample thickness to yield the raw attenuation value at the selected frequency.

Table 2. Heat Treatments, Microstructure, and Properties.

Alloy	Annealing Temperature	Grain[a] Size, μm	Volume Percent Pearlite, %	Lower Yield Strength	Tensile Strength	Transition Temperature	Attenuation at 5 MHz
A	none[b]	30.3	2.5	25.6	42.6	10	1.08
	1250	21.7	0.0	27.9	45.8	0	1.08
	1650	34.5	0.7	22.2	40.6	47	1.21
	1700	53.7	2.8	19.1	40.4	-	2.05
	1700[c]	35.8	3.5	24.0	43.6	-	1.63
	1750	55.7	2.5	20.0	40.2	-	2.10
	1800	65.7	2.2	16.1	40.3	-	2.91
	1850	81.4	2.5	14.3	40.0	-	4.62
	1900	104.7	2.2	12.8	39.6	-	5.39
	2000	113.3	2.9	13.7	40.0	103	6.00[d]
	2275	238.6	4.0	13.8	38.7	-	12.18[d]
	2300	212.4	2.8	16.6	41.9	128	8.12[e]
B	1575[f]	20.8	10.2	32.8	50.9	33	1.53
	1650	39.8	9.9	19.9	47.2	84	1.30
	1950	107.7	11.6	16.6	46.7	93	4.97
C	1575[f]	13.7	15.4	38.8	60.3	-72	0.83
	1650	34.8	19.3	31.0	57.2	8	1.18
	1950	78.4	16.6	25.6	55.7	10	4.57
D	1650	60.4	21.4	21.9	53.2	108	2.63
	1950	84.5	23.2	21.0	53.2	112	3.95
E	1525[f]	11.9	24.4	40.2	69.4	-25	1.15
	1650	31.1	34.9	34.9	66.5	18	5.60
	1950	55.8	36.4	30.4	65.5	25	3.20

Table 2. Heat Treatments, Microstructure, and Properties (continued).

Alloy	Annealing Temperature	Grain[a] Size, μm	Volume Percent Pearlite, %	Lower Yield Strength	Tensile Strength	Transition Temperature	Attenuation at 5 MHz
F	1250	28.9	2.6	30.9	49.7	42	2.58
	1675	37.8	1.6	30.1	47.4	94	2.07
	1750	43.1	1.9	29.4	47.1	96	1.81
	1875	59.9	1.9	27.2	46.3	92	2.20
	2000	88.7	2.4	22.9	46.2	140	3.88
	2150	102.6	2.7	21.6	45.9	137	4.82
G	1250	18.4	7.5	34.2	54.9	72	1.65
	1600	26.4	7.7	29.9	49.9	115	1.78
	1675	30.8	6.1	30.6	49.7	115	1.74
	1750	35.0	6.2	29.2	50.6	102	1.90
	1875	71.2	9.7	20.3	48.9	162	5.40
	2000	83.5	8.9	20.0	49.0	177	4.35
H	1250	17.4	11.7	39.4	62.1	75	1.42
	1550	25.3	11.3	32.4	57.1	157	1.45
	1675	29.1	12.4	32.3	56.4	128	2.34
	1875	92.1	16.6	21.0	55.0	224	5.70
	2000	105.0	14.2	20.3	54.1	218	5.68
I	1250	11.5	22.0	42.8	72.7	72	1.35
	1500	19.5	19.6	36.4	68.4	145	1.39
	1675	50.8	27.0	31.1	69.9	163	2.23
	1750	55.7	26.4	29.1	68.8	204	2.92
	1875	59.7	27.6	27.9	69.0	190	2.83
	2000	65.2	28.1	29.0	69.1	194	3.23

[a] Grain size is herein defined as d, the mean ferrite intercept.

[b] As rolled condition.

[c] Air cooled rather than furnace cooled.

[d] Attenuation based on three back echoes due to the large attenuation.

[e] Attenuation based on two back echoes due to the large attenuation.

[f] To minimize pearlite banding, the plate was given a preliminary heat treatment of 10 minutes at 2425 °F, normalized at the indicated temperature and annealed at 1250 °F.

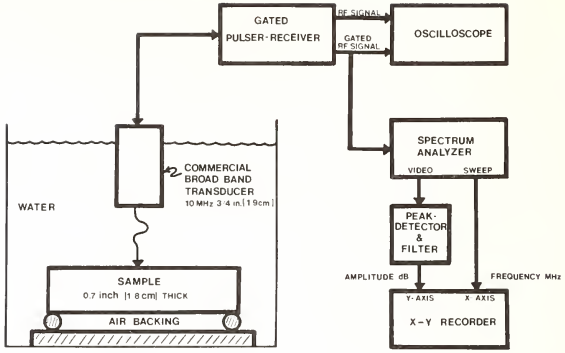

Figure 1. Ultrasonic test configuration.

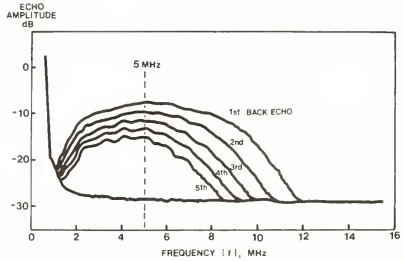

Figure 2. Back echo frequency spectrum data for sample F annealed at 1675 °F (1186 °K).

Correction of the raw data for reflection loss from the front surface of the sample was made by first measuring the loss from the first to second back echo with a sample completely immersed in water and then repeating this measurement with the same sample backed in air. The average of several such tests yielded a correction factor of 0.7 dB per reflection. This figure agrees with the expected theoretical loss from a plane interface of materials with the acoustical impedance of water and steel.

The attenuation data were not corrected for diffraction effects. Consistent with the literature [25-27], a classic piston diffraction pattern was not detectable for the highly damped commercial transducer. All ultrasonic attenuation data were collected within the near-field as calculated classically for the diameter of the transducer. Since the same systematic error is included in all of our measurements (at each frequency), lack of a correction for diffraction should have little effect on our correlation of attenuation with properties. The diffraction correction must be made if measurements at various sample thicknesses, different water path lengths, different frequencies, or from different transducers are to be quantitatively compared.

The front and back reflecting surfaces of the ultrasonic samples were smooth (0.81 μm rms finish) and parallel to within 0.02 percent. Transducer alignment normal to the sample surface was obtained by adjusting the transducer until the front surface echo indication was peaked. Prior to final machining into mechanical test specimens, the tensile and Charpy impact test coupons were ground and ultrasonically tested exactly as were the ultrasonic test specimens. All samples were, in addition, ultrasonically tested at least three times at different

ocations. Ultrasonic attenuation was measured in the through-thickness direction of the late. For data presented in this paper, all attenuation values were calculated at 5 MHz.

4. Experimental Results

Metallographic examination revealed a satisfactory range in grain size and pearlite for ur experimental purposes, namely, 11.5 to 239 μm mean ferrite intercept and zero to 36 per- ent pearlite (table 2). The typical microstructure was equiaxed polygonal ferrite and andomly distributed pearlite islands (fig. 3a). Some plates, especially of alloys B, C, D, nd E, developed marked pearlite banding (fig. 3b). Such banding may occur in commercial roduct, and it was therefore included in our analysis. Grange [28] showed that neither trength nor transition temperature of longitudinal specimens is significantly affected by anding, and our results support his findings. A close analysis of our data revealed that anding had no effect on ultrasonic attenuation when the measurement is in the through- hickness orientation.

Figure 3a. Polygonal ferrite and pearlite in alloy G after annealing at 1600 °F (100X, Nital etch).

Figure 3b. Pearlite banding in alloy C after annealing at 1650 °F (50 X, Nital etch).

Mechanical test results are summarized in table 2 and figures 4, 5 and 6. Figure 4 is a lot of lower yield strength versus the reciprocal square root of the mean ferrite intercept. he data support the fact that grain size influences lower yield strength in accordance with he Hall-Petch relationship, eq. (1), and are in good agreement with those of others, in articular with Morrison's results [29], which are superimposed in figure 4. As seen in igure 4, the effect of our composition variations is about half that of our grain-size ariations. This result is consistent with reports in the literature [29-31]. The variation f Charpy transition temperature versus grain size is presented in figure 5[2]. A strong dependence of the transition temperature on both grain size and composition is evident. igure 6 presents the tensile strength data plotted as a function of the grain size. As xpected, the grain size has a relatively small effect on the tensile strength, composition eing the most significant factor. The curves drawn on figures 5 and 6 are visual estimates drawn solely to illustrate the separation of the data by composition and the trend with grain ize. Although not included in table 1, the data on elongation and reduction in area showed little variation with grain size.

The metallographically measured mean ferrite intercept is plotted against the ultrasonic attenuation in figure 7. The classical cubic relation between grain size and attenuation, eq. (3), has been fitted to the data in the Rayleigh region. The cubic fit is made for the fraction of our data below one-half the critical grain size d_c, where $d_c = c/2\pi f$ and c is the ultrasonic longitudinal velocity. Restriction of the fit to $d_c/2$ points up the fact that for grain size approaching a significant fraction of d_c the Rayleigh relation is not expected to be valid [3]. Others [3,5] have pointed out the need to be in the Rayleigh region to best predict grain size. However, figure 7 makes the additional point that too small a grain size, or equivalently too low a frequency since λ/d is the significant parameter of the experiment (in

[2] In contrast to figure 4, figures 5 and 6 are plotted with grain size as the abscissa in order to illustrate their similarity to the graphs of the ultrasonic data, figures 11 and 12.

our case the data below approximately 35 μm grain size at 5 MHz), greatly reduces resolution. This is due to the fact that in that initial portion of the Rayleigh region the cubic curve is nearly horizontal. Statistical analysis of the data indicated that attenuation is not significantly influenced by the composition or percent pearlite.

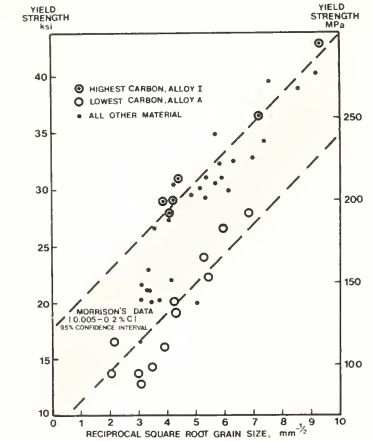

Figure 4. Lower yield strength versus the reciprocal square root of the metallographically measured grain size.

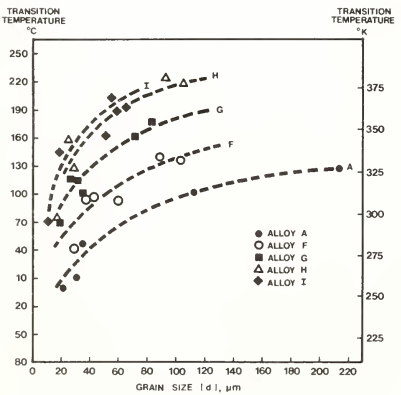

Figure 5. Transition temperature versus grain size.

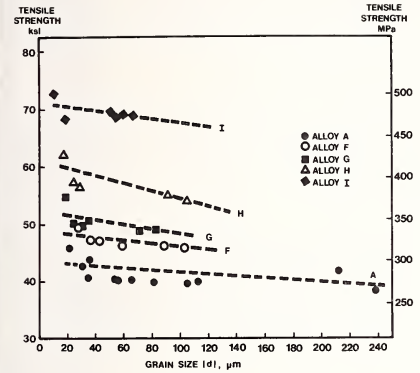

Figure 6. Tensile strength versus grain size.

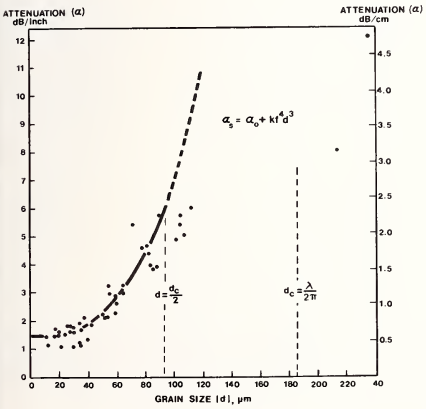

Figure 7. Metallographically measured mean ferrite intercept (grain size d) versus the ultrasonic attenuation at 5 MHz.

Figure 8 illustrates the frequency dependence of the attenuation for one particular alloy with grain size as a parameter. The Rayleigh relation, eq. (3), could be fitted to this data. However, as pointed out in the literature [3,12,32] the f^4 dependence is not quite correct due to the typical distribution in actual grain size through the sample. The curves drawn are only visual estimates to illustrate the grouping by grain size and continuity with frequency. The decrease in attenuation with increasing frequency for the sample of finest grain size is an indication of the small degree to which diffraction errors affect the results.

Since the Hall-Petch equations predict certain properties to be linear in $d^{-\frac{1}{2}}$, it is appropriate to relate $d^{-\frac{1}{2}}$ and attenuation. Figure 9 shows the dependence of $d^{-\frac{1}{2}}$ on attenuation. Due to the nonlinear nature of the Rayleigh relation, eq. (3), the data were simply fit to the highest order statistically significant polynomial in α, which for our data was the third order. The best fit shown in figure 9 has been made for data between grain sizes of 35 and 115 μm. Since an empirical power fit is being made, strict adherence to the $d < d_c/2$ criterion is not followed.

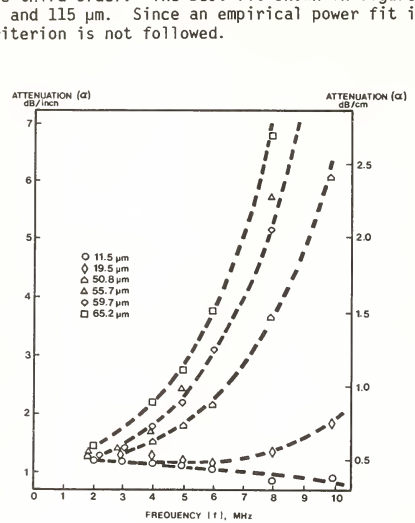

Figure 8. Attenuation versus frequency for alloy I, with grain size as parameter.

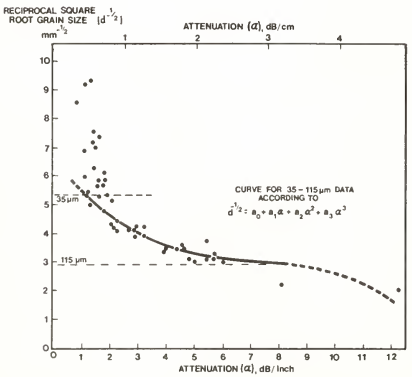

Figure 9. Reciprocal square root grain size ($d^{-\frac{1}{2}}$) versus ultrasonic attenuation (α) at 5 MHz.

Figure 10 is a plot of the lower yield strength data versus attenuation. The plot illustrates that there is a qualitative trend of yield strength with attenuation, and that variations in composition systematically increase the apparent scatter of the data. Grouping of the data by composition is illustrated by the systematic separation of points for one high and one low carbon alloy. In conjunction with figure 7 and eq. (3), the nearly vertical

lignment of the data at the smaller grain size, below approximately 35 μm, indicates that igher frequencies, approaching 20 MHz, would be required for resolution of these higher trength steels. Transition temperature data versus attenuation is plotted in figure 11. onsistent with the results of figure 5, attenuation by itself is shown to be a poor indicator f transition temperature. However, addition of the composition clearly improves the situation. astly, figure 12 illustrates that, consistent with the data in figure 6, the tensile strength s not strongly dependent on attenuation, composition being the most significant factor in etermining this mechanical property.

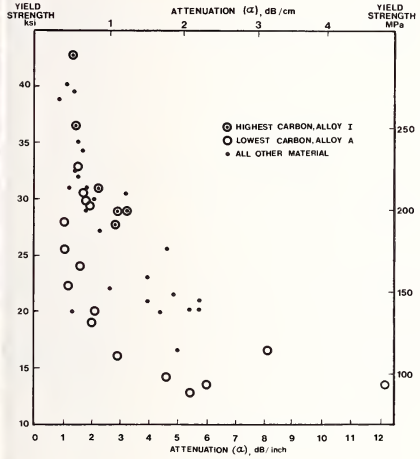

Figure 10. Lower yield strength versus the ultrasonic attenuation (α) at 5 MHz.

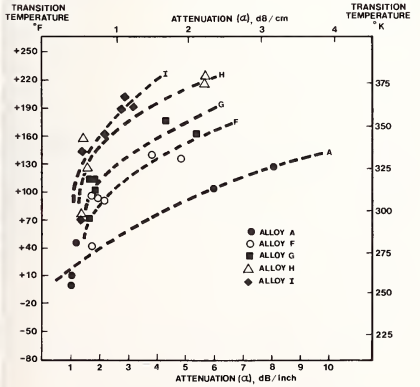

Figure 11. Transition temperature versus the ultrasonic attenuation (α) at 5 MHz.

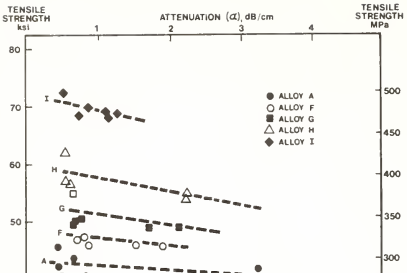

Figure 12. Tensile strength versus the ultrasonic attenuation (α) at 5 MHz.

5. Regression Results

Regression analysis was used to evaluate the effectiveness of the attenuation measurements in predicting the mechanical properties through the use of attenuation as a proxy for metallographic grain size and to compare the relative importance of grain size and composition in predicting mechanical properties. Because our data were "nested" (i.e., 46 plates of varying grain size were derived from nine ingots), composition was handled in the analysis by the "indicator variable" technique [33,34]. Thus, all compositional effects were aggregated into one variable for each ingot, and we have not attempted, for example, to distinguish the effect of carbon from that of manganese. Regression equations with the alloy indicator variables and $d^{-\frac{1}{2}}$ as independent variables, the second equations of tables 3, 4, and 5, yielded Hall-Petch slopes of 3.1 ksi-mm$^{\frac{1}{2}}$ (22 MPa-mm$^{\frac{1}{2}}$), 0.95 ksi-mm$^{\frac{1}{2}}$ (6.5 MPa-mm$^{\frac{1}{2}}$), and -22F-mm$^{\frac{1}{2}}$ (-12 °K - mm$^{\frac{1}{2}}$), respectively, for yield strength, tensile strength, and transition temperature. The excellent agreement of these slopes with values reported in a large body of literature confirms the normality of our data and the validity of the regression analysis.

Table 3. Regression-Equation Statistics for Lower Yield Point.

Form of Equation	Statistics			
	For All Data		For 35 μm<d<115μm	
	Variance Explained	95% Confidence Interval	Variance Explained	95% Confidence Interval
1. LYP = b_0(Alloys)	.521	±11.7 ksi (±80.7 MPa)	.755	±6.3 ksi (±43.4 MPa)
2. LYP = b_0(Alloys) + $k_y d^{-1/2}$	.945	±4.0 ksi (±27.6 MPa)	.966	±2.5 ksi (±17.2 MPa)
3. LYP = b_0 (Alloys) + $b_1\alpha$ + $b_2\alpha^2$ + $b_3\alpha^3$	-	-	.954	±3.2 ksi (±22.1 MPa)

Table 4. Regression-Equation Statistics for 15 FT-LB Transition Temperatures.

Form of Equation	Statistics[a]			
	For All Data		For 35 μm<d<115μm	
	Variance Explained	95% Confidence Interval	Variance Explained	95% Confidence Interval
1. $TT = b_0$ (Alloys)	.666	±91 °F (±51 °K)	.949	±36 °F (±20 °K)
2. $TT = b_0$ (Alloys) + $k_t d^{-1/2}$	.948	±37 °F (±21 °K)	.973	±27 °F (±15 °K)
3. $TT = b_0$ (Alloys) + $b_1\alpha + b_2\alpha^2 + b_3\alpha^3$	-	-	.985	±23 °F (±13 °K)

[a] Only five, rather than all twelve, specimens of Alloy A were Charpy tested.

Table 5. Regression-Equation Statistics for Tensile Strength.

Form of Equation	Statistics			
	For All Data		For 35 μm<d<115μm	
	Variance Explained	95% Confidence Interval	Variance Explained	95% Confidence Interval
1. $TS = b_0$ (Alloys)	.965	±4.2 ksi (±30.0 MPa)	.994	±1.8 ksi (±12.4 MPa)
2. $TS = b_0$ (Alloys) + $k_t d^{-1/2}$	.988	±2.5 ksi (±17.2 MPa)	.998	±1.2 ksi (±8.3 MPa)
3. $TS = b_0$ (Alloys) + $b_1\alpha + b_2\alpha^2 + b_3\alpha^3$	-	-	.997	±1.5 ksi (±10.3 MPa)

The form of the regression equations for the lower yield point and their statistics are shown in table 3. In the first equation, the b_o (alloy) terms are actually the average yield points of all the plates (with various grain sizes) of each alloy. In the second and third equations, the b_o (alloy) terms are the yield points of each alloy extrapolated (by least squares) to zero $d^{-\frac{1}{2}}$ and α, respectively. The latter two equations assume, of course, that composition has no effect on k_y or on the relation between grain size and attenuation. The significant point in table 3 is given by the statistics. For all the data, the alloy terms alone explain half of the variance (scatter). Adding the $d^{-\frac{1}{2}}$ term makes a very significant improvement in "explained variance" and a quite marked tightening of the "95 percent confidence interval". Restricting the data to grain sizes of between 35 and 115 μm, as was done for figure 9, we note that empirically substituting as α polynomial for $d^{-\frac{1}{2}}$ slightly decreases the "explained variance" and slightly increases the confidence interval. However, these differences are relatively small. Comparison of the first and third equations indicates that adding the α terms to the alloy term as independent variables clearly improves the fit and tightens the confidence interval.

Similar comments apply to the analysis of the transition temperature (table 4), except that substituting an α polynomial for $d^{-\frac{1}{2}}$ slightly increases the "explained variance" and slightly decreases the confidence interval. As opposed to the case for yield strength and

transition temperature, the tensile strength (table 5) is predominantly affected by composition. Including either $d^{-\frac{1}{2}}$ or α in the equation, however, still increases the "explained variance" and decreases the confidence interval.

On the basis of the above results, we conclude that the α polynomial is a satisfactory proxy for $d^{-\frac{1}{2}}$, at least for steels with grain size between 35-115 μm, and that the addition of attenuation terms to prediction equations based on composition would significantly improve the precision of the prediction of yield strength, tensile strength, and transition temperature.

6. Conclusion

Our work supports previously published studies indicating that the ultrasonic attenuation due to grain boundary scattering can be used to successfully predict the grain size in plain carbon steel. We have demonstrated that only a portion of the Rayleigh region is useful for the prediction of grain size or mechanical properties.

Whereas the mechanical properties of plain carbon steels are dependent on composition, percent pearlite, and grain size, the through-thickness ultrasonic attenuation is not influenced by the alloy, percent pearlite, or the presence of banding but is strongly and systematically dependent on grain size. Though ultrasonic attenuation cannot by itself be used to predict mechanical properties in a variety of steels, it can in combination with chemical composition serve to predict yield strength, transition temperature, and tensile strength in plain carbon steels.

Results of the regression analysis indicate that the nondestructive prediction of yield strength and tensile strength may approach the accuracy required for practical application. Although the experimental work was conducted under laboratory conditions with one ultrasonic frequency and one plate thickness, the results point to the possibility of developing an ultrasonic attenuation-based on-line method of predicting the mechanical properties of steel.

References

[1] Roderick, R. L. and Truell, R., The measurement of ultrasonic attenuation in solids by the pulse technique and some results in steel, J. Acoust. Soc. Amer., 23, 267 (1952).

[2] Papadakis, E. P., Ultrasonic attenuation and velocity in three transformation products in steel, J. App. Phys., 35, 1474 (1964).

[3] Papadakis, E. P., Revised grain scattering formulas and tables, J. Acoust. Soc. Amer., 37, 703 (1965).

[4] Papadakis, E. P., Ultrasonic attenuation caused by scattering in polycrystalline metals, J. Acoust. Soc. Amer., 37, 711 (1965).

[5] Aurich, D. and Martin, E., Prerequisites, possibilities, and limitations of grain size determination by ultrasonic attenuation measurement, Arch. Eisenhuettenw., 41, [3] Henry Butcher 8186, ed., (1970).

[6] Armstrong, R. W., The influence of polycrystal grain size on several mechanical propertie of materials, Met. Trans., 1, 1169 (1970).

[7] Armstrong, R. W., Advances in Materials Research, Vol. 4, pp. 101-146, Interscience, (New York, 1970).

[8] Hall, E. O., Yield Point Phenomena in Metals and Alloys (Plenum Press, New York, 1970).

[9] Gladman, T., et al., Work hardening of low-carbon steels, J. Iron Steel Inst., 208, 172 (1970).

[10] Papadakis, E. P., Ultrasonic attenuation and velocity on SAE 51200 steel quenced from various temperatures, Met. Trans., 1, 1053 (1970).

[11] Kettler, R., et. al., Surface ultrasonic measurement of grain size of silicon iron sheet, Met. Trans., 5, 952 (1974).

[12] Kesler, H. A., and Shraifel'd, L. I., Dispersion of ultrasonic waves in polycrystalline metals with statistically distributed grain size, Soviet J. NDT., 1, [1] (1975).

[13] Papadakis, E. P., Ultrasonic nondestructive test for the detection of improper heat treatment of steel, Mater. Evaluation, 23, 136 (1965).

[14] Matsumoto, S. and Kimura, K., The relation between grain size and ultrasonic attenuation coefficient in austenitic stainless steels and irons, Trans. Nat. Inst. Metals, 14, 21 (1972).

[15] Adhikari, B. C., et al., Measurement of grain size by ultrasonic attenuation, Trans. Indian Inst. Metals, 28, 498 (1975).

[16] Juva, A. and Haarvista, M., On the effects of microstructure on the attenuation of ultrasonic wave in austenitic stainless steels, Brit. J. NDT, 19, 293 (1977).

[17] Von Gunter Bott, et al., Utilization of the ultrasonic attenuation measuring method to sort out normalized and not annealed sheets, Materialpruefung., 19, 251 (1977).

[18] Beecham, D., Ultrasonic scatter in metals its properties and its application to grain size determination, Ultrasonics, 5, 67 (1967).

[19] DiGiacomo, G., et al., Development of an ultrasonic method for determination of grain size in cast steel, Mater. Evaluation, 28, 271 (1970).

[20] Kopec, B., Ultrasonics inspection of grain size in the materials for railway wheel sets, Ultrasonics, 13, 267 (1975).

[21] Goebbels, K., Evaluation of steel structure with scattered ultrasonic pulse, Materialpruefung., 17, 231 (1975).

[22] Fay, B., Determination of the grain size of steel using the ultrasonic backscatter method, Arch. Eisenhuettenw., 47, 119 (1976).

[23] Goebbels, K., et al., Ultrasonic determination of the structure of steels. Final Report, British Iron and Steel Institute Translation 15536 (1977).

[24] Papadakis, E. P., et al., Ultrasonic attenuation by spectrum analysis of pulses in buffer rods: Method and diffraction corrections, J. Acoust. Soc. Amer., 53, 1336 (1973).

[25] Papadakis, E. P. and Fowlder, K. A., Broad band transducers, radiative field and selected applications, J. Acoust. Soc. Amer., 50, 729 (1971).

[26] Gitis, M. B., Diffraction corrections in the pulsed regime, Soviet Phys. Acoust., 18, 33 (1972).

[27] Rose, J. L., Effects of selected electrode shapes on basic ultrasonic field parameters, Mater. Evaluation, 34, 114 (1976).

[28] Grange, R. A., Effect of microstructural banding in steel, Met. Trans., 2, 417 (1971).

[29] Morrison, W. B., The effect of grain size on the stress-strain relationship in low-carbon steels, ASM Trans., 59, 824 (1966).

[30] Pickering, F. B. and Gladman, T., An investigation into some factors which control the strength of carbon steels, in Metallurgical Developments in Carbon Steels, Special Report 81, Iron and Steel Inst., 10-20 (1963).

[31] Grozier, J. D. and Bucher, J. H., Correlation of fatigue limit with microstructure and composition of ferrite-pearlite steels, J. Materials, 2, 393 (1967).

[32] Papadakis, E. P., From microstructure to grain size distribution with ultrasonic applications, J. Acoust. Soc. Amer., 35, 1586 (1964).

[33] Draper, N. R. and Smith, H., Applied Regression Analysis (Wiley, New York, 1966).

[34] Daniel, C. and Wood, F. S., Fitting Equations to Data (Wiley, New York, 1971).

National Bureau of Standards Special Publication 596, Ultrasonic Materials Characterization, H. Berger and M. Linzer, eds., Proceedings of the First International Symposium on Ultrasonic Materials Characterization held at NBS, Gaithersburg, Md., June 7-9, 1978. Issued November, 1980.

ASSESSMENT OF MATERIAL PERFORMANCE IN FATIGUE WITH ACOUSTIC METHODS

Z. Pawlowski and G. Funke

Institute of Fundamental Technological Research
of the Polish Academy of Sciences
Swietokrzyska 21, 00-049 Warszawa
POLAND

The possibilities created by the use of ultrasonics and acoustic emission to detect cumulative damage during alternating straining of material are reviewed. In ultrasonics, three possible measures of damage accumulation are discussed, the attenuation of longitudinal waves, the attenuation of surface waves, and direct observation of fatigue crack growth in large structures.

Ultrasonic methods, although sensitive to the changes in materials subjected to cyclic straining, do not indicate clearly enough the beginning of the crack propagation stage. Measurements of the acoustic emission count rate, however, clearly shows the separation between the crack propagation and crack incubation stages in both notched and unnotched specimens.

It is shown how the prediction of fatigue life can be carried out after analyzing the statistical distribution of acceleration of acoustic emission counts. An example of controlled fatigue crack growth in service is also presented.

1. Introduction

Methods of following damage accumulation during alternating straining have been reported for about 20 years [1][1]. In fatigue, a crack or flaw grow slowly before reaching critical dimensions after which rapid crack propagation sets in.

The fatigue life may be divided into two stages, the incubation stage and crack propagation one. It appears that the large dispersion in fatigue life observed at the same stress level is connected with the incubation stage during which the mechanisms of crack nucleation operate. As about 90 percent of failures may be ascribed to the fatigue of material, the need to have continuous or random information on fatigue damage, which nucleates with time, is obvious.

Since the critical crack size can be estimated using fracture mechanics approaches, nondestructive testing methods able to supply information on the position and dimensions of the crack or flaw become a valuable tool in the assessment of fracture risk.

The changes in physical state of a material may conveniently be recognized and followed with ultrasonic and acoustic emission methods. Ultrasonic methods allow one to detect a crack and measure its growth from a very early stage by observing the reflection of ultrasonic waves from the discontinuity. Another possibility is to look for structural changes which occur in the strained zones before the crack starts to propagate and then to observe it up to the final fracture. Thus, there may be direct or indirect methods of the observation of crack growth. Some examples in the estimation of fracture risk or prediction of fatigue life are given in this paper.

[1]Figures in brackets indicate the literature references at the end of this paper.

2. Ultrasonic Attenuation

Changes in the attenuation of ultrasonic waves which are transmitted through the region where fatigue cracks initiate may be detected either with longitudinal [1-3] or surface waves [4,5]. It was suggested [2,3] that three parameters are the potential sources of information on the damage accumulation in fatigue. These parameters are, the absolute increase in the attenuation of ultrasonic waves, the gradient of attenuation increase or the attenuation increase per cycle,and the attenuation recovery after the cyclic straining has been stopped (fig. 1).

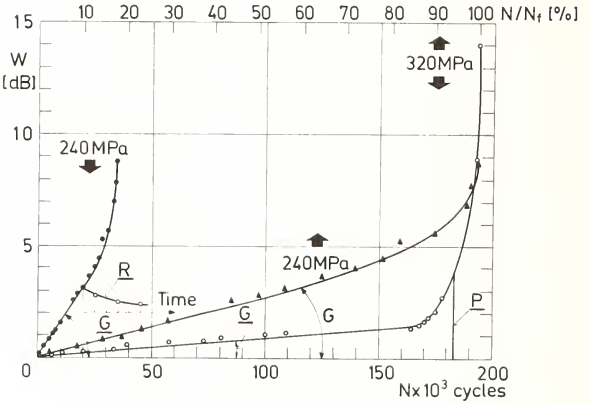

Figure 1. Three possible measures of damage accumulation in fatigue: P - the absolute increase in ultrasonic wave attenuation, G - gradient of attenuation increase, R - recovery of ultrasonic wave attenuation after the test has been interrupted. Arrows indicate the horizontal axis to which the curves correspond.

2.1. Longitudinal wave attenuation

The absolute increase in attenuation may be used as a damage measure only in those cases when a reference level is established and the changes in attenuation are large enough so they could not be masked by the dispersion in attenuation measurements. These measurements may be carried out with a transducer which is either fixed to the specimen or coupled separately at the time of each measurement.

It may easily be concluded from figure 1 that larger increases in attenuation are observed in the last periods of fatigue life. The absolute increase in attenuation is, in general, too small in the early stages of fatigue life to be measured repeatably if the probe is attached to the object at the time of each measurement.

If this difficulty could be overcome, there exists a practical realization of fatigue monitoring based on measuring the absolute and monotonic increase in attenuation. The results presented until now [1] show that only an increase of a few decibels may be expected. There

s also a spread in the absolute values and without a larger collection of statistical data, howing the range of changes to be expected, one cannot draw definite conclusions from single ttenuation measurements.

2.2. Surface wave attenuation

Using the surface waves as an indicator, many of the above mentioned difficulties could e overcome. In figure 2, results of changes in ultrasonic surface wave attenuation are resented for mild steel and an aluminum alloy $AlMg_5$. All curves in the figure were ormalized with respect to the final fatigue life in order to get an idea of the similarity of he changes in the surface wave attenuation.

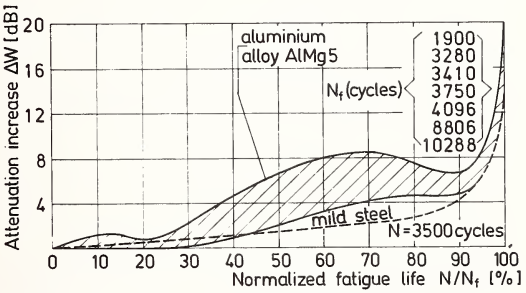

Figure 2. Ultrasonic surface wave attenuation for mild steel and aluminum alloy $AlMg_5$ in low-cycle fatigue. For mild steel the results for only one specimen are presented, whereas for aluminum alloy, the range from results for seven specimens is indicated.

The scheme of measurement of the surface wave attenuation is shown in figure 3. The samples were fatigued in reverse bending at various levels of deformation. The height of the echo from the sample edge was set to an arbitrarily chosen reference level and the amplification of the ultrasonic instrument to maintain the same echo height was noticed. The surface waves traveled twice through the fatigue region, once from the transducer head to the sample edge, the second time in reverse direction after the reflection from the target.

As can be deduced from the arrows in figure 4, which indicate the first visible crack and the onset of rapid crack propagation, about 50 to 70 percent of the total fatigue life is spent in the incubation period. In the case of steel, no special sign could be visible in the curves of attenuation vs. normalized fatigue life (figs. 1 and 2). Quite another situation seems to exist for aluminum alloys. The curves obtained for seven specimens show sufficient similarity. However, for those samples with shorter fatigue life, an increase in attenuation up to about 50 percent of fatigue life was observed. It was then followed by a decrease in attenuation by 2-6 dB until the onset of rapid crack propagation. This point, marked by an arrow 2 in figure 4, occurs at about 95 percent of the total fatigue life.

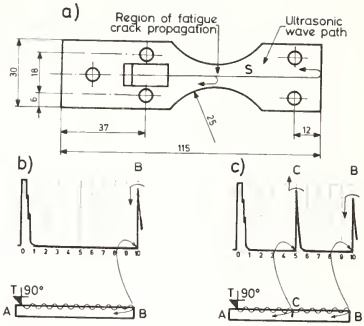

Figure 3. Method of measuring the attenuation of ultrasonic surface waves: a) the shape of samples used in experiments; b) screen image before the crack is nucleated; and c) screen image when the macroscopic crack started to grow.

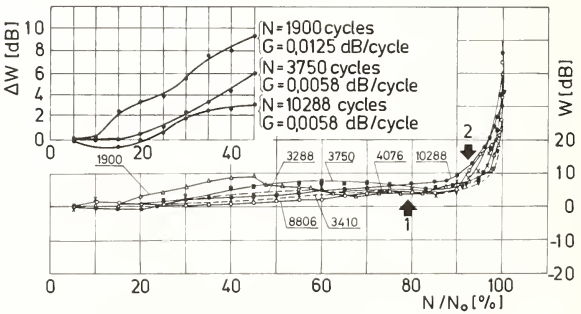

Figure 4. Changes of ultrasonic surface wave attenuation for six aluminum alloy samples tested in bending in low-cycle fatigue. Arrows indicate the first visible crack (1) and the onset of rapid crack propagation (2).

A careful examination of the curves in figure 4 leads one immediately to the conclusion that in the case of the aluminum alloy used in our experiments various fatigue life values may correspond to the same level of attenuation increase. Such a lack of monotonic increase in the attenuation in the case of aluminum alloys excludes the possibility of fatigue life estimation on the basis of single attenuation measurements. Of course, if the history and the response of the sample is known from the beginning, a reasonable prediction could be made.

The advantage of the use of surface waves for fatigue monitoring has to be stressed for several reasons. In contrast to the case of longitudinal wave attenuation, it is quite easy to obtain in practice the same reference level. The changes are comparatively large compared to the sensitivity of modern ultrasonic instruments which is about 0.1 dB. Reproducibility of the measurements is very satisfactory. There is no need to calculate the attenuation related to the given path length, which in reality cannot be known exactly as the fatigue process is a localized one. It is, therefore, sufficient with this approach to follow the relative increase in attenuation irrespective of the dimensions of the region where the stress concentration exists.

2.3. Attenuation gradient

The gradient of the attenuation appears to offer additional possibilities for fatigue monitoring. It can be measured during the whole fatigue life at short intervals, e.g., 10-100 cycles, and is to some degree independent of reference level and instrumentation used.

Some measurements of the gradient were introduced in figure 4. In the case of steel, a monotonic function obtains; thus, the gradient has a continuously increasing value. For aluminum alloy samples showing a very short life in low-cycle fatigue, the gradient changes sign. The initial value of gradient is connected with the total life as it can be seen from figure 4.

It seems probable that the zero value of the gradient may be connected with the end of incubation period. However, no additional support could be obtained with other methods at this stage of research. In general, the rate of attenuation as a function of fatigue life lends further support to the conclusion presented earlier [2,3].

By combining the absolute increase in surface waves attenuation with the gradient of the attenuation increase per cycle, we obtain additional information on the damage process and the length of the fatigue life.

3. Acoustic Emission During Fatigue Straining

In general, when the acoustic emission response is recorded, one is able to measure the cumulative counts and then calculate the rate of acoustic emission counts $n' = \Delta n/\Delta t$ or the acceleration of acoustic emission counts $n'' = \Delta n'/\Delta t$. Further, the spectrum of acoustic emission signals could be recorded and analyzed. In our experiments, only the first three parameters have been taken into account.

It was reported [5] that the cumulative counts of acoustic emission increase with the number of fatigue cycles. However, the number of cumulative counts depends largely on the sensitivity of the instrumentation. Due to the irreversibility of acoustic emission, no valid conclusion may be drawn if the counts are not registered continuously. More information is obtained when one measures the rate of acoustic emission events or acceleration of acoustic emission counts [5]. An example is shown in figures 5 and 6. Two samples, with and without notches, present a typical response. Irregular rates of acoustic emission counts are generally observed for unnotched specimens in the early fatigue life. This behavior may be ascribed to the plastic deformation occurring in various regions of the fatigued zone, before the fatigue crack starts to propagate.

Such a period was almost absent in notched specimens. In this case, due to the stress concentration around the crack tip, one expects a shorter period of crack incubation. No random signals originate from various regions which may deform plastically before the damage concentrates around a stress raiser.

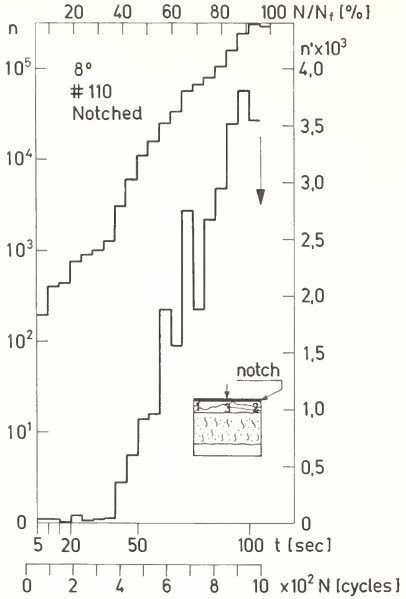

Figure 5. One of the typical acoustic emission responses of an $AlMg_5$ alloy sample in low-cycle fatigue. The cumulative counts are presented in intervals of 10 seconds.

The graphs in figure 6 suggest that differentiation between the incubation and crack propagation stages is possible. For the notch configuration used in the experiments, the decrease of the incubation period can be estimated for about 20 percent of fatigue life. Another important point to be stressed is that information about the crack propagation stage could be collected sooner than was possible with ultrasonic wave attenuation.

4. Fatigue Life Prediction

Further analysis of acoustic emission response seems to be conclusive enough to predict fatigue life by making short random measurements. For 37 samples, tested in low-cycle fatigue, the absolute values of acceleration of acoustic emission counts were collected after 20, 40, 50, 60, 70, 80, and 90 percent of fatigue life. For each sample, only three values of the acceleration of acoustic emission counts, at the given life stage, were taken. The absolute values of acceleration were calculated as the differences in the rates of counts in three successive seconds. In the case considered, one second of life corresponded to about 10 alternating strain cycles.

The distribution of 117 values of these statistical samples is shown in figure 7. The probability was calculated from the formula $P = i/(n+1)$ with i = sample number and n = total number of samples. The points, for the given fatigue life, are dispersed randomly along the straight line; thus the distribution may be considered as a normal distribution.

The mean values, taken at 50 percent of probability, served to construct the graph for predicting fatigue life if the mean value of acceleration counts is known. The graph in figure 8 is indicative of the observed trends. However, the dispersion of counts is very large and the application of standard methods of mean calculation could be troublesome and sometimes misleading. In this case, sequential analysis [6] may be of great help in estimating the fatigue life from a short series of measurements.

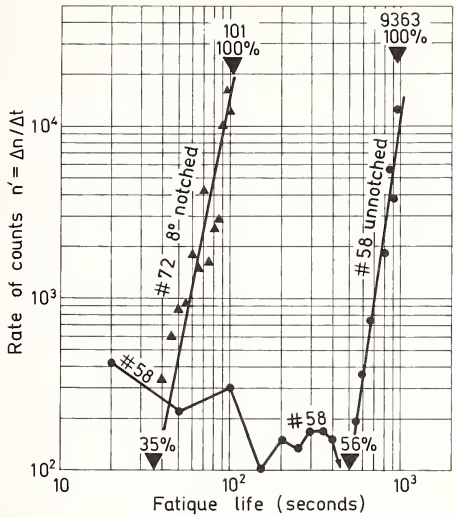

Figure 6. The rate of acoustic emission counts against fatigue life for a notched and unnotched $AlMg_5$ alloy specimen. The average values of the rates, taken for a longer period, were introduced in the figure.

To discriminate between two hypotheses $N \quad N_o$ and $N \quad N_1$, where $N_1 > N_o$, with probability α of rejecting the hypothesis $N \quad N_o$, when it is true, and the probability β of rejecting the alternative hypothesis $N \geq N_1$, when it is true, one arrives to the useful inequality [6]:

$$\frac{\sigma^2}{N_1 - N_o} \ell n \frac{\beta}{1-\alpha} + m \frac{N_o + N_1}{2} < \sum_{i=1}^{m} \left| n''_i \right| < \frac{\sigma^2}{N_1 - N_o} \ell n \frac{1-\beta}{\alpha} + m \frac{N_o + N_1}{2}$$

with σ^2 = standard deviations and m = ordinal number.

Graphical presentation of this inequality is given in figure 9 with two examples of discrimination between the hypotheses N_1 = 70 percent and N_o = 40 percent. The probabilities α and β were taken as 0.05, and the standard deviation from figure 7 was σ = 0.9.

Two sets of successive measurements were taken from the data for two samples. One of the sets was chosen in the neighborhood of 50 percent of fatigue life, the other in the neighborhood of 35 percent. The sum

$$\sum_{i=1}^{m} \left| n''_i \right|$$

of absolute acceleration counts was drawn against the number of successive measurements in the intervals of one second. In the first case, the hypothesis N_1 = 60 percent was accepted

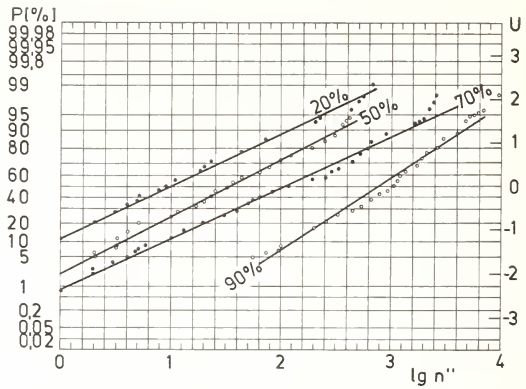

Figure 7. The distribution of acoustic emission acceleration counts in various periods of fatigue life. The values were collected from 37 samples, three values in one second intervals for each sample.

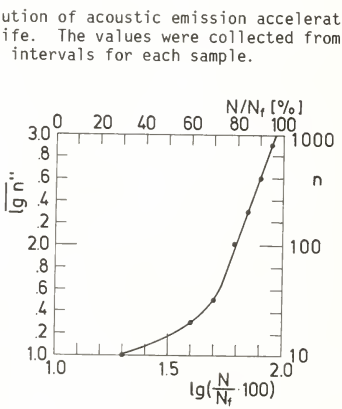

Figure 8. Acoustic emission acceleration counts plotted against fatigue life. The mean values of figure 7 has been used.

against the alternative hypothesis N_o = 40 percent after 7 trials. In the second case, the hypothesis N_o = 40 percent was accepted and the hypothesis N_1 = 70 percent rejected.

These two examples, selected at random, may serve to demonstrate one possible way of estimating the fatigue life from acoustic emission tests.

5. Direct Observation of Crack Growth

As mentioned earlier there may be direct and indirect approaches to the prediction of fatigue life still remaining in the sample. When large objects made of high toughness material are considered, the fatigue crack dimensons may attain considerable values, e.g., the depth of fatigue crack may be of the order of 40 to 50 percent of the sample diameter before rapid crack propagation starts. In such cases, due to the considerable dimensions of the crack, the ultrasonic method can be used for direct measurement of fatigue crack growth.

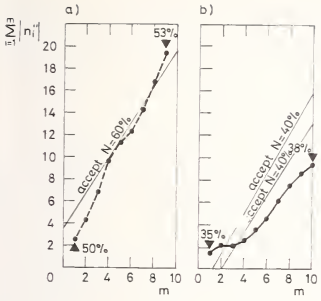

Figure 9. Sequential analysis applied to the estimation of fatigue life. Examples of discrimination between two hypotheses.

One such example occurs in the case of columns of hydraulic presses. The columns work in corrosive environments. Their length ranges up to 10 m, their diameter is about 0.35 m and they bear a pulsating load of 7.4 mn. The fatigue crack usually starts perpendicular to the axis of the column, at the end of the thread, about 0.5 m from one of the ends of the column. Such cracks may easily be detected with 1 MHz ultrasonic longitudinal waves, introduced from the head surface of the column. Once detected, its growth may be followed at given time intervals during technical overhauls.

The critical crack depth for a column stressed at a 100 MPa pulsating load could be estimated to about 40 percent of the column diameter. An example of controlled fatigue crack growth is presented in figure 10.

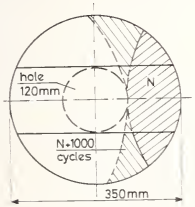

Figure 10. Two fatigue crack fronts in a column of a hydraulic press. The pulsating load was 7.4 MN and the column diameter 350 mm. The indicated crack front increase occurred after 1000 cycles.

Two front lines of a growing fatigue crack, shown in the figure were separated by about 1000 loading cycles. In this stage, the column was replaced by a new one. Even with such a large crack, it was possible to operate the press safely until the scheduled time of technical overhaul [7].

6. Conclusions

Depending on the configuration of the sample subjected to fatigue straining, various methods can be used. The changes of attenuation of ultrasonic surface waves offer prospects for a successful fatigue monitoring parameter. For aluminum alloy samples, a nonmonotonic increase in attenuation was observed for comparatively short fatigue lives, of the order of 1000 to 4000 cycles. For longer fatigue lives, this phenomenon was absent.

The analysis of acoustic emission responses seems to be more sensitive for detection of the transition between the incubation and crack propagation stages. It also offers the possibility for estimating fatigue life when only random measurements of acoustic emission response are made.

Another approach is the direct observation of crack growth. Knowing the fracture toughness of materials, the critical crack size can be calculated. In this case, the task of ultrasonic methods is to monitor the crack growth in order to provide a reliable service performance. Thus, acoustical methods, due to their great flexibility and sensitivity to changes in materials structure, may supply much information on performance of materials strained in fatigue.

References

[1] Green, Jr., R. E., Ultrasonic attenuation detection of fatigue damage, Ultrasonic International 1973 Conference Proceedings, pp. 187-193, IPC Business Press Ltd., London (1973).

[2] Pawlowski, Z., Internal friction of metals and the problem of damage cumulation with static and variable loadings, Proc. Vibration Problems (Warsaw), 1, 43-64 (1963).

[3] Pawlowski, Z., Ultrasonic attenuation during cyclic straining, in Proc. Fourth Intern. Conf. on Nondestructive Testing, pp. 127-130, Butterworths, London (1964).

[4] Brokowski, A. and Pawlowski, Z., Ultrasonic and fractographic investigation of fracturing processes during fatigue, in Bulgarian, Fourth National Conf. on Nondestructive Testing, pp. 103-113, Varna, Bulgaria (28-30 June 1972).

[5] Funke, G. and Pawlowski, Z., Acoustic emission and fractographic analysis applied to the estimation of crack growth during low cycle fatigue, in Proc. Eighth World Conf. Nondestructive Testing, Paper 3K10, Cannes (1976).

[6] Hald, A., Statistical Theory with Engineering Applications (J. Wiley, New York, 1952).

[7] Pawlowski, Z., Problem of identification of physical state of constructional materials with nondestructive testing methods (in Polish), Fourth National Symposium on Exploitation of Technical Appliances, pp. 147-152 OPT Katowice, Vol. 4 (1977).

National Bureau of Standards Special Publication 596, Ultrasonic Materials Characterization, H. Berger and M. Linzer, eds., Proceedings of the First International Symposium on Ultrasonic Materials Characterization held at NBS, Gaithersburg, Md., June 7-9, 1978. Issued November, 1980.

HOW CAN PHASE ANALYSIS OF SHORT PULSES INCREASE THE ACCURACY OF TIME MEASUREMENTS

I. Bredael and F. Merli

Commission of the European Communities
Joint Research Center of Ispra
Materials Science Division
Nondestructive Testing Laboratories, B33
I-21020 Ispra (Varese) ITALY

Accurate time position of a short pulse is not intuitive on a scope screen. Therefore, some mathematical data treatment is needed. The method described here provides a means to determine accurately time position, phase angle, and modulus of a short pulse. The method is well adapted to implementation with a minicomputer.

1. Introduction

Time position measurement of a short pulse is useful for the determination of sample thickness, velocity of sound, etc. Unfortunately, on short pulses this determination is quite difficult because it is inappropriate simply to use the peak value; this value for lightly damped pulses may correspond with the maximum of the amplitude modulus generating the pulse. In the same way, it is inappropriate to take the mean time value because generally the pulse is not symmetrical (fig. 1).

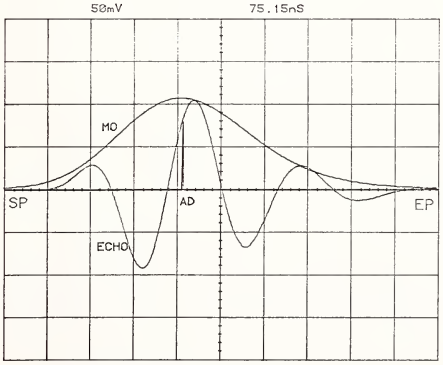

Figure 1. Echo and modulus for Plexiglas.

In a preceding paper, a method was presented to determine the phase of the pulse using the Hilbert Transform [1][1]. This paper presents a method based on the same principle but using the Fourier transform, which is more suitable for use with minicomputers because these perform the convolution using the Fast Fourier Transform (FFT).

2. Method Description

After digitization of the signal, the quadrature of the original signal and the modulus of the original signal can be computed. The time of the maximum of amplitude of the modulus represents the moment of maximum energy in the analyzed signal. This moment can be taken as characteristic for a given acoustic interface between two different media.

A first step in the computation consists in selecting a part of the original echo signal, using a manually selected starting and ending point. The signal is then extended to cover the whole screen and serves as the selected original signal. A second step is noise filtering. This is done by FFT analysis. All the frequencies higher than two times the frequency of maximum response are eliminated, using a window with smooth slopes. Then it is necessary to compute the quadrature of this signal, using the Hilbert Kernel (fig. 2). In Appendix 1, three ways are indicated to compute the quadrature. The first and third methods use the convolution algorithm. In a minicomputer this is generally done by using the products of the FFTs followed by IFT (Inverse Fourier Transform). To spare time and increase precision, the second method using the IFT of the crossed real and imaginary parts given by the FFT of the original signal is recommended.

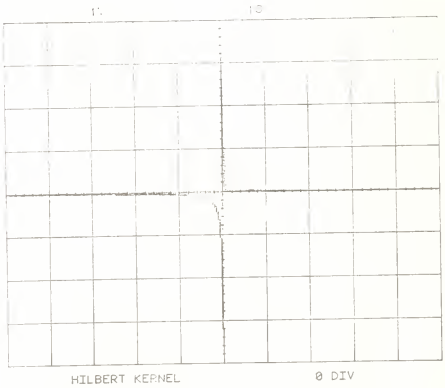

Figure 2. Hilbert kernel.

Using the selected and filtered original signal and its quadrature, we can compute the modulus of the original signal (fig. 3), taking the square root of the sum of the squared original signal and the squared quadrature. Unfortunately, this modulus contains noise such as windowing noise, nonlinear distortions, etc.; this noise must be filtered out. The filtering may be done in two ways, as explained in Appendix 2. The fastest is FFT filtering, cutting-out all the frequencies higher than the frequency of maximum response. Of course, in this way we introduce a heavy windowing effect, but the computer address AD corresponds with the exact delay. The second method, using auto-convolution of the modulus, is accurate over the entire original signal.

[1]Figures in brackets indicate the literature references at the end of this paper.

Now it is possible to find the exact time delay of the pulse multiplying the address of the largest modulus (AD = number of points on the time axis) by the time base factor. This delay is very useful, for example, for determination of material thickness in thin layers where it is necessary to use short acoustic pulses at high frequencies.

3. Example of Applications

The modulus of the echo pulse is computed by taking the square root of the sum of the squares of real and imaginary parts of the signal; that is of the original waveform and the quadrature signal. At a given address AD (corresponding to a time position), corresponds to the maximum of this modulus. This time position (DELYED) summed to the delay of the delaying time base (DELYING) gives the total delay (TOTDLY) between transmission pulse and echo.

Knowing the address AD, it is possible to find the phase angle of the modulus taking the arctangent of the ratio of the value of the quadrature signal at the address AD, divided by the value of the original signal at the same address.

The equipment used for this work includes the following:

1) Panametrics Pulser Receiver PR 5052.

2) Tektronix Fast Transient Recorder (7A13, 7B92A) or Tektronix Digital Processing Oscilloscope (7A13, 7D11, 7B92A).

3) DEC/PDP-11/05 Minicomputer with 32K Memory and BASIC.

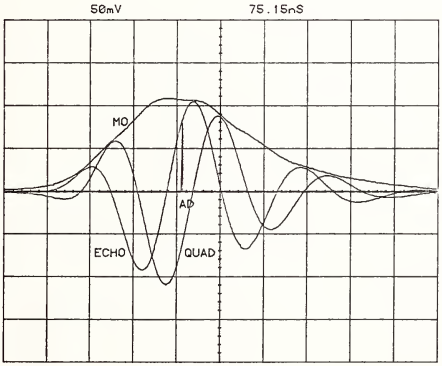

Figure 3. Echo and modulus for Plexiglas.

The data, as well as the polar graph give an idea on the interaction of ultrasound on materials as indicated in the following examples. Using arrays of 512 points with 8 or 10 bits dynamic range, peak to peak error in time is one address point, i.e., 1.6° and 0.34 percent on modulus. The address error for a hard damped ultrasonic probe (Q = 1.2) at 10 MHz corresponds to 1 ns. The time needed for this computation is in the range of several seconds without graphing.

3.1. Quartz and Lucite (Plexiglas) samples in water

Samples of quartz (1.5 cm thickness) and of Plexiglas (0.3 cm thickness) were tested in water. In figures 4 and 5, the front echoes on glass and Plexiglas are shown. The damping potentiometer was set in such a way that the two upper half waves were at about the same level. This eliminates the phase shift introduced by the equipment and the water path.

Notice that the indicated phase angle is about 0°. The shapes of the two echoes are quite similar.

Figures 6 and 7 represent the first reflected echoes from the rear part of the samples. Here, the shapes are no more similar and a determination of the time position of the maximu modulus becomes difficult. As expected there is about a 180° shift between the front echo and first rear echo. These last echoes are used as references.

Figures 8 and 9 show the shape of the second rear echoes. Here the discrepancies are noticeable. The delay differences on the same material represent two times the travel time through the analyzed sample. This delay permits the computation of the longitudinal sound velocity in the sample at the actual working frequency. In the same way the relation of the moduli provides a measure of the absorption and complex reflection coefficient. These graph are plotted as a function of time in the clockwise direction.

Figures 6, 7, 8, and 9 show that quartz and Plexiglas react in opposite directions (respectively + 13.4° and - 30°) at about 6 MHz (fig. 10). Thus, at 6 MHz, the phase shift for quartz is 4.47° per cm and - 50° per cm for Plexiglas. Also, at 6 MHz the time delay difference between figures 6 and 8, and 7 and 9 permit one to compute the longitudinal sound velocities of 5682.5 and 2979.1 ms. The four digit precision of these data is limited only by the single precision computational capability of the PDP-11/05 and the accuracy of the sample thickness measurement.

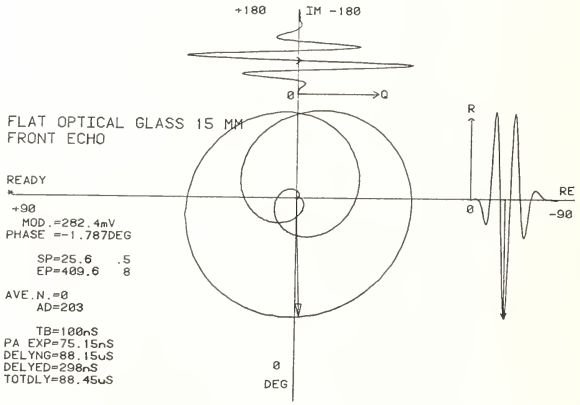

Figure 4. Reflector characterization by phase on D.P.O.

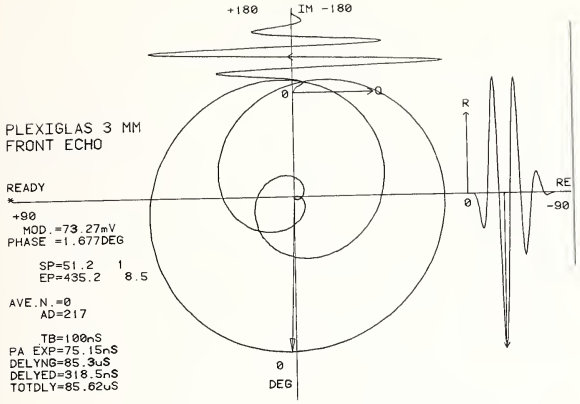

Figure 5. Reflector characterization by phase on D.P.O.

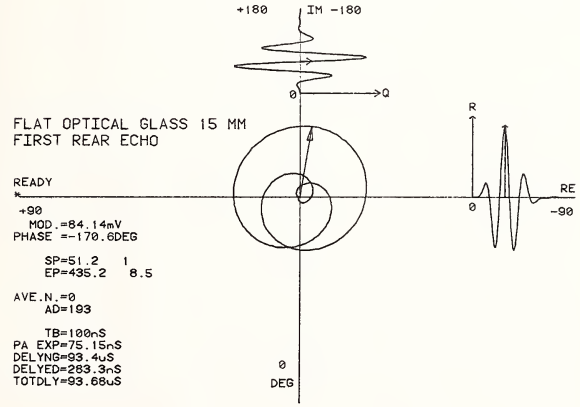

Figure 6. Reflector characterization by phase on D.P.O.

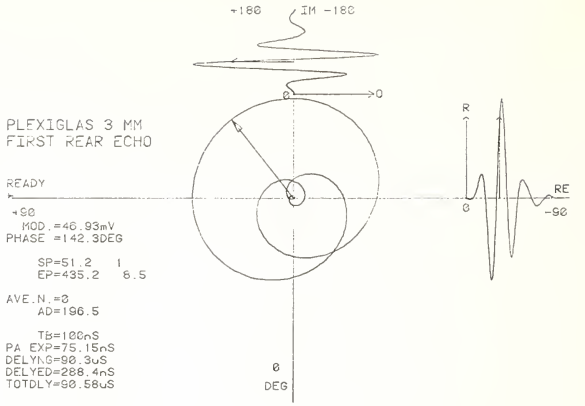

Figure 7. Reflector characterization by phase on D.P.O.

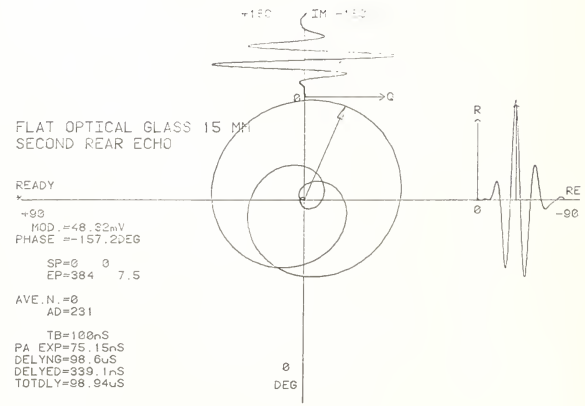

Figure 8. Reflector characterization by phase on D.P.O.

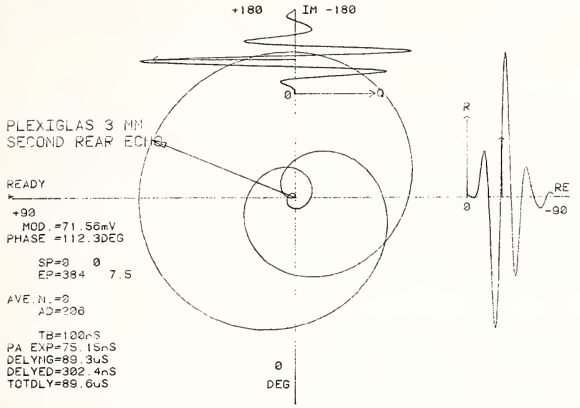

Figure 9. Reflector characterization by phase on D.P.O.

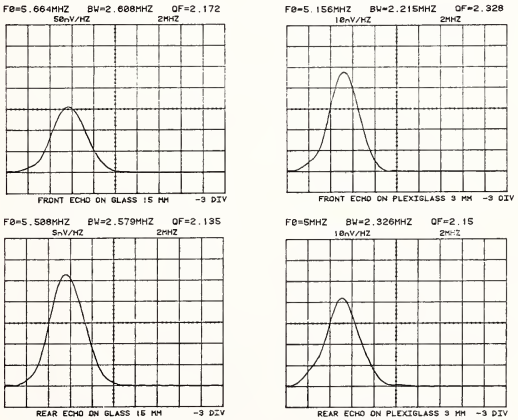

Figure 10. Echoes from Plexiglas.

References

[1] Bredael, I., Jehenson, P., and Merli, F., Proposal for material characterization using phase analysis of ultrasonic pulsed echoes, J.R.C. Ispra, NDT Section, Materials Science Div., Atti II Congresso Nazionale SISUM, Roma, 12/13/6/1976.

Appendix 1

```
*** HILBERT KERNEL IN ARRAY 'B' FORMULATION ***

     * BASED ON 1/(3.1416 * T) *
       BASIC PROGRAM:KERNEL IN ARRAY 'B' AND QUADRATURE IN ARRAY 'C' OF 512
    POINTS:
FOR I=Ø TO 255:LET B(I)=-1/(3.1416*(I-256)):NEXT I
FOR I-257 TO 511:LET B(I)=-1/(3.1416*(I-256)):NEXT I
CONV A,B,C,D (A=ENTIRE CONVOLUTION, C=1D.PART, D=2D.PART)
LET C=A      (QUADRATURE IN ARRAY 'C')
END


     * BASED ON FFT'S REAL AND IMAGINARY CROSSING *
     ORIGINAL WAVEFORM IN ARRAY 'A',QUADRATURE IN ARRAY 'C'
FFT A,B,D       (B=REAL, D=IMAGINARY)
     IFT D,B,C  (D USED AS REAL, B USED AS IMAGINARY, C=QUADRATURE)
     DEPENDING ON THE FFT ALGORITHM IT MAY BE NECESSARY TO INVERT THE 'C'
MATRIX AS FOLLOW:
FOR I=Ø TO 255:LET XX=C(I):LET C(I)=C(511-I):LET C(511-I)=XX:NEXT I
END


     * BASED ON IMAGINARY PART OF A STEP FUNCTION *
     SYNTHETIC STEP FUNCTION IN ARRAY 'D'
LET D=1:FOR I=256 TO 511:LET D(I)=-1:NEXT I
FFT D,C,B  (THE RESULTING KERNEL IS IN ARRAY 'B')
CONV A,B,C,D      (A=ENTIRE CONVOLUTION,  C=1D.PART,  D=2O.PART)
LET C=A           (QUADRATURE IN ARRAY 'C')
END
```

APPENDIX 2

```
*** MODULUS FILTERING (ARRAY 'B') ***

  * BASED ON FFT'S HIGH FREQUENCY CUT ,STARTING FROM CENTRAL FREQUENCY
(XF) OF PROBE *
  N.B.:THIS CUTING INTRODUCES WINDOWING ERRORS ON THE WAVEFORM,BUT THE
POSITION OF MODULUS MAX. IS CORRECT
  *BASIC PROGRAM:'FILTERED MODULUS' IN ARRAY 'D'*
FFT D,E,F  (E=REAL, F=IMAGINARY OF FFT)
LET D=E*E+F*F:LET XF=CRS(D,MAX(D))
FOR I=XF TO 511:LET E(I)=Ø:LET F(I)=Ø:NEXT I
IFT E,F,D:LET AD=CRS(D,MAX(D))
  N.B.:AD ,IS THE ADDRESS IN TIME OF THE MODULUS MAXIMUM
END

  * BASED ON AUTO CONVOLUTION IN ARRAY 'D' FROM 'PD' (MODULUS) *
  N.B.:THE CONV.SUBROUTINE GIVES THE CONVOLVED RESULT OF D AND D IN D
WHERE LAST D REPRESENTS THE COMPRESSED ARRAYS E AND F IN D
  *BASIC PROGRAM*
LET D=PD:CONV D,D,E,F  (D=ENTIRE CONVOLUTION, E=1D.PART, F=2D.PART)
LET AD=CRS(D,MAX(D))     (AD=ADDRESS IN TIME OF MODULUS MAXIMUM)
LET D=D*D:LET D=D/D(AD):LET D=D*PD(AD)  (NORMALIZATION)
  N.B. :'AD' ADDRESS MAY BE TAKEN IN ARRAY 'E' OR 'F' FOR MORE ACCURACY
END
```

National Bureau of Standards Special Publication 596, Ultrasonic Materials Characterization, H. Berger and M. Linzer, eds., Proceedings of the First International Symposium on Ultrasonic Materials Characterization held at NBS, Gaithersburg, Md., June 7-9, 1978. Issued November, 1980.

ULTRASONIC LENGTH MEASUREMENT IN SINGLE CRYSTAL AND POLYCRYSTALLINE AGGREGATE WITH PREFERRED ORIENTATION

J. N. C. Chen

W. P. Dobson Research Laboratory
800 Kipling Avenue
Toronto, Ontario M8Z 5S4
Canada

and

C. A. Carey

Sanders Associate
Nashua, NH

Traditional methods of ultrasonic length measurements require the understanding of grain orientation (for single crystal) or grain orientation distribution (for polycrystalline aggregate). This is due to the fact that sound velocities are very sensitive to orientation changes.

This paper introduces a composite velocity, which is a combination of longitudinal and shear velocities. The novel feature of this composite velocity is its insensitivity to grain orientation (for single crystal) or grain orientation distribution (for polycrystalline aggregate) despite the fact that its constituent velocities are orientation dependent. Several applications of this composite velocity have also been explored. They include ultrasonic length measurement independent of grain orientation information, as well as measurement of pure elastic properties of a polycrystalline material. Independent experimental data on textured copper and chromium steel have been used to illustrate the performance of the composite velocity in contrast to the traditional velocities.

1. Introduction

The modulus of a metal depends on many factors such as defect concentration (dislocations, inclusions), relaxation (grain boundary, diffusion), and basic crystalline state (grain size, orientation). Even in a laboratory environment it is difficult to control all these factors simultaneously. For instance, annealing can remove dislocations, but the grain size and orientation (texture) is also changed in such a process. Nondestructive applications in mills or on production lines generally allow even less control of the pertinent variables which determine the speed of sound in a polycrystalline medium. In many engineering applications, the modulus is used to monitor some variable or determine thickness or temperature. However, the author [1][1] and others [2] have found that variations in modulus due to grain orientation distribution in polycrystalline samples often obscure the measurement process. A simple technique using only ultrasonic measurements is proposed which removes the texture effect from the measurement.

Three types of waves propagate in a single crystal along any specific direction [3]. The three waves - one longitudinal and two shear - have distinctive displacement vectors

[1]Figures in brackets indicate the literature references at the end of this paper.

and velocities of propagation. The magnitude of the sound speed of each wave type also varies as a function of crystal orientation. The velocity of a specific type of sound wave in a polycrystalline material depends both on the texture and the boundary between individual crystals of the medium. The velocity of any type of sound wave in a polycrystalline aggregate could ideally be determined if a knowledge of the grain orientation distribution function is known. The modulus (or sound speed) for an isotropic polycrystalline sample can be calculated for the limiting cases of constant stress [4] or constant strain [5] across the individual crystallite boundaries. It has been shown [6] that the effective modulus should always lie between the Voigt and Reuss bounds. Actually, a set of more stringent bounds has been derived by Hashin and Shtrikman [7] for polycrystals with random grain orientation distribution. These two sets of bounds are generally referred to as upper (Hashin), lower (Shtrikman) bounds as well as highest upper (Voigt) and lowest lower (Reuss) bounds. For materials of high anisotropy, the Voigt and Reuss bounds are very widely separated and could not give a reasonable approximation of effective modulus. Hashin and Shtrikman bounds could give reasonable approximation of modulus only for randomly oriented polycrystals. Thus, some method of calculating effective modulus for all the conditions seems to be unavailable.

The present paper introduces a composite velocity (or modulus) which is a combination of the three velocities in a single crystal. An extension of the composite velocity to describe orientation effects on a polycrystalline aggregate is proposed. The uniqueness of this composite velocity is that in materials of cubic structure, its amplitude appears to be a constant for any grain orientation or grain orientation distribution. In addition, the composite modulus can be constructed from three ultrasonic measurements without prior knowledge of the texture of the sample.

The present paper also introduces the possible applications of this new composite velocity, which includes ultrasonic thickness measurements as well as elastic property indications independent of grain orientation or grain orientation distribution.

The theory for this composite modulus could be exactly derived from the wave equation for a single crystal of cubic structure [8]. A similar composite modulus has also been reported by Date [2] et al., for certain wave guides. However, experimental data collected indicates a simplified theory elaborated on in the present paper can be used for polycrystalline infinite media and wave guides.

2. Theory

The basic equation used in ultrasonic transmission measurements relates the path length along the measurement direction (L), the ultrasonic transit time ($t(\theta)$), and the speed along the direction of measurement ($V(\theta)$). If θ represents the angle of the direction of propagation relative to the crystal axis, the basic equation becomes

$$L = V_K(\theta)\, t_K(\theta) \quad , \tag{1}$$

where K represents a particular mode of sound (longitudinal, shear). Ultrasonic measurement in a polycrystalline aggregate is a more complicated problem. There are many grains in a polycrystal, and each one has a specific orientation. The sound speed, in this case, is the mean velocity. If P(i) is the weighting function for the ith crystal in the whole volume under the sound beam, the mean velocity is

$$\bar{V}_K = \sum_i P_K(i)\, V_K(\theta_i) \quad , \tag{2}$$

where $V_K(\theta_i)$ is the K-mode sound velocity in the ith crystal, and θ_i represents the direction of sound propagation in this crystal. It is important to point out that $V_K(\theta_i)$ could be different when the ith crystal is in single crystal form or when it is a member of a polycrystalline aggregate.

A relation similar to eq. (1) also exists for polycrystalline aggregate:

$$L = \bar{V}_K \, \bar{t}_K \quad , \tag{3}$$

where $\bar{t}_K$ is the transit time for the sound wave to propagate through the thickness (L).

Equations (2) and (3) indicate that ultrasonic transit time determinations could be used for ultrasonic length measurements in a polycrystalline material if the orientation distribution functions were known. Thus, the necessary and sufficient condition for using ultrasonic transit time for thickness measurement is a detailed knowledge of the grain orientation for a single crystal and grain orientation distribution function for a polycrystal. However, it is possible to make several transit time measurements to render the knowledge of grain orientation or grain orientation distribution unimportant in the ultrasonic thickness measurement under discussion.

It is well known that three types of waves can propagate in an indefinite isotropic medium. These are one longitudinal (velocity V_ℓ) and two shear (velocities V_{s1}, V_{s2}).

Each of the three wave velocities varies in amplitude with the direction of sound propagation. However, it has recently been found [8] that a simple relation always exists among three velocities independent of grain orientation. The relation for a single crystalline material of cubic structure is

$$V_\ell^2(\theta) + V_{s1}^2(\theta) + V_{s2}^2(\theta) = \frac{C_{11} + 2C_{44}}{\rho} \tag{4}$$

where ρ is the density of the material and C_{11}, C_{44} are elastic constants.

With eq. (4), another interesting relation is also found. If t_ℓ, t_{s1}, t_{s2} are the three transit times for a thickness L measured with the three waves, the relation among L, V and t could be represented as

$$V_\ell(\theta) = \frac{L}{t_\ell(\theta)} \quad , \quad V_{s1}(\theta) = \frac{L}{t_{s1}(\theta)} \quad , \quad V_{s2}(\theta) = \frac{L}{t_{s2}(\theta)} \quad . \tag{5}$$

From eqs. (4) and (5), it can be derived that

$$L = \sqrt{\frac{(C_{11} + 2C_{44})/\rho}{[1/t_\ell^2(\theta) + 1/t_{s1}^2(\theta) + 1/t_{s2}^2(\theta)]}} \quad . \tag{6}$$

Equation (6) indicates that the thickness L could be determined using the three transit times of the three types of waves, and without a knowledge of the grain orientation.

A relationship similar to eq. (4) has been found to be empirically true for polycrystals. Actually, several sets of independent data analyzed in the next section indicate that a relation

$$\bar{V}_\ell^2 + \bar{V}_{s1}^2 + \bar{V}_{s2}^2 = \text{constant} \tag{7}$$

exists in polycrystalline aggregate. Equation (7) suggests that an ultrasonic thickness measurement similar to eq. (6) can be worked out for polycrystalline aggregate, independent of grain orientation distribution information.

A method has been presented, which will allow thickness measurement in both single and polycrystalline materials without any knowledge of the grain orientation or grain orientation distribution. The validity of the theory will be compared with some of the existing data in the next section. Both moduli and velocities will be used interchangeably in the text using the relations

$$V_\ell = \sqrt{\frac{E}{\rho}} \quad , \quad V_{s1} = \sqrt{\frac{G_1}{\rho}} \quad , \quad V_{s2} = \sqrt{\frac{G_2}{\rho}} \quad ,$$

where E is Young's modulus and G is the Shear modulus.

It is important to note that: (a) in some orientations, the two shear waves degenerate to have the same velocity, and (b) the shear wave in certain wave guides is actually torsional in character, and has only one torsional wave velocity since the torsional mode automatically averages the stress in two perpendicular directions.

The composite modulus (or velocity) also appears to be a useful engineering parameter for cubic material. In a single crystal, it gives a very-easy-to-measure elastic property of the material. Elastic constants (C_{11},C_{12},C_{44}) are measurable only with a clear knowledge of grain orientation. Young's and shear modulus can be easily measured. However, they do not have a definitive meaning for the material because of their variation with grain orientation. This composite modulus can be easily measured, and it also gives a definitive meaning of the elastic property of a certain material.

In a polycrystalline aggregate, the composite modulus allows a unique means to measure the mean elastic properties of the constituent grains. Two major factors normally exist in Young's or shear modulus measurement: (a) the elastic properties of the constituent grains and (b) the orientation of the constituent grains. Separation of the two factors seems to be of great interest in many engineering applications, such as fracture mechanics. This composite modulus appears to offer a unique method to accomplish such a separation.

3. Discussion of the Theory and Experimental Results

Several examples of the orientation invariance of the composite modulus are presented here. Firstly, it is shown that eq. (4) is obeyed along certain directions in a single crystal. Then, three sets of experimental data related to polycrystals from different sources are discussed.

Close examination of these examples indicates the value of the composite modulus appears to be invariant while Young's and shear moduli change drastically.

3.1 Single crystal

The three velocities [9] propagating in a cubic crystal along the [100] direction are

$$V_\ell = \sqrt{C_{11}/\rho} \quad , \quad V_{s1} = \sqrt{C_{44}/\rho} \quad , \quad V_{s2} = \sqrt{\frac{C_{44}}{\rho}} \quad .$$

The three velocities in the [110] direction are

$$V_\ell = \sqrt{\frac{C_{11} + C_{12} + 2C_{44}}{2\rho}} \quad , \quad V_{s1} = \sqrt{C_{44}/\rho} \quad , \quad V_{s2} = \sqrt{\frac{C_{11} - C_{12}}{2\rho}} \quad .$$

The three velocities in the [111] direction are

$$V_\ell = \sqrt{\frac{C_{11} + 2C_{12} + 4C_{44}}{3\rho}} \quad , \quad V_{s1} = \sqrt{\frac{C_{11} - C_{12} + C_{44}}{3\rho}}$$

$$V_{s2} = \sqrt{\frac{C_{11} - C_{12} + C_{44}}{3\rho}} \quad .$$

In all three directions, the three velocities are found to satisfy eq. (4).

3.2. 99.9 percent OFHC polycrystalline wire (0.26 cm diameter)

The grains in the wire are believed to be aligned due to the wire making process. 100 kHz acoustic waves were used to measure both the Young's and torsional moduli as a function of temperature [1]. Figures 1 and 2 show the torsional and extensional moduli measured. For comparison purpose, also included are the theoretically predicted moduli from the four models (Voigt, Hashin, Shtrikman and Reuss). In a polycrystalline aggregate of random grain orientation, the Young's and torsional moduli should fall between the Hashin and Shtrikman limits. In figures 1 and 2, both moduli consistently lay outside the upper (Hashin) and lower (Shtrikman) limits. Furthermore, Young's moduli throughout the temperature range are higher than the upper limit while the torsional moduli are consistently lower than the lower limit. As described in eq. (7), there is a composite velocity which is insensitive to grain orientation distribution. This equation could be presented using the moduli, as follows:

$$\bar{E} + \bar{G}_1 + \bar{G}_2 = C = \text{constant} \qquad (8)$$

where C is the composite modulus.

The C values are found to be very close to the theoretically predicted values despite the fact that both Young's and torsional moduli deviate drastically from theoretical predictions. Thus, eq. (7) is substantiated.

In figure 3, the deviations of moduli from the theoretical predictions for Young's torsional and composite moduli at 200 °C, 300 °C, 400 °C and 500 °C are presented (the mean of Hashin and Shtrikman values is used as theoretical predictions just to make the comparison simple). The figure indicates that the deviation for the composite modulus is consistently lower compared to Young's and torsional moduli for all the temperature ranges. The mean deviation for the composite modulus is 2.8 percent, while for Young's and shear is 10.8 percent and 7.2 percent, respectively. The 2.8 percent deviation for the composite modulus may well be due to the variations of copper materials chosen. However, the 7.2 percent and 10.8 percent deviations for shear and Young's moduli are apparently too large and could not be due to variations of copper samples.

It is believed that the copper sample used has strong preferred grain orientation due to the wire manufacturing process. The theoretically predicted moduli are, however, for polycrystalline material of random grain orientation. The grain orientation distribution is believed to cause the high deviations for Young's and shear moduli reported in figure 3. This analysis also indicates that the composite modulus is very insensitive to the preferred orientation or texture.

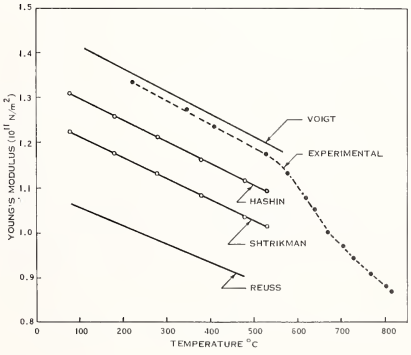

Figure 1. Young's moduli vs. temperature for polycrystalline copper wire.

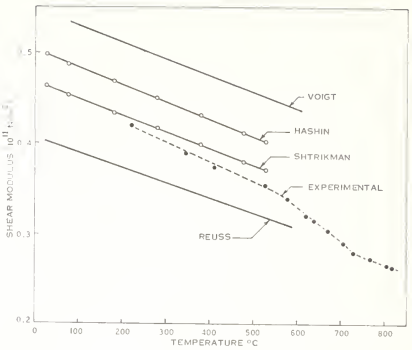

Figure 2. Shear moduli vs. temperature for polycrystalline copper wire.

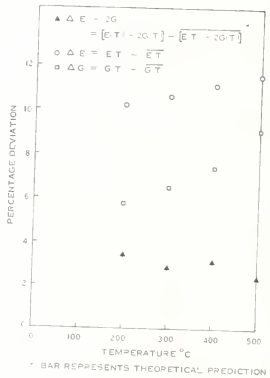

Figure 3. Deviations of the three moduli from their theoretically calculated values at different temperatures.

3.3. Electrolytic copper rods (1.3 cm diameter) [10]

Young's and shear moduli were determined by vibration techniques. The data were taken as a function of annealing temperature as well as annealing time. Figures 4 and 5 show how Young's and shear moduli change as a function of annealing time at 240 °C and 280 °C. It is quite evident that the two moduli (Young's and shear) are always heading in opposite directions as their values vary. The maximum deviation, which is defined as the difference of the highest and lowest values divided by the mean of the two values, is also presented on figures 4 and 5. At both annealing temperatures, the maximum deviations for the composite modulus is about one order of magnitude smaller than that for the Young's and shear moduli.

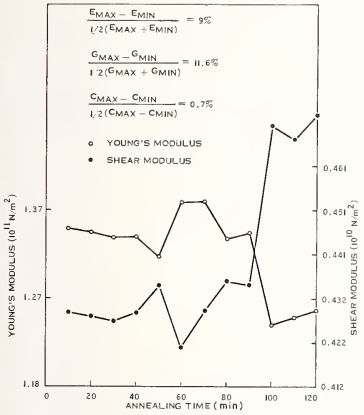

Figure 4. Young's and shear moduli of copper bar as a function of annealing time (280 °C).

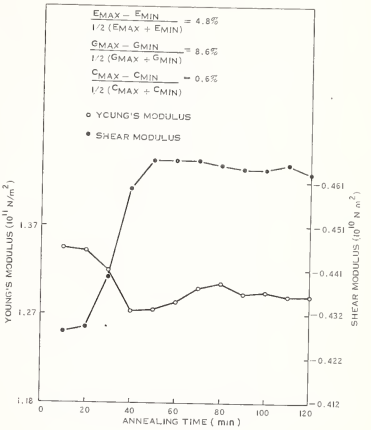

Figure 5. Young's and shear moduli of copper bar as a function of annealing time (240 °C).

3.4. 17 percent chromium steel plates [2]

Young's and shear moduli as a function of direction were measured with resonance techniques. Figure 6 shows Young's and shear moduli measured in different directions. It is evident that the two moduli are always heading for the reverse directions as they vary. However, irrespective of the drastic variation of Young's and shear moduli as functions of direction of measurement, the composite modulus varies very little. The maximum deviation of the three moduli is also indicated in figure 6. The maximum deviation for the composite modulus is 2.6 percent, which is significantly smaller than the 8.4 percent for the shear modulus and 11.8 percent for Young's modulus.

All of the analysis described above appears to indicate that the composite velocity is insensitive to grain orientations in a single crystal or grain orientation distribution in a polycrystalline aggregate. Thus, ultrasonic thickness measurement using this composite modulus described in the theory section appears to be substantiated by the experimental data.

4. Summary

A composite velocity is introduced. The most important feature of this velocity (or modulus) is its independence to grain orientation in single crystals of cubic structure. Experimental evidence indicates that a composite effective modulus for polycrystalline aggregate also has similar characteristics.

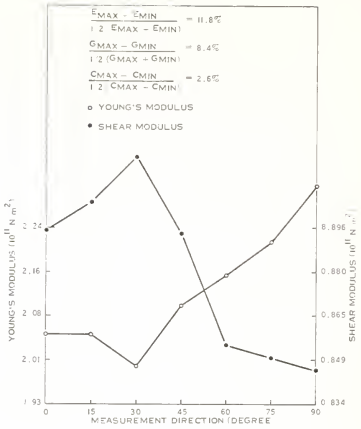

Figure 6. Young's and shear moduli for 17 percent chromium steel as a function of measurement directions.

Two of the most important applications of this composite modulus conceived by the authors are:

(1) It is a useful parameter for science and engineering, because (a) it gives one easy-to-measure definitive meaning of the elastic property of a specific single crystal material, (b) it defines the elastic properties of a polycrystalline aggregate which is not affected by grain orientation.

(2) It could be used to make ultrasonic thickness measurements independent of grain orientation or grain orientation distribution. This application includes thickness measurements for materials with preferred orientation, which cannot be accomplished by existing state-of-the-art techniques.

The authors are especially indebted to Dr. O. A. Kupcis and Dr. D. V. Leemans of Ontario Hydro for many valuable discussions.

References

[1] Chen, J. N. C., Ph.D. Thesis, Boston College, p. 113 (1976).

[2] Date, E. H. F., and Andrews, K. W., Anisotropic and composition effects in the elastic properties of polycrystalline metals, Brit. J. Appl. Phys. 2, 1373 (1969).

[3] Kettle, C., Introduction to Solid State Physics, p. 119, (John Wiley, New York, 1967).

[4] Voigt, W., Lehrbuch der Kristallphysik, p. 962, (Teūbuer, Leipzig, 1928).

[5] Reuss, A., Z. Angew. Math. Mech., 9, 49 (1929).

[6] Hill, R., The elastic behaviour of a crystalline aggregate, Proc. Phys. Soc., A65, 349 (London 1952).

[7] Hashin, Z. and Shtrikman, S., A variational approach to the theory of the elastic behaviour of polycrystals, J. Mech. Phys. Solids, 10, 343 (1962).

[8] Musgrave, M. J. P., Crystal Acoustics, p. 108, (Holden Day, San Francisco, 1970).

[9] Mason, W. P., Physical Acoustics and Properties and Solids, p. 370 (Van Nostrand, Princeton, 1958).

[10] Wara, H., Modulus of elasticity for cold drawn copper as functions of anneal time, Wire and Wire Products, 54 (July 1968).

National Bureau of Standards Special Publication 596, Ultrasonic Materials Characterization, H. Berger and M. Linzer, eds., Proceedings of the First International Symposium on Ultrasonic Materials Characterization held at NBS, Gaithersburg, Md., June 7-9, 1978. Issued November, 1980.

METALLURGICAL CHARACTERIZATION BY ULTRASONICS

Hervé Recroix
DDEC/SDEEC/GET
CEN Cadarache
BP no 1
13115 St. Paul lez Durance
FRANCE

A method is presented for the metallurgical measurement of thin plates, the principle of which is based on very precise measurements of the longitudinal and transverse velocities.

This method of testing makes it possible to separate the two static parameters (E, σ) of the medium's viscoelastic characteristics (internal frictions, dislocation resonances), and to measure the degree of cold working of the thin plate with more discrimination than with a classical traction test.

1. Introduction

This paper presents an account of a method of metallurgical analysis based on very precise measurements of the velocities of longitudinal and transverse sound waves of very high frequency. This technique of measurement is not only applicable to thin plates with parallel faces, but it is also relevant to the testing of the cold working rate of metal plates.

The originality of this method depends on the quality of the measurements in which the relative precision needs to be better than 1 part in 4×10^{-4}, so that the choice of practical working frequency extends from 15 to 50 MHz, depending on the absorption of the material. This explanation of the analysis of the measurements requires an understanding of the physics and electronics involved. The paper ends with a series of examples on different types of stainless steel.

2. Principles of Measurements

Given that $C_L(\nu)$ and $C_T(\nu)$ are the respective phase speeds of the longitudinal and transverse waves, of frequency ν, two basic configurations can be obtained, one for each type of wave:

2.1. Measurements associated with $C_L(\nu)$

Figure 1a shows the arrangement of the transducers by which measurement is made either by transmission-reception or by transmission. Medium 1 is always a liquid; medium 2 may be a liquid or a gas (in a transmission-reception situation). To analyze the different signals S_0, S_1, S_2, S'_1, S'_2, the coefficients of reflection and transmission from medium (i) to medium (j) are denoted by r_{ij} and t_{ij}. Theoretically, if the media were dispersive, the coefficients would be complex and denoted by r^*_{ij} and t^*_{ij}. In practice, the acoustic impedances of the media 1 and 2 are always insignificant following that of medium 0, and only the the phase change across t^*_{10} influences the measurement. Thus:

$$t^*_{10} = t_{10}\, s(\nu)\, e^{j\phi_L(\nu)} .$$

The value of the angle $\phi_L(\nu)$ is given by the equation:

$$\phi\ (\nu) = \arctan \frac{d_L\ C_L}{2\pi\nu} \quad ,$$

where $\phi_L(\nu)$ is the longitudinal wave attenuation corresponding to the viscoelastic properties of medium (0). Then by using the relationship

$$Z_{01} = -Z_{10} > 0$$

where

$$Z_{01} = e^{i\pi} Z_{10}$$

for plane waves and a similar coefficient of proportionality, the various signals may be written:

$$S = \exp j\omega t$$

$$S_0 = Z_{01} \exp j\omega(t + \pi/\omega)$$

$$S_1 = T_{10}\ t_{01}\ Z_{02} \exp j\omega(t - 2e/C_L + \phi_L/\omega)$$

$$S_2 = t_{10}\ t_{01}\ Z_{02}\ Z_{01}\ Z_{02} \exp j\omega(t - 4e/C_L + \phi_L/\omega)$$

$$S'_1 = t_{10}\ t_{02} \exp j\omega(t - e/C_L + \phi_L/\omega)$$

$$S'_2 = t_{10}\ t_{02}\ Z_{02}\ Z_{01} \exp j\omega(t - 3e/C_L + \phi_L/\omega) \quad .$$

Strictly, the measurements of the times between the signals S_1, S_2 or S'_1, S'_2 give:

$$\delta_L(\nu) = 2e/C_L(\nu) \quad ,$$

while S_0, S_1 give:

$$\delta_L(\nu) = 2e/C_L(\nu) + (\phi_L + \pi)/\omega \quad .$$

For this reason, measurements of $\delta_L(\nu)$ are made as the differences $S_1 - S_2$ or $S'_1 - S'_2$.

The thickness e is not known with precision, only this measurement makes it possible to study the development of C_L in relation to one frequency ν_0. For that it follows:

$$C_L(\nu) = C_L\ (\nu_0)\ [1\ g_L(\nu)] \quad ,$$

where

$$g_L\ (\nu_0) = 0 \quad .$$

By using the following relationship:

$$\frac{d\ C_L}{C_L} = -\frac{d\ \delta_L}{\delta_L}$$

this expression is obtained:

$$g_L\ (\nu) = 1 - \frac{\delta_L(\nu)}{\delta_L(\nu_0)} \quad ,$$

2.2. Measurements associated with $C_T(\nu)$

As with the preceding measurement, Figure 1b shows the arrangement of transducers for two configurations, transmission-reception and transmission. The phase relationship corresponding to viscoelastic phenomena may be written:

$$\phi_T(\nu) = \arctan \frac{d_T(\nu)\ C_T(\nu)}{2\pi\nu} \quad ,$$

and this may be solved by making use of the signals S_1 - S_2 or S'_1 - S'_2.

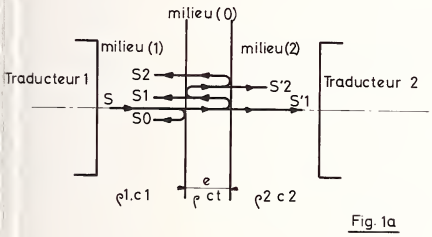

Fig. 1a

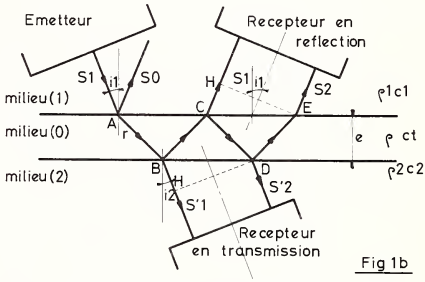

Fig 1b

Figure 1. (a) Transducer arrangements for measurements associated with $C_L(\nu)$.
(b) Transducer arrangements for measurements associated with $C_T(\nu)$.

This time, however, there is a new problem. With oblique reflections and transmissions, as for perfectly elastic media, the coefficients r_{ij} and t_{ij} are complex. Between the signals S_1, S_2 or S'_1, S'_2, there is a phase rotation given quite closely by the equation:

$$\phi_s = -4 \arctan \left[\frac{Z_L}{Z_T} \frac{1}{\tan^2 2Z} \right] \quad ,$$

where

$$Z_T = \rho_0\ C_T/\cos Z$$

$$Z_L = \rho_0\ C_L/\sinh Z$$

and

$$\sin Z/C_T = \sin i/C_1 = \cosh \theta/C_L \quad .$$

By setting

$$\delta_T = \frac{2e}{C_T} \cos Z$$

the delay measurement of each of the differences S_1 - S_2 or S'_1 - S'_2 corresponds to:

$$\delta = \delta_T + \phi_s/\omega \quad .$$

To eliminate the phase change ϕ_s/ω, it is necessary that the angles of refraction r in the neighborhood of the two faces should be 45°. The value of i corresponding to the maximal C_T (which is then the true velocity) is given by the formula:

$$C_T = 1/\sqrt{\left[\frac{\delta^2}{4e^2} + \frac{\sin^2 i}{C_1^2}\right]} \quad .$$

To satisfy this condition, the measurement of oblique incidence should be given with a good precision:

$$\delta_T(\nu) = \frac{2e}{C_T(\nu)} \cos Z(\nu)$$

where

$$\sin Z(\nu) = C_T(\nu) \sin i/C_1 \quad .$$

To study the development of C_T with respect to one frequency ν_0, set

$$C_T(\nu) = C_T(\nu)_0 \, [1 + g_T(\nu)]$$

$$g_T(\nu_0) = 0 \quad ,$$

and, by making use of the relationship

$$\frac{d\,\delta_T}{\delta_T} = -\frac{\lambda}{\cos^2 Z} \frac{d\,C_T}{C_T}$$

the function g_T corresponds to the expression:

$$g_T(\nu) = \cos^2 Z_0 \left(1 - \frac{\delta_T(\nu)}{\delta_T(\nu_0)}\right)$$

where

$$\sin Z_0 = C_T(\nu_0) \sin i/C_1.$$

2.3. Function associated with the ratio δ_L/δ_T

Choosing the values

$$\delta_L = \frac{2e}{C_L}$$

and

$$\delta_T = \frac{2e}{C_T} \cos Z$$

at a given point in the specimen, study of the ratio δ_L/δ_T makes it possible to eliminate the thickness e. To do this, set

$$C_L(\nu) = C_L(0) \, [1 + G_L(\nu)]$$

$$G_L(0) = 0$$

$$C_T(\nu) = C_T(0) \, [1 + G_T(\nu)]$$

$$G_T(0) = 0 \quad .$$

By expressing the characteristic velocities $C_L(0)$ and $C_T(0)$ for a perfectly elastic medium with Young and Poisson coefficients E and σ, for any frequency ν, for the corresponding δ_L/δ_T, q may be written:

$$q = \frac{1}{\cos Z \sqrt{2}} \left[\sqrt{\left(\frac{1 - 2\sigma}{1 - \sigma}\right)}\right][1 + G_T(\nu) - G_L(\nu)] \quad .$$

In order to be sensitive to the physical parameters of the medium, the following function is used:

$$G = \cos Z \, (\sqrt{2}) \, q$$

which can be calculated for the frequency ν_0:

$$G(\nu_0) = [\sqrt{(\frac{1 - 2\sigma}{1 - \sigma})}][1 + G_T(\nu_0) - G_L(\nu_0)] \quad .$$

3. Experimental Results

In order to demonstrate these variations in velocity, and to establish a connection between these measurements and the metallurgical status, several sets of samples of sheet were prepared with slightly different properties.

In each series a range of plates cut from the same slightly work-hardened sheet of given thickness was reduced by several passes through a rolling mill, so as to make the rate of work hardening from around 0 percent to more than 80 percent.

In practice the measurements are made by transmission using the assembly shown in figure 2. Essentially they consist of time measurements made visually on an oscilloscope with a time resolution of the order of 100 picoseconds. The transducers, which are wide-band types, are excited by trains of waves of length less than three or four cycles.

3.1. Derivation of $C_L(\nu)$

The measurement of time makes it possible to calculate $g_L(\nu)$ without any particular difficulty. Provided that the incidence i is close to zero, the error introduced by this parameter is second order. The fluctuations in the function g_L are small and manual exploitation of this variable is not possible. In practice, values of dg_L of the order of 2×10^{-5} are obtained for 1 percent work hardening.

An example is given in figure 3 for specimens of 304L stainless steel work hardened from zero to 80 percent. These measurements were taken using a programmable time interval meter having a statistical precision improved by a factor of ten.

3.2. Derivation of $C_T(\nu)$

As has already been indicated, this measurement requires knowledge of the incidence i_0 minimizing the phase change ϕ_s at the surface. Finding this value depends on varying i and, knowing the value of the thickness e, calculating the speed "C_T" (which is then not necessarily the true speed) for each incidence. The maximum of this function corresponds to i_0 and gives the true speed C_T. The curves in figure 4 give several examples of this measurement for a series of specimens of 304L steel. The coupling liquid is distilled water thermostatically controlled at 25 °C. This allows the testing of one sheet or a series of specimens to be achieved at one time.

Knowing i_0, for a series of measurements of δ_T on a specimen, the following expression can be calculated:

$$\cos^2 \overline{Z}_0 = 1/(1 + \frac{4\overline{e}^2}{C_1^2} \frac{\sin^2 i_0}{\overline{\delta}_T^2})$$

for the smallest values of $\overline{e}$ and $\overline{\delta}_T$ for the specimen. The function $g_T(\nu)$ is then given by the equation:

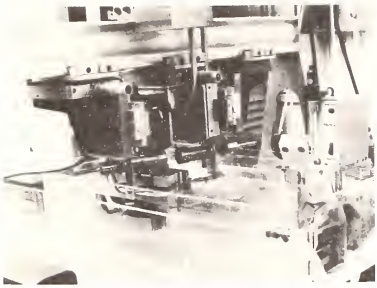

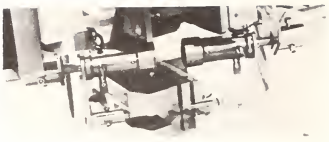

Figure 2. Experimental set-up. (a) General view. (b) Specimen position.

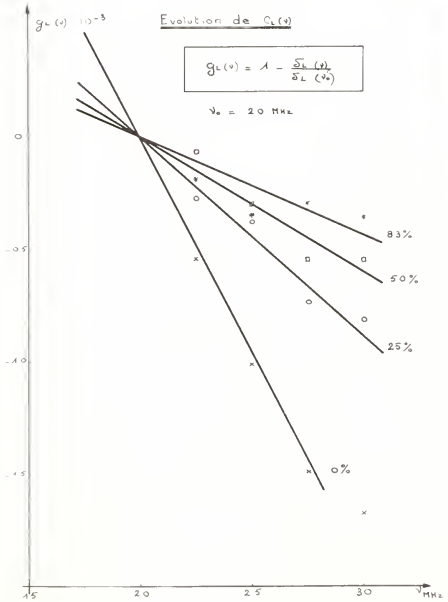

Figure 3. Derivation of $g_L(v)$, for various degrees of work hardening; v_0 = 20 MHz.

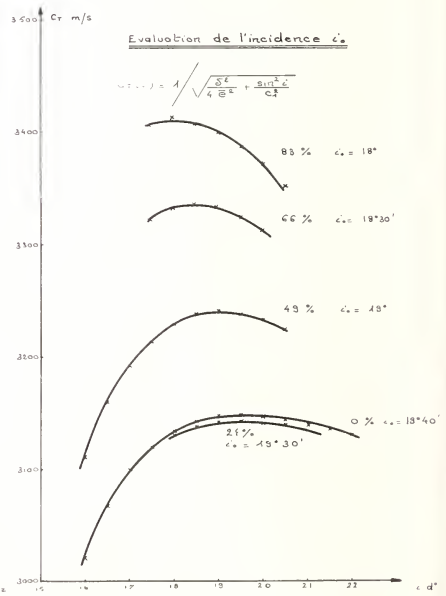

Figure 4. Derivation of i_0, for various degrees of work hardening; v_0 = 20 MHz.

$$g_T(\nu) = \cos^2 Z_0 \left(1 - \frac{\delta_T(\nu)}{\delta_T(\nu)_0}\right) \quad .$$

The rolling process causes an anisotropy in the sheet and at every point it is necessary to make two measurements of δ_T, one parallel and the other perpendicular to the rolling direction. Figure 5 shows the function of g_T for the series of specimens of 304L. The variations of dg_T are slightly greater than those of g_L (about three or four times).

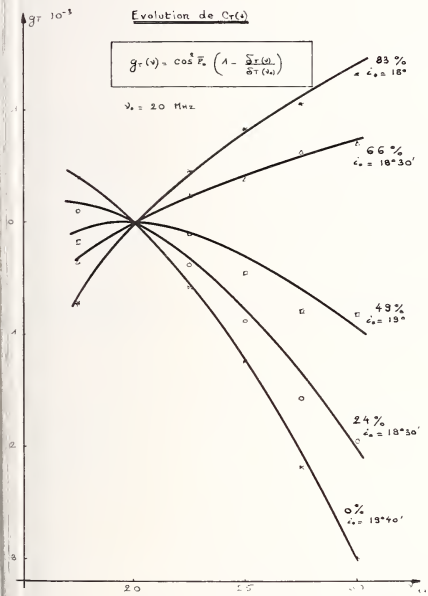

Figure 5. Derivation of $g_T(\nu)$, for various degrees of work hardening; ν_0 = 20 MHz.

Although requiring very precise measurements and numerical analysis of the results, the data given by g_T (and by g_L) are of great interest because they depend on the viscoelastic properties of the material. In the case of laminated sheets, the resonances of dislocations represent the principal factor (number, statistical length, etc.) and therefore afford a method of arriving at the relative density of these dislocations per unit volume.

3.3. Function G

The velocity C_T was not isotropic in the sheet; it is the same as the function G. A series of samples is therefore characterized by two functions $G_{\parallel}$ and $G_{\perp}$ (measured parallel and perpendicular to the rolling direction). The variations in dG/G are, relative to the previous situation, very large and may reach 1.5×10^{-3} for one percent work hardening. In deriving the variation dG/G with $\sigma \sim 0.3$, the following approximate expression is obtained:

$$\frac{dg}{G} \cong -\frac{1}{2}\frac{d\sigma}{\sigma} + dG_T - dG_L \quad .$$

Now experience shows that for ν_0 = 20 MHz, the difference

$$dg_T\ (\nu_0) - dG_L\ (\nu_0)$$

remains below a few thousandths, that is around ten times smaller than dG/G. If they are neglected, it may be concluded that G is closely representative of the development of the Poisson coefficient σ.

Three examples for three grades of different stainless steels are given in figures 6, 7 and 8. The results show evidence of the grade, but in every case, the functions $G_{\parallel}$ and $G_{\perp}$ are rather more linear for specimens with work hardening of more than 20 percent. From zero to 20 percent, the relationships are complex and difficult to interpret on the basis of the metallurgy. For each of these graphs, the precision of measurement is such that the fluctuations are less than about a millimeter at each point.

4. Conclusion

The diversity of the results obtained show that ultrasound is sensitive to a number of parameters characteristic of the grade and metallurgical state of a metal. It seems that the functions $G_T(\nu)$ and $G_L(\nu)$ are poorly related to dynamic phenomena connected with dislocation resonances and so provide an indication of the density of dislocations. The function G seems to more influenced by the value of the Poisson coefficient σ so that it may be interpreted as giving a "static" measure of the metal (resulting, for example, from a traction experiment).

A more advanced analysis of the results assumes a complete knowledge of all the metallurgical parameters of the specimens. The study has been carried out on a large number of well characterized plates.

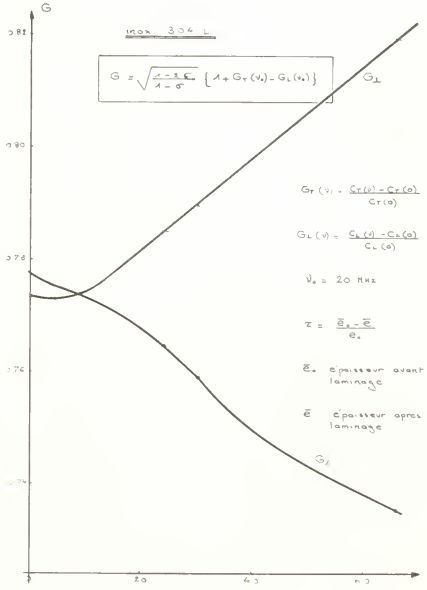

Figure 6. Values of G for 304L stainless steel; ν_0 = 20 MHz.

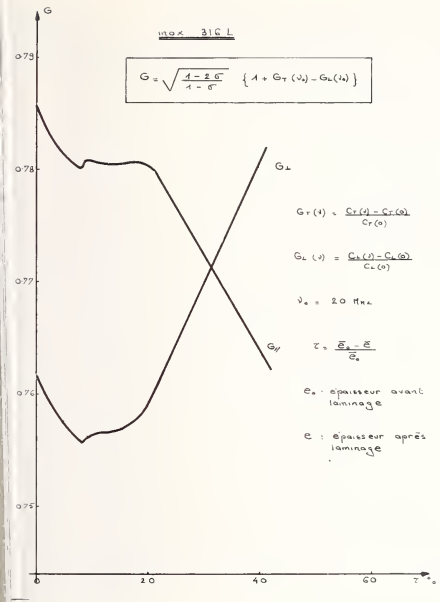

Figure 7. Values of G for 316L stainless steel; ν_0 = 20 MHz.

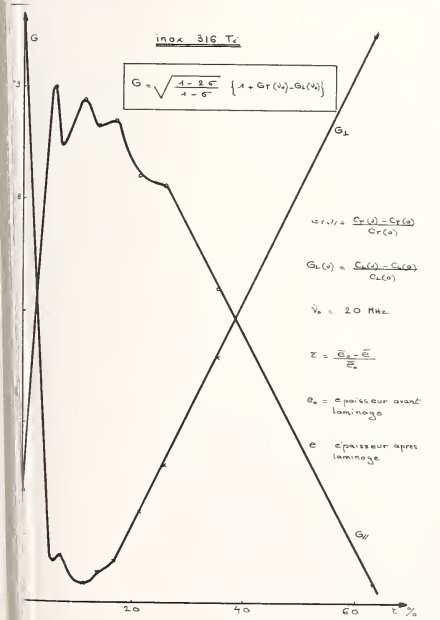

Figure 8. Values of G for 316 Tc stainless steel; ν_0 = 20 MHz.

In practice these measurements could be made in industrial applications in the continuous examination of the relative homogeneity of a metal sheet. The measurement could be carried out automatically using commercially available equipment. This automation makes it possible to examine a great number of work points to exploit the results on a statistical basis to obtain good precision.

National Bureau of Standards Special Publication 596, Ultrasonic Materials Characterization, H. Berger and M. Linzer, eds., Proceedings of the First International Symposium on Ultrasonic Materials Characterization held at NBS, Gaithersburg, Md., June 7-9, 1978. Issued November, 1980.

ULTRASONIC CHARACTERIZATION OF ALUMINUM MATRIX COMPOSITES FOR THEIR MODULI

G. V. Blessing, W. L. Elban and J. V. Foltz

Research Department
Naval Surface Weapons Center
Silver Spring, MD 20910

The ability to make meaningful elastic moduli measurements ultrasonically is reported for potential application to the nondestructive evaluation of aluminum matrix composites. The materials were monitored for a change in elasticity as a function of heat treatment that would affect the material's residual stress state. We evaluate initial results obtained on two unidirectional (UD) systems: (1) continuous graphite (Gr) fiber reinforced Al, and (2) discontinuous SiC whisker reinforced Al. The requisite five elastic moduli C_{ij} for a UD system were obtained by measuring bulk acoustic velocities, first in the as-fabricated material. The engineering constants, e.g., longitudinal and transverse Young's moduli, were in good agreement with available tensile test data. The samples were then subjected to single cycle liquid nitrogen and elevated temperature excursions, and the elastic moduli remeasured at room temperature. Results indicate a significant effect on the residual stress state (specifically, a reduction in modulus of Gr/Al, but no effect on SiC/Al.

1. Introduction

The initial results of an ultrasonic study to nondestructively characterize metal matrix composite elastic properties are reported. Single cycle thermal treatment effects on the Young's and shear moduli, relevant to the end item fabrication process, are given for two specific unidirectional (UD) aluminum matrix composites. For one of these, SiC/Al, the as-cast billet moduli are compared to the extruded rod anisotropic values. Also, a comparison of the ultrasonically determined moduli with machine tensile values is made where possible.

The two UD metal composite systems addressed in this paper are (1) a continuous fiber Thornel 50 graphite reinforced 201 aluminum alloy (Th 50/201 Al); and (2) a discontinuous fiber silicon carbide whisker reinforced aluminum (SiC/Al). Both composites possess a nominal 30 percent by volume (30 V/o) reinforcement fiber array.

The motivation for thermal treatment studies is twofold. First, the as-fabricated residual stress state of a composite with constituent materials possessing different coefficients of thermal expansion is of concern. Secondly, the effects of net-shape material forming at elevated temperatures need to be evaluated.

Substantial efforts have been made in recent years to ultrasonically evaluate the engineering moduli of non-metal composites, with reasonable success [1-6][1]. The work in metal matrix composites has been much more limited [7,8]. However, the evolution of new inexpensive metal composites with very attractive features will accelerate the pace of metallic system development. Closer agreement can be expected between the ultrasonically determined dynamic moduli and the statically measured tensile values for metal rather than non-metal composites. This is due both to the strong viscoelastic frequency dependence of most non-metals and the effects of adiabatic heating (ultrasonic method) versus isothermal tests (static method). Both phenomena are negligible in non-viscous highly conductive metals. However, geometric dispersion (caused by an orderly array of fibers in the matrix) can dominate the apparent

[1]Figures in brackets indicate literature references at the end of this paper.

elasticity's frequency dependence in both metal and non-metal composites and, therefore, needs to be evaluated when making a direct comparison of dynamic and static test values [9,10]. Finally, we note that whether or not an absolute comparison can be confidently made between the ultrasonic and tensile values, the ultrasonic method is invaluable for accurately determining relative changes as a function of temperature, thermal treatment, and composition.

2. Experimental Technique

2.1. Samples

Figure 1 illustrates the two composite systems investigated. The Gr/Al sample was available in single-ply plate form 2.6 mm thick[2]. The plate was formed from a multilayer of precursor Gr/Al wires diffusion bonded with 0.15 mm of 2024 Al on both surfaces. The precursor wires, with a nominal diameter of 1 mm, were formed by liquid metal infiltration of graphite fiber bundles. The measured plate density was 2.44 gm/cm^3, indicating a net 30 V/o graphite fiber reinforcement. Parallel face samples approximately 3.0 mm in length were cut transverse to and at 45° relative to the fiber direction. Figure 2 presents a 30X magnification normal to the transverse cut, illustrating the random fiber-aluminum matrix geometry[3].

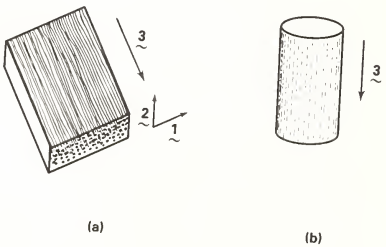

Figure 1. Pictorial illustration of unidirectional (a) continuous fiber reinforced Gr/Al plate, and (b) discontinuous fiber (whisker) reinforced SiC/Al extruded rod. The principal fiber direction is $\underset{\sim}{3}$, with the plane of isotropy transverse to it.

The SiC/Al sample was available in a 50 mm long by 40 mm diameter cast cylindrical billet with a 27 V/o reinforcement[4]. The SiC whisker dimensions are only approximately known about 85 percent are particulate, and the remaining 15 percent have a nominal aspect ratio (ℓ/d) of 30, where d is $\sim$0.5 μm, after billet fabrication. The sample section taken from the 10:1 extruded bar was approximately 20 mm in length and 10 mm diameter. The extrusion process was expected to align the whiskers by shear viscous flow to produce a UD composite. From this extruded section, a 3.0 mm thick parallel face cut at 45° to the extrusion direction was taken for three of the velocity measurements.

[2]Plate material fabricated by DWA Composite Specialties, Inc., Chatsworth, California.
[3]Scanning electron micrograph taken by M. K. Norr, NSWC, Silver Spring, Maryland.
[4]Billet fabricated by A. P. Divecha, NSWC, Silver Spring, Maryland.

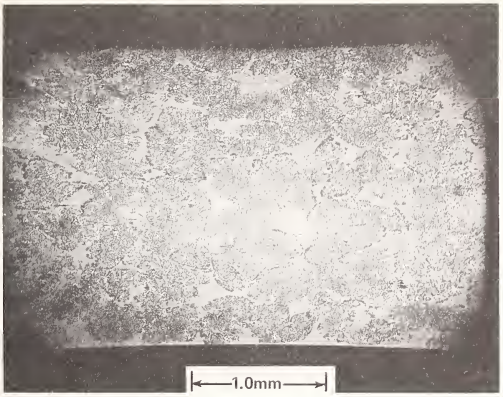

Figure 2. A 30X SEM photo of 30 V/o Gr/Al plate sliced transverse to the $\underset{\sim}{3}$ (fiber) direction.

2.2. Ultrasonic system

Bulk acoustic velocity measurements of both longitudinal and shear waves were made in specific directions relative to the composite fibers. All measurements were made at room temperature by direct contact of transducer to sample or via a relay rod.

The experimental system used is shown in figure 3. The sharp spike voltage excitation of a heavily damped PZT ceramic transducer for longitudinal waves, and of a $LiNbO_3$ single crystal for shear waves, produced broadband acoustic pulses with a nominal 10 MHz center frequency. Time of flight velocity measurements were made by pulse-echo overlap using the time delay of a 7000 series Tektronix oscilloscope. The digital readout time display provided a resolution of 1 ns for a precision $\sim$1:1000, with a like precision for the velocity. Minimum acoustic path lengths, defined by the sample dimensions, were 6 mm round trip measured to a resolution of 4 μm or $\sim$1:1000.

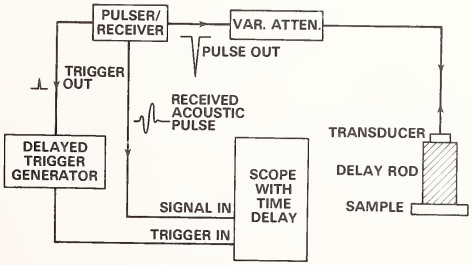

Figure 3. Broadband ultrasonic system used to measure sound velocity by the time-of-flight pulse-echo overlap technique.

2.3. Analysis

By means of the stress-strain constitutive relationships for orthotropic media, the elastic constants C_{ij} were calculated knowing the material density ρ and the direction of acoustic propagation $\underset{\sim}{k}$ relative to the fiber direction $\underset{\sim}{3}$. Table 1 summarizes these relationships for a UD system, one that is transversely isotropic or specially orthotropic. There are five independent C_{ij} as originally shown by Mason [11], Musgrave [12], and others, but eight independent measurements are conveniently made for three directions of wave propagation relative to the fibers: $\underset{\sim}{k} \parallel \underset{\sim}{3}$, $\underset{\sim}{k} \perp \underset{\sim}{3}$, and $\measuredangle(\underset{\sim}{k}, \underset{\sim}{3}) = 45°$. The additional three measurements serve to check the other measurements.

Table 1. Equations relating the measured ultrasonic velocities Vn to the elastic moduli C_{ij} for a UD composite with fibers in the $\underset{\sim}{3}$ direction.

	Eq. #			Wave Type & Prop. Dir.[a]
1	ρV_1^2	=	C_{33}	Long: $\underset{\sim}{k} \parallel \underset{\sim}{3}$
2	ρV_2^2	=	C_{11}	Long: $\underset{\sim}{k} \perp \underset{\sim}{3}$
3	ρV_3^2	=	C_{44}	Shear: $\underset{\sim}{k} \parallel \underset{\sim}{3}$, $\underset{\sim}{\varepsilon} \perp \underset{\sim}{3}$
4	ρV_4^2	=	C_{44}	Shear: $\underset{\sim}{k} \perp \underset{\sim}{3}$, $\underset{\sim}{\varepsilon} \parallel \underset{\sim}{3}$
5	ρV_5^2	=	C_{66}	Shear: $\underset{\sim}{k} \perp \underset{\sim}{3}$, $\underset{\sim}{\varepsilon} \perp \underset{\sim}{3}$
6	ρV_6^2	=	$1/2 \left\{ \frac{C_{11} + C_{33} + 2C_{44}}{2} + \left[\left(\frac{C_{33} - C_{11}}{2} \right)^2 + \left(C_{13} + C_{44} \right)^2 \right] 1/2 \right\}$	Quasi-Long: $\measuredangle(\underset{\sim}{k}, \underset{\sim}{3}) = 45°$
7	ρV_7^2	=	$1/2 \left\{ \frac{C_{11} + C_{33} + 2C_{44}}{2} - \left[\left(\frac{C_{33} - C_{11}}{2} \right)^2 + \left(C_{13} + C_{44} \right)^2 \right] 1/2 \right\}$	Quasi-Shear: $\measuredangle(\underset{\sim}{k}, \underset{\sim}{3}) = 45°$ $\underset{\sim}{\varepsilon}$ in plane ($\underset{\sim}{k}$,
8	ρV_8^2	=	$1/2 \left(C_{44} + C_{66} \right)$	Shear: $\measuredangle(\underset{\sim}{k}, \underset{\sim}{3}) = 45°$ $\underset{\sim}{\varepsilon} \perp$ plane ($\underset{\sim}{k}$,

[a] $\underset{\sim}{k}$ is the acoustic propagation vector, and $\underset{\sim}{\varepsilon}$ is the shear wave polarization direction.

With the above-mentioned time resolution in the velocity measurement, the precision of the calculated C_{ij} is $\sim$ 4:1000. Provided all controllable variables such as acoustic frequency and sample dimensions are kept constant, we can then monitor changes in C_{ij} as a function of thermal treatment to better than 0.5 percent. The absolute uncertainty of this technique is estimated to be less than 1 percent for the C_{ij}. For C_{13}, the number of variables involved in eqs. (6) and (7) indicate a somewhat reduced precision. In fact, we have experienced the accuracy of C_{13} to be very much reduced, as have other investigators [1,3].

Finally, to relate the composite bulk elastic properties so obtained to engineering quantities such as Young's modulus, we refer to table 2. The Emn, Gmn, and ν_{13} are, respectively, Young's moduli, shear moduli and Poisson's ratio, where the second subscript refers to the stress direction. The specific modulus type and property direction are given in the last column of table 2. Similar relationships exist for the other two Poisson's ratios pertinent to a UD composite. The precision of the longitudinal Young's modulus, E_{33}, a principal quantity of interest for materials design, is estimated to be better than 1 percent with the above-described measurement technique.

Table 2. Equations relating engineering moduli to the ultrasonically determined elastic moduli C_{ij} for a UD composite with fibers in the $\underset{\sim}{3}$ direction.

Eq. #	Eng. Modulus	=	Function (Cij)	Type & Dir. Relative to Fibers
9	E_{33}	=	$C_{33} - \frac{C_{13}^2}{C_{11} - C_{66}}$	Young's: Long., Parallel to Fibers
10	E_{11}	=	$\frac{4\, C_{66} \left[C_{33}\left(C_{11} - C_{66}\right) - C_{13}^2 \right]}{C_{11}\, C_{33} - C_{13}^2}$	Young's: Transverse to Fibers
11	G_{13}	=	C_{44}	Shear: In-Plane, Parallel to Fibers
12	G_{12}	=	C_{66}	Shear: In-Plane, Perpendicular to Fibers
13	ν_{13}	=	$\frac{C_{13}}{2\,(C_{11} - C_{66})}$	Poisson's Ratio: Stress Parallel to Fibers, Strain Measured in Transverse Plane

2.4. Thermal treatments

Two sets of Gr/Al samples were subjected to separate thermal treatments. One set was subjected to a two-part cycle: first quenched in liquid nitrogen (LN_2), then heated at 260 °C in a vacuum furnace for twenty minutes. This sample set was observed to have slightly expanded dimensions ($\lesssim$0.5%) after treatment. The second set was simply heated at 500 °C under vacuum for twenty minutes. The LN_2 quenching step was applied to relieve the residual stress state of the as-fabricated plate material. The elevated temperature excursions simulate excursions the plate material experiences in net-shape hardware fabrication and/or in-service.

Only the 45° cut from the SiC/Al sample set was exposed to thermal treatment. It was heated at 500 °C in the vacuum furnace for twenty minutes as the Gr/Al sample set. After thermal treatment, the elastic moduli of all specimens were remeasured ultrasonically at room temperature.

3. Results

3.1. Gr/Al composite

Table 3 provides a sample set of data for the 25 V/o Gr/Al specimens, together with the calculated C_{ij} moduli. Additional C_{44} and C_{13} values (C_{44}-2, C_{13}-2, etc.) are calculated from the additionally measured velocities V_6, V_7 and V_8. A computer program[5] has been written to calculate the C_{ij} and the related engineering moduli for an arbitrary angle of the fibers relative to the acoustic propagation $\underset{\sim}{k}$. Table 2 above gives these relationships (eqs. (6), (7), (8)) for the special case of $\theta = \sim 45°$ [2,3]. In Table 3, note that nine C_{ij} values have been calculated from eight velocity measurements. The last value, C_{13}-3, was obtained by subtracting eqs. (6) and (7) to solve for C_{13}.

[5]Program written by A. L. Bertram, NSWC, Silver Spring, MD.

Table 3. Sample data set for as-fabricated 30 V/o Th 50/201 Al with a density of 2.44 gm/cm^3.

Velocity (mm/μs)	Equations used from table I	C_{ij} (GPa)[a]
V_1 = 8.642	1	C_{33} = 182.
V_2 = 4.040	2	C_{11} = 39.8
V_3 = 2.783	3	C_{44}-1 = 18.9
V_4 = 2.783	4	C_{44}-2 = 18.9
V_5 = 2.073	3 & 8 or 4 & 8	C_{44}-3 = 18.8
V_6 = 6.166	5	C_{66} = 10.5
V_7 = 3.070	1, 2, 3, & 6	C_{13}-1 = 25.6
V_8 = 2.450	1, 2, 3, & 7	C_{13}-2 = 25.5
	1, 2, 3, 6, & 7	C_{13}-3 = - 4.69

[a] 1 GPa = 10^9 Nt/m^2. To obtain C_{ij} in units of 10^6 psi (or Msi), multiply # GPa by 0.145.

Some of the C_{ij} calculations deserve special attention, in particular the C_{13} and C_{44} values. The large variation of C_{13}, even being negative, is not understood at this time but has been reported by other investigators [1,3]. Since the V_7 measurement yielded the most meaningful and consistent results from sample to sample for both composite systems, C_{13}-2 was used throughout to calculate E_{11}, E_{33} and ν_{13} according to the relationships in table 2. Concerning the C_{44} values, although the particular data set in table 3 shows excellent agreement for all three measurements, there was as much as a 9 percent difference observed in another sample between C_{44}-1 and C_{44}-2. This is well in excess of the experiment precision of 0.5 percent. This may possibly be attributed to geometric dispersion since the acoustic wavelength at 10 MHz is comparable to the average fiber spacing [8,9]. And these two shear measurements are made in one case with $\underset{\sim}{k}$ parallel to the fibers, and the other with $\underset{\sim}{k}$ perpendicular to the fibers.

Table 4 summarizes the effects of two separate heat treatments on two sets of Gr/Al samples and compares the ultrasonic (UT) values with theoretical model predictions for as-fabricated plate before heat treament. The UT as-fabricated values were calculated according to eqs. (9-13) using the raw data of table 3. Model predictions assumed perfect bonding of the graphite fibers to the Al matrix [13,14], in addition to static stress conditions. In spite of this, the second and third columns of table 4 show good agreement between experiment and theory, except for Poisson's ration ν_{13}. At this point, we only note that ν_{13} is proportional to C_{13}, a quantity which itself presents interpretation difficulties. Finally, we note that E_{33} modulus was in good agreement with the range of values (131 to 165 GPa) obtained on a series of tensile specimens taken from the same sample plate. In addition, ultrasonic E_{11} and G_{13} values were in good agreement with available static test results obtained on similar plate material[6].

A comparison of the last two columns of table 4 with the first column shows a measurable reduction in Young's moduli, in particular E_{33}, after thermal treatment. The changes in the shear moduli, however, are negligible. Lastly, although the experimental precision is sufficient to detect a real change in Poisson's ratio, the strong dependence on C_{13} (eq. (13)) clouds any significance that might be attached to its apparent increase.

[6] Tensile data provided by NETCO, Long Beach, CA.

Table 4. Ultrasonic moduli (in GPa) of 30 V/o Th 50/201 Al before and after two separate heat treatments, including theoretical model predictions

ng. Modulus	As-Fabricated Plate		Post-Heat Treatment	
	UT	Model[a]	500 °C	LN2 Quench[b] & 260 °C
E_{33}	160.	166.	148.	141.± 3.
E_{11}	29.7	32.6	29.7	26.9
G_{13}	18.6	18.5	18.6	19.3
G_{12}	10.3	10.8	11.0	9.6
ν_{13}	0.43	0.34	0.47	0.53

[a] Continuous fiber reinforcement model by Hashin [14].

[b] Relatively large error in precision due to different specimen used.

Possible physical mechanisms for the reduction in E_{33} can only be conjectured at the present time. The possible formation of Al_4C_3 at the Gr/Al interface is unreasonable for such short duration heat treatments (twenty minutes) at 260 °C and 500 °C [15-17]. It is more plausible to consider the effects on the residual stress state of the material, although reductions on the order of the 10 percent measured are unexpected [18]. Future heat treatments will help to elucidate the mechanism.

3.2. SiC/Al composite

Table 5 compares ultrasonic moduli of 27 V/o SiC/Al before and after extrusion, including theoretical model predictions for the (presumed) unidirectional extruded rod. The reinforced cast billet values in the first column represent a 70 percent increase in stiffness over the isotropic Al matrix values of 70 and 27 GPa, respectively, for E and G. The last two columns show good agreement between the ultrasonic values and theoretical model predictions. The difficulties experienced in the calculation of C_{13} for Gr/Al were not encountered with the SiC/Al data. The discontinuous fiber reinforcement model assumes 100 percent alignment of the elongated whiskers in the direction of extrusion [19, 20]. In addition, equal longitudinal and transverse Young's moduli for whisker elasticity, estimated at 480 GPa, is assumed. More recent evidence that the value may be closer to 700 GPa (similarly for shear) might be cause for ultrasonically measuring modulus values E_{33} (and G_{12}) larger even than those predicted by a model assuming perfect whisker-matrix bonding.

The high percentage of particulate with $\ell/d \sim 1$ is reflected by the high elastic isotropy (nearly equal shear moduli G_{12} and G_{13}) measured. The available tensile data on this sample, a three-test average value of 117 GPa for E_{33}, showed reasonable agreement with the ultrasonically determined value of 132 GPa[7].

Table 6 presents data on SiC/Al before and after a twenty-minute heat treatment at 500 °C. The calculated engineering moduli are bracketed to indicate that the before-heat treatment data was necessarily used in part for these calculations. Since only the 45° cut (to the extrusion direction) sample was available for heat treatment, only the V_6, V_7, and V_8 measurements could be made on the heat treated specimen. However, the consistency of the three measurements, indicating a constant or slightly increasing stiffness, lends confidence to the bracketed values. In addition, data on several other heat treated specimens of extruded SiC/Al has consistently demonstrated a slight increase in modulus value with elevated temperature excursions. Both a more comparable thermal coefficient of expansion between SiC and Al, and the short discontinuous fiber nature of SiC reinforcement, corroborates the lesser heat treatment effects observed on the elasticity of SiC/Al than on Gr/Al.

[7] Tensile data provided by R. C. Crowe, NSWC, Silver Spring, MD.

Table 5. Ultrasonic moduli (in GPa) of 27 V/o SiC/Al before and after extrusion, including theoretical model predictions.

Eng. Modulus	CAST BILLET	EXTRUDED ROD	
	UT	UT	Theor. Model[a]
E_{33}	116.	132.	124.
E_{11}	-	116.	117.
G_{13}	44.8	44.8	45.5
G_{12}	-	43.7	40.7
ν_{13}	0.29	0.29	0.30

[a]Discontinuous fiber reinforcement model by Halpin and Tsai [18].

Table 6. Ultrasonic moduli (in GPa) of 27 V/o SiC/Al extruded rod before and after heat treatment at 500 °C for 20 minutes.

Eng. Modulus	BEFORE	AFTER
E_{33}	132.	[134.][a]
E_{11}	116.	[117.]
G_{13}	44.8	[44.8]
G_{12}	43.7	[43.7]
ν_{13}	0.29	[0.28]

[a]Brackets [ ] indicate values calculated using BEFORE heat treatment data in part.

4. Conclusions

The most significant result is the effect of thermal treatment on the two metal matrix composites' elasticity: a measurable reduction in stiffness for Gr/Al but no reduction for SiC/Al. Secondly, the reasonable and, in many cases excellent, agreement of the ultrasonic values with machine tensile test data and model predictions demonstrates that the ultrasonic technique can be used to meaningfully characterize the material moduli.

An unresolved difficulty is the inconsistency of the C_{13} calculations from the 45° velocity measurements for Gr/Al. This principally reflects itself in questionable values for the Poisson's ratio which are anomalously large in some cases. The small increase upon extrusion in the longitudinal modulus E_{33} for SiC/Al indicates that the use of better quality reinforcement whiskers should improve that material's already attractive properties.

Future investigations will be first to examine the effects of repeated heat treatments on the material's elasticity. Secondly, multi-ply Gr/Al laminates stacked at specific fiber angles (to improve the transverse properties) will be studied. Finally, some long-range goals for the program include making a reliable nondestructive estimate of Young's modulus for a UD composite by means of a simple longitudinal velocity measurement and to relate the material's strength to ultrasonic parameters.

In addition to those cited throughout the report, the authors wish to recognize helpful discussions with Drs. C. R. Crowe and S. G. Fishman, Research Department, NSWC. This work was supported by the NAVSEA Metal Matrix Composites Block Program SF 54 594594.

References

[1] Dean, G. D. and Turner, P., The elastic properties of carbon fibres and their composites, Composites, 4, 174 (1973).

[2] Smith, R. E., Ultrasonic elastic constants of carbon fibers and their composites, J. Appl. Phys., 43, 2555 (1972).

[3] Zimmer, J. E. and Cost, J. R., Determination of the elastic constants of a unidirectional fiber composite using ultrasonic velocity measurements, J. Acoust. Soc. Am., 47, 795 (1970).

[4] Markham, M. F., Measurement of the elastic constants of fibre composites by ultrasonics, Composites, 1, 145 (1970).

[5] Reynolds, W. N. and Wilkinson, S. J., The propagation of ultrasonic waves in CFRP laminates, Ultrasonics, 109 (1974).

[6] Russel, W. B. and Acrivos, A., On the effective moduli of composite materials: Experimental study of chopped fiber reinforcement, J. Appl. Math. and Phys., 24, 838 (1973).

[7] Read, D. T. and Ledbetter, H. H., Elastic properties of a boron-aluminum composite at low temperatures, J. Appl. Phys., 48, 2827 (1977).

[8] Ledbetter, H. M. and Read, D. T., Orthorhombic elastic constants of an NbTi/Cu composite superconductor, J. Appl. Phys., 48, [5], 1874 (1977).

[9] Sutherland, H. J. and Lingle, R., Geometric dispersion of acoustic waves by fibrous composites, J. Composite Matls., 6, 490 (1972).

10] Sutherland, H. J., Dispersion of acoustic waves by fiber-reinforced viscoelastic materials, J. Acoust. Soc. Am., 57, [4], 870 (1975).

11] Mason, W. P., Physical Acoustics and the Properties of Solids, pp. 371-2, (D. Van Nostrand Co., 1958).

12] Musgrave, M. J. P., On the propagation of elastic waves in aeolotropic media, II. Media of hexagonal symmetry, Proc. Roy. Soc. A, 226, 356 (1954).

13] Hashin, Z. and Rosen, B. W., The elastic moduli of fiber-reinforced materials, J. Appl. Mech., 31, 223 (1964).

14] Hashin, Z., Theory of Fiber Reinforced Materials, NASA CR-1974 (N72-21932, Univ. PA); and private communications to be published for a transverse matrix modulus larger than the transverse fiber modulus.

15] Khan, I. H., The effect of thermal exposure on the mechanical properties of aluminum-graphite composites, Metallurgical Trans. A, 7, 1281 (1976).

16] Blankenburgs, G., The effect of carbide formation on the mechanical behavior of carbon-aluminum composites, J. Austr. Inst. of Metals, 14, 236 (1969).

17] Baker, A. A., Shipman, Mrs. C., and Jackson, P. W., The short-term compatability of carbon fibres with aluminum, Fibre Science and Tech., 5, 213 (1972).

18] Daniel, I. M. and Liber, T., Effect of laminate construction on residual stresses in graphite/polyimide composites, Exper. Mech., 21 (1977).

[19] Halpin, J. C. and Tsai, S. W., Environmental factors in composite materials design, AFML TR 67-423.

[20] Ashton, J. E., Halpin, J. C., and Petit, P. H., Primer on Composite Materials: Analysis, pp. 77-84 (Technomic Pub. Co., Westport, CT, 1969).

National Bureau of Standards Special Publication 596, Ultrasonic Materials Characterization, H. Berger and M. Linzer, eds., Proceedings of the First International Symposium on Ultrasonic Materials Characterization held at NBS, Gaithersburg, Md., June 7-9, 1978. Issued November, 1980.

ULTRASONIC MEASUREMENT OF ELASTIC CONSTANTS AT TEMPERATURES FROM 20 TO 1100 °C

D. L. Donsbach and M. W. Moyer

Union Carbide Corporation, Nuclear Division
Oak Ridge Y-12 Plant[1]
P. O. Box Y, Building 9203
Oak Ridge, TN 37830

This paper describes in detail techniques developed to allow determination of the elastic moduli of structural materials of interest to the Liquid Metal Fast Breeder Reactor and the High Temperature Gas Reactor programs using acoustic techniques. Measurements of the elastic moduli of a number of different materials were performed at temperatures from 20 to 1100 °C. A two-step process was required to complete the measurements. First, the acoustic velocities were accurately measured using bulk samples at room temperature. Wire samples were then used to obtain elevated-temperature measurements by using a magnetostrictive transducer and an automatic data acquisition system. A computer was used to calculate the moduli and plot the data. A detailed summary has been made of the sources of error and a calculation of the precision of the measurements is given.

1. Measurement of Velocity

Room-temperature velocity measurements were made using conventional (piezoelectric) transducers on bulk samples. To perform velocity measurements at temperatures up to 1100 °C, a magnetostrictive transducer was used to generate ultrasonic waves in a wire buffer rod attached to a wire-like sample. Velocity measurements made using a magnetostrictive transducer do not have as high an absolute accuracy as room-temperature measurements made with a conventional transducer since a magnetostrictive transducer operates at a lower frequency. However, magnetostrictive transducers can be used to accurately measure small changes in velocity so that the measurement of velocity as a function of temperature can be normalized to the room-temperature wire measurement and multiplied by the room-temperature bulk measurement to yield an accurate high temperature velocity measurement.

1.1. Room-temperature velocity measurement on bulk samples

Measurement of the ultrasonic velocity, V, involves the measurement of length, X, and time, t, since V = X/t. In a pulse-echo measurement, the time must be measured for a round trip in a specimen of length, L, so:

$$V = 2L/t \quad . \tag{1}$$

The sample length can be measured using gage blocks or a micrometer. Accuracy in the determination of the length (L) will depend upon how flat and parallel are the sample faces. Measurement of time must be made electronically and is subject to certain systematic errors for which there must be an accounting.

The technique used to measure the transit time is a double-pulse method which is similar to the pulse-echo overlap method described by Papadakis [2][2]. The double-pulse technique consists of an oscillator and gating circuitry which allows two successive oscillations to trigger the transducer. The frequency of the oscillator is adjusted to obtain superposition

[1]Operated by the Union Carbide Corporation's Nuclear Division for the Department of Energy.
[2]Figures in brackets indicate the literature references at the end of this paper.

of the multiple reflections in the sample caused by the two excitation pulses. The transducer response adds the two wave trains to generate a combined waveform. A block diagram and the associated time traces are presented in figure 1. The time traces show the signals at each point in the system. When the superposition of two successive multiple reflections is obtained, a counter enables the oscillator period and thus the transit time in the sample to be measured.

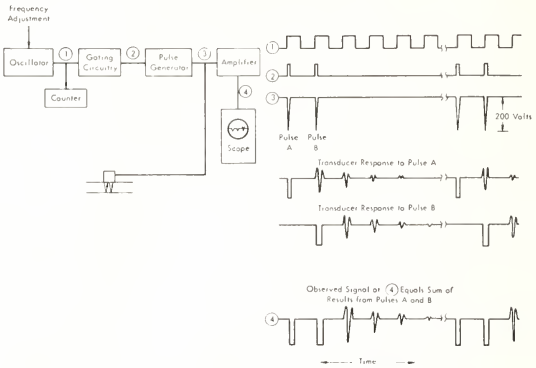

Figure 1. Double-pulse system to measure sonic velocities.

1.2. Analysis of errors on bulk-sample measurements

Since the measurement of ultrasonic velocity requires that both the sample length, L, and transit time, t, be measured, an estimate of each is required. Papadakis [3] describes some of the errors involved in measuring the transit time in the sample: 1) the precision in overlapping the multiple echoes; 2) phase shift associated with bond thickness between the transducer and sample; 3) phase shift associated with diffraction; 4) counting errors, and 5) vagaries in the electronics. Two additional sources of error must be considered, namely: 6) the anisotropy of a sample, and 7) variations between samples of the same material.

These seven sources of error will be considered one at a time.

1) An estimate of the ability to overlap echoes can be obtained by repeating each measurement several times. The average time, t, and a standard deviation, δt, can then be calculated.

2) Measurement of the phase shift associated with bond thickness is more difficult. McSkimin [4] has shown that the combination of a transducer plus a couplant against one surface of a sample causes a phase shift of a signal reflected from the surface. (This behavior implies that the transducer plus couplant represents a complex acoustic impedance.) This phase shift will occur for each reflection. McSkimin presents a technique to measure the bond-thickness error which requires measurements to be made with a tuned system. Since the velocity measurements in this study were made on a wide-bandwidth system, a different technique was used to eliminate the bond-thickness error. Incidentally, this technique was also useful for eliminating delays in the timing system caused by the cabling and amplifiers.

The technique involves measuring the transit time in several different blocks of the material with different thicknesses and determining the best straight-line fit to the data. The phase shift due to the coupling thickness is constant for all sample thicknesses. Thus, if the velocity fit is extrapolated to a zero sample thickness, the offset time can be determined. In practice, only two thicknesses were available for each material. Although one

ould normally determine a correction for a given material, in this case the zero-thickness ffset was determined by averaging the offset measured on 22 different materials. This verage offset was then used as a transit-time data point for zero thickness in the calcu- ation of velocity for each material. This technique provides several additional benefits. ince more than one sample is measured, the velocity is an average between samples. Also, ll the electronic delays are constant so the zero-thickness offset includes the electronic elays.

3) The diffraction-phase shift error for the longitudinal wave must be estimated. he phase of a plane-wave radiation from a piston source changes by $\pi/2$ radians between he surface of the piston and infinity. If the transit time is measured between two mul- iple echoes, a phase shift will be present between the two echoes because they have raveled different distances. This phase shift will result in an error in the time mea- urement so it is important that it be estimated. The phase change has been calculated y a number of authors [4-5] as a function of a normalized distance, S_d, where:

$$S_d = Z\lambda/a^2 = ZV/a^2f \quad . \tag{2}$$

y eq. (2):

Z = propagation distance
λ = wavelength
a = transducer radius
V = sonic velocity
f = transmitted frequency.

lost calculations for diffraction phase shifts were made for narrow-bandwidth transducers; owever, Papadakis [7] extended the calculations to cover broad-bandwidth pulses and pro- ided plots of the diffraction phase shift as a function of S_c and transducer bandwidth (where S_c is the normalized bandwidth at the center frequency of the transmitted pulse).

Papadakis computed a weighted average of the diffraction phase shift as a function of he transducer bandwidth. Once the diffraction phase shift is determined as a function of he normalized distance, S_d, an increment of time, Δt, can be determined which must be added to the measured travel time to obtain the true travel time with which to compute the elocity. Thus:

$$\Delta t = [\phi(S_2) - \phi(S_1)]/2\pi f_c \quad , \tag{3}$$

where:

$\phi(S_1)$ represents the diffraction phase shift in radians for the first multiple at a normalized distance, S_1, and $\phi(S_2)$ the diffraction phase shift for the second multiple at a normalized distance, S_2.

Normally, the $\phi(S_i)$ would be determined from one of the curves generated by Papadakis. he transducers used in this study had approximately an 80 percent bandwidth, so a least- quares polynomial fit was made to the curve generated by Papadakis to facilitate the calcu- lation of $\phi(S_i)$. The transmitted frequency, f, was measured by using a spectrum analyzer to observe the response of the transducer to an echo.

4) The counting statistics on the audio-frequency oscillator which drives the double-pulse system generates an error. By using a period-averaging counter to count for 10^3 to 10^4 periods, a 0.1 ns measurement can be made.

5) Vagaries in the electronics include delays caused by cabling and time jitter caused by triggering the audio oscillator. The electronic delays are corrected at the same time as the coupling-thickness phase shift is measured, by measuring several samples of dif- ferent thickness. The jitter is averaged by using a period-averaging counter.

6) Another error is due to the anisotropy of the sample. To estimate the anisotropy of the samples, shear-velocity measurements were made with polarization directions at 0 and 90 degrees. An average shear-velocity value was used to calculate the moduli. If the anisotropy is excessive, the model used to calculate the moduli from the measured velocities becomes invalid and must be modified. The solution to this problem is beyond the scope of this paper.

7) Variations in velocity between different samples of the same material are averaged at the same time the coupling phase shift is measured by measuring several different thickness samples.

It should be mentioned that the use of broad band pulses can generate additional errors, particularly when the measurements are made on attenuating materials. Attenuation is frequency dependent so that higher frequencies are attenuated more than lower frequencies. This difference causes a pulse-shape change, resulting in errors in the transit time measurement. The materials examined in this study had relatively low attenuation, thus keeping this error to a minimum.

1.3. Sonic-velocity measurements at elevated temperatures

Measurement of the sample transit time at temperatures to 1100 °C presents a whole new set of problems. No suitable transducers are available which operate at these elevated temperatures, so the transducer must be coupled to the sample through a buffer rod. Difficulties arise for longitudinal velocity measurements because beam reflections at the buffer-rod surface cause a mode conversion which makes it difficult to measure the sample velocity. In addition, long buffer rods are required, causing attenuation problems, and coupling the sample to the buffer rod at high temperatures presents another problem (silver solder will melt).

If a thin wire is used in which the diameter is less than 0.1 the wavelength of sound, extensional and torsional waves can be generated using a magnetostrictive transducer. Extensional waves are similar to longitudinal waves except that they have a radial component of particle motion and have a lower velocity than longitudinal waves in bulk material.

Torsional waves are shear waves with a circumferential particle motion and have the same velocity as shear waves in bulk material. With the magnetostrictive system, pulse frequencies are limited to 100 to 200 kHz. For typical materials, the wavelength would range from 25 to 50 mm, and the maximum wire diameter would be limited to a range of 2.5 to 5.0 mm. Thus, samples approximately 2.5 mm in diameter were used. To obtain sufficient length to make a reasonably precise measurement, these samples needed to be longer than those used for the bulk-sample measurements. A sample length of about 100 mm was found to be satisfactory.

The magnetostrictive transducer consists of a section of magnetostrictive wire (wire which undergoes strain when placed in a magnetic field) and an exciting coil. The magnetostrictive wire was coiled and drawn through a die to produce a helical structure.

This structure enables both extensional and torsional waves to be generated simultaneously. These waves can be separated because of their different velocities. The helical structure of the magnetostrictive wire is annealed at a fairly low temperature so that it is necessary to weld a 304 SS buffer wire to the transducer wire. The samples are then welded to the 304 SS buffer wire and inserted into a furnace.

The double-pulse technique used on the bulk samples requires an operator adjustment to determine the transit time in the sample. Since many measurements were required on each of the wire samples to determine the velocity as a function of temperature, an automatic system was set up to make time measurements. Figure 2 is a block diagram of this system. The furnace has an automatic controller to heat and cool to the desired temperature at a constant heating rate.

A heating rate of 10 °C/min was used for all elevated-temperature measurements. A Chromel/Alumel thermocouple was attached to the center of the sample to measure its temperature; an argon gas purge was used to reduce sample oxidation.

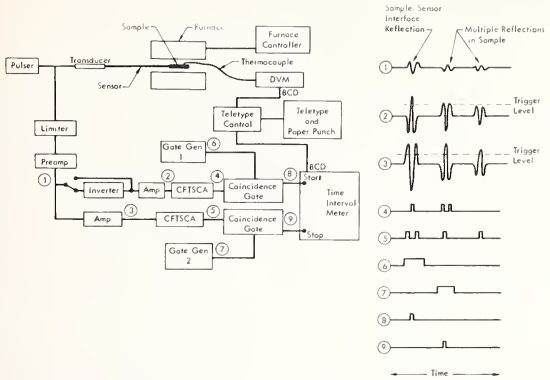

Figure 2. Elevated-temperature sonic-velocity measurement system.

The ultrasonic excitation system consists of a transducer and a pulser. The time traces show the signals found at points throughout the system. Echoes from the sample are fed through a limiter (to clip the excitation pulse), a preamplifier, and then to two parallel amplifiers. When two reflections are chosen to measure the time, these parallel amplifiers are used to adjust the amplitude of the two pulses to be equal. An inverter is included to make the two pulses of the same polarity. The amplifier outputs are supplied to two constant-fraction-timing, single-channel analyzers (CFTSCA). The CFTSCA provides a trigger pulse at a time which is a constant fraction of the peak pulse height. Thus, changes of the pulse amplitude do not cause the time location of the trigger pulse to change. Two gate generators are provided to set a gate on the pulses of interest. The signals from the gates and the CFTSCA are routed to coincidence circuits to provide timing signals which are sent to a time interval meter.

A timer was used to initiate readings of the time intervals and thermocouple voltage at 100-second intervals (equivalent to 17 °C increments at the heating rate used) and punch the readings on paper tape for later analysis on a computer. By doing this, the system required a minimal amount of attention to acquire transit time as a function of temperature data. Four runs were taken on each sample - two extensional wave runs and two torsional wave runs. Each run involved data acquisition during both the sample heating and cooling cycles.

2. Calculation of Moduli

2.1. Processing of room-temperature data

Once transit times for the bulk samples were measured and corrected for the diffraction phase shift, the thickness was measured and the velocity was calculated using a special least-squares fit. The thickness of each sample was measured ten times with a micrometer, and the average thickness and standard deviation were calculated. Precision-ground gage blocks were also measured to determine the micrometer accuracy. The transit time was measured a number of times so that the average and standard deviation could be calculated. Thus, for each material at least three data sets (two thicknesses plus the zero thickness offset time) were available which contained an independent measurement of thickness and time with an estimate of the repeatability of each measurement. An adaptation of a technique described by Graybill [8] which is used to calculate the slope and offset of a least-squares straight-line fit to data of the form x_i, δ_i, y_i, δy_i and to obtain an estimate of the standard deviation of the slope and offset is given in the Appendix. A computer program using this technique was written to calculate the room-temperature velocities for each sample.

Following are listed the equations necessary to calculate all the moduli and Poisson's ratios for a bulk sample knowing the longitudinal and shear velocities, and the density:

$$\sigma = \frac{1 - 2(V_S/V_L)^2}{2 - 2(V_S/V_L)^2} \tag{4}$$

$$V_E = V_L \sqrt{\frac{(1 + \sigma)\ (1 - 2\sigma)}{(1 - \sigma)}} \tag{5}$$

$$Y = V_L{}^2 \rho \frac{(1 + \sigma)\ (1 - 2\sigma)}{(1 - \sigma)} \tag{6}$$

$$S = V_S{}^2 \rho \tag{7}$$

$$K = \frac{Y}{3(1 - 2\sigma)} \tag{8}$$

Also, it is necessary to calculate an estimate of the standard deviation of each variable. An estimate of the standard deviation of a function of more than one variable can be obtained by taking the partial derivative with respect to each variable as follows:

$$\delta F(a,b) = \left[\left(\frac{\partial (F)}{\partial a} \right)^2 (\delta a)^2 + \left(\frac{\partial (F)}{\partial b} \right)^2 (\delta b)^2 \right]^{1/2} \tag{9}$$

Using eq. (9), an estimate of the standard deviations of the moduli and Poisson's ratio can be made by taking the partial derivatives of eqs. (4-8) and evaluating them according to eq. (9). Doing this calculation, other equations can be derived:

$$\delta\sigma = \left[\frac{V_L{}^2 V_S{}^4 (\delta V_L)^2 + V_S{}^2 V_L{}^4 (\delta V_S)^2}{(V_L{}^2 - V_S{}^2)^4} \right]^{1/2} \tag{10}$$

$$\delta V_E = \left[\frac{(1 + \sigma)\ (1 - 2\sigma)\ (\delta V_L)^2}{(1 - \sigma)} + \frac{V_L{}^2 \sigma^2 (\sigma - 2)^2 (\delta\sigma)^2}{(1 - \sigma)^3 (1 + \sigma)\ (1 - 2\sigma)} \right]^{1/2} \tag{11}$$

$$\delta Y = \left[\frac{4 V_L{}^2 \rho^2 (1 + \sigma)^2 (1 - 2\sigma)^2 (\delta V_L)^2}{(1 - \sigma)^2} + \right. \tag{12}$$

$$\frac{V_L{}^4 (1 + \sigma)^2 (1 - 2\sigma)^2 (\delta\sigma)^2}{(1 - \sigma)^2} +$$

$$\left. \frac{4\sigma^2 (\sigma - 2)^2 V_L{}^4 \rho^2 (\delta\sigma)^2}{(1 - \sigma)^4} \right]^{1/2}$$

$$\delta S = \left[4 V_S{}^2 \rho^2 (\delta V_S)^2 + V_S{}^4 (\delta\rho)^2 \right]^{1/2} \tag{13}$$

$$\delta K = \left[\frac{(\delta Y)^2}{9(1 - 2\sigma)^2} + \frac{4 Y^2 (\delta\sigma)^2}{9(1 - 2\sigma)^4} \right]^{1/2} \tag{14}$$

where:

F = function of a and b

δF = standard deviation of F

δa = standard deviation of a

δb = standard deviation of b

V_L = longitudinal velocity

δV_L = standard deviation of V_L

V_S = shear velocity

δV_S = standard deviation of V_S

V_E = extensional velocity

δV_E = standard deviation of V_E

σ = Poisson's ratio

$\delta\sigma$ = standard deviation of σ

Y = Young's modulus

δY = standard deviation of Y

S = shear modulus

δS = standard deviation of S

K = bulk modulus

δK = standard deviation of K

ρ = sample density

$\delta\rho$ = standard deviation of ρ.

For several materials, wire samples were received without bulk samples. This necessitated performing the room temperature velocity measurements on the wire samples. To make reliable contact with the magnetostrictive wire, the sample must be welded to the wire. This presents a problem in knowing the length of the sample with accuracy sufficient for the velocity measurements. In addition, the variable frequency oscillator used in the double-pulse system for bulk samples did not have a long enough period to allow it to be used on the longer wire samples. To overcome these problems, the same timing system used for the elevated temperature measurements was used to perform room-temperature velocity measurements on the wire samples. This was done by clamping a reflector to the wire sample and making a measurement of the time interval between the partial reflection of the pulse from the weld interface and the reflection of the pulse from the reflector. The distance from the end of the wire to the reflector was then measured (using precision gage blocks and a dial micrometer) and the reflector moved toward the weld. This process was repeated four or five times to obtain transit time versus reflector position (distance) data. The velocity could then be determined from the slope of a straight-line fit to the data using the least-squares technique described in the Appendix.

The equations used to calculate the moduli and Poisson's ratio from wire data are different from the equations used for bulk samples since the extensional velocity, V_E, and torsional velocity, V_S, are measured (instead of longitudinal and shear). These equations are:

$$Y = V_E^2 \rho \tag{15}$$

$$S = V_S^2 \rho \tag{16}$$

$$\sigma = \frac{Y}{2S} - 1 \tag{17}$$

$$K = \frac{Y}{3(1 - 2\sigma)} \tag{18}$$

$$V_L = \frac{V_E}{\sqrt{\frac{(1 + \sigma)(1 - 2\sigma)}{(1 - \sigma)}}} \tag{19}$$

$$\delta Y = \left[4V_E^2 \rho^2 (\delta V_E)^2 + V_E^4 (\delta \rho)^2 \right]^{1/2} \tag{20}$$

$$\delta S = \left[4V_S^2 \rho^2 (\delta V_S)^2 + V_S^4 (\delta \rho)^2 \right]^{1/2} \tag{21}$$

$$\delta \sigma = \left[\frac{(\delta Y)^2}{4S^2} + \frac{Y^2 (\delta S)^2}{4S^4} \right]^{1/2} \tag{22}$$

$$\delta K = \left[\frac{(\delta Y)^2}{9(1 - 2\sigma)^2} + \frac{4Y^2 (\delta \sigma)^2}{9(1 - 2\sigma)^4} \right]^{1/2} \tag{23}$$

$$\delta V_L = \left[\frac{(1 - \sigma)(\delta V_E)^2}{(1 + \sigma)(1 - 2\sigma)} + \frac{V_E^2 \sigma^2 (\sigma - 2)^2 (\delta \sigma)^2}{(1 - \sigma)(1 + \sigma)^3 (1 - 2\sigma)^3} \right]^{1/2} \tag{24}$$

2.2. Processing of elevated temperature data

Once the room-temperature data were obtained for the samples, elevated-temperature data were taken. A normalizing technique was used to limit the number of parameters which needed to be measured.

If a sample of length, L, is heated, the length changes as a result of thermal expansion. If the temperature changes from some initial temperature to some other temperature, T, then the new length, L', is given by:

$$L' = L(1 + \alpha \Delta T) \tag{25}$$

where $\Delta T = T - T_o$.

Then, at temperature, T, the velocity is given by:

$$V = 2L'/t = \frac{2L(1 + \alpha \Delta T)}{t} \quad , \tag{26}$$

where t represents the two-way transit time in the sample.

A normalized velocity can then be calculated by:

$$N_V = \frac{V}{V_o} = \frac{\frac{2L(1 + \alpha \Delta T)}{t}}{\frac{2L}{t_o}} = \frac{t_o}{t}(1 + \alpha \Delta T) \tag{27}$$

where:

N_V = normalized velocity

t_o = two-way transit time in sample at T_o.

It can be seen that the length of the sample is not required. In a like manner, the oung's and shear moduli can be calculated. Repeating eq. (15):

$$Y = V_E^2 \rho \tag{15}$$

hen, at some temperature, T

$$\rho \simeq \rho_o/(1 + 3\ \alpha\Delta T) \tag{28}$$

here:

ρ_o = density at T_o
ρ = density at T.

Thus, a normalized modulus can be calculated from:

$$N_y = \frac{Y}{Y_o} = \frac{V_E^2 \rho}{V_{E_o}^2 \rho_o} = N_{V_E}^2/(1 + 3\ \alpha\Delta T) \tag{29}$$

here:

N_y = the normalized Young's modulus
Y_o = Young's modulus at T_o.

Likewise, the normalized shear modulus is given by:

$$N_S = \frac{S}{S_o} = N_{V_S}^2/(1 + 3\ \alpha\Delta T) \tag{30}$$

here:

N_S = normalized shear modulus
S_o = shear modulus at T_o.

The actual velocities and moduli can be calculated by multiplying the normalized values by the room-temperature values. This fact is the reason accurate room-temperature values of sonic velocity are required.

2.3. Computer calculations of high-temperature moduli

Four sets of data are taken on each wire sample - two extensional runs and two torsional runs. Each run can have as many as 300 sets of data (transit time and thermocouple voltage). Figure 3 is a block diagram of the computer program. A two-program package was written to do the data analysis and data plotting on a PDP-15/20 and a PDP-15/35 computer. The first program reads the data tapes from the four runs and calculates the normalized velocities correcting for the coefficient of thermal expansion (eq. (25)) and temperature. These data are plotted to check for errors and written in data files on magnetic tape in a standard format. The second program combines the two extensional runs and the two torsional runs. The room-temperature velocities and moduli are supplied, and the program calculates the actual velocities and moduli as a function of temperature.

A least-squares program fits an equation of the form:

$$\left[M = M_o \quad 1 + A(T - T_o) + B(T - T_o)^2 + C(T - T_o)^3\right] \tag{31}$$

to both the Young's and shear moduli data. An estimate of the standard deviation of the fit is also made. These equations are required to calculate the Young's and shear moduli at equal temperature increments to use in the calculation of the bulk modulus and Poisson's ratio since the extensional and torsional velocities were not measured at the same temperatures. Once Poisson's ratio is calculated, a least-squares routine is used to fit an equation of the same form as eq. (31) to Poisson's ratio. Finally, a table of moduli versus temperature is generated; and all the velocity, moduli, and Poisson's ratio data are plotted along with the fitted curves.

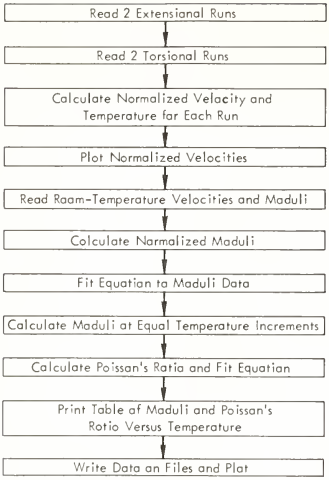

Figure 3. Computer program to calculate elevated-temperature sonic moduli.

3. Results and Conclusions

Table 1 is a list of some of the samples tested using the system described here. Typical results from sample 9MA (a 2.25 Cr-1 Mo steel) are listed in tables 2 through 4 and outlined in figures 4-10. Table 2 gives the results of the room-temperature velocities and moduli calculations (to convert moduli from psi to Pa multiply by 6.894757 E + 03). The velocities were calculated using the least-squares fit routine described earlier and in the Appendix. Shear-velocity measurements were taken twice with the polarization direction rotated 90 degrees between measurements. This is done to obtain an estimate of the anisotropy of the sample. The standard deviation of the average shear velocity is calculated from:

$$\delta V_S = \left[\delta V_{S_0}^2 + \delta V_{S90}^2 \right]^{1/2} \tag{32}$$

The anisotropy is calculated from:

$$A = \left[\frac{V_{S_0} - V_{S_{90}}}{2} \right] \tag{33}$$

As mentioned earlier, a measure of the anisotropy of a sample is important. The equations used (eqs. (5-9) and (15-19)) assume a homogeneous isotropic material. Calculations of the moduli of a sample may be invalid if the sample has excessive anisotropy. The moduli were calculated using the average shear velocity.

It should be pointed out that the uncertainties given are standard deviations on the repeatability of the measurements; i.e., precision. Since no velocity standards are available, it is difficult to know how accurate these measurements are. As described earlier, an attempt has been made to eliminate all identifiable errors.

Table 3 contains the coefficients of the least-squares fit to the elevated-temperature data for sample 9 MA. The elevated-temperature data were fitted to an equation of the form:

Table 1. Specimens for sonic dynamic properties.

Code	Material: Alloy	Material: Dimension (in)	Material: Dimension (mm)	Material: Form	Test Range Room Temperature To: (°F)	Test Range Room Temperature To: (°C)	Orientation of the Specimen Axis[1]	Specimen Condition[1]: Block for Room Temperature	Specimen Condition[1]: Wire for Elevated Temperature
9	2.25 Cr-1 Mo	1	25	Plate	1200	649	Parallel to the RD	MA	MA
9	2.25 Cr-1 Mo	1	25	Plate	1200	649	Parallel to the RD	AT	AT
9	2.25 Cr-1 Mo	1	25	Plate	995	538	Parallel to the RD	CT	CT
9	2.25 Cr-1 Mo	1	25	Plate	-	-	In Plane Perpendicular to the RD	Annealed[2]	
9	2.25 Cr-1 Mo	1	25	Plate	-	-	Perpendicular to the RD	Annealed	
17	9 Cr 1 Mo	0.5	13	Plate	1200	649	Parallel to the RD	MA	MA
15	Incoloy 800H	1	25	Plate	1650	899	Parallel to the RD	SA	SA
1	Type 304 SS	1	25	Plate	1600	871	Parallel to the RD	SA	SA
1	Type 304 SS	1	25	Plate	1000	538	Parallel to the RD	CT	CT
1	Type 304 SS	1	25	Plate	1600	871	Parallel to the RD	AT	AT
2	Type 304 SS	1	25	Plate	-	-	In Plane, 45° to the RD	SA	-
3	Type 304 SS	1	25	Plate	-	-	In Plane, Perpendicular to the RD	SA	-
4	Type 304 SS	1	25	Plate	-	-	Perpendicular to the Plane	SA	-
5	Type 304 SS	2.75	70	Plate	-	-	Parallel to the RD	SA MA	-
6	Type 304 SS	2	51	Plate	1600	871	Parallel to the RD	SA MA	SA
7	Type 304 SS	2.5	64	Plate	-	-	Parallel to the RD	SA MA	
8	Type 304 SS	3	76	Bar	1600	871	Parallel to the RD	SA MA	SA
10	Type 308 SS	-	-	FFTF Weld	1600	871	Parallel to the WD	AW	AW
13	Type 316 SS	1	25	Plate	1600	871	Parallel to the RD	SA	SA
16	Hastelloy X	0.75	19	Rod	2000	1093	Parallel to the RD	SA	SA
19	Hastelloy N	1	25	Plate	2000	1093	Parallel to the RD	SA	SA
11	Inconel 718	0.75	19	Plate	1000	538	Parallel to the RD	AH MA	AH
12	Inconel 718	-	-	Weld Deposit	1000	538	Parallel to the WD	-	AH[3]
18	Inconel 617	1	25	Plate	1800	982	Parallel to the RD	SA	SA
21	Inconel 82	-	-	Weld Deposit	1300	704	Parallel to the WD	-	SR[3]
21	Inconel 82	-	-	Wrought	1300	704	Parallel to the RD	-	SA[3]
22	Type 16-8-2	-	-	Weld Deposit	1300	704	Parallel to the WD	-	SA[3]
20	Pt-30 Rh-8 W	-	-	Sheet	1975	1079	Parallel to the RD	-	SA[3]

(1) The following notations are used:
AH = Age Hardened
AT = Treated to Give Recrystallized Fiber Texture
AW = As Welded
CT = Treated to Give Cold-Worked Fiber Texture
MA = Mill Annealed
RD = Rolling Direction
SA = Solution Annealed
SR = Stress Relieved
WD = Welding Direction

(2) No elevated-temperature data.

(3) Room-temperature properties taken on wire samples.

$$x = x_o(1 + A_1\Delta T + A_2\Delta T^2 + A_3\Delta T^3), \text{ or} \tag{34}$$

$$y = A_1x + A_2x^2 + A_3x^3 \tag{35}$$

where:

$$y = \left(\frac{x}{x_o}\right) - 1$$

$$x = \Delta T.$$

The standard deviation of the fit was then calculated from the equation:

$$\sigma = \left\{ \frac{\sum_{i=1}^{n} [(A_1x_i + A_2x_i^2 + A_3x_i^3) - y_i]^2}{n - 1} \right\}^{1/2} \tag{36}$$

where:

$$y_i = \frac{x_i}{x_o} - 1 \quad .$$

The fitted equations were then used to calculate the data reported in table 4.

Table 2. Room-temperature ultrasonic velocity and modulus measurements.

Sample: 9MA, 2.25 Cr-1 Mo, Heat Treat: 20017, Mill Annealed, Measurement Parallel to Rolling Direction
Sample Configuration: Bulk

Ultrasonic Velocity Calculations: 9MA

Longitudinal Velocity	=	5929.747	0.822 m/μs
0-Degree Shear Velocity	=	3267.996	1.318 m/μs
90-Degree Shear Velocity		3268.141	0.574 m/μs
Average Shear Velocity		3268.068	1.438 m/μs
Anisotropy of Shear Velocity		0.073	

Ultrasonic Moduli Calculations: 9MA

[illegible] Velocity	5929.747	0.822 m/μs
	233454.61	32.36 m/μs
Shear Velocity	3268.068	1.438 m/μs
	128664.09	56.61 m/μs
Longitudinal Velocity	5232.731	1.963 m/μs
	206013.62	77.28 m/μs
Density	7.83320	0.00050 g/m^3
Poisson's Ratio	0.281872	0.000289
Young's Modulus	214.4845	0.1615 GPa
	0.311083E-08	0.234241E-08 psi
Shear Modulus	83.6607	0.0738 GPa
	0.121394E-08	0.107052E-08 psi
Bulk Modulus	160.8826	0.2498 GPa
	0.233709E-08	0.362788E-08 psi

[illegible] 14.18 [illegible]

Table 3. Elevated-temperature ultrasonic modulus measurements.

Sample: 9MA, 2.25 Cr-1 Mo, Heat Treat: 20017, Mill Annealed, Measurement Parallel to Rolling Direction
Temperature Measurement Range: 24 - 663° C
Least Square Fit
$X = X_0(1 + A_1\Delta T + A_2\Delta T^2 + A_3\Delta T^3)$,

or $y = A_1x + A_2x^2 + A_3x^3$ where $y = (X/X_0) - 1$ and $x = \Delta T$

	X_0	A_1	A_2	A_3	Standard Deviation of Fit	
Young's Modulus	3.110836E-7	3.05032E-4	6.22360E-9	1.71081E-10	6.87155E-4	psi
Shear Modulus	1.213396E-7	2.09753E-4	4.53940E-7	2.72752E-10	9.35099E-4	psi
Poisson's Ratio	0.281872	4.66649E-4	2.19339E-6	2.13668E-9	2.79229E-4	

Table 4. Moduli and Poisson's ratio at elevated temperatures

Sample - 9MA, 2.25 Cr-1 Mo, Heat Treat - 20017, Mill Annealed, Measurement Parallel to Rolling Direction

Temperature (° C)	Temperature (° F)	Young's Modulus (X 10^6 psi)	Shear Modulus (X 10^6 psi)	Bulk Modulus (X 10^6 psi)	Poisson's Ratio
24	75	31.12	12.14	23.79	0.282
38	100	30.99	12.10	23.52	0.280
52	125	30.86	12.06	23.27	0.279
66	150	30.72	12.02	23.04	0.278
79	175	30.59	11.98	22.84	0.277
93	200	30.46	11.94	22.65	0.276
107	225	30.32	11.89	22.49	0.275
121	250	30.19	11.84	22.34	0.275
135	275	30.06	11.79	22.21	0.274
149	300	29.92	11.74	22.09	0.274
163	325	29.78	11.69	21.98	0.274
177	350	29.65	11.63	21.89	0.274
191	375	29.51	11.58	21.81	0.274
204	400	29.37	11.52	21.73	0.275
218	425	29.23	11.46	21.67	0.275
232	450	29.09	11.40	21.62	0.276
246	475	28.94	11.34	21.58	0.276
260	500	28.80	11.27	21.54	0.277
274	525	28.65	11.21	21.51	0.278
288	550	28.50	11.14	21.48	0.279
302	575	28.36	11.08	21.46	0.280
316	600	28.20	11.01	21.44	0.281
329	625	28.05	10.94	21.43	0.282
343	650	27.90	10.87	21.42	0.283
357	675	27.74	10.80	21.41	0.284
371	700	27.58	10.73	21.39	0.285
385	725	27.42	10.66	21.38	0.286
399	750	27.26	10.59	21.37	0.287
413	775	27.09	10.51	21.35	0.289
427	800	26.92	10.44	21.33	0.290
441	825	26.75	10.36	21.30	0.291
454	850	26.58	10.29	21.26	0.292
468	875	26.40	10.21	21.22	0.293
482	900	26.22	10.14	21.17	0.294
496	925	26.04	10.06	21.10	0.294
510	950	25.85	9.98	21.03	0.295
524	975	25.67	9.90	20.93	0.296
538	1000	25.47	9.83	20.83	0.296
552	1025	25.28	9.75	20.70	0.296
566	1050	25.08	9.67	20.56	0.297
579	1075	24.88	9.59	20.40	0.297
593	1100	24.68	9.52	20.22	0.297
607	1125	24.47	9.44	20.01	0.296
621	1150	24.26	9.36	19.78	0.296
635	1175	24.04	9.28	19.53	0.295
649	1200	23.82	9.21	19.25	0.294
663	1225	23.60	9.13	18.95	0.292

Finally, the data and calculated curves were plotted, as seen in figures (4-10). One of the samples (sample 1CT-75, a 2.25 Cr-1 Mo steel with 70 percent cold work) was mistakenly tested above the annealing temperature. The normalized extensional velocity data are shown in figure 11 for two thermal cycles. The first run shows the effect of annealing on the velocity after the sample reached approximately 550 °C. (The offset between the start and finish of the test is indicative of the modulus change due to annealing.) The second run then shows the results for an annealed sample.

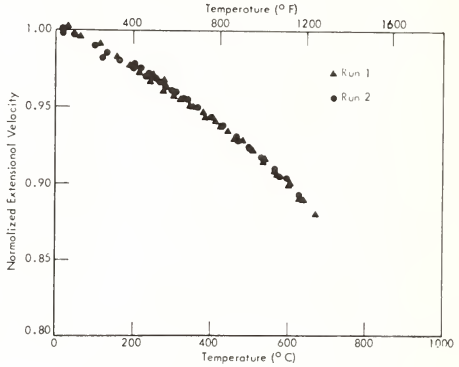

Figure 4. Normalized extensional velocity of sample 9 MA.

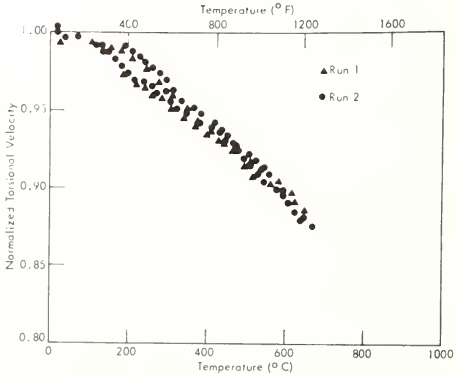

Figure 5. Normalized torsional velocity of sample 9 MA.

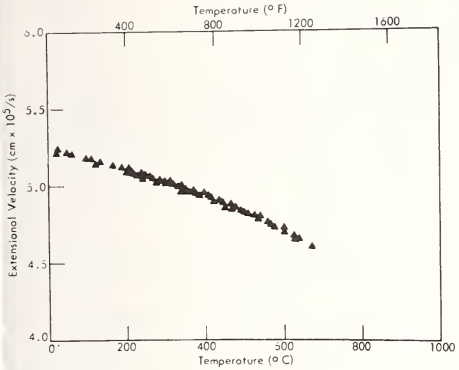

Figure 6. Extensional velocity of sample 9 MA.

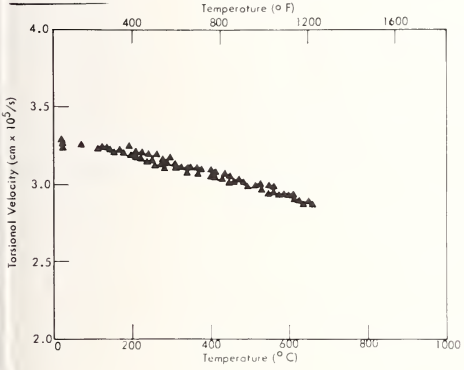

Figure 7. Torsional velocity of sample 9 MA.

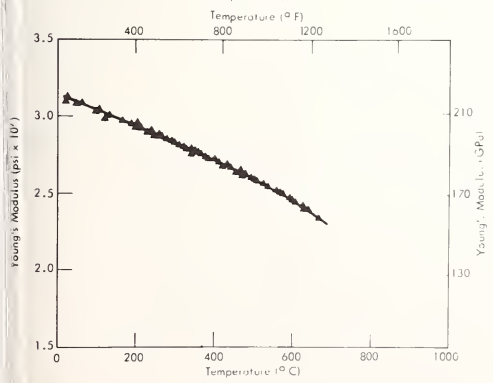

Figure 8. Young's modulus of sample 9 MA.

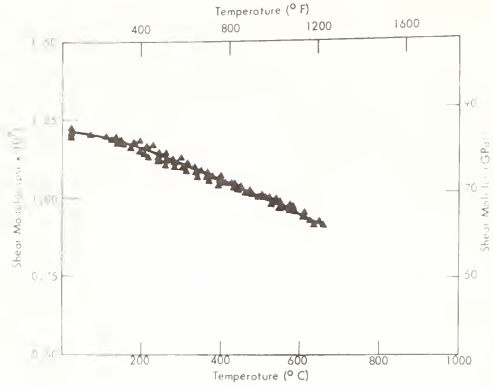

Figure 9. Shear modulus of sample 9 MA.

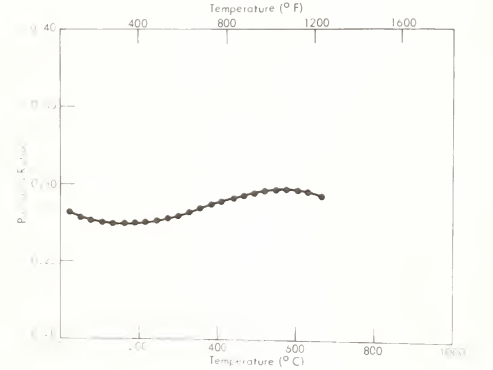

Figure 10. Poisson's ratio of sample 9 MA.

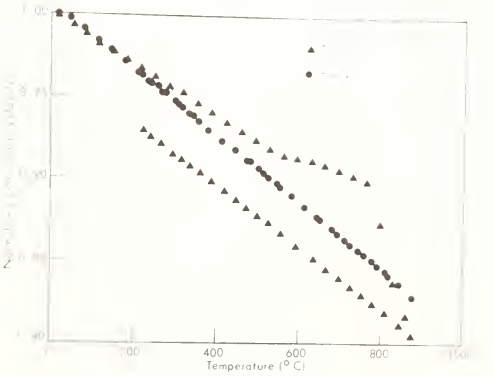

Figure 11. Normalized extensional velocity of sample 1 CT-75.

Appendix: Technique to determine a least-squares fit.

Herein, a technique is presented that can determine a linear least-squares fit to data in which both x and y are subject to error. A fit of the form:

$$y = \alpha + \beta x \tag{A-1}$$

is desired as well as an estimate of the standard deviation of both α and β.

A method is outlined by Graybill [8] to obtain an estimate of σ_e^2, α, and β for the functional relationship of eq. (A-1). The technique requires that λ be known, where λ is defined as a ratio:

$$\lambda = \frac{\sigma_x^2}{\sigma_y^2} \quad . \tag{A-2}$$

An estimate of σ_x^2 is obtained from the equation:

$$\sigma_x^2 = \frac{\sum[(n_i - 1)\sigma_{x_i}^2]}{\sum n_i - N} \tag{A-3}$$

where:

n_i = number of samples used to determine σ_{x_i}

N = number of data points used for the least-squares calculation.

Likewise:

$$\sigma_y^2 = \frac{\sum[(n_i - 1)\sigma_{y_i}^2]}{\sum n_i - N} \tag{A-4}$$

The maximum-likelihood estimates are given by:

$$\hat{\beta} = \pm (U^2 + \frac{1}{\lambda})^{1/2} + U \tag{A-5}$$

where:

$$U = \frac{\sum (y - \bar{y})^2 - \frac{1}{\lambda}(x - \bar{x})^2}{2\sum (y - \bar{y}) \quad (x - \bar{x})} \tag{A-6}$$

Also:

$$\hat{\alpha} = \bar{y} - \beta\bar{x} \tag{A-7}$$

$$\sigma_e^2 = \frac{1}{N - 2} \quad [\sum (y - y)^2 - \hat{\beta} \sum (y - \bar{y}) \ (x - \bar{x})] \quad . \tag{A-8}$$

Using the following identities, these equations can be simplified for calculations:

$$\text{let } S = N\sum x_i y_i - \sum x_i \sum y_i = N[\sum (x - \bar{x})(y - \bar{y})] \tag{A-9}$$

$$C = N\sum y_i^2 - (\sum y_i)^2 = N\sum(y_i - \bar{y})^2 \tag{A-10}$$

$$D = N\sum x_i^2 - (\sum x_i)^2 = N\sum(x_i - \bar{x})^2 \tag{A-11}$$

where:

$$\bar{y} = \frac{\sum y_i}{N} \tag{A-12}$$

$$\bar{x} = \frac{\sum x_i}{N} \quad . \tag{A-13}$$

Then, simplifying eqs. (A-6) through (A-8) gives:

$$U = \frac{C\lambda - D}{2\lambda S} \tag{A-14}$$

$$\hat{\alpha} = \frac{\sum y_i}{N} - \beta\,\frac{\sum x_i}{N} \tag{A-15}$$

$$\sigma_e^2 = \frac{1}{N(N-2)}\,[C - \beta S] \tag{A-16}$$

where $\hat{\beta}$ is determined by eq. (A-5). The sign is chosen by the sign of S. Thus, if S is positive, $\hat{\beta} = U + \sqrt{U^2 + 1/\lambda}$; and, if S is negative, $\hat{\beta} = U - \sqrt{U + 1/\lambda}$.

John Mandel [9] then presents a method for calculating approximate estimates of $\hat{\sigma}_{\hat{\beta}}$ (standard deviation of the slope), and $\hat{\sigma}_{\hat{\alpha}}$ (standard deviation of the intercept). Assuming that errors in y are uncorrelated with errors in x, the estimates given by Mandel reduce to:

$$\hat{\alpha}_{\hat{\beta}} = T\hat{\sigma}_e \tag{A-17}$$

$$\hat{\sigma}_{\hat{\alpha}} = \sigma_e\sqrt{1/N + (T \cdot \bar{x})^2} \tag{A-18}$$

where:

$$T = \frac{(1 + \lambda\hat{\beta}2}{\sum(x_i - \bar{x})^2\left[1 + 2\lambda\hat{\beta}^2 + \left(\frac{\sum(x_i - \bar{x})^2\sum(y_i - \bar{y})^2}{[\sum\ (x_i - \bar{x})(y_i - \bar{y})]^2}\right) \cdot \lambda^2\hat{\beta}^4\right]^{1/2}} \tag{A-19}$$

σ_e^2 is given by eq. (A-16). Using eqs. (A-9) through (A-13), T can be expressed as:

$$T = \frac{(1 + \lambda\hat{\beta}^2)}{\{(D/N)\,[1 + 2\lambda\hat{\beta}^2 + D \cdot C\lambda^2\hat{\beta}^4/S]\}^{1/2}} \quad . \tag{A-20}$$

The authors wish to express their gratitude to J. P. Hammond for initiating this program; to T. W. Dews for taking and reducing the data presented here, to C. M. Davenport and D. M. Darby for providing the computer programming, and to R. W. Counts for providing the statistical treatment for calculating the standard deviation of the velocity.

References

[1] Moyer, M. W. and Hammond, J. P., Ultrasonic measurement of elastic constants at temperatures from 20 to 1100 °C, Y-2047, Union Carbide Corporation-Nuclear Division, Oak Ridge Y-12 Plant, Oak Ridge, Tennessee, available from the National Technical Information Service, Springfield, Virginia (1976).

[2] Papadakis, E. P., J. Acoust. Soc. Amer., 42, 1045-1051 (1967).

[3] Papadakis, E. P., Absolute accuracy of the pulse-echo overlap method and the pulse-superposition method for ultrasonic velocity, J. Acoust. Soc. Amer., 52, 843-846 (1972).

[4] McSkimin, H. J., Pulse superposition method for measuring ultrasonic wave velocities in solids, J. Acoust. Soc. Amer., 33, 12-16 (1961).

[5] Seki, H., Granato, A., and Truell, R., Diffraction effects in the ultrasonic field of a piston source and their effects upon accurate ultrasonic attenuation measurements, J. Acoust. Soc. Amer., 28, 230 (1956).

[6] Papadakis, E. P., Diffraction loss and phase change in anisotropic materials, J. Acoust. Soc. Amer., 37, 711 (1965).

[7] Papadakis, E. P., Ultrasonic diffraction and phase change for broad-band pulses, J. Acoust. Soc. Amer., 52, 847-849 (1972).

[8] Graybill, F. A., An Introduction to Linear Statistical Models 1, p. 191 (McGraw-Hill Book Company, 1961).

[9] Mandel, J., A simple approach to straight line fitting with correlated errors in both variables, presented at the 19th Fall Technical Conference of the American Society for Quality Control, Chemical Division, and the American Statistical Association, Section on Physical and Engineering Sciences, Denver, Colorado (October 30, 1975).

National Bureau of Standards Special Publication 596, Ultrasonic Materials Characterization, H. Berger and M. Linzer, eds., Proceedings of the First International Symposium on Ultrasonic Materials Characterization held at NBS, Gaithersburg, Md., June 7-9, 1978. Issued November, 1980.

THE ELASTIC CONSTANTS OF REFRACTORY MATERIALS AT HIGH TEMPERATURES

J. F. W. Bell, J. Y. F. Chen, and K. R. Chaplain

University of Aston
Birmingham B4 7PB
United Kingdom

A knowledge of the elastic constants of refractory materials is necessary for carrying out stress analysis of high temperature structural designs. Together with internal friction, such measurements can give useful NDT information.

Techniques for these measurements based mainly on disks, but including rods and rings, are described. Observations on conventional materials such as silica, molybdenum, and tungsten have been extended to graphite, graphite composites, and the silicon nitrides. In general, these materials have very stable thermophysical properties but show wide variations from batch to batch. This is currently a major obstacle to their use.

1. Introduction

The vibrational spectrum of a solid body is a function of its geometrical form and the elasticities of its materials. In a limited number of simple geometrical cases, the exact theoretical spectrum can be obtained and these have been used in material characterization over a wide temperature range for stress analysis programs and in nondestructive testing. Of particular value is the in-plane spectrum of thin disks which can give the elastic constants of isotropic, orthotropic and empirically anisotropic, and composite materials. Where only thin rods and rings are available, Young's Modulus can be obtained by using longitudinal modes of vibration.

The pulse echo system already reported which is effective at frequencies from 10 to 1000 kHz is used for all measurements [1,2][1]. By observing resonant frequencies, the low order modes are obtained and at high frequencies, where the modes are close together, time-of-flight measurements enables surface channels to be explored. Internal friction can also be measured and this is useful in analyzing batches of materials for anomalies such as poor bonding in fiber composites.

2. Experimental Techniques

Figure 1(a) shows the pulse-echo system in its simplest form and 1(b) typical echo returns. The longitudinal vibrations of the wire will couple to the component of the modal vibration parallel to the wire. Thus a single radial drive will couple effectively to the first four modes shown in table 1, but the shear mode requires an angled drive. In many cases, the frequencies of two modes can be too close to be resolved separately. By using a double wire drive, one can be suppressed. For example, in aluminum, the 1,3 and 1,R modes frequencies are coincident (fig. 2). A double drive at opposite ends of a diameter will excite the 1,R mode when in phase and the 1,3 when in reverse phase. These phase relationships are obtained by adjusting the position of the coil to make the line lengths either equal, for "in phase", or different by $\lambda/2$, for "push pull". An essential feature of the system is the use of long lengths of line. This, as well as separating the transmission

[1]Figures in brackets indicate the literature references at the end of this paper.

from the echo return, avoids standing waves on the line which would give a reactive loading on the resonator and therefore a false frequency. The line loading is thus resistive only. Useful lines vary in diameter from 0.1 to 3 mm, the choice being to give sufficient coupling to the required mode. Only the transducer section of the line need be of magnetostrictive material and for high temperature measurements the rest is chosen for low attenuation and furnace environment compatibility.

In a typical measurement at 100 kHz, a line 2 m long can have a burst of 80 oscillations (λ,5 cm) before standing waves occur. The burst can be repeated every 10 ms without interaction. The echo is usually about 30 dB less than the transmitted signal. A noise limitation due to backscattering from the line can be significant when the wavelength becomes comparable to the grain size in a metal but is negligible for fused quartz and other glasses.

Figure 1(a). The electronic box allows digital control of frequency, burst number and recurrence period over wide ranges. It includes a transmit/receive switch, power amplifier, and other sonar type circuits.

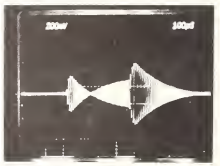

Figure 1(b). An echo return for the signal frequency equal to one of the resonator frequencies. There are 60 oscillations in the signal transmission, the null--a sensitive indication of resonance--occurs after 13 oscillations and the final long decrement is the retransmission of the energy stored in the resonance.

Table 1. Nomenclature of the principal modes used. The first shear mode has an antinode (maximum rotation) at the center. All the others have central nodes which are classified as circles.

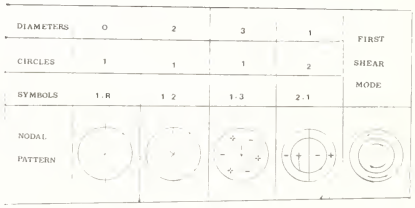

3. Disks

The disk geometry has been the most used by the authors for elasticity measurements. The principle as given by Onoe depends on the feature that while the distortion modes [1,2; 1,3, etc.] are governed principally be the shear modulus, the 1,R; 2,1 and 2,R are more dependent on Young's Modulus [3]. This is understandable as the area change in the former group is small while in the latter it is large. The dimensionless frequency constant used is the

ratio of the frequency circumference product to the plate wave velocity in the material. The choice of plate velocity is arbitrary but is widely used. Figure 3 shows graphs of the frequency constant as a function of Poisson's Ratio for various modes. The slopes of the distortion modes are negative and that of the others positive. Comprehensive high precision values of K have been calculated by Chaplain over the Poisson's Ratio range of -0.2 to +0.5 at intervals of 0.01 [4]. Tables are given enabling Poisson's Ratio to be calculated from the 1,R and 2,1 modes frequencies and those of distortion modes at adjacent frequencies. The plate velocity can then be obtained from one of the mode frequencies.

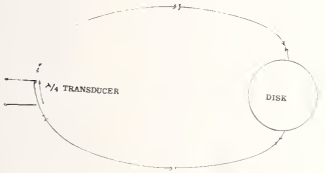

Figure 2. The transducer drive sends equal signals in both directions. By positioning the coil "push-pull" or "push-push" drives are obtained. This technique enables a desired resonance to be obtained.

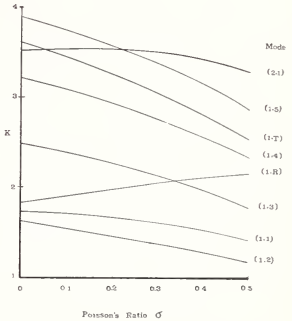

Figure 3. The dependence of the dimensionless frequency constant (K) on Poisson's Ratio is shown for the modes generally used. The (1,T) is the first shear mode. Determination of Poisson's Ratio required a comparison of the (1,R) or (2,1) modes with any of the others shown.

Silica is typical of the materials investigated. A disk 5 cm diameter was fused to a 1 mm diameter silica tube about 60 cm long. The tube was then joined to a magnetostrictive line of diameter giving a good acoustic match. The disk was then located in the isothermal region of a furnace. The silica tube being in the region of the temperature gradient thus kept the magnetostrictive joint at room temperature. The 1,3 and 1,R mode frequencies were measured as the disk temperature was slowly cycled. Figure 4 shows the variation of Poisson's Ratio and the plate velocity with temperature. Typical of most materials, Poisson's Ratio increases with temperature but most uncharacteristically the velocity increases with temperature to the limit of the particular experiment. A similar specimen form is employed for various grades of graphite. The disk and line are cut from a sheet of material, thus avoiding the problem of making a high temperature joint between line and disk. Figure 5 gives the logarithmic display used when both velocity and expansion data are available.

Disks of simple anisotropy, where the maximum and minimum elasticities are perpendicular, have been investigated empirically. The moderate anisotropy which occurs in rolled metal sheets, is evident only at the lowest mode, that with two nodal diameters. The elasticity removes the mode degeneracy and the mode becomes double. In one, the nodal diameters are symmetrical about the elastic axes and in the other they are aligned. As the wire drive has maximum coupling at an antinode, placing the drive at an elastic axis excites only the symmetrical mode. As it is moved to the 45° position, the second mode appears and in turn becomes separately excited with maximum coupling.

Materials similar in structure to wood can be made from layers of graphite fabric sheet held together by a carbon matrix. When these are cut perpendicular to the layers, a highly anisotropic material results. Disks cut in this plane have been investigated. Driven along

the diameter of maximum elasticity, the disk exhibits simple longitudinal modes which are almost harmonic. The frequencies are close to those of a rod of length equal to the diameter and cut in the direction of maximum elasticity. Driven at right angles, along the direction of minimum elasticity, the modes are close to those of an isotropic disk of the carbon matrix material. Measurements have not yet been carried out on nonclassified materials.

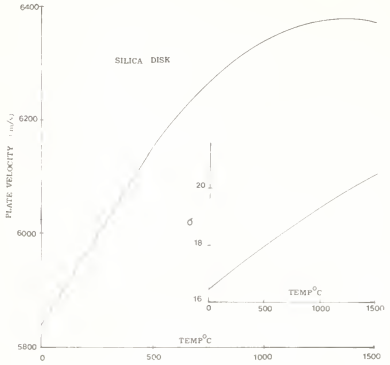

Figure 4. Data on silica. Poisson's Ratio increases linearly with temperature. The plate velocity reaches a maximum as the melting point approaches. Lack of information on expansion prevents exact interpretation of the data.

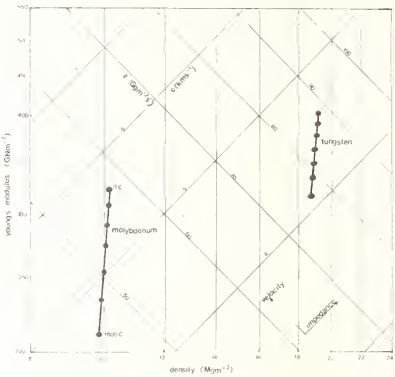

Figure 5. Where expansion and velocity dat are available, a four axis logarithmic gr gives a comprehensive data display. The terials shown, tungsten and molybdenum, a widely used metal refractories.

4. Rods, Rings and Other Resonator Forms

Thin rods and rings sustain longitudinal vibrations. In the former, the frequencies are harmonically related and in the latter follow an $(S^2+1)^{\frac{1}{2}}$ law where S is an integer. S=0 gives the radial "breathing" mode much used as acoustic radiators for identifying deep water oceanographic probes. Since these structures are thin, only one constant is readily obtainable. Rods are particularly useful for internal friction measurement [5]. Rings are important in giving hoop strength to various structures and, as a carbon fiber in polymer composite, for ultra-centrifuge work. In the latter case, the frequency of the longitudinal circu ferential waves is in the region of high density distortion modes. To avoid exciting these modes, a double drive is used in which the wires are angled to produce only a circumferentia component. In many cases, the overtone modes depart significantly from the $(S^2+1)^{\frac{1}{2}}$ law due to fabrication anomalies. This is under investigation as an NDT technique and for productio quality control.

5. Typical Results

The main engineering interest in the elasticity of materials arises when stress analysi is to be carried out over a wide temperature range. In a rocket motor, the throat material which is chosen for its thermal properties rather than intrinsic strength is bonded to a steel frame which may be cryogenically cooled. The calculation of thermal stresses at the bond requires a knowledge of the elasticities as well as other more obvious thermophysical properties. Similarly, in high power internal combustion engines, low thermal conductivity liners can result in a conspicuous reduction in cooling requirements. A variety of graphite including isostatically pressed, extruded, pyrolytic (the orthotrophic form) and carbon fibe and carbon fabric-carbon composites are potentially usable. Two types of silicon nitride, reaction formed and hot pressed, are useful because of their very stable dimensional and other properties.

These have been examined over their engineeringly useful temperature range and in common with other properties the elasticities vary only very slightly in comparison with metals. A conspicuous deficiency is, however, at once apparent. This is the large variation of properties from specimen to specimen even from the same batch. Thus the production variation far exceed that of any temperature effect. Data on specimens of the two materials are shown in figures 6 and 7. The large difference in values of Poisson's Ratio for graphite can have a large effect on bonded structure.

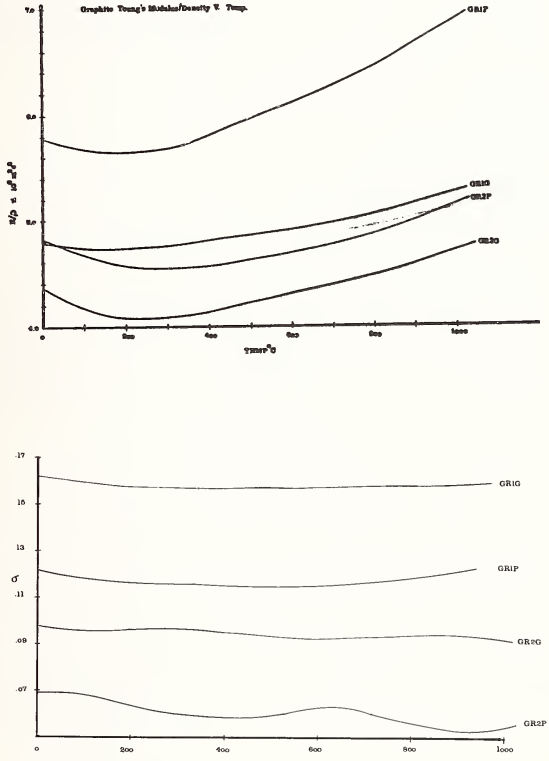

Figure 6 (a) (top) Shows the elasticity graphs and (b) (bottom) those of Poisson's Ratio. The material was made from powdered coke extruded with a tar binder and then graphitized. Specimens were cut with the grain (G) and perpendicular (P). The variations with temperature are all similar. P cut has the greater elasticity, but the lower Poisson's Ratio. The difference between the two specimens is conspicuous.

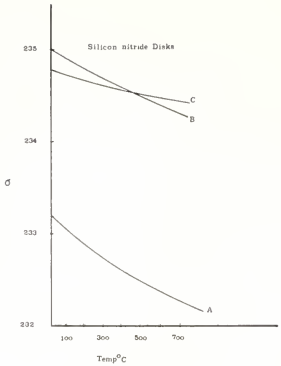

Figure 7. The specimens are nitrided, sintered silicon biscuits. All three are from the same batch. The Poisson's Ratios are virtually identical but, as in graphite, the specimen variations exceed the temperature effect.

References

[1] Bell, J. F. W., Johnson, A. C., and Sharp, J. C. K., J. Acoust. Soc. Amer., 57, 1085-1093 (1975).

[2] Bell, J. F. W. and Sharp, J. C. K., Rev. Int. Htes. Temp. et Réfract., 12, 40-43 (1975).

[3] Onoe, M., J. Acoust. Soc. Amer., 28, 1158-1162 (1956).

[4] Chaplain, K. R., Ph.D. Thesis, University of Aston (1978).

[5] Bell, J. F. W. and Pelmore, J. M., J. Phys. E., 10, 1145-1149 (1977).

National Bureau of Standards Special Publication 596, Ultrasonic Materials Characterization, H. Berger and M. Linzer, eds., Proceedings of the First International Symposium on Ultrasonic Materials Characterization held at NBS, Gaithersburg, Md., June 7-9, 1978. Issued November, 1980.

ULTRASONIC MEASUREMENT OF RESIDUAL STRESS

Robert E. Green, Jr.[1]

Polymer Science and Standards Division
Center for Materials Science
National Bureau of Standards
Washington, DC 20234

This paper serves as an introduction to the section on Materials Characterization: Residual Stress. Since most of the papers presented deal with ultrasonic measurement of residual stress in structural materials, this overview will be primarily confined to that subject.

General definitions of the various types of residual stresses are presented as well as a discussion of acoustoelasticity. A brief historical review of theoretical and experimental considerations for ultrasonic residual stress measurements follows. Finally, several problems associated with ultrasonic residual stress measurements are discussed and areas where additional research may be fruitful are pointed out.

1. Introduction

This paper is to serve as an introduction to the subject of nondestructive measurement of residual stress. Since most of the papers to follow deal with ultrasonic measurement of residual stress in structural materials, this overview will be confined to that subject.

At the onset it should be pointed out that the term residual stress is used in the present article in order to conform to conventional usuage; however, what is actually measured in all cases is residual strain. The residual stresses are conventionally calculated from the measured strain values using linear elastic stress-strain relations for a homogeneous isotropic solid.

As a result of forming, joining, and heat treating processes, a solid material is often found to be in a state of internal stress (strain) even though all externally applied stresses have been removed. This internal stress state is commonly termed residual stress and consists of several different components, generally classified as macrostress, microstress, and pseudo-macrostress.

Macrostress refers to internal stresses whose magnitude and direction are reasonably constant over large regions of a solid body, and is the type of internal stress engineers usually mean when they use the term "residual stress". Residual macrostresses cause a portion of a solid body to deform spontaneously when that portion is removed from the bulk of the body. Macrostresses produce x-ray line shifts and changes in ultrasonic wave velocities.

[1]Permanent address: Mechanics and Materials Science Department, The Johns Hopkins University, Baltimore, MD 21218.

Microstress refers to internal stresses whose magnitude and direction are reasonably constant only over small regions of a solid body. Residual microstress does not cause a portion of a solid body to deform spontaneously when that portion is removed from the bulk of the body. Microstresses produce x-ray line broadening and extremely small changes in ultrasonic wave velocities. They may, however, produce large changes in the attenuation of the ultrasonic waves, particularly those of higher frequency.

Pseudo-macrostress refers to the type of internal stress in which an x-ray line shift is observed, but no spontaneous deformation of a portion of the body is observed upon removal from the bulk. Such internal stress distributions are observed in some materials following plastic deformation. The exact nature and causes of pseudo-macrostresses have not been determined. The effect of such stresses on ultrasonic waves has not been investigated.

Although x-ray diffraction techniques have historically been the nondestructive method most often used in actual practice to measure residual stress, they are not optimally suited for field applications partially because the necessary equipment is heavy and bulky, and, perhaps more importantly, because they suffer from the fact that they only serve to determine the state of stress in surface layer of a material, while in many practical cases a knowledge of the bulk stresses is desired. Nevertheless, the majority of practical nondestructive residual test measurements are made using an x-ray diffraction technique.

Ultrasonic residual stress measurements have been made far less frequently, probably because of lack of familiarity with nonlinear elasticity and the experimental techniques necessary to obtain the desired measurement accuracy. However, properly applied, these techniques offer the potential to measure both surface and bulk stresses rapidly over large areas and throughout large volumes of structural materials.

2. Acoustoelasticity

Acoustical birefringence or acoustoelasticity are the terms often used to describe the experimental ultrasonic technique which permits measurement of applied or residual stress in materials. The names describe the phenomenon of variation of ultrasonic transverse wave velocity with different polarizations in stressed isotropic solids. The names derive from the analogy with optical birefringence or photoelasticity. The fact that in a rigorous sense the analogy is not correct has been pointed out in a paper by Henneke and Green [1][2] in which general consideration is given to the analogies that exist between the propagation of light waves and the propagation of ultrasonic waves in anisotropic media. Since the material constitutive equations required to describe elastic wave propagation are of higher order (second-order tensors related by fourth-order tensors) than those required to describe electromagnetic wave propagation (vectors related by second-order tensors) a direct one-to-one analogy will never be attained for all phenomena. Thus when a transverse ultrasonic wave is incident normally on the face of an anisotropic solid it does not simply resolve into pure-mode transverse waves with different polarizations and velocities as in the case for light (double refraction or birefringence), but it is generally resolved into three waves, one quasi-longitudinal and the other two quasi-transverse (triple refraction). However, in the special case when a transverse ultrasonic wave is incident normally on the face of an anisotropic solid such that the normal to that face is a principal symmetry axis, it is resolved into two pure-mode transverse waves which possess different polarizations and propagate with different velocities. This special case is directly analogous to optical double refraction. In the even more special case, when an initially isotropic solid is subjected to a set of co-planar stresses which converts it to a plane-stress anistropic solid and a transverse ultrasonic wave is incident normally to the stressed plane, acoustoelasticity (acoustical birefringence) is analogous to photoelasticity (optical birefringence).

3. Historical Background

The fundamental theoretical foundation for ultrasonic residual stress measurement dates back to Murnaghan [2] who in 1937 published a definitive treatment of finite deformation of

[2]Figures in brackets indicate the literature references at the end of this paper.

elastic solids which he expanded and updated in 1951 [3]. The historical origin of using ultrasonic waves to make measurements in stressed solids is attributed to Firestone and Frederick [4] who, in 1946, showed that when transverse waves were propagated through an isotropic solid at right angles to the direction of applied stress, the transverse wave with particle displacement perpendicular to the direction of applied stress propagated with a slower wave velocity than the transverse wave with particle displacement parallel to the direction of applied stress. In 1953, Hughes and Kelly [5] derived seven expressions for infinitesimal elastic waves propagating in stressed isotropic solids and used an ultrasonic pulse technique to measure the seven different wave velocities. In 1959, Benson and Raelson [6] employed the acoustoelastic effect to study the stressed state of an isotropic solid.

The existence of acoustoelasticity and all other phenomena which are capable of being used for ultrasonic measurement of residual stress depend on the fact that nonlinear elastic behavior is induced in an otherwise linear elastic solid due to the presence of an applied or residual stress. A comprehensive treatment of both linear and nonlinear elastic wave propagation in isotropic and anisotropic solids was published by the present author in 1973 [7]. This publication contained a detailed survey of previous work on ultrasonic wave propagation in stressed solids from both theoretical and experimental viewpoints.

An important reference overlooked prior to publication of the above mentioned book was the paper by Ratcliffe [8] who in 1969 reviewed the various experimental techniques for using ultrasonic waves for measurement of stress within materials. In 1974, Hsu [9] published a paper in which he described the use of a rotatable shear wave transducer to measure stress-induced acoustical birefringence in solids. The same year, an entire book devoted to ultrasonic nondestructive methods of determination of stress in solid bodies was published in Russia [10]. The next year, Noronha and Wert [11] reported results of using an ultrasonic technique for measurement of residual stress. Also in 1975, a special workshop was held on nondestructive evaluation of resdual stress at which five papers were presented on ultrasonic residual stress measurement [12]. In 1976, Blinka and Sachse [13] applied ultrasonic-pulse-spectroscopy measurements to experimental stress analysis and Buck and Thompson [14] presented a paper on acoustic interactions with internal stresses in metals at the ARPA/AFML Review of Progress in Quantitative NDE. At a similar meeting held in 1976, a paper was presented on computerized reconstruction of ultrasonic velocity fields for mapping of residual stress [15]. Most recently, Smith et al., [16] reported on measurements of ultrasonic shear wave birefringence in order to determine residual stress levels in bridge members.

4. Discussion

As has been pointed out by numerous previous investigators, the major difficulty associated with reliable ultrasonic residual stress measurement is that the change in elastic wave velocities in solid materials due to residual stress in small and other factors which can cause greater velocity changes may mask residual stress effects. The major factor in this regard is the fact that all real structural materials are initially anisotropic. The prime reason for this is that the solidification or forming and heating processes associated with material preparation does not permit a random distribution of crystallographic orientations among the grains of the polycrystalline aggregate and often does not even permit a uniformity in grain size. Therefore, real polycrystalline solids possess a "texture" and this texture strongly influences the mechanical properties of the solid including ultrasonic wave propagation. Thus the ultrasonic residual stress measurement problem becomes one of measuring changes in anisotropy before and after stressing rather than the commonly treated theoretical problem of stress-induced anisotropy of an originally isotropic solid. For this reason it is quite pertinent to include papers in this session, and to pay close attention to papers presented in other sessions, concerning the influence of a variety of material parameters, other than residual stress, on ultrasonic velocity measurements.

The fact that ultrasonic techniques offer the possibility of measuring bulk residual stresses in thick sections of materials can also lead to problems, since the same section of a material may contain both compressive and tensile stresses whose effects integrated over the path of the ultrasonic wave will cancel.

Most methods used to measure residual stresses ultrasonically have been concerned with measuring only one stress component, even though stress and strain are tensor quantities with six different components each, if we limit attention to linear elasticity where the stress and strain tensors are symmetric.

Although most ultrasonic measurements of residual stress made to date have been based on stress-induced acoustical birefingence of an isotropic solid, other ultrasonic techniques can be used to make such measurements. For example, five of the equations derived originally by Hughes and Kelly [5] relate an elastic wave velocity to a stress component in the material. These equations can be used either singly or in appropriate combination to determine individua stress components from experimental measurements of various ultrasonic wave velocities. Moreover, other features of nonlinear elastic wave propagation such as harmonic generation, as studied by Buck and Thompson [14], or temperature dependence of ultrasonic velocity, as studied by Salama and Ippolito [17], can be used for residual stress determinations.

The papers to follow either deal with improvements in existing techniques or describe new techniques for ultrasonic residual stress measurements in solid materials.

References

[1] Henneke, E. G., II and Green, R. E., Jr., J. Acoust. Soc. Amer., 45, 1367 (1969).

[2] Murnaghan, F. D., Amer. J. Math., 49, 235 (1937).

[3] Murnaghan, F. D., Finite Deformation of an Elastic Solid (John Wiley, New York, 1951, Dover, New York, 1967).

[4] Firestone, F. A. and Frederick, J. R., J. Acoust. Soc. Amer., 18, 200 (1946).

[5] Hughes, D. S. and Kelly, J. L., Phys. Rev., 92, 1145 (1953).

[6] Benson, R. W. and Raelson, V. J., Prod. Eng., 30, 56 (1959).

[7] Green, R. E., Jr., Ultrasonic Investigation of Mechanical Properties, Volume III Treatise on Materials Science and Technology (Academic Press, New York, 1973).

[8] Ratcliffe, B. J., Britsh J. of NDT, 11, 48 (1969).

[9] Hsu, N. N., Experimental Mechanics, 14, 169 (1974).

[10] The Fundamentals of Ultrasonic Nondestructive Methods for Determination of Stress in Solid Bodies, A photocopy of this book was kindly supplied by Dr. Michael Lauriente, Office of Systems Engineering, Department of Transportation, Washington, DC.

[11] Noronha, P. J. and Wert, J. J., J. of Testing and Evaluation, 3, 147 (1975).

[12] Alers, G. A., Ultrasonic methods-overview; Szabo, T. L., Ultrasonic dispersion; Hsu, N. N., Shear wave birefringence; Buck, O., Harmonic generation; Bray, D. E., Measurement of longitudinal stresses in railroad rails by acoustic wave velocity, in Proc. Workshop on Nondestructive Evaluation of Residual Stress, NTIAC-76-2, Nondestructive Testing Information Analysis Center, Southwest Research Institute, San Antonio, Texas 78284 (1976).

[13] Blinka, J. and Sachse, W., Experimental Mechanics, 16, 448 (1976).

[14] Buck, O. and Thompson, R. B., Acoustic interactions with internal stresses in metals, in Proc. ARPA/AFML Review of Progress in Quantitative NDE, AFML-TR-44 (1977).

[15] Hildebrand, B. P. and Hufferd, D. E., Computerized reconstruction of ultrasonic velocity fields for mapping of residual stress, Acoustical Holography, Vol. 7, L. W. Kessler, ed., pp. 245-262 (Plenum Press, New York, 1977).

[16] Smith, V. D., King, R. R., Cerwin, S. A., Barton, J. R., and McGogney, C. H., in Paper Summaries, National Spring Conference of the American Society for Nondestructive Testing, New Orleans, Louisiana, p. 293 (April 1978).

[17] Salama, K. and Ippolito, R. M., in Proc. of 11th Symposium on Nondestructive Evaluation, p. 62, San Antonio, Texas (April 1977).

Naticnal Bureau of Standards Special Publication 596, Ultrasonic Materials Characterization, H. Berger and M. Linzer, eds., Proceedings of the First International Symposium on Ultrasonic Materials Characterization held at NBS, Gaithersburg, Md., June 7-9, 1978. Issued November, 1980.

ULTRASONIC TOMOGRAPHY FOR MAPPING RESIDUAL STRESS

B. P. Hildebrand and T. J. Harrington[1]

Battelle, Pacific Northwest Laboratories
Battelle Boulevard
Richland, WA 99352

It is known that internal stress concentrations can give rise to microcracks which then grow when the structure is subjected to external forces. It has also been found that the velocity of sound is altered as it propagates through a region of stress. In this paper, we discuss a technique called Computer-Assisted Tomography (CAT) and describe an application of the CAT technique that provides pictures of stress fields. We report the results of both simulated and experimental models used to evaluate the technique. We conclude that the CAT approach has great potential for locating and mapping residual stress in metals.

1. Introduction

One of the outstanding problems of nondestructive testing is the location and measurement of areas of residual stress. In the manufacture of large structures, such as pressure vessels, a number of very large welds are required. The heat-affected zone surrounding the welds will contain residual stresses due to uneven cooling rates. In practice, these stresses are relieved by heating the entire vessel to some appropriate temperature and then carefully controlling the cooling rate. This standard procedure has not always been successful in relieving the residual stress that is induced by the welding process [1][2]. Structural designers realize this, and try to compensate for the possibility of stress concentrations by overdesigning. This leads to penalties in terms of both added weight and cost. Consequently, there is high motivation for finding and delineating such concentrations.

Currently, there is no satisfactory test for measuring the success of stress-relief procedures. Thus, it may happen that high residual-stress regions exist in the pressure vessel. If these regions occur in critical areas (such as nozzle-to-vessel joints), cracks may develop, which would require subsequent plant shut-downs and expensive repair. If it were possible to detect and map residual stress, local stress relief could be applied, and future problems could be avoided.

Standard Nondestructive Testing (NDT) examinations consist of radiography and ultrasonic pulse-echo. Neither of these techniques can reveal the presence of residual stress; the former because it shows only density variations, and the latter because stress regions are not sharply defined; hence, they do not reflect much sound. It is known, however, that the velocity of sound in a solid is affected by stress. This phenomenon is a third order effect, and has been used primarily to determine the Lamé and Murnaghan elastic constants for various materials.

A number of studies have shown that it is possible to measure velocities with sufficient accuracy to detect and calculate residual stress [2-4]. Typically, for steel, the stress-acoustic constant is approximately 0.197 ns/cm/6895 kPa. This constant means that a 6895 kPa increment in stress produces a 0.5 ns change in travel time through a 2.54 cm thick specimen. Since it is relatively easy to measure time-of-flight changes to this accuracy, the sensitivity of the proposed method should be approximately 6895 kPa.

[1]This research is sponsored by the Electric Power Research Institute under Contract RP5-4-2.
[2]Figures in brackets indicate the literature references at the end of this paper.

At the present time, a number of researchers have made velocity measurements for the computation of stress. This data, however has been obtained in the form of spot measurements or profiles. No one has yet attempted to take a number of profiles at different angles in order to reconstruct a cross section of a velocity anomaly, and hence a cross section of the residual stress. The purpose of this paper is to discuss our efforts to develop a method for mapping stress anomalies utilizing velocity information and an image reconstruction technique known as Tomography.

A Tomogram could be described as a picture of a slice. Over the past several years Computer-Assisted Tomography (CAT) scanners have revolutionized the field of diagnostic medicine. This technique uses x rays to obtain visible, thin slices through any section of the human body. We are applying the same reconstruction algorithms used in medical applications, except for the substitution of ultrasound for the x rays, to generate velocity maps of cross sections of thick metal sections.

In the following section we briefly discuss the principles of Tomography and describe the Algebraic Reconstruction Technique (ART). We are using ART to construct the velocity profile. Section 3 describes several computer simulations for testing the ART algorithm. In section 3 we also discuss the effect of varying several parameters and describe the effect they have on the quality of the reconstruction. In section 4, we describe an experimental apparatus, which we have developed in our laboratory, for obtaining time-of-flight measurements. Section 4 also includes a discussion of reconstructions generated from these experimental data, and a description of the calibration procedure we are using in order to relate the velocity of sound to stress. In our conclusion, (section 5), we comment on the validity of this method for mapping residual stress and also describe a prototype instrument that we are building to test this technique.

2. Principles of Image Reconstruction in Computed Tomography

As we noted in the introduction, Tomography has had its greatest impact to date in the field of diagnostic medicine. A good source of references on medical Tomography can be found in a paper by Brooks and Dechiro [5]. The principles of image reconstruction using Tomography have also been applied in a number of other disciplines: Electron Microscopy [6-8], Radio Astronomy [9], and Nondestructive Testing [10,11].

To clarify the discussion that follows, a brief digression into the principles and terminology of Tomography will be necessary. Consider figure 1a, which is a particular cross section of a general three-dimensional object. Define the velocity distribution of the object as $v(x,y,z)$. Assume an ultrasound pulse, transmitted from location t, traverses the object along path 1 to a point r where it is received. The time-of-flight along path 1 is a function of the velocity distribution along the path, and is given as the line integral

$$t_\Theta(\rho) = \int_1 \frac{ds}{v}$$

where ρ and Θ define the path 1 from t to r. If the variable ρ is allowed to vary continuously over the object at a constant angle Θ, a one-dimensional projection of the velocity distribution will be obtained.

The reconstruction problem is to estimate the velocity of the cross section $v(x,y,z_o)$ from the projection values. Clearly, this can only be done if the projection values are available for a large number of angles Θ_i. Also, in actual practice the projection values are available only at a discrete number of the ρ_j for each angle Θ_i. Thus, the reconstruction is an approximation to the actual velocity field, with resolution being a function of the spacing between rays $\Delta\rho_j$ and the degrees between angles $\Delta\Theta_i$.

In theory, the velocity field can be reconstructed quite easily from the projection information. To see this, visualize a square grid superimposed over the object of figure 1a as shown in figure 1b. If we assume that the velocity within each square (pixel) is constant, then the total travel time through the grid becomes the sum of the travel times in each of the pixels. Each ray that passes through the velocity field will intersect various pixels. The length of the ray segment in each pixel can be determined quite easily by using geometry. If a ray of length l_k lies in a cell with velocity v_k, the travel time through the cell is l_k/v_k. Thus, the total time-of-flight can be expressed as a linear equation

whose unknowns are the velocities v_k. By using a number of independent rays that is equal to the number of grid cells, a linear system of algebraic equations can be generated and solved for the unknown velocities.

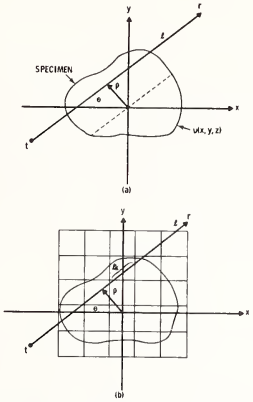

Figure 1. Concepts of reconstruction from Tomography.

The difficulty with solving for the unknown velocities by inverting a system of algebraic equations is that, even for small grid systems, the size of the resulting matrix is prohibitive. For example, consider a grid system of 20 by 20 pixels. This means that there are 400 unknown velocities to solve for. If we take 20 independent views with 20 rays per view the result is 400 equations in 400 unknowns, or a 400 by 400 matrix to invert. Furthermore, the matrix will be sparse, since each ray will usually intersect less than 30 pixels.

Other reconstruction algorithms are available that overcome the limitations imposed by the matrix inversion method, some of these alternatives are as follows:

1) convolution, which is based on the work of Johann Radon [12,13] (who first solved the equations governing image reconstruction in 1917);

2) Fourier transform, which is the spatial frequency version of convolution [14];

3) back projection, which was used in the first attempts to produce Tomograms of living patients;

4) and iterative techniques, which are probably the most widely used reconstruction methods.

3. Iterative Reconstruction Algorithms

All the iterative algorithms start with an "initial guess" as to what the image looks like. Typically, the average value of the projections is divided among all the pixels that make up the image. The algorithms then adjust the pixel values to bring them into better agreement with the measured projections. These algorithms are iterative in that they continually sequence through the set of projection data, updating the pixel values until a stopping criteria is met. An example of a stopping criteria would be a measurement of the change that has been made to the image during an iteration. If the change is less than some prespecified minimum, the iteration is stopped.

The three most popular iterative reconstruction algorithms currently in use are: the Iterative Least Square Technique (ILST) of Goitein [15], the Simultaneous Iterative Reconstruction Technique (SIRT) introduced by Gilbert [16], and the Algebraic Reconstruction Technique (ART) discovered by Gordon, et al. [7]. Our preliminary investigation of both ART and SIRT indicates that ART produces better reconstructions than SIRT, given the amount and nature of the data that is available.

You will remember from the discussion earlier in this section that the time-of-flight for a given project can be approximated as a sum of the time-of-flights in individual pixels. Briefly, the ART algorithm works as follows: for each ray in the data set, ART compares the experimentally obtained time-of-flight with the time-of-flight calculated using the current pixel values. If they are different, ART updates the velocity in each of the pixels as a function of the length of the ray path in the pixel. After the pixels along the ray have been modified, the time-of-flight calculated from the pixel values matches that obtained experimentally. ART then cycles through the remainder of the rays in the data set, repeating the process described above. However, as each new ray is processed, the value of previously updated pixels will be changed. This is the reason for the need to iterate. It has been shown, however, that the image improves after each iteration and converges to the best solution in a least squares sense [17].

The majority of medical CAT scanners in use today employ one of two geometries for obtaining profiles. These two geometries are usually referred to as fan beam and parallel beam. Figure 2 points out the differences between these two approaches. In the parallel beam method a set of measurements are obtained by scanning the source and detector linearly past the patient. The entire scanner assembly is then rotated by a fixed amount and the scan is repeated. In the fan beam approach, the source rays are formed into a fan of narrow beams that encompass the patient. The rays are received simultaneously by an array of detectors. For this geometry, the source and detector array are also rotated about the patient. Since the fan beam method does not require a linear translation of the source and detector, it is capable of much superior performance.

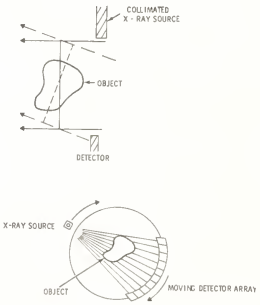

Figure 2. Two reconstruction geometries.

5. Simulated Data

To test the feasibility of using time-of-flight information along with the ART algorithm to reconstruct velocity fields, we have simulated several different images on the computer. As mentioned in the previous section, the time-of-flight for a particular ray crossing a velocity field is given by the line integral

$$t_\theta(\rho) = \int_1 \frac{ds}{v} .$$

To obtain simulated time-of-flights on the computer, this integral can be discretized to:

$$t_{\theta_i,\rho_j} = \sum_{k=1}^{K} l_{kij}/v_k \quad ,$$

where l_{kij} is the path length of the ray defined by θ_i and ρ_j through the cell k, and K is the set of all cells which intersect the line l.

To visually compare the reconstructions with the simulated velocity fields that were used to generate the data, we construct both isometric views and black-and-white gray scale images of the reconstruction. We will use both of these techniques to display results in this paper. To obtain a more qualitative idea of how the reconstructions compare with the original image, we calculate several error parameters at each iteration of the ART algorithm. The discrepancy is defined as:

$$\delta^q = \left\{ \frac{\sum_k (V_k^q - V_k)^2}{\sum_k (V_k - \bar{V})^2} \right\}^{1/2} .$$

This is a normalized Euclidian norm where V_k is the velocity value of the k^{th} pixel of the test image, $\bar{V}$ is the average velocity of the test image, and V_k^q is the velocity of the k^{th} pixel after the q^{th} iteration. This equation shows that the discrepancy is the ratio of the root-mean-square error to the standard deviation of the test picture. This measure was suggested by Gilbert [16], and has since been used by Herman, et al. [17] and Colsher [8].

The second error parameter we calculate is the mean relative (or average) error which is defined as:

$$E_{av}^q = \frac{\sum_k |V_k^q - V_k|}{\sum_k V_k}$$

This has also been used by Sweeney [18] and Colsher [8].

The final error function that we calculate is the residual, which is defined by:

$$R^q = \left\{ \sum_i \sum_j \left[P(\theta_i, \rho_j) - P^q(\theta_i, \rho_j) \right]^2 \right\}^{1/2}$$

where $P(\theta_i,\rho_j)$ is the actual measured time-of-flight for the ray path defined by θ_i and ρ_j and $P^q(\theta_i,\rho_j)$ is the computed time-of-flight for the same path using the pixel values after the q^{th} iteration. This measure indicates the degree to which the reconstructed image satisfies the measured time-of-flight data. Notice also that this is the only error measure of the three that is valid for experimentally obtained data. This criterion has been employed by Colsher [8].

An obvious deficiency of the first two error criteria is that the test image must be discretized. Several of the velocity fields that we used to generate our simulated data are circular and thus difficult to discretize. This problem tends to negate the usefulness of these two criteria.

All of our reconstructions were performed on a PDP 11/70 minicomputer. It is not valid to discuss execution time, since this computer operates in a multi-user environment. On the average, however, each iteration of the ART algorithm required approximately 30 s of wall clock time and 5 s of computer time. All of the isometric and gray scale images presented in this report were post processed after the ART reconstruction program was completed.

In our initial investigation of the ART algorithm we simulated a parallel beam geometry, as described in the previous section. Figure 3a represents a velocity field having two islands of 2 percent velocity increase in a uniform region. Figure 3b shows the reconstruction when time-of-flight profiles are taken over a full 180° field of view. Notice that the tops of the two islands in this reconstruction are fairly flat and the steep sides approximate the test image very well. In figure 3c a 90° field of view as available to the reconstruction algorithm. In this image the tops of the islands are somewhat irregular and the sides have less slope than the 180° field of view reconstructions. The 90° data base, however, still provides an adequate reconstruction of the test image. Figure 3d shows the result of using a 45° data base. In this reconstruction, the two islands have been smeared into the uniform velocity region. The tops of the islands are rough, and the height does not represent a 2 percent velocity difference. The walls of the islands in this reconstruction also have a very shallow slope. The reason for the poor reconstruction with a 45° field of view is that the majority of the rays pass through one of the two islands. As discussed in the last section, the velocity differences are divided among all the pixels in the path of the ray. Since there are few rays which pass completely outside the two velocity islands, the smearing effect is not counteracted.

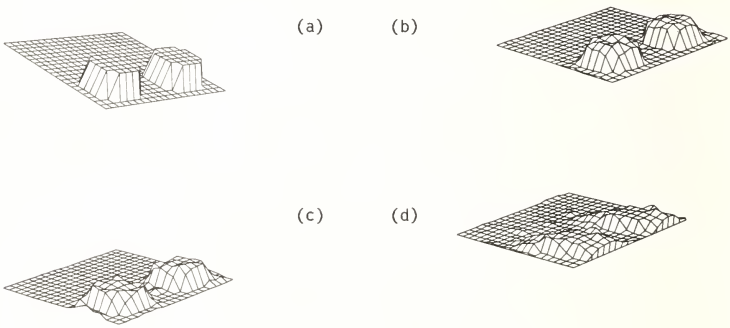

Figure 3. Test image, (a) and reconstructions, (b) 180° field of view, (c) 90° field of view, and (d) 45° field of view.

A major goal of our present work is to develop procedures for mapping residual stress in thick metal sections (typically 10 to 20 cm). In many practical situations, it may not be feasible to obtain time-of-flight profiles by either of the geometries discussed in the previous section. For instance, it may be physically impossible to position a detector inside a pressure vessel.

To overcome this difficulty, we have been investigating the feasibility of locating both the transmitter and the receiver on the same side of the metal section. Figure 4a and 4b illustrate the differences between this geometry and those discussed in the last section. Figure 4a illustrates the case in which both sides are accessible. The only way in which different angular profiles can be taken is to launch the waves at different angles by tilting the source. Theoretically, it is possible to launch waves over a ±90° field. However, note that the receiver would need to be moved further away with increasing angle. Hence, a practically obtainable field of view with this method is realistically ±45°.

Figure 4 illustrates the dilemma produced by the requirement for single surface inspection, and the solution. The back surface of the section is used as a reflector, with the receiver placed to receive the reflected signal. Note, however, that the reconstruction will now include a mirror image as well as the object itself. Also note that in both cases the total geometric path length changes as a function of angle of view. Both of these peculiarities must be taken into account by the reconstruction algorithm.

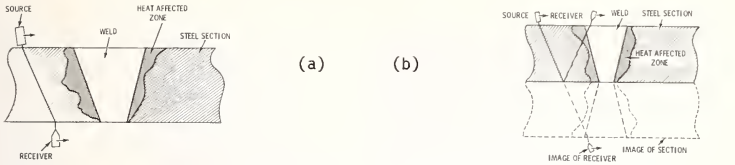

Figure 4. Scanning thick sections by transmission (a) and reflection (b).

In order to evaluate the reflected beam approach we developed a test model as shown in Figure 5. In this model two islands of 2 percent lower velocity reside in a steel body. The velocity islands have the Gaussian shape, so that the magnitude of the velocity distribution in the steel can be determined as:

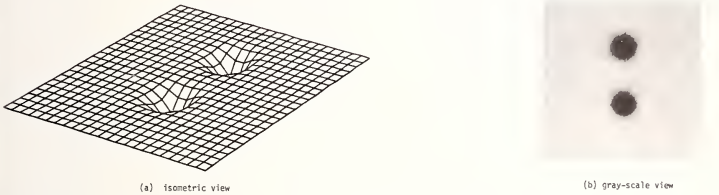

Figure 5. Simulated velocity anomalies of 2 percent in steel.

$$|V(x,y)| = V_o \left\{ 1.0 - 0.02 \exp\left[\frac{(x-x_1)^2 + (y-y_1)^2}{0.25}\right] - 0.02 \exp\left[\frac{(x-x_2)^2 + (y-y_2)^2}{0.25}\right] \right\}$$

where V_o = velocity of sound in steel

$$(x_i, y_i) = (3.8, 1.27) \text{ and } (3.8, -1.27) \text{ (units in cm)}$$

Note that the maximum deviation is 2 percent.

Time-of-flight information was determined by using the procedure discussed earlier in this section. We assumed that the transducers were equally spaced along a 10.2 cm thick section and that the two velocity island were located 3.8 cm from the reflecting side.

The time-of-flight data is generated by letting each point-transducer, in turn, act as a transmitter while all the other transducers become receivers. We have defined the field of view for this geometry as the included angle between the two transducers with maximum distance between them. For example, if we want a 120° field of view for a 10.2 cm thick metal section, the two transducers at opposite ends of the array must be approximately 38 cm apart.

Figure 6a-c shows the reconstruction with 21, 31, and 41 point transducers in a fixed field of view of 125°. Notice that as the number of rays increases the amount of information available increases and the reconstruction of the test image improves.

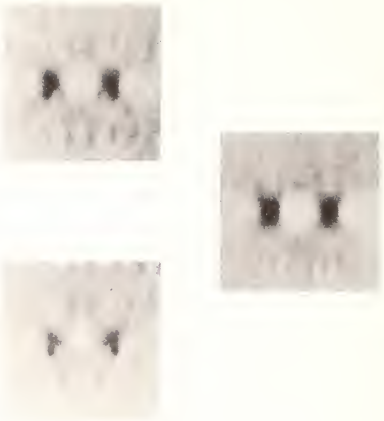

Figure 6. Reconstructions with a fixed field angle of 125° and (a) 21, (b) 31, and (c) 41 rays.

Figure 7a-d shows reconstruction with a 75°, 100°, 125°, and 150° field of view and a fixed number of point transducers (in this example 31 transducers were simulated). The different fields of view are obtained by changing the spacing between the transducers.

It is quite obvious from the reconstruction in figure 7 that, for a fixed number of transducers, an optimum field of view can be determined. With a 75° field of view the two velocity islands are elongated and not well-defined. At the opposite extreme, a 150° field of view, the islands are out of focus. The reason for this effect is that the transducer spacing at 150° has a detrimental effect on the resolution.

Using equally spaced transducers causes some of the pixels in the reconstruction array to have a large number of different ray paths through them, while other pixels have very few. We are currently investigating the effect of unequally spaced transducers. Our preliminary determinations indicate that spacing the transducers closely in the center of the array and increasing the spacing as we move toward the ends seem to improve the quality of the reconstruction. The reason for this improvement is that the number of ray paths through each pixel is more even.

6. Experimental Data

To obtain actual data to test our proposed reconstruction method, we ran several different experiments. Our first experiment was designed to test the accuracy of the equipment we were planning to use. For this experiment we used the parallel beam geometry to collect time-of-flight data from objects submerged in a water bath. In our second experiment we also used parallel beam geometry but made measurements on a section of type 1018 mild steel, in which we embedded an oversized pin to induce stress. In our current work we are employing a variation of the reflected beam geometry to analyze the physical characteristics of the reconstruction.

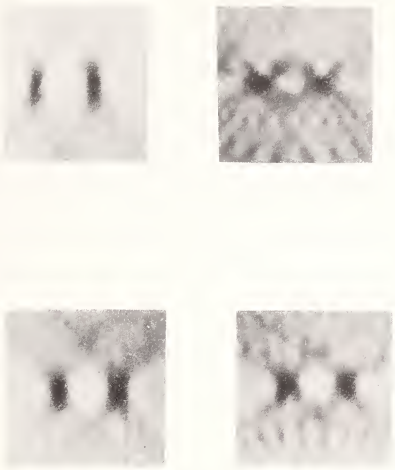

Figure 7. Reconstruction with 31 rays and field of view of (a) 75°, (b) 100°, (c) 125°, and (d) 150°.

The equipment we are using to measure time-of-flight includes: 1) Velonex Model 570 Pulser, 2) Metrotek MP 215 Pulser, 3) Metrotek MR 101 Receiver-Amplifier, 4) Metrotek MG 703 Time Interval Gate, 5) Nortec No. VM 16-2.25 O Broadband Unfocused Ultrasonic Transducer, 6) Hewlett Packard 5345A Time Interval Counter, and 7) Hewlett Packard 9825A Desk Calculator/ Computer.

The Velonex 570 Pulser generates a 0.5 μs, 600V pulse with a repetition rate of 2000 Hz. This pulse starts the Time Interval Counter and energizes a Nortec V-Z-16-2.25-O 2.54 cm, wide-band transducer. A Nortec R-Z-0.025-10-O, 0.064 cm, wide-band receiver senses the pulse, a sense amplifier amplifies and thresholds it and sends it to the Time Interval Counter. The counter, a Hewlett Packard 5345A, measures the time between the start pulse and the received pulse by counting internal clock pulses generated in the interval. The instrument can be set to average over intervals from 10 ns to 20 000 s; its worst-case accuracy is ±0.7 ns and its worst-case resolution is ±11 ps. With a 1 s averaging time we have consistently seen a repeatibility better than ±0.3 ns.

A Hewlett Packard 9825A Calculator was added to the equipment list prior to our most recent experiment. This calculator allows us to semiautomate the data gathering process; it has been programmed to control a set of stepping motors that are used to scan the transducer assembly past the object being examined. The calculator also has the capability to plot the data as it is being taken. This gives us visible assurance that the measurements being made are correct. Finally, the calculator has a permanent storage capability in the form of removable magnetic tape cartridges. In our current configuration, the time-of-flight measurements are recorded on the magnetic tape while the experiment is in progress. After all the data has been collected, it is read off of the magnetic tape and transmitted over a communications line to a PDP 11/70 Minicomputer, where the reconstruction is performed.

7. First Experiment

In our first experiment, we wished to test the feasibility of the measurement system. To accomplish this, we developed a model consisting of a rubber glove filled with a water-alcohol mixture. The ratio of water to alcohol was intended to provide a 2 percent increase in the velocity of sound over the surrounding water. We found this model to have several advantages: 1) ease of implementation, 2) easy adjustment of the velocity of sound in the sample to any desired value in the range of interest, and 3) a well-defined shape for reconstruction testing.

Three disadvantages of this model became apparent as we moved toward smaller velocity differentials. First, a variation with temperature in the density of the ambient fluid gave rise to an observable, slowly varying velocity change which must be accounted for in the data analysis. Fortunately, because the thermal mass of the water bath is sufficiently large, data correction is not difficult. Second, the rubber glove sample is sufficiently pliant to make it sympathetic to small turbulences brought about by mechanical movement of the scanning apparatus within the tank. This is overcome by allowing a short settling-time between positioning of the apparatus and data collection. The third and greatest difficulty that we encountered with this model is that the abrupt edges of the glove gave rise to refraction and reflection "edge effects."

Figure 8 shows the measurement system used for this early set of experiments. The transducer assembly is scanned past the model with time-of-flight measurements taken at discrete intervals. The object is then rotated on the turntable through a fixed angle and the transducers are again scanned past the model.

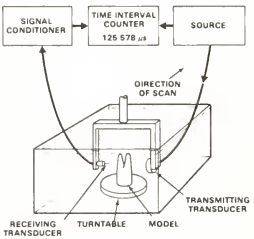

Figure 8. The measurement system used for the early set of experiments.

Figure 9 shows a reconstruction obtained when the two fingers of the rubber glove are filled with a water-alcohol mixture corresponding to a 2 percent velocity increase. The data base for this reconstruction consists of 19 scans taken at 5° increments from 0° to 90°. Each scan consists of 20 rays taken at 0.0254 cm intervals over a span encompassing the two fingers.

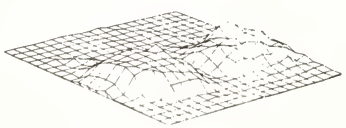

Figure 9. Reconstruction of 2 percent velocity model.

8. Second Experiment

In our second experiment, we developed a model that we feel provides a realistic test in steel as well as a controlled stress field of known shape. As shown in figure 10a, a slab of type 1018 mild steel 5.08 x 1.27 x 7.62 cm was used as the base metal. A 0.635 cm hole was drilled as shown. A pin, of diameter 0.639 cm, was also fabricated from the same steel stock. The pin was cooled in liquid nitrogen (-190 °C), the block was heated to 1000 °C and the pin was inserted in the hole. After the model stabilized to room temperature, the sides were ground to remove scale and to assure constant thickness. The model was then mounted on the turntable and scanned. In this case, due to refraction, the angle through which the model was rotated was nonlinear. That is, the angular increments were calculated to achieve 5° increments in the steel. Fifty-one measurements were made per scan over a 2.29 cm span centered on the pin.

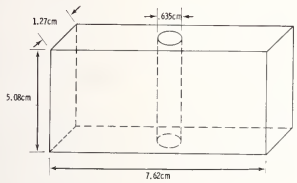

(a) (b)

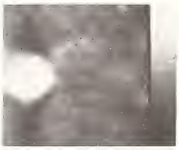

Figure 10. Steel model: (a) drawing, (b) reconstruction.

Rough computations show that the pin is subjected to about 6.895 x 10^8 kPa compressive stress, which must be balanced in the surrounding metal with a distributed tensile stress. Figure 10b shows a reconstruction of the velocity field in the steel section in the vicinity of the pin. The reconstruction shows that, inside the pin itself, the velocity has decreased indicating compressive stress. The region surrounding the pin has a higher velocity than the base line, indicating an increase in tensile stress.

9. Current Experiments

In our current experiments we are testing the reflected beam ART algorithm. We are again using a water-alcohol mixture in a water bath to simulate changes in velocity due to stress. In these experiments, however, the transmitter and receiver are positioned on the same side of the object. A mirror centered between the two transducers (and on the opposite side of the rubber glove) is used to simulate reflection off the back wall of a metal section.

The Hewlett Packard Calculator was included in the data acquisition loop to accomplish the control, data storage, and quality assurance tasks mentioned earlier in this section. Using the calculator decreases the time needed to obtain a complete data set by almost 50 percent over our earlier manual mode. This is important because, as was discussed earlier, the temperature of the water bath changes during the day and this causes changes in the velocity of sound in water.

For the current experiment, we took 23 different views at included angles from 10° to 120° in steps of 5°. At each angle, 31 time-of-flight measurements were taken as the transducer assembly was scanned past the object. The distance between measurements was 0.732 cm.

Figure 11a shows a 3-D plot of the reconstruction obtained from this data. It definitely indicates a sharp velocity change in the region of the finger. The computer calculated a maximum velocity change for this reconstruction of 2.7 percent, which is close

to our measurement of actual velocity in the glove. Figure 11b shows the same reconstruction, using a gray-scale plot to indicate velocity change.

(a)

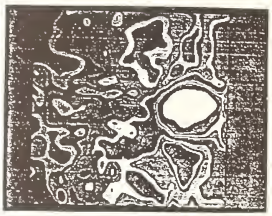

(b)

Figure 11. Reconstruction of velocity profile using reflected beam Tomography: (a) isometric, (b) gray-scale.

10. Calibration Experiments

In order to relate velocity measurements to stress, we have initiated a calibration experiment. The purpose of this experiment is to obtain velocity measurements as a function of stress, both tensile and compression. To accomplish this, we have fabricated a 6.45 cm, A516-74A, grade 70, pressure vessel steel plate into tensile and compression specimens. These were placed in an MTS 810 material-test-system machine located in our laboratory.

Time-of-flight measurements were made with a system consisting of a Metrotek MP 215 High-Energy Pulser (driving a wide-band transducer), and a Metrotek MR 101 Receiver and Metrotek MG 703 Interval Gate (driving an HP 5345A Time Interval Counter). The transducer was coupled directly to one side of the specimen and stress was applied. The MG 703 was set to gate out the first and second echoes from the back surface of the specimen. This eliminates any possible error due to the coupling thickness. We have found this measurement to be repeatable to 0.1 ns. Transverse strain was measured with a Lion Precision Corporation Metri-Gap 300-3 Capacitive Micrometer to a precision of 25 μm. A thermocouple was also attached to the specimen to keep track of the temperature as the specimen was stressed.

We have obtained time-of-flight data for one tensile and one compressive sample. The data have not been reduced as yet, but there are indications that the expected velocity variations are present.

11. Conclusions

We have discussed an application of Computer-Assisted Tomography (CAT) for locating and mapping regions of residual stress. The simulations and experiments described have demonstrated that velocity anomalies of 2 percent can be quite easily resolved. In work not reported here we have also experimentally mapped velocity anomalies as low as 0.2 percent and feel that 0.05 percent is technically feasible. These velocities translate to a sensitivity of 6895 kPa in a 2.54 cm thick region.

We feel that the reflected beam geometry represents an important advance in the development of methods for inspecting structures which do not physically lend themselves to either the parallel beam or the fan beam geometries. Thus, the reflected beam geometry could have important applications in the area of in-service inspection. In the remainder of this paper we will describe the design of an instrument which could be used for this purpose.

We are currently designing a prototype instrument for measuring stress in an on-line production environment. The instrument, as we envision it, will consist of an array of transducers placed in contact with the metal surface. Two elements of the array would be

elected to form a pitch-catch arrangement. One is used to transmit a pulse and the other o receive it. The choice of elements defines the angle of the ray to be measured. After a ime-of-flight measurement has been made, the selected set of two elements are electron- cally moved over by one element and a second measurement made. In this way, a whole rofile can be made very quickly.

After one profile is made, the separation between the two elements is changed by electing two different transducers and the process is repeated, giving another profile at a different angle. All of the necessary data can thus be taken in a few seconds or less, depending upon the accuracy desired.

The time-of-flight measurements are fed directly into the memory of either a small minicomputer or a microprocessor. When a complete set of data is available, the computer executes the ART algorithm and displays the resulting reconstruction on a CRT display. Even using only a small minicomputer, it should be possible to obtain reconstructions in a matter of minutes. If velocity anomalies appear to be present in the reconstructions, local stress relief procedures could be applied.

References

[1] Gott, K. E., Residual stresses in a weldment of pressure vessel steel, AB Atomenergi Report, NyKöping, Sweden (1978).

[2] Hsu, N. H., Acoustical birefringence and the use of ultrasonic waves for experimental stress analysis, Experimental Mechanics (May 1974).

[3] Smith, R. T., Stress-induced anisotropy in solids--the acousto-elastic effect, Ultrasonics (July-September 1963).

[4] Noronha, P. J. and Wert, J. J., An ultrasonic technique for the measurement of residual stress, J. Test. Eval., 3 (March 1975).

[5] Brooks, R. A. and DiChiro, G., Theory of image reconstruction in computed Tomography, Radiology, 117, 561-572 (December 1975).

[6] DeRosier, D. J. and Klug, A., Reconstruction of three-dimensional structures from electron micrographs, Nature, 217, 130-134, London (1968).

[7] Gordon, R., Bender, R., and Herman, G. T., Algebraic reconstruction techniques (ART) for three-dimensional electron microscopy and x-ray photography, J. Theoretical Biology, 29, 471-481 (1970).

[8] Colsher, J. G., Iterative three-dimensional image reconstruction from projections: applications in electron microscopy (Ph.D. Thesis) University of California/Livermore, UCRL-52179 (December 1976).

[9] Bracewell, R. N. and Riddle, A. C., Inversion of fan-beam scans in radio astronomy, Astrophys. J., 150, 427-434 (1967).

[10] Kruger, R. P. and Cannon, T. M., The application of computed Tomography, boundary detection, and shaded graphics reconstruction to industrial inspection, Materials Evaluation, 36, (April 1978).

[11] Falconer, D. G. and Gates, D. C., Reactor-component inspection with computed Tomography, EPRI NP-213, Project 610-1 (July 1976).

[12] Radon, J., Uber die bestimmung von funktionen durch ihre integralwerte langs gewisser mannigfaltigkeiten, Ber. Akad. Wiss. (Leip Zig) Math. Phys. Klass., 69, 262-277 (1917).

[13] Rammachandran, G. N. and Lakshminarayanan, A. V., Three-dimensional reconstruction from radiographs and electron micrographs: applications of convolutions instead of Fourier transforms, Proceedings of National Academy of Science U.S.A., 68, 2236-2240 (September 1971).

[14] Mersereau, R. M. and Oppenheim, A. V., Digital reconstruction of multidimensional signals from their projections, IEEE, 2, 1319-1338 (1974).

[15] Goitein, M., Three-dimensional density from a series of two-dimensional projections, Nucl. Instr. Meth. 101, 509-518 (1972).

[16] Gilbert, P., Iterative methods for the three-dimensional reconstruction of an object from projections, J. Theoret. Biol., 36, 105-117 (1972).

[17] Herman, G. T., Lent, A., and Rowland, S. W., ART: mathematics and applications a report on the mathematical foundations and the applicability to real data of the algebraic reconstruction techniques, J. Theoret. Biol., 42, 1-32 (1973).

[18] Sweeney, D. W., Interferometric measurement of three-dimensional temperature fields (Ph.D. Thesis), University of Michigan/Ann Arbor (1972).

National Bureau of Standards Special Publication 596, Ultrasonic Materials Characterization, H. Berger and M. Linzer, eds., Proceedings of the First International Symposium on Ultrasonic Materials Characterization held at NBS, Gaithersburg, Md., June 7-9, 1978. Issued November, 1980.

MEASUREMENT OF STRESS FIELD IN METALS

G. S. Kino, J. B. Hunter, G. C. Johnson
A. R. Selfridge, D. M. Barnett, G. Hermann, and
C. R. Steele

Stanford University
Stanford, CA 94305

An acoustic technique for measuring inhomogeneous stress in externally loaded solids is described. This method requires a measurement of transit time of a longitudinal acoustic wave through a stressed thin metal specimen using a small diameter water coupled acoustic transducer. The transducer is mechanically scanned over the surface of the sample by a computer controlled system to take stress field contour plots. The results compare well with theory.

1. Introduction

An ultrasonic technique has been developed for the measurement of acoustic wave velocity. By use of a mechanically scanned transducer the technique has been employed to measure stress variations across several different types of metal samples. Measurements are made through the thickness of planar metal samples by normally incident longitudinal waves. A mechanical scanning system is used to move a water coupled acoustic transducer from point to point on a stressed specimen and acoustic transit time variations with applied stress are measured at each point in the scanned area.

As a calibration, uniaxial tension specimens of aluminum and steel have been tested to determine the third order elastic constant governing the dependence of velocity on stress with results comparable to earlier measurements [1-4][1]. Acoustic behavior of aluminum and steel have been examined and inplane loaded panels containing edge notches and central holes have been scanned. These tests are conducted in a specially constructed hydraulically operated testing machine that permits specimen loading and transducer scanning in a water bath. The scanning and measurement systems are automatically controlled by a minicomputer. Data is stored, processed, and plotted to produce contour maps of the uniform stress fields in the scanned area.

It has been shown by Hughes and Kelly [5] that for a wave propagating in the principal direction along x_1, the wave velocity is

$$V_1 = \left(\frac{\lambda + 2\mu}{\rho_o}\right)^{1/2} \left[1 + \frac{(2\ell + \lambda)\theta + (4m + 4\lambda + 10\mu)\varepsilon_{11}}{2(\lambda + 2\mu)}\right]$$

$$V_2 = \left(\frac{\mu}{\rho_o}\right)^{1/2} \left[1 + \frac{(\lambda + m)\theta + 4\mu\varepsilon_{11} + 2\mu\varepsilon_{22} - \frac{1}{2} n \varepsilon_{22}}{2\mu}\right] \quad (1)$$

$$V_3 = \left(\frac{\mu}{\rho_o}\right)^{1/2} \left[1 + \frac{(\lambda + m)\theta + 4\mu\varepsilon_{11} + 2\mu\varepsilon_{33} - \frac{1}{2} n \varepsilon_{22}}{2\mu}\right]$$

[1]Figures in brackets indicate the literature references at the end of this paper.

where $\theta = \varepsilon_{kk}$, the dilitation in the deformed state, λ and μ are the classical Lamé constants, ℓ, m and n are the Muragham or third order elastic constants, and ε_y is the state strains.

The velocity V_1 represents a longitudinal wave along the x_1 principal axis, while V_2 and V_3 represent shear waves propagating in the x_1 direction with particle motions, in the x_2 and x_3 principal directions, respectively.

The experimental work covered in this paper falls into the area of plane stress with the acoustic waves propagating normal to the plane of stress. Thus if θ_{ij} is the stress, $\sigma_{11} = 0$ and it follows that

$$\begin{aligned} \varepsilon_{11} &= -(\nu/E)\ (\sigma_{22} + \sigma_{33}) \\ \theta &= \frac{1 - 2\nu}{E}\ (\sigma_{22} + \sigma_{33}) \end{aligned} \tag{2}$$

where ν is Poisson's ratio and E is Young's modulus. The longitudinal velocity change $\Delta V_1/V_1$ is proportional to the sum of the principal stresses, so we can write

$$\frac{V_1}{V_{10}} = \frac{\mu\ell - \lambda(m + \lambda + 2\mu)}{(3\lambda + 2\mu)(\lambda + 2\mu)}\ \sigma_{22} + \sigma_{33} = K(\sigma_{22} + \sigma_{33}) \quad . \tag{3}$$

The constant term K can be directly determined experimentally.

2. Experimental Apparatus and Techniques

Electronic and mechanical systems were developed for imaging nonuniform stress fields and studying acoustoelastic effects. An unfocused 3 mm diameter commercial longitudinal wave ultrasonic transducer was used in a reflection mode near a 12.5 MHz operating frequency. The metal samples employed were typically 10 mm thick. Immersion of the transducer and specimen in water provided an acoustic path and permitted easy scanning of the transducer. Two-dimensional motion and location of the transducer at measurement positions is accomplished by a perpendicular pair of digital stepping motor driven translatory slides. These slides, manufactured by Unislide Corp., have a 250 mm span and a positioning accuracy of 0.1 mm.

A loading machine with tensile and compressive load capability of 100,000 Newtons was developed for these experiments. The machine has provisions for precisely maintaining the relative position and alignment of transducer and specimen. A water filled tank for immersion of the specimens and transducer is an integral part of the assembly. Loading is provided by a hydraulic cylinder supplied with oil at an accurately controlled pressure. A Lebow Resistance Bridge Load Cell monitors applied force. Specimens are held in pinned grips which reduce alignment and bending errors.

Point by point acoustic measurements along straight lines at one millimeter spacings are taken over areas as large as 20 cm^2. These measurements are repeated for each value of applied load. Collection and analysis of this data is handled by a PDP-11T-10 minicomputer. By using interpolation on the computer X - Y plots showing stress field contours of the scanned area can be generated for each load level. Artificially generated fringe contours, similar to photoelastic stress images can also be displayed on a TV screen.

The electronic system for making precision acoustic measurements was designed with the aim of carrying out all measurements under computer control. Thus techniques such as the usual pulse overlap methods were not appropriate. We employed, however, a modification of the pulse echo overlap technique. A longitudinal acoustic pulse from the transducer traverses the water path to be reflected by the front and back faces of the specimen.

The transit time of the pulse through the double thickness of the specimen is indicated by time delay in the return of the back echo after the front echo. Variations in transit time are measures of changing thickness and pulse velocity. Because the returning pulses travel the same water path, variations in temperature and water path length should not affect the transit time measurement.

Two 12.5 MHz rf tone bursts approximately 1 μs long are injected into the transducer. The pulses are short in comparison to the transit time through the sample, so that thickness resonances cannot be excited in the metal. The time separation of the two transmitted pulses is adjusted to be equal to the transit time through the specimen and back so the front and back face echoes overlap, as shown in figure 1.

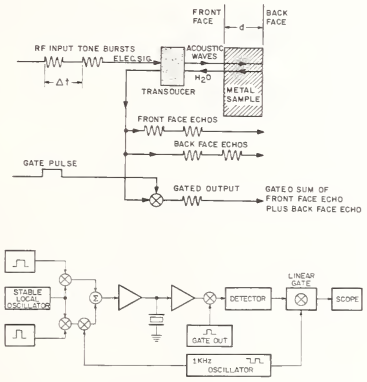

Figure 1. Block diagram of the double pulse echo system.

The total phase change between the front and back face echoes is

$$\phi = 2\omega\, d/V \tag{4}$$

where ω is the radian frequency of the rf carrier, d the sample thickness and V the acoustic velocity. Because the sample thickness and acoustic velocity are dependent on stress, the phase of the emerging pulse is altered by changes in applied stress, as it is by a change in frequency. So by logarithmically differentiating eq. (4) it will be seen that

$$\frac{\Delta\phi}{\phi} = \frac{\Delta\omega}{\omega} + \frac{\Delta d}{d} - \frac{\Delta V}{V} \quad . \tag{5}$$

If zero phase change ($\Delta\phi = 0$) is maintained during the measurement by adjustment of frequency ω, then

$$\frac{\Delta\omega}{\omega} = \frac{\Delta V}{V} - \frac{\Delta d}{d} = \frac{\Delta V}{V} - \varepsilon_{11} \tag{6}$$

The system used for phase change measurements is shown in figure 1. The double pulses have an 8 kHz repetition rate, and the pulse train that produces the front echo face echo is modulated with an additional 1 kHz square wave. After detection and passage through a 1 kHz filter, we obtain a signal after filtering with a 1 kHz component corresponding to the product of the two rf pulses. After filtering it follows from the Nyquist sampling theorem that these sampled signals can be treated as quasi-cw and phase differences measured.

The sum of the coincident echo signals from the transducer is of the form

$$G(t) = A \cos(\omega t + \phi)\cos\Lambda t + B \cos\omega t \tag{7}$$

where A and B are amplitudes of the front and back face echoes, Λ is the 1 KHz modulation frequency, and ϕ the total phase shift of the carrier produced by passage through the specimen. The signal is detected in a square law detector to give an output of the form

$$G^2(t) = A^2\cos^2(\omega t + \phi)\cos^2\Lambda t + 2AB \cos\omega t \cos(\omega t + \phi)\cos\Lambda t + B^2\cos^2\omega t \quad . \tag{8}$$

Passage of this signal through a 1 KHz filter (Λ) leaves only that part of the 2nd term with a frequency Λ. This term can be written in the form

$$S(t) = A\ B \cos\phi\ \cos\Lambda t \tag{9}$$

A linear gate (Keithly Instruments), gated by the 1 kHz square wave removes the 1 kHz component from the signal giving a cd output level that varies as cos ϕ. This output signal will be zero when $\phi = \pi/2 + n\pi$. The presence of this null is easily sensed by the computer. During testing, the computer interatively adjusts the carrier frequency produced by a Hewlett Packard Stalo source to maintain and track a particular null. The system is capable of setting a null at 12.5 MHz to within 60 cycles, or 5 parts in 10^6.

3. Experimental Results

The initial tests were performed on aluminum and steel uniaxial tension specimens and panels. For the plane stress state of these specimens it follows from eqs. (2) and (3) that transverse strain $\varepsilon_{11} = \Delta d/d$ and velocity change $\Delta V_1/V_{10}$ is proportional to the sum of the principal stresses. Thus it follows from eq. (6) that the relative frequency change is proportional to the sum of the principal stresses or first stress invariant

$$\frac{\Delta f}{f} = \frac{\Delta\omega}{\omega} = \frac{\Delta V}{V} - \varepsilon_{11} = B(\sigma_1 + \sigma_2) \ , \tag{10}$$

where B is the proportionality constant.

Uniaxial specimens machined from a rolled bar of 6061-T6 aluminum and a plate of pressure vessel steel[2] were used to determine B. All specimens were loaded parallel to the rolling direction. The aluminum specimen had a (12.0 x 12.5) mm x 75 mm long measurement section. Strain gages were applied in both longitudinal and transverse directions. Figure 2 shows relative frequency change vs stress for the aluminum specimens. The slope of this plot is the constant B with a value $B = 18 \times 10^{-6}$ MPa^{-1}.

For steel the measured value of B is 2×10^{-6} MPa^{-1} again consistent with previous work [2,4]. Because system accuracy is 5 parts in 10^6, the limit of stress resolution for aluminum and steel are respectively 0.28 MPa and 2.5 MPa.

A second set of measurements was then carried out on a specimen whose state of stress was inhomogeneous. For this purpose a 6061-T6 aluminum panel with a central circular hole was chosen because comparison could be made with the available theoretical solution for this plane stress problem [7]. The panel dimensions were 63 x 120 x 10 mm with a 19 mm

[2]Supplied by Dr. K. Stahlkopf, EPRI, Palo Alto, CA.

central hole as illustrated in figure 3. One quadrant of the panel was scanned as shown with a 1 mm point spacing. A scan at zero load provided initial data for the determination of relative changes.

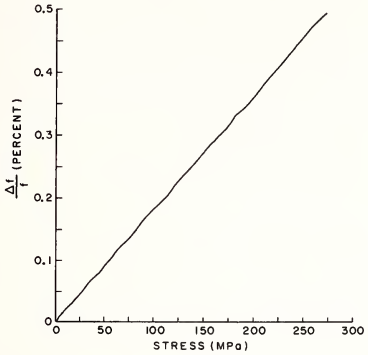

Figure 2. Relative frequency change vs stress uniaxial tension for 6061-T6 Aluminum.

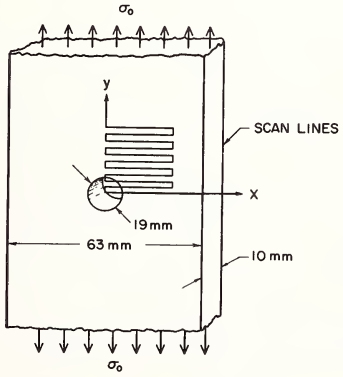

GEOMETRY OF THE PLATE WITH A CIRCULAR HOLE IN TENSION.

Figure 3. Specimen geometry for 6061-T6 aluminum panel with central hole.

Experimentally and theoretically determined contours of the first stress invariant normalized with respect to the far field uniaxial stress are in figure 4 for a far field stress of 85 MPa. The theory for this finite panel predicts that the stress maximum at the edge of the hole is approximately 3.3 times the remote uniaxial stress and that the top of the hole is in a state of lateral measurements near the edge of the hole. It will be seen from the figure that the experimental results are in agreement with the theory throughout the panel. In particular the contour separating the compressive and tensile regions is well defined experimentally. The value of the acoustoelastic constant B used in figure 3 is that value which was determined by the uniaxial test. The value of B which gives the best fit of the experimental data to theory differs from B(uniaxial) by less than 5 percent.

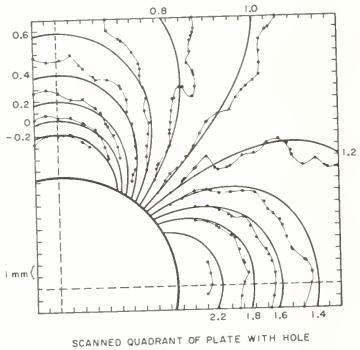

Figure 4. Stress contour plots of results of 6061-T6 aluminum panel with central hole normalized stress invariant (solid line) theory; acoustic experiment (dotted line).

In another set of experiments a double edge notched panel under remote uniaxial tension was scanned and stress field contours prepared. The width and thickness of the specimen illustrated in figure 5 are 60 mm and 8 mm. Two collinear 20 mm deep notches with a 0.5 root radius were cut perpendicular to the panel edges. Stress field contours obtained for a load of 30,000 Newtons and 1 mm scan point spacing are shown in figure 6 with a numerical elastic solution for comparison. The results give a value of B within a few percent of that for the calibration sample.

It will be noted that at higher stress shown in figure 7 the region near the crack tip is in the yield range. Now the corresponding contours near the crack tip have moved away from the tip, as might be expected.

4. Conclusions

It has been shown that quantitative acoutoelastic measurement of stress field profiles can be made. The highly precise measurements can be made over large areas of relatively thin specimens.

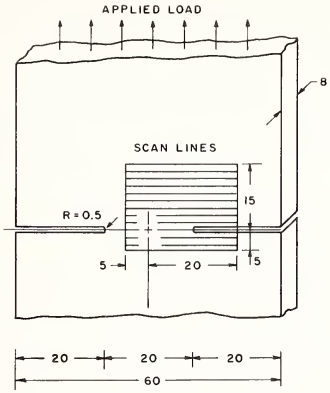

Figure 5. Specimen geometry for double edge notched 6061-T6 aluminum panel showing scanned area dimensions in millimeters.

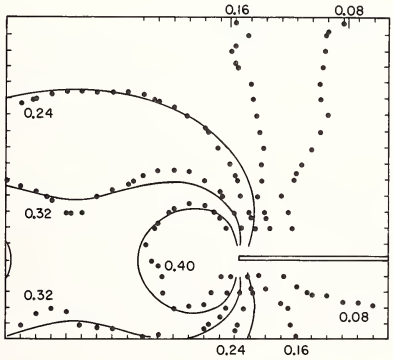

Figure 6. Stress and frequency contour plots of results for 6061-T6 aluminum double edge notched panel, 30,000 Newton tensile load.

Ongoing work concerns the acoustic behavior of plastically yielded material. A technique for carrying out similar scanning measurements with shear wave measurements may avoid the necessity of measuring the thickness, and make it possible to work with samples of nonuniform thickness. Furthermore, the use of such techniques should make possible the determination of magnitudes and directions of the principles stresses.

This work was supported by EPRI Contract No. RP-609-1 and NSF Contract No. DMK-76-00726 through the Center for Materials Research at Stanford University.

References

[1] Crecraft, D. I., The measurement of applied and residual stresses in metals using ultrasonic waves, J. Sound Vib., 5 173-192, (1967).

[2] Smith, R. T., Stern, R., and Stephens, R. W. B., Third-order elastic moduli of polycrystalline metals from ultrasonic velocity measurements, J. Acoust. Soc. Amer., 40, 1002-1008, (1966).

[3] Hsu, N. N., Acoustical birefringence and the use of ultrasonic waves for experimental stress analysis, Exp. Mech., 14 169-176, (1974).

[4] Egle, D. M. and Bray, D. E., Measurements of acoustoelastic and third-order elastic constant for rail steel, J. Acoust. Soc. Amer., 60, 741-744, (1976).

[5] Hughes, D. S. and Kelly, J. L., Second-order elastic deformation of solids, Phys. Rev., 92, 1145-1149, (1953).

[6] Murnaghan, F. D., Finite Deformations of an Elastic Solid, (Wiley, New York, 1951).

[7] Howland, R. C. J., On the stresses in the neighborhood of a circular hole in a strip under tension, Trans. Roy. Soc. (London), Ser. A., 229, 49-86, (1930).

National Bureau of Standards Special Publication 596, Ultrasonic Materials Characterization, H. Berger and M. Linzer, eds., Proceedings of the First International Symposium on Ultrasonic Materials Characterization held at NBS, Gaithersburg, Md., June 7-9, 1978. Issued November, 1980.

THE USE OF TEMPERATURE DEPENDENCE OF ULTRASONIC VELOCITY TO EVALUATE INTERNAL STRESSES

K. Salama and R. M. Ippolito

Mechanical Engineering Department
University of Houston
Houston, TX 77004

Basically, the temperature dependences of the elastic constants of a solid are due to the anharmonic nature of the crystal lattice, and are directly related to the coefficients of higher-order terms in the strain energy function. A measure of the temperature dependence of the ultrasonic velocity can, therefore, be used to evaluate the state of internal stress in the solid. Experiments undertaken on pure aluminum and copper plastically deformed in compression showed that the ultrasonic velocity, in the vicinity of room temperature, changed linearly with temperature, and the slope of the linear relationship changed considerably as the amount of prestrain was varied. In aluminum the relative changes of both the temperature dependences of longitudinal and shear velocities first increased as the amount of prestrain was increased, until they attained a maximum of about 23 percent at a prestrain of approximately 13 percent. In copper, however, the maximum in the temperature dependence of longitudinal velocity was smaller and occurred at a lower value of prestrain. A second broader maximum of smaller value was also observed in the heavily deformed copper specimens.

1. Introduction

Residual stresses are those contained in a body which has no external traction or other sources of stress, such as thermal gradients or body forces. When the body is externally loaded, these stresses are called internal stresses, and accordingly, residual stresses may be considered as a special case for vanishing external loads. Residual stresses result from non-uniform plastic deformation which includes cold working, forming, forging, heat treatment, etc. Their presence in manufactured components plays an important role in determining the behavior of the component when it is subjected to service loads and environment.

It is important to distinguish between two kinds of residual stresses, namely, the macroscopic stresses which extend over distances of the order of millimeters or greater, and the microscopic stresses which act over short distances and are highly localized from point-to-point. The macroscopic residual stresses vary continuously through the volume of the body and at any point are the combination of the components of stresses in the three principal axes. The microscopic residual stresses (internal stresses) vary greatly from grain to grain and are important to dislocation motion and structure which control many of the material properties. From dislocation theory, it is known that internal stress is proportional to the square root of the dislocation density and is also related to the flow stress of the solid [1,2][1].

Only in the case of surface stresses in components made of crystalline materials, can nondestructive evaluation of residual stresses be performed by x-ray diffraction [3]. Although considerably improved in the last ten years, this method still suffers from serious problems which severely restrict its applications. Ultrasonic methods appear to be most

[1]Figures in brackets indicate the literature references at the end of this paper.

promising in measurements of the bulk residual stresses in both crystalline and noncrystalline materials [4]. At present, there are three approaches in which ultrasonic techniques are employed, namely: dispersion [5], birefringence [6], and harmonic generation [7,8], employed. All these approaches are believed to utilize the anharmonic properties in solids; however, the exact mechanism in each case is not yet established.

2. Theoretical

Basically, the temperature dependences of the elastic constants are due to the anharmonic nature of the crystal lattice, and can be related to the pressure dependences of these constants. If we consider the isothermal bulk modulus B_T to be a function of pressure and temperature, it follows that [9]

$$\left.\frac{\partial B_T}{\partial P}\right|_T = \frac{1}{\beta B_T}\left[\left.\frac{\partial B_T}{\partial T}\right|_V - \left.\frac{\partial B_T}{\partial T}\right]_P , \tag{1}$$

where β is the volume coefficient of thermal expansion. Swenson [10] has shown empirically that for many materials

$$\left.\frac{\partial B_T}{\partial T}\right|_V = 0 , \tag{2}$$

and it can also be shown by differentiating $(B_S - B_T)$ that

$$\left.\frac{\partial B_S}{\partial P}\right|_T = \left.\frac{\partial B_T}{\partial P}\right|_T \tag{3}$$

to an accuracy of a few percent. Thus, it follows that if Swenson's rule is correct,

$$\left.\frac{\partial B_S}{\partial P}\right|_T = \frac{-1}{\beta B_T}\left.\frac{\partial B_T}{\partial T}\right|_P \tag{4}$$

to an accuracy of a few percent. The right-hand side can be calculated from the measurements of the temperature dependence of the second-order elastic constants. The left-hand side is calculated from the third-order elastic constants C_{ijk}, and eq. (4) is then expressed as [11]

$$\frac{\partial B}{\partial T} = \frac{\beta}{9}\left[C_{111} + 3C_{112} + 3C_{113} + 2C_{123}\right] \tag{5}$$

More rigorous relationships can be derived [12,13] for the temperature dependence of the longitudinal or the shear modulus which is related to the temperature dependence of the ultrasonic velocity V as,

$$\frac{\partial \ell n M}{\partial T} = 2\,\frac{\partial \ell n V}{\partial T} \tag{6}$$

From this general argument, it can be seen that the temperature dependence of the ultrasonic velocity (longitudinal or shear) is a measure of the anharmonic effects generated when the solid is subjected to a stress. A wide range of values for the apparent third order elastic constants were obtained in copper when measurements were made on specimens with different dislocation contributions [9]. Changes in the anharmonic properties due to the presence of internal stresses can therefore be detected by the changes in the slope of the relationship between the ultrasonic velocity and the temperature. This slope can be determined with a high accuracy as its value depends only on measurements of the relative changes in the velocity and not on the absolute values.

3. Experimental

The aluminum and copper employed in the present investigation were acquired from Materials Research Corp. in the form of polycrystalline rods of 99.999 percent purity and 0.25 in (6.35 mm) in diameter. After being prepared for ultrasonic measurements, the length of the specimens was approximately 0.5 in (1.27 mm). Before ultrasonic measurements were made, the specimens were annealed in a vacuum at 500 °C for about five hours. Prestraining was performed in compression in different amounts, by means of an Instron machine. The amount of prestrain was calculated from the change in length of the specimen after being deformed.

The ultrasonic velocity was measured using the pulse-echo-overlap method which was fully described elsewhere [14]. Figure 1 displays the experimental system used in this investigation. A pulse of approximately 1 μs duration of variable pulse-repetition rate is generated by the ultrasonic generator and impressed on a transducer of fundamental frequency 10 MHz which is acoustically bound to the specimen. The reflected rf echoes are received by the same transducer, amplified and displayed on the screen of an oscilloscope. Two of the displayed echoes are then chosen and exactly overlapped by critically adjusting the frequency of the cw oscillator, and the division factor on the decade divider. This frequency f, accurately determined by the electronic counter, is employed to compute the ultrasonic velocity using the relation $V = 2\ell f$, where ℓ is the length of the specimen. X- and Y-cut transducers are used for the generation of the longitudinal and the transverse waves respectively. A continuous flow cryostat in conjunction with a temperature control arrangement is used to maintain the temperature of the specimen at any desired value between 350 and 200 °K. The system is capable of measuring changes in the ultrasonic velocity to an accuracy of better than 1 part in 10^5, and the temperature of the specimen to within ±0.1 °C.

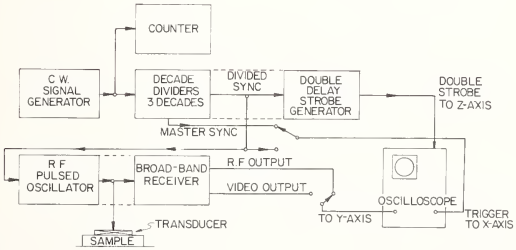

Figure 1. Pulse-echo-overlap system.

4. Results

4.1. Aluminum

Five aluminum specimens designed at A, B, C, D, and E are investigated in the present work. The specimens are prestrained up to 50 percent, and longitudinal as well as shear waves

are employed in the measurements. Typical examples of the longitudinal and the shear velocities in the temperature range between 300 and 230 °K are illustrated in figures 2 and 3 respectively. The results are obtained on specimen C after it is prestrained 0, 2.3 percent, and 10.6 percent. From both figures, it can be seen that in the temperature range investigated, the velocity increases linearly as the temperature is decreased. In addition, the absolute value of the velocity is decreased while its temperature dependence is increased as the amount of prestrain is increased. The latter behavior, however, is reversed when the specimen is heavily deformed.

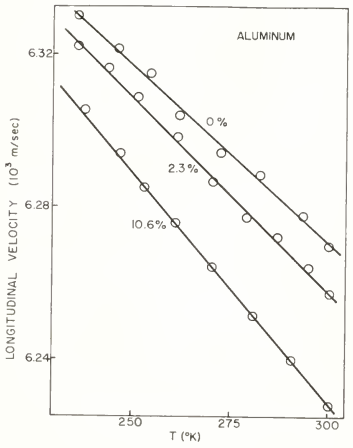

Figure 2. Ultrasonic longitudinal velocity as a function of temperature in aluminum prestrained 0 percent, 2.3 percent, and 10.6 percent.

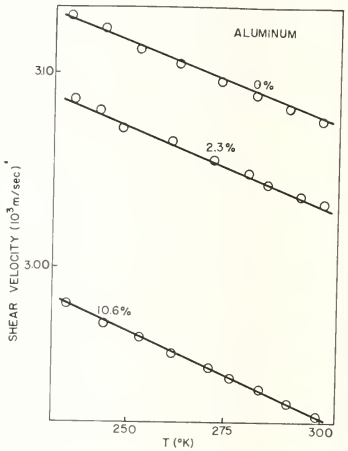

Figure 3. Ultrasonic shear velocity as a function of temperature in aluminum prestrained 0 percent, 2.3 percent, and 10.6 percent.

Table 1 summarizes the results obtained on the five specimens when longitudinal and shea waves are employed in the measurements. Included in the table are the values of the velocity V, and its temperature dependence $\partial \ell nV/\partial T$ as a function of the amount of prestrain given to t specimens. The table also contains the percentage change in the quantity $\partial \ell nV/\partial T$ with respec to its value at zero prestrain. From the table, it can be seen that the absolute values of the longitudinal velocity, obtained on the five specimens when they are in the annealed state are equal to within ±0.7 percent, while those of the shear velocity agree to within ±1.5 percent. The discrepancy in the latter seems to be due to the anisotropy in the specimens which has more effect on the shear propagation. Also, at zero prestrain, one finds that the values of the temperature dependence of the longitudinal or the shear velocity among the five specimens differ by ±5 percent. This difference lies outside the estimated error of these

Table 1. The effect of prestrain on the absolute values and the temperature dependence of the longitudinal and the shear velocities of ultrasonic waves in polycrystalline aluminum.

		Longitudinal			Shear		
Specimen	% Prestrain	V (10^3m/s)	$-\partial\ell nV/\partial T$ (10^{-4}/°K)	$\partial\ell nV/\partial T$ %	V (10^3m/s)	$-\partial\ell nV/\partial T$ (10^{-4}/°K)	$\partial\ell nV/\partial T$ %
A	0	6.231	1.36	0	3.036	2.48	0
	6.9	6.196	1.61	18	3.040	2.63	6
B	0	6.210	1.45	0	2.984	2.51	0
	30.0	6.148	1.76	21	2.962	3.04	22
C	0	6.266	1.44	0	3.077	2.44	0
	2.3	6.306	1.59	10	3.032	2.47	1
	10.6	6.212	1.77	23	2.923	2.91	19
	10.6	6.228	1.77	23			
	50.0	6.079	1.32	-8	2.958	2.81	15
D	0	6.306	1.45	0	3.082	2.63	0
	0				3.076	2.67	0
	6.6	6.242	1.61	11	3.009	3.10	18
	6.6	6.249	1.61	11			
	14.6	6.186	1.78	22	3.047	2.93	11
	27.4	6.183	1.67	15	3.109	2.59	-1
E	0	6.256	1.48	0	3.076	2.72	0
	0				3.064	2.73	0
	7.1	6.195	1.80	20			
	12.0	6.172	1.81	21	2.924	3.56	31
	20.8	6.196	1.71	15			

measurements, and is apparently due to the differences in the level of the internal stresses in the specimens when they are in the annealed state. Measurements made on the same specimen at zero prestrain, show that the values of $\partial \ell nV/\partial T$ can be reproduced to within ±2 percent.

Figure 4 displays the dependence on prestrain of the absolute values of the longitudinal velocity obtained in the five specimens. Although the scatter in the data is rather considerable, a straight line with a negative slope is found to represent the general behavior of V_ℓ as a function of prestrain. When the absolute values of the shear velocity as a function of prestrain is plotted, the data exhibit much scatter, which makes it difficult to determine a general behavior of V_s vs. prestrain. The scatter in the data is believed to be due to the strong influence of the anistropy in the specimens on the propagation of the shear waves. These velocities are measured when the shear waves are polarized in the plane perpendicular to the direction in which the specimen is deformed. However, no specific polarization direction was kept constant during the entire set of measurements.

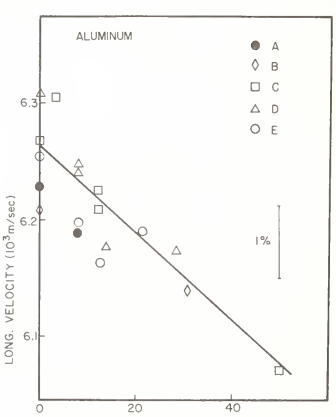

Figure 4. The effect of prestrain on the room temperature ultrasonic longitudinal velocity in aluminum specimens A, B, C, D, and E.

The effect of prestrain on the relative change in the temperature dependence of the longitudinal velocity is plotted in figure 5. The plot shows that the percentage of $\partial \ell nV/\partial T$ first increases linearly as the amount of prestrain is increased. It reaches a maximum value of about 23 percent when the amount of prestrain is approximately 13 percent. More prestraining however, results in a linear decrease in the quantity $\partial \ell nV/\partial T$ which, in a heavily deformed specimen, can reach a value smaller than that determined when the specimen is in the annealed state. The decrease in the temperature dependence of the longitudinal velocity in the high prestrain region is more gradual than the sharp increase exhibited when the specimens are deformed with small amounts. It is also interesting to note that the extrapolation of the linear relationship to zero prestrain intersects the $\partial \ell nV/\partial T$ axis at zero value.

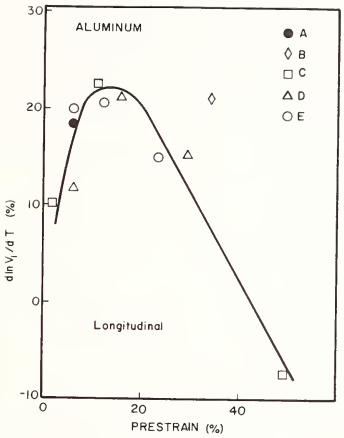

Figure 5. Percentage change in the temperature dependence of ultrasonic longitudinal velocity as a function of prestrain in aluminum specimens A, B, C, D, and E.

The relative changes in the temperature dependence of the shear velocity as a function of prestrain is shown in figure 6. In this case, the data exhibit two peaks at about the same value of prestrain (12 percent), but with relative changes in $\partial \ell nV/\partial T$ of approximately 21 percent and 31 percent. Again, it appears that the sensitivity of the shear propagation to the anisotropy in the specimens is the primary reason for the two peaks. A study of the temperature dependence of the shear velocity in specimens prestrained in various directions should examine this behavior.

4.2. Copper

Two copper specimens designed A and B are investigated in the present work. The specimens are prestrained up to 50 percent and only longitudinal waves could be employed in the measurements. The shear velocity was difficult to measure due to the excessive scattering of ultrasonic waves in the specimens after they were vacuum annealed. Typical examples of the longitudinal velocities in the temperature range between 300 and 240 °K, are illustrated in figure 7. The results are obtained on specimen A after it is prestrained 0, 11 percent, and 15 percent. From the figure, it can be seen that in the temperature range investigated, the velocity increases linearly as the temperature is decreased. In addition, the absolute value of the velocity is decreased while its temperature dependence is increased as the amount of prestrain is increased. The latter behavior, however, is reversed when the specimen is heavily deformed.

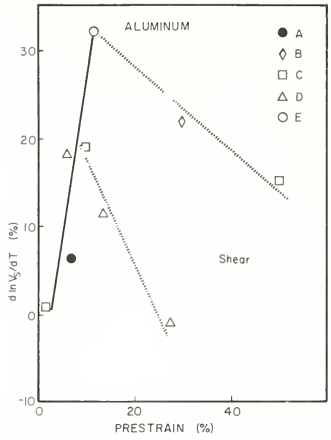

Figure 6. Percentage change in the temperature dependence of ultrasonic shear velocity as a function of prestrain in aluminum specimens A, B, C, D, and E.

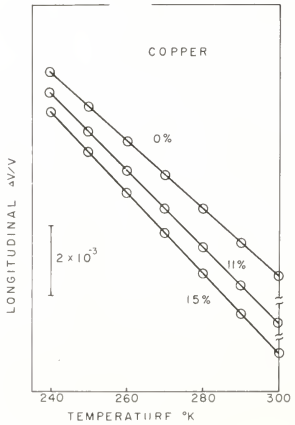

Figure 7. Longitudinal velocity as a function of temperature in copper prestrained 0 percent, 11 percent, and 15 percent.

Figure 8 displays the dependence on prestrain of the absolute values of the longitudinal velocity obtained in specimen B. Again, a straight line with negative slope seems to be the best fit to the experimental data, with the exception of the high prestrain value at 48.9 percent. The effect of prestrain on the relative change in the temperature dependence of the longitudinal velocity is plotted in figure 9. The plot shows that the percentage of $\partial \ell nV/\partial T$ with respect to its value at zero prestrain first increases linearly as the amount of prestrain is increased. It reaches a maximum value of about 18 percent when the amount of prestrain is approximately 11 percent. Again more prestraining results in a linear decrease in the quantity $\partial \ell nV/\partial T$ which can reach a value smaller than that determined when the specimens are in the annealed state. As the amount of prestrain is further increased, the temperature dependence of the velocity is increased exhibiting a second maximum at about 30 percent prestrain. These results and those of figure 5 shows that the temperature dependence of the longitudinal ultrasonic velocity in aluminum and copper behaves similarly when the specimens of these metals receive moderate amounts of prestraining.

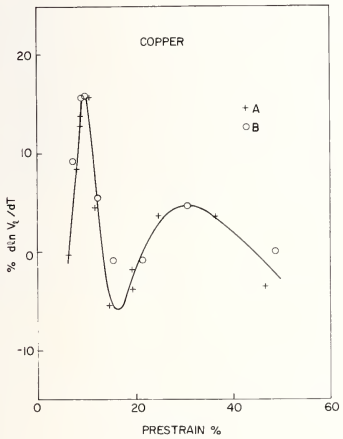

Figure 8. The effect of prestrain on the room temperature ultrasonic longitudinal velocity in copper specimen B.

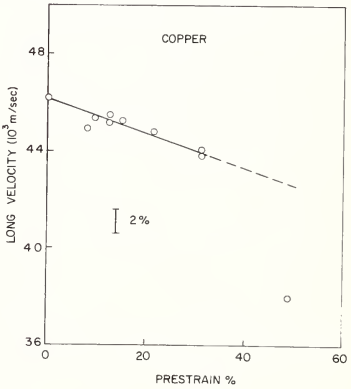

Figure 9. Percentage change in the temperature dependence of the longitudinal ultrasonic velocity as a function of prestrain in copper specimens A and B.

5. Discussion

The results shown in figures 5 and 9 indicate that the temperature dependences of the longitudinal ultrasonic velocities in aluminum and copper vary considerably as the amount of plastic deformation is varied. This implies that measuring the slope of the ultrasonic

velocity as a function of temperature can be employed to evaluate the level of internal stresses in these metals. The sensitivity of this temperature dependence to plastic deformation seems to be higher than that of the absolute velocity measurements where the errors are usually comparable to the measured changes. At present, however, the temperature dependence gives qualitative evaluation of the internal stresses, and measurements on specimens subjected to known stresses are required to qualitatively evaluate these stresses. In addition, figures 5 and 9 show that the behavior of the temperature dependence with prestrain does not give unique values for the stress levels in the specimens tested. A more regular behavior is expected in commercial materials which usually contain high dislocation densities and small average loop length.

The linear decrease observed in the longitudinal velocities with prestrain is consistent with the measurements of Alers and Salama [15] on single crystals of copper employing much smaller deformations. These results were interpreted in terms of an increase in the average effective loop length and a smaller change in the dislocation density, while the specimen is subjected to the external deformation. In the present study, where large prestrains are employed, the decrease in the velocity is likely to be predominantly due to the increase in the dislocation density in the deformed specimens. According to the analysis presented in reference [15], the ultrasonic velocity is expected to decrease as the dislocation density and/or the average dislocation loop length is increased. As the temperature and stress dependences of the velocity are related, it will be also expected that the temperature dependence can be influenced by the two dislocation parameters affecting the absolute values of the velocity. The contribution due to increases in the dislocation density predominates at lower values of prestrain where dislocation multiplications increase fast while the specimens are in the annealed state. As the amount of deformation is increased, the increase in the dislocation density is expected to be small and the temperature dependence will be predominantly lowered by the large decrease in the average loop length. When the two contributions are equal, the temperature dependence as a function of prestrain exhibits a maximum. This maximum occurred at 13 percent prestrain in aluminum and at 11 percent prestrain in copper. In heavily deformed specimens, these effects are no longer linear, and higher order terms in dislocation density and average loop length can result in reversing their contributions to the changes of the temperature dependence with prestrain.

This work is sponsored by the Air Force Office of Scientific Research under Grant No. 77-3457.

References

[1] Salama, K. and Roberts, J. M., Phys. Stat. Solidi (a) 3, 511 (1970).

[2] Salama, K. and Roberts, J. M., Scripta Met. 4, 749 (1970).

[3] Residual stress measurement by x-ray diffraction, SAE J. 784a, 199 (1971).

[4] Ratcliffe, B. J., Brit. J. Nondestructive Testing, 11, 48 (1969).

[5] Noranha, P. J., Chapman, J. R., and Wert, J. J., J. Testing and Evaluation, 1, 209 (1973).

[6] Noranha, P. J., Wert, J. J., and Kimser, D., Proc. IEEE Ultrasonic Symposium, 230 (1973).

[7] Scorey, C. R., J. Appl. Phys., 41, 2535 (1970).

[8] Thompson, R. B., Buck, O., and Thompson, D. O., J. Acous. Soc. Amer., 59, 1087 (1976).

[9] Salama, K. and Alers, G. A., Phys. Rev., 161, 673 (1967).

[10] Swenson, C. A. in Physics of Solids at High Pressures, C. T. Tomizuka and R. M. Emrick, ed., p. 548 (Academic Press Inc., New York, 1963).

[11] Thurston, R. N. and Brugger, K., Phys. Rev., 133A, 1604 (1964).

[12] Stern, E. A., Phys. Rev., 111, 786 (1958).

[13] Garber, J. A. and Granato, A. V., Phys. Rev., 1311, 3990 (1975).

[14] Papadakis, E. P., J. Acous. Soc. Amer., 42, 1045 (1967).

[15] Alers, G. A. and Salama, K., Dislocation Dynamics, A. R. Rosenfield, et al., eds., p. 211 (McGraw-Hill, 1968).

National Bureau of Standards Special Publication 596, Ultrasonic Materials Characterization, H. Berger and M. Linzer, eds., Proceedings of the First International Symposium on Ultrasonic Materials Characterization held at NBS, Gaithersburg, Md., June 7-9, 1978. Issued November, 1980.

APPLICATION OF THE ACOUSTOELASTIC EFFECT TO RAIL STRESS MEASUREMENT[1]

D. M. Egle

University of Oklahoma
Norman, OK 73019

and

D. E. Bray

Texas A & M University
College Station, TX 77843

An ultrasonic probe has been designed, evaluated, and shown capable of measuring longitudinal stress changes in railroad rails. The probe utilizes the effect of applied stress on wave velocity (acoustoelastic effect) to determine the stress change. In both laboratory and field evaluations, it has shown that the probe is capable of measuring stress changes with an accuracy of ± 6.9 MN/m^2 (± 1 ksi).

1. Introduction

The goal of the work reported here was to develop a technique for the in-situ measurement of rail stresses. These stresses are primarily caused by changes in ambient temperature but are also affected by installation practice and train traffic over the rail. This paper is based on the final report [1][2] of a two-phase study to determine the feasibility of using the acoustoelastic effect for the measurement of longitudinal rail stresses.

Thermal expansion phenomena are particularly evident in railroad rails since they are exposed to the full range of outdoor temperatures, typically 47.7 °C to -41.7 °C (118 °F to -43 °F). Actual rail temperature is often much higher than the ambient because of the absorption of radiant heat from the sun [2].

The effect of the rail expansion and contraction is more noticeable in continuous welded rail (CWR) than in bolted (or jointed) rail in which the relative motion within the joints can reduce the stresses. High maintenance costs and the propensity for fatique cracks at the joint, plus the occurrence of end batter on the rail, have all led to the replacement of jointed rail with continuous welded rail. In most cases, these strings of CWR are 439 m (1440 feet) long. These rails, while clearly superior to the old jointed rail, do not have the ability to release the expansion and contraction forces through linear movement along the rail length. Instead, these forces are accomodated by the resulting lateral and vertical strain and by longitudinal stress. Typical high temperature stresses for properly installed rail have been estimated to be near 83.7 MN/m^2 (12 ksi) [3].

Several techniques for the nondestructive measurement of stresses have been developed and successfully applied by other industries. X-ray diffraction is perhaps the most well known today. Other methods which are emerging from the laboratory into field usage are

[1]Supported by the Federal Railroad Administration, Department of Transportation, Contract OS-40091, with a contribution by the American Association of Railroads.
[2]Figures in brackets indicate the literature references at the end of this paper.

Barkhausen Noise Analysis and shear wave acoustic birefringence which is based on the acoustoelastic effect. X-ray diffraction and Barkhausen Noise Analysis [4,5] are both surface-effect techniques, that is, they are techniques used to measure surface stresses. Although these techniques have shown feasibility in some applications, the reliable measurement of body stresses through rough steel surfaces, such as occur on the rail, has not been demonstrated. The acoustic birefringence technique appeared to be the one warranting further study since it can be used to measure body stresses and can be made less dependent upon the surface condition.

Another topic of concern that applies to any proposed technique is the choice of the proper area of the rail to use in measuring the stresses. Operationally, the top of the rail would be best since it is always clear of obstruction. This surface, however, is rendered unusable due to deformation caused by the regular passage of trains. This deformation also affects the sides of the rail head rendering it unuseable as a measuring location. The best choice appears to be the midpoint of the rail web, near to the neutral axis. A summary of early work on the acoustoelastic effect has been given in an interim report of this study and will not be repeated here [6].

2. An Ultrasonic Probe for Longitudinal Stress Measurement

The measurement of the acoustoelastic properties of rail steel [7] showed that the effect is greatest for longitudinal waves propagating in the direction of the applied stress. This fact, coupled with the possibility of long gage lengths, dictated that the probe should be capable of generating and receiving a longitudinal wave traveling parallel to the rail axis (also called a P-wave). The measurements of longitudinal wave speeds in several samples of new and used rail reported in reference [6] indicated that if an absolute measure of stress is needed a reference wave speed would probably be necessary. For this reason, the probe was designed to also propagate and receive a shear wave parallel to the rail axis.

The same data also indicated that the variations in longitudinal, surface, and shear wave speeds for several samples of new and used rail were smaller in the rail web as compared to the rail head. These smaller variations further support the choice of the web as a more desirable portion of the rail in which to measure the wave speeds. Further, using the rail web allows measurement on two opposite surfaces which has the advantage of minimizing the effects of surface curvature by averaging. The data presented in reference [7] showed that the relative change in speed for longitudinal waves propagating along the direction of the applied stress is

$$\frac{dV_L/V^o_L}{d_\varepsilon} = -2.45 \tag{1}$$

where V_L - speed of longitudinal waves

V^o_L - speed of longitudinal waves in the absence of stress

ε - longitudinal strain corresponding to stress σ.

The relative change in travel-time may be shown to be

$$\frac{d(t_L/t^o_L)}{d_\varepsilon} = +2.45 \tag{2}$$

or, in terms of the change of applied stress $d\sigma$

$$dt_L = \frac{2.45\ t^o_L}{E}\, d\sigma \tag{3}$$

where E is Young's modulus and t_i, t_i are longitudinal wave travel-times. Proceeding in the same manner, change in transverse wave travel-time may be shown to be

$$dt_T = \frac{0.25\ t_T^o}{E}\ d\sigma \qquad (4)$$

The probe was designed to measure the wave travel-times over a nominal distance of 216 mm (8.5 in). Typical wave speeds in rail steel are 5.9 km/s ($\sim 2.32 \times 10^5$ in/s) and 3230 m/s (1.27×10^5 in/s) for longitudinal and transverse waves, respectively. Hence the changes in travel-times are expected to be near 0.44 ns/MN/m^2 (3 ns/ksi) and 0.09 ns/MN/m^2 (0.6 ns/ksi) respectively.

The probe design, which evolved through four steps, is shown in figure 1. It consists of two transmitters and four receivers held in position by a steel frame. The transmitters and receivers use the conventional technique of diffraction through a plastic-steel interface for generating and detecting waves parallel to the rail surface. Incident angles in the plastic wedges are 28° and 55°, respectively for the longitudinal and transverse waves. The transducers are 25.4 mm (1 in) square PZT-5 piezoelectric plates of 1.27 mm (0.050 in) thickness and have a nominal resonant frequency of 1.6 MHz. The transducers were epoxy bonded to the plastic wedges and electrical connection made through BNC connectors on the metal frame. Receiver probe spacing and vertical flexibility was maintained through a 2 mm thick steel plate bolted to the wedges.

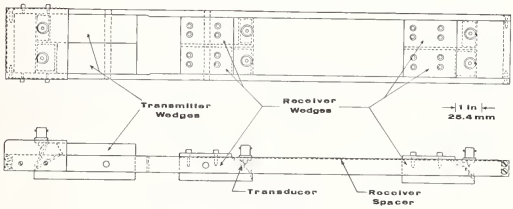

Figure 1. Ultrasonic probe for measuring rail stresses.

A differential technique for measuring wave travel-times was employed to eliminate or reduce extraneous effects such as temperature-induced changes in wave speed in the plastic wedges or surface condition of the rail. Thus, the time for the wave to travel the distance spanned by the two receivers is determined by subtracting the travel-times from the generator to each of the receivers.

Several techniques for measuring the wave travel-times were evaluated for accuracy and repeatability. The most consistent results were obtained with a pulse overlap technique, similar to the pulse superposition technique described in reference [8]. A schematic of the instrumentation is shown in figure 2. The oscillator drives a frequency divider, which produces a single pulse with a period 100 times the oscillator period, T. A double pulse having a separation of period T is also generated. The leading edges of the single pulse and the first double pulse are coincident. The single pulse is used to trigger a short duration pulse from the pulse generator which in turn drives the transducer pulser. The received signal is amplified 40 dB in the preamp and further amplified 10 to 30 dB in the receiver. A typical received signal is shown in figure 3a. This signal and the double pulse are superimposed on the scope. The oscillator period is adjusted such that the leading edge of the second pulse coincides with the first positive going zero crossing of the received signal as shown in figure 3b. The time from pulse initiation to reception of that zero crossing then equals the oscillator period which is measured to 0.1 ns by averaging over 1000 periods and then rounded to 1 ns.

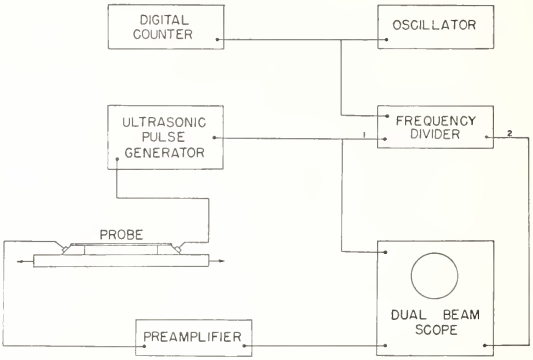

Figure 2. Electronic instrumentation for travel-time measurements.

The accuracy of the travel-time measurements with this system is about 3 ns. The major cause of inaccuracy in the measurement is in superimposing the two traces. Nevertheless these errors were found to be less than variations introduced by other sources.

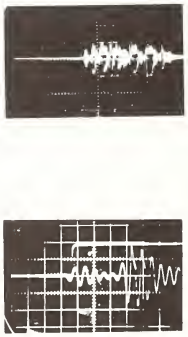

Figure 3. Typical oscilloscope traces for travel-time measurements; (a) sweep rate 10 μs/cm; (b) sweep delay 35 μs, sweep rate 1 μs/cm.

2.1. Repeatability of wave travel-time measurements

Evaluation of the repeatability of the probe measurements was conducted in three steps. First, repeated measurements were made on a laboratory specimen machined from the head of a new rail. These tests were conducted to assess the effect of factors other than specimen surface condition and curvature. A sequence of ten measurements of both P wave and shear-wave travel-times were made as described earlier. After each measurement set (of four travel-times) the probe was removed and cleaned, the couplant reapplied, and the probe clamped to a cleaned specimen. This sequence of ten measurements was repeated numerous times in order to evaluate the effects of different couplants, clamping techniques, and minor modifications to the probe. Typical results indicated that the expected variations based on one standard deviation is ± 3 ns for the longitudinal and shear wave travel-times.

The second step in evaluating probe repeatability was to make repeated measurements on a typical rail surface. Data typical to these measurements showed the expected variations to be ± 3 ns for both measurements. It should be noted that temperature effects are minimal since these sequences of measurements can be conducted within a time span of about 60 minutes. Temperatures of the respective surfaces were monitored and showed maximum changes of 0.2 °C in the laboratory.

The conclusion drawn is that a travel-time measurement made on surface typical of rail webs or better can be expected two times out of three to be within three nanoseconds of the average value obtained over many measurements. The degree of repeatability is considered very good for the purpose for which this probe is intended.

The third step consisted of measuring travel-times for eight different rail web surfaces over a longer period of time. A sequence of three measurements on each surface was repeated on three sucessive days. Repeatability in these measurements was not as good as that obtained previously but was ± 6 ns or less.

2.2. Changes in wave travel-times due to varying elastic properties

One of the problems associated with using the acoustoelastic technique for stress measurement lies in the fact that nominally identical materials exhibit slightly different wave speeds. For this reason measuring changes in stress is significantly simpler than measuring absolute values of stress. If however the variations of wave speed due to elastic property changes can be determined, an absolute measure of stress becomes feasible. As was mentioned previously this concern led to the incorporation of both longitudinal and shear wave travel-time measurements in the probe design. The longitudinal wave was monitored for changes in stress; the shear wave travel-time may be considered as a reference measurement to be used for determining the value of the longitudinal wave travel-time in the absence of stress. We consider next an hypothesis of the effect of the variations in material properties on wave speeds in order to test its applicability to the present measurement.

If we assume the variations in elastic properties are caused by variations in the rolling process by which the rail is formed, then, following Bradfield [9], it is reasonable to assume the bulk modulus of the rail is constant. We also assume the density is constant, thus requiring that the bulk velocity remain unchanged. The bulk velocity is related to the longitudinal and shear velocities by

$$V_B^2 = V_L^2 - \frac{4}{3} V_T^2 \qquad (5)$$

where

V_B is the bulk velocity

V_L is the velocity of longitudinal waves

V_T is the velocity of transverse waves.

If V_B is constant, then

$$\frac{dV_L}{dV_T} = \frac{4}{3}\frac{V_T}{V_L} \quad . \tag{6}$$

Equation (6) can also be written as

$$\frac{dt_L}{dt_L} = \frac{3}{4}\left(\frac{t_T}{t_L}\right)^3 \quad . \tag{7}$$

For the typical wave travel-times associated with the probe, eq. (7) yields

$$\frac{dt_T}{dt_L} = 4.28 \tag{8}$$

Figure 4 shows the travel-time measurements before and after annealing a cold rolled bar of 4140 steel. The measurements were made at six locations along 3.66 m (13 ft) length of a bar of cross section 25.4 x 102 mm (1 x 4 in). The travel-times were measured on opposite sides of the bar and averaged to eliminate curvature effects. The bar was heated to 815 °C (1500 °F) for an hour and oven cooled for 24 hours. The travel-time measurements after annealing show coherence indicating that the initial differences were probably due to residual stresses. Also shown in figure 4 is the expected change in travel-times for constant bulk velocity. The agreement enforces the theory that the plastic deformation to which the material has been subjected produces no change in the bulk velocity in the absence of residual stresses.

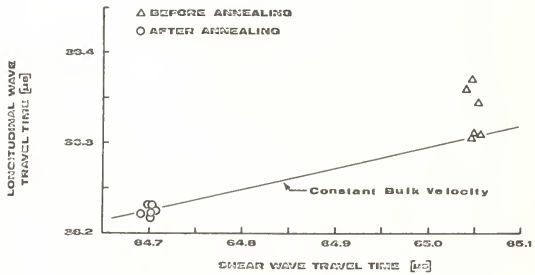

Figure 4. Travel-time measurements before and after annealing a 4140 cold rolled steel bar.

2.3. Travel-time measurements in new rail

The results of travel-time measurements at several locations on two full length rails are shown in figure 5. The data for rail 13, with the exception of two points, do show reasonable agreement with the constant bulk velocity line. Two possibilities for the disagreement with the expected variations are first that other uncontrolled parameters are affecting the measurements, and secondly, the presence of residual stresses in the rail web is causing changes in the travel-times.

A plot of the longitudinal wave travel-time as a function of position on the rail web is shown in figure 6. Only the data from these locations allowing travel-time measurements on both sides of the web are shown. If it is assumed the variations in longitudinal wave travel-time are due to stress, this data indicates a range of residual stress of 96 MN/m^2 (14 ksi), which is not unreasonable.

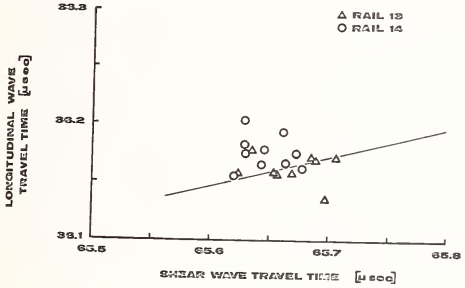

Figure 5. Travel-time measurements at several locations on two new full length rails with probe IV.

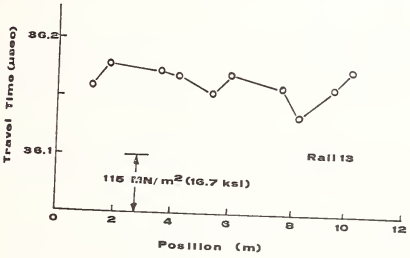

Figure 6. Longitudinal wave travel-time on the web and along the length of a new 119 lb, 11.9 m (39 ft) rail.

3. Field Evaluation of the Probe

3.1. Field test at Norman

A preliminary test to assess the operational procedures and measurement repeatability was conducted on the main line of the Atchison, Topeka, and Santa Fe Railway at Norman, Oklahoma. Ultrasonic travel-times, rail temperature and ambient temperatures were measured at a single station near mile-post 400. Two data sets were obtained in the early morning and evening of the same day. Although the longitudinal wave travel-times were greater than expected and the shear-wave travel-times showed unexplained changes, the results did indicate that measurements could be made in the field with reasonable precision.

3.2. Field tests at Pueblo

The principle field tests were conducted at the Department of Transportation, Transportation Test Center (TTC), Pueblo, Colorado in December, 1976. The weather was generally favorable to conducting the tests. Four stations were instrumented by TTC personnel for strain and temperature data. These locations were 91.4 m (100 yards) apart toward the middle of a 609 m (2000 feet) tangent section of the access track to the test section used for operating the linear induction motor (LIM) rail vehicle. Stations 26 and 35 were located near a weld. Station 26 was 1.2 m (4 ft) and station 35 was 0.51 m (2 ft) from the nearest weld. Stations 29 and 32 were located near the center of a rail. Station 29 was 4.5 m (15 ft) and station 32 was 3.6 m (12 feet) from the nearest weld.

Each station was instrumented to read longitudinal strain at the neutral axis on each side of the rail, vertical strain at the same location and lateral strain at the top of the rail. Rail temperature was also recorded. Each of the four test stations was instrumented with five 350 ohm bonded strain gages and two thermocouples. Temperature compensation for each strain gage was provided by applying compensating bridge strain gages to three-foot lengths of unstressed rail. This compensating rail was placed parallel to the test rail at each of the four test points. Data from all four test stations were multiplexed and recorded on a 14 track FM tape recorder. IRIG-4 time code was recorded. Real time data were available through a seven channel strip chart recorder.

The ultrasonic probe was alternately placed on each side of the rail at each station and a full set of travel-time data was recorded for both the shear wave the the longitudinal wave The ultrasonic instrumentation was housed in a van located on the road adjacent to the track. Two 15.2 m (40 foot) coaxial cables were used to transmit the electronic signals to and from the ultrasonic probe. One was connected to the sending transducer and the other would be alternately connected to each of the receiving transducers for the particular wave travel-time being measured.

The probe was held in place by C-clamps as shown in figure 7. The rail surface was prepared by wire brushing and wiping the web area. Precautions were taken to be sure that both the rail and the probe surface were free from grit and other loose particles since this presence would yield erratic readings. Low viscosity oil was used as the ultrasonic couplant.

A 1 m (3 ft) length of 110 lb/yd AREA rail located near each measuring station was used as a reference. Travel-time measurements on the reference rail were used to assess temperature effects and to detect abnormalities in the probe.

3.3. Results of the Pueblo field test

The strain histories recorded at the two rail stations are shown in figure 8. Similar, although less complete, data were obtained at stations 32 and 35. This strain is that associated with the thermal stress in the rail since the strain due to thermal expansion is compensated for by the gages on the unstressed rail. The strains plotted are not absolute strains but are relative to the strain present in the rail when the bridges are initially balanced. Because of operational difficulties all of the bridges were not balanced at the same time, hence, the data shown represent changes in strain from an unknown reference. The strains are plotted as functions of time beginning at about 2200 hours on 10 December 1976 (shown as -2 hrs) and continuing to about 2100 hours on 11 December 1976. The dotted lines shown in the figure are interpolations during periods when the data recorded were obviously in error or when the data were not recorded. The discontinuities which are seen in several of the strain histories, e.g. at station 26, the vertical strain on the gage side of the rail at 0700 hours, are due to bridge rebalancing necessitated by operational problems and should be disregarded.

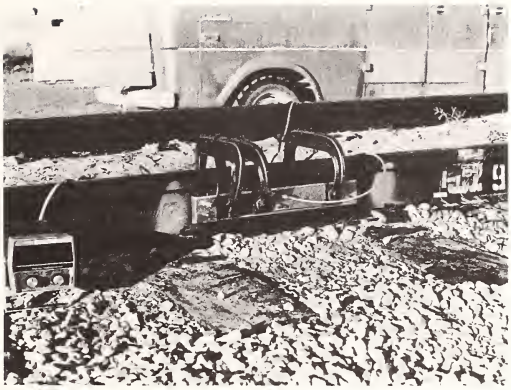

Figure 7. Ultrasonic probe clamped to rail web.

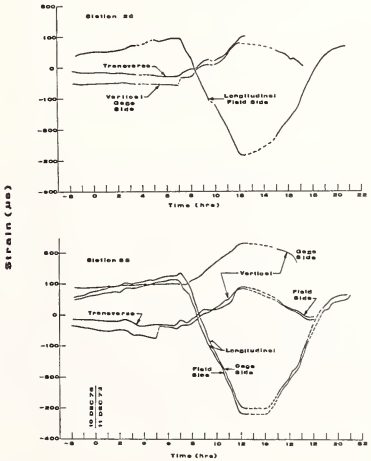

Figure 8. Strain histories at stations 26 and 29-Pueblo field test.

The strain histories are reasonably consistent with expectations. The maximum longitudinal tensile strain occurs at all four stations at approximately 0700 hours which was shortly after sunrise. The histories show rapid changes from 0700 to 1200 hours due to solar heating, and a rapid increase in tensile strain due to cooling from 1500 hours to 1800-1900 hours. Most of the vertical transverse strain histories show trends consistent with the longitudinal strains.

The stress changes computed from the measured longitudinal strains at the four stations are shown as a function of rail temperature in figure 9. Although the scatter is higher than is normally expected with strain gage measurements, the trend of the data agrees with the expected change of 2.24 $MN/m^2/°C$ (325 psi/°C). The data at station 35 show a shift of 16.6 MN/m^2 (2.4 ksi) because those strain gages were not operational for the full span of the test and, hence, were zeroed at a different strain level than the remainder of the gages. The scatter in figure 9 can be attributed to three causes. First, unequal temperatures between the unstressed lengths of rail upon which the bridge completion gages were located and the rail will cause an apparent strain. Secondly, flexure induced in the rail due to unequal heating of one side of the rail will cause apparent discrepancies. Thirdly, inaccuracies in temperature measurement may be responsible for some of the scatter because rail head temperatures were used in figure 9.

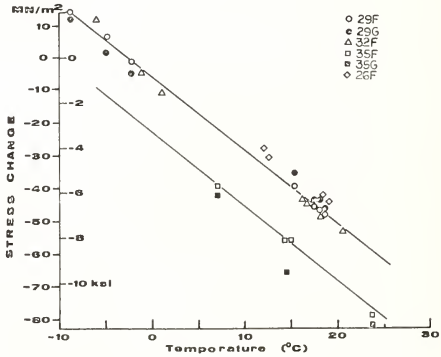

Figure 9. Stress changes measured with strain gages during the Pueblo field test.

The results of the travel-time measurements on the reference rail are shown in figure 10. The longitudinal-wave measurements show the expected change with temperature. The shear-wave measurements, however, show considerable scatter, the cause of which is not evident. The slope of the longitudinal wave travel-time data agrees very well with the slope measured in the Norman field test. The average slope of the shear wave data is greater than that measured in the Norman field test but is approximately the same as measured in the laboratory.

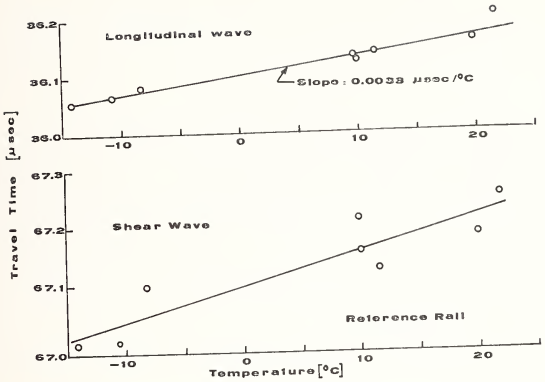

Figure 10. Travel-time measurements on reference rail during Pueblo field test.

The travel-time measurements at the four stations on the rail are shown in figures 11 and 12. Each data point shown is the average of measurements made on the field and gage sides of the rail web and has been temperature corrected for the variations shown in figure 10. Additionally the stress change data for station 35 have been incremented by 16.6 MN/m^2 (2.4 ksi) to account for the different zero stress level at this station as noted above.

The experimental data at station 26 shows more inconsistency than the data at the other three stations. However the data for stations 29, 32, and 35 agree within ± 6.9 MN/m^2 (± 1 ksi) with the expected relationship between stress changes and longitudinal wave travel-time. That is they have a common slope of 0.44 μs m^2/MN (3 ns/ksi) shown by the two straight lines in figure 11.

The absolute travel-time data at stations 29 and 32 are less than the travel time data at stations 26 and 35. That difference could be due to different longitudinal stresses or to different material properties. Note that stations 29 and 32 are both located near the center of a rail, and 26 and 35 are both near welds. That fact implies that the difference in absolute travel-times may be associated with different rail-web stresses caused by the manufacturing process or the welding process. Note also that the difference in absolute travel-time between the two sets of data, which is about 0.02 μs, is within the variation of longitudinal wave travel-times measured on the new 119 lb rail as shown in figure 6.

The shear wave travel-times shown in figure 12 for station 26, 32 and 35 are relatively independent of stress level but the data for station 29 show larger variations than were expected. Further the shear wave data for stations 26, 29 and 32 show reasonable agreement but that, for station 35, is considerably lower. This indicates that the elastic properties at station 35 are significantly different than those at the other locations.

3.4. Stress relieving tests at station 32

After all of the ultrasonic and strain gage data had been compiled for the 24 hour period of the test, a decision was made to cut the rail at station 32 in order to establish the true stress levels throughout the 24 hour test. Full strain gage data were recorded for the stress relieving test but no ultrasonic measurements were made.

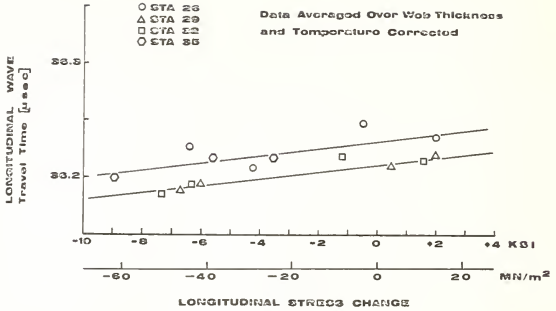

Figure 11. Longitudinal wave travel-time measurements on four rail stations at pueblo

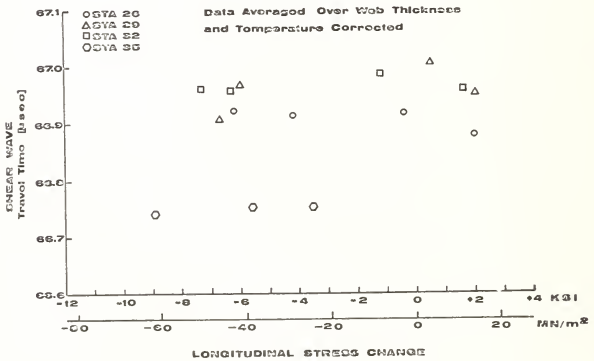

Figure 12. Shear wave travel-time measurements on four rail stations at pueblo.

The tests were conducted in five stages at a time in the afternoon when rail temperature was reasonably uniform at approximately 26.1 °C (79 °F). First strain data were recorded with the rail fully constrained. The strain data were recorded after each of the following steps. The rail clips were removed from seven ties on the side of the planned cut containing the strain gage. Then, the tie plates were removed from the same seven ties Following that, the rail was saw cut. Finally, the loose rail was hit with a hammer along its length in order to be sure that it was lying free on its ties.

The strain data behaved as expected. The longitudinal strains on either side of the rail were not severely affected until after the saw cut. However, greater longitudinal strain was recorded on the gage side of the rail compared to the field side indicating that the rail was not entirely straight. With this data, the true rail stress can be estimated. The mean stress free temperature is approximately 24.5 °C (76.1 °F). For the temperature encountered during the ultrasonic tests, the true longitudinal rail stresses ranged from approximately 6.9 MN/m^2 (1 ksi) to 74.5 MN/m^2 (10.8 ksi) in tension.

4. Conclusions

Based on the results of the field evaluation, it is concluded that the ultrasonic probe is capable of measuring longitudinal stress changes at specific locations in rail with an accuracy of ± 6.9 MN/m^2 (± 1 ksi). Although temperature induced changes in wave speed affect the probe, the differential travel-time measurement technique along with the stress-free reference measurement provide a means to cancel these undesirable effects.

The ability of the probe to measure absolute stresses has not been demonstrated at the present time. Although the variations in absolute travel-time measurements are possibly due to variations in stress along the length of the rail, that question will be answered only with a more extensive comparison of the ultrasonic measurements with absolute stress measurements.

References

1] Egle, D. M. and Bray, D. E., Nondestructive measurement of longitudinal rail stresses. Part 1-application of the acoutoelastic effect to rail stress measurement, Final Report DOT project OS-40091, report no. FRA/ORD-77/09.1 (Jan. 1977).

2] Coombs, D.H., ed., British Railway Track, London, Permanent Way Institution (1971).

3] Hay, W. W., Railroad Engineering (New York, John Wiley, 1953).

4] Pasley, R. L., Barkhausen effect -- An indication of stress, Materials Evaluation, 28, 157-161 (1970).

5] Klug, H. P. and Alexander, L. E., X-Ray Diffraction Procedures (New York, Wiley, 1954).

6] Egle, D. M. and Bray, D. E., Nondestructive measurement of longitudinal rail stresses, Interim report, DOT project DOT-OS-40091, report no. FRA-OR&D-76-270 (June 1975).

7] Egle, D. M. and Bray, D. E., Measurement of acoustoelastic and third-order elastic constants for rail steel, J. Acous. Soc. of Amer., 60, 741-744 (1976).

8] Schreiber, E., Anderson, O. L., and Soga, H., Elastic Constants and Their Measurement (New York, McGraw-Hill Book Company, 1973).

9] Bradfield, G., Strength, elasticity and ultrasonics, Ultrasonics, 10, 166-172 (1972).

lational Bureau of Standards Special Publication 596, Ultrasonic Materials Characterization, l. Berger and M. Linzer, eds., Proceedings of the First International Symposium on Ultrasonic laterials Characterization held at NBS, Gaithersburg, Md., June 7-9, 1978. Issued lovember, 1980.

ACOUSTIC POLARIMETRY AND THE ACOUSTO-ELASTIC EFFECT[1]

J. Rouge

Thomson-CSF, ASM Division
Chemin des Travails
06802 Cagnes/Mer
FRANCE

and

A. Robert

STCAN Groupe MSCN
8 boulevard Victor
75732 Paris Cedex 15
FRANCE

and

Y. Le Corre

Faculté des Sciences Paris VII
Paris - FRANCE

Until now, studies on the acousto-elastic effect and its application to nondestructive testing consisted in the measurement of the velocity difference between two transverse acoustic waves which were polarized parallel and perpendicular to the applied uniaxial stress direction. This acoustic birefringent measurement should only be applied to the case of a material which is isotropic in its initial state. But usually, materials exhibit an initial elastic anisotropy whose amplitude and direction are modified by the applied stress. We want to measure this anisotropy (amplitude and direction) for each value of the applied stress.

For this purpose, we developed an acoustic polarimeter which measures the change in shape of a transverse acoustic wave after going through the sample. The principle uses the mapping of a transverse acoustic wave on the Poincaré sphere. A short review of the properties of this sphere shows how a wave can be represented by a matrix; it is the same thing for other parameters such as linear, elliptic,and circular birefringent operators and linear or elliptic filters. This powerful means of computation allows for a fast and simple analysis of the way the acoustic polarimeter works.

An experiment has been done which agrees well with the theory. The sensitivity and the accuracy of the method enable us to measure the weak initial elastic anisotropy of a sample and to check its evolution for an applied stress.

1. Introduction

Most solids have an intrinsic elastic anisotropy, the acousto-elastic effect is the ›erposition of this intrinsic anisotropy with an anisotropy induced by an applied stress. ese two different anisotropies are of the same order of magnitude but have different ori- tations for the principal axes; therefore, velocity measurements should be performed on ear acoustic waves polarized in parallel with the principal axes of anisotropy.

›rk sponsored by DRET, Paris, France.

In order to make such a measurement, we have built an acoustic polarimeter which gives the angle θ of the fast birefringent axis of the sample, referred to a reference direction, and the phase shift γ between two shear acoustic waves polarized parallel to the fast and slow axis respectively.

These two parameters θ and γ are a characteristic of the elastic anisotropy of the sample for a given state of stress. If the stress is varied, θ and γ vary.

To explain this polarimeter, we use the Poincaré method which represents a shear wave elliptically polarized by a point on a sphere of unit radius.

2. Poincaré Method

An elliptical wave is characterized by two parameters, as seen in figure 1: the angle α, between the long axis of the ellipse and the Ox direction, and the flatness of the ellipse which is defined by an angle λ such that $|\tan \lambda| = b/a$, where a is half the long axis and b half the short axis.

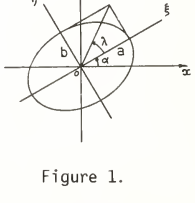

Figure 1.

In the equatorial plane of the Poincaré sphere [1][2] (see fig. 2) the Ox direction is the image of the reference direction Ox. In this plane, let us consider the situation such that $\widehat{XOm} = 2\alpha$, which is twice the angle α as previously described. In the meridian plane PmP', let us consider OM such that $\widehat{mOM} = 2\lambda$. M represents the elliptical wave of figure 1.

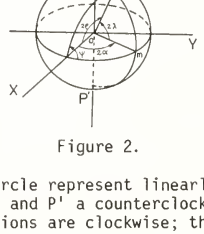

Figure 2.

The points on the equatorial circle represent linearly polarized vibrations. P represents a clockwise circular vibration and P' a counterclockwise circular vibration. In the upper hemisphere ($\lambda > 0$), the vibrations are clockwise; they are counterclockwise in the lower hemisphere ($\lambda < 0$).

Referred to Ox, Oy, a vibration ω can be written as follows:

$$\begin{array}{c|cc} Ox & \cos\rho & \cos \omega t \\ Oy & \sin\rho & \cos(\omega t + \Psi) \end{array} \quad . \qquad (1)$$

[2]Figures in brackets indicate the literature references at the end of this paper.

On the Poincaré sphere, $\widehat{XOM} = 2\rho$ and Ψ is the rotation angle around OX which brings the equatorial plane into the plane XOM. A rotation applied to the vibration modifies α in $\alpha+R$, stays unchanged. The rotation matrix R_{2R} is:

$$R_{2R} = \begin{vmatrix} \cos 2R & -\sin 2R & 0 \\ \sin 2R & \cos 2R & 0 \\ 0 & 0 & 1 \end{vmatrix} . \qquad (2)$$

The matrix representation of the vibration M is:

$$[OM] = R_{2\alpha} \begin{vmatrix} \cos 2\lambda \\ 0 \\ \sin 2\lambda \end{vmatrix} . \qquad (3)$$

For the phase γ, an operator, B_γ^θ, can be defined, as follows:

$$B_\gamma^\theta = R_{2\theta} \; B_\gamma \; R_{-2\theta} \qquad (4)$$

th

$$B_\gamma = \begin{vmatrix} 1 & 0 & 0 \\ 0 & \cos\gamma & -\sin\gamma \\ 0 & \sin\gamma & \cos\gamma \end{vmatrix} . \qquad (5)$$

3. The Acoustic Polarimeter

3.1. Description

The acoustical part of the device includes an acoustic transmitter applied on a flat ice of the sample and an acoustic receiver applied on the opposite side. These are connected mechanically in order to adjust their orientation on the sample, as can be seen on gure 3.

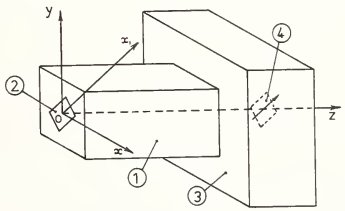

Figure 3.

In the emitter, there is a birefringent acoustic buffer ① referred to the axes , Oy, Oz. The fast axis is parallel to Ox, the slow axis is parallel to Oy and the wave opagation is along Oz. The transmitting shear transducer ② is cemented onto the buffer, s axis of polarization is along Ox_1, which bisects the Ox and the Oy axes.

While going through the buffer ① , the wave components along Ox and Oy undergo a lative phase shift Φ. The other face of the buffer is fixed on the sample to be studied ③ whose anisotropy is characterized by the two unknowns; the angle θ and phase shift γ. receiving transducer ④ is fixed on the other face of the sample; its polarization axis along Ox_1 like the transmitting transducer ② . The various axes are shown in figure 4.

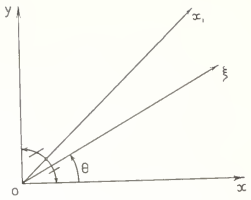

Figure 4.

3.2. Matrix representation

Referred to Ox, the transmitted acoustic wave can be represented by the following parameters: $\alpha = \frac{\pi}{4}$ and $\lambda = 0$. Its components on the Poincaré sphere are:

$$\begin{vmatrix} 0 \\ 1 \\ 0 \end{vmatrix} .$$

At the output of the birefringent buffer with phase shift ϕ the vibration is:

$$B_\phi \begin{vmatrix} 0 \\ 1 \\ 0 \end{vmatrix} .$$

In going through the sample, the birefringence has an orientation θ and a phase shift γ. The vibration on the Poincaré sphere is then:

$$[OM] = R_{2\theta}\, B_\gamma\, R_{-2\theta} B_\phi \begin{vmatrix} 0 \\ 1 \\ 0 \end{vmatrix} .$$

This vibration reaches the receiving transducer which acts as a linear filter with an orientation $\beta = \frac{\pi}{4}$, the matrix operator being $|010|$.

The parameter ρ_1 of the detected vibration is given by:

$$\cos 2\rho_1 = |010|\; R_{2\theta}\, B_\gamma\, R_{-2\theta}\, B_\phi \begin{vmatrix} 0 \\ 1 \\ 0 \end{vmatrix} \qquad (6)$$

which can be written as a function of θ and γ:

$$\cos 2\rho_1 = \sin^2 2\theta \cos\phi + \cos 2\theta\, (\cos 2\theta \cos\phi \sin\gamma - \sin\phi \sin\gamma) \quad . \qquad (7)$$

The electrical signal delivered by the receiving transducer is:

$$u = A \cos \rho_1 \cos \omega t \quad . \qquad (8)$$

3.3. Signal processing

Signal processing is done to determine θ and γ of eq. (7), knowing eq. (8). A null method is used for improved accuracy. Beside a null indicator, the device only includes a frequency variation knob.

Without sample, i.e., with the receiving transducer directly set against the transmitter, the signal processing is such that a null occurs at f_o, corresponding to a phase shift Φ_o in the buffer.

3.4. Principal axis of anisotropy

After inserting the sample and setting the frequency at f_o, the transmitter-receiver system is rotated until we get a new null. This is achieved when θ is equal to $\pi/4$ or $3\pi/4$ (see fig. 4). In this case, eq. (7) can be written:

$$\cos 2\rho_1 = \cos \phi_o \quad .$$

In this position, the fast axis (if $\theta = \pi/4$) or the slow axis (if $\theta = 3\pi/4$) is parallel to the polarization direction of the acoustic waves.

3.5. Phase shift measurement

Starting from the previous position, the acoustic transducer is rotated by 45°. θ is then 0 or $\pi/2$. Equation (7) is then:

$$\cos 2\rho_1 = \cos(\phi + \gamma) \qquad \theta = 0$$

or

$$\cos 2\rho_1 = \cos(\phi - \gamma) \qquad \theta = \frac{\pi}{4} \quad .$$

The frequency is then adjusted to f_1 for a new null. The phase shift φ becomes ϕ_1 such that:

$$\phi_1 + \gamma = \phi_o$$

ϕ_1 being known, γ is then given by:

$$\gamma = \phi_o \frac{f_o - f_1}{f_1} \quad .$$

If γ is positive, the fast axis of the sample is parallel to the fast axis of the buffer.
If γ is negative, the slow axis of the sample is parallel to the fast axis of the buffer.

4. Test Results

A test block of an aluminum alloy cylinder of 10 cm diameter has been cut into dimensions of 3 cm x 3 cm x 4 cm with the 4 cm length parallel to the axis of the cylinder. The compressive stress has been applied in the same direction.

The variation of the anisotropy parameters of the test block under the effect or an uniaxial loading is shown on figure 5. The curve I (upper) is relative to the orientation θ of the fast axis of the sample with the direction of the compressive stress. One can see that the direction of that fast axis has a tendency to draw nearer to the loading direction.

Curve II (lower) is the phase difference γ of the anisotropy, the nonlinear variation of which shows that there is a combination of initial anisotropy and of a load induced anisotropy. To show the sensitivity of the process, an overload of 1.4 10^6 N/m² (200 psi) applied to the block loaded at 25.10^6 N/m² (3600 psi) made the value of the phase difference γ grow 0.15

degree. The test apparatus works with two transducers fixed up on the opposite faces of the sample. With the same general working principle, an apparatus for which only one transducer is needed to monitor the transmitted and received pulses, is still under study.

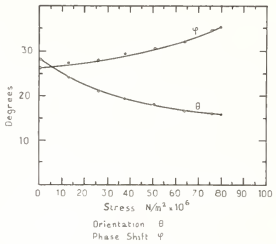

Figure 5.

5. Conclusion

The test results have shown that our new method of acoustical polarimetry offers the following advantages:

- measurement of the two characteristics of the elastic anisotropy of a solid: orientation θ of the principal axis and phase difference γ between the two components of an ultrasonic wave polarized in a parallel direction of these axes;

- discrimination between the fast axis and the slow axis of sample anisotropy;

- precision of the measurement and high resolution;

- and compact, easy to use device.

References

[1] Born, M. and Wolf, E., Principles of Optics, p. 30-31 (Pergamon Press, New York, 1959). Examples illustrating this method are given in H. G. Verrard, J. Opt. Soc. of Amer., 44, 634 (1954).

National Bureau of Standards Special Publication 596, Ultrasonic Materials Characterization, H. Berger and M. Linzer, eds., Proceedings of the First International Symposium on Ultrasonic Materials Characterization held at NBS, Gaithersburg, Md., June 7-9, 1978. Issued November, 1980.

APPLICATION OF ACOUSTICAL HOLOGRAPHIC INTERFEROMETRY TO THE STUDY OF STRESS IN MATERIALS

W. S. Gan

Acoustical Services Pte Ltd.
29, Telok Ayer Street
Singapore 1, Republic of Singapore

We have applied acoustical holographic interferometry (AHI) to the study of stress in materials. Our purpose is to locate where the stresses are, both outside and especially inside an object. We use double exposure AHI and time-averaged AHI. We have performed a theoretical analysis of the principles of the technique. We have obtained expressions for the intensity of the interference fringes and fringe spacing. From the fringe structure of the interferogram, we obtain stress information. We give a brief description of the proposed experimental setup. For time-averaged AHI, we obtain an expression for the intensity of the interference fringes in terms of the geometry of the experimental setup. It is a complicated expression conveying information about different angles of illumination and observation. We also give a brief description of the proposed experimental setup. We use two plates with stress present in one of them. We induce vibrations in the plates and apply time-averaged AHI to them. The interference pictures for these plates differ strongly from each other and show different frequency response. In the regions where there is stress, one observes an increase in intensity, since the plate is weakened and the oscillations have their largest amplitude at this point. The greatest advantage of AHI over optical holographic interferometry is its capability of detecting stresses inside objects.

1. Introduction

In industrial processes, much cost has been incurred because of damages due to the presence of unnoticed stresses and cracks induced by these stresses. There are several known methods for detection of stress but they are limited mainly to surface stress measurements. We have developed a new method using sound waves which can penetrate optically opaque objects with the ultimate aim of detecting and relieving the stresses before cracks occur. This method is carried over from optical holographic interferometry. In optics, there is a standard method of double exposure holographic interferometry for the detection of stress. We first perform a theoretical analysis of the principles of double exposure AHI and show how it differs from the optical case.

2. Derivation of Intensity of Interferograms and Fringe Structure of Double Exposure AHI

Let the x axis be the scanning direction of the transducer. The reflected wave U_{01} from the object before stress is applied, the reflected wave U_{02} from the object after stress is applied, and the reference wave U_r are given by:

$$\begin{aligned} U_{01}(x) &= A_0(x)[\cos \omega t + \phi_0(x)] \\ U_{02}(x) &= A_0(x)[\cos \omega t + \phi_0(x) + \Delta\phi_0(x)] \\ U_r(x) &= A_r(x)[\cos \omega t + \phi_r(x)] \quad . \end{aligned} \tag{1}$$

Before stress is applied, the intensity recorded on the hologram is

$$I_1(x) = \{A_0(x)\exp[i(\omega t + \phi_0(x))] + A_r(x) \exp[i(\omega t + \phi_r(x))]\}\{A_0(x)\exp[-i(\omega t + \phi_0(x))] + A_r(x) \exp[-i(\omega t + \phi_r(x))]\} \quad . \tag{2}$$

After stress is applied, the intensity recorded on the hologram is

$$I_2(x) = \{A_0(x)\exp[i(\omega t + \phi_0(x) + \Delta\phi_0(x))] + A_r(x) \exp[i(\omega t + \phi_r(x))]\}\{A_0(x)\exp[-i(\omega t + \phi_0(x) + \Delta\phi_0(x))] + A_r(x)\exp[-i(\omega t + \phi_r(x))]\} \tag{3}$$

The intensity of the interferogram is then

$$I(x) = I_1(x) + I_2(x) \tag{4}$$

The interference fringes are due to stress inside or outside the object. If the object is in a normal unstressed condition, there will be no interference fringes, and the two holograms will be identical. Equation (4) reduces to

$$\begin{aligned} I(x) &= 2A_0^2(x) + 2A_r^2(x) + A_0(x)A_r(x)\{\exp[i(\phi_0(x) - \phi_r(x))] \\ &+ \exp[-i(\phi_0(x) - \phi_r(x))]\} + A_0(x)A_r(x)\{\exp[i(\phi_0(x) \\ &+ \Delta\phi_0(x) - \phi_r(x))] + \exp[-i(\phi_0(x) + \Delta\phi_0(x) - \phi_r(x))]\} \\ &= 2A_0^2(x) + 2A_r^2(x) + 2A_r(x)A_0(x)\cos[\phi_r(x) - \phi_0(x)] \\ &\quad + 2A_0(x)A_r(x)\cos[\phi_r(x) - \phi_0(x) - \Delta\phi_0(x)] \quad . \end{aligned} \tag{5}$$

If the interferogram shown in eq. (5) is put into its original position, and illuminated with a laser beam representing the reference beam $U_r(x)$, it follows immediately from eq. (5) that the reconstructed wavefield will have a term proportional to $U_r U_r^* (U_{01} + U_{02})$. Assuming that $U_r U_r^* = 1$ which is the case for a plane wave and very closely approximates the case for a spherical wave, it follows that the reconstructed image field is $(U_{01} + U_{02})$. The resultant field vector at each point in the reconstructed image field may be written explicitly as

$$U_{image}(x) = U_{01}(x) + U_{02}(x + \Delta x) \quad . \tag{6}$$

Because the amount of displacement Δx is generally very small, one may conclude that the image field vector in the reconstructed image U_{image} given at each point is simply the vector sum of the corresponding fields reconstructed as the two superimposed images, given by U_{01} and U_{02}. Under these conditions, one may write the intensity distribution in the reconstructed image as

$$\begin{aligned} I_{image} &= (U_{01} + U_{02})(U_{01}^* + U_{02}^*) \\ &= \{A_0(x)\exp[i(\omega t + \phi_0(x))] + A_0(x)\exp[i(\omega t + \phi_0(x) \\ &\quad + \Delta\phi_0(x))]\}\{A_0(x)\exp[-i(\omega t + \phi_0(x))] + A_0(x) \\ &\quad \exp[-i(\omega t + \phi_0(x) + \Delta\phi_0(x))]\} \\ &= 2A_0^2 + 2A_0^2 \cos\Delta\phi_0(x) \\ &= 2A_0^2(1 + \cos\Delta\phi_0(x)) \end{aligned} \tag{7}$$

where $\Delta\phi_0(x)$ is a direct measure of the amount of stress Δx given by

$$\Delta\phi_0(x) = \frac{2\pi}{\lambda} \times \Delta x \quad . \tag{8}$$

Equation (7) describes the "contour map" interferogram obtained by double exposure AHI.

3. Brief Description of Proposed Experimental Setup

We shall describe a setup based on that of K. Suzuki et al., [1][1] but with some modifi-
tions, since our purpose is slightly different from that of Suzuki, et al. The apparatus
Suzuki [1] has to be modified to be able to measure the stresses over long periods of time.
this application, a portable scanner would be positioned with respect to a fiduciary point
the foundation of a nuclear reactor, for example. An ultrasonic hologram of a particular
nponent would be made and filed. After some period, say a year, the scanner would be set
again and a second hologram made. The two holograms would then be used to determine if
resses had occurred in the intervening time interval. Suzuki's [1] paper is concerned with
tection of the flaws at a particular instant and not over a period of time.

4. Derivation of Intensity of Interferograms and Fringe Structure of Time-Averaged AHI

We have to consider the two different interference fringes on two different plates, one
thout stresses and one with stresses.

4.1. Plate without stresses

Let $A_\ell \cos(\Omega t + \psi(\underline{r},t))$ describe the vibration of the object where Ω = frequency of
ration and $\psi(\underline{r},t)$ = phase difference due to object movement. When a sound wave is inci-
nt on the vibrating object, the scattered sound wave will be given by

$$U_\ell = A_\ell \cos(\Omega t + \psi(\underline{r},t)) \quad , \tag{9}$$

ere $\ell = 1, 2, 3\ldots$, each correponding to a successive position of the object at given times
Following the paper of Powell and Stetson [2], the reconstructed image point field value
l be given by:

$$U(\underline{r}) = \frac{1}{T} \int_0^T U(\underline{r},t)\, dt \quad , \tag{10}$$

ere the $\underline{r}$ vector describes the position of a point on the object. Substituting (9) into
0), we have

$$U(\underline{r}) = A_\ell \frac{1}{T} \int_0^T \exp[i(\Omega t + \psi(\underline{r},t))]\, dt \quad . \tag{11}$$

If the exposure time in making the hologram is much longer than the vibration period
e., $T >> 2\pi/\Omega$) and if the exposure is linearly recorded as an amplitude transmittance,
n using the results of Powell and Stetson [2], the intensity of the reconstructed image
the object is

$$I(\underline{r}) = |U(\underline{r})|^2 = |A_\ell|^2 \left| J_0\left(\frac{2\pi}{\lambda}\right) 2d_0 \right|^2 \tag{12}$$

ere d_0 = amplitude of object movement.

4.2. Plate with stresses

With stresses in the plate, eq. (9) will be modified to

$$U_\ell = |A_\ell| \cos(\Omega t + \psi(\underline{r},t) + \Delta\psi(\underline{r},t)) \quad . \tag{13}$$

[1] gures in brackets indicate the literature references at the end of this paper.

Substituting eq. (13) into eq. (10), we have

$$U'(\underline{r}) = |A_{\ell}| \frac{1}{T} \int_0^T \exp[i(\Omega t + \psi(\underline{r},t) + \Delta\psi(\underline{r},t))]\, dt \quad . \tag{14}$$

Now

$$\psi(\underline{r},t) = \left(\frac{2\pi}{\lambda}\right)2d = \left(\frac{2\pi}{\lambda}\right)2d_0 \sin \omega t \tag{15}$$

where d represents object movement. From eq. (15),

$$\Delta\psi(\underline{r},t) = \left[\left(\frac{2\pi}{\lambda}\right)2d_0\, \omega \cos \omega t\right] \Delta t \quad . \tag{16}$$

Replacing eq. (16) back into eq. (14), we have

$$U'(\underline{r}) = |A_{\ell}| \left|J_0\left(\frac{4\pi 0}{\lambda}\right)\right| + |A_{\ell}| \left|J_1\left(\frac{4\pi 0}{\lambda}\right)\right| \quad . \tag{17}$$

Then the intensity of the reconstructed image of the object is given by

$$I'(\underline{r}) = |A_{\ell}|^2 \left|J_0\left(\frac{4\pi 0}{\lambda}\right)\right|^2 + |A_{\ell}|^2 \left|J_1\left(\frac{4\pi 0}{\lambda}\right)\right|^2 . \tag{18}$$

From eq. (18), we can see that with stresses in the plate, the fringes will be modulated by an extra term. The presence of stresses in the plate will be manifested by changes in the fringes due to the increase in the amplitude of oscillations.

5. Brief Description of Proposed Experimental Setup

We shall follow the experimental setup of M. D. Fox et al., [3]. We have to modify the setup for the object so that both the plates can vibrate.

6. Advantages of AHI Over the Optical Holographic Interferometry

First, both double exposure and time-averaged AHI can enable one to detect stresses ins the object, whereas, optical holographic interferometry is limited to detecting stresses at surface of the object. Second, time-averaged AHI can detect very small distortions in an ob due to the preservation of the phase of the movement of the object, whereas, the optical hol graphic interferometry is not able to do this.

7. Suggestions for Future Work

The next step would be to map stress fields using double exposure and time-averaged AHI Secondly, we must investigate how the various stress components can be determined from the holographic fringe structure.

References

[1] Suzuki, K., Takahashi, F., and Michiguchi, Y., Application of shear wave focused image holography to nondestructive testing, Acoustical Holography, pp. 583-598 (Plenum Press, New York, 1977).

[2] Powell, R. L. and Stetson, K. A., Vibration analysis by holographic interferometry, J. Opt. Soc. Amer., 55, 1593 (1965).

[3] Fox, M. D., Ranson, W. F., Griffin, J. R., and Pettey, R. H., Acoustic holographic interferometry, Acoustical Holography, pp. 103-120 (Plenum Press, New York, 1974).

National Bureau of Standards Special Publication 596, Ultrasonic Materials Characterization, H. Berger and M. Linzer, eds., Proceedings of the First International Symposium on Ultrasonic Materials Characterization held at NBS, Gaithersburg, Md., June 7-9, 1978. Issued November, 1980.

ACOUSTIC IMAGING TECHNIQUES FOR NONDESTRUCTIVE TESTING

G. S. Kino, T. M. Waugh[1], P. D. Corl,
C. S. DeSilets and P. M. Grant

Edward L. Ginzton Laboratory
Stanford University
Stanford, CA 94305

A review is presented of our real time analog and digital phased array B scan acoustic imaging systems. We discuss the recent results taken with our analog FM chirp focused system operating in the gated mode. This technique removes completely the sidelobes which have degraded earlier systems. With it, we have been able to obtain acoustic images in metal samples with surface waves, Lamb waves, shear waves, and longitudinal waves. We have detected small reflectors of less and more than 1 mm diameter in the neighborhood of an end wall and have obtained images of small cracks, both when they are placed parallel and at large angles to the acoustic array. The principles of two alternate digital imaging systems, one based on chirp focusing and the other a synthetic aperture approach, will also be described. The latter system samples and stores the return echo signals in digital memories for subsequent processing, in real time, to produce the focused image only. The principles of these systems are described here.

1. Introduction

We have used our chirp focused phased array B-scan imaging system [1,2][2] to make reflection mode images in aluminum and stainless steel. The basic system was originally designed to operate at frequencies of the order of 2.5 MHz in water, and would not be expected to have sufficient resolution using longitudinal waves in metals (where the acoustic velocity is approximately 4 times that in water), to give useful images. We therefore decided to excite and receive the scanned focused acoustic beam in water, and mode convert to shear waves in the metal, for which the acoustic wave velocity is approximately twice that in water. We were able to demonstrate that the beam remains focused and can be scanned, and we obtained good two-dimensional cross sectional images of arrays of holes in the metal. Later we were able to demonstrate that good imaging could be obtained using Rayleigh waves on the surface of the metal, or Lamb waves in thin sheets of metal. The latter result was encouraging because it involved the use of highly dispersive waves. As the focusing system behaves like a very rapidly moving lens scanning a focused beam along a line parallel to the array at a velocity comparable to the velocity of acoustic waves, considerable deterioration in the focusing might have been expected in such media. This was not, in fact, the case. As far as we are aware, this is the first real time scanned focused images that have been obtained with Rayleigh waves and Lamb waves in thin metal sheets. We have also studied methods for reducing the sidelobe responses in this system. Considerable success has been obtained with a gating technique, which now permits us to image small reflectors in the neighborhood of a large reflector, such as an end wall. Finally, the the development of two new digital imaging systems, based on both the earlier chirp and a new synthetic focus technique will be reported.

[1]Now at Varian Associates, Salt Lake City, Utah.
[2]Figures in brackets indicate the literature references at the end of this paper.

2. Principle of Operation

The basic principles of operation [1,2] of chirp focused system and the detailed theory [3] has been given in other papers, so we will only give a short outline of how the system operates.

A linear FM chirp signal of frequency $\omega = \omega_1 + \mu t$ is fed into a tapped acoustic surface wave delay line, there being one tap for each element of a linear acoustic transducer array. This gives rise to an acoustic wave propagating along the delay line with a parabolic variation of phase:

$$\phi_n = \omega_1(t-x_n/v) + (\mu/2)(t - x_n/v)^2$$

where v is the surface wave velocity and x_n is the coordinate of the n-th tap.

The signals from each tap are mixed with a constant frequency signal of frequency ω_2 so as to excite rf signals with a center frequency $\omega_s = 2\pi f_s = \omega_1 - \omega_2$ with the same parabolic variation of phase. These signals, after amplification, are inserted into the corresponding elements on the transducer array. They give rise to an acoustic beam with a parabolic phase variation along the transducer array which is scanned rapidly along the array at a velocity v, determined by the acoustic surface wave velocity. This is just the type of beam which would be emitted by a moving lens moving at a velocity v parallel to the array and excited by a plane wave, as illustrated in figure 1. As we have shown earlier [3], the equivalent focal length of this lens is

$$z = \omega_s v^2/zv_w \quad .$$

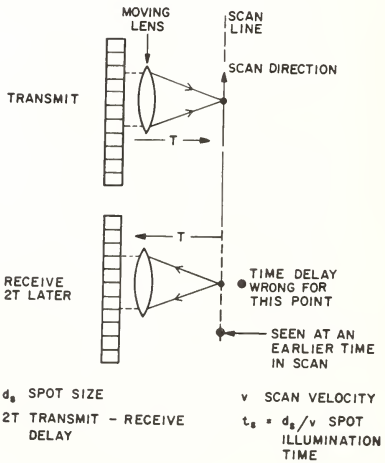

Figure 1. A schematic of the principles of the B-scan system in which the device is regarded transmitting or receiving a moving focused beam with a lens moving parallel to the array.

In operation the system is used to focus on a line a distance z from the array, and scan along this line. Then after a time delay $T = 2z/v_w$ where v_w is the velocity in the medium, the system is operated as a receiver with the same type of chirp focusing and scanning. The system is then refocused on another line at a different distance from the array, the time delay between transmit and receive is changed correspondingly, and a complete raster is scanned in this way as shown in figure 2.

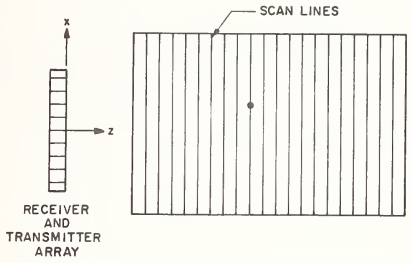

Figure 2. A schematic of the raster scanned with phased array B-scan system.

The calculated definitions in the x and z directions are given by

$$d_x = z\lambda/D$$

$$d_z = v_w z\lambda/Dv$$

respectively, where $\lambda = v_w/f_s$ and D is the width of the lens, i.e., the spatial length of the chirp along the array.

Suppose now we use the array system in water and allow the center of the beam (the ray normal to the array) to be incident at an angle θ_1 on the surface of a metal. Then it follows from Snell's law that the center of the beam leaves the surface of the metal at an angle θ_T where

$$\frac{\sin \theta_T}{\sin \theta_i} = \frac{v_M}{v_w} \quad ,$$

v_M is the wave velocity in the metal and v_w is now the wave velocity in water.

We note that for paraxial focusing ($\sin \theta_i \approx \theta_i$; $\sin \theta_T \approx \theta_T$), θ_T is still proportional to θ_i and the beam still remains focused within the metal at a point which can be calculated. This is not too critical because of the relatively large depth of focus of this system, as the range resolution is determined by time delay. However, it should be noted that the beam will still scan along a line parallel to the array at a distance determined by the total delay time to this line and back. We can estimate the required time delays fairly easily, especially, if the array is placed quite close to the metal surface.

It will be noted that by tilting the array sufficiently, the angle θ_i can be made large enough so that the longitudinal waves in the metal are cut off and only shear waves can be excited. When the angles are made still larger, the shear waves are cut off and only Rayleigh waves are excited and $\theta_T = 90°$. At intermediate angles, Lamb waves of various kinds can be excited, but all these waves can be focused and scanned by the chirp focusing system.

3. Experimental Chirp Focused System

The systems which we have constructed have been operated with scan velocities between 1 and 2.5 mm/μs. A block diagram of the system is shown in figure 3. It uses a Bismuth Germanium Oxide (BGO) surface acoustic wave delay line with a center frequency of 50 MHz. This line has a total of 60 taps spaced 1 μs apart along the line, although we have only elected to use the first 28 elements of the line due in part to defects in the line and in part to the fact that only 30 channels of transmitter and receiver electronics have been constructed. The digital control electronics generates a sequency of pairs of ramp pulses which are used to generate the chirp waveform in the voltage-controlled oscillator (VCO). The first ramp is used on transmit while the second identical ramp is for receive. As the system focuses further from the array, each scan line of the sequence of ramp pulses decreases amplitude, simultaneous with an increase in delay between transmit and receive to compensate for the increased range. The peak output power of the system is approximately 0.25 watts into each element of the array.

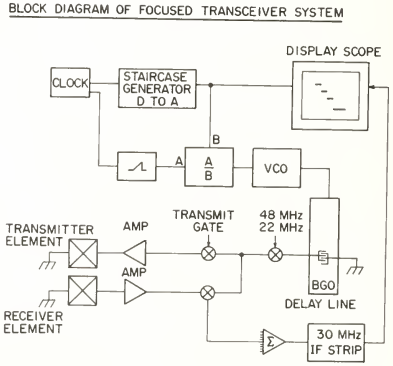

Figure 3. Block diagram of transceiver system used for shear, Rayleigh, and Lamb wave ultrasonic imaging.

A number of different transducer arrays all using PZT-5 on a tungsten epoxy backing have been used. The array elements are 1 cm long and are on either 0.5 mm or 0.64 mm centers depending upon the particular array used. The center frequency of these arrays is in the range of 1.2 to 2.7 MHz. Both the transmitter and the receiver were electronically apodized to reduce the sidelobe level into the range 25 dB to 30 dB below the main lobe. In addition, the individual elements are connected in pairs to decrease the first gating lobe. However, when imaging close to a strong reflector, e.g., end wall, there is still a considerable problem with the sidelobes which mask out small targets.

This deficiency has been overcome by operating in a gated mode where the transmitter and receiver are only switched on for a short period once each scan line. This removes both sets of sidelobes due to transmit mainlobe-receiver sidelobe, and transmit sidelobe-receiver mainlobe. With the system scanning at 2 mm/μs across an x = 6 cm wide sample we have incorporated a 1.6 μs duration gate pulse, which traverses across the display in 16 discrete steps. When imaging over area Z = 10 to 30 cm from the array, at 2 mm line spacings, the gating circuit reduced the display rate from 30 frames per second to approximately two. Thus the considerable improvement in image quality is obtained at the expense of TV compatible frame rates. It is therefore desirable to view the display on a scan converter.

4. Reflection Mode Imaging

Using our focused and scanned system in a reflection mode, we have been able to produce a number of B-mode images using longitudinal, shear, Rayleigh, and Lamb waves. For optimum resolution in both directions, we would like to have $v = v_M$ where v_M is the acoustic wave velocity in the material of interest. Thus we have attempted to match the scan velocity v to the velocity of the medium v_M. For imaging in aluminum with shear waves, Rayleigh waves, or Lamb waves, we require a scan velocity of approximately 3 mm/μs for optimum resolution, while we are actually using a scan velocity of 2 mm/μs.

We can produce shear wave B-mode images in aluminum by tilting the array past the critical angle (13.8°) for longitudinal waves, then a longitudinal wave coming from water will be mode converted at the surface of the block to a shear wave. By cutting the end of a target block so that the shear waves propagate straight down the block, as shown in figure 4, we have been able to image arrays of holes drilled in the block. As illustrated in figure 5, we have carried out shear wave imaging at a number of different frequencies with different scan velocities and have found that when we use a target of approximately 1 wavelength in diameter, the theoretical 3 dB transverse resolution is 2.5 mm, with a measured transverse resolution of 2.6 mm; the theoretical 3 dB range resolution is 3.9 mm, and the measured range resolution is 3.5 mm. These measurements were made at a center frequency of 2.75 MHz on targets which were 150 mm from the array, with a scan velocity of 2 mm/μs.

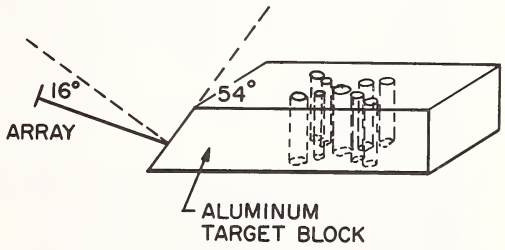

Figure 4. A schematic of the mode conversion scheme used to produce shear waves.

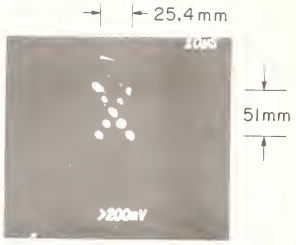

Figure 5. B-mode shear wave images of 2 mm diameter holes in aluminum block. f_o = 2.75 MHz; scan velocity 3.0 mm/μs; central hole is 150 mm from input end of target block.

In another experiment, we have used 3 MHz longitudinal waves in aluminum to obtain an image of a flat bottomed hole. The results are shown in figure 6, where it will be seen that the top surface of the hole can be observed, as well as the front and back walls of the metal sample. The hole has a diameter of 3 mm and a length of 25 mm. It will be noted that the diameter and length of the hole can be measured directly by this technique, without further interpretation of the results. Because the surface of the hole is a specular reflector, we only observe its top surface, a point of great importance in NDT problems.

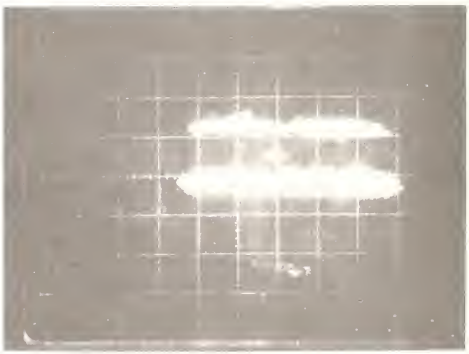

Figure 6. An acoustic image of flat bottomed hole (3 mm diameter x 25 mm deep) using 3 MHz longitudinal waves in an aluminum sample.

By changing the experimental setup slightly, so that we now have the array tilted to the critical angle for Rayleigh waves, as illustrated in figure 7, we have been able to image the same targets using Rayleigh waves. Because the velocities for Rayleigh waves and shear waves are approximately the same in aluminum (3.16 mm/μs for shear waves and 2.96 mm/μs for surface waves), the expected resolutions are also very similar. For 2.75 MHz surface waves incident on a 1 mm target located 165 mm away from the array with a scan velocity of 2 mm/μs, we obtain a theoretical transverse resolution of 2.5 mm and measured resolution of 3 mm with a theoretical range resolution of 3.7 mm and a measured range resolution of 4 mm. Thus, we have now been able to image the same set of targets with both shear waves and Rayleigh waves, and are able to obtain comparable images with both of these methods.

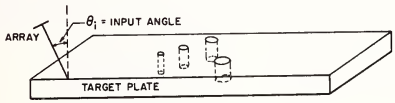

Figure 7. A schematic of mode conversion scheme used to produce Rayleigh waves and Lamb waves.

Figure 8 shows Rayleigh wave images obtained in gated mode of an artificial crack 1 cm long, ~100 μm wide, eloxed in a metal sample, figure 9. This sample can be rotated in the surface wave field, so that the crack can be aligned at an angle to the transducer array. When the crack is parallel to the array ($\theta = 0$), the crack is clearly seen, as shown in figure 8(a). Because the crack is a specular reflector, when it is turned at an angle, no signal will be returned to the array from the middle of the crack; only the two ends of the crack will be observed. The results for $\theta = 0°$, 45°, and 90° are shown in figures 8(a), 8(b), and 8(c), respectively. The scattering from the crack ends can clearly be seen. These studies confirm the results obtained in theoretical work on scattering from cracks. The two ends of the cracks behave like sources, and the imaging technique shows the presence of the sources directly, rather than resting on an indirect inference based on the interference phenomenon between the two sources, as would be obtained with simple plane wave transducers.

Another example in gated mode is shown in figure 10 in which two small holes are observed at a distance 8 mm from the end of a sheet of metal along which Rayleigh waves are propagating. With sufficient intensity we can observe both the top of the metal sheet and the reflection from the surface wave passing around the two corners at the end of the metal sheet. As the intensity is turned down, one observes in addition, the holes in front of the first corner.

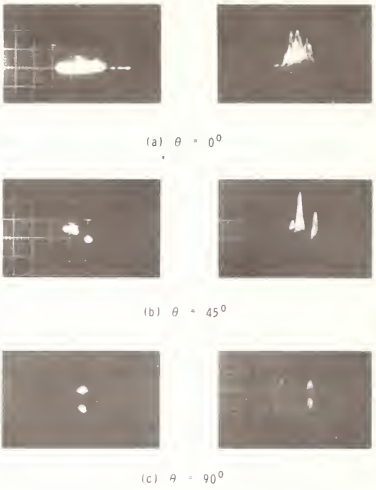

Figure 8. Photographs of a surface crack taken in the gated mode with the crack facing the array (0°) at 45° to the array and at 90° to the array. The configuration shown in figure 7 is used to excite Rayleigh waves.

Figure 9. Detail of simulated surface crack. Scale: 1 mm/small division.

Thus the gated technique is capable of giving a considerable improvement in sidelobe levels at the expense of a relatively slow scan which permits us to image a small target close to a large reflector. The disadvantage of such a slow scan is not only that of speed but also the display problem becomes more severe as each point in the image is only illuminate for a very small portion of the total time.

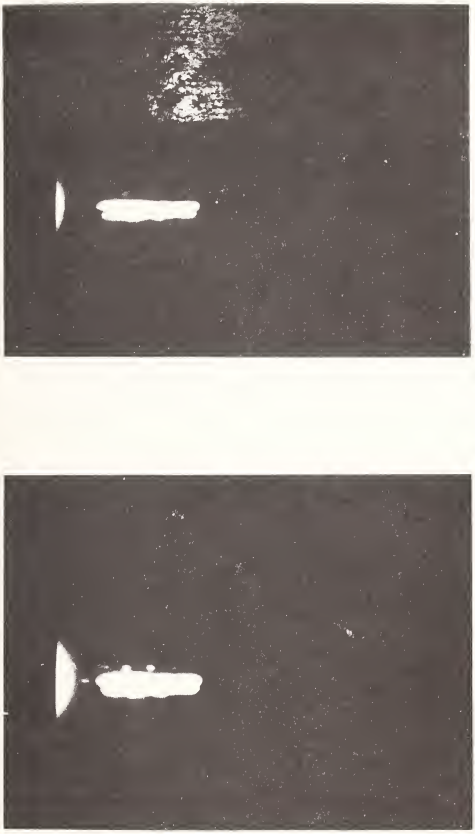

Figure 10. Photographs of two small holes 8 mm from the end of a metal surface. The less intense image shows reflections from the two corners of the sample. Image taken in gated mode.

5. New Developments

The successful results obtained to date on our analog chirp focused acoustic imaging system, have led us to develop new improved systems. One approach, adopted by Bates and

Shaw [4], is to develop a digital chirp focused system. They use a digital shift register to switch 16 different phase references into individual elements of the array. This should yield a sidelobe level, due to sampling, of the order of 30 dB. The advantage of this new approach is that the FM chirp can be digitally programmed and need not be limited to the paraxial form. In addition the scan velocity can be varied at will, or stopped to image a single point. An interesting application of such systems is to phase contrast imaging. This digital imaging system is being built to obtain improved accuracy and better images of stress fields with electronic scan rates.

Another approach to imaging system design is to employ analog-to-digital converters on each element to realize a digital time delay focused system. Such a system is not practical at the present time for the frequencies employed in nondestructive testing because of the high cost of high speed A-to-D converters. It is, therefore, necessary to employ some stratagem to decrease the number of A-to-D converters and the complexity of the system required.

We have constructed a synthetic aperture system for this purpose [5]. A short pulse is emitted from a single transducer and enters the object of interest. Reflected echoes are received on the same transducer then passed through an amplifier and A-to-D converter into an 8 x 1024 bit RAM. The process is then repeated for the next element in the array, and the signals from that element are stored in a separate RAM. By using a clock rate several times the signal frequency, several samples per rf cycle are obtained. Thus it is necessary to employ a high frequency video A-to-D converter. By the time the process is finished, information from the whole field of view is stored in the RAM memories and is available for reconstruction of an image. To image a particular point in the field, signals are taken from the appropriate points in the RAM corresponding to the correct time delays. Thus any line in the image can be scanned in any direction to generate a complete raster image.

The system has the advantages of great flexibility and superior definition over other imaging systems operating at the same frequency. The major disadvantage of the system is that its sensitivity will not be as good as a system which uses a focused transmitter and receiver, as only one element is excited at a time. On the other hand, as only one transmitter, amplifier, and A-to-D converter is used in combination with a multiplexer, the system is relatively simple. The transmitter and receiver amplifier can then be designed with special care. Thus it is possible to work with a higher voltage transmitter than is possible with a multi-element system, to use a pulse train with a matched filter, and to design for the lowest possible amplifier noise figure. It is, of course, vital to use transducers with as high an efficiency as possible. Thus in our early experiments we are constructing transducers with quarter wavelength matching to water [6] and a measured return loss of approximately 11 dB at 3.5 MHz, whereas the earlier chirp focused array had a return loss of the order of 40 dB.

It is apparent that digital techniques are extremely flexible, and that new methods and ideas can be tried out almost at will by programming from a computer. We therefore believe that such processing schemes are likely to be the most promising techniques to use in the future, especially as in the NDT field the speed necessary to observe rapidly moving objects, such as that required for medical heart scans, is not really required.

6. Conclusions

We have shown that imaging techniques are very powerful ones for determining the position of the flaw, and for finding information on its size and shape. Careful attention to the design of these imaging systems is necessary to keep the sidelobe levels low enough so that small flaws can be observed in the neighborhood of a large scatterer, such as a metal wall. Operation of these systems is quick and simple, and provides an increase in speed on the order of 100 times over that of a purely mechanically scanned system. In B-scan operation, the transverse definition in these systems is comparable to the range definition, a major advance in capability over present systems.

New systems are now designed and constructed which show promise of being capable of eliminating most of the difficulties associated with our first earlier system. The design concept is based on digital in preference to analog circuitry, which is dropping in price all the time. Thus it should eventually lead to an inexpensive and flexible enough approach to make an electronically controlled system with full three-dimensional focusing and dynamic scanning in the near future.

This research was sponsored by the Center for Advanced NDE operated by the Science Center, Rockwell International for the Advanced Research Projects Agency, and the Air Force Materials Laboratory under Contract RI 74-20773.

References

[1] Kino, G. S., DeSilets, C., Fraser, J., and Waugh, T., New acoustic imaging systems for nondestructive testing, p. 94-101, IEEE Ultrasonics Symposium Proceedings (1975).

[2] Fraser, J., Havlice, J., Kino, G. S., Leung, W., Shaw, H. J., Toda, K., Waugh, T., Winslow, D. K., and Zitelli, L. T., A two-dimensional electronically focused imaging system, p. 19-23, IEEE Ultrasonics Symposium Proceedings (1974).

[3] Souquet, J., Kino, G. S., and Waugh, T., Chirp focused transmitter theory, Acoustical Holography, Volume 7 (1976).

[4] Bates, K. N. and Shaw, H. J., Digitally controlled electronically scanned and focused ultrasonic imager, Acoustical Holography, Vol. 8 (1978).

[5] Corl, P. D., Kino, G. S., DeSilets, C. S., and Grant, P. M., A digital synthetic focus acoustic imaging system, Acoustical Holography, Vol. 8 (1978).

[6] DeSilets, C. S., Fraser, J. D., and Kino, G. S., Design of efficient broadband transducers, IEEE Trans. Sonics Ultrasonics SU-25, 115-125 (1978).

National Bureau of Standards Special Publication 596, Ultrasonic Materials Characterization, H. Berger and M. Linzer, eds., Proceedings of the First International Symposium on Ultrasonic Materials Characterization held at NBS, Gaithersburg, Md., June 7-9, 1978. Issued November, 1980.

SYNTHETIC APERTURE ULTRASONIC IMAGING IN METALS

C. VandenBroek, M. B. Elzinga, J. R. Frederick, and S. Ganapathy

2046 East Engineering Building
University of Michigan
Ann Arbor, MI 48109

Images of flaws in metals obtained by a synthetic aperture focusing technique for ultrasonic testing (SAFT UT) are presented. The technique uses a single scanning transducer operating in pulse-echo mode; echo signals are digitized and stored on disc. A description is given of the subsequent data processing which results in flaw images with high resolution ($\sim 1\ \lambda$) both laterally and longitudinally. Flaw images from test samples with both artificial and real flaws are analyzed with the aid of position-amplitude plots, contour plots, and gray-scale displays. The images are inherently quantitative, and, therefore are directly suitable for evaluation using the ASME Section XI Boiler and Pressure Vessel Code.

1. Introduction

A synthetic aperture focusing technique for ultrasonic testing (SAFT UT) has been under development at the University of Michigan over the past four years under sponsorship of the United States Nuclear Regulatory Commission [1-3][1]. The primary goal has been to obtain improved resolution with respect to other NDT methods, and in this way to obtain a better idea of the size, shape, and orientation of a discontinuity in the pressure vessel or piping. It is expected that this new approach will provide more and better information that will be useful in the implementation of the ASME Section XI Boiler and Pressure Vessel Code. The purpose of this paper is to describe SAFT UT as implemented at the University of Michigan and present some of the results that have been obtained.

2. Synthetic Aperture Imaging

The original application of the synthetic aperture technique was to airborne radar terrain imaging [4]. The extension to ultrasonic imaging soon followed but met with limited success due primarily to the elaborate optical processing that was being used [5-9]. SAFT UT at the University of Michigan makes use of a digital data acquisition and processing scheme to be described later.

Basically, synthetic aperture imaging takes advantage of the nonlinear phase shift of a target response as it is being linearly scanned. Use of this phase shift allows a more precise determination of the target's lateral position, thus resulting in a finer lateral resolution than can be obtained by using the physical beam width alone.

Consider the case of a transducer which is linearly scanned over a test specimen which contains a point target. As shown schematically in figure 1, the echoes for scan positions laterally displaced from the target location are delayed in time due to the greater distance they have traveled. The locus of echo phase shifts created by the scanning process is generally hyperbolic in form with its apex positioned at the location corresponding to minimum echo travel time. In fact, if the scanning and surface geometries are known, it is possible to accurately predict the shape of the locus of echoes. If the individual A-scan signals are now shifted forward in time by an amount equal to their predicted phase delays, they will come into phase with one another. Consequently, if the signals are coherently summed, the result will be a single large response as shown in figure 2. The A-scan signals included in

[1]Figures in brackets indicate the literature references at the end of this paper.

this process constitute a synthetic aperture. The same process is repeated with a new synthetic aperture displaced by one scan position from the previous aperture as shown in figure 3. In this case, however, the phase shift compensation does not produce a set of in-phase echoes. Destructive interference occurs during summation which results in a significantly smaller response. The process is directly analogous to that which occurs in a conventional transducer with a physical focusing lens. Repeatedly shifting the new aperture by one scan position and producing a new output signal each time has the effect of producing a scanning synthetic aperture. By reducing the aperture size at the edges of the raw data, it is possible to generate a processed data scan of exactly the same size as the raw data scan. The achievable lateral resolution is proportional to the aperture width[2], however, and as such the edges of the processed data will be reduced in resolution somewhat.

Thus far, the discussion of the synthetic aperture focusing technique has been described in terms of a linear scan. In reality, the typical data scan is two-dimensional and requires a two-dimensional aperture. The locus of echoes from a point target is thus actually a hyperboloid and the phase shifts are figured accordingly.

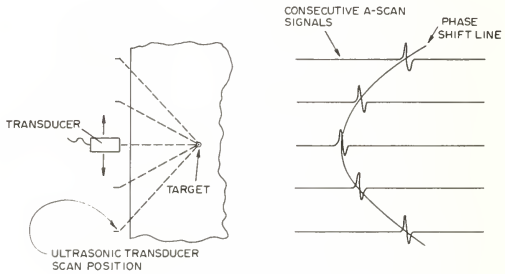

Figure 1. Scanned transducer response.

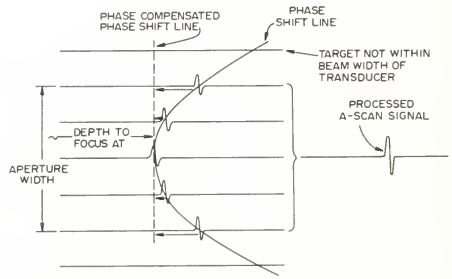

Figure 2. Single aperture phase correction.

[2]From reference [4], the lateral resolution, ρ_x, will be approximately equal to $[\lambda/(4 \sin(\Delta\theta/2))]$ where λ is the ultrasonic wavelength in the medium in which the target is located, and $\Delta\theta$ is the total angle over which the target is illuminated. If we assume an illumination angle of 30°, a reasonable value for a focused transducer in steel, then ρ_x is approximately equal to λ, or 2.6 mm in stainless steel at 2.25 MHz.

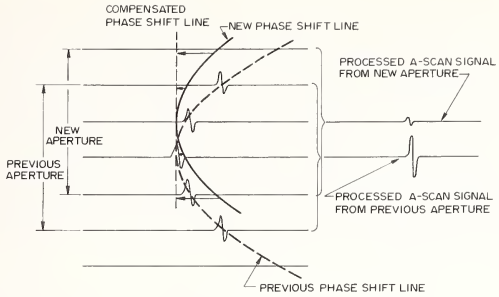

Figure 3. Consecutive synthetic apertures showing resolution improvement.

3. Data Collection

All data collection and management is currently done digitally with an Interdata 7/32 minicomputer. During data acquisition a test specimen is immersed in a tank of water and scanned under computer control by a single scanning transducer operating in pulse-echo mode. Highly damped, focused transducers are used. Scanning is done in a single plane in raster fashion with the test specimen generally oriented so that the focal point of the transducer is always located on the specimen surface. The movement of the transducer is performed by stepping motors attached to ball screws in a jig located over the water tank. User control is by way of a FORTRAN program through which the appropriate parameters such as the size and depth of the scan are entered.

At each scan position the minicomputer causes the ultrasonic transducer to be pulsed. The resulting A-scan RF signal is sampled and converted to a digital value at equal time intervals as shown in figure 4. Again, parameters which specify the desired sampling are supplied by the operator. The time delay between the pulsing of the transducer and the first sample (ID), the subsequent delay increment between successive samples (DI), and the number of samples (NP) are recorded for future use.

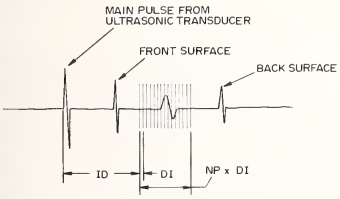

Figure 4. Sampling of an A-scan rf signal.

Additionally, the operator may choose to employ signal averaging to reduce the random noise introduced by wideband amplifiers in the system. In this case, at each scan position, the transducer is pulsed repetatively and the resulting sampled signals are averaged. For truly random noise a signal-to-noise ratio improvement equal to the square-root of the number of signals averaged can be achieved. Signal averaging is important in SAFT UT because large amounts of gain are needed to produce reasonable signal levels with wide beamwidth transducers and thick section steels.

An electronic flow-chart is shown in figure 5. A free running trigger under manual control is used to set the transducer pulse repetition rate, typically about 1 kHz. When data are required, the programmable digital delay generator (DDG) is loaded with a BCD (binary coded decimal) number from the computer. On the next available pulse from the free running trigger, the DDG emits 2 pulses--an initial pulse and a delayed pulse which is a function of the BCD value. The initial pulse is sent to the high voltage pulse generator which applies a very short, high voltage spike to the transducer causing it to emit an ultrasonic pulse. The high voltage spike is gated out in order to protect the wide-band amplifier which follows. The wide-band amplifier is preceded by a manual attenuator so that the signal of interest is brought to the proper level for the sample-and-hold module. The sample-and-hold module captures the ultrasonic signal at the instant of the delayed pulse from the DDG. The output of the sample-and-hold module is converted to a 12-bit digital representation by an analog-to-digital converter.

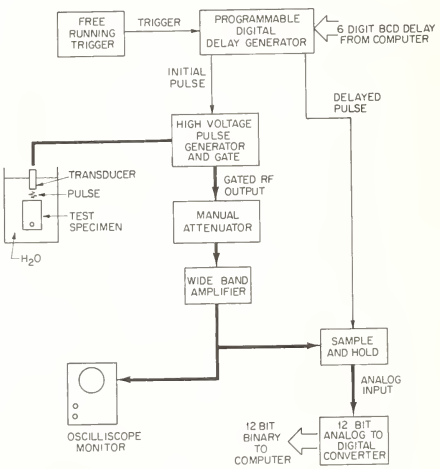

Figure 5. Data acquisition system block diagram.

On receipt of the 12-bit representation by the computer, the process is repeated with different BCD delay values as often as necessary to describe the entire A-scan waveform of interest. Delay increments can be set as small as 10 ns giving an effective maximum sampling frequency of 100 MHz.

4. Data Processing and Display

Figure 6 is a flow chart of the digital routines employed to generate SAFT UT flaw images. The scan program collects data as discussed above, and its output is a raw data file which is stored on a magnetic disc. To give a feel for the acquisition time required, a single A-scan signal made up of 250 points (used to generate data for figure 10) and summed 20 times to improve the signal-to-noise ratio takes approximately 5 seconds to collect.

The SAP3D routine constructs a synthetic aperture for each of the original scan positions. Each of the signals in the synthetic aperture are shifted individually by the amount necessary to focus at the assumed target location and then added into a summing vector. Dividing the summing vector by the number of signals added into it then gives the required output signal.

Because the amount of phase shift necessary is a function of the depth of the assumed target as well as of the position of the signals within the aperture, the output signal has high resolution only at the depth of the assumed target. The current processing routine uses this depth as an input parameter which is held constant. The output data file is thus focused at one plane. The choice of focal plane is made by an inspection of the raw data. Another input parameter is the number of signals comprising an aperture. To maintain a given resolution, the effective angle of insonification must remain constant. Hence, the number of signals included in an aperture increases as the square of the focal depth.

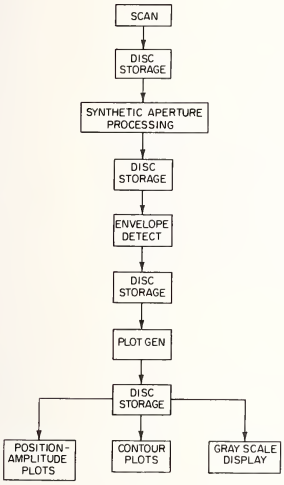

Figure 6. Data processing block diagram.

Again, to give a feel for time, the 250 point A-scan signal mentioned above can be processed in a 25 x 25 aperture (625 shifted and added signals) in approximately 19 s, most of which is disc I/O time.

An envelope detection routine is used to remove the rf waveform leaving only the amplitude envelope. This is done digitally with the aid of the Fast Fourier Transform. Time required for a 250 point signal is approximately 2.5 s.

Current techniques for display of an ultrasonic image require transforming the output of the envelope detection routine from a four-dimensional data set (X, Y, Z, and echo amplitude) to a three-dimensional data set (amplitude plus two spatial dimensions). This transformation is done by the PLOTGEN program, and the output data is then suitable for display as a position-amplitude plot, a contour plot, or a gray-scale display. The process of PLOTGEN and display occurs with sufficient speed that the researcher can obtain the desired results in an interactive fashion at the computer terminal.

5. Ultrasonic Images

Figures 8 to 10 show some of the results obtained with the SAFT UT system. These include images from a post-test wedge cut-out from the Oak Ridge National Laboratory Intermediate Test Vessel V-7B and also images from a weld specimen from GARD, Inc.

Some preliminary information is helpful in understanding the images from the Oak Ridge block. The block was cut from a test vessel as depicted in figure 7. The slot machined into

the side of the vessel served as a crack initiator for the hydraulic pressure test which followed. After the vessel was pressurized to failure, the area surrounding the slot was removed in the form of a wedge-shaped block as shown. For further details on the origin of the block see reference [10]. Three SAFT UT scans were made over the right-side face of the block.

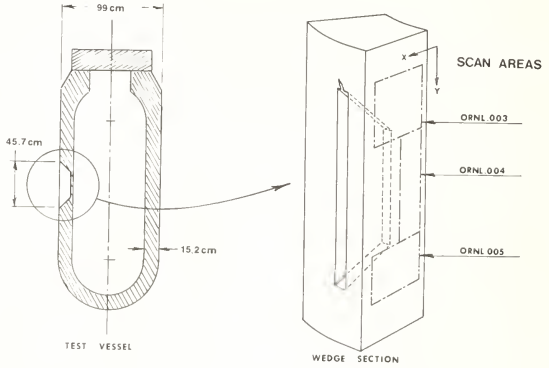

Figure 7. Diagram of Oak Ridge National Laboratory Intermediate Test Vessel V-7B and wedge cut-out.

A position-amplitude plot of the scan area labeled ORNL.003 is shown in figure 8. The X-Y reference coordinates must be observed for proper orientation. In this case, the PLOTGEN program was used to search the Z dimension at each X-Y location for the maximum echo amplitude and the display routine plotted this out in the form of a perspective drawing. In this sense the plot is very similar to a C-scan.

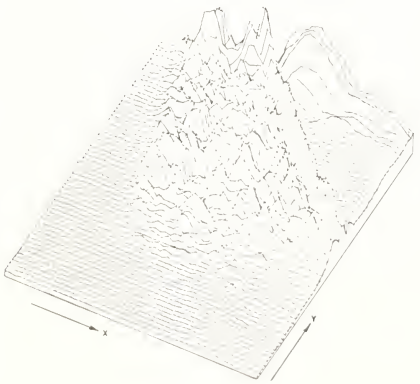

Figure 8. Position-amplitude plot of inspection volume ORNL.003.

The same data set together with the corresponding sets from the adjacent scan areas have been displayed on a gray-scale unit. Photographs of these displays are fitted into the composite shown as figure 9. Also included in figure 9 is a sketch showing the scan areas, slot, and flaw location. It should be emphasized that the flaw outline is an interpretation of the gray scale display shown in the figure since no sectioning results were available. Sources of variations within the composite include differences in focus depth and differences in the process of photographic reproduction.

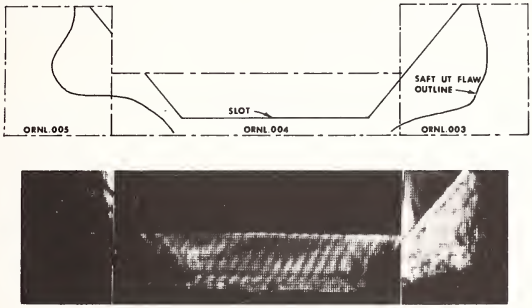

Figure 9. Gray-scale display of inspection volumes ORNL.003, ORNL.004, and ORNL.005.

The GARD, Inc. weld specimen is depicted in figure 10 together with examples of the third display technique, the contour plot. The specimen was made from reactor pressure vessel grade 533B steel with a multipass, 60° included angle, vee-butt weld. Slag was intentionally left in the weld.

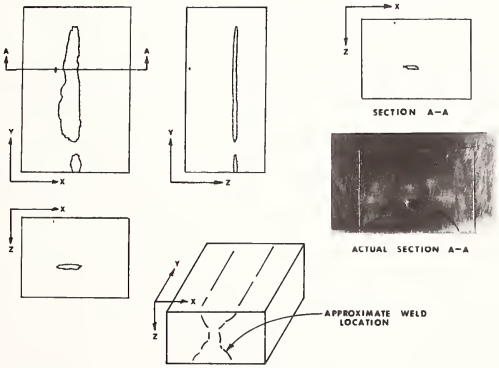

Figure 10. Contour plots and sectional view of the GARD, Inc. weld specimen.

The X-Y, Y-Z, and X-Z plots of figure 10 are all derived from PLOTGEN files of the same type as used for figures 8 to 9. In this case, however, the display routine plotted only those points corresponding to a specific amplitude. Each view corresponds to a projection of the internal discontinuities in one of the three orthogonal directions. One can think of the volume as being transparent with opaque discontinuities. It is also possible to produce

sectional views at arbitrary locations within the inspection volume as shown in the upper right hand corner of figure 10. Sectional views differ from projections in that they only show discontinuities which intersect the section line. The sample was destructively sectioned along the plane marked A-A, and a photograph of this surface is included for comparison. The weld line and inspection volume boundaries have been artificially enhanced for clarity. Note that the small void in the upper left corner of the computer-generated section A-A corresponds correctly with the actual section. The depth (Z dimension) of the flaw as shown does not represent the depth of the flaw due to the fact that sound transmission has been effectively stopped by the slag so that the bottom surface of the flaw lies in a shadow. The indicated width dimension of the flaw, however, is representative of the actual flaw width. The depth of the computer generated contour represents the uncertainty or resolution in the longitudinal, or Z, direction.

6. Conclusion

The images presented here demonstrate the ability of SAFT UT to quantitatively characterize discontinuities in metal. However, they are only interim results of an ongoing effort. Current activities include improvements in all phases of the system. A transient recorder is being implemented so that an entire A-scan signal can be digitized by the use of one outgoing pulse. This will drastically reduce data acquisition time. A new processing algorithm is being developed so that the output data will be focused at every plane instead of a single plane as is presently the case. The display systems are being improved with the goal of presenting simulated three-dimensional images with interactive control so that it will be possible to zoom in on and rotate any desired portion of the inspection volume. Concurrent with these efforts is the ongoing task of validating the ultrasonic images by comparing them with the sectioned test specimens. This procedure together with a quantitative description of the capabilities of SAFT UT is necessary for field implementation.

References

[1] Frederick, J. R., Seydel, J. A., and Fairchild, R. C., Improved ultrasonic nondestructive testing of pressure vessels - First Annual Report, NUREG-0007-1, University of Michigan, Ann Arbor, Michigan (January 1976).

[2] Frederick, J. R., Fairchild, R. C., and Anderson, B. H., Improved ultrasonic nondestructive testing of pressure vessels - Second Annual Report, NUREG-0007-2, University of Michigan, Ann Arbor, Michigan (September 1977).

[3] Frederick, J. R., Fairchild, R. C., Vanden Broek, C. J. H., and Elzinga, M. B., Improved ultrasonic nondestructive testing of pressure vessels - Third Annual Report, University of Michigan, Ann Arbor, Michigan (to be published) (January 1978).

[4] Brown, W. M. and Porcello, L. J., An introduction to synthetic-aperture radar, IEEE Spectrum, 6, 52-62 (September 1969).

[5] Flaherty, J. J., et al., Synthetic aperture ultrasonic imaging systems, U. S. Patent No. 3548642, December 22, 1970 (Filed March 2, 1967).

[6] Prine, D. W., Synthetic aperture ultrasonic imaging, Proc. Symp. on Engineer. Applications of Holography, 287-294, Los Angeles, California (February 16-17, 1972).

[7] Burckhardt, C. B., et al., Methods for increasing the lateral resolution of B-scan, in Acoustic Holography, Vol. 5, P. S. Green, ed., pp. 391-413 (Plenum Press, 1974).

[8] Griffiths, J. W. R., et al., Synthetic phased array for nondestructive testing, Ultrasonics, 12, 246-247 (November 1974).

[9] Greguss, P., Acoustical holography, Physics Today, 42-48 (October 1974).

[10] Whitman, G. D., and Bryan, R. H., Heavy-section steel technology program quarterly progress report for July-September 1977, ORNL/NUREG/TM-166, Oak Ridge National Laboratory, Oak Ridge, Tennessee (March 1978).

National Bureau of Standards Special Publication 596, Ultrasonic Materials Characterization, H. Berger and M. Linzer, eds., Proceedings of the First International Symposium on Ultrasonic Materials Characterization held at NBS, Gaithersburg, Md., June 7-9, 1978. Issued November, 1980.

THE USE OF FOCUSED PROBES FOR DETECTION, IMAGING, AND SIZING OF FLAWS

A. M. Touffait, M. T. Destribats, M. Roule, and R. Saglio

Centre d'Etudes Nucleaires de Saclay
B. P. N° 2, 91190 GIF Sur Yvette
France

During the last seven years, focused probes have been used at the French Atomic Energy Commission at Saclay on various applications, especially on thick specimens (up to one meter of steel). Several very important advantages have appeared: the characteristics of the acoustical beam in the zone used for the testing, that is the focal zone, are accurately known; misoriented flaws are more easily detected; it is possible to image flaws through cladding without distortion of the image; the lens may be corrected for specimen geometry (testing of cylindrical or spherical components) or the use of inclined beams. Higher signal-to-noise ratio is obtained, especially on very thick specimens and on stainless steel weldings; very small defects are detected, even at a very long distance from the testing surface; flaws can be sized. The results obtained on sizing artificial or natural defects on weldment are presented. Focused transducers are used for many very different applications in various fields such as control of petrochemical vessels or nuclear energy components. They are utilized in the different pre- or in-service inspection devices which have been developed by the French Atomic Energy Commission to control the pressurized water power reactor built in France. Some of these applications are described.

1. Introduction

Ultrasonic inspection must be able to detect, image, and size flaws to be credible and valuable. Focused probes permit great progress in those three areas.

2. Focused Probe

The focused probe is identical in its composition to a conventional probe. Focusing is obtained by machining the front part to get an acoustical lens. The following formulae give a good approximation of the diameter (d) and the length (L) of the focal zone for a drop of 6 dB.

$$d = \lambda \frac{F}{D}$$

$$L = 4\lambda \left(\frac{F}{D}\right)^2 \qquad \text{L measured in water}$$

The beam diameter can be measured either in water or in solid material and it is possible to know its variation as a function of the gain (fig. 1). The focal zone defines the region of the part actually inspected by the transducer.

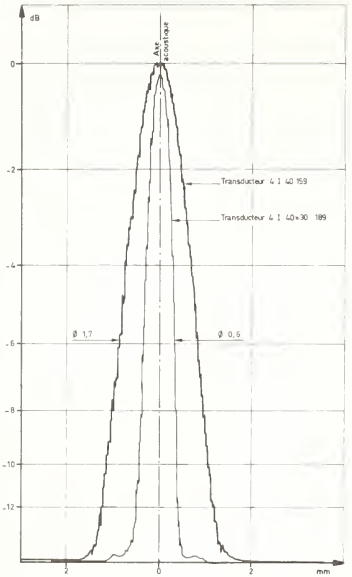

Figure 1a. Beam diameter of focal zone in water, experimental results.

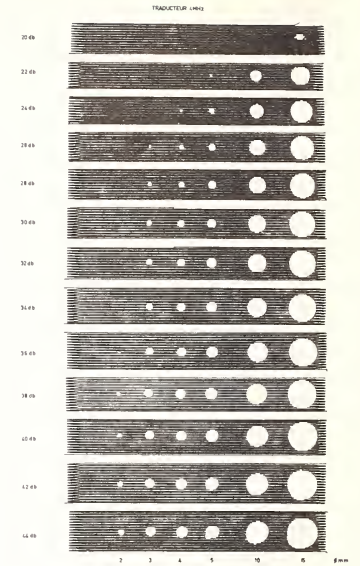

Figure 1b. Beam diameter of focal zone in steel.

The beam diameter changes with gain according to the formula:

$$d_{n(6\ dB)} = (n + 1)\frac{d}{2}(6\ dB)$$

To take into account the different interfaces encountered, it is important to correct the acoustical lens for the focusing or defocusing induced by the interface. In the same way, when an angled beam is used, the lens is adjusted so that the focal point is placed on the axis of the refracted beam.

3. Detection of Flaws

When conventional ultrasonic inspection is possible, the use of a focused probe does not increase the number of detected flaws, but it allows a better knowledge of the flaws because of its better resolution. For example, a focused probe at 4 MHz, 350 mm focal distance, 60 mm in diameter, 50 mm of water path, will have a focal zone of 2 mm in diameter and will be able to resolve 2 defects separated by 3 mm. Another point is the better detection of large misoriented flaws [1,2][1]. In some cases, only inspection with focused probes gives the required results. Four examples are given below.

3.1. Detection of cracks in cladding

Figure 2 presents the problem of determining whether or not a crack in the cladding has extended into the base metal. With a conventional transducer, because of the divergence of the beam, it is not possible to detect a difference between the different echoes. However, with a thin focal zone, the differences in the time paths will be sufficient to indicate if the crack is in the cladding or in the base metal.

[1]Figures in brackets indicate the literature references at the end of this paper.

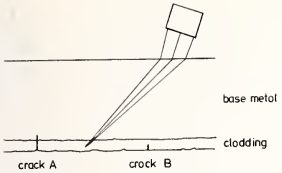

Figure 2. Crack detection in cladding.

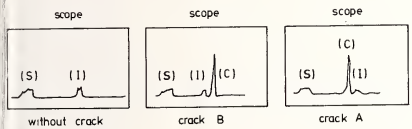

(S) = surface echo

(I) = interface echo

(C) = crack echo

3.2. Detection of cracks in threads

The detection of cracks in studs of PWR reactors is an important problem. The interface between water and metal causes a cylindrical beam to focus at a point located at 10 mm under the surface, far from the zone of interest. With such a beam, the signal-to-noise ratio is very bad. With lens correction, the signal-to-noise ratio increases and it is possible to detect a 0.5 mm crack.

3.3. Inspection of a flange in γ shape

The access to the weld is very difficult and is impossible from the interior or the bottom. The only solution is the use of a sufficiently narrow beam insensitive to the geometry, as shown in figure 3. The focused beam is rotated so that it interrogates all the weldment. A mechanism with local immersion is used in that case and a mirror rotates the beam.

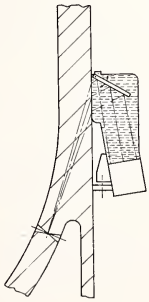

Figure 3. Sketch of the pressurizer lower head weld. Principle of ultrasonic testing.

3.4. Inspection of the flange weld for a 900 MWe PWR

The inspection is to be done from the joint of the flange (fig. 4) to detect a defect perpendicular to the inner surface of the reactor. The distance in the material is 900 mm. The transducer used has a frequency of 2 MHz, a diameter of 125 mm and a focal distance of 3850 mm in water. The beam diameter in the focal zone is 19 mm. To inspect all the weld, the focused probes tilt from -3°30' to 1° in water. It is possible to detect a 2 mm hole at the distance of 900 mm with a signal-to-noise ratio of 18 dB.

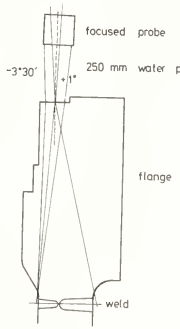

Figure 4. Inspection of the flange weld.

4. Imaging

The two different types of imaging most used to define a flaw are B-scans and C-scans. B-scans present a cross section view and are very useful for the inspection of specimens presenting a complex geometry. When a B-scan presentation is used with a focused probe, the orientation of the defect with respect to the axis of the acoustical beam can be determined. If the surface of the flaw is perpendicular to the axis of the beam, there will be no variation in time path so the image will be flat. If the defect is spherical, there will be a difference of the time path and the image will be round. The C-scan presentation enables one to size the defect, as described below.

5. Sizing

5.1. Principle

The procedure we describe is very simple and allows the sizing of defects with a precision equal to the size of the focal beam diameter [3,4]. When a flaw is detected, it is possible to measure the maximum amplitude A_m and to make C-scan images at different levels A_m + 6 dB, A_m + 12 dB, A_m + 18 dB, etc.

On each of those images, it is possible to measure the size L of the image in each direction ($L_{6\ dB}$, $L_{12\ dB}$, $L_{18\ dB}$, etc.)

If $L_{6\ dB}$ is equal to the beam diameter d, $L_{12\ dB}$ is 1.5 d and $L_{18\ dB}$ is 2 d, then the defect is smaller than the focal beam. To size the defect, it will be necessary to use a probe with a smaller focal zone or, if that is not possible, to estimate the defect with regard to a calibration hole.

If $L_{6\ dB}$ is greater than the beam diameter, and the variation between $L_{18\ dB}$ and $L_{6\ dB}$ is only d, then the dimension is that of the image at 6 dB.

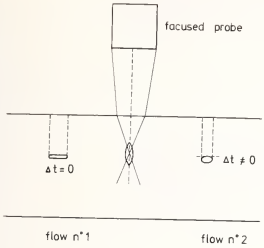

Figure 5. B-scan presentation.

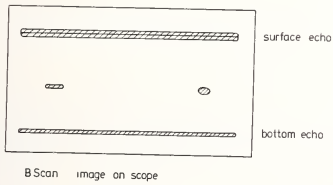

If $L_{6\ dB}$ is greater than the beam diameter and $L_{12\ dB}$ varies from $L_{6\ dB}$ by more than half d (some zones of less reflectivity have been revealed), it is necessary to make additional C-scans in steps of 6 dB until two consecutive images vary by only d/Z. The size of the last image is the one of the defect; this size is known to an error of d/2.

5.2. Example

Three natural flaws existing in a weld have been characterized. Figure 6 shows the images obtained at different levels.

The characteristics of the defects are noted on the following table:

defects	depth (mm)	dimensions
1	35	smaller than beam diameter
2	37	14 x 9
3	35	6 x 3

The transducer used was 4 MHz and had a 3 mm focal beam diameter. The dimensions of the flaws have been confirmed.

6. Conclusion

The focused probes have allowed great progress in detecting, imaging and sizing the defects. In many cases, they provide the only way of obtaining enough information about the

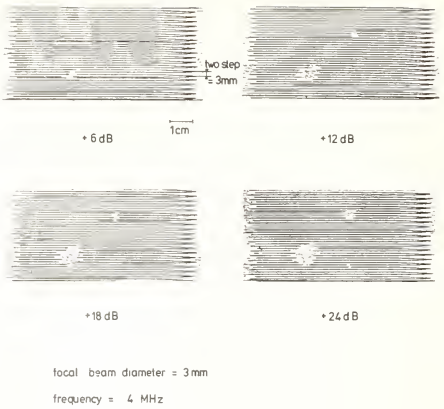

Figure 6. C-scan presentation.

defect with regard to its existence, size and orientation. Research is now in progress to study all the possibilities of the sizing method, especially by comparison of the results obtained by focused ultrasound with the true size of the real flaws.

References

[1] DeVadder, D., Dimensioning badly oriented flaws by means of focused probes, Ecole Centrale des Arts et Manufactures (Chatenay-Malabry France).

[2] Saglio, R., Better detection of large poorly oriented plane defects by ultrasonics, NDT International (August 1976).

[3] Saglio, R., Prot, A. C., and Touffait, A. M., Determination of defect characteristics using focused probes, Materials Evaluation, 36, 62 (1978).

[4] Saglio, R., Foulquier, H., Roule, M., and Touffait, A. M., Application of focused probes to measure the dimension of defects in welds, in Proc. 8th World Conference on NDT - Cannes, France.

National Bureau of Standards Special Publication 596, Ultrasonic Materials Characterization, H. Berger and M. Linzer, eds., Proceedings of the First International Symposium on Ultrasonic Materials Characterization held at NBS, Gaithersburg, Md., June 7-9, 1978. Issued November, 1980.

DEVELOPMENT AND APPLICATION OF FOCUSED PROBES FOR ULTRASONIC ANGLE BEAM TESTING

T. Yamazaki

Nippon Kokan K. K.
1 Kumozukokancho Tsu City Mie Pref.
Japan

and

T. Fuji

Industrial Research Institute
7-1-1 Shinkawa Chuo-ku
Tokyo, Japan

The depth and height of a flaw from the surface are the two most important factors in determining the strength of a welded structure. Ultrasonic angle beam testing is used to detect such flaws, but so far, the measurement precision is not sufficient to evaluate the flaws. Angle beam focused probes were produced, based on the curved surface reflection method. Probes with refraction angles of 45° and 70° were designed. These probes accurately indicate the depth of the flaw from the surface and the height of the flaw itself.

1. Introduction

The height and depth of a flaw from the surface are the two most important factors in determining the strength of a welded structure. Ultrasonic angle beam testing is used to detect such a flaw, but so far, the measurement precision has not been sufficient to evaluate the flaws. This may be due to the directivity of the ultrasonic beam. Therefore, the measurement of the defect size would be more precise, provided that the beam from the probe could be converged or focused.

Angle beam focused probes were designed based on the curved surface reflection method. For simplicity of the design, it was assumed that the ultrasonic wave emitted from the transducer was straight and without diffraction. A concave mirror of spherical surface, made by the method of lens polishing, was used as the curved surface. For the purpose of calculating the spread of the ultrasonic beam from the transducer, a few points on the surface were selected and only waves from these points were taken into account. The angle of refraction is the angle by which the ray from the center of the probe refracts at the contact surface.

Probes with refraction angles of 45° and 70° were designed. Figure 1 shows the path of the ultrasonic wave rays used for the calculation; U, V, R, and α are variables and were evaluated as $X_1 \cong X_2$, where $X(X_1 = X_2)$ is the focus distance. The ultrasonic beam produced by the angle beam focused probes converge into a narrow beam and the degree of convergence was examined. Using this information, the most applicable probe was applied in measuring artificial and natural flaws in welded parts.

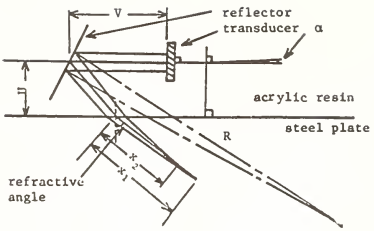

Figure 1. Path of beam emitted from the transducer.

2. Experimental Method

2.1. Experimental equipment

Ultrasonic flaw detector: Krautkramer USIP 11
Angle probe:
(1) new design focused probes for 45°;
FP-1 (R=105), FP-2 (R=228), FP-3 (R=320) for 70° FP-4 (R=105);
(2) Krautkramer : MWB45, MWB70;
(3) Tokyo keiki : PZT. 5Mhz, 10x10mm angle 45° (refer to this as PZ-5).

2.2. Experiment with respect to verification of focus

2.2.1. Focus for depth direction

Generally, as an ultrasonic beam path increases in length, the width of the beam spreads accordingly. On the other hand, for an angle beam focused probe, the focus distance is the path length before the beam begins to spread. Figure 2 shows the testing blocks utilized in this experiment. The scanning graph was drawn along the path at 5 mm intervals between 15 and 70 mm in order to investigate the spread of the beam. This result verified the convergence of the beam when the scanning graph of the focused probes was compared with a conventional probe.

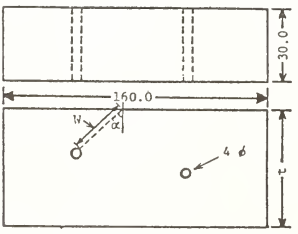

α = 45° or 70°
W=15,20,25,30,35,40,45,50,55,60,65,70
t=34.7, 77.0, 37.3, 30.4, 23.6

Figure 2. Testing blocks for depth focus.

2.2.2. Focus for lateral direction

The depth of a small defect is measured more efficiently provided that the beam is onverged in the lateral direction. Therefore, the focus was verified using the testing lock as shown in figure 3. The method is similar to that described above (2.2.1.).

2.2.3. Spread of acoustic field

A scanning graph was drawn using the testing block as shown in figure 4. This was sed to examine the spread of the scanning graph to a perpendicular flaw of 2 mm at about 0 mm path length.

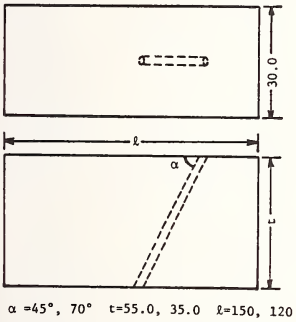

Figure 3. Testing blocks of lateral focus.

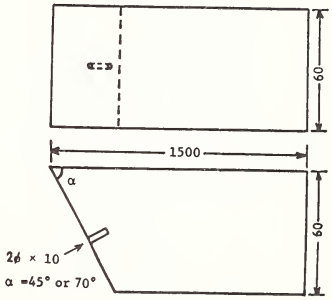

Figure 4. Testing blocks for the spread of acoustic field.

2.3. Test of artificial and natural defects in a welded part

Only depth and height of flaws were measured. Artificial defects were used with the ooves as shown in the figure of table 1. The detection of the depths and heights of ie flaws was achieved through the use of echoes received from the upper and lower edges f the defects. The size and the condition necessary to distinguish the two echoes was erified.

Two types of test specimens were used. Number 1 type test specimens have natural de- ects of slag inclusions, incomplete penetration and transverse cracks, as shown in figure Number 2 type specimens have three different cracks in the welded part, as shown in igure 6. The parameters α, d, hr, hr', and l are represented in figure 6. The limit of ie measurement by the shape of flaws was verified.

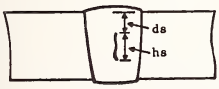

Figure 5. Number 1 type specimen.

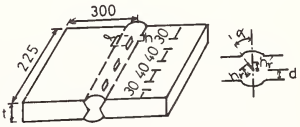

Figure 6. Number 2 type specimen.

3. Experimental Results

3.1. Experimental results with respect to verification of focus

Figure 7 shows representative scanning graphs of depth and lateral scans at 20 mm path length. It is clear that the beam of the focused probes is converged more than the one of the common probe. The depth scanning of the focused probes for 45° was examined in particular detail. The degree of convergence of the beam changes with the difference in curvature of the reflection surface. The lateral resolution is worse than the depth resolution because of the use of a spherical surface as the reflection surface. In designing the probe, greater emphasis was placed on the depth convergence resulting in less convergence of the lateral focus.

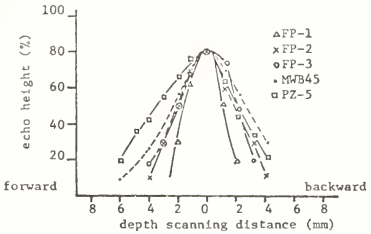

Figure 7-1. Depth scan for 45°.

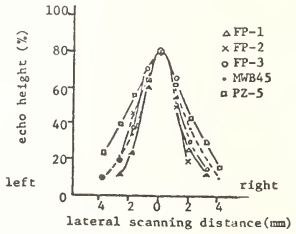

Figure 7-2. Lateral scan for 45°.

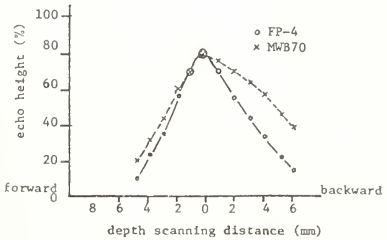

Figure 7-3. Depth scan for 70°.

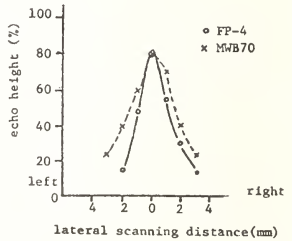

Figure 7-4. Lateral scan for 70°.

As seen from the depth scanning graph, the beam of the focused probe for 70° is well focused when the path length is short, but when the path length increases, the difference between focused and conventional probes becomes negligible. The reason is due to the large refraction angle, resulting in the upper and lower beam paths not coinciding in a single focal point. Instead, the focus results in a series of points along the beam path.

3.2. Spread of acoustic field

The spread of the acoustic field differs between the probes for 45° and 70° as considered in 3.1. From figure 8, the spread of the acoustic field of the focused probe for 45° is narrow and the scanning distance in which the echo height reaches 70 percent of the peak on axis is about 2 mm. The lateral resolution of the 70° probe is considerably broader and it is very difficult to measure quantitatively.

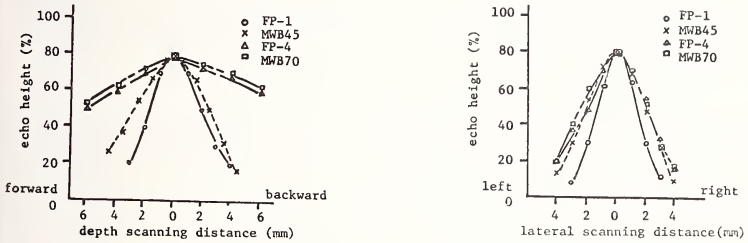

Figure 8. Spread of acoustic field.

3.3. Test of artificial defects

In examining the peaks of the upper and lower edge echo of the artificial defects, the focused probe separated these echoes for smaller defects to a greater extent than was possible with the conventional probe. There was complete separation for the conventional probe with respect to large defects but the pattern was not clear compared to the pattern received from the focused probe. When the conventional probe was used, the second echo was comparable to the noise echo and often difficult to evaluate. Table 1 shows the test result.

Table 1. Test of artificial flaws.

Probe / Test Block	ds	hs	FP-1 du	FP-1 hu	MWB45 du	MWB45 hu	PZ-5 du	PZ-5 hu	FP-4 du	FP-4 hu	MWB70 du	MWB70 hu
1 - 1	10.0	1.0	-	-	-	-	-	-	-	-	-	-
1 - 2	19.0	1.0	19.7*	0.7	-	-	-	-	-	-	-	-
1 - 3	10.0	2.0	10.8	1.8	11.6*	1.6	11.3*	2.4	11.2*	2.4	-	-
1 - 4	18.0	2.0	17.6	1.8	19.7*	0.7	17.9*	2.5	18.3*	2.2	-	-
2 - 1	10.0	4.0	10.5	4.2	8.9	5.1	9.9*	4.5	9.6	4.7	11.5*	5.2
2 - 2	16.0	4.0	15.8	3.9	15.4	4.3	15.8*	4.2	15.9	3.5	17.0*	7.7
2 - 3	10.0	8.0	10.1	8.2	10.4	6.4	10.2	8.1	9.6	7.4	12.1*	8.0
2 - 4	12.0	8.0	12.3	8.1	12.5	6.9	12.3	7.7	10.7	8.3	11.5*	9.1

ds: real depth (mm)
hs: real heighth (mm)
du: measured depth (mm)
hu: measured depth (mm)
- : this cannot test artificial flaw

When the defect was small, there was incomplete separation of the two echoes. In order to determine the location of the second echo, a line was drawn from the lowest point between the two peaks to the base line. These were marked by an asterisk. The focused probe for 45° could separate flaw echoes from a defect of 2 mm but the conventional probe could not separate the two echoes unless the defect was larger than 4 mm. The focused probe thus gave better results than the other in the evaluation of flaw echo patterns.

The 70° focused probe could separate flaw echoes from defects of 4 mm; the conventional probe could separate the flaw echoes but the evaluation was difficult to distinguish from the noise echo. Although better results were achieved using the focused probe compared to the conventional probe, the performance of the 70° probe did not measure up to the expected level.

3.4. Test of natural defect in welded part

The shape of natural defects is complicated but with respect to simple shapes, the focused probe may be better than the conventional probe in searching the upper and lower echo. Table 2 shows only the results for the 45° probe for the Number 1 type specimen. The focused probe had a precision in determining the defects within 0.5 mm. The conventional probe gives only one edge echo. Figure 9 shows the difference between the real depth or height and test results.

Table 2. Testing of natural flaws.

Probe / Test Block			FP-1		MWB45	
	ds	hs	du	hu	du	hu
TC - 1	5.5	10.0	4.7	9.2	7.2	7.4
TC - 2	9.0	6.0	9.7	4.2	8.3	7.7
TC - 3	12.7	3.4	10.5	4.9	10.0	5.0
IP - 1	9.0	5.3	9.3	5.3	9.3	4.6
IP - 2	8.7	6.0	8.2	5.7	7.2	7.1
IP - 3	6.8	1.2	11.4	1.1	-	-
SI - 1	12.0	3.0	11.8	2.5	-	-
SI - 2	7.4	7.0	7.5	7.1	7.6	7.8
SI - 3	7.4	8.4	7.9	6.7	7.2	6.8

TC: transverse crack
IP: incomplete penetration
SI: slag inclusion
- : uncertain

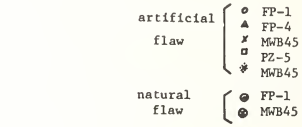

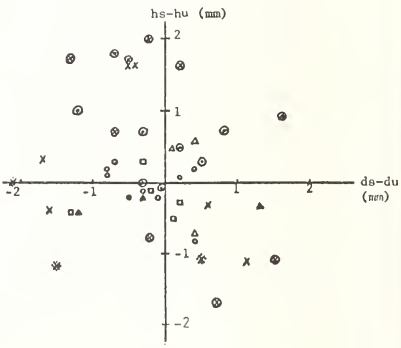

Figure 9. Difference between real heights or depth and test results.

Figure 10 shows the test result for the Number 2 type specimen; hu and hu' are the results for ultrasonic testing. The results show a good relation between the real defect and the result for ultrasonic testing; γ, σ and $\bar{\varepsilon}$ represent the correlation coefficient, standard deviation of error and mean value of error respectively.

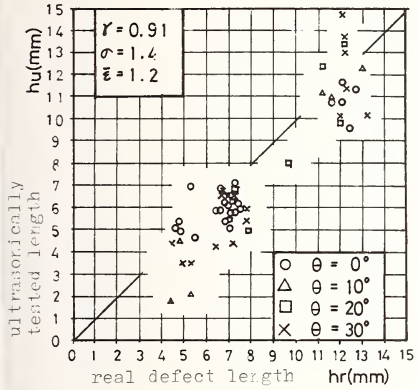

Figure 10-1. Relation between maximum value of hu and hr.

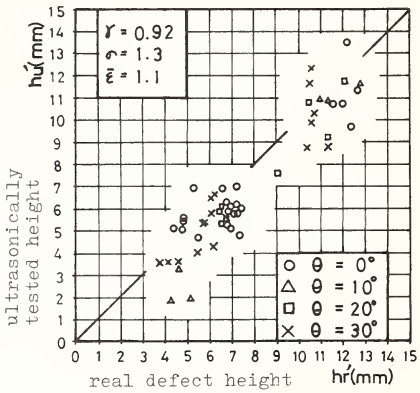

Figure 10-2. Relation between maximum value of hu' and hr'.

4. Conclusion

This work has shown that focused angle probes, based on the curved surface reflection method, can be used for the measurement of the depth and height of a flaw. The 45° focused probe could separate completely flaw echoes from defects of 2 mm, while conventional probes could not separate two echoes unless the defect was larger than 4 mm. In particular, the second echo for the focused probe was clear and separated completely from the noise echo.

Further development is necessary to utilize the full potential of focused probes. For example, in utilizing the spherical surface as a curved surface, it is easy to produce a wedge focal zone, but there is the additional possibility of line focusing, as in the case of the 70° probe. Therefore, in order to obtain a point focus, smooth curvature, gradually different in radius, is necessary. Also, the shape of the wedge is important. It is necessary to produce a wedge of small size to reduce the spread of the reflection signal. Finally, the aberration of a curved surface and the apparent location of a transducer is important in calculating the shape of the focused probe. However, no theoretical solution is available at the present.

National Bureau of Standards Special Publication 596, Ultrasonic Materials Characterization, H. Berger and M. Linzer, eds., Proceedings of the First International Symposium on Ultrasonic Materials Characterization held at NBS, Gaithersburg, Md., June 7-9, 1978. Issued November, 1980.

THE FOCUSED SOUND FIELD - A VERSATILE TOOL FOR ULTRASONIC EVALUATION OF MATERIALS

Udo Schlengermann

Krautkrämer GmbH
Postfach 420250, D-5000 Köln 41
Cologne, W. Germany

The focusing of sound fields for materials testing and medical applications is mainly achieved through diffraction. This also applies to the plane circular piston transducer with the structure of the field determined by the dimension 2a of the sound source and by the wave length λ. In the case of the lens-focused sound field, the radius of curvature r of the lens and the refraction index c_1/c_2 are additionally available as variables for controlling the sound field. This is why focusing transducers provide greater potential in practical testing applications.

Based on a generally applicable model of the focused sound field, it is demonstrated by some examples of practical applications how to find the transducer (mostly focusing) that provides an optimal solution of the test problem avoiding the troublesome trial and error method; the plane transducer is included in our considerations as a limiting case.

For both detection and measurement of critical reflectors, these focusing transducers can be of advantage.

1. Introduction

With ultrasonic nondestructive materials testing, it is important to arrange the interction between the sound waves and the medium so that the measured effect is as great as ssible. Assuming that the test problem is defined, the parameters of the sound field or und source must then be chosen so as to obtain an optimal interaction. However, troubleme trial and error approaches should be avoided if possible. In this paper, the followg will be discussed: Why focused sound fields provide greater opportunities for optimizing e interaction; how to obtain generally applicable data for focused sound fields using appropriate models; how to make use of these generally applicable correlations for particular testg problems; and the possibilities provided by focused sound fields in determining the sizes reflectors.

Because it is most commonly used, only a transducer with a circular piston oscillator d a spherical lens will be considered here; however, the essential conclusions of this per apply also to other methods of forming focused sound fields and to other types of cillators. The properties of the focused sound field will be compared, as far as possie, with those of the known sound field from a plane circular piston and the similarities all be pointed out.

2. Matching a Sound Field

Figure 1 demonstrates in principle what is meant by "matching a sound field": Properes of the material under test are to be determined within a given depth zone Δz. The sound eld parameters must now be chosen so that the field covers this depth zone Δz.

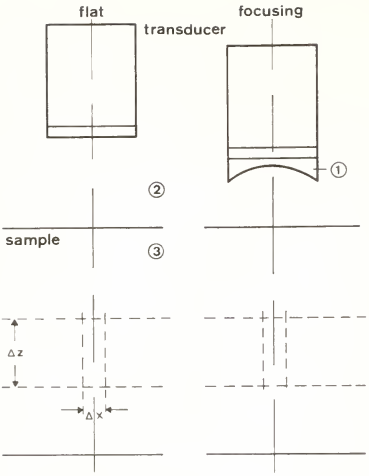

Figure 1. Matching a sound field.

Suppose, for instance, a plane transducer is chosen with a particular frequency; it will then be possible only to make the sound field coincide with the depth zone Δz by changing the delay path v. However, this no longer allows the beam width to be matched to the zone width Δx; moreover, the signal transit times may become excessive due to a long water delay path v. The focusing transducer, however, at the same time enables matching to the depth zone Δz with a given width Δx and a given water delay path v. This is because in the case of the focusing transducer, additional parameters determine the structure of the sound field, thus increasing the degrees of freedom for the matching [1][1].

The sound field structure (pressure P) from a plane transducer depends on the transducer radius a, the frequency f, the sound velocities c_2 and c_3 involved and the delay path v:

$$P = f(a,f,c_2,c_3,v) \quad . \tag{1}$$

In the case of a transducer focusing through a lens, the effects of the lens curvature r and the sound velocity c_1 of the lens are included:

$$P = f(a,r,f,c_1,c_2,c_3,v) \quad . \tag{2}$$

In practical testing, the sound field frequently has to meet the following requirements: How to achieve a required testing sensitivity within the given scanning zone; how to achieve a desired lateral resolution; how to obtain as even a pressure distribution as possible within the scanning zone; and how to achieve the signal transit times desired, i.e., the test velocities.

3. Characteristics of the Focused Sound Field

In ultrasonic testing within the MHz range, the wavelength λ is not negligibly small in relation to the dimensions of the transducer. Therefore, diffraction influences the structure of the sound field [2-4]. Because of the coherence of ultrasonic waves, the field obtained will always be characterized by interference patterns. With sound fields from circular sources, whether focused or not, these structures are always rotationally symmetric with respect to the field axis.

[1]Figures in brackets indicate the literature references at the end of this paper.

The field data which is mainly of interest in practical testing are the sound pressure distribution and the phase relationships, the latter with reference to measurement techniques and, in particular, to imaging techniques.

Figures 2 and 3 show an example for an immersion-type 5 MHz transducer, 20 mm in diameter. The pressure distribution on the acoustic axis in figure 2 shows a near field with varying pressure followed by the focal region [2,3]. The point of the highest sound pressure is taken as the focus because it is also experimentally easy to identify. It is not identical with the point at which all elementary waves are in phase [2,3]. The sound pressure profile at the in-phase point is identical with the diffraction pattern of the sound source [2-4]. With a circular transducer, the pressure distribution is determined by the Bessel function (fig. 3):

$$P = 2J_1(X)/X \quad \text{with} \quad X = 2\pi q/\lambda z_f \quad , \tag{3}$$

where q is the lateral distance from the axis and z_f is the focal distance.

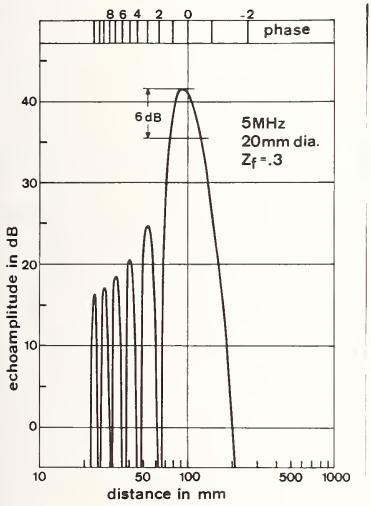

Figure 2. Sound pressure distribution acoustical axis.

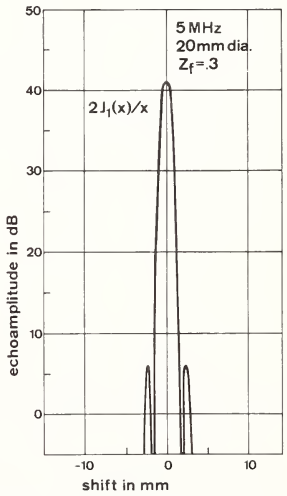

Figure 3. Sound pressure profile distance z(0).

Within the focal region, the cross-sectional profiles correspond to the same function as the profiles in the distant far field (infinity) of the unfocused sound field. This similarity is easier to understand when looking at the phase relationships in the sound field of the circular piston transducer. Sound pressure extremes (maxima or zeros) on the acoustic axis always occur when the path difference between the central ray and the ray from the transducer's edge just equals a multiple of $\lambda/2$ [5]. If the difference is $n\lambda/2$, then the cross-sectional profile has n extremes there. Because of the symmetry there are maxima on the axis if n is odd-numbered and zeros if n is even-numbered. These multiples of n to the phase relationship are drawn on the top of figure 2 [2]. Whereas with a plane transducer having no lens the travel distance of the edge ray is always longer than that of the central ray (the difference is zero only at infinity), the inverse case occurs with the focused field beyond the focal range: the travel distance of the edge ray is shorter than that of the central ray and that is why a negative sign is shown at the top of figure 2. The phase difference δ now increases as the distance to the transducer increases. At infinity it is given by

$$\delta_{max} = \frac{h_a}{\lambda_2}\left(\frac{c_2}{c_1} - 1\right) \quad , \quad \text{with } h_a = r - \sqrt{r^2 - a^2} \quad . \tag{4}$$

As the sign is of no importance for the phase difference, part of the near field reappears in the focused sound field beyond the focal range.

Consequently, this part of the field must be excluded from being used for testing for the same reasons as is the near field region of the plane transducer. Also, for imaging, the focal region should be used exclusively because a plane wave front exists only in that region and not at greater distances.

4. General Relationships

The relationships of the field parameters of the plane circular transducer can be transformed by means of appropriate normalization so that generally applicable relationships are established independent of the size of the transducer, the frequency and the material.

This is also attained to a great extent with focused sound fields when using the same normalizations:

For the distance z:

$$Z = z\,\lambda/a^2 \tag{5}$$

For the transverse shift q:

$$Q = q/a \tag{6}$$

These values will be referred to as the relative distance and relative transverse shift, respectively.

With the focused sound field, the following relative values are required in addition:
For the curvature r:

$$R = r\lambda/a^2 \tag{7}$$

For the focal distance z_f:

$$Z_f = z_f\lambda/a^2 \tag{8}$$

The value Z_f is known as the focusing factor [2,3].
For the beam width 2b at the focal distance z_f:

$$2B = 2b/a = \text{constant } Z_f \tag{9}$$

Hence, a simple linear relation exists between the focal distance and the beam width, an advantage of the normalization.

The constant is dependent on the dB-drop which is used for defining the beam width; for 6 dB, the constant equals 0.514. The focusing factor ranges always between 0 and 1 [2,3]. If one succeeds in establishing relationships between the sound field properties, which are important for the test, and these normalized values, and in particular with the focusing factor Z_f, then focused sound fields can be matched for any transducer size, for all frequencies and any medium to the particular test problem.

The following relationships are of particular interest: What is the relationship between the relative lens curvature R and the focusing factor Z_f (relative focal distance)? What is the relationship between the focal sound pressure and the focusing factor? What is the relationship between the relative length of the focal range (Z_a-Z_e) and the focusing factor? What is the relationship between the relative width of the focal range 2B and the focusing factor?

The last relationship is described by eq. (9), while the first three are given in figure 4. Based on extensive computations, figure 4 shows the following general functions of the focusing factor Z_f which are of interest for refraction coefficients ranging between

0.55 and 0.60: the increase in amplitude with respect to the unfocused field ($Z_f = 1$); the relative radius of curvature R of the lens; the relative start Z_a and end Z_e of the focal range (6 dB echo drop). (Also refer to the appendix.) The absolute values are then obtained from eqs. (5-10).

As focusing is a phenomenon of diffraction, there are, of course, limitations to focusing which are related to the ratio a/λ, whereby the possibilities of focusing increase as a/λ increases [6]. With focusing transducers, approximately 1.5 λ is the smallest beam width (6 dB echo drop) realizable in practice [7].

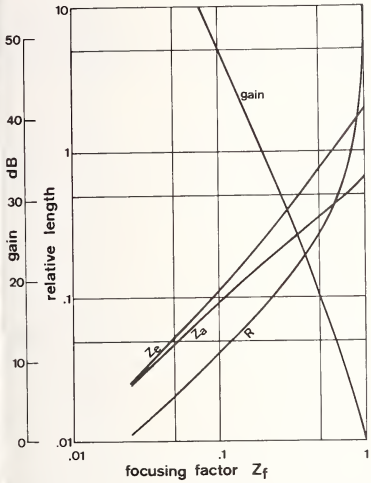

Figure 4. Functions of focusing factor.

Theoretical focusing effects will, of course, only be realized if the entire transducer area is able to radiate into the work piece. Figure 5 shows that limitations exist here, too. With both liquid and solid delay paths, it may happen, particularly with angle testing, that the outer portion of the sound beam is totally reflected from the interface, thus failing to contribute to the sound field; the focusing effect will be correspondingly weaker [6].

5. Matching the Focused Sound Field

The curves in figure 4 help to find immediately the focusing data for a given transducer. But how does one proceed in the reverse case, i.e., how does one find the focused sound field and the associated transducer which is appropriate to a given testing problem? As previously explained in connection with figure 1, the focal region (Z_a-Z_e) should exactly cover exactly the depth zone $\Delta z = z_1 - z_3$ (eqs. (11,12)). Requirements on the beam width or testing sensitivity result in requirements on the near field length N (eq. (13)). Requirements on the delay path are often to be met at the same time (eq. (13)). Using the general parameters p_i and q_i, the simultaneous equations below are established:

$$Z_a N_2 - v = (c_3/c_2) z_1 \qquad (10)$$

$$Z_e N_2 - v = (c_3/c_2) z_3 \qquad (11)$$

$$N_2 = f(p_i) \qquad (12)$$

$$v = g(q_i) \qquad (13)$$

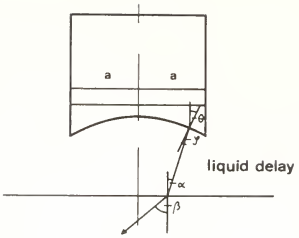

Figure 5. Limitations of focusing.

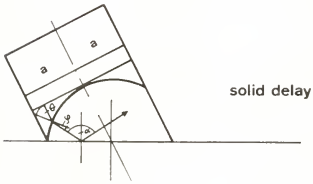

These four simultaneous equations for the two variables N_2 and v have a solution only if the following conditions are fulfilled at the same time:

$$(c_3/c_2)(z_3-z_1) = f(p_i)(Z_e-Z_a) \tag{14}$$

$$(c_3/c_2)(z_3Z_a-z_1Z_e) = g(q_i)(Z_e-Z_a) \tag{15}$$

As an explanation, two examples of practical significance will be given in the following: 1) The multiple echoes from the delay path v must not interfere with the echo signals from the range $\Delta z = z_1-z_3$:

$$v \geq (c_2/c_3)z_3 \tag{16}$$

From eqs. (14,15), it can be seen that all solutions are acceptable which fulfill the following:

$$\frac{Z_e}{Z_a} \leq \frac{z_3\left[1 + (c_2/c_3)^2\right]}{z_1 + (c_2/c_3)^2 z_3} \tag{17}$$

2) A beam width of 2b is desired within the zone $\Delta z = z_1-z_3$. The following results for N_2:

$$N_2 = 4b^2/\text{const.}Z_f^2\lambda_2 \quad . \tag{18}$$

Eqs. (14,15) show that any focusing is acceptable which fulfills the following:

$$\frac{Z_e - Z_a}{Z_f^2} = \frac{\text{const.}^2\, c_3(z_3 - z_1)}{4b^2 f} \quad . \tag{19}$$

Again, the constant equals 0.514 for a 6 dB echo drop.

In order to solve such problems, it is important to know the course of the functions z_e/Z_a or $Z_e - Z_a/Z_f^2$. This is shown in figure 6.

From equations like (17) and (19), one can determine whether the problem can be solved, and if so, what focusing factor is to be used. The unknown parameters a, r, and v can then be obtained from figure 4 or eqs. (5-9). Examples of this can be found in reference [6].

6. Examples of Applications

The theoretical characteristics of focused sound fields described above will now be complemented by some practical applications. Using these results, it was immediately possible to select or build the optimum focusing transducer for each of the test problems studied. The desired properties were then verified experimentally.

6.1. Tube testing employing a focused sound field

Figure 7 is a schematic representation of the sound beam travel in tube testing applications. Reflectors are to be detected on the inner surface within a half skip distance and on the outer surface within a full skip distance. The transducer must be chosen so that its

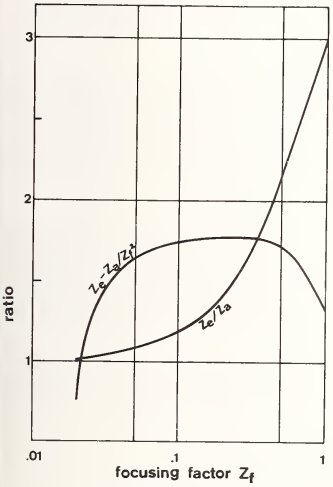

gure 6. Functions of focusing factor.

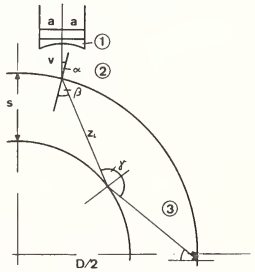

1. $v \geq 2(c_i/c_s)\, z_i$
2. $v \geq Z_a(a^i/\lambda_i) - (c_s/c_i)\, z_i$
3. $v \leq Z_e(a^i/\lambda_i) - 2(c_s/c_i)\, z_i$
4. $v \geq Z_a(a^i/\lambda_i)$
5. $v \leq Z_f(a^i/\lambda_i)$

Figure 7. Tube testing with focusing transducers.

ound field provides sufficient sensitivity within this flaw expectancy range for detecting e reflectors which are often extremely small (smaller than the wavelength λ). At the me time, there should be no interference with the sound beam on the tube surface other an refraction at the angle β.

The best results could be proven by systematic experiments when the transducer was osen in accordance with the following considerations: The flaw expectancy range in the be must be within the focal range of the sound field (6 dB echo drop), eqs. (21,22); the ter/tube interface must be located between the start of the focal range z_a and the focal int z_f, eqs. (23,24); and multiple echoes from the delay path v are to be prevented from lling into the flaw expectancy range by the transit time, eq. (20).

Set up a pattern of equations as follows, so that requirements are obtained for the delay path v, and implicitly for the transducer size 2a and the radius of the lens r at a given frequency f.

$$v \geq 2(c_2/c_3)z_i \tag{20}$$

$$v \geq Z_a(a^2/\lambda_2) - (c_3/c_2)z_i \tag{21}$$

$$v \leq Z_e(a^2/\lambda_2) - 2(c_3/c_2)z_i \tag{22}$$

$$v \geq Z_a(a^2/\lambda_2) \tag{23}$$

$$v \leq Z_f(a^2/\lambda_2) \tag{24}$$

6.2. Testing titanium forgings

The forgings for aircraft construction were 260 mm in diameter. They had to be tested in the entire area from 30 mm below the surface through to the core, the scanning sensitivity being as uniform as possible. A reflector with a circular disk equivalent to 1.2 mm was to be reliably detected.

An investigation of the attenuation properties showed that only frequencies below 10 MHz were suitable. Based on the above considerations, a transducer was built with a commercial 5 MHz transducer, 40 mm in diameter. With a focusing factor of $Z_f = 0.33$ at a 35 mm water delay path, the desired reflectors could be detected in the entire testing range of 100 mm titanium without any electronic compensation and with amplitude variations smaller than 6 dB.

6.3. Detection of inclusions in welded plate

In the case of welded heavy steel plate destructive testing showed that there were substantial differences in the elongation properties in the direction of thickness. It was assumed that this behavior might have been due to differing degrees of purity of the plates involved. A nondestructive testing method was therefore sought which could be used for determining the number of inclusions in the parent material within the heat-affected zone and the weld.

A system for determining the degree of purity in roller-bearing steels in accordance with ASTM was used for testing these 160 mm thick welds while the evaluation of the system was slightly altered (fig. 8). A transducer had to be developed which was capable of detecting inclusions of 0.2 mm circular disk equivalent even at these great thicknesses.

Because of the sound attenuation in the material, the only suitable frequency was 5 MHz. With a 40 mm diameter transducer, a focal range length of 50 mm in steel could be obtained. In order to enable the number of inclusions to be exactly allocated to their location, the evaluation was carried out separately in five depth zones (fig. 8). In each case, the tested volume was only $(120 \cdot 10 \cdot 3)\text{mm}^3 \approx 3.5\ \text{cm}^3$. In the lower diagram of figure 8, the counter outputs from the two hatched depth zones (that is from approximately 7 cm^3 in each case) are drawn over the track on which they had been detected. The circular disk equivalents were 0.5 mm, 0.7 mm and 1.0 mm. The example in figure 8 is a plate which is not very pure.

Whereas the number of inclusions remains statistically constant in the parent material, the heat-affected zone shows a considerable increase in inclusions far beyond the level of the parent material.

The melted material itself is flaw free. It is assumed that the inclusions contained in the parent material widen due to the heat influence thus causing a different elongation behavior of the sample in the direction of thickness. In any case, the number of inclusions obtained from different plates could be correlated with the differing elongation behavior.

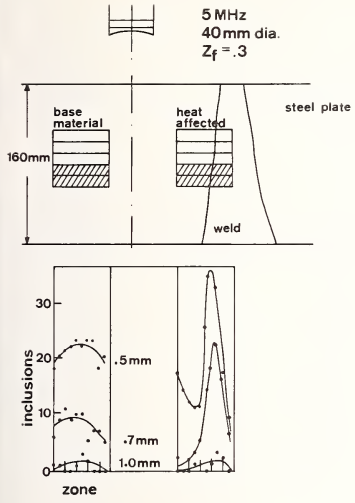

Figure 8. Counting inclusions in thick welded plate.

6.4. Testing thick welds

Immersion testing is frequently not feasible on samples having thick welds as, for nstance, pressure vessels. That is why for this test application, focusing transducers ere developed for direct contact [7]. Because of the direct coupling, these transducers re designed for a certain scanning zone, (fig. 9). Table 1 shows a range of such direct ontact transducers, their scanning zones joining one to each other (also shown in fig. 9). he transducers for normal testing (angle 0°) operate on longitudinal waves, the transducers or angular testing (angle 45°) on transverse waves. This table also shows the maximum and inimum limits of the 6 dB focal range for steel (in depth direction, fig. 9) as well as the eam width at the focal point. These transducers are coupled by means of running water.

Table 1. Scanning zones of transducers.

Type	Angle	Upper	Lower	Beam
NQP2-34	0°	40 mm	90 mm	5.0 mm
NQP2-50	0°	80 mm	165 mm	6.5 mm
NQP2-75	0°	150 mm	270 mm	8.0 mm
WQP2-34	45°	40 mm	100 mm	5.0 mm
WQP2-50	45°	85 mm	190 mm	6.0 mm
WQP2-75	45°	160 mm	300 mm	7.0 mm

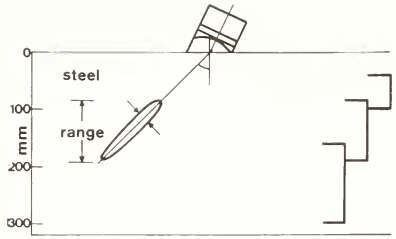

Figure 9. Weld testing with direct-contact focusing transducers.

type	angle	upper	lower	beam
NQP2-34	0°	40mm	90mm	5.0mm
NQP2-50	0°	80mm	165mm	6.5mm
NQP2-75	0°	150mm	270mm	8.0mm
WQP2-34	45°	40 mm	100 mm	5.0 mm
WQP2-50	45°	85 mm	190 mm	6.0 mm
WQP2-75	45°	160 mm	300 mm	7.0 mm

7. Flaw Size Evaluation Using a Focused Sound Field

The methods for evaluating the size of reflectors most commonly used today are classified in two groups: 1) determination by means of echo amplitude (A-scan), and 2) determination by means of scanning the reflector with the sound beam (C-scan).

When detecting and measuring reflectors using a focused sound field, either approach can only rely on the focal region as only there the required testing sensitivity can be obtained. Also, an approximately plane wave front with a sound pressure profile, as occurs in the far field, with the plane transducer exists only in that region.

The adaptability of the focused sound field is also of advantage when determining reflector sizes. The testing sensitivity can be increased selectively or the ratio between sound beam width and the reflector diameter selectively changed [9].

As mentioned previously, the same physical conditions exist in the focal range as in the far field of the unfocused field. All considerations with regard to flaw size determination in the far field of the plane circular transducer can thus be applied to the focused sound field [7].

As the cross-sectional distribution of the sound pressure in the focal range is determined by the Bessel function (eq. (3)), DGS diagrams can be developed for focused sound fields just as for unfocused ones [8]. Using these, the testing sensitivity can be adjusted without a reference block containing reference reflectors.

In the case of the scanning methods, the known rules for unfocused fields [10,11] can be transferred to focused ones when scanning the reflectors with the profile at the focal distance. When scanning reflectors, the factors, (demonstrated in fig. 10, top) which are to be considered are as follows. A point reflector (left) always produces a shift to each threshold level and the shift is much greater than the extent of the reflector due to the size of the measuring sound beam. Also, a reflector which is smaller than the beam width associated with the chosen threshold level will be over-estimated in its size [10]. Thus, an accurate determination of reflectors which are smaller than the beam width is only

ssible using the echo amplitude (DGS method). If the reflector diameter is greater than e beam diameter, then it is possible to determine the size by scanning, (fig. 10, top ght). The measured shift, however, is not simply the addition of the reflector size d the sound beam width, and correction curves have to be used [10,11].

Approximately, the 20-dB sound-beam width can be used as a limit, $2\rho'$, between the two thods. If the reflector diameter 2ρ is expected to be smaller than this limit, the DGS thod is to be chosen; otherwise, the scanning method:

$$2\rho' = 0.869\ a\ Z_f \quad . \tag{25}$$

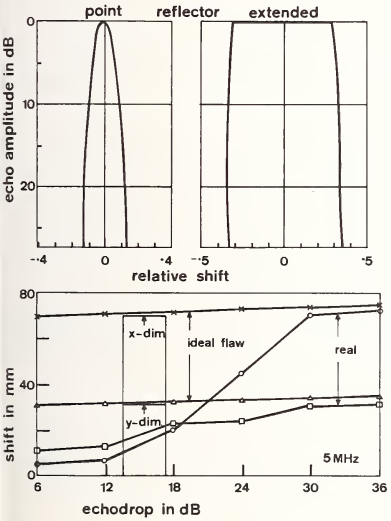

Figure 10. Flaw sizing by scanning.

According to eq. (9) the beam width for the focused sound fields can now be selectively osen so that it remains below the limit as per eq. (25). Exact scanning results are then so obtained from reflectors of only a few millimeters in size. However, only ideal re- ectors are independent of the threshold [7,12]. With rough and irregularly-shaped reflec- rs, the echo amplitude varies greatly, even if the reflector is fully covered by the sound am. Only if the threshold is set sufficiently below the maximum indication, the actual ze of the discontinuity will be obtained [12].

For demonstration purposes, the scanning results from an ideally smooth reflector of 1.70)mm^2 are compared in figure 10 (below) with the results from an equally-sized rough lue to fracture) reflector at a frequency of 5 MHz for different thresholds [7]. Only the rgest continuous shift was rated as a reflector elongation (separately for the X and Y rection). The curves for the ideal reflector (x,Δ) show that the true size of x = 70 mm d y = 31 mm was determined with a threshold of 6 dB below the maximum. With lower thresh- ds, the measured shift is larger than the reflector. The increase seems to be linear with spect to the threshold lowering rate but this is due to the scale of figure 10. The sound am used is only about 3.5 mm wide and therefore the increase appears to be linear; however, e increase has a Bessel function dependence (eq. (3)) (see fig. 3), getting smaller with a wer threshold.

According to eq. (26) the maximum possible error Δ in the case of a non-corrected size determination is as follows:

$$\Delta = 0.610 \; a \; Z_f \quad . \tag{26}$$

It is derived through the following consideration. With the 6-dB echo drop, the reflector size is exactly determined [10], the axis of the sound field points exactly to the transducer edge, that means that only half the sound beam is still on the reflector. When the complete beam is next to the reflector then the dB drop is infinite. So, a greater error than half beam width is not possible (echo amplitude drop to zero). However, between the zero points, the total sound beam width (eq. (3)) is $2b = 1.220 \; a \; Z_f$. Half of it gives eq. (26).

Also in the lower diagram of figure 10, the measuring error, in the case of the ideal reflector, can only amount to about 4 mm, even if the threshold is very low.

As the curves (□ ,o) demonstrate, the real reflector seems to be divided into a number of individual reflectors. It is only with a threshold around 30 dB below the maximum indication that the scanning result represents the reflector dimensions in the x and y direction approximately correctly.

As desirable as the heavy constriction of the sound beam is for reflector scanning, with real reflectors it may have undesirable effects. The narrower the sound beam and the shorter the wavelength, the stronger is the reflector behavior formed by the position and quality of the reflector area. This is why in most cases a focused sound field can be used for measuring plane reflectors, but not for detecting them. As the example of the welded plate with inclusions shows, the directional characteristic is no longer all that important for very small reflectors; here it is solely the scanning pattern which has to be carefully matched to the small sound beam width of the focused field.

A remedy to such splitting up of the testing methods into detection and measuring techniques will be provided as soon as focused sound fields with their advantageous properties in testing can be made controllable; that is, when the detection technique automatically turns into a measuring technique the moment a reflector has been detected.

Appendix

The normalization eqs. (5-9) given in the paper provides generally applicable functions enabling all the important data of the focused sound field for various transducer sizes, frequencies and sound velocities to be analyzed. However, with the exception of eq. (9), these functions are by no means linear with Z_f or with the value a^2/λ contained therein as is demonstrated by figure 4.

The basic values for the curves in figure 4 obtained through exact computation were therefore approximated by suitable polynomials according to the method of least squares. Depending on the nature of the functions, log/log of lin/log functions are recommended for this. With good accuracy in the interval $0.01 \leq Z_f \; 1$ or $0.01 \leq R \leq 3$, the following mathematical expressions are the results for the most commonly used curves of figure 4:

$$\log Z_f \approx -0.08844 + 0.28781(\log R) - 0.24581(\log R)^2 + 0.00839(\log R)^3 + 0.00134(\log R)^4 \tag{A1}$$

$$\log(Z_e - Z_a) \approx 0.11696 + 1.18464(\log Z_f) - 1.84700(\log Z_f)^2 - 1.73982(\log Z_f)^3 - 0.57720(\log Z_f)^4 \tag{A2}$$

References

1] Schlengermann, U., Die automatische Ultraschallprüfung mit der Impus-Echo-Methode als Informationssystem; DGZfP-Jahrestagung Nijmegen, NL (1974).

2] Schlengermann, U., Schallfeldausbildung bei ebenen Ultraschallquellen mit fokussierenden Linsen, Acustica, 30, 291-300 (1974).

3] Schlengermann, U., Focusing ultrasonic transducers and their characteristics, ASNT Fall Conf., Detroit, MI (1977).

4] Penttinen, A. and Luukkala, M., Sound pressure near the focal area of an ultrasonic lens, Phys. D. Appl. Phys., 9, 1927-1936 (1976).

5] Stenzel, H., and Brosze, O., Leitfaden zur Berechnung von Schallvorgängen, Springer-Verlag, Berlin, 74ff (1958).

6] Schlengermann, U., Kriterien zur Auswahl fokussierender Ultraschall-Prüfköpfe, Materialprüf., 19, 416-420 (1977).

7] Schlengermann, U., Fehleranalyse mit fokussierenden Prüfköpfen, React. Safety-Seminar, IZfP, Saarbrücken (1978).

8] Wüstenberg, H., and Kutzner, J., Empfindlichkeitseinstellung beim Einsatz fokussierender Prüfköpfe in der Ultraschall-Prüfung an ebenen und gekrümmten Bauteilen, Materialprüf., 19, 441-444 (1977).

9] Kanevskii, I. N., and Nisnevich, M. M., Enhancement of ultrasonic flaw detection sensitivity by means of focusing systems, Sov. J. Nondestr. Test., 12, 428-438 (1976).

10] Schlengermann, U., and Frielinghaus, R., Beitrag zur Fehlergrößenbestimmung mit Ultraschall durch Fehlerabtastung mit relativer Schwell, Materialprüf., 15, 50-56 (1973).

11] Schlengermann, U., Beitrag zur Fehlergrößbestimmung mit fester Schwelle, Materialprüf., 16, 319 (1974).

12] Saglio, R., Prot, A. C., and Touffait, A. M., Determination of defect characteristics using focused probes, Mater. Evaluation, 36, 62-66 (1978).

National Bureau of Standards Special Publication 596, Ultrasonic Materials Characterization, H. Berger and M. Linzer, eds., Proceedings of the First International Symposium on Ultrasonic Materials Characterization held at NBS, Gaithersburg, Md., June 7-9, 1978. Issued November, 1980.

OPTIMIZATION OF ULTRASONIC TUBE TESTING WITH CONCENTRIC TRANSDUCERS

Jean-Pierre Dufayet and Raymond Gambin

DDEC/SDEEC/GET
CEN Cadarache BP no. 1
13115 St Paul lez Durance
FRANCE

Tube testing can be carried out without rotation by the use of concentric transducers, with conical and helical mirrors to detect transverse and longitudinal defects, respectively. This principle has already been described in many publications, notably at the Eighth World Congress on Nondestructive Testing [1,2][1]. Complementary studies have been carried out to improve the technique, so that it is now in a fully operational state. The respective advantages of a system with rotating masks, or employing sector transducers, are discussed.

1. Introduction: Objective of the Work

One of the standard methods of detecting flaws in an object is by ultrasonic testing, which in particular gives evidence of the presence of possible cracks (discontinuities of the surface reflect ultrasonic waves). To improve the sensitivity of the method, focused transducers are generally used; it is then necessary to set the object in motion, so that it can be totally examined.

In the case of cylindrical objects (tubes and bars), the examination is customarily made in a helical pattern. Two methods are then possible: either the transducers can be fixed, with the object having a helical motion (being driven forward while being rotated), or the transducers can be given a rotary movement (rotating head), with the object being advanced. With either method, the rotational movement requires complex and awkward mechanics if adequate test data are to be obtained at high speed.

The development of ultrasonic techniques has resulted in an elegant solution to these difficult problems. The annular array, with the advantage of circular symmetry, makes a complete examination possible without rotation, and has the advantages of mechanical simplicity and the capability of much increased translational speed, of up to around a meter per second.

The apparatus consists essentially of annular transducers which emit a homogeneous sheet of ultrasound parallel to the axis of the object, and associated concentric mirrors which reflect this sheet according to a predetermined geometry constant across the beam. There are two mirrors, one of conical form to detect transverse flaws, and the other with the surface of a screw (i.e., helical) to detect longitudinal flaws. The object is moved longitudinally along the center of the array. The annular array is completely immersed in a bath of water, which provides the ultrasonic coupling. Each transducer is connected to an electronic measuring system.

2. Principle of Operation

2.1. Detection of transverse defects

Transverse defects present a maximally reflecting surface to waves progressing across the cracks. Therefore, the angle of incidence should be along the meridian. It is easy to

[1] Figures in brackets indicate the literature references at the end of this paper.

see from figure 1 that, to obtain a constant angle of incidence i, a conical mirror is required. Its apical angle is:

$$2\,\delta = \pi/2 + i\ .$$

The illuminated zone at any given moment is a defined length of tube:

$$b = 0.5\ (D - d)\ (\tan i + \cot \delta)$$

where D and d are respectively the external and internal diameters of the sheet of ultrasound emitted by the transducer. The phase relationship between the incident and refracted waves allows the detection of a crack lying within b. The defect gives a maximal echo provided that it lies in the corresponding direction.

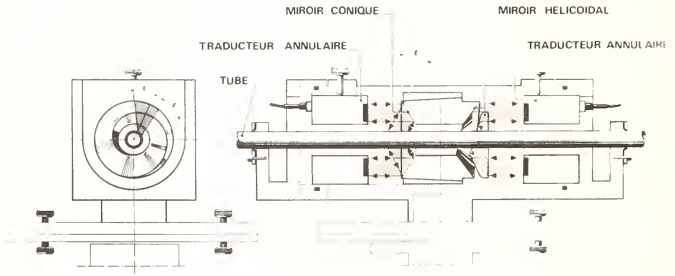

Figure 1. Quality control of cylindrical materials by ultrasound; view in the position of the inspection tank; transverse view left side of figure; longitudinal view on the right.

2.2. Detection of longitudinal defects

Longitudinal defects present a maximally reflecting surface to waves traveling in the long direction (ray R). The angle of incidence should be equatorial (see fig. 1). It can be seen that, to obtain constant angle of incidence i in this direction, the equatorial sections of the interposed mirror should be developed from a circle of the ray a = R sin i. The surface of the mirror is given by an equation in cylindrical coordinates:

$$z = \sqrt{(p^2 - a^2 + \theta a)}\ .$$

It is constructed by extending the tangent of the circular helix of the ray a of pitch $p = 2\pi a$; this can be done by turning.

The illuminated zone at any instant is a parallelogram of rotation limited by two arcs and by two complete whorls of helices of pitch p. The distance between the two whorls along the axis is:

$$c = 0.5\ [\sqrt{(D^2 - 4a^2)} - \sqrt{(d^2 - 4a^2)}]\ .$$

The phase relationship between the incident and refracted waves results in a wavefront of length c/sin i. The defect gives the maximal echo provided that it lies on the whorl of the helix corresponding to this direction. A cyclical resonance phenomenon is obtained for $c \cong p$; the defect is then seen on more turns with high intensity.

The continuity of the phase front is also better than that obtained with transducers with linear focusing; there are more than about ten cycles instead of only a few, and this compensates for the loss of sensitivity due to the lozenge-shaped emitter. Moreover, no parasitic echoes are generated.

3. Essentials of the Assembly

Several requirements have to be taken into consideration: in the first place, the quality of the transducer; the parallelism of the sheet of ultrasound, and the homogeneity of the field; next, the quality of the mirrors; conformity of the actual surface to that theoretically required, and coaxial alignment of this surface with the object under test.

The assembly is designed to satisfy these requirements as closely as possible. Figure 2 is a diagram of the arrangement. In the central part of the tank, there are the two surfaces of the mirrors (conical and helical); the annular transducers are in the other part of the tank. If it is necessary to increase the sensitivity of detection (by improving the signal-to-noise ratio), it is possible to add a system with a rotating mask which, by presenting a window of adaptable shape, samples only a portion of the sheet of ultrasound; it is then necessary, in order to study the entire surface of the object, to rotate the mask. Another method of achieving this sampling of a part of the sheet of ultrasound is simply to excite angular sectors of ultrasonic transducers in sequence by electronic commutation. The components of the assembly are listed in the following sections.

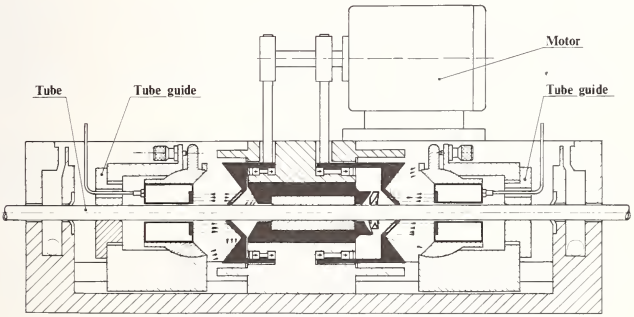

Figure 2. Inspection tank with rotating masks.

3.1. Tank

The tank is designed to contain the coupling liquid. It is a flow type, with three compartments, at a constant level [3]. The central compartment is the test section, and the lateral compartments are for overflow and recovery of the water. Two shafts cross the tank longitudinally. They serve to align the assembly.

3.2. The transducer assembly

This is composed of the transducer [4] and transducer mounting, as shown in figure 3; the two blocks face their respective mirrors. The transducer mounting permits precise adjustment of the transducer. The coincidence of the optical axis of the sheet of ultrasound with the geometrical axis of the assembly can be achieved by a knuckle-joint supporting the housing of the transducer. The alignment rings, independent of the knuckle-joint, define the axis of the system with precision. The transducers are easily demountable.

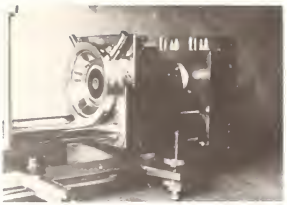

Figure 3. Transducer assembly.

3.3. The mirror assembly

This is composed of mirrors and the mirror mounting. The two mirrors are independent, mounted facing each other by a cylindrical adjustment, permitting centering.

3.4. Rotating masks

Because of the importance of the reflecting surfaces in the annular assembly, there is a residual ultrasonic noise which is simply of geometrical origin, and which is troublesome when searching for the maximum detection sensitivity. This problem may possibly be solved by the use of a mask [5] which intercepts part of the sheet of ultrasound, and so improves the signal-to-noise ratio; in order to maintain cylindrical inspection, it is then essential to rotate the mask, at a speed which depends on the shape of the mask and the speed of translational movement of the object during the course of its testing.

The system includes two types of screen (fig. 4), one for the detection of transverse defects, and the other for the detection of longitudinal defects. Attached to the corresponding mirrors, they are mounted respectively on two ball bearings, and rotated by a motor at constant speed (about 1500 revolutions per minute maximum), by means of ribbed belts.

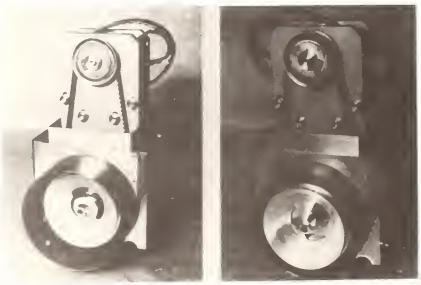

Figure 4. Masking arrangements. (a) With the helical mirror. (b) With the conical mirror.

The screens contain windows of shapes according to the type of detection. For transverse defects, the mask consists of one or more sector openings (in general, three at 120° intervals); in the case of longitudinal defects, the opening is helical, simply made up of two portions constructed on circles staggered by 180° and limited by the two concentric circles of the annular transducer.

3.5. Sector transducers [5]

The annular shape of the transducer is cut up into several sectors, the number and shape of which depends, as in the case of the rotating mask, on the type of detection.

For Transverse Defects. Very good results are obtained with three sectors staggered by 120° (see fig. 5[2]).

For Longitudinal Defects. Two sectors staggered by 180° are generally sufficient (see fig. 5[2]).

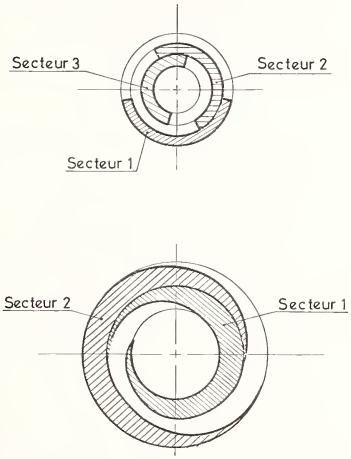

Figure 5. Transducer sectors. For transverse defects (top): 3 sectors of 170° with 50° overlap. For longitudinal defect (bottom): 2 sectors offset by 180°.

4. Results

The performance of the apparatus depends on the condition of utilization; i.e.: without rotating mask, with rotating mask, and without rotating mask, with sector transducer.

To put the matter into perspective, results obtained on stainless steel tubes of 8.65 mm diameter and thickness 0.575 mm are given below; the range of standard defects studied comprised internal and external longitudinal and transverse gaps of length 0.75 mm and of depth varying between 15 μm and 60 μm.

4.1. Performance of rotating mask

Figures 6 and 7 show the circumferential uniformity of the amplitude of the signal (transverse and longitudinal defects) without the rotating mask and with the rotating mask, for the same transducer and the same mirror. The observations follow.

[2]It is apparent from figure 5 that the active zones of the sectors overlap circumferentially. This is why these sectors are divided up on concentric annuli. The results which follow show in effect that such overlapping is necessary for uniform circumferential sensitivity in the detection of faults.

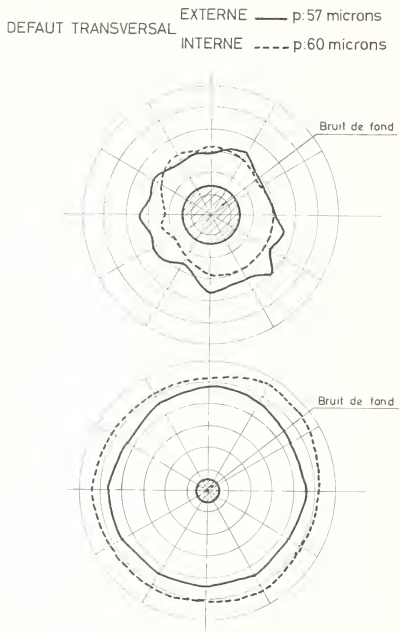

Figure 6. Circumferential homogeneity, transverse defect. Without mask (top). with mask (bottom).

Transverse Defects. Without mask: sufficiently important fluctuations of the order of ±20 percent, are seen. The received signal is on the average twice the base noise for a defect of 60 μm depth; a defect of 30 μm depth is lost in the noise. With mask: the variations in amplitude fall to ±5 percent. The received signal is equal to 5 times the base noise; a defect of 15 μm depth is clearly detectable. The oscillograms in figure 8 show the difference in the response to a defect, with and without masking.

Longitudinal Defects. Without mask: the amplitude varies on average by ±45 percent. The mean signal-to-noise ratio is four; at the limit, it should be possible to detect a defect of 15 μm in depth. By improving the quality of machining of the mirrors, it might be possible to reduce the fluctuations to ±20 percent. With mask: as with the transverse view, an improvement in sensitivity uniformity (around ±5 percent) can be demonstrated; and it also appears that the mask improves the signal-to-noise ratio by a factor of about two[3].

[3]The results on the uniformity of the amplitude of the signal were obtained with a very slow speed of rotation of the mask. The results deteriorated noticeably at higher speed.

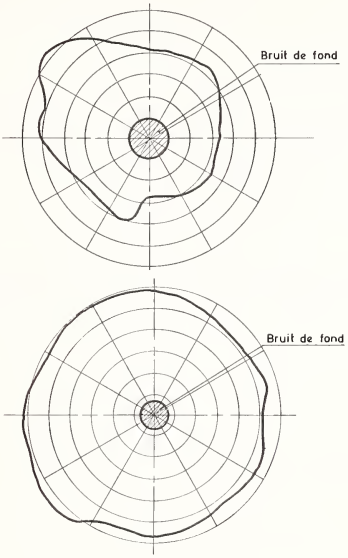

Figure 7. Circumferential homogeneity, longitudinal external defect (p: 60 µm). Without mask (top). With mask (bottom).

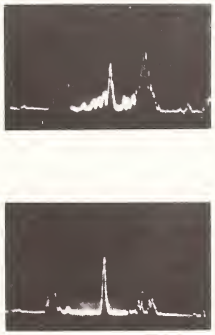

Figure 8. Transverse defect, L: 0.75 mm, p = 57 µm. Without mask (top). With mask (bottom).

4.2. Utilization of sector transducers

Transverse Defects. With the configuration of the split into three sectors, the diagram shown in figure 9 was obtained. It can be seen that the signal amplitude remains almost constant over the major part of the sector, and diminishes towards the edges. It can easily be appreciated that an overlap of 50° is necessary to avoid a large dip in the response. It can also be demonstrated that the signal-to-noise ratio is satisfactory. It is about three times better than with the same transducer when not sectored.

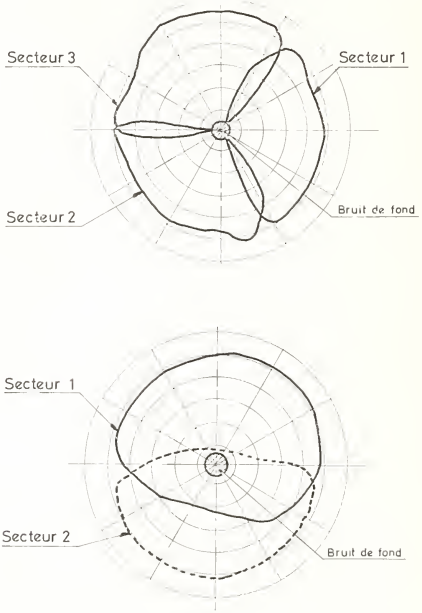

Figure 9. Division of the slab into 3 sectors (top): response to a transverse defect. Division of the slab into 2 sectors (bottom): response to a longitudinal defect.

There has therefore been positive progress. More is available by supplementary adjustment, because it is possible, if it should be necessary, to equalize the sensitivity of the sectors by selecting the gain of the corresponding electronic circuit.

Longitudinal Defects. The division following the two-sector configuration makes it possible to obtain the diagram shown in figure 9. The improvement with respect to the non-sectored arrangement is similar to that obtained with the transverse view.

4.3. Summary of results

The apparatus with rotating masks results in a considerable gain in detection uniformity and sensitivity, above all with the transverse view. This advantage is counteracted by a reduction in the rate of the examination. With a mask rotation speed of 1500 revolutions per minute, it is possible to obtain an object translational speed of around 15 cm/s with a fluctuation in amplitude of ±20 percent (about ±2 dB). This apparatus is not necessary for the detection of microdefects; in such conditions, the simple annular assembly is adequate to ensure satisfactory testing at pass speeds of 1 m/s.

Finally, the sectorization of the transducer makes it possible to provide a very good ensitivity and a small variation in investigation at speeds which depend on the speed of lectrical commutation and which can reasonably be around 0.25 - 0.5 m/s.

5. Conclusions

In order to optimize the performance of an annular array, it is necessary above all to onstruct a very high precision mechanism incorporating a number of refinements; the ransducer should be mounted on a ring, and the tube guide should be adjustable.

To obtain a small variation in testing quality, and great sensitivity to defects, two olutions are possible. They each have advantages and disadvantages: the rotating mask ives the better performance, without modifying the electronics or the transducers. But ertain inherent limitations remain in rotating machines: the mechanism is complex, and the peed of translation is limited.

With the transducer divided into 2 or 3 sectors, the mechanics remain simple, without ny rotating parts, and the speed of testing is accelerated. On the other hand, the lectronics are complicated because each sector has a measurement channel and specially abricated transducers are required.

References

1] Perdijon, J., Le contrôle des tubes par ultra sons sans mise en rotation, Revue Métallurgie, January 1976. Communication IC9, presented at the Eighth World Congress on Nondestructive Testing (Cannes, 1976).

2] Dufayet, J-P., Perdijon, J., and Dacosta, D., Communication ID12, presented at the Eighth World Congress on Nondestructive Testing (Cannes, 1976).

3] Brevet Commissariat à l'Energie Atomique; no D6117 (30 April 1970).

4] Brevet Commissariat à l'Energie Atomique; no 70.160.42 (26 December 1973); no 391675 (4 November 1975).

5] Brevet Commissariat à l'Energie Atomique; no 78.03854 (10 February 1978).

ational Bureau of Standards Special Publication 596, Ultrasonic Materials Characterization,
. Berger and M. Linzer, eds., Proceedings of the First International Symposium on Ultrasonic
aterials Characterization held at NBS, Gaithersburg, Md., June 7-9, 1978. Issued
ovember, 1980.

B-SCAN RESOLUTION ENHANCEMENT USING FOURIER TRANSFORM HOLOGRAPHY

M. I. J. Beale

Instrumentation & Applied Physics Division
Harwell AERE
Didcot, Oxon
England

A method is described whereby a B-scan type display may be obtained with greatly enhanced lateral resolution by processing the ultrasonic signals holographically [1][1]. Depth resolution is by time of flight rather than by the subjective assessment of optimum focus associated with conventional holography.

An equipment has been developed based on the scanned holography system developed at Harwell for the NDT center there. However, a recently developed parabolically focused synthetic phase reference replaces the original planar reference to enable Fourier Transform holograms to be recorded.

The holograms are recorded with a transducer which repeatedly scans the linear aperture; between each scan line a narrow time gate is moved in increments until the full depth of the object has been scanned. During each scan line the signal arriving within the time gate is processed with the parabolic reference whose focal length is dynamically varied to correspond to the depth being imaged. Each scan line results in a linear Fourier Transform hologram and the stack of holograms which results from scanning a range of depths is reconstructed optically. Using astigmatic optics a B-scan type display can be formed with all depths simultaneously in focus.

The parabolic reference generator is described in outline. The form of the recorded holograms is derived and a distortion in the images shown to exist. An optical system designed to reconstruct a distortion free image is described and some practical results obtained with the system are presented.

1. Introduction

The B-scan display, which shows a cross section in depth of an object, is widely used and offers a format convenient for interpretation. Using conventional B-scan techniques the lateral image resolution is defined by the diameter of the ultrasonic beam at the depth being imaged. Practical beam profiles result in an image whose resolution varies with depth.

If holographic processing is used the resolution is defined by the effective cone angle of rays generated by the transducer and is depth independent. Using a focused transducer the lateral resolution is approximately equal to the size of the focal spot. An additional benefit from using a wide cone angle is the sensitivity of planar specular reflectors oriented over a wide range of angles.

Conventional hologram reconstructions consist of a superposition of C-scan type images. A plan view of each depth may be brought into focus by altering the parameters of the reconstruction system; objects from other depths appear superimposed but out of focus. The depth of an object is determined subjectively by optimizing its focus.

[1] Figures in brackets indicate the literature references at the end of this paper.

An experimental system has been developed which retains the resolution advantages of holography but which displays the images in the B-scan format enabling both lateral position and depth to be measured directly without the need for subjectively optimizing the focus of each object. The system is based on that developed at Harwell for the NDT center there [2], however the planar phase reference has been replaced by a recently developed parabolically focused phase reference. The focused phase reference enables Fourier Transform holograms to be recorded by the system.

To form a hologram the transducer repeatedly scans the linear aperture; during each stroke the signal from a small depth section is selected by a time gate, processed electronically and recorded as a line on a facsimile recorder. At the start of each stroke the time gate is advanced and the signal from the next depth section processed and recorded. In this way the full depth of the object is recorded as a stack of lines. The effective focal lengt of the phase reference is dynamically varied to be equal to the depth of the section being scanned; thus each recorded line is a Fourier Transform hologram of a thin depth section of the object.

The resultant hologram is reconstructed using an astigmatic optical system to give a B-scan type display. Unlike conventional holograms however the Fourier Transform holograms reconstruct with all depths simultaneously in focus. A distortion is present in the image whereby, though a point object forms a point image, it has a depth dependent lateral position. A modification to the optical system is described which enables a distortion free image to be obtained.

2. Fourier Transform Holography

To record an exact Fourier Transform hologram the phase reference must be a point sourc lying at the same depth as the object being scanned. However, to explain some of the features of the recorded holograms, it is necessary to analyze the more general case where object and reference are in arbitrary positions. The electronic phase reference is only an approximation to a point source and its effect on the recorded hologram is included in the analysis.

With the scan geometry illustrated in figure 1 the signal at y in the aperture from a point reflector acting as the phase reference is:

$$\text{Cos}\left[\frac{4\pi}{\lambda}\sqrt{x_1^2 + (y + a)^2} + wt\right] \qquad (1)$$

and from the point object is:

$$\text{Cos}\left[\frac{4\pi}{\lambda}\sqrt{x^2 + y^2} + wt\right] \qquad (2)$$

x_1, x = depth of reference and object points respectively
y = coordinate in scan direction
a = lateral separation of reference and object

The amplitude terms have been neglected to simplify the notation.

In practice the electronic phase reference generates the following approximation to th true point source of eq. (1).

$$\text{Cos}\left[\frac{4\pi}{\lambda}\frac{(y + a)^2}{2x_1} + wt\right] \qquad (3)$$

The hologram processing entails the multiplication of the reference and object signals followed by low pass filtering and results in a recorded hologram of the form:

$$B + \text{Cos}\left[\frac{4\pi}{\lambda}\left(\frac{(y + a)^2}{2x_1} - \sqrt{x^2 + y^2}\right)\right] \qquad (4)$$

B = bias to enable bipolar signal to be recorded on unipolar facsimile recorder.

To simplify the analysis of the hologram the parabolic approximation to the spherical wavefront from the point object will be used. The errors involved are not significant unde normal imaging conditions.

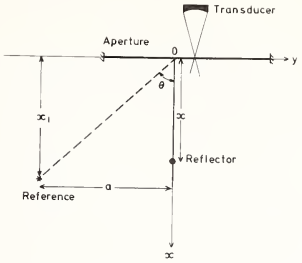

Figure 1. Scanning a point reflector.

Equation 4 becomes:

$$B + \text{Cos}\ \frac{4\pi}{\lambda}\left(\frac{(y+a)^2}{2x_1} - x - \frac{y^2}{2x}\right) \qquad (5)$$

If an exact Fourier Transform hologram is recorded i.e., object and reference at the same depth ($x = x_1$) the hologram becomes:

$$B + \text{Cos}\ \frac{4\pi}{\lambda}\left(\frac{ay}{x} + \psi\right) \qquad (6)$$

$$\psi = \frac{a^2}{2x} - x = \text{a phase constant}$$

The hologram is a sinusoidal grating of space frequency proportional to $\frac{a}{x}$. Note that the space frequency is dependent on both lateral position and depth; all points lying along lines of constant $\frac{a}{x}$ i.e., constant θ (fig. 1) will give rise to fringes of identical space frequency. This relationship is shown later to result in an image distortion referred to as isoclinic distortion.

Under practical recording conditions the width of the time gate and the transmitted pulse duration are a compromise between depth resolution and signal to noise ratio. Thus the signal from a point object is recorded over a number of scan strokes each processed with a slightly different effective focal length of phase reference. Analysis of eq. (5) reveals that this results in a space frequency change between lines making the fringes slightly nonparallel and, in addition, a phase shift that introduces an overall tilt on the fringes. This may be observed on figure 7, the hologram recorded under the conditions illustrated in figure 6; each, batch of fringes corresponds to one of the wires imaged and can be seen to be slightly nonparallel and also tilted.

A detailed analysis will not be pursued as the effect of fringe nonparallelicity is in practice negligible and the optical system has been designed to be insensitive to fringe tilt.

3. Equipment Details

The Harwell system scans the aperture with a transducer operating in pulse-echo, the received signal is processed using an electronically generated phase reference and the output recorded on a facsimile recorder. The recording is reduced photographically to a 35 mm transparency which can then be reconstructed optically. The basic system has been described elsewhere [2] and only the recently developed parabolic reference will be discussed here.

On a B-scan display lateral resolution in only one dimension is displayed directly. Thus holographic processing is required only in that one dimension to enhance the image resolution. The lateral resolution in the undisplayed dimension is defined by the beam profile in both conventional and holographic B-scans.

To generate the focused phase reference a phase delay varying parabolically with scan position is required. The original Harwell system contains a phase modulator which produces a phase delay proportional to a DC control voltage. An electronic unit has been developed which generates a voltage, which is a parabolic function of the scan position, to drive the phase modulator. This control voltage is generated digitally and is synchronized to the transducer's position.

At the start of the hologram a store is loaded with a number that determines the lateral position of the effective focal point of the phase reference relative to the scanned aperture. This enables either on-axis or off-axis holograms to be recorded. The contents of this store is incremented by unity at each sampling point and squared digitally. The modulus of the square is calculated with respect to a number which determines the effective focal length. The output drives the phase modulator via a Digital to Analog converter thus generating a parabolically focused phase reference.

At the start of each scan line the store whose contents determine the effective focal length is incremented to make the effective focal length increase to track with the advancing time gate. The lateral offset is reloaded and the process repeated until the full depth has been scanned.

If the parabolic phase reference is used to form a hologram with a normally incident plane wave, a zone plate is formed. Two such zone plates are shown in order to demonstrate the operation of the phase reference (fig. 2 a, b); the former was recorded on-axis the latte off-axis. In practice an off-axis reference is used to separate the image from the undiffracted light arising from the DC bias used to record the hologram.

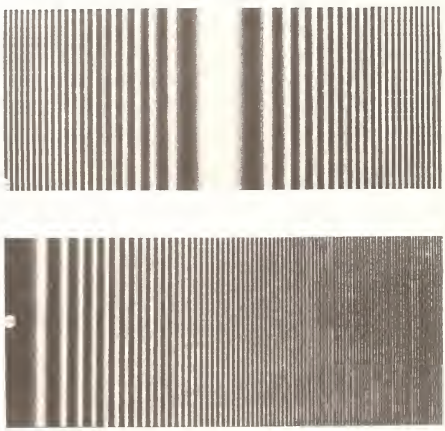

Figure 2. (a) On-axis zone plate generated by electronic reference. (b) Off-axis zone plate generated by electronic reference.

The phase reference was developed to demonstrate the principles of this type of holography and as such can image on a single hologram over a range of depths limited to 2:1. This limitation is due to the amount of digital storage available and is not an inherent limitation of the system.

4. Hologram Reconstruction Requirements

A Fourier Transform hologram of a point reflector is a sinusoidal grating of space frequency proportional to $\frac{a}{x}$ as shown in eq. (6). This grating exists on a number of the stack of lines comprising the hologram. The lateral position of each point in the aperture is encoded as this space frequency while depth is encoded directly as the position of the grating along the depth axis of the hologram, e.g. compare the array of wires scanned (fig. 5) and the resultant hologram (fig. 7).

To reconstruct the image we require the Fourier Transform of the lateral dimension while leaving the depth dimension unchanged. The one dimensional Fourier Transform of each recorded grating would produce a pair of lines whose separation was proportional to the space frequency of the grating. These lines would be symmetrically positioned about a third line arising from the undiffracted light from the bias term used to record the hologram. For the one dimensional Fourier Transform required, each line would have a length and position in the depth dimension determined by the length and position of the grating on the hologram.

A cylindrical lens can be used to perform the one dimensional Fourier Transform. The properties of the lens will not be analyzed here but reference is made to the literature [3]. The hologram is illuminated with parallel coherent light and the transmitted light passed through a cylindrical lens oriented such that its lens function is confined to the lateral dimension of the hologram (fig. 3). In the back focal plane of the lens is the one dimensional Fourier Transform of the hologram.

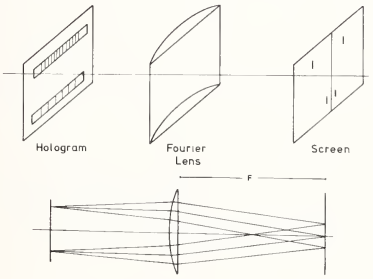

Figure 3. Cylindrical lens used to perform one dimensional Fourier transform.

The scale and aspect ratio of the image are now determined. The lateral scale is determined by the recording conditions, the photographic demagnification and the reconstruction conditions. The photographically reduced hologram from eq. (6) is of the form:

$$B + \text{Cos}\ \frac{4\pi}{\lambda}\left(\frac{a}{x}\, m\, y\right) \qquad (7)$$

m = demagnification factor. The phase constant Ψ is neglected.

Illuminating this grating with light results in two plane parallel beams, each diffracted at an angle ϕ to the undiffracted beam:

$$\text{Sin}\ \phi = \lambda_{\ell} \cdot \frac{2}{\lambda}\frac{a}{x}\, m \simeq \phi \text{ in small angle theory} \qquad (8)$$

The diffracted beams are each brought to a line focus in the back focal plane of the lens with a separation from the undiffracted beam's line focus of (by geometrical optics):

$$Y = F\ \text{Tan}\ \phi \simeq F\phi \simeq \left(\frac{a}{x}\right)\frac{\lambda\ell}{\lambda}\, 2mF \qquad (9)$$

F = focal length of lens.

Thus the lateral displacement is proportional to $\frac{a}{x}$, i.e. to θ, the isoclinic distortion referred to earlier. However each point object results in a uniquely positioned point image and though the distortion is undesirable the image can still be uniquely and correctly interpreted.

The depth scale of the image is determined entirely by the recording conditions and the photographic reduction, under the conditions used a very narrow, deep image results. In addition to the isoclinic distortion the image suffers from three other problems. First, th depth dimension appears as the diffraction pattern of each narrow strip of grating and hence forms a distorted image. Second, the narrow, deep aspect ratio of the image cannot be altered on reconstruction. Thirdly, the effect of the previously mentioned tilt on the fringes, equivalent to a component of space frequencies in the depth dimension, is to introduce depth errors in the image. The space frequency component in the depth dimension result in the light transmitted by the hologram being diffracted in that dimension and hence result in the error in the position of the image points. An optical system has been designed which in addition to correcting the isoclinic distortion, overcomes the problems outlined above.

5. Practical Reconstruction System

To cancel the effect of the isoclinic distortion which results in lateral image positio being inversely proportional to depth, a reconstruction system is required in which lateral magnification varies linearly along the axis corresponding to the depth dimension. This may be achieved using a cylindrical lens with the hologram positioned after the lens and hence illuminated with a cylindrical wavefront. The scale of the Fourier-Transform appearing in the back focal plane becomes [3] (cf. eq. (9)):

$$Y = \frac{a}{x}\frac{\lambda\ell}{\lambda} 2m\ d \qquad (10)$$

where d = distance of hologram from the Fourier Plane. This equation becomes equal to eq. (9) when the hologram is positioned against the lens with d = F or when it is illuminated with parallel light.

Hence, by tilting the hologram as in figure 4, d varies linearly with the depth dimension of the hologram and the required magnification function is achieved. Thus the isoclinic distortion can be exactly corrected without the introduction of further optical components.

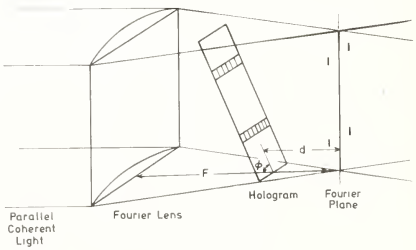

Figure 4. Hologram tilted to correct isoclinic distortion.

The three remaining problems in reconstructing the image can be solved by the introduction of two further cylindrical lenses, one to image the depth dimension of the hologram onto the screen, the other to image the lateral dimension of the Fourier Plane onto the screen (fig. 5).

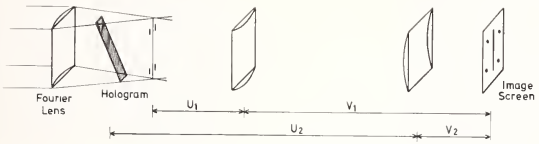

Figure 5. Practical optical system.

The lens imaging the depth direction is rotated 90° about the optic axis relative to the Fourier Transform lens thus; its lens function is confined to the depth dimension. When the lens and screen are positioned to form a focused image of the depth dimension both the diffraction spreading of the image and the depth distortion due to the fringe tilt are removed. The lens imaging the Fourier Plane onto the screen is oriented to act only on the lateral dimension. The magnification produced by the two additional lenses is V_1/U_1 for the lateral and V_2/U_2 for the depth dimension as defined by geometrical optics. Thus any aspect ratio required may be obtained by suitably positioning the screen and lenses. In this way the image may be reconstructed with the aspect ratio of the scanned object. Additional magnification of the image can be obtained using a spherical lens positioned between the image plane and the screen.

6. System Performance

To determine the capabilities of the system two objects have been imaged each consisting of an array of wires in a waterbath. Ultrasound of 10 MHz (λ = 0.148 mm) and wires of 0.25 mm diameter were used. Both arrays consisted of wires lying parallel to the scan plane with the long axis of each wire lying along the dimension not displayed on the B-scan. Hence the expected images would consist of a point corresponding to each wire.

The first array consisted of 8 wires on a 13 mm square grid, the recording geometry is illustrated in figure 6 and the resultant hologram in figure 7. The images reconstructed without tilting the hologram to remove the isoclinic distortion are shown in figure 8 where the entire Fourier plane is displayed and also the image alone. Tilting the hologram to remove the distortion results in figure 9, which is reconstructed with a 1:1 overall aspect ratio.

The second array was designed to verify that the lateral resolution is depth independent and defined by the transducer cone angle and not its beam diameter at the depth imaged. The scan geometry is illustrated in figure 10, the array consists of wires of from 1 mm to 5 mm spacing. To prevent possible shadowing of deeper objects by shallower ones the array was positioned alternately at each of the three depths illustrated; the equipment was not otherwise altered between each position.

The reconstructed images are shown in figure 11. At all depths the 2 mm and coarser spaced wires are resolved. The 1 mm spaced wires are not resolved on the shallower arrays but are just resolved on the deepest array. This apparent increase of resolution with depth is probably due to slight differences in the spacing of the wires at the three depths and may be taken as an indication that the 1 mm spaced wires are on the edge of being resolved. The spot size of the transducer used and hence its expected resolution is approximately 1 mm.

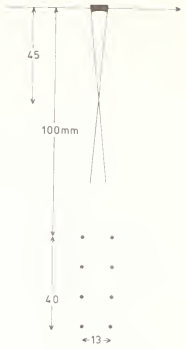

Figure 6. Geometry for scanning on array of wires.

Figure 7. Hologram formed by scanning the array of wires of figure 6.

Figure 8. Fourier plane from figure 7 showing isoclinic distortion and image of wire array showing isoclinic distortion.

Figure 9. Fourier plane from figure 7 after correcting the distortion and image of wire array after correcting the distortion.

If conventional B-scan processing had been used the lateral resolution would be of the same order as the beam diameter at the depths of the objects imaged, i.e. from ≃8 mm for the closest array to ≃13 mm for the deepest.

7. Conclusion

An experimental system has been developed which gives a conventional B-scan type display but with greatly enhanced and depth independent lateral resolution. Images have been obtained of simple objects indicating depth independent lateral resolution approximately equal to the spot size of the focused transducer used.

The equipment was conceived as a useful option to have available on a conventional scanning holography system as it enables the depth of an object to be determined by time of flight without the necessity for subjective assessment of optimum focus. It is planned to extend the depth range available on a single hologram and then to image defects in steel samples to assess the potential of the technique in NDT.

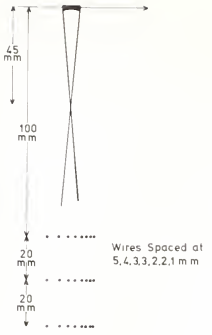

Figure 10. Geometry for scanning an array of wires to test lateral resolution.

Figure 11. Image of wire array in figure 10. Isoclinic distortion corrected.

Many thanks to E. E. Aldridge, A. B. Clare and D. A. Shepherd for their great assistance and fruitful discussions concerning this work. Also to the European Coal and Steel Community and the Mechanical Engineering and Machine Tools Requirements Board (DoI), UK for their financial support.

References

[1] Burckhardt, Grandchamps and Hoffman, Methods for increasing the lateral resolution of B-scan, Acoustical Holography, 5 (Plenum Press, 1973).

[2] Aldridge, E. E., Acoustical Holography (Merrow, 1971).

[3] Goodman, J. W., Introduction to Fourier Optics (McGraw Hill, 1968).

National Bureau of Standards Special Publication 596, Ultrasonic Materials Characterization, H. Berger and M. Linzer, eds., Proceedings of the First International Symposium on Ultrasonic Materials Characterization held at NBS, Gaithersburg, Md., June 7-9, 1978. Issued November, 1980.

ULTRASONIC IMAGING

B. J. McKinley

University of California
Lawrence Livermore Laboratory
P. O. Box 808
Livermore, CA 94550

This paper describes a portion of the Lawrence Livermore Laboratory (LLL) Ultrasonic Imaging Project. The project's purpose is to increase resolution and produce accurate graphic ultrasonic images. Improved methods for quantitative evaluation of bond strength, cracks, and joining are required by current LLL programs. From these requirements the necessity of a two transducer test bed has become evident. The major emphasis of the paper is to describe this sophisticated new concept in ultrasonic test beds now under development.

1. Introduction

An Ultrasonic Imaging Project is in progress at Lawrence Livermore Laboratory (LLL). e purpose of the project is to increase resolution and produce accurate graphic ultrasonic ages. The word "image" is used in a broad sense to include a variety of methods for splaying quantitative test results. A central feature of the project, and, the one phasized in this paper, is the two transducer ultrasonic test bed.

The motivation for this project comes from the need to satisfy a variety of LLL trasonic inspection requirements. The overall project goal is to make pertinent quantitive material evaluations with the highest attainable accuracy. Our requirements generly fall into four categories: first, bond strength evaluation; second, accurate surface ack depth measurement; third, definition of the size, shape, and orientation of material fects such as cracks, voids, and inclusions; and fourth, the inspection of one of the ove three categories in some complex configuration.

2. Ultrasonic Imaging Project

There is presently a two person effort in the area of theoretical work; we are reviewing e literature on solutions to elastic wave equations. Specifically, we are interested in lutions on approaches which can be applied to practical problems. In general, we are terested in the approximate theories. Two examples are the diffracted ray theory and the ries of integral equation solutions which started with the Born approximation and has olved to the extended quasistatic approximation.

We are perfecting the signal analysis techniques which we use for time and frequency main analysis. Our major effort at this point is improvement in range resolution. Recent periments have shown (fig. 1) that we have the capability of resolving two pulses which e separated in time by 35 ns. Estimates of the relative amplitudes were also calculated.

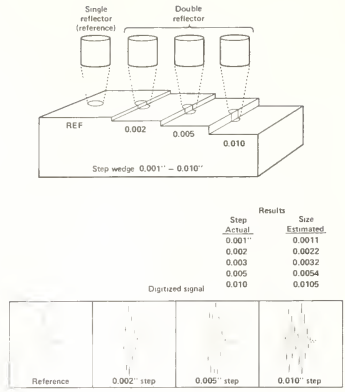

Figure 1. Increased range resolution experiment, (0.001 in = 25.4 μm).

A development effort is directed toward design and fabrication of the two transducer ultrasonic test bed. The features of this test bed represent the highest precision, versatility, and reliability. Central features are shown in figure 2. The mechanical motions are completely computer controlled. Data acquisition, signal processing, graphic displays, and feedback control are all computerized. The base of the test bed is a five meter square granite block one meter thick. Both a horizontal and vertical spindle are included for rotating symmetric test objects. The sturdy overhead ways provide rectilinear motion of both transducers simultaneously in a controlled scan mode or for positioning the central cylindrical section relative to the test object. The central section provides two cylindrical motions which allows the two transducers to be independently positioned to any point within a 0.40 m diameter cylinder 0.30 m high. The accuracy goal is to position the transducer at a point in the space of the cylinder within a sphere of uncertainty 125 μm in diameter with reproducibility of position within 10 μm. There are two orthogonal angular motions which allow the transducer to "look at", or be directed at, any point in the cylinder completely independent of the position motions. This is a new concept for positioning the transducers relative to the test object (see fig. 3).

The principle of the concept is to have the point of incident of the beam on the test object fixed while changes in incident angle are made. This greatly improves accuracy and simplifies the motions necessary to "map the field"; mapping the field at the water-to-part interface, is considered the most common mode of operation. For example, suppose we were to inspect a weld in a sphere. We would mount the sphere on the horizontal spindle with the weld in the vertical plane. The transmitting transducer would be positioned and the angle set for a refracted shear wave incident on the weld zone. The scattered field at the outside surface of the sphere would be recorded by manipulating the position of the receiving transducer over the necessary surface area while constantly changing its angular directions to be normal to the wave fronts of the scattered field. At each point in the field the simplifying feature which makes this possible is that the motion used to position the transducers in space is completely independent of motions used to change the direction which the transducer "looks" at that position in space.

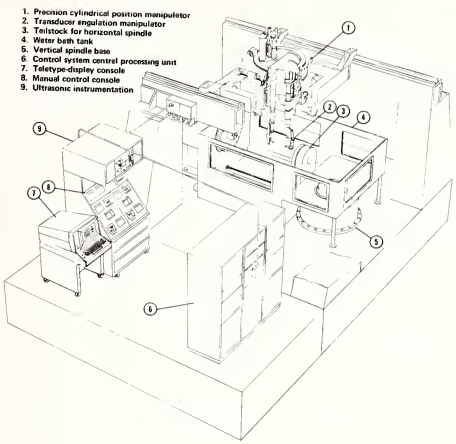

Figure 2. Ultrasonic test bed.

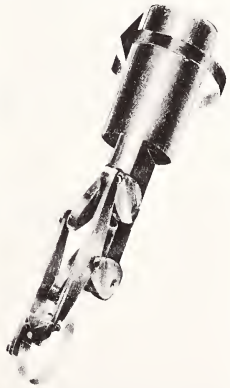

Figure 3. Transducer angulation manipulator.

There are fourteen precision axes of motion on this text bed. The computer control system, (fig. 4), will provide various control modes, including a "teach mode" which allows the operator to establish a routine for moving the transducer over an object. This is especially important when the test object is not a simple shape or accurate dimensions are not available.

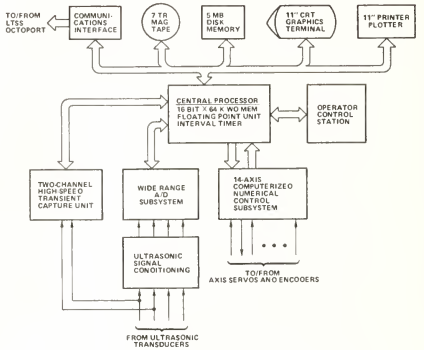

Figure 4. Computer control schematic.

A new addition to our ultrasonic system is a high speed digitizer. It has a 500 MHz sampling rate with six bit accuracy for a single recording cycle which is 1024 data points. Improved resolution is easily attained by averaging.

The ultrasonic system was designed with calibration in mind. For example, it has a built in 25 MHz reference signal which is used to calibrate amplifiers and the peak rF amplitude to dc conversion section. We are looking for better methods of making this conversion which will increase the linear dynamic range. We periodically calibrate or at least tabulate the following system parameters:

Pulser - peak voltage, width, overshoot, repetition rate.

Receiver - gain bandwidth, linearity, sensitivity/noise figure, overload recovery time for both large and small overloads.

Gates - width, position accuracy (jitter).

Peak Sampling - linearity, dynamic range, effective bandwidth.

3. Unique Test Bed Capabilities

The most fundamental motive for building the two transducer ultrasonic test bed is the growing necessity in routine inspection for two transducers, a transmitter, and a receiver, which are accurately and independently manipulated.

The mathematical models now being generated are new approximate solutions for which no complete solutions exist. The mechanical versatility and accuracy of the two transducer ultrasonic test bed is absolutely necessary to verify the approximate solutions.

A very significant use of this test bed will be in feasibility studies the purpose of which are to identify, quantitatively, all the parameters necessary to design a production line inspection fixture. The largest portion of our effort has been in the design of the fixturing. A problem we constantly face is the one of designing a test bed to do a feasibility study which later is used in the production test. There are several problems with that approach: more versatility must be designed into the system to do the feasibility study than is necessary to do the actual test. There is a problem with the time lapse necessary to build anything. The cost of adequate systems is prohibitive for a small program. When the job is complete the system goes to the production line and we are left with nothing but a technical report from which to start on the next task.

4. Conclusion

An ultrasonic imaging project is underway at Lawrence Livermore Laboratory. We are addressing the theoretical problems of mathematical modeling of scattering by realistic defect geometries. We are perfecting the instrumentation and analytical techniques necessary for adequate ultrasonic signal analysis. We are building the sophisticated precision two transducer ultrasonic test bed necessary to achieve the full potential of ultrasonics as a quantitative nondestructive test.

National Bureau of Standards Special Publication 596, Ultrasonic Materials Characterization, H. Berger and M. Linzer, eds., Proceedings of the First International Symposium on Ultrasonic Materials Characterization held at NBS, Gaithersburg, Md., June 7-9, 1978. Issued November, 1980.

ACCURATE ULTRASONIC MEASUREMENTS WITH THE BIOMATION 8100 TRANSIENT RECORDER

R. K. Elsley

Rockwell International Science Center
1049 Camino Dos Rios
Thousand Oaks, CA 91360

The Biomation 8100 Transient Recorder performs 8-bit analog-to-digital (A/D) conversions at a 100 MHz sample rate and is widely used for data acquisition of high frequency ultrasonic signals. Due to the nature of the A/D method used, the accuracy is substantially less than 8-bits under some conditions, particularly at high frequencies. The errors which occur are found to be partially random and partially systematic (called "preferred states" by the manufacturer). The accuracy which can be obtained depends not only on the signal which is being acquired, but also on what features of that signal the experimenter is interested in measuring. By using signal averaging and offset variation, dynamic ranges in excess of 70 dB (12-bits) have been obtained, and subtle but important features in the signals being analyzed have been thereby measured.

1. Introduction

The Biomation 8100 transient recorder [1][1] does 8 bit A/D conversions at a 100 MHz rate into 2048 words of internal digital memory. It is completely programmable by a host computer and is therefore very flexible. However, at high slew rates (high frequency and large amplitude), it is not accurate to 8 bits. The inaccuracies range from very large to very small depending on the signal being studied and the features of the signal which are of interest. Also, unless the experiment is synchronized to the Biomation's free running sample clock, there will be an apparent trigger jitter of up to 1 sample interval. These factors, combined with true trigger jitter and electrical noise in the experiment, invite the use of signal averaging. In order to overcome these sources of error, we have used signal averaging combined with input offset shifting. The nature of the inaccuracies are discussed in the first two sections. Then the averaging technique used is described and evaluated. Finally, examples of applications to 2 types of ultrasonic waveforms are presented.

2. Unused Amplitude Levels

At low frequencies (e.g. less than 500 kHz) or for low amplitudes, the A/D conversion process is indeed accurate to 8 bits. However, as the slew rate (i.e. instantaneous slope, in levels per ns) of the signal increases, the accuracy decreases. The inaccuracy manifests itself in terms of "preferred states": at high slew rates, it is very unlikely for the signal to be assigned to some of the 256 output levels, thereby reducing the number of levels used and the effective number of bits of the A/D conversion. The preferred states can be observed by setting the instrument to repeatedly acquire and then varying the input signal (e.g. by varying the input offset knobs). The bright spots on the display (output) oscilloscope are seen to stay at constant level as the signal shifts.

In order to evaluate the preferred states phenomenon, asynchronous triangle waves of nearly full scale amplitude at frequencies not commensurate with the sampling frequency (100 MHz) were acquired and a record kept of how often each of the 256 levels was occupied. Figure 1 shows the results. In each case, 250 waveforms of length 512 samples each were accumulated for a total of 128,000 conversions.

[1]Figures in brackets indicate the literature references at the end of this paper.

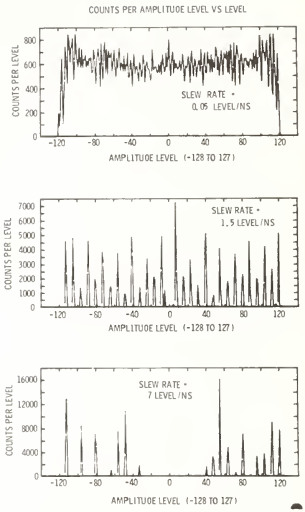

Figure 1. Distributions of number of times the input voltage was assigned to each amplitude level, showing unused amplitude levels at high slew rates.

At low slew rates (fig. 1a), all levels receive approximately equal occupancy. Note that the variations from equal occupancy are almost exactly symmetric about level 0. This is because the instrument "folds" negative voltages into positive ones and uses a single s of 128 comparators. The variations from equal occupancy represents the quality of calibra of the 128 comparators. In this case the quality is rather good.

At higher slew rates (fig. 1b), a remarkable phenomenon develops. Many of the 256 levels have no occupancy whatsoever. For example, at a slew rate of about 1.25 level/ns (3 MHz triangle wave), the levels are occupied in a regular sequence of 2 occupied followe by 6 unoccupied:

...OOuuuuuuOOuuuuuuOO...

In no case does the signal occupy both of an adjacent pair of occupiable levels on a giver sweep past those levels, but rather picks levels 8 apart. Upward slewing and downward slewing perform the same. The behavior at this slew rate is much like that of a 5 bit A/D converter.

At a still higher slew rate (fig. 1c), more and more of the occupiable levels become unoccupiable. The lack of occupiable levels is most pronounced around zero, where high slew rate portions of a waveform are most likely to occur.

Figure 2 shows the fraction of levels which are occupied vs. slew rate. The progressive ss of levels can be observed by setting the instrument to perform continuous acquisitions d varying the frequency in the input waveform.

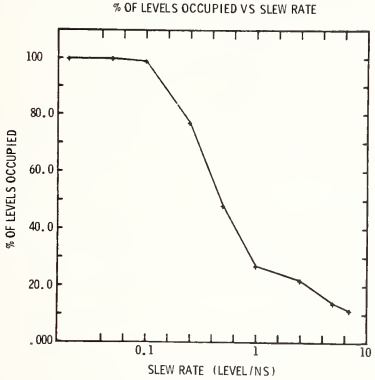

Figure 2. Percent of amplitude levels used vs. slew rate of input voltage.

What is the effect of the unused amplitude levels on the accuracy of measurements made the acquired waveforms? That depends on what features of the waveforms are of interest. aks and valleys are regions of low slew rate. Therefore, for example, the time of occur- nce and amplitude of extrema can be measured much more accurately than the time of occur- nce of zero crossings. If frequency spectra are calculated, the noise energy due to the rors in the regions of high slew rate will be spread fairly uniformly across the spectrum ecause the errors are functions). The overall accuracy depends also on trigger jitter d signal averaging considerations discussed below.

3. Trigger Jitter

The sampling process in the Biomation 8100 is controlled by a 100 MHz crystal clock. the experiment triggers the Biomation, but is not synced to this clock, then the digital mples will be delayed from the trigger pulse by a random amount between 0 and 1 sample terval. Recall that if a sine wave is acquired at 5 samples per cycle, then the error gnal between 2 such acquisitions which differ by 1 sample interval is itself a sine wave ich is bigger than the input wave. Therefore, arrival-time-dependent features of the gnal can be greatly affected. On the other hand, arrival-time-independent features, such power spectrum, are not affected.

The trigger jitter causes a distribution of apparent arrival times of the signals. The pected RMS variation of arrival time of 0.29 sample interval is, in fact, observed. Note at the jitter is as much as 1 sample interval, not 1 clock cycle. Therefore, at slower mpling rates, the error is proportionately bigger.

In addition to this apparent trigger jitter, there is usually true trigger jitter in the periment. When our Panametrics 5052PR triggers the Biomation, we observe about 5 ns peak to ak jitter, or about ½ of that of the Biomation. Therefore, the approach of using a synchro- ed external source of both 100 MHz and trigger pulses (Tektronix type 184) to control both e Panametrics and the Biomation resulted in only a modest reduction in jitter. However, en doing signal averaging, trigger jitter is not all bad as discussed below.

When an ensemble of waveforms are averaged, the resultant has the mean arrival time of the ensemble and it has lost high frequencies according to

$$\text{sinc}\left(\frac{\pi f}{2f_n}\right)$$

where

$\text{sinc}(x) = \sin(x)/x$
f = frequency
f_n = Nyquist frequency .

This is not a very serious loss, amounting to less than 1 dB at the center frequency of an ultrasonic transducer (i.e. at $f = \frac{1}{2} f_n$). Thus, an averaged signal will have a well defined arrival time. Also, jitter is beneficial in that it moves the signal back and forth past the few occupiable amplitude levels, thereby giving better resolution.

4. Signal Averaging With Offset Shifting

In order to obtain better waveforms than are obtainable from a single acquisition, we have made use of the fact that our signals (ultrasonic NDE signals) are available for long enough that signal averaging can be used. Simple signal averaging helps, but because of the missing amplitude levels (preferred states), there are still "flat spots" on the resultant waveform.

To make further improvement, it is desirable to "move" the signal with respect to the amplitude levels during averaging so as to improve resolution. The trigger jitter of the free running sample clock or of the signal itself accomplishes this to some extent, with the side effects described above. Adding a small amount of noise to the signal is a commonl used method of accomplishing this, but the amount needed depends on the input range being used and the noise itself must be averaged away.

The programmability of the Biomation 8100 provides a better way. By varying the input offset level between waveforms, the signal can be moved up and down by the large amounts needed to span the missing amplitude levels without introducing a corresponding amount of noise. Figure 3 shows a block diagram for this procedure.

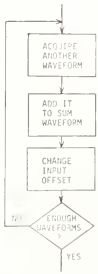

Figure 3. Block diagram for signal averaging with input offset level shifting.

In practice, it is faster to perform several acquisitions at each offset level. Our instrument is interfaced to a Data General Eclipse S/200 computer by a DMA interface withou add-to-memory capability. The software addition loop used for the averaging (plus cycle stealing by the DMA) takes 9 μs per point. Because there is a 10 ms dead time associated w changing the input offset, we acquire 10 waveforms at each offset level in order to spread out that 10 ms overhead. Naturally, an add-to-memory DMA interface or simply storing the individual waveforms for later averaging would speed the acquisition process.

Because the input offset levels (1/100) are incommensurate with the A/D conversion levels (1/128), it is possible to resolve within each conversion level. In particular, if 25 adjacent offset levels are used, then each conversion level is divided into 25 equally spaced parts.

Figure 4 shows the errors remaining after signal averaging over a given number of waveforms and a given number of input offset levels. The quantity plotted is the $\log_{10}$ of the mean squared error of an ensemble of waveforms each obtained by signal averaging in the given manner, compared to a "true" waveform. The test waveform is 10 cycles of a 14 MHz sine wave acquired at 0.01 μs sample interval, and the ensembles contained 500 waveforms. The number of averages are

1, 5, 10, 25, 50, 100, 200, 250 .

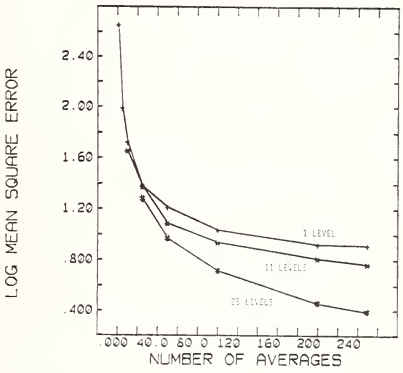

Figure 4. Error of averaged waveform from true waveform for a variety of combinations of signal averaging and offset shifting.

The "true" waveform could have been obtained from an independent instrument if one had been available. However, the accuracy of that instrument would then need to be determined. Therefore, we used as the "true" waveform the result of doing a substantial amount of averaging with the Biomation. In this case, we used 250 waveforms at 25 levels, which is the same as the lowest data point in figure 4.

Note first that a substantial improvement (18 dB) is obtained simply by averaging without level shifting (1 level). This is believed to be due to the trigger jitter effect of the synchronous sample clock, as discussed above. An additional gain of 5 dB is achieved by the use of the offset shifting.

5. Examples

Below are two examples of the effect of signal averaging on signals encountered in ultrasonic NDE. In each case, 3 types of averaging are compared: a single waveform, 250 waveforms without level shifting, and 250 waveforms with 25 levels of level shifting.

5.1. The tale of a long echo train

Figure 5(a) shows the train of echos received when a short pulse from a 15 MHz transducer is reflected from a layered structure consisting of an aluminum-adhesive-aluminum sandwich. A front surface echo is seen at the left, followed by a multiplicity of echos fro within the structure. The latter part of the echo train, while of low amplitude, contribute substantially to the sharpness of the layer thickness resonances in the frequency spectrum.

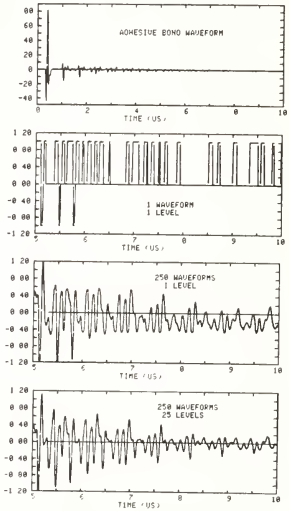

Figure 5. Adhesive bond echo waveform and 3 different acquisitions of its tail, showing improved resolution.

Figures 5(b), (c), and (d) show the last 5 μs of the echo train acquired in the 3 mann listed above. Because the tail does not contain high slew rates, unoccupiable amplitude levels are not a problem. For a single waveform the resolution is, of course, 1 level. Fo 250 averages resolution is substantially improved, due to trigger jitter, but there is a flattening of the negative half cycles at the -0.4 level. With the addition of offset shif the flattening disappears. The noise level visible on these signals (~0.06 level) is about 72 dB down from the full scale range of the instrument. Note that this is just what is expected for an 8 bit (48 dB) A/D converter combined with a $\sqrt{250}$ (24 dB) improvement from averaging. Note also that there may still be systematic errors larger than the -72 dB, whi the present averaging technique is not capable of removing. (This brings to mind the adage "Random errors may be discovered systematically, but systematic errors can only be discover randomly").

5.2. Frequency spectrum of an 0.5 MHz transducer with substantial harmonic content

Figures 6(a), (b) and (c) show the magnitude of the frequency spectrum of an 0.5 MHz transducer which has energy at odd harmonics of its fundamental frequency. The noise level is seen to improve from -45 dB to -55 dB to -65 dB as the averaging technique improves. Ir figure 6(c), the 23rd harmonic of the transducer fundamental is discernable.

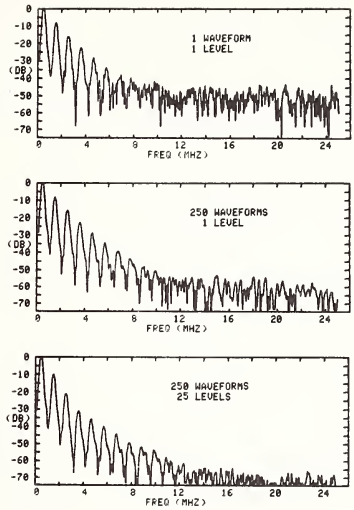

Figure 6. Frequency spectra of an 0.5 MHz transducer with high harmonic content, showing improved noise level with signal averaging. The 23rd harmonic is visible in the bottom figure.

6. Conclusions

The accuracy of data acquisition with the Biomation 8100 is limited by 1) amplitude inaccuracies at points where the input voltage has a high slew rate (e.g. at zero crossings) and 2) trigger jitter due to the asynchronous sample clock. By using signal averaging and input offset shifting, the accuracy can be greatly improved.

The extent to which these inaccuracies effect a given measurement depends greatly on what feature of the waveforms is being studied. In applications where only a single repetition of the waveform is available, careful consideration must be given as to whether the accuracy of the instrument is adequate.

The author would like to thank Roy Tottingham of Biomation, Inc. for helpful discussions of the principles of operation of the Biomation 8100.

References

[1] Biomation, Inc., 4600 Old Ironsides Dr., Santa Clara, CA 95050.

National Bureau of Standards Special Publication 596, Ultrasonic Materials Characterization, H. Berger and M. Linzer, eds., Proceedings of the First International Symposium on Ultrasonic Materials Characterization held at NBS, Gaithersburg, Md., June 7-9, 1978. Issued November, 1980.

A PIPELINE DISTRIBUTED PROCESSING SYSTEM FOR REAL TIME PATTERN RECOGNITION APPLICATIONS[1]

Howard A. Sholl

Electrical Engineering and Computer Science Department
University of Connecticut
Storrs, CT 06268

and

Dominic A. Pagano

Dapco Industries
Ridgefield, CT 06877

A pipeline distributed processing system is described whose intent is to allow high speed, real time, pattern recognition tasks to be accurately carried out. The modular system consists of typically three processing stages: a high speed microprogrammed preprocessing stage whose function is to carry out low level, high speed data "filtering" functions including A/D conversion; a micro- or minicomputer level whose function is statistically-based feature extraction/detection; and a mini- or maxi-computer level whose function is pattern classification, file storage, and display. The system design (both hardware and software) is general in nature to allow its rapid application to many real time pattern recognition tasks. System design has been verified by the construction and testing of a prototype unit which has been successfully applied to the real time ultrasonic inspection of rails.

1. Introduction

One of the problems involved with automatic processing and classification of sampled data in real time is the time required for the system to make a classification decision. Often, the desired data input rate is not compatible with its computer processing time, necessitating a two stage classification process, where a data collection stage occurs first, followed by a classification and decision making stage which processes the collected data sets in non-real time. This paper describes an alternative system organization which has taken advantage of the mini- and microcomputer revolution to achieve a high performance system design which can carry out many real time pattern classification tasks.

1.1. Background

Recent advances in LSI (large-scale-integration) have created a new set of ground rules for digital systems designs. Whereas logic component and memory costs were once the controlling organizational factor creating many years of single processor systems, they no longer need play a dominant role. As a result, considerable interest in research and development is occurring in the area of multiprocessor (parallel-processing) systems, and in methods of decomposing computational tasks to take advantage of parallel processing [1,2,3][2]. One organization which is particularly well suited for data collection and analysis is the dis-

[1]This work was done at the University of Connecticut under a research contract with Dapco Industries, Ridgefield, CT.
[2]Figures in brackets indicate the literature references at the end of this paper.

tributed pipeline, which is shown in figure 1 [4,5]. The pipeline approach, as a design organization, has been applied for many years; however, most applications have been directed toward developing single processor systems which are capable of performing the same low level function on successive data sets [6]. In this way, efficient single processor manipulation of data arrays was possible. Multiple processor pipelines, however, are now feasible and being considered/proposed for a number of applications [4,7].

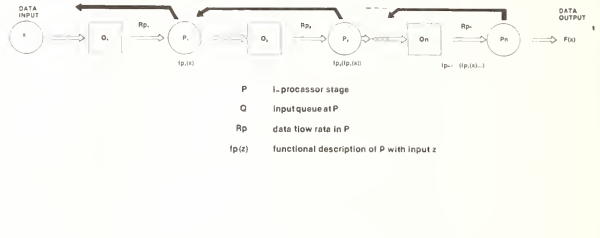

Figure 1. Distributed pipeline organization.

The remainder of this paper considers some of the basic constraints in the design and use of a distributed pipeline, and describes a specific and flexible system which was designed, constructed, and applied to the real time ultrasonic inspection of rails.

2. General Pipeline System Properties

2.1. Basic operational properties/constraints

The distributed pipeline shown in figure 1 has a set of typifying operational properties and constraints: let

T_{P_i} = the processing time for stage P_i

R_{P_i} = the input data rate at stage P_i

L_{Q_i} = the queue length of queue Q_i

T_{Q_i} = the time a data element resides on the queue.

Assume:

1) T_{P_i} has a geometric distribution (see fig. 2).

2) P_i has an expected data mapping factor F_P .

3) Each stage P_i is independent in execution time from the other stages.

Figure 2 illustrates the assumed behavior of processing stage P_i. Note that T_{P_i} has a fixed component, t_{i0}, and an iterative component t_{i1}. Thus if $q = 0$, T_{P_i} has a fixed time t_{i0}; whereas if $0 < q < 1$, T_{P_i} behaves iteratively. These models then provide crude models of processing functions which do not loop, or loop, respectively. The data mapping factor,

F_{P_i}, provides a means of describing the increase or decrease in data flow rate that may occur in processing function P_i. Thus, for example, if processor P_j delivers, on the average, as output two words of information for every four words of input, $F_{P_j} = 2/4 = 0.5$. Queueing is required between each stage to allow for the variations in data arrival/departure rates.

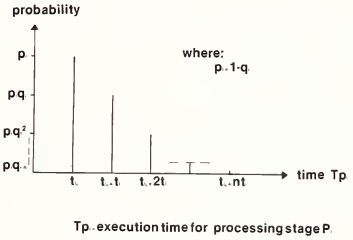

Figure 2. Geometric execution time.

2.2. Expected processing time per stage

$E(T_{P_i}) = \sum_{j=1}^{\infty} t_j(\text{prob of } t_j)$, where E(x) indicates the expected value of x.

From figure 2, $$E(T_{P_i}) = t_{i0} + \left(\frac{1-p_i}{p_i}\right) t_{i1} \quad . \tag{1}$$

2.3. Operational constraints

Let T_{IN} = the expected time between successive data input sets. For continuous operation, assuming potentially infinite queues, both

$$E(T_{P_i}) \leq T_{IN} \text{ seconds} \tag{2}$$

nd

$$E(T_{P_i}) \leq \frac{E(T_{P_{i-1}})}{F_{P_{i-1}}} \text{ seconds for } 1<i\leq n \text{ must be true.} \tag{3}$$

These requirements insure that for each queue, Q_{i-1}, the average data output rate equals r exceeds the data input rate thus preventing continuous queue build-up. Consider the data ate viewpoint

$$E(R_{P_j}) = \frac{1}{E(T_{P_j})} \quad \text{data units/s at the input of stage } P_j \text{ and output of queue } Q_{J-1}. \tag{4}$$

Since processing stage P_j delivers F_{P_j} data units for each data unit accepted, the data rate at the output of P_j is $(R_{P_j})(F_{P_j})$. Thus the prior constraint expressed in data rate terms is

$$E(R_{P_1}) \geq E(R_{IN}) \quad \text{data units/s} \qquad (5)$$

and

$$E(R_{P_j}) \geq E((R_{P_{j-1}}))(F_{P_{j-1}}) \quad \text{data units/s} \quad . \qquad (6)$$

We may also express the rates in terms of data input units. This is useful because it allows a viewpoint of the passage of an input data packet through the pipeline. Since for each successive stage a data unit may represent part of, or more than, a single input data unit, the following is true:

1) At stage P_j input (Q_{j-1} output), each data unit represents $\frac{1}{F_{P_{j-1}}}$ data units of the preceding stage.

2) By induction, at stage P_j, each data unit represents $\prod_{i=i}^{j} (\frac{1}{F_{P_i}})$ input data units.

Thus,

$$E(R_{P_j}) = \frac{\prod_{i=1}^{j} \left(\frac{1}{F_{P_i}}\right)}{E(T_{P_j})} \quad \text{data input units per second} \quad . \qquad (7)$$

2.4. Continuous processing rate

Again assume potentially infinite queues. The slowest, or "bottleneck" processing stage, P_B, is identifiable by the following:

$$\max_j \left[\frac{E(T)_{P_j}}{\prod_{i=1}^{j} F_{P_j}} \right] = \max_j \left[\frac{1}{R_{P_j}} \right] = t_{10} + (\frac{1-p}{p_1}) t_{11} \quad . \qquad (8)$$

Since (eqs. (5,6)) must be true, P_B occurs at j=1 for a properly designed pipeline. The continuous expected processing rate is now:

$$R_C = \frac{1}{t_{10} + (\frac{1-p_1}{p_1}) t_{11}} \quad \text{data input item/s.} \qquad (9)$$

2.5. Pipeline delay, T_D and queue length, L_{Q_j}

T_D represents the time required for $\prod_{j=1}^{n} (\frac{1}{F_{P_j}})$ data input items to have "passed through the pipeline. Note that since a single data item (or its effect) may often be rejected

due to F_{P_j}) at a stage P_j, $j<n$, a relevant measure of T_D may be based on the expected number of input data items that are utilized to create each pipeline output response.

$$T_D = T_P + T_Q \tag{10}$$

where: $T_P = \sum_{j=1}^{n} E(T_{P_j})$ total time contribution due to the n successive processing stages (11)

$T_Q = \sum_{j=1}^{n} E(T_{Q_j})$, total time contribution due to the expected waiting time in the n queues. (12)

T_P is easily determinable from knowledge of the modelling statistics of each independent processing stage:

$$T_P = \sum_{j=1}^{n} \left[t_{j0} + \left(\frac{1-p_j}{p_j}\right) t_{j1} \right] . \tag{13}$$

T_Q is a more difficult parameter to evaluate. Evaluation of T_{Q_j} requires the establishment of the statistics of the number of data items in Q_j for the situation where both the arrival and serving processes have geometric properties as shown in figure 2. Since the model is discrete, and the execution times, t_{i0} and t_{i1}, are continuous, a nonlinear analysis is required. This problem may be approached more easily by simulation, and not considered further in this paper. A system designer, however, should establish these statistics such that he may evaluate the probability of Q_j becoming full (p_F) as a function of queue length L_{Q_j}. Q_j may then be selected such that p_F is sufficiently small to allow the system to behave as if it had infinite length queues. Typical values of p are 10^{-4} [8]. Also from the statistics of the number of data items, the expected time T_{Q_j} may be evaluated.

Let N_{Q_j} = the number of data items in Q_j.

$$E(T_{Q_j}) = E(N_{Q_j})\ E(T_{P_j}) \tag{14}$$

2.5. Functional decomposition

To apply a distributed pipeline system to a specific task requires a careful decomposition of the entire task, F(X), into a set of sequential processing functions, $f_{P_i}(X)$, such that the above properties are achieved, where

$$f_{P_i}(X) = f_{P_i}(f_{P_{i-1}}(\text{---}f_{P_2}(f_{P_1}(X))\text{---})) \tag{15}$$

3. Distributed Pipeline Design/Implementation

3.1. Overview

The remaining part of this paper describes a real distributed pipeline system that was applied to the problem of real time ultrasonic rail inspection; however, the design was intentionally organized in a general format such that the hardware/software system is applicable

to many real time pattern recognition problems. Figure 3 illustrates the functional decomposition that was used for the system problem of pattern recognition. The overall problem was divided into three logical data processing functions: P_1 analog and digital signal processing, P_2 feature extraction, P_3 pattern classification. In reality, this subdivision was adjusted to fit timing constraints such that part of the feature extraction process is actually performed in P_1 stage, and part may also be performed as the "front-end" of stage P_3, depending on the featural complexity required for the specific problem. System control and management is carried out in a hierarchical manner, such that each higher level stage has a command set which it uses to control its next lower stage. In this manner each level need not be aware of the intricacies required to carry out the command. The highest control level is the user; the lowest the processing stage P_1. Acknowledgment of commands is included to provide a suitable system "awareness" of possible error conditions.

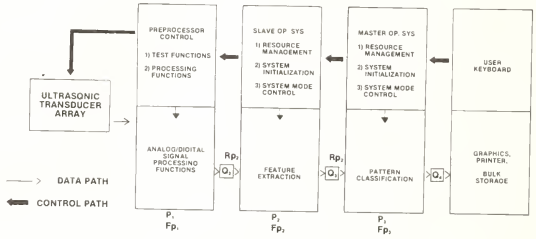

Figure 3. Functual decomposition.

3.2. Description/implementation of processing stages

Implementation of the system is shown in figure 4. A description of each stage follows.

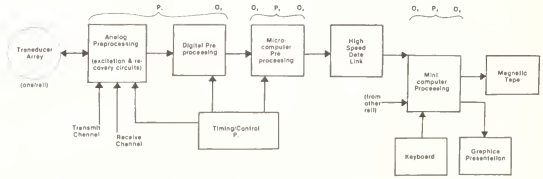

Figure 4. System description - signal processing.

3.3. Stage P_1 analog/digital preprocessor

This stage was designed using a microprogrammed special function computer (designed specfi-
ly for this application) as the control and timing element. The control and timing signals
used to perform the following functions:

a) excitation of a selected transducer,
b) multiplexing (one of sixteen) of an amplified analog response into an analog processing unit, which suitably amplifies (linearly or logarithmically) and envelope-detects the response,
c) sample and hold,
d) 10 bit A/D conversion at an 800 KHz rate,
e) digital detection and magnitude correction of waveform peaks (if a proper mode command was given) at 800 KHz rate,
f) conversion of magnitude to a floating point 8 bit format at an 800 KHz rate,
g) magnitude thresholding,
h) preparation and storage (Q_2) of a descriptive data set of test response including transducer identification, location of test (within the rail being tested), size of the data set, and the time of occurrence for each 8 bit magnitude response,
i) and transfer via DMA (direct memory access) of the data set to the memory (Q_2') of processing function P_2 at a rate of 800 KHz.

Figure 5 illustrates the processing of analog data. Figure 6 illustrates the data set
anization. Since all preprocessing functions occur synchronously, the only queuing re-
red is at the output (Q_2).

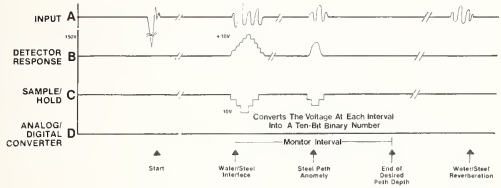

Figure 5. Analog signal description (P_1).

The preprocessor, P_1, receives and executes a set of commands from the higher level
ess, P_2. These commands allow the following functions:

a) Specification of a magnitude threshold value (8 bits floating point format).
b) Specification of the desired delay between the excitation of a transducer and the start of the data collection process (0 to 319 μs in units of 1.25 μs).
c) Specification of the desired duration of the data collection process (0 to 319 μs in units of 1.25 μs).
d) Specification of mode of the peak extraction process: on - save only peaks for thresholding; off - save all samples for thresholding.
e) Specification of the desired transmit and receive transducers.
f) Specification of the desired destination address (in processing function P_2's memory) where the collected data set is to be delivered.
g) Start immediate.
h) Start synchronized (with an external signal source).

rly the command set allows processing function P_1 a versatile set of facilities.

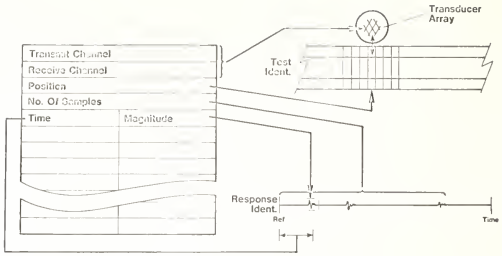

Figure 6. Digital signal description (P_1, P_2) - (data set)

3.4. Stage P_2 feature extraction

This stage was implemented with an LSI-11 microcomputer; thus the design was entirely software. The control function (operating system) at this stage, under command of processing function P_3, carries out three tasks: management of memory resources (Q_2', Q_3); initialization functions, (primarily initial program loading); and mode control functions which allow variations in commands to P_1 and in the data analysis task called feature extraction. Specifically, the following tasks/operations are performed:

a) initial program load;
b) test initiation, either a single test at a time, or a sequence of tests, or an iterative sequence of tests, depending upon the specified mode. A test consists of a cycle of operation as described in the prior section (P_1);
c) while the test is being carried out in P_1, the processor performs a feature extraction algorithm on the next data set in Q_2'. During this process an output data set in Q_3 is prepared which contains a compact representation of the featural content of the input data set. Two modes of operation are allowed here: a raw data mode, in which all input data is passed through to P_3; and the feature extraction process described later;
d) for each analyzed cyclic sequence of tests, a DMA to DMA word transfer is initiated to convey the analyzed data set to the memory of processing function P_3, where it arrives to form queue Q_3';
e) and completion of the input and output transfers is indicated by interrupts, which then allow P_2 to control its memory facilities. In addition, commands to P_2 from P_3 are sent over the DMA data link, and announced by interrupt.

Feature extraction is accomplished by storing in memory a two-dimensional set of decision boundaries (time, magnitude) for each transmit/receive transducer pair that form a used set (channel). Figure 7 illustrates this situation. In this figure "Feature 1" corresponds to an expected response on ch i. A decision boundary is shown which may be positioned as desired to control the probability of making an incorrect decision (e.g. deciding the event did occur when, in fact, it did not, and vice versa). Positioning of the boundary requires a priori knowledge of the two dimensional density function of the expected response. "Feature 2" shows a similar time-magnitude area in which a response is unexpected. Feature occurrence is then determined from the input data set by "mapping" the input time-magnitude

air in the decision regions. If the event is a feature which is unexpected, a mapping into hat region is recorded and the time-magnitude pair preserved; if the event is a feature hich is expected, a lack of mapping into that area is recorded; all other responses are iscarded. Thus, by selecting desired decision boundaries, a flexible set of features may e observed and recorded, such that the total bit content of the data is reduced.

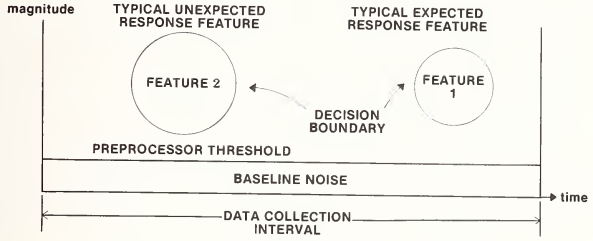

Figure 7. Feature extraction (P_2).

The DMA to DMA data link was designed to link two PDP-11's in a high speed, 16 bit ord, transfer. Implicit queuing was used to allow each end of the transfer path to oper- e asynchronously, while enabling a continuous transfer for each processor. A software rotocol is used to insure a reliable and nonconflicting operation. A second, more expen- ve, alternative link was also developed, which allows higher performance. This second ethod utilizes a shared memory, which occupies a logical address block of each processor. n this way no actual data transfer is necessary between the processors. Memory control is tomatically achieved through a microprogrammed control unit (invisible to each processor). gain a software protocol is necessary.

3.5. Stage P_3: pattern classification

Stage P_3 was implemented in a PDP-11/04 minicomputer, with a suitable bulk storage de- ce (e.g. magtape or disk), keyboard, printer, and graphics terminal. A Tektronix 4010 rminal was used for the keyboard and graphics functions. This stage of processing has th control and data processing functions. The control-related functions are:

a) communicating via the keyboard and printer/graphics terminal to receive and interpret commands from the user,

b) management of memory space to support input data queuing, Q_3 and output data queuing, Q_4, for the peripheral devices,

c) system initialization for each operating mode specified by the user,

d) control of the scheduling of the various jobs in a coherent and balanced manner,

e) and management of the DMA-DMA data link to command processor P_2.

Operating of P_3 occurs in the following manner. After the user has specified a suit- le set of test tables to be used for operation, P_3, performs a system initialization nction. It also receives commands from the user to set up the desired modes of operation d conveys these to the lower level process, P_2, if necessary. The operating modes cover th the testing format to be used (as described for process P_2), and the data analysis

functions to be performed. Some of these were described in the prior section as they relate to process P_2. In P_3 three alternatives are possible: store raw data as it arrives; store semi-processed data; store only the results of the pattern classification process.

Pattern classification is arranged as a two stage process: transformation and sequential finite state classification. Each input data indication represents a time/magnitude pair for a specific channel. Since, at least for many ultrasonic applications, the time sequence of data arrivals may not directly correspond to the spatial sequence of the test piece locations that caused the response, the data arrivals are sorted and placed in a data structure representing a three dimensional model of the test piece. This process is called spatial transformation. As each section of the test piece is completely scanned, the corresponding contents of the data structure are sequentially reviewed by the pattern classification process. At this point a featural combination is allowed (any boolean expression of the occurrence or non-occurrence of the features selected in P_2). The outcome of these evaluations is then monitored by finite state procedure which recognizes a regular event for each desired pattern [8]. This approach thus allows a direct application of syntactic pattern recognition research results, since a descriptive regular grammar (for each desired pattern class) is recognizable by a finite state machine. It is expected that for specific and unique applications the formulation of the pattern classification process may be varied; however, the method utilized and described above has a wide range of potential application.

3.6. Application potential

While the preceding description illustrates a solution aimed primarily at a time-magnitude featural evaluation of ultrasonically-derived signals, the distributed pipeline system has a much wider breadth of application. Some of the possible variations are described below:

3.6.1. Signal source variations

If the analog preprocessing section is varied to allow other transducer types to be connected, a time-magnitude evaluation may be carried out in exactly the same manner as described above. In the existing prototype system, up to 16 channels of analog information are supported, and are monitored in a time multiplexed fashion.

3.6.2. Digital preprocessing variations

If the basis for evaluation is to be frequency-magnitude rather than time-magnitude, the digital preprocessing function must be supplemented with an FFT function before the data is entered into stage P_2. The remaining stages of processing (P_2,P_3) are entirely unaffected since the modes of analysis are independent from the labelling of the dimensions of concern.

4. System Performance

Since the system design was intended for real-time application (classification of rail anomalies), it was important to control the processing time for each stage. This section briefly summarizes the performance properties of the system as they apply to real time use.

4.1. Processing stage P_1

Operation of this stage was described earlier. It was noted that for a specific transducer test channel, the operating time for that test consisted of three factors: a delay time, T_D, (from transducer excitation until response monitoring was desired); a monitoring interval, T_M; and a data transfer time T_T, (to allow the collected data to be transferred into the memory of P_2-LSI-11). Following this sequence, a software latency period occurs to allow the processor (P_2) to react and issue the next desired test. For typical testing in the pattern recognition mode, the following results were noted:

$$E(T_{P_1}) = E(T_D + T_M + T_T + T_L) = 385\ \mu s \text{ per data set} \qquad (16)$$

ere

$$E(T_D + T_M) = 250\ \mu s \quad (17)$$

$$E(T_T) = 10\ \mu s \quad (18)$$

$$E(T_L) = 125\ \mu s \quad (19)$$

$$F_{P_1} \cong 0.1 \quad (20)$$

ese results indicate system performance where $E(T_{P_2}) \leq E(T_{P_1})$ such that no delay of test itations occurred caused by the overflow of Q_2'. It should be noted that the measures licated reflect the settings of the various thresholds; thus a lower performance level urs for "raw" data cases.

4.2. Processing stage P_2

This stage functioned by starting the next desired test as soon as the data set from current test arrived in memory. The time to do this corresponded to T_L of the prior ge. After this function, the featural extraction process, T_F, was applied to the next a set in the queue while the next test was being carried out. After a cyclic sequence of a sets had been processed, the results were transferred to processing stage P_3, in time For these functions during pattern recognition operation the following results were ed:

$$E(T_{P_2}) = E(T_T + T_L + T_F + T_0) = 382\ \mu s \text{ per data set} \quad (21)$$

re:

$$E(T_T + T_L) = 135\ \mu s \text{ (see above)}$$

$$E(T_0) = 7\ \mu s \quad (22)$$

$$E(T_F) \cong 240\ \mu s \quad (23)$$

$$F_{P_2} \cong 0.1 \quad (24)$$

These results indicate that stage P_2 was able to keep up with stage P_1, depending here n the settings of the featural decision thresholds. However, except for 125 μs of soft- e latency, the transducers were operated at a maximum rate. In our testing a latency iod was necessary to allow prior test energy decay in the coupling device such that the tware latency was not a wasted time interval. It should be noted that higher-speed sions of LSI-11s or PDP-11 minicomputers could be substituted for the ones in current use gain a higher level of performance with only minor, if any, changes in system design.

4.3. Processing stage P_3

This stage is the most difficult to evaluate, since the desired output data sets may be ferent in intent and detail for different applications. In our application, classifica- n of rail anomalies, a specific classification is made for each rail column-cross sec- nal "slice" of rail. Typically a rail column was set at 5 mm (although our design al- ed program control of this parameter over a much wider range). Since, for 98 percent or e of the columns, a "good rail" anomaly class is expected, it was expedient for us to ume that conclusion initially. Thus, following a rapid "anomaly"/"non-anomaly" decision, aximum amount of time was available to sort out the best anomaly class, if, in fact, one occurred. Analysis of this stage considered the following factors:

T_0 = processor time committed to receiving data from stage P_2 (DMA),

T_X = time committed to spacial transformation,

T_P = time committed to pattern classification,

T_V = overhead (latency) time required to manage memory space and convey the results to output peripherals.

$$E(T_{P_3}) = E(T_0 + T_X + T_P + T_V) \cong 357 \text{ μs per data set} \quad (25)$$

$E(T_0) = 7$ μs (see above)

$$E(T_X + T_P) \cong 300 \text{ μs} \quad (26)$$

$$E(T_V) \cong 50 \text{ μs} \quad (27)$$

$$F_{P_3} < .02 \quad (28)$$

These figures must be considered in context with the specific application, detail of recognition, and amount of output data storage; thus we expect that while they are typical of our results, they may vary considerably for other modes of operation and the level of detailed analysis that is applied. Again we note that $E(T_{P_3}) \leq F(T_{P_2})$ illustrating that the system may function continuously. Since only 2 percent or less of the rail columns are expected to contain an anomalous condition, the available time interval to perform $T_X + T_P$ for an anomalous column is about 15 ms, per data set, assuming a "good rail" condition is determinable in about 100 μs. It should also be noted that for our testing n channels and data sets ($n \leq 14$) were used for each rail column.

5. Conclusions

A prototype distributed pipeline system was described which is suitable for many real time pattern recognition problems. A summary of distributed pipeline design parameters was given, as well as an operational description of the prototype. Finally, a brief summary of the values of the relevant system parameters was provided as they applied to a specific real time pattern recognition problem. The primary conclusion is that a distributed pipeline system is a feasible and flexible computing structure for handling real time pattern recognition problems. Finally, it should be noted that the system performance, as described in the prior section, may be easily upgraded to a higher level by: substituting faster processor for P_2, P_3 (which are available in compatible form); using parallel pipelines dedicated to specific recognition subclasses; or by moving the transformation process to a separate process (lengthening the pipeline).

References

[1] IEEE Transactions on Computers (special issue on Parallel Processors and Processing) (Feb. 1977).

[2] Wei, M. C. and Sholl, H. A., Computation expressions and their applications in an adaptive computer system, Proceedings of the Sixth Texas Conference on Computing Systems (Nov. 1977).

[3] Reddi, S. S. and Feustel, E. A., A restructurable computer system, IEEE Trans. Computers (Jan. 1978).

[4] Cooper, R. G., The distributed pipeline, IEEE Trans. Computers (Nov. 1977).

[5] Pagano, D. A., Sholl, H. A., et al., A real-time computer-based instrumentation system applied to ultrasonic inspection of rails, presented at 2nd National Conference on Nondestructive Testing (American Society on Nondestructive Testing) (Sept. 1976).

[6] Ramamoorthy, C. V. and Li, H. F., Pipelined processors - a survey, Proceedings 1975 Sagamore Computer Conference on Parallel Processing (Aug. 1975).

[7] Roesser, R. P., Two-dimensional microprocessor pipelines for image processing, IEEE Trans. Computers (Feb. 1978).

[8] Fu, K. S., Syntactic Methods in Pattern Recognition (Academic Press, 1974).

National Bureau of Standards Special Publication 596, Ultrasonic Materials Characterization, H. Berger and M. Linzer, eds., Proceedings of the First International Symposium on Ultrasonic Materials Characterization held at NBS, Gaithersburg, Md., June 7-9, 1978. Issued November, 1980.

INTRODUCTION TO ACOUSTIC MICROSCOPY TECHNIQUES

L. W. Kessler

Sonoscan, Inc.
720 Foster Avenue
Bensenville, IL 60106

1. Introduction

The acoustic microscope is an analytical tool whose course of development and importance the technical community may parallel that of the scanning electron microscope. Though in relatively early stage of development compared with electron microscopy, acoustic microscopy s demonstrated a broad range of applications in materials technology and nondestructive aluation. By way of contrast to imaging techniques described in other articles in this lume in which low frequency (1-10 MHz) ultrasonic energy is employed, acoustic microscopes e frequencies ranging from 100-3000 MHz in order to reveal microstructure. Unfortunately, e high acoustic frequency is also associated with increased attenuation losses in materials. e increase is often so severe that in the "microscopy" regime, the conventional applications low frequency ultrasound are entirely precluded. On the other hand, the greatly increased solution has made possible the solution of problems in materials inspection and character- ation that could not be solved by low frequency equipment.

The purpose of this introductory article is to describe the basic techniques for acoustic croscopy. The articles that follow deal with some specific applications and current de- lopments in the field. For the reader interested in obtaining a general background of the eld, two review papers [1,2][1] are listed in the bibliography.

2. Techniques

A great variety of methods can be thought of for acoustic microscopes. Some of these e used at low frequencies and may also be adaptable for microscopy. There may also be many w ones which will likely be developed in the future when it becomes economical to justify e task. At the present time, however, essentially two techniques have emerged as viable, actical acoustic microscopes. The scanning laser acoustic microscope (SLAM) and the scan- ng acoustic microscope (SAM). The end result of both techniques is the production of high solution acoustic images; however, the imaging technologies, capabilities, and areas of olicability are quite different as will be seen in this and the following articles.

3. The Scanning Acoustic Microscope

In the scanning acoustic microscope (SAM) [3-5], an incident acoustic wave is launched o a water medium by a piezoelectric transducer bonded onto one end of a cylindrical sap- re rod. The other end of the rod has a concave spherical surface ground into it causing e acoustic beam to be focused a short distance away. A receiver rod, geometrically the ne as the transmitter rod, is colinearly and confocally aligned with the transmitter to ieve maximum signal and resolution. For visualization, a thin sample is placed at the al zone and it is systematically indexed mechanically. Variations in the sonic trans- sion amplitude or phase are used to brightness modulate a CRT display. The position put signal of the sample drive mechanism is synchronized to the X and Y axes of the play. Horizontal scanning is accomplished by a rod attached to a vibrating loudspeaker ne. The vertical mechanism is a small precision hydraulic piston. A block diagram of the ustic system is shown in figure 1.

[1] gures in brackets indicate the literature references at the end of this paper.

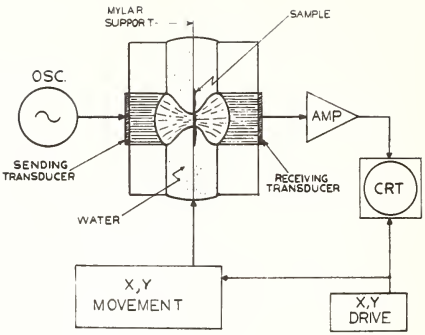

Figure 1. Schematic diagram of the Scanning Acoustic Microscope (SAM)

In all imaging systems, the theoretical resolution limit depends upon the frequency of the illumination (or insonification). The frequency of operation of the SAM seems to be limited by the ultrasonic attenuation in the fluid path (usually water) between the transmitting and receiving rods. The attenuation of signal depends upon the separation distance between the lens surfaces; this, in turn, depends upon the radius of curvature of the lens. The total path length can be decreased if the lens radius is made smaller. The first reported SAM experiments in 1973 were at 160 MHz [4] with a lens radius of 1.59 mm. The focal zone is located about 13 percent farther out than the center of curvature of the lens. Therefore, the lens-to-lens separation is about 3.6 mm and the consequent attenuation loss in the water path excluding that due to the specimen is about 20 dB at room temperature. In the most recent experiments, the reported operating frequency is 3 GHz [6] where the wavelength of sound in water (0.5 μm) is comparable to that of visible light. However, because of the extremely high ultrasonic absorption in water, viz., 8000 dB/cm at 60 °C, the lens-to-lens distance must be considerably reduced. Thus, Jipson and Quate [6] did their 3 GHz experiments with a lens whose radius is only 40 μm.

4. The Scanning Laser Acoustic Microscope

In the scanning laser acoustic microscope (SLAM), a specimen is viewed by placing it on a stage where it is insonified with plane acoustic waves (instead of focused waves as in SAM) and illuminated with laser light [9,10]. The block diagram of this system [11,12] is shown in figure 2. The principle upon which the laser beam is employed as a detector is based upon the minute displacements which occur as a sound wave propagates. As shown in figure 3, an optically reflective surface placed in the sound field will become distorted in proportion to the localized sound pressure. The distortions are dynamic in that the pressure wave is periodic and the mirror displacements accurately follow the wave amplitude and phase. At every instant of time, the mirror surface is an optical phase replica of the sound field. The laser is used to sense and measure the mirror displacements. By electronically magnifying the area of laser scan to the size of the CRT monitor and brightness modulating the display, the acoustic micrograph is made visible. If the sample is not polished, (for example, unprepared solid material), a plastic mirror (coverslip) is placed in contact with the sample to relay the sonic information into the laser beam.

The laser detection process is further explained with reference to figure 3. A light beam incident upon the mirror will be reflected at an angle equal to the incident angle. When the surface is locally tilted by the sound pressure, the reflected light is angularly modulated (spatially). If all the reflected light is captured by a photodiode, its electrical output signal will only be a dc level because the light power reaching the detector will not change as a function of angle. However, if a portion of the light beam

s blocked by an obstacle (or knife-edge) then the amount of light reaching the photodiode ill depend upon the instantaneous angular position of the beam. Thus, the electrical signal utput will now consist of a dc component plus a small ac term coherent with the acoustic ignal.

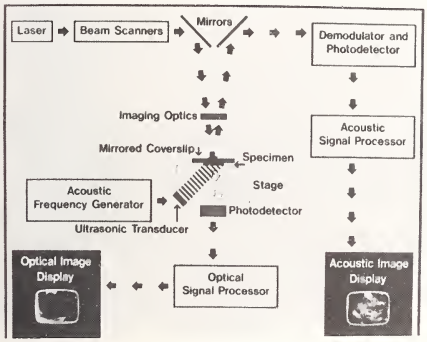

igure 2. Schematic diagram of the Scanning Laser Acoustic Microscope (SLAM)

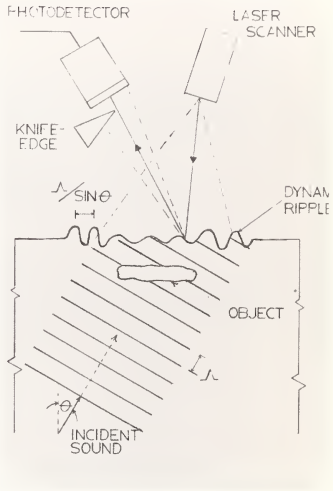

Figure 3. Laser detection of acoustic energy at an interface

As a by-product of the laser scanning technique, a corresponding optical image of the ample is obtained simultaneously as shown in figure 2. In the case of optically translucent amples, such as biological materials and some solid materials such as polymers and ceramics, "partially silvered" coverslip is employed. Here, a fraction of the probing laser light an penetrate the mirror and sample. This transmitted light is detected and the resulting ignal fed to an adjacent CRT monitor, thus constituting an optical image. In the case of a eflective specimen, an optical reflection image is produced. The importance of the simul- aneous optical image is very great to the user, for it permits newly obtained information, coustically, to be immediately compared to a familiar optical frame of reference. This is ccomplished without repositioning the sample or disturbing its environmental circumstances.

The frequency of operation of the SLAM is usually between 100 and 500 MHz, the frequency f choice being dictated by intrinsic attenuation of signal in thick samples. Compared to the AM wherein thin samples are optimum since a lossy fluid path is needed to establish acoustic ocus before entering the specimen, the SLAM needs only a thin fluid film to couple the ound from the stage to the sample. Thick samples are not as much of a problem with the AM except for losses within the samples themselves. Another distinction between the tech- iques is that with the SLAM, the sample remains stationary and the light beam does the canning. Unlike the SAM whose ultimate resolution limit depends upon the precision of a ens and the acoustic frequency generated, the limit of resolution in SLAM is governed by the avelength of the laser light detector, which is about 0.5 μm.

5. Applicability of Acoustic Microscopy

Where does acoustic microscopy fit in the broad spectrum of materials characterization nd testing? Although the answers to this question depend upon one's vantage point, below is collection of statements which pertain to the question.

(1) Suitable materials: ceramics, composites, geological finds, glasses, metals and alloys, polymers and plastics, semiconductors and electronic materials.

(2) Typical studies: anisotropy, bonding, defect characterization, coatings, delamination, dynamic behavior, elastic modulus and density variations, heat affected zones, fracture studies, polymerization defects, porosity, welding and brazing powder metallurgy, stress analysis.

(3) Advantages over other characterization and testing techniques:

A. Higher resolution than conventional low frequency methods, thus permitting microstructural features to be detected.

B. Subsurface and interior structures detectable.

C. Detects changes in elastic properties of samples on a microscopic scale.

D. Nondestructive to sample, serial sectioning not necessary.

E. Planar view images are produced for ease of interpretation.

F. New information is revealed which may not be detectable by other techniques.

G. Penetration of optically opaque samples.

H. Can determine bulk properties of materials instead of just surface properties.

I. Extremely sensitive to planar delaminations which cannot be determined by x-ray or neutron radiography.

(4) Disadvantages over other techniques:

A. Requires fluid coupling or solid contact to get acoustic energy into sample. Cannot propagate through air gap.

B. Resolution at present is poorer than can be obtained with electron microscopy.

C. Only small number of acoustic microscopes exist at present time; therefore, it is not yet as readily accessible as is scanning electron microscope, for example.

D. Limited penetration compared with low frequency ultrasonic techniques due to attenuation mechanisms in materials.

References

[1] Kessler, L. W. and Yuhas, D. E., Acoustic microscopy - 1979, Proc. IEEE, 67, 526-536 (1979).

[2] Kessler, L. W., A review of progress and applications in acoustic microscopy, J. Acoust Soc. Amer., 55, 909-918 (1974).

[3] Lemons, R. A. and Quate, C. F., Acoustic microscope - scanning version, Appl. Phys. Lett., 24, 163-165 (1974).

[4] Lemons, R. A. and Quate, C. F., A scanning acoustic microscope, IEEE 1973 Ultrasonics Symp. Proc., IEEE Cat. # 73CHO 807-8 SU, pp. 18-21, J. de Klerk, ed. (IEEE, New York, NY, 1973).

[5] Lemons, R. A. and Quate, C. F., Advances in mechanically scanned acoustic microscopy, IEEE 1974 Ultrasonics Symp. Proc., IEEE Cat. # 74CHO 896-ISU, p. 41, J. de Klerk, ed. (IEEE, New York, NY, 1974).

[6] Jipson, V. and Quate, C. F., Acoustic microscopy at optical wavelengths. Ginzton Laboratory Report No. 2790 on Contract AFOSR-77-3455 and NSF APR75-07317; also published Nikkei Electronics (Japan), 40-45 (Aug. 21, 1978).

[7] Korpel, A. and Kessler, L. W., Comparison of methods of acoustic microscopy, in Acoustical Holography, A. F. Metherell, ed., Vol. 3, pp. 23-43 (Plenum Press, New York, NY, 1971).

[8] The promise of acoustic microscopy. Mosaic 9, p. 35, National Science Foundation, Washington, D. C. (March/April 1978).

[9] Korpel, A., Kessler, L. W., and Palermo, P. R., Acoustic microscope operating at 100 MHz, Nature, 232, 110-111 (July 9, 1971).

[10] Kessler, L. W., Korpel, A., and Palermo, P. R., Simultaneous acoustic and optical microscopy of biological specimens, Nature, 239, 11-112 (Sept. 8, 1972).

[11] Kessler, L. W. and Yuhas, D. E., Structural perspective, Industrial Research, 20, 53-56 (1978).

[12] SONOMICROSCOPE TM 100, manufactured by Sonoscan, Inc., Bensenville, IL 60106.

National Bureau of Standards Special Publication 596, Ultrasonic Materials Characterization, H. Berger and M. Linzer, eds., Proceedings of the First International Symposium on Ultrasonic Materials Characterization held at NBS, Gaithersburg, Md., June 7-9, 1978. Issued November, 1980.

COHERENT TECHNIQUES IN ACOUSTIC MICROSCOPY

S. D. Bennett and E. A. Ash

Department of Electronic and Electrical Engineering
University College London
Torrington Place
London WC1E 7JE
England

This paper describes the development of a novel method of measuring small changes in the mechanical properties of specimens on a microscopic scale. Complex transmission or reflection functions are measured using a Quate acoustic microscope and a phase coherent detection scheme. Data are recorded digitally and, by numerical comparison of two or more complex records, a third image may be obtained which depends on the changes which have occurred between the two recordings. The assessment of the performance of this system is described and typical results for test specimens are presented. The scope of application of the technique is indicated.

1. Introduction

The principles of Quate acoustic microscopy are now well established and have been extensively described in the literature [1-4][1]. It has been demonstrated by Lemons [2] that it is possible to present acoustic micrographs which depend for their contrast upon both the amplitude and phase modulation of the acoustic beam brought about by the object. Wickramasinghe has also described a method whereby the phase information may be separately extracted from the transmitted or reflected acoustic energy [5]. The fact that both amplitude and phase data are available from the Quate acoustic microscope implies that it is in principle possible to characterize completely the acoustic transmission properties of a specimen. A recording of the amplitude and phase of the transmitted beam, or the real and imaginary parts of the output signal, then carries essentially the same information as a hologram.

This observation suggests a novel technique in the field of acoustic microscopy: by recording two images consecutively and in exact registration, it should be possible to derive a third image which corresponds to the changes which have occurred to the specimen between the two recordings. The technique is directly analogous to optical double exposure holographic interferometry. The potential value of the technique, which we describe in this paper, stems from the fact that we are able to make both qualitative and quantitative evaluations of the changes in the mechanical characteristics of the specimen which take place between two or more images.

Our main objective was to construct an experimentally flexible system which would allow the inspection of specimens of practical interest while avoiding the difficulties of very high frequency operation. The microscope we have constructed operates at 50 MHz and 150 MHz, giving a maximum resolution of about 10 μm. The mechanical scanning of the object is achieved by means of a pair of orthogonal micrometer slides driven by stepper motors. The stepper motors inevitably give a slow frame rate but this implies little restriction on the class of object changes which may be recorded. The stepper motor system has the advantages that it is relatively easy to ensure accurate registration between records and that the system lends itself to control by digital electronics.

[1] Figures in brackets indicate the literature references at the end of this paper.

An alternative and equally viable approach would be to use a conventional Quate system where the frame rate is typically of the order of 1 Hz. The data would then be recorded using the very fast analog-to-digital converters which are now available and conveyed to a digital frame store. In this scheme no attempt would be made to achieve a high degree of registration at the recording stage; rather the specimen would be mounted with reference markers to allow registration to be achieved at a later time. Even without markers, the registration could be effected using a maximum correlation criterion. A system of this kind would be more expensive to implement but has the advantage of almost real time recording.

2. Implementation

The data we require for the double exposure processing is available at the output of the acoustic microscope in the form of a radio frequency carrier which has been modulated in amp litude and phase by the complex transmission (or reflection) properties of the specimen. We make two measurements using a phase coherent detector in which the reference phase may be shifted by 90°, thus providing two orthogonal signals. When the reference is mixed with the microscope signal and filtered, one obtains quantities which are proportional to the real and imaginary parts of the complex function we are seeking to measure (fig. 1). Both the scan ning of the object and the measurements are controlled by an HP 9825A calculator. The system is shown schematically in figure 2. A typical measurement cycle proceeds as follows:

(i) move specimen to a particular point;
(ii) set the reference phase to 0° and measure the detector output;
(iii) change reference phase to 90° and remeasure the detector output;
(iv) store data in calculator read/write memory;
(v) move object to new location and repeat until the frame log is complete.

In our current experiments the recordings have been made for frames of just 100 x 100 picture points in order to reduce the time for recording and subsequent processing to a minimum.

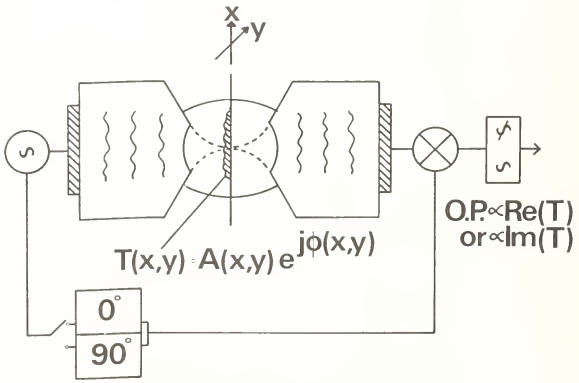

Figure 1. Schematic diagram of microscope.

Two forms of display of the recorded data are available. One is a storage video display hich has the advantage of speed but disadvantage of poor grey level quality. The second form f display is a facsimile machine which takes about 5 minutes to produce a frame and re- uires photographic processing but produces a print of up to 16 grey levels.

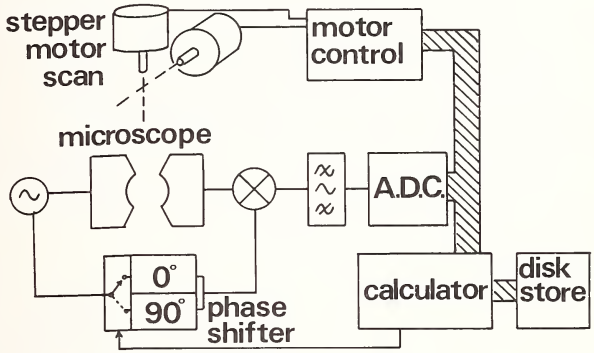

Figure 2. Data logging system.

One important feature of the system we have constructed is the fact that the phase shift n the reference arm does not need to be accurately set to 90°. It is possible to measure ne actual phase shift; any error in either amplitude or phase of the reference signal may nen be corrected numerically by means of a very simple algorithm applied to the data, as it s read into the calculator. The actual phase shift is determined using a vector voltmeter hich allows an accuracy of better than 0.2°. In practice the phase shift is set to within)° of the required value of 90°, this being a tolerance which is easily achieved. After easuring the error to ±0.2°, the resulting accuracy of the quadrature measurement is of the ame order.

The stepper motors provide a resolution of 1.25 μm in the object position; this is con- iderably less than the 10 μm minimum spot size of the current system. The translation tages used are straight to within ±1 μm over their full travel.

3. System Characterization

A careful program of characterization has been adopted; we are primarily concerned ith the assessment of system performance and the development of a suitable test specimen.

A very simple trial was carried out to ensure that the system was indeed capable of esolving phase changes which take place in the microscope. The water bath which provides ne acoustic coupling to the specimen in normal use was filled with warm water and allowed o cool. The acoustic velocity of water is a function of temperature and therefore a peri- dic phase variation is measured at the output as the delay through the water bath is aried by several wavelengths. An example of the output from this experiment is shown in igure 3. The results of the trial enable us to be confident that we are able to measure ne two quadrature components of the transmitted signal with the anticipated accuracy. ne temperature dependent fluctuation of attenuation causes less than 0.2 dB change in mplitude over the range of the measurement and therefore the simulation is of an essen- ially "pure phase object".

This experiment, however, also highlights a possible problem: the system is very sensitive to temperature fluctuations. This could potentially cause some difficulty if the variations of bath temperature were more than 0.1 °C during the recording of a single frame. We are currently planning to monitor the bath temperature and if the changes are significant we will simply make numerical corrections to the data on the basis of continuously monitored temperature compared with a calibration experiment such as the one just described. This problem does not arise in systems where the frame rate is much higher.

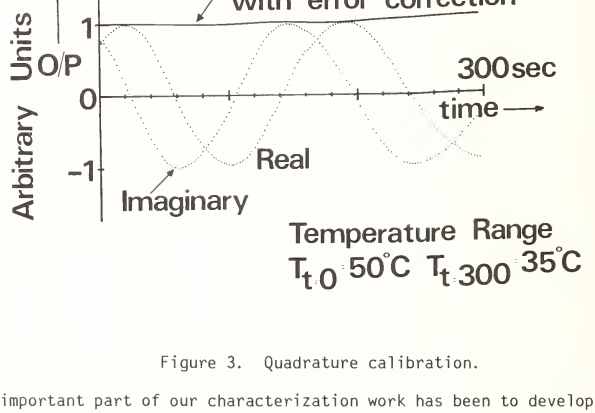

Figure 3. Quadrature calibration.

The most important part of our characterization work has been to develop a suitable tes specimen. This proved to be somewhat more involved than we had anticipated since the specimen must possess a number of not readily reconcilable characteristics. It must permit controlled change within the water bath so that exact registration is ensured; the changes must be easily controlled and must be capable of external measurement to verify the findings of the acoustic microscope system. The dynamic range of the specimen contrast must not exceed the dynamic range of the detector, about 30 dB in the present instrument. In practice it would not be uncommon to find objects which have very much greater dynamic range than 30 dB but for the purposes of characterization this is undesirable. One typical problem associate with this issue is that if, for example, the amplitude of the transmitted signal is locally effectively zero then the phase is undefined at that point. With the simple signal processing currently employed, this leads to certain difficulties in reconstructing phase images. The object should also exhibit significant levels of both phase and amplitude contrast.

The test object we have developed for this purpose is shown diagrammatically in figure It consists of an aluminium foil which is partially transparent at the frequency used in the trials (50 MHz), with a thick layer (about 10 μm) of positive photoresist deposited on one side. The photoresist is exposed to ultraviolet light with a fine wire mesh acting as a mas In this way a grid pattern with a period of 150 μm is defined in the resist: at this stage the resist is not developed. The plane layer of resist shows almost no amplitude contrast variation across the field of view and so a small dot of varnish was placed on top of the resist to provide an aid to focussing the object. Figure 5a shows the logged and reconstructed amplitude frame of a typical field of view; the varnish dot is clearly visible but the resist pattern is almost invisible. The phase information extracted from the same frame of logged data, however, shown in figure 5b, clearly indicates the pattern. We may deduce from this that the exposure of the resist causes a velocity change but very little change in attenuation.

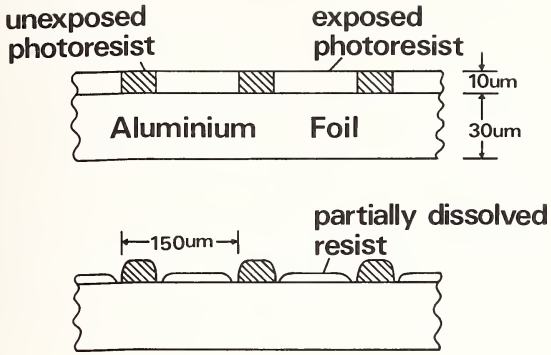

Figure 4. Test object.

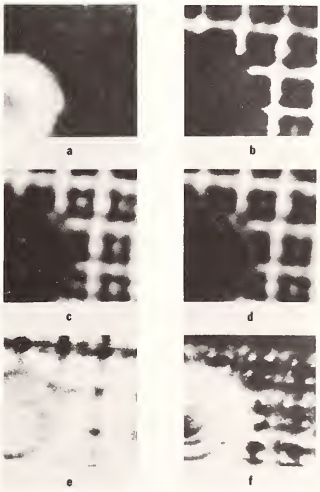

Figure 5. (a) Amplitude image (undeveloped); (b) phase image (undeveloped); (c) amplitude image (partially developed); (d) as (c) after further development; (e) amplitude image formed from the subtraction of the complex records used for (c) and (d); (f) phase image corresponding to (e).

The specimen is used to demonstrate the principle of double exposure processing as follows. The specimen is focussed in the microscope cell and a recording is made of the complex transmission function over the field of view, typically 500 μm x 500 μm. The water in the bath is then replaced with a dilute solution of the resist developer so that the exposed regions of the resist start to dissolve. After a period of time the differential solubility of the exposed and unexposed resist allows the definition of a multithickness specimen as indicated in figure 4. The developer tends to remove the resist nearest to the unexposed bars first, which slightly enhances the contrast at the edges of the grid pattern. There is also some evidence of undercutting of the varnish dot. All of these observations may, of course, be verified by examination with an optical microscope. When a suitable change has occurred in the specimen the resist is removed and the bath is refilled with water and the development process is halted. The specimen then remains unchanged during the period of recording the next frame. A typical sequence of results is shown in figures 5c - f. Figure 5c is the amplitude image extracted from a complex record of a partially developed specimen. The origin of the contrast seen here is associated with the impedance matching effect of the resist between the foil and the water. The transmission through the system is actually increased when the spot passes over a region of resist which is about one quarter wavelength thick. This interpretation of the contrast mechanism has been further supported by a simple experiment in which the object was a plane layer of photoresist on an aluminium foil. The specimen was held stationary and the complex transmission function was measured for a single spot while the layer was gradually dissolved by a weak solution of developer. The results of this experiment are shown in figure 6 and compared with the approximate theoretical effect of a matching layer of resist on aluminium [6].

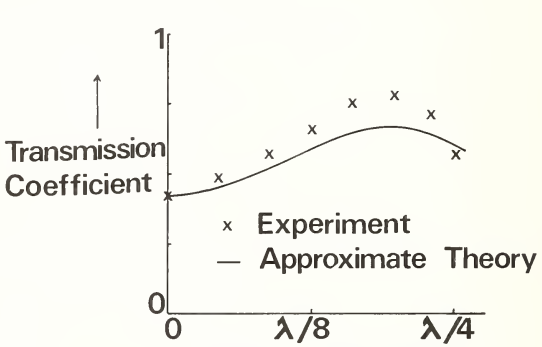

Figure 6. Transmission coefficient as a function of thickness of photoresist layer on aluminum foil.

Figure 5d shows the same field of view as figure 5c but after further development of the resist. Once again this is an amplitude image taken from the complex frame record. The two complex records used to produce figures 5c and 5d were subtracted to produce a third, difference frame. Figures 5e and 5f show the resulting differences in amplitude and phase respectively. It is quite clear that the greatest amplitude changes that have taken place (indicated by the light regions in the amplitude image) are in the centers of the grid pattern, close to the edge of the bars. This is in accord with expectations. The changes which are apparent in the region around and underneath the varnish dot are attributed to the undercutting mentioned above. This effect is of particular interest since it shows ring-lik

nges which represent interference between the two complex frames. These fringes are also dent in the phase image as would be expected. The phase image carries in addition further ormation about the changes which have taken place in the centers of the resist pattern. exact form of the distribution is not well understood at the present time; it is note- thy because these patterns were not expected. They therefore reveal something about the cess which was not evident from the other images.

4. Conclusions

We have demonstrated a novel method of measuring small changes in the mechanical perties of specimens on a microscopic scale. The system is essentially an interferometer, arm of which is a Quate acoustic microscope. One possible implementation of the method been described and the techniques adopted to characterize the system and assess its formance have been indicated.

The results we have presented here are typical of the test specimens we are currently ng. We are now able to proceed with confidence to specimens of more intrinsic interest. are particularly interested in the possibility of studying biological processes such as l growth and division and osmotic effects. It is important to appreciate that unlike the ical holographic interferometry methods which are largely confined to dimensional changes, technique we are proposing is capable of highlighting changes in any parameter which tributes to acoustic contrast. It is therefore conceivable that small changes in ionic centration in living cells may be monitored.

All the results presented have been transmission recordings but it is equally possible operate the system in a reflection mode. Indeed it would be possible to operate in both es simultaneously. We should then be able to measure elastic constants directly on a roscopic scale.

Financial support for both the experimental program and one of the authors (S.D.B.) provided by the National Research and Development Corporation and is gratefully ac- wledged.

We are also grateful to Mr. M. Gillett for his contributions to the design of the roscope system and to Mr. E. Seaford for his work on the stepper motor control. Mr. Nichols designed and constructed the phase shifter and detector system. Mr. M. Shute igned and constructed the interface used to control the facsimile machine.

References

] Lemons, R. A. and Quate, C. F., Acoustic microscope - scanning version, Appl. Phys. Lett., 24, (1974).

] Lemons, R. A., Ph.D. Dissertation, Microwave Laboratory, Stanford, (ML Report No. 2456), 1975.

] Lemons, R. A. and Quate, C. F., Integrated circuits as viewed with an acoustic micro- scope, Appl. Phys. Lett., 25 (1975).

] Kompfner, R. and Lemons, R. A., Nonlinear acoustic microscopy, Appl. Phys. Lett., 28 (1976).

] Wickramasinghe, H. K. and Hall, M., Phase imaging with the scanning acoustic micro- scope, Electronic Letters, 12 (1976).

] Brekhovskikh, L. M., Waves in Layered Media, pp. 56-68 (Academic Press, 1960).

National Bureau of Standards Special Publication 596, Ultrasonic Materials Characterization, H. Berger and M. Linzer, eds., Proceedings of the First International Symposium on Ultrasonic Materials Characterization held at NBS, Gaithersburg, Md., June 7-9, 1978. Issued November, 1980.

ACOUSTIC MATERIAL SIGNATURES USING THE REFLECTION ACOUSTIC MICROSCOPE[1]

R. G. Wilson and R. D. Weglein

Hughes Research Laboratories
Malibu, CA 90265

We show, for the first time, the characteristic acoustic signatures for a variety of bulk materials and thin films of one material on a different material, and how the signatures differ with the thickness of the surface layer. Some attempts at modeling this phenomenon are discussed. We show the relationship between this phenomenon and image contrast and reversal and how the image changes with large displacement from the focal plane.

1. Introduction

The basic principles of the scanning acoustic microscope operating in the cw transmission mode or the cw or pulsed reflection modes have been described adequately in the literature [1-5][2]. During a study of the surfaces of integrated circuits in which the pulsed reflection mode was used, we observed and reported [3] striking contrast and image reversal. In another study of the origin of these phenomena, we discovered that each bulk material exhibits a characteristic reflected acoustic signal pattern as the sample surface is translated from the calculated focal distance toward the lens surface. The contrast and image reversals that are observed can be explained by the superposition of these patterns from different regions of a composite surface. We will refer to these patterns as acoustic material signatures (AMSs). In the analytical treatment of this phenomenon advanced in reference [6], it is pointed out that the presence of a layer of a different material on a surface alters the acoustic velocity of the layered structure and, therefore, the characteristic AMS. This effect is described in this paper for varying thickness of a gold layer on a well characterized [100] surface of silicon. Also described are the AMSs for different bulk materials and for several layer/substrate combinations. Some trends in the experimental data are pointed out that may aid in developing models and analytical treatments of this phenomenon.

2. Acoustic Material Signatures

Acoustic material signatures (AMSs) for six selected materials are presented in two different formats in figures 1 and 2. In figure 1, the relative power reflection coefficient is plotted as the sample-to-lens spacing is varied uniformly from just beyond the focal distance toward the lens surface. Figure 2 presents time exposures of the reflected signal as the sample-to-lens spacing is varied for the same six materials. Figure 2 contains both the time and intensity information for the reflected signal. The acoustic microscope geometry for obtaining AMSs is shown in figure 3. The primary reflection occurs when the sample surface is at the focal distance from the lens, as shown in the upper right of figure 3. When the sample surface is farther away than the focal plane, the acoustic beam crosses over and much of the acoustic energy is reflected outside the lens. In this region, the signal decreases approximately as $\mathrm{sinc}^2\, a\Delta z$ for a pulse length of 50 ns or less. At a spacing of f/2, the focal point is folded onto the lens surface as illustrated in the lower right of figure 3. A "folded reflection" occurs at this location. These three distinguishable regions of an AMS are illustrated in figure 4, which is a qualitative

[1] This research was funded by the advanced Research Projects Agency Order 2397 through the National Bureau of Standards' Semiconductor Technology Program Contract 5-35898.
[2] Figures in brackets indicate the literature references at the end of this paper.

representation of the AMSs shown in figure 1. A total AMS spectrum is shown in the top trace of figure 4. Just below is shown the characteristic of the sample-immersion fluid interface, centered about the focal distance. This pattern does not depend on the sample material properties. The third trace shows the region from the focal plane to the lens, where a series of periodic maxima and minima occurs, characterized by a period Δz_N.

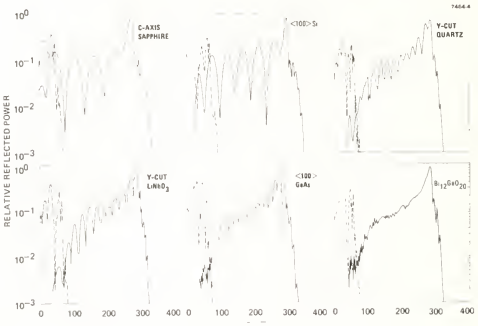

Figure 1. AMSs for six selected materials: relative reflected power versus lens-to-sample spacing.

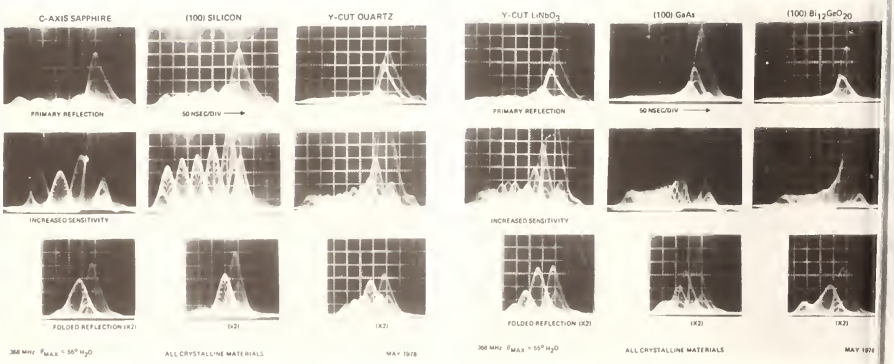

Figure 2. AMSs for six selected materials: time exposures of the reflected acoustic signal as the lens-to-sample spacing is varied as in figure 1.

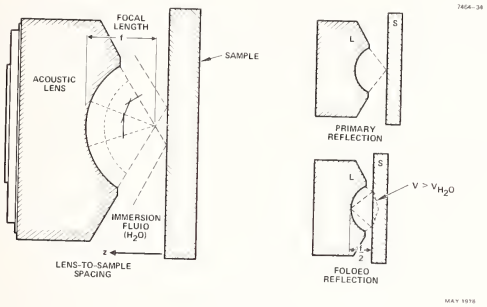

Figure 3. Reflection acoustic microscope geometry for AMSs.

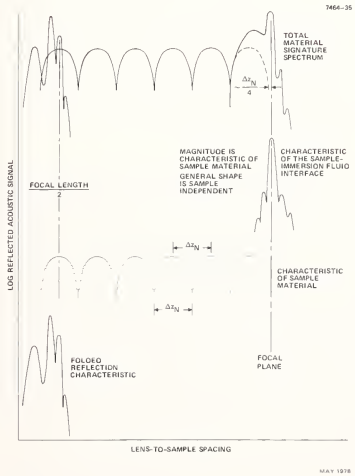

Figure 4. The structure of AMSs.

This region is characteristic of the sample's mechanical properties: it varies with the material, as do the depth of the minima and the relative magnitudes of the maxima. As shown below, Δz_N may be multivalued or may vary with z when a layer or layers of different materials comprise the sample surface. Finally, the bottom trace shows a folded reflection characteristic. All three regions are then combined in the top trace. The folded reflection spectrum is independently superimposed; the material-independent interface spectrum and the material-dependent spectrum add to produce a composite spectrum as shown. Measured AMSs for a variety of materials with a wide range of acoustic velocities have shown that the distance between the focal distance and the location in z of the beginning of the first cycle of the material-dependent oscillations is (0.27 ± 0.07) Δz_N or approximately $\Delta z_N/4$.

The "folded" reflection traces of figure 2 occur at very nearly the same time that the first interface maximum occurs, but only after the lens-to-sample spacing has been decreased by one-half of the focal distance (225 ± 2 μm). For all materials studied, the first primary peak in the folded reflection maximum occurs ∿ 13 ns closer to the lens than the corresponding reflected primary interface maximum, which corresponds to ∿ 10 μm is lens-to-sample spacing, using the longitudinal acoustic velocity in water. In figure 1, these folded reflections occur between 0 and 70 μm. Their shapes and spacings do not have a one-to-one or any apparent regular correspondence to the primary spectrum.

In forming the traces of figure 1, the magnitude of the reflected acoustic power is obtained in the manner shown in the upper trace of figure 5. As one AMS maximum is decaying (points 7, 8, and 9), the next maximum is already increasing (points 10, 11, and 12). Plotting the reflected power versus the spacing produces the cyclic spectrum illustrated in the lower left, which corresponds to the plots of figure 1. However, when the locations in time of the reflected signal maxima (see fig. 2) are plotted versus spacing, a bivalued plot results, as is illustrated in the lower right of figure 5. A full trace of this type is shown in figure 6 for a layered surface (6000 Å of gold on a [100] silicon surface) where five cycles of maxima/minima are observed together with a linear region. The mean slope (velocity) of the data in figure 6 is ∿ 0.76×10^5 cm/s, which, when corrected for the round trip path length in the water immersion fluid, gives the known acoustic velocity in water. The velocity slopes in the regions of material-dependent oscillations are less than one-half of the general velocity slope. The velocity slope in the region beyond the focal distance where the beam crosses over in front of the sample surface and returns mostly outside of the lens cavity is about 2×10^5 cm/s, which is about 2.7 times the velocity in water. The general velocity slope of the folded reflection region is somewhat less than that corresponding to the velocity in water. Some distortion might be expected because of the closeness of the outer radius of the lens to the sample surface and the irradiation of an area of the sample surface that is nearly as large as the lens itself (∿ 44 wavelengths in water).

We have measured AMSs in the three principal planes of silicon: [100], [110], and [111]. The Δz_N spacings vary directly as the square of the mean Rayleigh velocities in these planes (see section on modeling). We have measured AMSs for polished and unpolished surfaces of crystalline materials; they seem to be relatively independent of the condition of the surface (etched or ground). In at least one case, the AMS has better defined minima for the rough surface than for the corresponding polished surface. This observation may be relevant for any model that requires propagation of surface acoustic waves where scattering from surface irregularities could have an effect. The acoustic wavelengths (longitudinal velocities) in our experiments vary in the range from 6 to 40 μm for most sample materials; surface irregularities of the order of hundreds of Angstroms probably would not produce an effect, but scratches on the order of one or a few micrometers probably would. We have measured AMSs for crystalline and amorphous samples of the same material (quartz). For fused quartz, the AMS was more regular and exhibited deeper minima than did the AMS for (y-cut) crystalline quartz. This suggests that the nature of AMSs depends on the degree of acoustic anisotropy of the sample.

Superimposed on top of every AMS pattern in the material-dependent region is another set of oscillations of fixed periodicity equal to 2.17 μm ± 10 percent, which is about one-half of the acoustic wavelength in the water immersion fluid (λ_{H_2O} = 4.17 μm at the acoustic operating frequency of 360 MHz), as shown in the third trace of figure 4. Since these fluctuations are small (∿ 5 percent) relative to the large oscillations

shown in figure 1, they are not shown here in figure 2. These oscillations are evident in the signature photographs of figure 1, where they appear as a brighter internal "herringbone" structure, much as in figure 5. These oscillations exhibit a periodicity of approximately one-half of the acoustic wavelength in water for all materials examined.

3. Composite Layered Surfaces, Contrast, and Image Reversal

AMSs are shown in figure 7 for a variety of composite layered surfaces. In most cases, these signatures are superimposed on the signatures for the surface without the top layer.

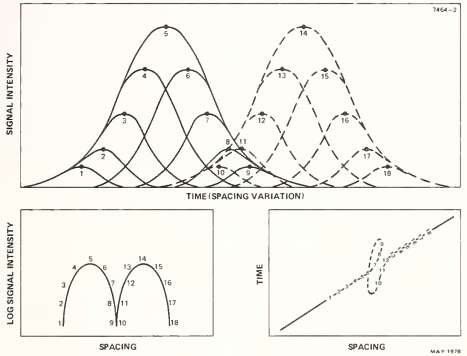

Figure 5. Presentation of AMSs.

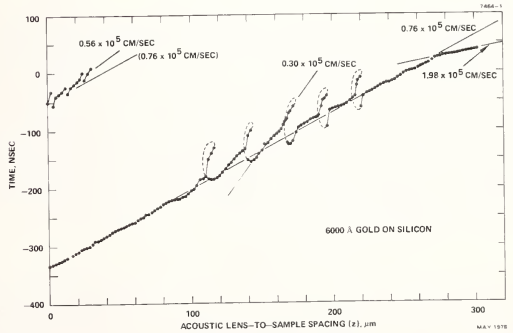

Figure 6. Time display of one AMS.

At any location in z where a distinguishable difference exists between the signatures with and without the layer, contrast occurs in an image of the surface; the larger the difference, the greater the contrast. As the lens-to-sample spacing z is varied, the contrast varies as shown in these plots. In many cases, little contrast occurs at the main interface maximum, and better contrast is obtained by moving the sample toward the lens. As this is done (see fig. 7), varying degrees of contrast can be achieved. Several image reversals occur as first one signature and then another exhibits a maximum. The layered structures exhibit complex patterns. In figure 7(b), the composite curve of a standard silicon-on-sapphire wafer is shown both with and without the silicon layer. This figure shows that the silicon is nearly "transparent". Little contrast exists between regions where silicon exists and does not exist on sapphire. However, figure 7(c) shows that the presence of either a thin or thick layer of aluminum causes a great difference in the signature and, therefore, that good contrast can be achieved, even near the interface maximum. Figure 7(a) shows that a layer of developed photoresist on a SiO_2/Si substrate causes a strong alteration in the acoustic signature and, therefore, is very easy to see in acoustic micrographs.

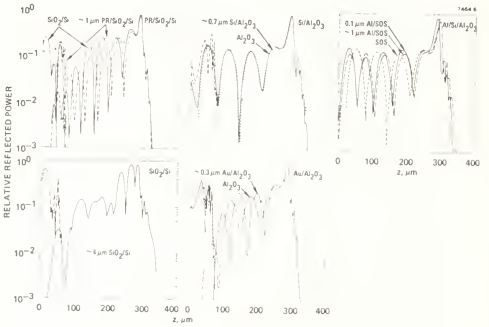

Figure 7. AMSs for several selected layered surfaces.

A special case of a layered surface is shown in detail in figures 8 and 9. Reflection acoustic information for a mesh of gold ~ 0.3 μm thick on a silicon substrate is shown in figure 8, in which mesh dimensions are indicated. Figure 9 illustrates the signatures for the silicon and gold-on-silicon regions, with values of z indicated where the data of figure 8 were obtained. The data of figure 8 include scanning acoustic reflection images, reflected acoustic pulses, and "A" traces across the mesh pattern. The zero reference for the z values was chosen as the location of the maximum for the silicon substrate, the predominant area. Image reversal and the changes in contrast that can be achieved are shown. Enhanced resolution capability is seen in the -14 μm plane where, by reducing the image intensity, the apparent mesh line width can be reduced to an artificial narrowness. The reflected pulses from the two regions of this sample are seen to be about 13 ns apart at all z values.

4. Layer Thickness Dependence

The effect on AMSs and, therefore, on the possibility of determining the thickness and uniformity of layers of one material on another is shown for one selected layered surface system in figures 10 and 11. Figure 10 shows AMSs for 11 thicknesses of gold on a well characterized surface of [100] silicon. Four selected thicknesses are shown in figure 11 in the pulse-time format as z is varied continuously (as done in fig. 2). The effect of increasing the thickness of the gold film is to generally decrease the

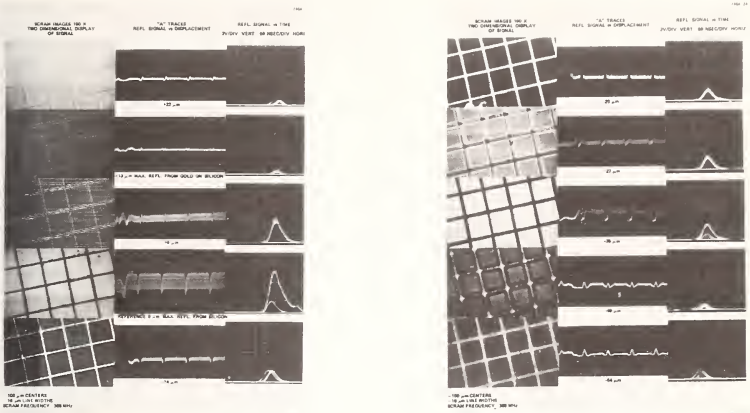

Figure 8. Reflection acoustic microscope information for a layered surface consisting of a 3000 Å gold mesh pattern on a silicon surface.

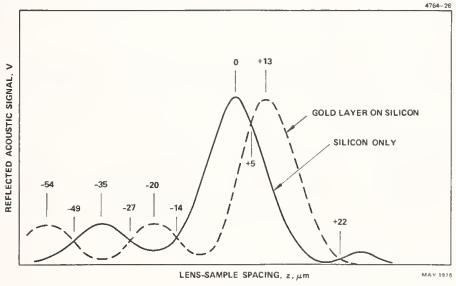

Figure 9. The AMS for the information of figure 8, showing the locations in z where the data were obtained.

periodic length Δz_N and the intensity of the material-dependent oscillations. For some thicknesses, irregular patterns develop; for others, two different regions, one for larger z and one for smaller z, seem to occur. The periodic variations characteristic of AMSs are absent for a quarter-longitudinal-wavelength thick gold layer (2.3 μm) at the operating frequency of 360 MHz.

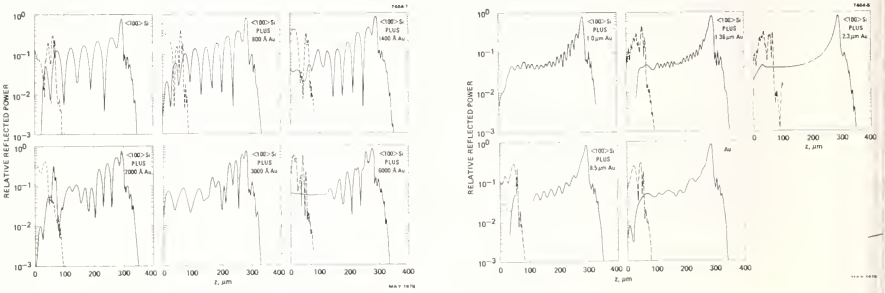

Figure 10. AMSs for increasing thicknesses of a gold layer on a [100] silicon surface.

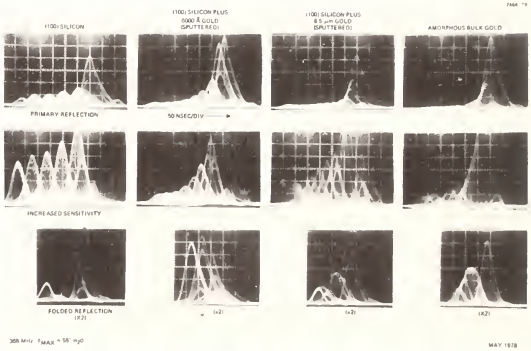

Figure 11. AMSs: reflected power versus time.

5. Depth of Focus

Defocusing effects using an acoustic beam with large convergence angle ($\theta_{max} \cong 55°$) are not well understood. We have found that large depth of focus is observed (i.e., reasonably

sharp images are obtained) as the object is translated up to 27 wavelengths away from the focal plane (compare the mesh images in fig. 8). Under these conditions, the incident acoustic beam width broadens correspondingly from its nominal focused spot size of about 2 μm to 77 μm. Simple ray-tracing analysis suggests that the observed effect may be a consequence of the large refractive index change ($n = v_{Al_2O_3}/v_{H_2O} \cong 7.5$) at the sapphire-water interface of the acoustic lens. Much of the beam apparently is deflected outside the circular transducer area, leaving an effectively smaller beam that emanates from the central, but correspondingly smaller, region of the irradiated surface.

6. Attempts at Modeling

Attempts to understand the origin of acoustic material signatures have met with only limited success. Two approaches, one using a computer analysis based on the angular decomposition of the converging beam into a spectrum of plane waves and the other using a "paraxial ray", have shown the material-dependent nature of these signatures [5]. The paraxial ray analysis appears to be in close agreement with their published experimental results.

The development of a model that explains the features of measured AMSs and predicts the behavior of unknown materials or allows classification of new materials on the basis of their AMSs would seem to be desirable. While analyzing AMSs for about 30 materials where acoustic velocities range over a factor of 3, the relationship that is summarized in table 1 and figure 12 was found. For 10 of the materials examined, the periodic spacing Δz_N of these material signatures varies as the square of the average Rayleigh wave velocity $\bar{v}_R$ in the sample plane. The values of $\bar{v}_R$ and Δz_N in the table and curves are referred (normalized) to the respective quantities in [100] silicon. For the anisotropic materials, where $\bar{v}_R$ is a function of direction, a weighted average was computed, based on published data [7-8]. The table shows that, except for the fastest (beryllium) and the slowest (tungsten) materials considered, the maximum error is about 8 percent and, for most examples, is 4 percent or less. Both beryllium and tungsten, which were assumed to be isotropic, may be partially crystalline, resulting in some variation of $\bar{v}_R$ from the published isotropic values. This agreement supports the conclusion that Rayleigh wave propagation is largely responsible for the observed periodic interference phenomenon. The square-law dependence of Δz_N on $\bar{v}_R$ further suggests the existence of a simple mechanism that may explain the observed relationship. The development of a heuristic model that is based on the observed behavior of Rayleigh wave propagation [9] at a solid-liquid interface is currently being pursued.

The data for Lucite are consistent with the observed dependence provided that the longitudinal velocity v_ℓ rather than the Rayleigh wave velocity is used. The Rayleigh velocity is sufficiently slow in Lucite that the application of Snell's law yields a critical angle θ_R such that $\theta_R > \theta_{max}$, where θ_{max} is the maximum beam convergence angle. In such cases, the longitudinal mode of propagation may be excited and behave similarly to the observed Rayleigh wave excitation [10]. Plastic materials such as Lucite are elastically very deformable (large Poisson ratio). A longitudinal wave propagating parallel to the liquid-solid interface would therefore be accompanied by a corresponding propagating transverse surface deformation that could interact with the liquid.

7. Conclusions and Summary

We presented and discussed experimental results and unique features of reflection acoustic microscopy, including material signatures and the effects of layers of different materials and varying thicknesses of one material on another. We have briefly discussed several attempts at modeling for these effects. The experimental results presented here are intended to aid in the further development of analytical treatments that will explain the complex phenomena.

Table 1. Periodicity of acoustic material signatures.

Material	Orientation	$\bar{v}_R$ [a,b]	$\bar{v}_R^2$	Δz_N [b]	Error %
W		0.49	0.24	0.28	-13
GaAs	100	0.53	0.28	0.29	- 2.2
7059 glass		0.53	0.28	0.28	+ 1.7
Al		0.56	0.33	0.36	- 8.3
Fused SiO_2		0.69	0.48	0.49	- 1.9
Si	111	0.93	0.88	0.91	- 3.6
Si	100	1.00	1.00	1.00	0
Al_2O_3	C-axis	1.16	1.35	1.33	+ 1.3
Be		1.59	2.52	2.27	+11
Lucite[c]		0.54	0.30	0.31	- 4

[a] Averaged Rayleigh velocities.

[b] Normalized to [100] silicon.

[c] Longitudinal velocity.

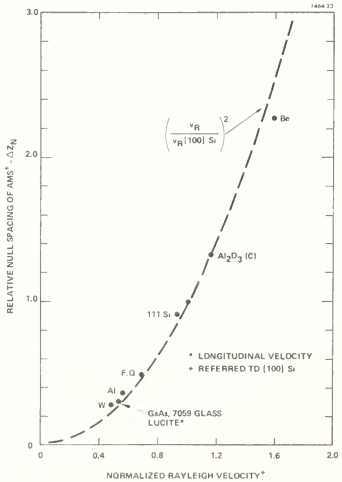

Figure 12. Relative spacings between minima or maxima in AMSs, normalized to [100] silicon and indicating a quadratic dependence on the Rayleigh velocity.

We gratefully acknowledge the technical support of Stephen M. Marks throughout this work. We are grateful to Hugh L. Garvin for sputtering the gold films of varying thickness on silicon substrates.

References

[1] Lemons, R. A. and Quate, C. F., Integrated circuits as viewed with an acoustic microscope, Appl. Phys. Lett., 25, 251-253 (1974).

[2] Quate, C. F., A scanning acoustic microscope, in Semiconductor Silicon 1977 Proc., Vol. 77-2, pp. 422-430, H. Huff and E. Sirtle, eds. (Electrochem. Soc., Princeton, NJ, 1977).

[3] Wilson, R. G., Weglein, R. D., and Bonnell, D. M., Scanning acoustic microscope for integrated circuit diagnostics, in Semiconductor Silicon 1977 Proc. Vol. 77-2, pp. 431-440, H. Huff and E. Sirtle, eds. (Electrochem. Soc., Princeton, NJ, 1977).

[4] Wang, S. K., Lee, C. C., and Tsai, C. S., Nondestructive visualization and characterization of material joints using a scanning acoustic microscope, in 1977 Ultrasonic Symposium Proceedings, IEEE Cat. No. 77CH1264-1SU.

[5] Weglein, R. D. and Wilson, R. G., Image resolution in the scanning acoustic microscope, Appl. Phys. Lett., 31, 793-795 (1977).

[6] Atalar, A., Quate, C. F., and Wickramasinghe, H. K., Phase imaging in reflection with an acoustic microscope, Appl. Phys. Lett., 31, 791-793 (1977).

[7] Slobodnik, Jr., A. J., Conway, E. D., and Delmonico, R. T., Microwave Acoustic Handbook, Vol. 1A, AFCRL-TR-0597 (1973).

[8] American Institute of Physics Handbook, chap. 3 (McGraw Hill Book Co., NY, 1957).

[9] Breazeale, M. A., Adler, L., and Scott, G. W., Interacton of ultrasonic waves incident at the Rayleigh angle onto a liquid-solid interface, J. Appl. Phys., 48, 530-537 (1977).

10] Neubauer, W. E., Ultrasonic reflection of a bounded beam at Rayleigh and critical angles for a plane liquid-solid interface, J. Appl. Phys., 44, 48-55 (1973).

National Bureau of Standards Special Publication 596, Ultrasonic Materials Characterization, H. Berger and M. Linzer, eds., Proceedings of the First International Symposium on Ultrasonic Materials Characterization held at NBS, Gaithersburg, Md., June 7-9, 1978. Issued November, 1980.

CHARACTERIZATION OF SURFACE FLAWS BY MEANS OF ACOUSTIC MICROSCOPY

Donald E. Yuhas

Sonoscan
720 Foster Avenue
Bensenville, IL 60106

A portion of the acoustic bulk wave energy impinging on a surface flaw from within the sample (transmission imaging) will be scattered at the flaw site. This scattering gives rise to characteristic image structure when materials are examined with the Scanning Laser Acoustic Microscope (SLAM). In this investigation a series of acoustic micrographs are obtained at 100 MHz on glass and ceramic samples containing surface cracks and regions damaged by Knoop indentations. The unique capability of the SLAM to independently view the scattered and transmitted sound field in the vicinity of a surface flaw is demonstrated. In a glass sample, a crack is revealed by direct visualization of mode converted surface waves generated at the fracture surface. In this case, a crack less than 30 μm in depth, leads to strong SAW generation. In unprepared, surface ground silicon nitride test bars, defects (Knoop indentations) are revealed by direct visualization of surface skimming bulk waves (SSBW) generated at the site of the flaw. This study represents the first use of surface skimming bulk waves for flaw detection at 100 MHz. Images produced using mode converted surface acoustic waves are strikingly similar to those obtained using surface skimming bulk waves. The primary advantage of the latter mode is that their propagation is relatively insensitive to surface roughness.

1. Introduction

A principle advantage of the Scanning Laser Acoustic Microscope (SLAM) is its ability to rapidly detect and characterize buried defects in optically opaque materials. Numerous examples of the application of this technique to localize subsurface flaws, inclusion and disbonded regions in a variety of materials (e.g. metals, ceramics, polymers) are contained in the literature [1-5][1]. In these applications, the elastic discontinuity of the buried flaw leads to sound scattering and/or absorption. The flaws are revealed as the result of the variation in the acoustic transmission in the vicinity of the defect and can be characterized by their morphology, size, degree of contrast, and magnitude of the change in sonic velocity. Although sound scattering plays an important role in determining defect visibility, the transmitted sound, not the scattered sound, is normally used to produce the acoustic image. In this investigation we illustrate how the SLAM can be used to visualize both the transmitted and scattered sound in the vicinity of a flaw.

Using a rapidly scanning laser beam to detect the sound field, the SLAM has the unique capability of independently visualizing the transmitted, scattered, and mode converted sound fields in the vicinity flaws. This arises because the laser scan is sufficiently rapid that the frequency of the detected signal is Doppler shifted from that of the acoustic wave. The amount of the Doppler shift is dependent on the direction and speed of sound. Scattered or mode converted energy will be perceived at frequencies different from that of the incident acoustic wave. Consequently, the various waves can be viewed separately by using appropriate electronic filtering.

[1] Figures in brackets indicate the literature references at the end of this paper.

The ability to separately visualize the transmitted, scattered and mode converted sound fields has proved to be important in the detection and characterization of surface flaws. Scattered and mode converted sound can propagate considerable distances from the flaw thus permitting easy detection of flaws at relatively low magnification. This is particularly important when the rapid detection of small, critical flaws in structural ceramics is required. Direct visualization of surface waves which result from mode conversion at the site of surface flaws and cracks can be used to evaluate sputtered films, polished surfaces and in development of surface acoustic wave devices.

2. Technique

The principle of operation of the SLAM has been described in detail previously, [6,7] and the instrument is commercially available under the trade name Sonomicroscope 100. In this section we will briefly discuss two aspects of the instrument. Namely (1) the conversion of acoustic energy to an electrical signal by the laser beam and (2) the Doppler shift of the detected signal. The concepts developed in this section will be useful in understanding the acoustic images produced in the vicinity of flaws.

The basic detection scheme employed by the SLAM is illustrated schematically in figure 1. An incident sound wave crossing or being reflected from the boundary will distort the interface. The particle displacement at the boundary is dynamic and occurs at the frequency of the acoustic wave, which is the same as the electrical drive frequency of the transducer. The phase front of the displacement wave, the dynamic ripple, propagates to the right with a velocity $C_b/\sin\theta$, where C_b is the sonic velocity and θ is the angle of incidence. The magnitude of this surface distortion, and hence the amplitude of the sound transmitted through the sample is detected by illuminating the interface with a focused laser beam. The reflected light beam is angularly modulated by the changing slope of the surface, and a knife edge detection scheme is used to convert this angular modulation to an intensity modulation [8]. Scanning the laser beam point by point across the surface is necessary to produce an image. Figure 1 shows an acoustically uniform field, i.e., the dynamic ripple has uniform amplitude across the surface. In samples containing elastic inhomogeneities, sharply defined shadows will be projected onto the interface.

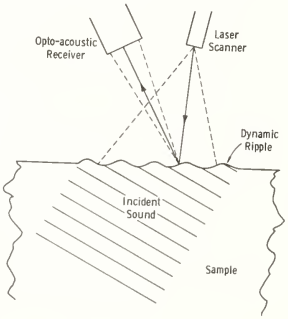

Figure 1. Schematic illustrating the operating principles of the SLAM. Sound impinging on an interface produces a dynamic ripple pattern which can be detected by a focused scanning laser beam.

The second aspect of the SLAM to be discussed is the Doppler shift of the detected signal. The Doppler shift arises because the laser beam is scanning rather than being stationary in space. The amount of the Doppler shift f_d is given by the expression:

$$f_d = \cos\phi \left[\frac{V_s \sin\theta}{\Lambda_b}\right] \qquad (1)$$

Where:

V_s is the laser scan velocity.

ϕ is the angle between the laser scan direction and the direction of the dynamic ripple, e.g., for $\phi = 0^o$ the laser scan is parallel to the dynamic ripple.

$\Lambda_b/\sin\Theta$ is the distance between equiphase points on the dynamic ripple pattern (see fig. 1).

Λ_b is the wavelength of the acoustic wave.

Equation 1 shows that the magnitude of the Doppler shift and hence the frequency of the etected signal is dependent upon an instrumental parameter, the scan velocity, as well as coustic parameters such as the direction and speed of the acoustic wave. Sound scattered om surface flaws or mode converted to surface waves will be perceived at frequencies dif- erent from that of the transducer drive frequency.

Perhaps the best way to conceptualize the separation of the transmitted, scattered and ode converted waves is in the frequency domain. Figure 2 shows a series of plots depicting he frequency spectrum of the detected acoustic signal in the presence of a surface flaw. ach plot contains three dark vertical bars corresponding to the nonscattered, transmitted ound (T) and two scattered or mode converted waves +s and -s. The drive frequency of the ansducer, f_o, if indicated in each figure by the arrow on the abscissa.

The position, in frequency, of the nonscattered wave (T) is downshifted from the drive requency of the transducer, f_o. In the normal imaging configuration the direction of the aser scan is parallel to the direction of the dynamic ripple. Thus, the Doppler shift is egative and the perceived frequency of this component is lower than the drive frequency of he transducer. The magnitude of the frequency shift (from f_o) is determined by the insoni- cation angle and speed of sound and is typically on the order of a few megahertz.

In the absence of any elastic inhomogeneities, the T component is the only one present. wever, when a flaw such as a surface crack is contained in the field of view, two addi- onal components +s and -s appear. These new components correspond to acoustic energy mode nverted at the flaw site into either surface waves or surface skimming bulk waves [9]. The o components, +s and -s, differ in that they correspond to scattered or mode converted waves aveling in different directions relative to that of the laser scan. The component at the west frequency indicates a wave propagating along the laser scan while the higher frequency mponent -s corresponds to a wave propagating antiparallel to the scan. Because the magnitude the Doppler shift depends on the direction of the mode converted wave, the location, in equency, of the mode converted components can be anywhere between +s and -s. Only the treme values are plotted here.

In each of the plots of figure 2 the position of the electronic filter, designated by e hashed area, has been changed to illustrate four different imaging modes. In figure 2a e passband of the filter is adjusted such that only the transmitted bulk waves are pro- ssed. This image mode is useful when only buried inclusions are of interest and structure ising from surface flaws is deliberately suppressed. In figures 2b and 2c, the passband of e filter is adjusted to look simultaneously at the transmitted and mode converted waves. these filtering configurations the acoustic images contain characteristic fringe patterns sulting from the interference of the two modes. In figure 2d only scattered component is the passband. The contribution of the nonscattered wave to the image has been completely ppressed. This configuration is analogous to dark field imaging in optical microscopy.

3. Observations of Surface Acoustic Waves (SAW)

The initial investigations were carried out on a quartz glass substrate which has been tallized over portions of its surface. The 2.0 mm thick sample contained a small fracture ich opened to the metallized surface and led to a strong generation of mode converted sur- ce waves. Acoustic images in the vicinity of the crack were obtained to illustrate the aracteristics of the data for the four different electronic filter configurations shown ematically in figure 2.

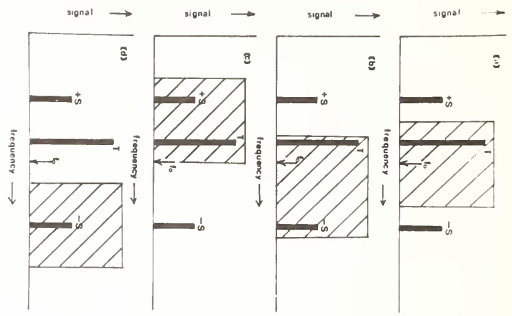

Figure 2. Electronic filtering configurations used for surface flaw investigations. The dark bars represent the dominant frequency components detected in the vicinity of a flaw while the hashed areas indicate the filter passband. Four different imaging modes are illustrated, a) normal acoustic image, b, c) mixed mode acoustic imaging, and d) acoustic dark field imaging.

The insonification geometry used to investigate this sample is illustrated in figure 3. One hundred megahertz sound is incident on the sample from below at an angle of 9.4° in water. The sound is refracted at the glass - water interface and waves impinge on the crack from below as illustrated. The acoustic images were obtained by using light reflected from the metallized areas on the top surface of the sample. The direction of the laser scan as well as the direction of the dynamic ripple resulting from the transmitted bulk wave are to the right in this schematic. Mode converted surfaces waves generated at the crack sight travel both to the right and to the left, (see arrows).

Figure 4a shows an acoustic micrograph obtained with the electronic filter positioned a illustrated in figure 2a. Only the transmitted bulk wave is within the passband of the filt The cracks (indicated by the arrow) that appear as a dark curved line in this micrograph, is approximately 800 μm long and is located in the upper right corner. The field of view size is 2.3 x 3.0 mm^2. This sample, a resolution test target, was metallized only over a portion of its surface. The bright regions of the micrograph record the level of sonic transmission through the metallized portions of the sample. The dark bars correspond to nonmetallized portions of the sample which reflect no laser light and hence yield no signal detection. The extension of the crack below the surface can be estimated by measuring the extent of the shadowed region to the right of the fracture. The width of this highly attenuating, dark zone is less than 30 μm which sets an upper limit on the crack depth. In addition to the crack and features caused by the metallization pattern, several dark filament-like structures corresponding to scratches in the metallization are also apparent.

Figure 4b is an acoustic micrograph obtained on the same region of the sample as depicted in figure 4a. In this case the passband of the filter includes both the transmitted acoustic signal and the mode converted surface wave generated by the crack. The surface wave is propagating to the left; thus we are using the filtering configuration illustrated in figure 2b. The fringe pattern seen in this micrograph results from the interference of the transmitted bulk wave and the mode converted surface wave generated by the crack. The crack curvature leads to a slight focusing of the surface waves which is apparent in this micrograph.

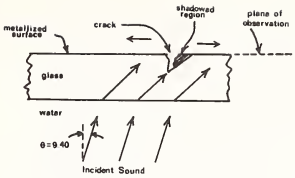

Figure 3. Schematic illustrating the insonification geometry used to detect surface flaws in a quartz glass sample.

Figure 4. A series of acoustic images obtained on a metallized glass substrate containing a surface crack (indicated by the arrow). The four images correspond to the four filtering configurations illustrated schematically in figure 2.

The spatial periodicity of the fringe pattern is directly related to the spatial periodicity of the two modes in the passband of the filter. In appendix A we describe how measurement of the fringe spacing in this micrograph can be used to determine the sonic velocity of the scattered component. A value of 3060 m/s was obtained for the sonic velocity of the surface wave generated at the crack site. Several aspects of the acoustic

images obtained in this filtering configuration should be pointed out. First the mode converted surfaces waves propagate a considerable distance from the site of the cracks; thus, the presence of a flaw can be easily detected even at relatively low magnification. Secondly, the crack, due to the strong surface wave generation is easily distinguishable from surface scratches, and third, the sensitivity to detecting surface features is enhanced in this filtering configuration. For example, in micrograph 4b weak surface wave generation can be seen at the boundaries between the metallized (light) and nonmetallized (dark bars) portions of the sample.

Figure 4c shows an acoustic micrograph obtained using the filter configuration illustrated in figure 2c. The crack has been moved so that it is near the center of the field of view. In this case both the dynamic ripple of the transmitted bulk wave and the mode converted surface wave traveling parallel to the laser scan direction (i.e. to the right) are within the passband of the filter. A characteristic fringe pattern similar to that of figure 4b is obvious. However, the fringe spacing is larger owing to the change in direction of the surface wave relative to the transmitted bulk wave. Surface wave velocity determined by measuring this fringe spacing was found to be 3110 m/s which agrees favorably with the value of 3060 m/s determined from figure 4b.

Figure 4d shows the acoustic micrograph obtained with only the scattered wave in the passband of the filter. In this case the transmitted bulk wave is excluded from the passband; thus, the regions where no mode converted waves propagate appear dark. This imaging mode is directly analogous to optical dark field imaging. The bright regions of the micrograph arise entirely from mode converted surface wave energy. The fringe patterns, characteristic of images 4b and 4c are suppressed in this micrograph because only one mode is being detected. At least two modes are required for interference. Some structure in the darker regions and a hint of fringing can be seen in this micrograph. Part of this structure can be attributed to surface wave generation in other portions of the sample and part is attributed incomplete suppression of the transmitted bulk wave component by the electronic filter.

Figure 5a and b are acoustic dark field interferograms obtained in the vicinity of the crack. The field of view is similar to that depicted in figure 4d. Interferograms are produced by combining the detected acoustic signal with an electronic reference signal which is coherent with the drive of the transducer. The fringe pattern observed here is produced electronically and not acoustically. In this case the fringe spacing yields a direct measure of the surface acoustic wave wavelength and a measure of the SAW velocity. A value of 3100 m/s determined from this micrograph is in good agreement with the previous two determinations.

Figure 5b is a second acoustic interferogram taken with the sample in the same orientation as that depicted in figure 5a. Here a few drops of water (dark regions) placed in the path of the mode converted waves produce a shadowed region to the right of the drops. This micrograph provides a simple, direct test proving that the waves originating from the crack are indeed surface waves. In the next section we discuss some of the characteristics of bulk waves scattered from surface flaws and find them to be relatively uneffected by the presence of water on the surface.

4. Observation of Surface Skimming Bulk Waves (SSBW)

The investigation described in the previous section was carried out on an optically reflective, metallized surface where surface acoustic waves are easily propagated. The requirement for an optically reflective surface poses no problem for the investigations of sputtered films, polished samples such as silicon wafers, and surface acoustic wave devices. Even some high strength ceramic components such as ball bearings have sufficiently smooth surface finished which permit flaw detection by visualizing surface waves. However, there are a number of applications where the surface finish of components is too rough to permit flaw detection at 100 MHz using surface acoustic waves. Observations presented in this section indicated that the presence of surface flaws in ceramics often lead to strong generation of surface skimming bulk waves (SSBW). These scattered bulk waves produce image characteristics similar to those observed on the metallized quartz substrate but do not require an optically smooth surface finish. Thus, many of the imaging options and advantages described in the previous section are directly applicable to detection of surface flaws in high strength ceramics with rough, textured surfaces.

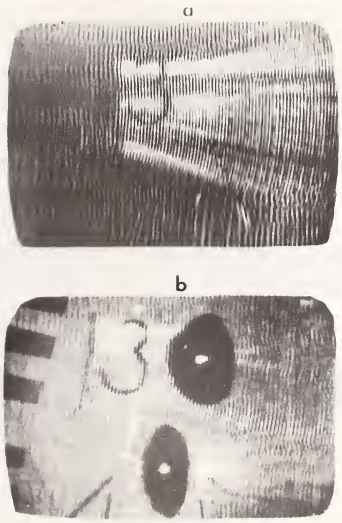

Figure 5. Acoustic interferograms obtained before (a) and after (b) placing a few drops of water on the sample surface (dark regions in b). Attenuation of the crack-generated surface acoustic waves by the water leads to a shadow to the right of the drops.

In unprepared samples, such as surface round structural ceramics, surface waves (at 0 MHz) quickly dissipate for two reasons. First, because the surface roughness is comrable to the surface acoustic wave wavelength, the waves are attenuated. Second, because e scanning laser method requires an optically reflective surface in order to produce an oustic image, a plastic mirror coverslip is coupled to the surface with a drop of liquid. is apparent from figure 5b that the presence of a liquid rapidly attenuates the acoustic rface waves.

In figure 6a we present an acoustic micrograph obtained in the vicinity of a surface aw in hot pressed silicon nitride, NC132. The sample is a 1/8 in (3.2 mm) thick test bar d the insonification geometry is identical to that depicted in figure 3 except that a mirred coverslip is coupled to the top surface with a drop of water. The surface flaw was tificially induced using a Knoop microhardness tester with a 10 kg load. The character of is acoustic image is remarkably similar to that observed in figure 4b and 4c. However, in is case the fringe pattern results from the interference between the transmitted bulk ve and the bulk wave (surface skimming bulk wave) scattered from the flaw. The filterg configuration used to obtain this micrograph is shown schematically in figure 2c. e dynamic ripple from the transmitted and scattered wave are both propagating to the ght. In addition to the structure directly attributable to the surface flaw a number striations running horizontally across the micrograph can be seen. These features e caused by the surface texture of the component.

Figure 6b shows the same surface flaw, but the filtering configuration has been changed to that illustrated schematically in figure 2b. In this case the fringe pattern results from the interference between the transmitted bulk wave and the wave scattered to the left. Note that the fringe spacing is smaller (compared to that of fig. 6a) as anticipated based on the analogous surface wave example. Either of these examples can be used to calculate the velocity of the scattered component (see Appendix A). A value of 5650 ± 100 m/s is obtained indicating that the scattered component is a shear wave [10].

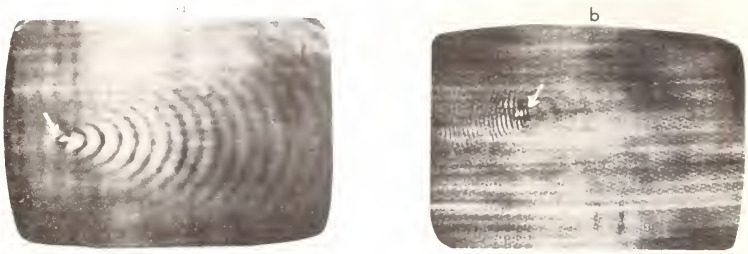

Figure 6. Acoustic micrographs showing surface damage on a test bar of silicon nitride. Images are mixed-mode acoustic micrographs. The scattered component propagates to the right in 6a and the left in 6b.

The advantages of the detection scheme illustrated in figure 6a and 6b as well as acoustic dark field imaging (not illustrated here) are the same as that described previously for surface wave imaging. Namely scattered waves propagate considerable distances from the site of the flaw; thus, small defects can be detected at relatively low magnification. The sensitivity for the detection of small flaws is increased by viewing the scattered waves. Surface damage resulting from Knoop indentations using loads as small as 1 kg have been detected. In addition, the results presented here were obtained on components whose surface finish was comparable to that generally encountered in fully processed components. The surface skimming bulk waves are relatively insensitive to the surface roughness.

5. Conclusions

Surface flaws in glass and ceramic materials were found to strongly scatter incident bulk acoustic waves. Depending upon the nature of the flaw, properties of the host materia and angle of insonification, the scattered energy can be partitioned between surface waves and surface skimming bulk waves. We found that for a 9.4° angle of incidence in water SAW was dominant in glass materials and SSBW was dominant in high strength ceramics.

We have demonstrated the capability of the SLAM to visualize both the scattered and nonscattered sound fields in the vicinity of the surface flaws. By appropriate electronic filtering the various modes can be viewed independently or in combination. The primary advantage of imaging the scattered sound field is the increased defect visibility and detection sensitivity. The visualization of mode converted surface acoustic waves can be applied to flaw detection in sputtered films, polished electronic substrates and high strength ceramic components with a good quality surface finish. The investigation of surface wave generation and propagation on nonpiezoelectric substrates may be important in SAW device development. The visualization of surface skimming bulk waves are found to be ideally suited for surface flaw detection in unprepared ceramic components. The detection sensitivity and image characteristics appear to be comparable to those found using

ode converted surface acoustic waves. However, the propagation of surface skimming bulk waves is relatively unaffected by surface texture. Thus, extensive surface preparation required for SAW visualization are not necessary for SSBW imaging schemes. Lastly, it should be pointed out that flaws detected using SSBW do not necessarily have to open to the surface. The images on ceramics result from the interference of transmitted and scattered bulk waves. Although the detection sensitivity is clearly optimal for surface features, inclusions, pores, and cracks buried at shallow depths will give rise to similar image structure.

Appendix A

Calculation of Velocity of the Scattered Wave

Whenever two or more modes are detected simultaneously in the SLAM the resultant acoustic image contains characteristic interference fringes. The fringes arise from the constructive and destructive interference between the two modes.

The nature of the problem is illustrated in figure 7 where we show two views of the dynamic ripple pattern in the vicinity of a surface flaw. In figure 7a, we illustrate the dynamic ripple resulting from the transmitted bulk wave, while in figure 7b, the dynamic ripple of the surface wave generated at the crack is shown. Although drawn separately here, these two ripple patterns will overlap spatially and lead to characteristic interference fringe patterns like those observed in figure 4b and 4c. The spatial periodicity of the observed fringe pattern is quantitatively related to the periodicity of the two modes which overlap.

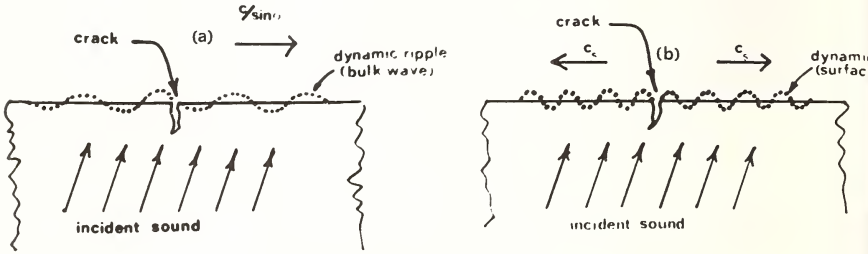

Figure 7. Schematic showing the dynamic ripple produced by the transmitted bulk wave (a) and the wave scattered from a surface flaw (b). Generally these two waves overlap spatially and can be separated by detection and filtering.

The relationship between the micrograph fringe spacing, Λ_m, and periodicity of the two modes is given by the expression:

$$\Lambda_m = \left| \frac{1}{\frac{\sin\theta}{\Lambda_b} - \frac{\cos\psi}{\Lambda_s}} \right| \qquad (2)$$

Where:

Λ_s is the surface wave wavelength.

Λ_b is the bulk wave wavelength.

θ is the incident angle.

ψ is the angle between the direction of the bulk wave dynamic ripple and the surface wave dynamic ripple, e.g. $\psi = 0_1$ corresponds to both ripple patterns propagating parallel to one another.

In this expression, Λ_s gives the spacing of the equiphase points on the surface wave dynamic ripple while the quantity $\Lambda_b/\sin\theta$ is the separation of equiphase points on the ripple pattern of the transmitted bulk wave (fig. 7).

The parameter, Λ_m, can be measured directly from micrograph 4b. The spacing, $\Lambda_b/\sin\Theta$, can be obtained from normal acoustic interferograms. The interferogram, one of four imaging modes available with the SLAM, is obtained by combining the detected acoustic signal (bulk wave ripple) with an electronic reference signal which is coherent with the drive of the transducer. The result is an image containing a series of fringes with spacing equal to $\Lambda_b/\sin\Theta$. The magnitude of this term is determined graphically from the interferogram micrographs and was found to be 92.9 μm for the insonification angle used in this study.

Equation 2 provides the relationship between the measured fringe spacing observed in mixed mode micrographs and the scattered mode wavelength. The normal dispersion relationship (i.e., $C_s = f\Lambda_s$) is then used to calculate the SAW or SSBW velocity, C_s. In micrograph 4b, $\psi = 150°$, $\Lambda_m = 25.9$ μm solving for Λ_s, we obtain a value of 31.2 μm. The acoustic frequency of 98.0 MHz gives a SAW velocity of 3060 m/s. Similarly the measured spacing of 48.3 μm in figure 4c ($\psi = 0_1°$) yields a value of 3110 m/s for the SAW velocity. The 1.5 percent difference between this determination is not significant considering the crude graphical (ruler) measurement techniques employed.

I am indebted to Dr. Lawrence W. Kessler for many valuable discussions. I am also grateful to J. J. Schuldies and the ARPA/Navy, Air Research ceramic program for supplying the ceramic samples used in this study.

References

[1] Kessler, L. W. and Yuhas, D. E., Structural perspective, Industrial Research, 20, 53-56 (1978).

[2] Kessler, L. W. and Yuhas, D. E., Listen to structural differences, Industrial Research/Development, 20, 102-107 (1978).

[3] Love, G. R. and Ewell, G. J., Acoustic microscopy applied to hybrid microelectronics, this volume.

[4] Kupperman, D. S., Dragel, G., and Yuhas, D. E., Evaluation of ceramic turbine blades with an acoustic microscope, this volume.

[5] Madeyski, A. and Kessler, L. W., Initial experiments in the application of acoustic microscopy to the characterization of steel and the study of fracture phenomena, IEEE Trans. Sonics and Ultrasonics SU-23, 363-369 (1976).

[6] Kessler, L. W., Palermo, P. R., and Korpel, A., Practical high resolution acoustic microscopy, in Acoustical Holography, Vol. 4, G. Wade, ed., pp. 51-71 (Plenum Press, New York, 1972).

[7] Kessler, L. W., The sonomicroscope, in Proc. 1974 IEEE Ultrasonics Symposium, J. deKlerk, ed., Cat. No. 74-CHO-896-1 SU, p. 735 (IEEE, N.Y., 1974).

[8] Whitman, R. L. and Korpel, A., Probing of acoustic surface perturbations by coherent light, Applied Optics, 5, 1667 (1966).

[9] Lewis, Meirion, Surface skimming bulk waves, SSBW, in Proc. 1977 IEEE Ultrasonics Symposium, Cat. No. 77-CHI-264-ISU, p. 744 (IEEE, New York, 1977).

[10] Hot pressed silicon nitride has a compression velocity in excess of 10,000 m/s and a shear velocity of 5650 m/s is typical.

ational Bureau of Standards Special Publication 596, Ultrasonic Materials Characterization,
. Berger and M. Linzer, eds., Proceedings of the First International Symposium on Ultrasonic
aterials Characterization held at NBS, Gaithersburg, Md., June 7-9, 1978. Issued
ovember, 1980.

EVALUATION OF CERAMIC TURBINE BLADES WITH AN ACOUSTIC MICROSCOPE[1]

D. S. Kupperman and G. Dragel

Materials Science Division
Argonne National Laboratory
Argonne, IL 60439

and

D. Yuhas

Sonoscan, Incorporated
Bensenville, IL

Ceramic components may fail because of the propagation of existing defects to a critical size. As a result, determination of initial defect characteristics and distribution in such components is important. The minimum flaw size that must be detected to assure reliable operation depends upon many factors such as stress, temperature, stress-intensity factor, component geometry, crack-growth rates, type of flaw, and time of operation.

Flaws with characteristic dimensions of the order of 10-100 μm will adversely affect the performance of silicon nitride used as a structural material for a gas turbine, as an example, where it will be exposed to temperatures up to 1400 °C and stresses up to 300 MPa. This flaw size is much smaller than critical flaw sizes in metals. Thus, the techniques developed for inspection of metallic components must be significantly improved or alternative methods applied to structural ceramic systems.

Detection and characterization of critical-size defects in silicon nitride components via ultrasonic methods appear feasible, although numerous obstacles must be overcome. Because of the necessity of detecting small flaws, frequencies of up to ~ 400 MHz may have to be employed (100 MHz was used in the present study).

Scanning laser acoustic microscopy may provide a means for high-frequency ultrasonic evaluation of ceramic gas-turbine rotors. The characteristics of turbine blades removed from blade rings, as revealed by acoustic microscopy, is discussed in the present report.

1. Introduction

There is an important need to develop ceramics for high-temperature engine components. mic materials that do not require cooling can be used to decrease fuel consumption and ove engine operating efficiency via higher turbine inlet temperatures. In addition, mic materials are often less costly and more corrosion-resistant than metals, and are ally fabricated from abundant, domestically available elements. Nondestructive

k supported by the U.S. Department of Energy.

evaluation methods employing ultrasonic techniques can help assure reproducible mechanical and physical properties, thus improving the operational reliability of such components as ceramic rotors.

The minimum flaw size that must be detected in order to assure reliable operation depends on many factors, such as desired operational time, operating stress, temperature, stress-intensity factor, part geometry, susceptibility of part to crack growth, and type of flaw (i.e., pores, inclusions, cracks, and/or large grains). For example, flaws with dimensions on the order of 10-100 μm will adversely affect the performance of silicon nitride as a structural material for a gas turbine, where it will be exposed to temperatures as high as 1400 °C and stresses up to 300 MPa [1][2]. Under laboratory conditions, flaws of this size can be detected in geometrically simple ceramic objects via ultrasonic techniques [1]. (The characteristic grain lengths of ceramic materials are of the order of several μm.) However, in-service testing, and testing of ceramic components with complex geometries, present formidable problems. A critical flaw size of 10-100 μm is ∿ 2 orders of magnitude smaller than critical flaw sizes in metals. Thus, the techniques developed for inspection of metalli components must be significantly improved, or alternative methods applied, to structural ceramic systems. For ultrasonic testing, this implies that frequencies of up to 400 MHz (approximately an order of magnitude higher than those conventionally used) may be required.

2. Acoustic Microscopy

The scanning laser acoustic microscope may provide a means for nondestructive evaluation of ceramic gas-turbine rotors at high ultrasonic frequencies. The instrument used in the present investigations is the SONOMICROSCOPE 100 (Sonoscan, Inc., Bensenville, IL), which is operated at an ultrasonic frequency of approximately 100 MHz [2]. This preliminary effort concentrated on the characterization of silicon nitride rotor blades. This included empirical definition of the normal structure.

The irradiation geometry used to produce the acoustic micrographs of samples studied in the present work is illustrated in figure 1. Ultrasonic energy is incident on the sample from below, at an angle of 10°. The transmitted acoustic energy imparts a slight oscillatory mechanical motion to the sample's top surface. These disturbances are detected, point by point, by a rapidly scanning focused laser beam (40,000 image points per micrograph) which drives an opto-acoustic receiver. The acoustic image is then displayed on the TV monitor; the darker areas of the micrographs are regions of higher ultrasonic attenuation. If the sample has a smooth surface finish, an acoustic image can be obtained directly from the ligh specularly reflected from the surface. Since this is not possible for silicon nitride blade a mirrored coverslip is placed in acoustic contact with the top surface of the sample and light reflected from the coverslip is used to form the acoustic image. The ten blades evaluated in the present study were removed from reaction-bonded silicon nitride rotor-blade rings supplied by Ford Motor Company. Two blade rings are shown in figure 2.

3. Results and Discussion

Data are presented in the form of photomicrographs obtained by sweeping the frequency over a variable bandwidth around 100 MHz. This eliminates coherent speckle and reveals features often masked by this speckle. In addition to displaying the acoustic amplitude distribution throughout the field of view, the SONOMICROSCOPE provides an acoustic-interference mode of operation. Acoustic interferograms show a series of alternating light and dark stripes. For acoustically homogeneous samples, these bands (interferences fringes) are parallel to one another and equally spaced. For samples that are elastically inhomogeneous, the interference lines will be distorted by localized variations in the sound velocity and/or sample thickness. A fringe shift to the left corresponds to an area of lowe ultrasonic velocity; a shift to the right indicates a region of higher ultrasonic velocity. Because many of the samples investigated in this report have controlled thicknesses, the character of the interferograms is determined solely by localized variations in the velocity of sound. These variations are related to variations in either the bulk density or elastic modulus of the sample constituents.

[2]Figures in brackets indicate the literature references at the end of this paper.

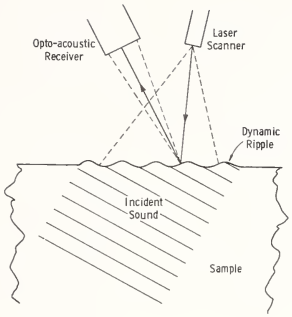

Figure 1. Schematic illustrating the detection scheme employed by the scanning laser acoustic microscope.

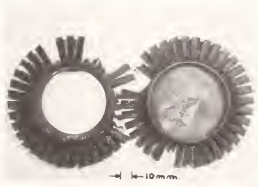

Figure 2. Two reaction sintered blade rings with (right) and without the center portion.

The first step toward localization and identification of important defects is to establish a definition of the normal structure. This was accomplished empirically in the present study, in which the "normal" structure is operationally defined as that which appears most often in actual rotor material. There are several advantages of working directly with "real" blades. First, the data obtained are directly applicable to the nondestructive testing of the intact blades. Secondly, the elastic properties may depend on the details of the fabrication process; thus, duplication of the microstructure observed in the blades may be difficult in test specimens with simple geometries. By analyzing the blades directly we study the properties of materials which have been part of the manufacturing cycle. Lastly, difficulties encountered in testing a blade with its complex geometry provide insight into th apparatus which would be required for the nondestructive testing of the entire turbine.

Although no modification of the SONOMICROSCOPE 100 was required for the present study, a scanning procedure was developed which permitted the rapid and systematic scan of a number of blades. The blades were placed in a sample holder (fig. 3) which consists of a 50 mm diameter stainless steel ring attached to a 4 μm thick Mylar base. Inside the holder, surrounding the sample, was a pliable spacer ring. The coupling medium, water, filled the holder to the level of the spacer ring. The coverslip rested on the spacer ring, close to the sample (fig. 3, top). Thus, it could be pressed down to make firm contact with the top surface of the blade (fig. 3, bottom). The coverslip (35x5x3 mm) was thinner than normal so that the contact with the sample was nearly planar (see fig. 3). The scanning of the blades was accomplished by first placing the coverslip in one position and translating the sample holder parallel to the long axis of the blade (to the left in fig. 3, top). After each longitudinal scan, the coverslip was indexed (e.g., moved to the left in fig. 3, bottom) and another longitudinal scan was made.

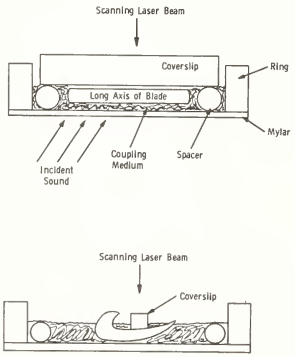

Figure 3. Configurations for scanning of ceramic rotor blade.

After acoustic scans suggested abnormally large defects in two blades, designated #18 and #28, radiographs of these blades were made to confirm the acoustic microscopy results. The blade was placed in contact with the film and x-rayed with the curved side down as well as up; two exposure times were used. The close proximity of the blade to the film made the resolution higher than can be achieved with ordinary radiographic techniques used for the intact blade ring. The flaw in blade 18 was determined by acoustic microscopy to be about 700 x 450 μm in size. All x-rays of blade 18 revealed a pore-like defect in the same area indicated by the acoustic microscopy. No other defects were seen on the x-ray film for bla 18. The anomaly was found to be 530 x 350 μm in size by x-radiography, in general agreemen with the acoustic measurement. Two types of acoustic micrographs of blade 28 are shown in figure 4. A flaw about 550 x 300 μm in size is suggested. X-rays of blade 28 revealed one

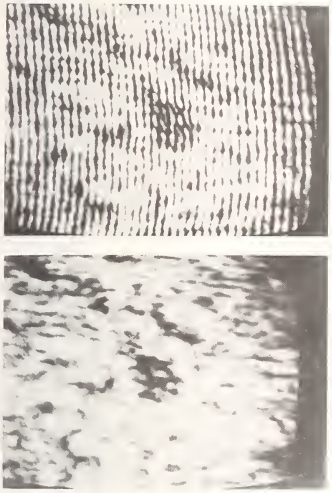

Figure 4. Amplitude and interference micrographs of turbine blade #28. Defect cluster (circled) observed in the flatter portion. The elastic microstructure surrounding the circled region is typical of that encountered throughout most of the blade. Interference lines, electronically added to the micrograph (bottom), are ∿ 80 μm apart.

e-like defect, evident in only one of four radiographs, in the area where an anomaly was ected by the acoustic microscope. A search for this flaw by metallographic sectioning at location suggested by the radiograph revealed a laminar-type defect with a pore at its e (fig. 5). The small size of the pore (∿ 100 μm) explains the difficulty in detecting it radiography. The advantage of detecting laminar-type flaws by acoustic microscopy is arly demonstrated in this sample, where such a flaw could be missed by radiographic hniques. Again, the size of the delamination, about 500 x 100 μm, is comparable to the x 300 μm size indicated by the acoustic microscope. From the cross section of blade 28 g. 5), the general porosity of the reaction-sintered blades can be seen. Pores on the er of 50 to 100 μm in diameter can be seen on the micrograph. These are not revealed by iographs. However, the acoustic microscopy did reveal anomalies on the order of 50 to μm in diameter with the same general frequency as seen on the micrograph.

4. Summary

This preliminary study employing acoustic microscopy techniques has indicated that:

1) Reaction-bonded silicon nitride rotor blades are acoustically transparent enough to be investigated at 100 MHz. The maximum thickness of the blades available for this study was 3 mm, which was easily penetrated at 100 MHz.

2) Although the blade geometry was complex, proper scanning procedures permitted direct imaging of the entire blade surface area.

Figure 5. Cross section of blade #28, 1.8 mm from end of blade, at location of pore indicated by radiography.

3) Subsurface defects or flaws can be distinguished from the normal or typical structure by this method.

4) The results demonstrate the feasibility of, and establish a data base for, the acoustic microscopic examination of intact ceramic turbines. Ultimately, this technique may allow ultrasonic examination of ceramic rotors with a degree of convenience approaching that of visual examination employing an optical microscope

---

We wish to thank Don Cassidy of Ford Motor Company for supplying the blade rings and Norm Lapinski for carrying out the radiography.

References

[1] Evans, A. G., Kuro, G. S., Khuri-Yakub, P. T., and Tittman, B. R., Mater. Eval. (Resear Suppl.), 85 (April 1977).

[2] Kessler, L. W., Palermo, P. R., and Korpel, A., Practical high resolution acoustic microscopy, in Acoustic Holography, G. Wade, ed., Vol. 4, p. 51 (Plenum Press, New York 1972).

ational Bureau of Standards Special Publication 596, Ultrasonic Materials Characterization,
. Berger and M. Linzer, eds., Proceedings of the First International Symposium on Ultrasonic
aterials Characterization held at NBS, Gaithersburg, Md., June 7-9, 1978. Issued
ovember, 1980.

ACOUSTIC MICROSCOPY APPLIED TO HYBRID MICROELECTRONICS

G. J. Ewell

Technology Support Division
Hughes Aircraft Company
Culver City, CA 90230

and

G. R. Love

Sprague Electric Co.
North Adams, MA 01247

The acoustic microscope has been shown to be a powerful new tool with the capability of characterizing nondestructively the internal structures of discrete components, substrates, and interconnections used in hybrid microelectronics. The resolution of the microscope when used in transmission is sufficient to allow inspection to the dimensional control required in both devices and substrates. Equally important, the acoustic transmission properties of a wide variety of electronically-useful materials can be important indications, not previously available, of the structural integrity and reliability of devices and substrates.

1. Introduction

The increasing usage of hybrid microcircuits in areas demanding very high reliability, uch as heart pacers and missile guidance systems, requires improved methods of non-estructive evaluation of both components and assembled systems. A NDE tool of great otential is the scanning laser acoustic microscope, an ultrasonic imaging technique that perates at very high frequencies (100 MHz to greater than 500 MHz). Described elsewhere n detail in this meeting, this instrument when used in transmission should allow high esolution viewing of the internal structures of discrete components and substrates. This aper briefly illustrates the application of the acoustic microscope to several hybrid areas: ultilayer ceramic capacitors, thick-film resistors, ceramic substrates, and interconnections.

2. Ceramic Capacitors

Ceramic capacitor "chips" exhibit many features common to all of hybrid microelectronic echnology, such as closely-spaced, multiple conducting layers, sharp and diffuse interfaces etween different materials, and occasional defects such as internal voids and lack of bonding. n addition, these devices present special examination problems because of exterior conformal etal coatings that partially mask their interior. The SONOMICROSCOPE 100 [1][1], operated at frequency of 100 MHz, was used to examine a series of capacitors, some preselected to ntain representative structural defects. The capacitors were of both terminated (with a red on silver-plus-frit system) and bare chips, of two physical sizes (table 1) and of two electric types. The majority of the chips examined were designed with an electrode paration of about 25 microns; in addition, a few chips with electrode separations up to 100 crons were also examined. Based upon several years of experience with conventional scanning trasonic inspection [2], the intent of this investigation was to evaluate the ability of e acoustic microscope to detect and examine the microstructural defects of major concern in pacitors--large voids and delaminations. During the study it became apparent that entirely w features could be explored; i.e., it was possible to document the location and alignment ecision of the stack of embedded electrodes.

[1] Figures in brackets indicate the literature references at the end of this paper.

Table 1. Experimental Design: Acoustic Microscope Evaluation.

Three factor, two level, full factorial design with
~ 25 percent redundancy

Factors:		
	Dielectric Type:	BX and NPO
	Case Size:	CDR02 and CDR05
	Part Quality:	Delaminated and defect-free, as screened by ultrasonic scanner.

Sample Size: Nominal 50 pieces per cell

Conventional ultrasonic scanning was used to screen parts initially. The parts were then screened and sorted with the SONOMICROSCOPE 100; all parts were examined and sufficient photographs were taken to document all defective parts, all anomalous structures, and a representative number of "good" parts, as well. The samples were then rescreened with the conventional ultrasonic scanner to determine the correlation between the two ultrasonic techniques. Then, representative samples of all possible combinations of "good" and defective parts were examined by standard DPA techniques [3], using serial sectioning to define, where possible, both the size and location of indicated defects.

2.1. BX-dielectric parts[2]

The experiments were an unqualified success for BX parts. Parts identified as delaminated by the acoustic microscope also appeared delaminated when examined by the ultrasonic scanner and by DPA techniques. In addition, the resolution of the acoustic microscope was so sensitive that layer separations as fine as 2 microns could be detected. The spatial resolution, moreover, was such that clusters of small (40-to-60 micron size) defects were individually resolved in acoustic micrographs, but were merged into a single defect in the ultrasonic scanner record.

In addition to this success, there were two unexpected benefits of the acoustic microscope. First, the speed of sound is greater in the embedded electrodes than in the surrounding dielectric. This difference is displayed as bends in the interference fringes (fig. 1). Such photographs contain information about both the location (relative size of side margins) and precision (accuracy of registry of successive electrodes) of the electrode stack. This information has never before been available nondestructively. The kind and quality of output data are illustrated by figures 1 to 4.

Another benefit occurs as a result of the oblique sound incidence. For the first time, it is possible to view under the cap of the silver termination, i.e., to examine even that portion of the chip covered by termination. Silver terminations are both porous and, therefore, sound dispersing and of varying thickness so that the examination is not ideal. These same characteristics permit qualitative evaluation of the coverage and uniformity of the termination itself.

2.2. NPO-dielectric parts

The interpretation of acoustic micrographs of NPO-dielectric parts is more complex. For the standard viewing conditions used for more than 90 percent of this study, the NPO parts displayed an additional acoustic feature--"speckle", which masked the features of interest (fig. 5). The term "speckle" is used here to describe the random image mottling occurring at a scale of about 80 microns. The intensity fluctuations are both above and below reference

[2] BX dielectrics are barium titanate-based ceramics, near-cubic in structure, and ferroelectric. NPO dielectrics are rare-earth titanates and non-cubic in structure.

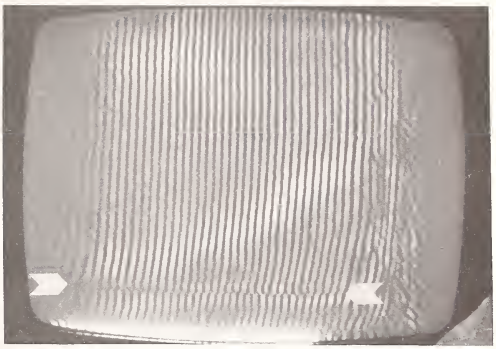

Figure 1. Acoustic micrograph of CDR06 BX chip capacitor without flaw or termination. Edge of electrodes shown with arrows. 30X magnification.

Figure 2. Acoustic micrograph of two CDR02 BX chip capacitors. Top chip shows misalignment in electrode stack; bottom chip shows well-centered electrode stacking. 30X magnification.

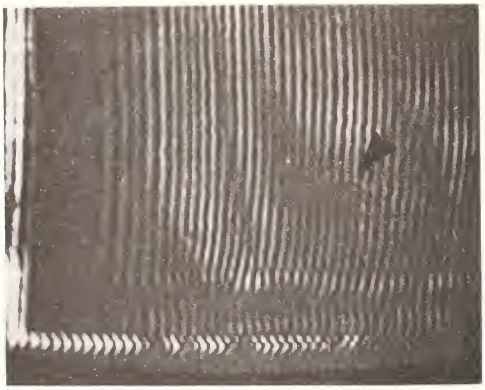

Figure 3. Acoustic micrograph of portion of flawed CDR06 BX chip. Circular delamination at arrow is about 200 microns in diameter. 30X magnification.

Figure 4. Acoustic micrograph of portion of flawed CDR06 BX chip. Gross delamination is indicated by opaque areas. 30X magnification.

evels, indicating that some focusing, or refraction, effect occurs. When the sample is otated with respect to the incident acoustic signal, the pattern does not rotate predictably ith the sample. Worst of all, the contrast of the speckle is frequently great enough that nterpretable features such as interference fringes and larger scale transmission variations annot be detected. Because of speckle, inspection of NPO dielectric parts was less success- ul. Stated more quantitatively, although the correlation between scanning ultrasonic inspec- ion and DPA was excellent, the acoustic microscope occasionally labeled good NPO parts "bad" nd bad parts "good" when compared with either of the other two techniques. Note that the rain size of the dielectric in these parts (8 microns max.) is certainly not greater than a enth of the speckle dimensions and that this dielectric also has a low level of porosity (3 ercent maximum).

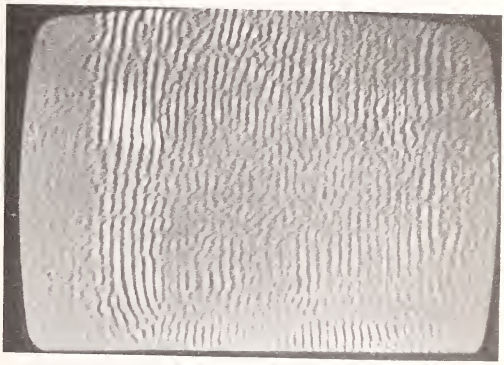

Figure 5. Acoustic micrograph of portion of CDR06 NPO chip. Compare to figure 1. Difference in transmission quality is due to "speckle". No detectable physical flaws when serially sectioned. 30X magnification.

One of the immediate actions taken was to try varying the angle of incidence of the coustic signal. An additional microscope stage was constructed with an angle of incidence 6°. This change led to a significant improvement in clarity and freedom from speckle in e acoustic micrographs of NPO parts. It was also noticed the speckle appeared to vary gnificantly with the orientation and spacing of the electrodes. For those parts showing tensive speckle, in the end margins where the electrode spacing doubles and in the side rgins where there are no electrodes, the speckle is much less severe. This suggested that unfortunate similarity between the acoustic wavelength in the NPO dielectric and the ectrode spacing might be aggravating this problem. A small number of parts with greater ectrode spacings were examined and found to be essentially speckle-free. Alternatively, it s been suggested that a minor change in the wavelength of the incident sound would reduce eliminate the speckle. It appears, therefore, that the problem of speckle in NPO electric capacitors can be solved.

3. Thick-film Resistors

Two varieties of thick-film resistors were examined in the scanning acoustic microscope. e variety is a resistor "chip" shown in figure 6 (with its acoustic micrograph) that consists a ruthenium oxide-based resistor material between metallization bands on an alumina substrate. is device was air-abrasive trimmed (arrows) after production and passivation to meet precise

electrical requirements. One area of concern is damage resulting from the trimming operatic
The acoustic micrograph indicates anomalies immediately adjacent to the trim line that may
indicate such damage. Parts showing such anomalies are now being sectioned to determine th
cause of the acoustic patterns.

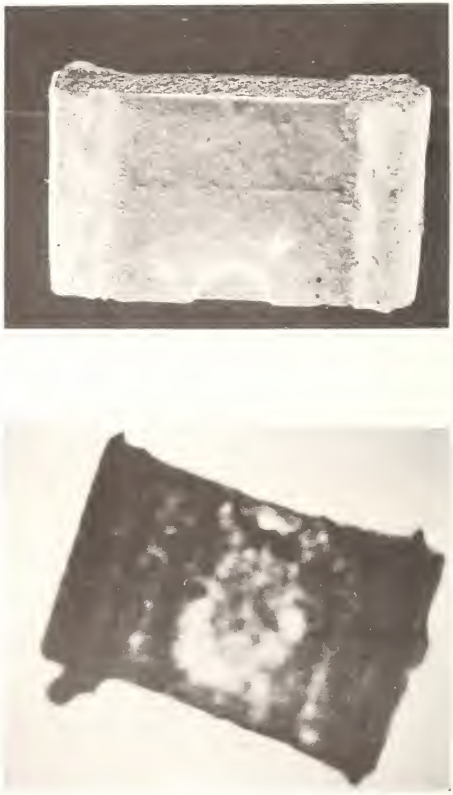

Figure 6. Thick-film chip resistor. Top view is SEM photo at 20X magnification. Arrows show trimmed region. Bottom view is acoustic micrograph showing anomalies adjacent to trimmed area. 40X magnification.

A second variety of thick-film resistor is the tin-oxide resistor formed by vapor depositing tin oxide around a cylindrical glass core. This resistor is trimmed by scribing
ral grooves and is then usually encapsulated. An unencapsulated device is shown in figure

f concern with this device is potential damage to the glass core resulting from the scribing. coustic micrographs and interference patterns of the part are shown in figure 8. The excel- ent transmission and sharp, even fringes in the acoustic interference pattern indicate the bsence of damage in the part examined.

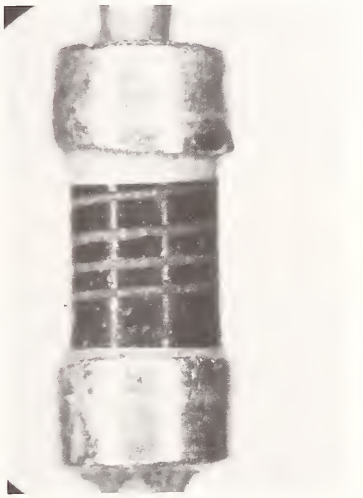

Figure 7. Unencapsulated tin-oxide resistor showing spiral trimming grooves. 30X magnification.

4. Multilayer Ceramic Substrates

To provide rugged, stable substrates for complex large scale integrated circuits (LSIs), ultilayer alumina substrates that contain internal metallization patterns are being developed. igure 9 shows one substrate with a metal ring for hermetic sealing of LSI devices. A portion f that substrate (96 percent Al_2O_3, metallized with platinum) was examined to determine the apabilities of the acoustic microscope to determine the alignment and location accuracy of n inner metallization pattern. Figure 10 shows the ability of the acoustic micrograph to esolve the buried metallization pattern (0.25 mm below the surface) and to accurately locate t with respect to the top surface pattern. Other defects such as areas of missing metal- ization and lack of bonding should also be resolvable.

Figure 8. Transmission acoustic micrograph (top) and interference pattern (bottom) of tin oxide resistor. No indication of part damage. 30X magnification.

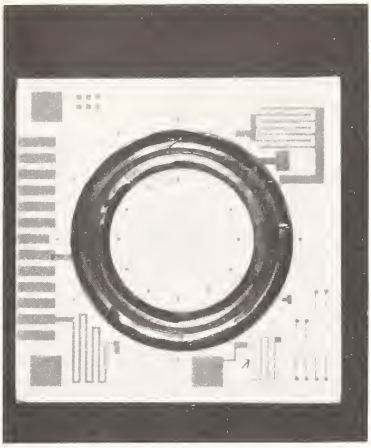

Figure 9. Overview of multilayer Al_2O_3 substrate with ring for LSI device. Area examined in acoustic microscope shown by arrow. 1.3X magnification.

5. Interconnections

Work by Tsai and co-authors [4] at Carnegie-Mellon and by Kessler [5] has shown the ›ility of the acoustic microscope to resolve voids in solder joints. A preliminary ›aluation of wire bonds (gold-to-gold) has also indicated an ability to identify some ›fects in both thermocompression- and ultrasonic-bonded wires.

6. Conclusions

A preliminary survey of potential application areas of a transmission acoustic croscope to hybrid microelectronic technology indicates a number of promising fields. mponents with hidden interfaces, multilevel substrates, and interconnections all appear enable to inspection by and thus improved control with an acoustic microscope. These plications all require detailed studies to correlate acoustic signatures with physical fects. Such a study has been initiated with multilayered ceramic capacitors and the results date indicate improved defect resolution and increased application ease when compared with ternate NDE techniques.

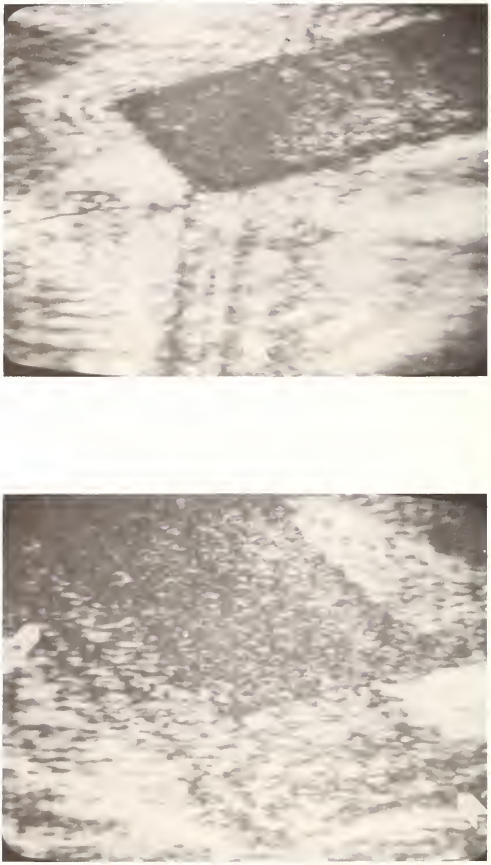

Figure 10. Acoustic micrographs of multilayer substrate shown in figure 9. Top view shows second layer run and contact (arrow) to top layer pad. Bottom view shows top and bottom (arrows) metallization patterns. 80X magnification.

References

[1] Available at Sonoscan, Inc., Bensenville, IL.

[2] Love, G. R., Nondestructive testing of monolithic ceramic capacitors, in Proc., 1973 International Microelectronics Symposium, ISHM, pp. 1A3-1A8 (1973).

[3] Ewell, G. J. and Jones, W. K., in Encapsulation, sectioning and examination of multilayer ceramic chip capacitors, in Proceedings IEEE-EIA Electronic Components Conference, pp.446-451, Arlington, VA (1977).

[4] Tsai, C. S., Wang, S. K., and Lee, C. C., Visualization of solid material joints using a transmission type scanning acoustic microscope, Applied Physics Letters, 31, 317-320 (1977).

[5] Kessler, L., private communication.

ational Bureau of Standards Special Publication 596, Ultrasonic Materials Characterization,
. Berger and M. Linzer, eds., Proceedings of the First International Symposium on Ultrasonic
aterials Characterization held at NBS, Gaithersburg, Md., June 7-9, 1978. Issued
ovember, 1980.

DETECTION AND CHARACTERIZATION OF ALLOY SPIKES IN POWER TRANSISTORS USING TRANSMISSION ACOUSTIC MICROSCOPY

C. C. Lee, J. K. Wang, and C. S. Tsai

Center for the Joining of Materials and
Department of Electrical Engineering
Carnegie-Mellon University
Pittsburgh, PA 15213

and

S. K. Wang and P. Hower

Westinghouse Research and Development Center
Pittsburgh, PA

Alloy spikes at the silicon-alloy interface are known to cause undesirable effect in drastically lowering the breakdown voltage of power transistors. By operating a 150 MHz transmission-type acoustic microscope at a combination amplitude and phase mode, we were able to determine both the location and size of the alloy spikes of a production-line power transistor. The alloy spikes have been clearly identified both from the difference in acoustic velocity between the silicon and the alloy layer and from the scattering loss of the focused acoustic beam spot caused by the alloy spikes.

1. Introduction

Several types of acoustic microscopes have been developed and used to visualize various inds of solid materials [1-9][1]. We have recently employed a transmission-type acoustic icroscope operating at 150 MHz to image and characterize the interfacial regions of a number f specially made joints as well as production-line solder bonds of die-attached transistor eaders with large thickness [3-5]. In this paper, we report on the concept and some experiental results obtained using the same microscope in determining both the size and the ocation of alloy spikes in a production-line power transistor. The detection of such alloy pikes was facilitated through the operation of the microscope at a combination amplitude nd phase mode.

2. Structure of the Power Transistor

The power transistor was formed by alloying a silicon wafer on a molybdenum preform hich has a thickness of 1.27 mm and a diameter of 23 mm. Prior to alloying, base and mitter diffusion had been made in the silicon wafer while aluminum metalization was made fter alloying. The orientation of the silicon is (111) and its thickness is around 150 μm. igure 1 shows the top surface of the power transistor on which the aluminum metalization is learly seen. A cross-sectional sketch of the power transistor is given in figure 2. The hickness of the alloy layer is about 50 μm. It is known that the alloy may penetrate into he Si layer to form the so-called alloy spikes. Such alloy spikes are known to cause ndesirable effect in drastically lowering the breakdown voltage of the power transistor and herefore to make the transistor useless.

[1] Figures in brackets indicate the literature references at the end of this paper.

Figure 1. Top view of the production line power transitor under study.

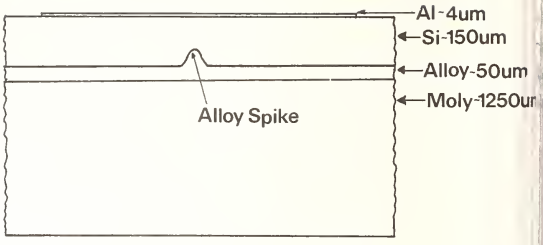

Figure 2. Cross-sectional sketch of the power transistor.

3. Acoustic Image of Moly Preforms and Silicon Wafers

Significant variations in both amplitude and phase can occur in the transmitted acoustic signal when the focused acoustic beam spot of the microscope coincides with the alloy spikes. In order to distinguish the amplitude and phase variations introduced inside the moly and silicon wafers from those caused by the alloy spikes, the acoustic images of a few typical moly preforms and silicon wafers were first taken. The relative phase and amplitude of the transmitted signals were measured by a HP Vector Voltmeter (model 8405A) which has a dynamic range greater than 80dB. Figure 3(a) is an acoustic amplitude image taken in a portion of a typical moly preform. Figure 3(b) shows the acoustic phase and amplitude variations along line A-B of figure 3(a). It is seen that the maximum phase and amplitude variations along line A-B are only 50° and 5 dB, respectively. The phase and amplitude variations obtained along other lines of scan in the same portion of the preform as well as in a number of different preforms also give similar results. With regard to the silicon wafer the measured variations in the amplitude and the phase are even smaller.

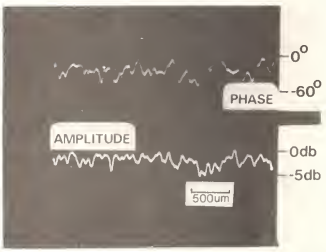

Figure 3. (a) Acoustic amplitude image of a typical moly preform. (b) Acoustic phase variation (upper curve) and acoustic amplitude variation (lower curve) along line A-B of (a).

4. Alloy Spikes Detection and Characterization

When a focused acoustic beam spot scans across an alloy spike with depth Δd penetrating into the silicon, the transmitted acoustic wave will encounter a phase change $\Delta\phi$ given by

$$\Delta\phi = 360^\circ \times \Delta d \, (1/\Lambda_{Si} - 1/\Lambda_{alloy}) \quad (1)$$

ere Λ_{Si} and Λ_{alloy} are the wavelengths of the acoustic wave in silicon and alloy. Since e composition of the alloy layer is dominated by silver, we assume that Λ_{alloy} is proximately equal to Λ_{Ag}. The longitudinal acoustic wave velocities of Ag and Si are 65 x 10^6 mm/s and 9.35 x 10^6 mm/s, respectively [10]. At 150 MHz, the operating frequency the microscope, Λ_{Si} and Λ_{Ag} are, respectively, 62 μm and 24 μm. Therefore, we have

$$\Delta\phi = 360^\circ \times \Delta d \, (1/62 \ \mu m - 1/24 \ \mu m)$$

$$= -360^\circ \times \Delta d/39 \ \mu m \quad (2)$$

$$\Delta d = -\Delta\phi/360^\circ \times 39 \ \mu m \quad (3)$$

e negative sign in eq. (2) simply means that an alloy spike penetrating into the silicon ll cause a decrease in phase in the transmitted acoustic signal.

In addition to this decrease in phase, a decrease in the acoustic amplitude is also pected because of the scattering loss caused by the spike and the impedance mismatch tween Si and Ag-dominated spike. This decrease in amplitude should increase with the total cursion and/or the sharpness, namely the absolute value of the slope, of the phase riation caused by the alloy spike. This correlation between phase and amplitude enables us identify the spikes.

Figure 4 shows the acoustic amplitude images of a portion of the power transistor tained with different adjustment of focus. In figure 4(a), the microscope was focused on e silicon surface and it clearly shows the Al metalization pattern. The image obtained by cusing at the Si-alloy interface is shown in figure 4(b). We see that the image of the uminum pattern is no longer as sharp. Finally, when the microscope was focused on the back rface of the transistor, the feature of the strips on the surface could be imaged. Figure shows the optical image of the front surface of the transistor. The area for which the tical image was taken is identical to that for the acoustic images shown in figure 4.

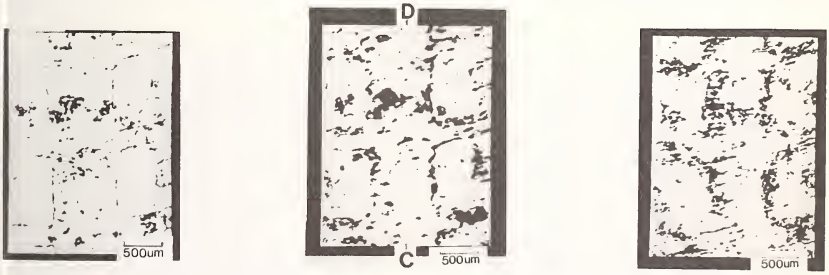

Figure 4. Acoustic amplitude images of a portion of the power transistor obtained with different adjustment of focus. (a) focused on the silicon surface, (b) focused at the silicon-alloy interface, and (c) focused on the transistor back surface.

Figure 5. Optical image (obtained from the silicon surface) of the area for which the acoustic images were taken.

Initially, we suspected that the dark areas which appeared in the acoustic image obtained by focusing on the Si-alloy interface were caused by the alloy spikes. To verify this speculation we then observed carefully both the acoustic phase and amplitude variations along several lines on the sample to see if they were correlated as expected. As an example, the acoustic phase and amplitude profiles along line C-D of figure 4(b) have been plotted and are shown in figure 6(a). Along line C-D, the acoustic beam did not cross the interdigitated aluminum pattern, and, consequently, no significant variation in either amplitude or phase, which would otherwise be caused by the transit of the acoustic beam through the interdigitated pattern, could be expected. Significant decreases in phase and amplitude are seen in the region marked "P" of figure 6(a). Consequently, this region was expanded in scale (fig. 6(b)) so that its detailed structures could be examined more closely. By comparing the phase profile with the amplitude profile, we observe that each sharp variation in phase is accompanied by a decrease in amplitude. This observation is in agreement with the expected correlation between the phase and amplitude variations caused by an alloy spike. Furthermore, we also observe that around the region "P" the decreases in phase and amplitude are, respectively, 140° and 23 dB which are much larger than what the moly preform itself could have produced (see fig. 3(b)). According to eq. (3), the depth of the spike is estimated to be 15 μm, and from figure 6(b) the width of the spike is estimated to be 100 μm. We have also observed alloy spikes as deep as 39 μm with a width of 40 μm.

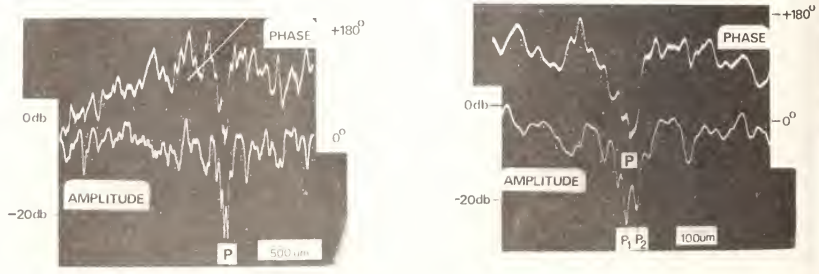

Figure 6. (a) Acoustic phase variation (upper curve) and acoustic amplitude variation (lower curve) along line C-D of figure 4(b), and (b) expanded version of (a).

In addition to the correlation between the phase and the amplitude depicted in the gion "P" of figure 6(b), we also observe two well-resolved amplitude dips marked "P_1" and $_2$". The distance between P_1 and P_2 is estimated to be 40 μm. This distance would mean at the resolution of the microscope is definitely better than 40 μm. Since the resolution a microscope depends not only on the parameters of the microscope itself but also on the rameters of the sample under testing, it is important to know the resolving power or the oustic beam spot size of the microscope when a sample is examined. The importance of owing the beam spot size can be illustrated by considering the effect of the finite beam ot size on the accuracy of the measurement made in detecting the alloy spikes. Because the asured size of an alloy spike is the space-averaged value of the actual spike with the oustic beam profile, the observed spike will not be as sharp as the actual one unless the am spot is infinitely smell. This degradation in image sharpness can be reduced, to some gree, by a deconvolution technique if the beam spot size is known.

5. Conclusion

In conclusion, we have utilized the transmission acoustic microscope operating at 0 MHz and at a combination amplitude and phase mode to determine both the location and e size of alloy spikes at the silicon-alloy interface of a production-line power ansistor.

The support from the Materials Research Laboratory Section, National Science Foundation, der Grant No. DMR72-03297-A03 is gratefully acknowledged.

References

] Lemons, R. A. and Quate, C. F., Integrated circuits as viewed with an acoustic microscope, Appl. Phys. Lett., 25, 251 (1974).

] Atalar, A., Quate, C. F., and Wickramasinghe, H. K., Phase imaging in reflection with the acoustic microscope, Appl. Phys. Lett., 31, 791 (1977).

] Tsai, C. S., Wang, S. K., and Lee, C. C., Visualization of solid material joints using a transmission-type scanning acoustic microscope, Appl. Phys. Lett., 31, 317 (1977).

] Tsai, C. S., Wang, S. K., and Lee, C. C., Acoustic imaging of joined surfaces, to be published in the Proceedings of ARPA/AFML Meeting on Review of Progress in Quantitative NDE, Cornell University, Ithaca, New York (1977).

] Wang, S. K., Lee, C. C., and Tsai, C. S., Nondestructive visualization and characterization of material joints using a scanning acoustic microscope, 1977 Ultrasonics Symposium Proceedings, pp. 171-175, IEEE Cat. No. 77CH1264-1SU.

] Weglein, R. D. and Wilson, R. G., Image resolution of the scanning acoustic microscope, Appl. Phys. Lett., 31, 793 (1977).

] Chubachi, N. and Sannomiya, T., Composite resonator using PVF_2 film and its application to concave transducer for focusing radiation of VHF ultrasonic waves, 1977 Ultrasonics Symposium Proceedings, pp. 119-123, IEEE Cat. No. 77CH1264-1SU.

] Bennett, S., Payne, D., and Ash, F. A., Reflection geometry for microscopy and NDT, 1977 Ultrasonics Symposium Proceedings, pp. 161-164, IEEE Cat. No. 77CH1264-1SU.

] Kessler, L. W. and Yuhas, D. E., Structural perspective, Industrial Research, 20, 52-58 (1978).

10] Auld, B. A., Acoustic Fields and Waves in Solids (John Wiley and Sons, 1973).

National Bureau of Standards Special Publication 596, Ultrasonic Materials Characterization, H. Berger and M. Linzer, eds., Proceedings of the First International Symposium on Ultrasonic Materials Characterization held at NBS, Gaithersburg, Md., June 7-9, 1978. Issued November, 1980.

THE INSPECTION OF BONDING AND LAYERS

G. A. Alers

Rockwell International
Science Center
Thousand Oaks, CA 91360

The joining of materials by adhesion has long been recognized as an optimum method of building a structure. Parts and subassemblies can be put together with a minimum of effort and no special provisions need to be made to accommodate fasteners or their installation tools. Furthermore, there is neither a need to maintain an inventory of fasteners, nor a requirement to guard against flaws introduced by the fastener holes. Also, the weight and materials penalty in the final structure is minimized.

With all of these advantages, it is surprising that this method of joining is not universally used. As a matter of fact, it is the inability to predict the strength of the completed adhesive joint that blocks its widespread utilization. No matter how conservative is the design or how carefully the manufacturing process is controlled, we are all reluctant to climb aboard an airplane that has no bolts or rivets and is held together by thin layers of adhesive polymers. We might feel much more confident if we knew that some instrument had been used on all the joints and had predicted the satisfactory strength of every section of adhesive bond on that airplane.

The papers in this section represent a good cross section of the current state-of-the-art aimed at developing the necessary techniques and instrumentation that will some day put a seal-of-approval on adhesive bonds so that they can be used for primary, load carrying structures. Of course, bonding is used now and there are techniques that can tell the difference between no bond and a physical connection. Also, as these papers attest, there are bonds that consist entirely of metal layers; these make joints that are much stronger than any adhesive bond. The problem which the papers in this session are actually addressing is the interaction of ultrasonic waves with a layered medium. Particularly, the case in which the layer is very thin. It is a far simpler problem than that of scattering from a small defect embedded in a solid and the mathematical description of these interactions is actually well established. What is not well defined is the detailed picture of the modes of failure - especially for failures that initiate or propagate right at the interface between the layers. The papers in this session address some of the defects that are known to cause weak joints such as porosity at the interface and water attack on the bulk adhesive within a bond. Other papers describe waves that propagate along the interface at the joint between dissimilar solids and show how a wave can propagate across a thin layer of air. These are all necessary to the assurance of strength in adhesively-bonded structures but they are not sufficient to really solve the problem of predicting the strength of a completed bond. It is quite easy to make a joint that fails because of weak chemical bonds across a contaminated interface. Also, we do not yet know how to describe the fracture mechanics of a layered, inhomogeneous medium so that the critical size of flaw can be specified. We must also realize that a bond can fail by peel as well as by shear and any device that is to predict the strength of a completed joint must have two output readings to describe both of these failure modes.

Therefore, my primary goal in introducing this section on bonding and layers is to point out that this is a very large problem which can and should be solved by a lot of hard, scientific work that is just beginning.

National Bureau of Standards Special Publication 596, Ultrasonic Materials Characterization, H. Berger and M. Linzer, eds., Proceedings of the First International Symposium on Ultrasonic Materials Characterization held at NBS, Gaithersburg, Md., June 7-9, 1978. Issued November, 1980.

ULTRASONIC SPECTROSCOPY AND THE DETECTION OF HYDROTHERMAL DEGRADATION IN ADHESIVE BONDS

E. A. Lloyd and D. S. Wadhwani

The City University
St. John Street
London E. C. 1V 4PB

When an adhesively bonded joint is subject to a combination of high humidity and temperature both irreversible and reversible degradation can occur. Ultrasonic Spectroscopy has been used since 1974 as part of a broadly based investigation into the integrity of adhesive joints of the single overlap type. It has been particularly successful in monitoring the hydrothermal degradation of adhesive joints and has provided an insight into the mechanisms of failure. Failure is due to a reduction of adhesion at the adhesive/adhered interface followed by corrosion of the exposed adhered surface.

1. Introduction

Most advocates of metal jointing with adhesives stress the advantages of fabricating higher strength-to-weight structures with smoother exterior surfaces than can be achieved with fasteners and rivets. In spite of this advocacy there are few structures today in which this potential has been fully realized. Lack of confidence in fabrication monitoring and the question of durability in service are probably the two main reasons why adhesively bonded structures are being so conservatively designed.

The very nature of an adhesively bonded assembly limits access and contributes largely to the problem of test and inspection. Although test coupons are routinely fabricated with the assembly and destructively tested, they are not always representative of the assembly. It is for this reason that nondestructive (N.D.T.) techniques are needed to guarantee the integrity of the assembly as fabricated and to monitor its durability in service.

During the fabrication process the wetting and attachment of the adhesive to the adherend is promoted by the application of heat ($\sim$ 175 °C) and pressure ($\sim$ 0.3 - 0.5 N/mm^2) for a period of up to 3 hours [1][1]. Adhesion is due to Van der Waal forces arising from dipole-dipole interactions between the polar adhesive and the metallic adherend [2]. Coupling agents too are being used to promote stronger covalent bonding between the adhesive and adherend. Although the presence of these covalent bonds results in an increase in the dry bond strength, water, for example, can now play a predictable role in modifying the bonds formed between the adhesive and adherend surface [3]. There is an extensive literature on the adverse effects of hot-humid conditions on the durability of aluminium joints bonded with epoxy based adhesives [4].

Others have reported a preference for regions near the adherend surfaces to be richer in solvents and additives than in the main body of the adhesive [5]. This and mono-layered contamination of the adherend surface are probably the other common contributors to poor adhesion.

To these considerations must be added the essential complexity of the bonded joint itself. At its simplest this consists of two adhered layers, usually metal, a bulk adhesive

[1]Figures in brackets indicate the literature references at the end of this paper.

which in itself may be subject to catalytic oxidation because of the presence of the metal adherend [6] and the two intermediate interfacial regions probably some hundreds of Angstrom units in thickness. With these interfaces determining the adhesion of the joint itself, it is not too surprising that few conventional N.D.T. techniques appear, at first sight, particularly suitable for the purpose of bond monitoring and inspection. Nevertheless, a pilot study carried out on specimens prepared at the Royal Aircraft Establishment, Farnborough, demonstrated that Ultrasonic Spectroscopy was indeed capable of differentiating between standard joints and those in which the fabrication process had been modified to produce examples of joints with reduced adhesive and cohesive properties [7,8].

2. Ultrasonic Reflectivity at an Interface

One of the difficulties in advocating the use of ultrasonic methods for the monitoring of bond quality, is to provide a convincing explanation for the demonstrable sensitivity of ultrasound to interfacial properties. This is particularly taxing when the wavelength of the interrogating ultrasound may be many orders greater than the effective thickness of the interface.

In this work it has been particularly useful to model the interface between two acoustic media with characteristic impedances Z_1 and Z_2 and to represent it as a compliance C. This avoids the necessity of ascribing to the interface an acoustic impedance, velocity and a dimension.

The stress wave amplitude $\sigma(x,t)$ associated with an ultrasonic wave $\Phi(x,t)$ in a medium with Young's Modulus (Y), density (ρ) and propagation velocity (c) can be expressed as,

$$\sigma(x,t) = -Y\partial\Phi(x,t)/\partial t \simeq - sc^2\partial\Phi(x,t)/\partial t \qquad (1)$$

Putting the boundary at the origin of the coordinate system (i.e., x = o), then $\Phi(x,t)$ in medium 1 will be the sum of the incident and reflected rays, figure 1.

$$\Phi_1(x,t) = A_o[\exp\ j\omega(t-x/c) - \alpha\ \exp\ j\omega(t + x/c)]$$

Whereas in medium 2,

$$\Phi_2(x,t) = A_o\{\beta\ \exp\ j\omega(t - x/c_2)\} \quad .$$

Applying the condition that stresses are equal across the boundary yields,

$$\sigma_1(t) = \sigma \text{ boundary} = \sigma_2(t)$$

From eq. (1) and putting x = 0 leads to the triple equality,

$$j\omega Z_1(1 - \alpha) = (1 + \alpha - \beta)/C = j\omega Z_2(\beta) \quad .$$

Solving for α, which represents the boundary reflectivity yields,

$$\alpha = [Z_1 - Z_2 + j\omega C(Z_1Z_2)]/[Z_1 + Z_2 + j\omega c(Z_1Z_2)] \quad .$$

To test the self-consistency of this result, we examine the following conditions:

1) When the boundary is rigid, $C \to 0$ and the expression above reduces to the more familiar representation for boundary reflectivity:

$$\alpha = [Z_1 - Z_2] \ / \ [Z_1 + Z_2] \quad .$$

2) When the boundary is soft, $C \to \infty$ and as anticipated

$$\alpha \to 1 \quad .$$

This is the condition for total reflection, i.e., media 1 and 2 are isolated by the large intermediate compliance.

3) When the compliance C is finite, the reflectivity α is complex and frequency dependent.

It is worthwhile examining how the amplitude and phase of a signal returned by such an nterface would be modified. The interfacial reflectivity α has been computed (figs. 1b, c) or some representative values of Z_1, Z_2 and boundary compliance. The most notable feature s the high sensitivity in the phase spectrum to small compliances at the boundary between imilar materials. This is a condition likely to be satisfied in a solvent bond, thermo-ompression bond or even a diffusion bond between identical materials and may indicate a ethod for their inspection. For an aluminium adherend and an epoxy adhesive, the ratio of mpedances across the interface is typically between 4 and 5 to 1. Referring to figures 1b, , this indicates that although the sensitivity to a boundary compliance is reduced, changes n the amplitude and phase spectra are still significant. The position would be less avorable had the adherend been, for example, steel instead of aluminium because of its igher acoustic impedance and consequent increase in the impedance ratio across the boundary.

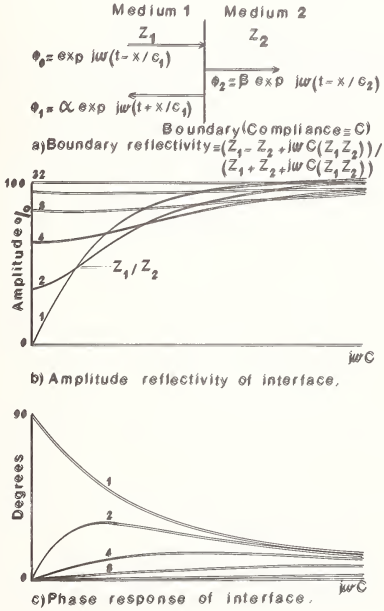

Figure 1. Analytical model of interface with compliance.

3. Ultrasonic Reflectivity of an Adhesive Joint

The most notable feature of the frequency domain reflectivity of an adhesive joint is the formation of principal and satellite responses (c.f. fig. 2b). The principal responses can all be associated with eigenmodes in the primary adherend layer, that is the adherend layer nearest the interrogating transducer. However, the position of the satellite responses could not readily be correlated with a measurable property.

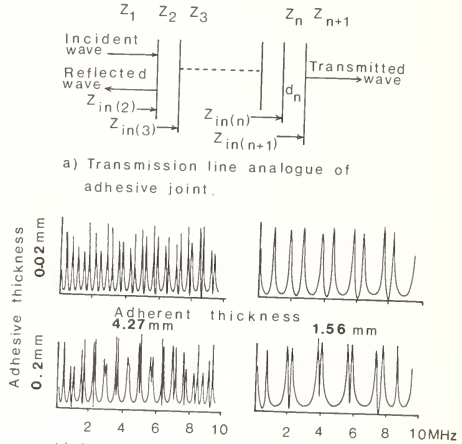

Figure 2. Full wave frequency domain response of adhesive joints.

4. Transmission Line Analog

In an attempt to clarify the position, a transmission line analog was considered figure 2a, (see also Brekhovskikh [9]). The reflectivity of a multi-layered joint can be represented by,

$$R = (A_{in(2)} - Z_1)/(Z_{in(2)} + Z_1)$$

where

$$Z_{in(n)} = Z_n(Z_{in(n+1)} + jZ_n \tan k_n d_n)/(Z_n + jZ_{in(n+1)} \tan k_n d_n)$$

and

Z_n = impedance of element n

$Z_{in(n)}$ = input impedance at interface to element n.

k_n = $2\pi/\lambda_n$, λ_n and d_n are the ultrasonic wavelength in and thickness of element n.

lutions to this equation have been computed for a representative range of adherend and dhesive properties, (fig. 2b).

The upper and lower traces on the right hand side represent the reflectivity of a joint n which the thickness of the adherend layers are equal and fixed at 1.56 mm. The lower race is for an adhesive layer 200 μm in thickness which reduces to 20 μm in the upper trace. n both cases the principal responses are the eigenfrequencies of the primary adherend layer hereas the separation between the principal and satellite responses is clearly inversely elated to adhesive thickness. However, this relationship is complex and the separation ecreases as the frequency of the principal response increases.

Similar conclusions can be drawn for the pair of left hand traces. In this case the rincipal responses have a decreased separation, because the adherend thickness has been ncreased, but the separation increases with a decrease in adhesive thickness as before.

In order to examine how variations in the interfacial properties might modify the pectral response, discrete and acoustically thin intermediate regions varying in their coustic properties were introduced into the model. No definite conclusions could be drawn owever; the results being significantly modified by the assumption used. It seemed more ppropriate to define a boundary that could contain an arbitrary compliance rather than deal ith an imposed solution.

5. Boundary Reflectivity Analog

The adhesive layer and the two associated interfaces with the adherends is shown chematically in figure 3a. An impulse traveling from medium 1 into the adhesive results in oth a reflected and transmitted wave train.

The first three terms in the reflected wave train are,

$$R_{(t)} = r_1\delta_o(t) + (1 + r_1)\, r_2(1 - r_1)\delta_o(t - \tau) + (1 + r_1)r_2(-r_1)(1 - r_1)\delta_o(t - 2\tau)$$

hereas in the frequency domain the total response can be represented very conveniently by

$$R_{(j\omega)} = [r_1 + r_2\Phi_{(j\omega)}]/[1 + r_1r_2\Phi_{(j\omega)}]. \quad . \quad . \qquad (2)$$

Here $\Phi_{(j\omega)}$ represents the phase shift by a double pass through the adhesive layer. In his form the boundary reflectivities r_1 and r_2 respectively can be associated with an rbitrary compliance and modifications to the spectrum of the signal returned from the dhesive studied.

Extension to an increasing number of interfaces is possible so that both adherends and dhesive can be modeled. However, this becomes an exercise in algebra and the essential echanisms tend to be masked.

There are also many cases in which the adhesive joint geometries are favorable and time esolved waveforms are generated with transducers operating below 15 MHz. Such a geometry is epresented in figure 3b. The first wave packet returned in this case is a resolved reflection rom the adhesive layer, that is R(jω) of eq. (2).

The second wave packet is, on the other hand, a composite waveform. It consists fig. 3b) of a secondary reflection from the adhesive layer to which is added a contribu- ion which has passed through the adhesive layer and has been reflected from the secondary dherend layer back through the adhesive.

Both these wave-packets can simply be expressed as follows:

$$R_1(j\omega) = R(j\omega)$$

$$\text{and } R_2(j\omega) = -r_oR^2_{(j\omega)} + r_3(1 - R^2_{(j\omega)})\Phi(j\omega) \quad .$$

In a practical test in which the interrogating transducer is water coupled to the adhesive joint, r_o represents the reflectivity of a water-metal interface whereas r_3 represents the reverse, a metal-water interface.

Therefore, $r_3 = - r_o$ and $R_{2(j\omega)} = - r_o \left[R^2_{(j\omega)} + (1 - R^2_{(j\omega)}) \Phi_{(j\omega)} \right]$

This expression has been computed in figure 3c for boundary conditions representing adhesive bonds formed between adherend aluminium layers. Experience too has shown that the transmissivity of the adhesive layer is important and this too has been varied in figure 3c.

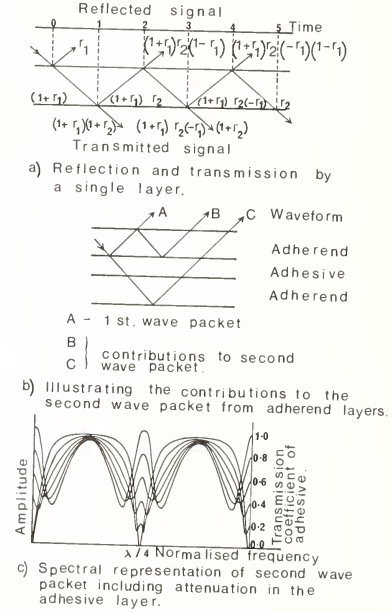

Figure 3. Reflectivity of adhesive joint.

The most notable feature is the peaking which occurs within the primary anti-resonance troughs. This is the contribution that has passed twice through the adhesive bond and is expressed by the second term in the equation for $R_{2(j\omega)}$ above. Evidently since $R_{2(j\omega)}$ can be determined uniquely from the first wave-packet, a double transit through the adherend layer can be derived with the effect of r_1 and r_2 equally weighted. A second but longer term objective is to explore the possibility of using the two expressions, both functions of r_1 and r_2, and to explore the possibility of determining r_1 and r_2 separately. The acoustic thickness is obtained separately from a measurement of the first anti-resonance frequency. The acoustic thickness (d/c_1), where d is the physical thickness of and c_1 is the longitudinal wave velocity within the adhesive, is equal to

$$d/c_1 = (2f_1)^{-1}$$

where f_1 is the first anti-resonant frequency.

At the same time, by taking the difference between the height of the peak in the second wave-packet at the first anti-resonance and subtracting from this the height of the trough for the first wave-packet, again at anti-resonance, the difference approximates to the double pass through the bond and avoids the necessity of signal processing. Thus when the two signals overlap, transmissivity is high and a positive result is recorded. When they fail to overlap, transmissivity is low and a negative result recorded.

6. Measurements

The analog equipment, figure 4, used for this purpose is similar in principle to that used by other workers in this field. The delivery recently of a PDP 11-34 will make it possible to go on-line and to employ signal processing. The transducers used are novel in the sense that their rear surfaces are dished prior to forming a tungsten loaded araldite packing onto them under pressure and in a mould. This results in a conductive loading which also acts as the rear electrical connection to the 1 cm diameter PZT 5 element.

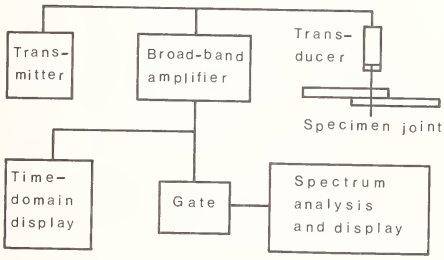

Figure 4. Block schematic of the analog instrumentation used in these measurements.

The advantages this dishing gives are two-fold. Firstly, the element has a lower mechanical Q than an equivalent planar structure; resulting in a short pulse broad band signal. Secondly, the higher frequencies are excited preferentially towards the center of the disc where the section is thinnest. Because of this the directivity of the transducer increases less dramatically than is the case with an equivalent uniformly excited element. Thus even with a proble operating over five octaves (0.5 to 16 MHz), the problem of probe-to-specimen alignment is reduced.

The nature of the measurements made are specimen dependent. For the thicker bonds, developed particularly by the supported adhesives and with adherend layers of 4 mm aluminium, the wave packets are well resolved and can be analyzed individually.

Figure 5a is a typical spectrum of the first wave packet returned from a 1 in (2.54 cm) single overlap joint, 2 in (5.08 cm) long. The anti-resonance minima are well defined and clearly illustrate the changing thickness in the bond-line. This figure also serves to illustrate the problem of defining a figure of merit for a joint. For example, if, as has been suggested, the "Q" of the anti-resonance trough were used as a quality factor then because both the depth of the trough and the 3 dB bandwidth vary with position, the indicated bond-quality would vary. In fact, it is the thickness of the adhesive which varies whereas the bond quality could be expected to remain sensibly constant over this comparatively small area.

The same limitations apply to the differential system adopted here if variations in attenuation with frequency were not taken into consideration. For example, in figure 5b, these results have been obtained by scanning across a one inch (2.54 cm) square overlap joint. In this case the adhesive was sufficiently thick to allow two anti-resonance troughs to be recorded. There is a substantial increase in bond attentuation with increase in frequency.

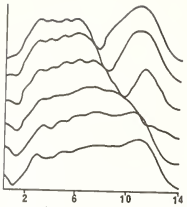

a) Illustrating the variation of bond-line thickness in a typical single overlap joint.

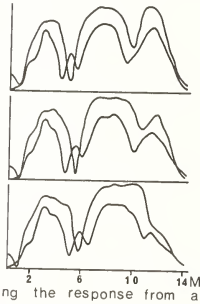

b) Illustrating the response from an acoustically thick bond.

Figure 5. Spectrum of resolved signals from thick adhesive/thick adherend specimen.

Another problem met with in the interpretation of experimental data is that adhesive joints do not fail homogeneously. To a first approximation joints which fail with evidence of a high adhesion to cohesion failure ratio were fabricated at the lower temperatures. This suggests a less adequate wetting of the adherend by the adhesive. As the temperature is increased, failure becomes homogeneous and is exclusively cohesive.

When the joint is first loaded, stress concentrations occur where the adherends end and the fillets begin. The nature of the forces operating are still a matter for conjecture but the load the joint will support does appear to be determined by the adhesive strength of the bond at the fillets because failure is predominantly adhesive in this region. The rest of the surface tends to fail cohesively. Are the joints formed at lower temperatures inherently inhomogeneous in their adhesive and cohesive properties? Higher resolution transducers than currently available would be required to investigate this hypothesis.

7. Hydrothermal Degradation

One of the least understood of the mechanisms of bond failure occurs when they are exposed to high humidity and elevated temperatures. In the field this degradation is unpredictable and may take many years to occur.

In order to accelerate this form of degradation, representative samples of adhesive joints were immersed in tap water at 60 °C and measurements taken at weekly intervals. All

The specimens had been prepared identically from 4.3 mm aluminium plate with FM1000 as the adhesive. The bond had a one inch (2.54 cm) overlap and was two inches (5.08 cm) wide. Measurements were taken on a five point grid, that is at the four corners and in the middle of the overlap. Blocks of specimens were started at fortnightly intervals; ensuring that in the event of a catastrophic change in bond characteristics, there would be a younger set available for examination.

The following observations were made:

1) During the first three weeks of exposure the differential ultrasonic measurements were both stable and reproducible. All test positions returned positive values for the differential measurement indicating high bond integrity and good transmission through the adhesive. Since these results were identical with those obtained in the pre-exposed state it is concluded that moisture had not at this stage entered the adhesive layer, or had entered but did not contribute significantly to a reduction in the adhesive modulus. There was, however, a marked modification to the fillets external to the joints. These had lifted and corrosion had occurred in their vicinity.

2) Between 5 and 8 weeks later, there was a progressive reduction in the transmissivity at the corners with the thicker bond-line. This loss of transmissivity is illustrated in figure 6a and 6b. What is particularly interesting is that by ceasing to expose the joint to water but maintaining the specimen at 60 °C, the original characteristic had been recovered within a week, (fig. 6c). During this period the anti-resonant frequency remained sensibly the same. This suggests that the moisture take up was not within the adhesive itself but had occurred interfacially. Furthermore, the fact that the phenomenon was reversible, suggests that the presence of moisture at the interface decreases the number of covalent bonds, which reform when the adhesive dries out.

3) With increased exposure, the thinner bond lines become increasingly affected and this modification appears to be irreversible. In all cases, measurements at the center of the joint remained stable until deterioration was well advanced at the outer test points. When all five test points returned highly degraded signals, the joint, through still intact, was very weak and could be snapped apart by hand. The most notable feature of the fractographic surfaces was the discoloration indicative of corrosion products.

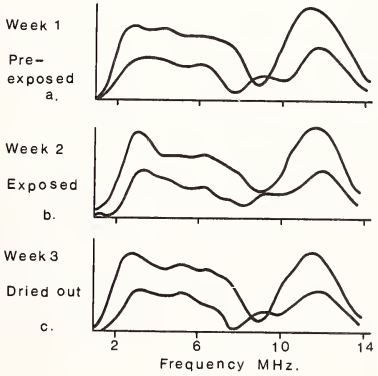

Figure 6. Evidence of the reversible nature of hydro-thermal degradation during early stage.

4) At this stage younger test samples, which had been started a fortnight and a month later, were pulled apart by peeling. The fractographic surfaces are reproduced in figure 7.

The most notable feature is the progression to failure which starts at the four corners and progresses towards the center. The fact that in the center failure is cohesive, confirms the ultrasonic prediction that adhesion there remained high and comparable with the unexposed state.

Around this central island is a halo of bright surface where failure had occurred adhesively along the interfaces. This is followed by a region where corrosion of the exposed metal surface had caused complete bond failure to occur prior to rupture.

A curious and notable feature is the change in the shape of the corrosion front. This appears to start as a rectangle, becomes elliptic and terminates as a circular island. Once started the progression to total failure is rapid. The most likely mechanism is that the formation of corrosion products at the adherend surface stresses the interface and promotes peeling.

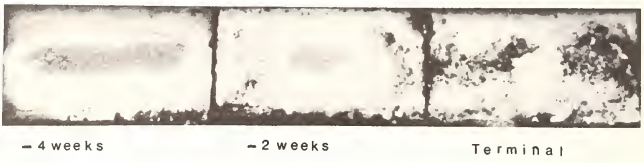

Figure 7. Fracture surfaces of hydro-thermally degraded joints at fortnightly intervals.

These results have been reproduced with more than a dozen representative specimens and one can, with confidence, relate the ultrasonic measurements with the state or the joint. For example both the corroded state and the central unmodified regions return stable and reproducible signals. The former is indicative of very low transmissivity and in a few cases a very poorly defined anti-resonance trough. The central reference region retains a high transmissivity throughout. Finally, there is the intermediate region where a progressive reduction in transmissivity is indicated by the ultrasonic measurement. Representative waveforms are related to their sources in figure 8.

The upper trace (a) in figure 8 is representative of the corrosion front. There is very low transmissivity through the joint; there is no anti-resonance trough in either spectrum and no evidence of a signal returned from the secondary adherend. Trace (b) occurs much later, when a low frequency anti-resonance occurs. By this time the adhesive and the adherends have most probably separated and water fills the interfacial region.

The middle traces represent the transitional phase in joint degradation and these have been correlated with those regions that fail adhesively. It is particularly interesting that when spectra of this type are returned from the outer edges of the joint, the mechanism is reversible. Earlier characteristics can be recovered by drying out. However, once the corrosion regime has started at the outer edges, inner regions returning this type of spectra do not recover.

Finally, the lower traces represent regions of high integrity. Here, trace (a) represents bond thickness thicker than that of trace (b). In both sets, the anti-resonant troughs are ell defined, and the contribution reflected back into the upper adherend from the lower dherend is well in evidence.

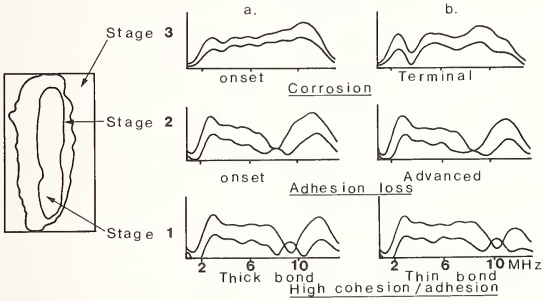

Figure 8. Correlation between the differential spectral signals and bond condition during hydro-thermal degradation.

8. Conclusions

Ultrasonic Spectroscopy has been demonstrated to be a valuable method for the monitoring f hydrothermal degradation of adhesively bonded joints. It has already provided an insight nto the mechanisms involved: the progressive reduction of adhesion at the adhesive/adherend nterface followed by corrosion of the exposed adherend surface.

In addition, these results have provided evidence that the method is particularly sensi- ive to the interfacial properties of the joint. Further evidence of this is the frequently bserved asymmetry in the joint response, when tested from one side and then the other. Could he ultrasonic spectroscopic method be unduly weighted towards an adhesion as opposed to a ohesion strength measurement?

This has important implications. For example, if the criterion for a well designed joint s that the mode of failure should be cohesive, that is, failure is confined to within the dhesive layer, then all the adhesive/adherend systems that we have examined have been esigned and fabricated to meet this objective. Indeed, when these specimens are loaded to estruction, failure has occurred almost predominantly within the adhesive.

The inescapable conclusion is that for these well designed joints, the adhesive strength, s fabricated, is substantially greater than that needed to support the ultimate cohesive trength of the adhesive itself. So much so that the variations in the adhesive strength of abricated joints monitored by ultrasonic spectroscopy would not be the mechanism governing ailure. As such these measurements would at least be poorly correlated with an estimate of ond strength (cohesion controlled) obtained by loading the joint to failure. In order to esolve this dichotomy, the excellent correlation between ultrasonic spectroscopic measure- ents and interfacial properties modified by hydrothermal degradation on the one hand nd the generally unsatisfactory relationship with bond strength at failure on the other, his sensitivity to interfacial properties needs to be reduced.

One possible approach is to examine the response at frequencies significantly below he first anti-resonance, where the increase in the wavelength of the interrogating ltrasound should de-emphasize the interfacial response and provide a better estimate of ohesive strength.

The authors wish to acknowledge Drs. D. E. W. Stone, B. C. Clarke, and J. L. Cotter of the R. A. E. Farnborough, for their support and interest in this work. The latter's review paper "Metal Jointing with Adhesives" Int'l Metallurgical Reviews 19, 103-115 (1974) is particularly recommended for those with an interest in this field.

References

[1] Allen, K. W., Aspects of Adhesion U. L. P., V1, p. 11 (1963).

[2] Keesom, W. H., Phys. Zeit., 22, 163 (1921).

[3] Plueddemann, E. J., Adhesion, 2, 184 (1970).

[4] Kerr, C. et al., Brit Polym. J., 2, 67 (1970).

[5] Peterson, J. M., Boeing Sci. Res. Labs., D1-82-1031 (1970).

[6] Black, J. M., Ind. Eng. Chem., 50, 918 (1958).

[7] Lloyd, E. A., Nondestructive Testing J., 7, 331 (1974).

[8] Lloyd, E. A., Aspects of Adhesion, 8, 345 (1976).

[9] Brekhovskikh, L. M., Waves in Layered Media (Academic Press, NY, 1960).

National Bureau of Standards Special Publication 596, Ultrasonic Materials Characterization, H. Berger and M. Linzer, eds., Proceedings of the First International Symposium on Ultrasonic Materials Characterization held at NBS, Gaithersburg, Md., June 7-9, 1978. Issued November, 1980.

APPLICATION OF ADAPTIVE LEARNING NETWORKS TO ULTRASONIC SIGNAL PROCESSING: CLASSIFYING FLAWS IN MULTI-LAYERED ADHESIVELY-BONDED STRUCTURES

Murray H. Loew and Anthony N. Mucciardi

7700 Old Springhouse Road
McLean, VA 22102

and

Richard K. Elsley

Rockwell International Science Center
Thousand Oaks, CA 91360

New methods have been developed that use ultrasound to locate and measure flaws in multiple-layered, adhesively-bonded structures. Two-, three-, and four-layer aluminum samples were manufactured with intentional defective bonds and scanned in a water tank; the reflected waveforms were used to characterize the sizes, shapes, and types of defects. Advanced nonlinear Adaptive Learning Network (ALN) signal processing techniques led to the extraction of a set of parameters from the time- and frequency-domain representations of the signals. The effects of the transducer and of any intervening layers were removed prior to the parameters' use in adaptive classification algorithms. A principal result is that the frequency domain provides the majority of the discriminatory power; time-domain parameters are of less value. A relatively small number of parameters was sufficient to discriminate among four types of defects with an accuracy exceeding 75 percent. The accuracy is not affected by the depth of the layer in the structure, nor by defects lying between the transducer and the layer of interest. This paper briefly describes the data acquisition, parameter extraction, and classifier design phases of the work and summarizes the results obtained to date.

1. Introduction

The goal of the work described here was the nondestructive determination of adhesive bond quality using ultrasound. Adaptive Learning Networks (ALN's) provided a way to establish nonlinear discriminant functions based on parameters extracted from the ultrasound waveform. Those functions then were used to classify the signal returned from a given adhesive layer as coming from either a good bond or one of a set of types of bad bonds.

The samples, described more fully in the next section, are intended to represent typical configurations considered for aircraft structural members; they have various geometries, thicknesses, and numbers of layers. Induced defects in some cases lie along the same inspection axis but in different layers and in other cases lie between the transducer and layers that are not defective. A signal returning from a given layer, therefore, may be modified by other layers before reception by the transducer. Small variations in the surface of the sample (e.g., warpage) can cause attenuation of the signal and artifactual changes in its frequency-domain representation. Those realistic kinds of problems were dealt with successfully in the design of the classifier.

2. Data Acquisition

2.1. Configuration of samples

Four kinds of samples were provided for this program (fig. 1). Each consists of from two to four layers of aluminum glued to one another, thereby providing from one to three layers of adhesive bonds. The thickness of the aluminum plates ranges from 0.025 in to 0.080 in and the adhesive layers are typically 0.005 in thick. The samples are 6 in across and 9 in deep. Each sample had one flat surface. It was intended that inspection will be done primarily from the flat side.

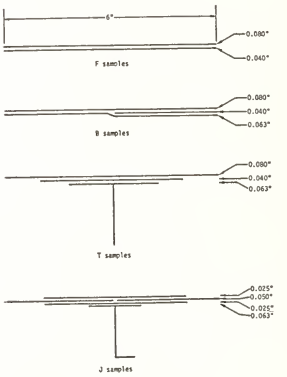

Figure 1. Schematic drawing of the metal layers in each of the four specimen types provided. The dimensions are the metal plate thicknesses (0.040 in = 1 mm).

Fifteen samples of each of the four geometries were provided, 10 with documentation for determining what kinds of defects were built in, and five without documentation, for testing purposes. Several examples of each type of defect (see Section 2.3) have been built into each geometry or part.

2.2. Apparatus and data acquisition

The parts were inspected in a water tank using conventional ultrasonic transducers mounted on a computer controlled x-y scanning mechanism. Figure 2 shows a schematic representation of the apparatus.

The primary inspection technique used was normal incidence pulse-echo inspection using high frequency (15 MHz, 0.5 in (1.27 cm) diameter) broadband nonfocused transducers. This selection was made to provide data with both broadband frequency content and long time coherence in order to test the full power of signal processing techniques.

Any imprecision in the scanning mechanism which leads to tilting of the transducer can cause interference and cancellation of the sound beam. High frequencies are affected more than low frequencies because of their shorter wavelengths. For example, a tilt of 0.2° causes a 6 dB drop in the peak amplitude of a 15 MHz pulse. That kind of error was prevented by the partial rebuilding of the scanning mechanism (which is 1 1/2 feet (45.7 cm) square to reduce tilt to 0.01°.

Another source of surface tilt in these experiments was the warpage of the samples hemselves. It has been found that the samples without stiffeners (the "B" and "F" samples) ave warpage as large as 0.2°. This is being treated as an inherent property of the amples which the testing system must deal with. The self-normalization procedure described n Section 3 does an excellent job of removing the effects of surface tilt from the frequency pectra.

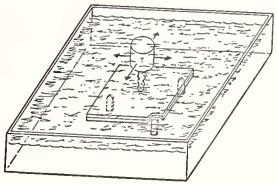

Figure 2. Schematic representation of water tank apparatus.

2.3. Defect types

Five types of defects were present in the samples. They were:

1) porosity

2) cracklike voids

3) circular voids

4) disbonds

5) bondline thickness variations

2.3.1. Description of defect types

The first three types are all examples of regions of missing adhesive material. They ffer in the sizes and shapes of the regions. Pores are zero-dimensional defects in that ieir dimensions are small compared to the wavelength of sound being used for inspection. acklike voids are one-dimensional. They are thinner than a wavelength of sound but have ngths comparable to or larger than the wavelength. Circular voids are regions both of ose dimensions are large.

Disbonds are regions where adhesive is present, but for some reason, such as a layer of ease or an unremoved release film, bonding to the metal plate did not occur. Bondline ickness variations can result from insufficient or excessive pressure during bonding.

2.3.2. Description of as-received defects

The documentation which the sponsor supplied with the samples indicates that four of the ve defect types were created successfully. Direct thickness measurements indicate that ndline thicknesses of as little as one-half of normal are present. Disbonds were ccessfully created by leaving release film atop the adhesive when bonding. These regions e readily detected in a conventional C-scan.

Porosity and large (i.e., "circular") voids have also been supplied. In some cases, rge adhesive cutout regions entirely filled themselves in during bonding due to the mperature and pressure used. However, numerous large voids remain. The large voids are so readily detected by conventional means.

The defects which most closely approach the configuration of cracklike voids are collections of small voids (or large pores) which are found strung together in a manner reminiscent of "leaves" and "branches".

2.4. Tabulation of data

Broadband normal incidence pulse-echo data have been acquired for all of the defects in the 40 documented samples. This provides a data base for developing and testing the defect characterization algorithms.

The data base consists of 59 linear scans, each of which passes over one or two of the documented defects. Each scan consists of, typically, 5 to 10 rf waveforms acquired at equally spaced intervals along a line parallel to either the X or Y axis of the part. The number of waveforms per scan was kept to a minimum consistent with providing data within, on the edge of, and outside of each defect.

Each waveform consists of 1,001 samples taken at 0.02 μs intervals, for a total of 20 μs. This therefore provides for frequency analysis from 50 kHz to 25 MHz. The ultrasonic transducer used provides useful data from about 1 to 20 MHz.

Figure 3 shows an example of two views of the ultrasound signal provided for each point examined on the specimen.

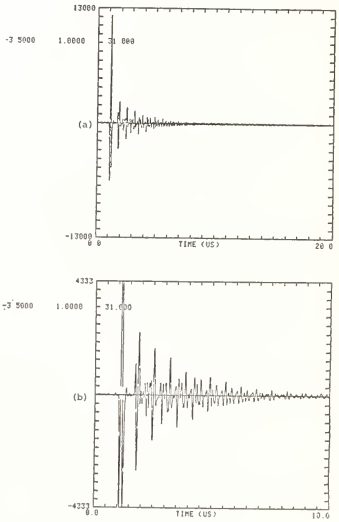

Figure 3. Typical waveform graphs produced by the computer from the digital data recorded on Run 31 at position x=3.5, y=1. (a) General view of entire waveform. (b) High gain, detailed view of the early part of the waveform.

3. Data Analysis

3.1. Segmentation and deconvolution

The multi-adhesive-layer nature of the samples and the fact that defects can occur in one or more layers beneath any surface location on the samples mean that it is desirable to

tract some features from the recorded time waveforms that are layer-specific. The goal is make all defects of a given type look alike, regardless of the adhesive layers in which ey occur. If that ideal can be realized, the problem will be simplified because cognition of a defect type will be independent of its location and depth.

Self-normalization may be used to achieve layer independence by noting two things. rst, the time waveform resulting from a pulse at a given location may be segmented, with ch segment containing information about a given layer. Second, the time segment for a ven adhesive layer will have been modified by the intervening adhesive layers, if any.

Self-normalization removes the effects of intervening layers from the time signal presenting a given layer by successive deconvolution. Thus, the front-surface signal hat characterizes the transducer) is deconvolved from the raw first-adhesive signal to eld a time signal that is characteristic of that adhesive only. (We use here the sumption that the aluminum contributes nothing to the signal; this is reasonable both om theoretical arguments [small-grain structure of aluminum] and from actual scans of ain aluminum sheets.) Then the raw first-adhesive time signal (that contains information t only about the first adhesive, but also about the transducer) is deconvolved from the me segment of the second adhesive, and so on, with each layer's signal being deconvolved om the signal from the next deeper layer.

The process of segmenting the signals takes advantage of our knowledge of the construc- on of the samples--knowledge that is likely to be available in nondestructive testing of al adhesively-bonded structures. The four geometries of samples--F, B, T, and J--(shown fig. 1) were illuminated on their flat sides by the ultrasound transducer. The F samples' at sides were defined to be the 0.080 in (80-mil) aluminum plates. Thus, the F, B, and T mples all presented to the transducer the sequence of layers 80-mil aluminum, 5-to-8-mil nesive, 40-mil aluminum, in that order; in parts of the B samples and all of the T samples, e additional layers were another 5-to-8-mil adhesive and a 63-mil aluminum. The J samples' vers are of different thicknesses from those of the other three geometries; this creates a ecial case for the segmentation algorithm.

Because the incident waves are normal to the surface, it is easy to compute the travel ne of the ultrasound in the aluminum and adhesive layers of the samples. Using longi- dinal velocities of 6.4 km/s and 1.17 km/s in aluminum and adhesive, respectively, we v construct the following table of one-way travel times in aluminum plates of various cknesses.

Thickness, mils	Time, μs
25	0.1
40	0.16
50	0.2
63	0.25
80	0.32

5-to-8-mil adhesive has a one-way travel time of 0.11 to 0.17 μs.

The front-surface echo, always the largest peak in the time waveform (see fig. 3), vides a reference point t_{fs} for delineation of the layers of the sample. If, for example, first layer of aluminum is 80 mils thick, an echo from its back surface should arrive 4 μs after the front-surface echo. The time waveform from an inspection of an F sample g. 3) does, in fact, have its second peak at 0.64 μs after the front-surface echo. An o from the back surface of the adhesive should arrive between 0.22 and 0.34 μs after the o from the first plate, but is difficult to observe because of the persistence of the lier waveform. One may, nevertheless, establish a time window beginning at t_{fs} + 0.64 ending somewhere between t_{fs} + 0.88 and t_{fs} + 0.96. The exact point is determined an algorithm that considers phase relationships and durations relative to the front- face echo.

Each waveform of the type shown (fig. 3) was submitted to the segmentation procedure. The resulting segments then were used in the deconvolution step to yield power spectra that were characteristic just of the defect type. The next step was extraction from the spectra of features that made the characterization explicit.

3.2. Feature extraction

The goal of feature extraction is the characterization of a sample by a set of measurements that are invariant to distortion, noise, measurement error, and inherent differences between samples of the same class. One cannot, in general, specify in advance a feature set that is guaranteed to possess all of those properties, nor can it be guaranteed that it is the smallest set capable of effecting accurate discrimination. Instead, a set of candidate features is postulated and its performance evaluated. If it performs well, one may then search for a subset that performs almost as well, trading off feature-extraction and processing costs against performance.

Work to date has resulted in the definition of the following types of features that were extracted from the quotient power spectrum for each segment (representing an adhesive layer at a given point on the sample) described in the previous section:

1) shape features of the cumulative spectrum;

2) proportion of power in various spectral bands;

3) and locations of peaks.

One feature from the time domain was used; the ratio of the rms value of a segment to the rms value of the front-surface echo.

This rms-ratio feature is intended to contain information regarding the presence or absence of adhesive. Because the echo energy for a given defect category decreases with increasing depth of the layer, a correction based on depth was used for segments for layers 2 and 3.

It is likely that the entire 1,001-point waveform described in Section 2.4 will contain useful information. To capture this, while retaining transducer independence and minimizing computational load, we computed the power spectrum of that entire waveform and extracted certain features from it. The ratios of those features to the same features extracted from the spectra of the front-surface waveforms provided eight additional features. The set of 2 features that resulted was the first candidate set used with the new data.

4. Results and Conclusions

An initial set of 274 waveforms was used to examine the value of our approach. The 274 waveforms accounted for 312 adhesive layer/location combinations. Appropriate time-gating was used to extract from each waveform the front-surface echo and the first occurrence of the echo from the adhesive layer(s) examined. Self-normalization, described in Section 3, requires the front-surface echo to characterize the transducer and to make all classifications independent of the transducer.

We defined, for this initial effort, four classes of layers: no defect, adhesive cutout, porosity, and release film. Partial/positive caul pressure, caul-plate cutout, and variable bond-line thickness, all intended to represent or induce a fifth type of defect, were omitted from this first classification effort because of insufficient evidence (from x-rays and C-scans) for most samples that the defect type was present. The remaining set of 265 feature vectors was partitioned into nonoverlapping sets for design and test of a classifier.

The matrix below indicates the number and proportion of layers of each type classified as each type.

No. of Samples	True Class	ND	AC	POR	RF
71	No defect (ND)	41(58%)	14(20%)	8(11%)	8(11%)
75	Adhesive cutout (AC)	9(12%)	57(76%)	2(3%)	7(9%)
67	Porosity (POR)	7(10%)	8(12%)	47(70%)	5(7%)
52	Release film (RF)	5(10%)	9(17%)	5(10%)	33(63%)

Note that the false alarm rate (the proportion of nondefective samples assigned one of the defect classes) is 42 percent, but that the false dismissal rate (the proportion of defective samples called nondefects) is 10.7 percent. Eight features were required on the average to make a classification.

The results achieved to date are promising. Current work is using a much larger set (1,124) of layer/location pairs. When model development is complete, a set of test samples will be used to evaluate the classification accuracy.

The work reported here was performed for the Air Force Materials Laboratory under Contract No. F33615-76-C-5079.

National Bureau of Standards Special Publication 596, Ultrasonic Materials Characterization, H. Berger and M. Linzer, eds., Proceedings of the First International Symposium on Ultrasonic Materials Characterization held at NBS, Gaithersburg, Md., June 7-9, 1978. Issued November, 1980.

ACOUSTICAL CHIRP FREQUENCY AND COMPUTER CORRELATION TECHNIQUE FOR DEBOND INSPECTION IN SOLID ROCKET MOTOR SECTIONS

H. D. Collins

Holosonics, Inc.
2400 Stevens Drive
Richland, WA 99352

This paper describes a chirp frequency system that detects and images incremental changes in the acoustical properties as a result of interface separations (i.e., debonds) between contiguous layers that comprise the rocket. The inspecting transducer is effectively loaded by the internal acoustic impedance of the rocket motor. Variations in the acoustic impedance are then translated into changes in the "Q" of the acoustic system and thus acoustic signatures are generated that describe the integrity of the motor.

An analytical model is constructed of the rocket motor's input impedance as seen by the transducer. Computer generated acoustic signatures of the various debonds are then analyzed and catalogued for correlation with the acoustic data.

Three test specimens were provided by the U.S. Air Force for the investigation of debonds in the dome section. The specimens were Minuteman First Stage Motors.

The experimental results verify the system's ability to detect and image various debonds in solid rocket motors with approximately 1 cm lateral resolution. The computer generated signatures have proven their viability in the defect identification analysis.

1. Introduction

Various acoustical and radiographical techniques have been employed to detect and image se/liner/propellant debonds in solid rocket motors. All of these techniques depend on anges in the physical properties of the intervening layers of the motor. A debond by defi- tion is a physical separation or discontinuity between two contiguous layers. The separa- ons consist of very thin air gaps or voids in the motor structure.

This paper describes a technique of debond inspection that depends on the variation of e acoustic impedance between intervening layers of the motor. It is tacitly assumed there sufficient acoustic energy to penetrate the numerous layers that influence the effective put impedance of the sensing probe.

This technique includes frequency chirping and determination of the system's "Q". An alytical model is constructed of the rocket motor's input impedance as seen by the trans- cer. Computer generated acoustic signatures (i.e., input impedance and "Q" signature) are en analyzed to determine the type of debond and the frequency range for imaging.

2. General Theory of Debond Inspection in Solid Rocket Motors

2.1. Input impedance or signature of a single layer system

We shall assume that an acoustic plane wave is incident on a uniform layer of thickness "y" at an arbitrary incident angle. Figure 1 illustrates the symbols used and the layer geometry.

The numbers 3, 2, and 1 denote the media through which the incident wave propagates into the intervening layers of the motor. The angles between the propagation directions and the normal in each medium will be denoted by θ_3, θ_2 and θ_1 respectively.

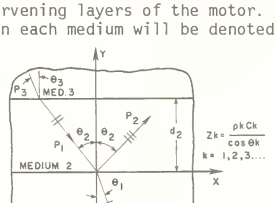

Figure 1. Single layer geometry.

Equation (1) represents the incident and reflected acoustic plane waves propagating in the Y-X plane with pressure amplitude P_1 and P_2:

$$P_2(x,y,t) = P_1\exp[j(\omega t - \beta_{2y}Y + \beta_{2x}X)] + P_2\exp[\omega t + \beta_{2Y}Y + \beta_{2x}X)] \qquad (1)$$

where ω = radian frequency, $\beta_{2y} = \frac{2\pi}{\lambda_2}\cos\theta_2$ and $\beta_{2x} = \frac{2\pi}{\lambda_2}\sin\theta_2$.

The two pressure amplitudes are usually not equal and may be complex quantities.

The particle velocity (u) is easily obtained from eq. (2) and using the following relationship between particle displacement and pressure gradient:

$$U_2(x,y,t) = \frac{1}{Z_2}\left\{P_1\exp[j(\omega t-\beta_{2y}Y + \beta_{2x}X)] - P_2\exp[j(\omega t + \beta_{2y}Y + \beta_{2x}X)]\right\} \qquad (2)$$

where

$$\frac{-\partial P_2}{\partial y} = \rho_2\frac{\partial^2\xi}{\partial t^2} = j\omega\left(\frac{\partial\xi}{\partial t}\right)\ \rho_2 = j\omega\rho_2 u_2 \qquad (3)$$

and ξ = displacement of a particle from the equilibrium position. The specific acoustic impedance (Z_{sp}) is defined as the complex ratio of the sound pressure to the particle velocity at a given point, in the sound field. The impedance is:

$$Z_{sp} = \frac{P_2}{u_2} = \frac{P_1\exp[-j(\beta_{2y}Y - \beta_{2x}X)] + P_2\exp[j(\beta_y Y + \beta_{2x}X)]}{P_1\exp[-j(\beta_{2y}Y - \beta_{2x}X)] - P_2\exp[j(\beta_{2y}Y + \beta_x X)]}\ Z_2 \qquad (4)$$

where we have omitted the time factor exp (jωt). At the boundary of layer (2) y = 0, the ratio P_2/u_2 must equal the impedance of medium 1; thus

$$Z_3 = \left[\frac{P_1 + P_2}{P_1 - P_2}\right] Z_2 \text{ and } \frac{P_2}{P_1} = \frac{Z_1 - Z_2}{Z_2 + Z_1} = R \quad . \qquad (5)$$

Now we can determine the input impedance at the front side of layer 2 (i.e., y = d_2). From eqs. (4) and (5) we obtain the input impedance of the layer:

$$Zin_2 = \left[\frac{P_1\exp(-j\beta_{2y}d_2) + P_2\exp(j\beta_{2y}d_2)}{P_1\exp(-j\beta_{2y}d_2) - P_2\exp(j\beta_{2y}d_2)}\right] Z_2 \qquad (6)$$

we substitute $P_2/P_1 = (Z_1-Z_2)/(Z_1 + Z_2)$ into eq. (6), the result is:

$$Zin_2 = \left[\frac{Z_1 - iZ_2 \tan \beta_{2y}d_2}{Z_2 - iZ_1 \tan \beta_{2y}d_2}\right] Z_2 \qquad (7)$$

ere $$Z_1 = \frac{\rho_1 c_1}{\cos\theta_3}\ ,\ Z_2 = \frac{\rho_2 c_2}{\cos\theta_2}\ ,\ \beta_{2y} = \frac{2\pi}{\lambda_2}\cos\theta_2$$

i d_2 = thickness of the layer .

2.2. Input impedance or signature of a multilayer system

Now we can extend the general theory to include multiple layers. Applying the identical ocedure, we can derive the input impedance of a multilayer system:

$$Zin_n = \left[\frac{Zin_{n-1} - iZ_n \tan \alpha_n d_n}{Z_n - iZin_{n-1}\tan \alpha_n d_n}\right] Z_n \qquad n = 2, 3, \ldots \qquad (8)$$

re Zin_n is the input impedance at the upper surface of the nth medium (see fig. 2).

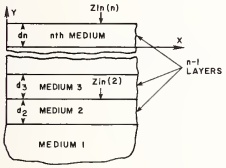

Figure 2. Multiple layer geometry.

The use of eq. (8) is quite simple if only a few layers are present, but the calculations ome extremely tedious when the number of layers exceeds three and thus, it is imperative to a digital computation technique.

3. Case/Liner Debond Signatures in Simulated Minuteman Motors

Figure 3 illustrates the various parameters in the two layer missile geometry.

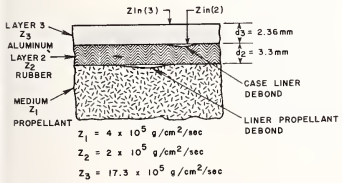

Figure 3. Simulated Minuteman missile case debond geometry.

Figure 4a graphically illustrates the acoustic input impedance of the simulated multilayer ile geometry with a case/liner debond. The frequency was varied from 1 MHz to 3 MHz and impedance minima occurred at 1.25 MHz and 2.5 MHz respectively which are the first and ond characteristic resonances for the aluminum case. The air gap debond essentially iso- es the case acoustically and the fundamental resonances are easily detected. The actual iles have external cases of cork/fiberglass, Avcoat/steel and cork/titanium which signifi- ly alter the signatures.

Figure 4b is the liner/propellant debond acoustic signature. There are numerous maxima and minima occurring between $10^{8.8}$ and $10^{4.8}$ impedance levels. The significant difference b tween the case/liner and liner/propellant signatures is the minimum ($10^{1.6}$ level) occurring 1.25 MHz in the case/liner signature. Case/liner and liner/propellant debonds can be easily identified by the number of minima occurring between 1 MHz and 3 MHz. Naturally, an impedan minimum implies a maximum "Q", and thus minimum transducer damping.

Figure 4c shows the acoustic impedance or signature of the multilayer system without th presence of a debond. It is similar to the case/liner debond signature. The major differen between them is the impedance levels and waveform shape. The case/liner debond minimums exhibit impedance levels of approximately 40 compared with the nondebond minimums of 10^5. The case/liner debond and nondebond maximums are $10^{8.8}$ and $10^{7.4}$ respectively. This extreme dif ference in levels significantly alters the "Q" of the system and thus allows debond detectio

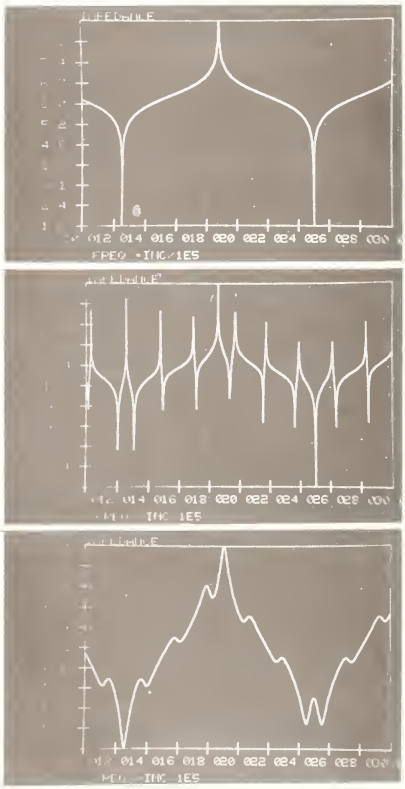

(a)

(b)

(c)

Figure 4. Computer generated, three layer acoustic signatures in simulated Minuteman dome motor section (aluminum/rubber/propellant): (a) case/liner debond, (b) liner/propellan debond, and (c) no debond condition.

3.1. Debond "Q" signatures in simulated minuteman motors

The frequency bandwidth of radiated acoustic power is determined by the mechanical "(the transducer. If we assume an input impulse or step function, the output waveform lengt ringing is a function of the system's "Q". This increase in the output pulse length of th

ansducer as it scans over the debond area provides the necessary conditions for detection and aging. A relatively simple inspection system can be used if this condition is sufficient.

The "Q" or quality factor of a transducer loaded at both sides is given by the following ation:

$$Qn = \frac{n\pi}{2}\left[\frac{Z_T}{Z_b + Zin}\right] \qquad (9)$$

re Z_T and Z_b are the acoustic impedances of the transducer and backing material. Zin is acoustic impedance or signature of the multilayer missile system. The factor n indicates harmonic mode (i.e., 1, 2, ...).

The mechanical "Q" is independent of the piezoelectric transducer dimensions and proportional to the ratio of the impedances. Z_T and Z_b are constants allowing Zin, the multilayer edance, to determine the "Q". Thus, the transducer loading on one side is completely determined by the impedance of missile structure and when the impedance approaches a minimum, "Q" approaches a maximum. In other words, the maximum "Q" values coexist with the minimum edance levels.

Figure 5a is the case/liner debond acoustic "Q" signature. The curve is very similar to corresponding acoustic signature (impedance) with the interchange of maxima and minima e fig. 4a). The "Q" values are given directly and not in powers of 10, as with the acoustic signature. The "Q" values vary from 0 to 31 in all three signatures. There are two maxi- "Q" values at 1.25 MHz and 2.5 MHz, the plate resonances between 1 MHz and 3 MHz. The air debond essentially simulates a free plate and thus the typical resonances exist.

The deep or liner/propellant debond exhibits a very unique "Q" signature as shown in fig- 5b. The maximum "Q" value occurs at 2.5 MHz corresponding to an impedance minimum at that quency. Figure 5c is the nondebond "Q" signature which closely resembles the case/liner ve. There appears to be a small amplitude modulation on the basic case/liner waveform. The ima and minima appear at approximately the same frequencies, but with different "Q" els. The important aspect concerning the three "Q" signatures is the unique differences ng impedance levels and waveform shapes.

These unique features or characteristics provide the necessary and sufficient conditions detection, differentiation, and imaging at internal debonds in solid rocket motors. Debond ges are constructed by proper frequency selection and time gating on the output transducer eform. The gate is adjusted to detect only the underdamped waveform at the preselected frecy corresponding to an impedance minimum (i.e., maximum "Q").

4. Chirp Frequency Debond Inspection System

4.1. Transducer and coupling system

Three basic subsystems make up the Chirp Frequency Debond Inspection System: 1) transer coupling system, 2) electronic signal processor, and 3) debond "Q" signature and image lay system.

The transducer coupling system is a device used for alignment and contains the couplant d. A thin rubber membrane is used between the couplant fluid and the missile case. The nsducer to missile case distance can be adjusted by the height adjustment screw. Axial inment is made by the angular adjustment screws. Couplant is introduced by a pressure tank ugh the couplant injection-pressure release valve. Air is released through the remaining e until the internal chamber is filled. Sufficient couplant pressure is introduced to luce a slight bulge in the flexible diaphragm. The amount of bulge is determined by the in which the system will glide over the test surface.

4.2. Electronic signal processor

The electronic signal processor block diagram is shown in figure 6. The following is a f description of the operation. The repetition rate and transmit pulse width generator is system clock. The repetition rate can be varied from 1 kHz to 10 kHz. The transmit pulse

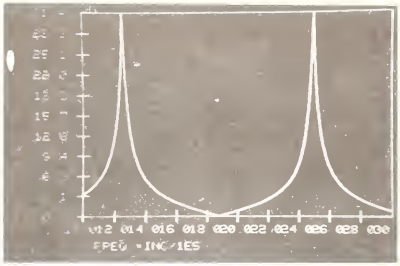

(a)

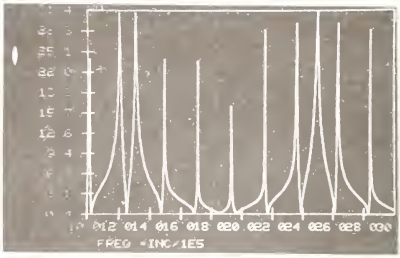

(b)

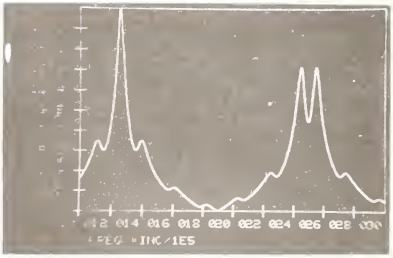

(c)

Figure 5. Computer generated transducer "Q" values in simulated Minuteman motor section (minum/rubber/propellant): (a) case/liner debond, (b) liner/propellant debond, and (c) r debond condition.

width can be varied from 1 μs to 1000 μs. The transmit pulse is used to enable the gated tage controlled oscillator and to initiate the frequency sequencer, gate delay, and reset t peak follower.

The frequency chirp or sequencer provides the control voltage to the voltage control oscillator. The frequency of the voltage controlled oscillator can be selected to vary i incremented steps. The voltage change occurs 150 μs after the transmit pulse to allow th oscillator to settle before the next transmit pulse. The same delayed staircase voltage applied to the X axis of signature monitor, where each frequency step provides a discrete X axis location.

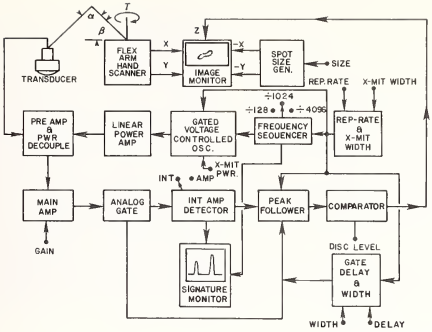

Figure 6. Electric signal processor.

The voltage controlled oscillator provides (rf) pulses of different frequencies to the put of the linear power amplifier. The number of sinusoidal oscillations in the pulse is termined by the transmit width and the frequency sequencer. The amplitude can be adjusted the transmit power control.

The linear power amplifier is a 10 watt (250 kHz to 30 MHz bandwidth) amplifier and pro- des the drive for the transducer. The preamplifier and power decoupler is a network of odes and wideband amplifiers that allow high level excitation of the transducer and recep- on of the low level reflected acoustic signals without damage or interference. The pre- plifier gain is approximately 34 dB.

The main amplifier provides additional gain of 0 to 45 dB adjustable by a manual control. e rf analog gate time selects the portion of signal to be processed. Timing is provided by e gate delay.

The intensity/amplitude detector consists of two separate detectors selected by a switch. e intensity detector is an amplitude squared type and the amplitude detector is a linear pe. The filtered output of the selected detector drives the vertical axis of the signature nitor and the peak detector. A peak detector is a special kind of sample-hold circuit. The put signal is tracked until the input reaches a maximum value and then the peak detector tomatically holds the peak value.

The adjustable comparator converts the amplitude information to bi-stable information. ere is an adjustable discriminator level. The output drives the Z axis of the image moni- r. The gate delay provides timing for the analog gate width and peak detector sections. th the gate delay and width are adjustable.

The sine/cosine generator and modulator has a sine and cosine output that drives the (-X) d (-Y) inputs of the image monitor. This displays a circle. The modulator modulates the ne and cosine output 100 percent resulting in a circle whose radius is constantly changing. e maximum diameter can be adjusted to simulate the resolution of the transducer.

The flex-arm hand scanner is an electromechanical device to which the transducer and upling system are attached. Transducer pos. ion is calculated and an X,Y voltage is pro- ded to the X,Y inputs of the image display monitor.

4.3. Debond "Q" signature and imaging display system

The "Q" signature monitor displays the "Q" as a function of frequency, the Y axis being e intensity or amplitude of the gated acoustic pulse, and the X axis being discrete frequency ep positions. The image display monitor is a bistable storage device that displays the tual debond area.

5. Experimental Results

5.1. Case/liner debond images in fired first stage motor dome section

Figure 7 shows the chirp frequency debond inspection system with the associated manual scanner attached to the dome section. The transducer is located in the wheel connected at one end of the scanning arm. The system is attached to the center of the dome section. The dome area is inspected for debonds by manual scanning with the transducer and coupling system. The effective "Q" signature and the selected debond image are constructed using the system. Figure 8 illustrates an operator manipulating the transducer over a selected inspection area of the dome section.

Figure 9 shows the case/liner debond geometries outlined on the external case. The simulated debonds were constructed by removal of the rubber liner from the steel case. This technique simulates an air gap between the liner and steel case.

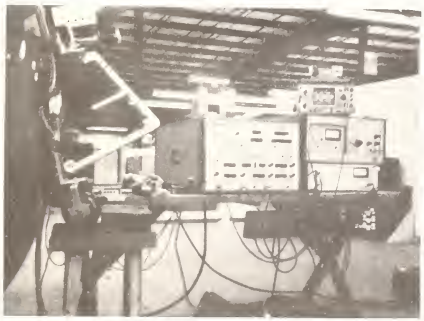

Figure 7. Chirp frequency debond imaging system electronics and manual scanner.

Figure 8. Variable frequency debond imaging system used in the inspection of the Minuteman dome section.

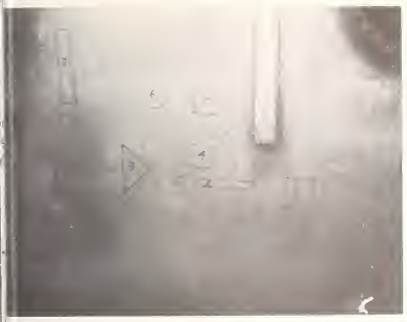

Figure 9. Outlines illustrating geometry of case/liner debonds constructed in Minuteman dome (fired section).

Figure 10 is the detailed schematic of the simulated case/liner debonds and the acoustic ages. The average debond size is approximately one inch (2.54 cm). The array of debonds nsists of two squares, one triangle, one rectangle, and one circle. The debond images were nstructed at 1.08 MHz using the wheel coupling system. The images are of excellent quality, aphically illustrating the system's performance. The image resolution is approximately one ch (2.54 cm). The debonds are easily recognized by their respective images.

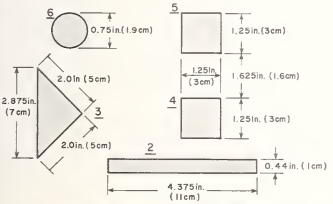

(a)

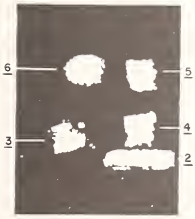

(b)

Figure 10. (a) Schematic of simulated case/line debonds; (b) acoustic images.

tional Bureau of Standards Special Publication 596, Ultrasonic Materials Characterization, Berger and M. Linzer, eds., Proceedings of the First International Symposium on Ultrasonic terials Characterization held at NBS, Gaithersburg, Md., June 7-9, 1978. Issued vember, 1980.

THROUGH-TRANSMISSION ULTRASONIC ATTENUATION MEASUREMENTS ON ADHESIVELY-BONDED STRUCTURES

W. E. Woodmansee

The Boeing Company
P. O. Box 3707
Seattle, WA 98124

Water-jet coupled ultrasound attenuation measurements have been performed on adhesively-bonded, metal-metal, aircraft structures to detect porosity occurring in the bondlines. Data collected during shuttle-index scanning was stored on a magnetic disk and multilevel C-scan attenuation maps were prepared on an electrostatic plotter. Single-level C-scans of the data were also generated by means of an interactive graphics display. The graphics presentation was used to measure the minimum, maximum, and average detected signal values as well as the amplitude distribution for selected portions of the stored data. Changing bondline thickness was the apparent cause of background signal variations measured on a series of production aircraft components. At 1 MHz the thickness-related signal variations were typically 3-5 dB. Attenuation increases caused by 5 to 7.5 mm pores were found to be 9 to 14 dB. The irregular C-scan patterns and increased attenuation associated with the porosity enabled this condition to be detected by through-transmission ultrasonics.

1. Introduction

Through-transmission ultrasonic scanning is commonly used for production inspection adhesively-bonded aircraft structures to locate unbonded components and to detect regularities in the bondlines. These tests are typically performed using commercial trasonic equipment coupled to facsimile recorders to prepare qualitative attenuation os over a limited dynamic range. This paper will describe a system developed at Boeing measure relative ultrasonic attenuation over 72 dB and to enable more quantitative aracterizations of adhesively-bonded components. The use of this system will be illustated in the development of a procedure for the detection of foliated porosity in tal-metal, laminated aircraft structures.

2. Data System

A functional diagram of the system used for attenuation measurements on bonded airaft structures is shown in figure 1. Vertically-opposed water jets were held by a yoke tached to a commercial scan bridge which moved the jets in a shuttle-index pattern over e test parts. The water streams which coupled the ultrasound between the transducers d test parts were 4.7 mm in diameter. The transducer elements were 18.75 mm diameter T-4 disks resonant at either 1.0, 2.25, or 5.0 MHz. The operating frequency was selecd by installing the appropriate transducer elements in the back of the water jets which re the same for all of the tests. The transmit transducers were driven by a Matec power cillator which generated variable amplitude and duration tone bursts at the appropriate equencies. The receive jet was coupled to a log compressor which permitted detection of gnals from 1 mV p-p to 3 V p-p. The compressed rf signal was then time-gated and ak-detected to develop a dc output signal proportional to the peak ultrasonic signal ceived in the gate interval.

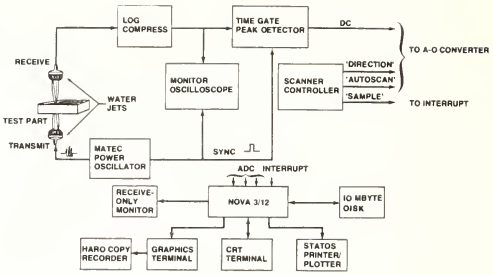

Figure 1. Data system functional diagram.

An encoder was added to the scan bridge to generate sampling pulses at 1 mm increments along the lengthwise scan direction. Signals from the scanner were also provided to establish the scan direction and to indicate when an automatic scan cycle was taking place. The "direction", "autoscan", and the detected ultrasonic signal were connected to the analog-to-digital converter inputs of a minicomputer. The pulses from the encoder were applied to the computer interrupt input to trigger sampling of the analog signals during a scan. While scanning was underway, the digitized voltages from the peak detector were stored in a buffer in the computer. When the direction voltage changed state at the end of a lengthwise scan, the data was transferred to the disk. In order to monitor portions of the sampled ultrasonic data in real time, a television display generated columns of numeric characters which paralleled the scan motions of the water jets on the test parts. The magnitudes of the characters were related to the amplitude of the ultrasonic data samples and the lowest signal increments were displayed as reverse-field characters to draw the operator's attention to a prolonged, low-level signal.

Following completion of a scan, hardcopy records of the data stored on the disk were prepared on a 22 in (55.9 cm) wide Statos printer/plotter. The magnitudes of the data samples were represented by numeric characters formed with a 3 x 5 dot matrix. Including the blank or no-write, thirteen discrete signal increments were represented on the plots. The number of dots used to form the numbers increases as their value increases. This provides both a qualitative and quantitative record of the signal amplitudes detected during a scan. The plotted symbols are a subset of the characters described by Patenaude, et al. [1][1].

The widths of the voltage increments corresponding to the plotted symbols are readily changed in order to alter the amplitude resolution although the majority of plots were prepared with 6 dB signal increments associated with each character. The normal plot sequence results in areas with higher attenuation appearing darker on the recordings although inverted plot sequences may be generated. Suppression of selected characters may also be used to enhance the representation of data. The stored data was also output on a Tektronix 4010-1 graphics terminal to develop single level C-scan maps. The terminal display was most effective in analyzing areas of relatively uniform attenuation. The multilevel hardcopy recordings were more informative in representing data varying due to differences in construction on complex test parts.

[1]Figures in brackets indicate the literature references at the end of this paper.

3. Test Samples

The samples examined during this study were typical aircraft components in which a ew film adhesive system was being qualified prior to production usage. Destructive esting of some of the initial panels prepared with this adhesive revealed the presence of orosity in the bondlines. The porosity, which typically exhibited a branching or oliated appearance, occurred predominantly in portions of the panels in which the bond- ine thicknesses were greater than the nominal value as a result of nonuniform bonding ressure. The individual pores were elongated with roughly a 3:1 length-to-diameter ratio nd their longest dimensions were generally between 2 to 8 mm. Closer examination of the ndividual pores revealed that they were filled with microscopic bubbles of foamed dhesive apparently containing air entrapped during assembly of the separate layers prior o bonding. As this condition was most commonly found in parts with extensive metal-metal onding used to form laminated edges of panels, several parts with this type of con- truction were selected for nondestructive evaluation. The laminated edges of the panels hosen had three bondlines joining aluminum sheets with thicknesses of 0.3, 0.5, 0.5, and .4 mm. The inner layers act as stiffeners and, in some instances, these inner sheets of luminum had regularly spaced "bleed-holes" to aid in the distribution of adhesive during he cure cycle. The adhesive films used had a nominal thickness of 0.25 mm. Ten areas ere selected for evaluation of five different production test parts. Two examples of hese parts may be seen in figure 2. All of the structures tested had laminated metal- etal bonding around the periphery of one or more areas of honeycomb construction. The hotograph was taken following completion of the ultrasonic tests and after portions of he laminated areas had been cut out of the panels and chemically milled to reveal the two uter bondlines.

4. Test Procedure

The goal of this project was to develop an inspection procedure that could be readily sed by production quality control personnel. Similarities between the laboratory and roduction data systems simplified this development and the subsequent transfer to roduction testing.

An initial scan of one of the test panels gave evidence of bonding anomalies of the ype being sought and low-kilovoltage radiography confirmed that foliated porosity was in ne or more of the bondlines of this part. Preliminary examination of the remaining test reas indicated that the attenuation in the metal-metal laminated segments was relatively niform. Based upon a survey of the attenuation in these areas conducted by manually oving the water jets over the test parts, a point was located on one panel which was used a reference for subsequent measurements. The magnitude of the signal received at this oint was adjusted by the Matec output amplitude control. The received signal value which s selected corresponds to the midpoint of one of the 6 dB increments used to prepare the ta plots. Data samples which were within 3 dB of the reference value were thus plotted a single character (the reference used was at the midpoint of the voltage increment ssociated with the ":" symbol). Sample points 4 to 9 dB below the reference were plotted "1"; points 10 to 15 dB below the reference appeared as "2", etc. Prior to each scan e part containing the reference point was positioned between the jets and the received gnal set to the desired level. The signal at this point was remeasured following each an and the differences between these values were consistently less than 1 dB.

The spacing between the water jets was maintained at 2 in (5 cm) throughout the sts. By controlling the water flow to the vertically-opposed jets, the fan of water rmed as they impacted was adjusted to be coplanar with the laminated edges of the test rts. The water fan also provided a means of verifying that the water jets were axially aligned and normal to the plane of the test parts. Prior to each scan a visual eck was made to ensure that the jets were directly opposed as evidenced by the formation a horizontal fan in the plane of the part being scanned.

Separate sets of scans at 1, 2.25, and 5 MHz were made of all of the test areas. The me jet bodies were used by interchanging the transducer elements for the different trasonic frequencies. Data collected for each frequency was stored on a separate magnetic sk to permit preparation of hardcopy records of all of the data sets and to enable mparative evaluation of the different parts with the graphics terminal. Although the

2.25 and 5 MHz recordings were more effective in revealing the bleed holes in some of the panels, the greater sensitivity to variations in adhesive thickness at these frequencies made interpretation of the recordings more difficult. The contrast of the porosity indications relative to the more variable background at 2.25 and 5 MHz was not significantly better than at 1 MHz. As a result, the recordings obtained at 1 MHz, which had more uniform background attenuation, were felt to be more suitable for production inspection requirements. Recordings made on two of these test parts at 1 MHz may be seen in figure 3. These test areas have been designated by the file names under which they are stored on the magnetic disks. The sample corresponding to DATUS 6 was later shown to be free of porosity while the DATUS 8 sample contained foliated porosity in all three of its bondlines.

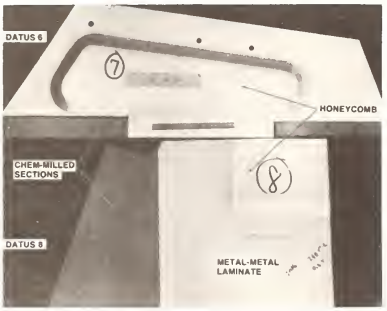

Figure 2. Typical test specimen.

a. WITHOUT POROSITY – DATUS 6

Figure 3a. Multilevel C-scan of sample.

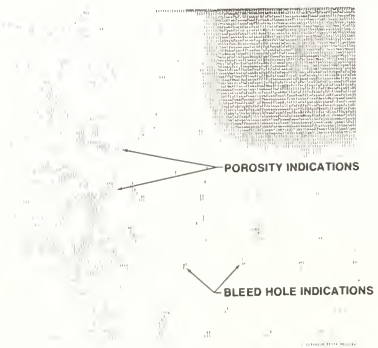

b. WITH POROSITY – DATUS 8

Figure 3b. Multilevel C-scan of sample (concluded).

The data stored on the disk from the 1 MHz scans was also output on the graphics erminal as single-level C-scans. The terminal cross-hair cursor was used to outline hose portions of each part which consisted of metal-metal laminations. By means of the ursor, up to 10 vectors could be drawn to designate the boundaries of the data to be xamined. This enabled selection of data from areas with complex configurations for easurement and permitted exclusion of data from portions of the structures with differing onstruction, e.g., areas with honeycomb. The median signal levels for the laminated ortions of each of the test parts were measured from the cursor-selected data and C-scan aps of these areas were generated with the write threshold set at the median level. The hreshold was then reduced in 1 dB steps to allow the spatial distribution of the ttenuation differences to be visualized. The normal mode of display with the graphics erminal caused sample points which fell below the threshold to be illuminated. As the hreshold was lowered, fewer sample points were displayed. For each test area, a level as selected which resulted in localized indications which were separable from the back- round and which were suspected to be caused by porosity. The threshold was reduced urther until all of the suspect indications were eliminated. The attenuation increments etween the median and the level at which the isolated indications are seen, and from that evel to the point at which all indications were eliminated, were measures of the varia- ility of the bondline attenuation and the increased attenuation associated with ossible flaws.

Examples of graphics displays generated from DATUS 6 and DATUS 8 may be seen in figures and 5. These are composites of separate C-scans generated on the two panels. The panel een in figure 4 did not contain porosity and the suspect indications seen in the middle isplay were eliminated by lowering the threshold 4 dB below the median value. The orosity indications as well as some of the bleed hole indications shown in figure 5, owever, persisted over a broader range of threshold values. The porosity was still isible with a threshold 14 dB below the median value for this panel. Figures 6 and 7 ive the amplitude distributions and the cursor-selected areas for the same panels. Many f the lower amplitude samples found in the DATUS 8 amplitude distribution are from the leed hole indications. The regular patterns of these indications in the graphics isplays and the recordings were helpful in distinguishing them from the irregular porosity ndications.

5. Summary

Upon completion of analysis of the data collected at 1 MHz, areas on each of the test anels were selected based upon the anomalous appearance of the attenuation on the record- ngs or the terminal displays. These areas were cut out of the panels and chemically- illed to remove the outermost two aluminum sheets. The samples then consisted of two ondlines which were visible, two additional layers of aluminum, and an interior bondline hich could not be seen. These sections were radiographed to determine if foliated orosity could be detected in the middle bondline. One sample, DATUS 8, had porosity in ll three bondlines and DATUS 9 had porosity in one of the outer bondlines. No porosity as detected in the selected areas of any of the other test samples. There were changes n the thicknesses of one or more of the three bondlines in those samples which did not ontain porosity and it is believed these were responsible for the relatively small ttenuation changes associated with these areas. The portion of the DATUS 8 sample that as chem-milled may be seen in figure 8 together with a section of the C-scan made from his part. The circled indications on the surface of the part are pores which could be ssociated with indications on the recordings. As noted above, porosity occurred in all hree bondlines on this part.

The measurements made on the laminated portions of these test samples are summarized n figure 9. The open bar shown for each sample represents the variability of the bond- ne as measured from the median signal level to the level at which discrete indications an be isolated from the background attenuation of the bondlines. The cross-hatched bar ows the range of attenuation over which the suspected indications persisted. In panels th the type of construction used for these tests, the measured range of attenuation from e median level to the disappearance of localized indications was 3 to 5 dB with accept- le bondlines. For the two samples found to contain porosity, the total variation was 9 14 dB. In addition to the magnitude of the increased attenuation, the porosity appears be distinguishable from normal part variations through differences in the spatial

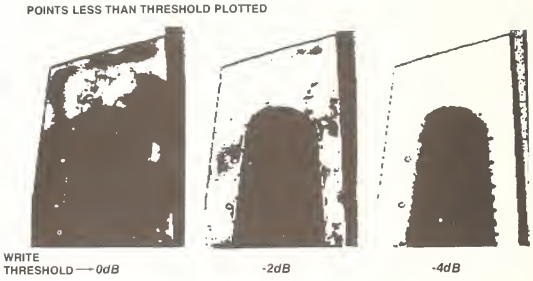

Figure 4. Graphics terminal display of DATUS 6.

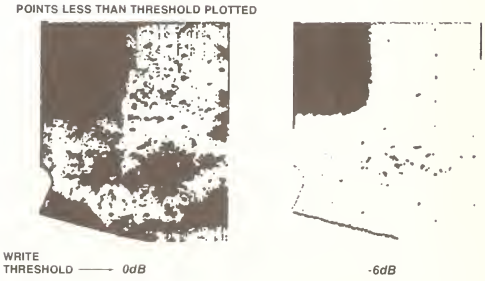

Figure 5. Graphics terminal display of DATUS 8.

AMPLITUDE DISTRIBUTION

VOLTS	SAMPLES	(%)
500	0.	0.0
520	0.	0.0
540	0.	0.0
560	0.	0.0
580	0.	0.0
600	0.	0.0
620	0.	0.0
640	0.	0.0
660	0.	0.0
680	1.	0.0
700	177.	1.0
720	822.	4.6
740	7065.	39.4
760	4852.	27.3
780	4943.	27.5
800	48.	0.3
820	0.	0.0
840	0.	0.0
860	0.	0.0
880	0.	0.0
900	0.	0.0
920	0.	0.0
940	0.	0.0
960	0.	0.0
980	0.	0.0

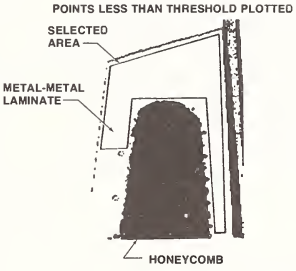

Figure 6. Amplitude distribution of DATUS 6.

AMPLITUDE DISTRIBUTION

VOLTS	SAMPLES	(%)
500	3.	0.0
520	15.	0.0
540	4.	0.0
560	20.	0.0
580	12.	0.0
600	34.	0.1
620	32.	0.1
640	79.	0.1
660	119.	0.2
680	164.	0.3
700	589.	1.1
720	867.	1.6
740	6901.	12.4
760	18264.	32.9
780	28364.	51.1
800	52.	0.0
820	0.	0.0
840	0.	0.0
860	0.	0.0
880	0.	0.0
900	0.	0.0
920	0.	0.0
940	0.	0.0
960	0.	0.0
980	0.	0.0

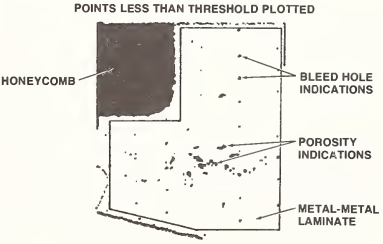

Figure 7. Amplitude distribution of DATUS 8.

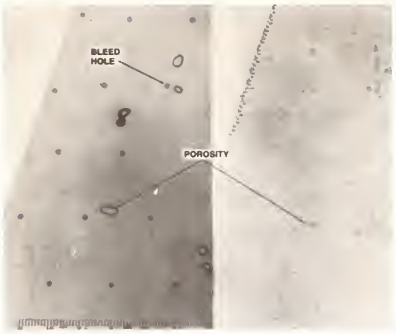

Figure 8. Chem-milled portion of DATUS 8 with recording.

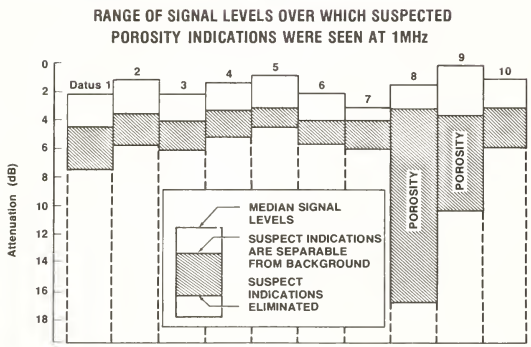

Figure 9. Range of signal levels ov which suspected porosity indicatio were seen at 1 MHz.

distribution of the porosity-related indications on the multilevel recordings and graphics displays. The porosity causes localized, irregular indications. Adhesive thickness variations resulted in comparatively large, uniform indications of slightly increased attenuation.

Larry Hazard developed the application software for the data acquisition and plot system. Pete Weidman prepared the software for the interactive display system with the graphics terminal. Their excellent work in support of this research is gratefully acknowledged.

References

[1] Patenaude, J., Bibli, K., and Reinisch, B. W., Direct digital graphics, American Laboratory, 95-101 (Sept. 1973).

lational Bureau of Standards Special Publication 596, Ultrasonic Materials Characterization, l. Berger and M. Linzer, eds., Proceedings of the First International Symposium on Ultrasonic laterials Characterization held at NBS, Gaithersburg, Md., June 7-9, 1978. Issued lovember, 1980.

ULTRASONIC EXAMINATION OF ELECTRICAL CONTACT ASSEMBLIES FOR BOND INTEGRITY

David C. Stewart

Cutler-Hammer, Inc.
P. O. Box 1158
Bowling Green, KY 42101

Although no absolute relationship between bond integrity and electrical life has yet been established, it is generally felt that the quality of the conductive bond between the electrical contact and the supporting member is critical to the overall functional life of an electrical contactor.

Due to the need to characterize the quality of this bond, a system of inspection techniques was developed to interrogate the braze joint on electrical contact assemblies, with immersion ultrasonics being the principle technique used. Careful selection of both electronics and transducers was done so as to develop a system that was particularly suited to this inspection. The system is designed to detect both disbond and inhomogeneous areas in brazed contacts that run parallel to the scanning motion of the immersion transducer.

The system can detect and print (C-scan) two 0.25 mm diameter flat bottom holes that are separated by their diameter, thus, giving us a tool with very good resolution. Other techniques used to support the ultrasonic data are destructive peel tests, metallurgical examination, and back etching. By using both A-scan and C-scan information coupled with destructive tests of selected samples, it is possible to statistically evaluate bond integrity for a large lot of assemblies.

1. Introduction

Cutler-Hammer, a major manufacturer of electrical control devices, produces a line of gh current ac contactors. The purpose of this paper is to discuss the ultrasonic techques for insuring the quality of the electrical contacts that are used in these devices.

AC contactors are used in many critical control applications. Due to the criticalness some of these applications we continue to search for ways to upgrade the overall quality d reliability of these devices. One area of concern is the electrical contact bond. though no absolute relationship between bond integrity and electrical life has yet been tablished, it is generally felt that the quality of the conductive bond between the elecical contact and the supporting member is critical to the overall functional life of the ntactor. Techniques have been established to better characterize the bond; thus, allowing to achieve further improvement.

2. What is a Contact?

A description of the morphology of the bond and the materials used to make up the conct assemblies would be in order to facilitate a better understanding of some of the inspecon problems. The contacts are part of the current carrying system of the contactor. The ps (contacts) are the actual points of electrical contact during opening and closing of the rcuit. In the case of high current ac contacts, the tips will see considerable heat and cing during normal use.

The severe environment under which we expect the contacts to operate requires the use special materials that are unique to the electrical field. Figure 1 shows a typical NEMA size 3 contact designed to carry a continuous 100 ampere load. The assembly consists of a silver cadmium oxide contact that is brazed with a silver solder to a copper carrier. The very nature of the contact material makes it difficult to inspect with ultrasonics. A micr graph of a cross section of the material (fig. 2) shows why. The contact material is a precipitate of cadmium oxide in a silver matrix. Typical cadmium oxide particle size runs from a few microns to approximately 0.25 mm. The area near the top of the photo is deplete of cadmium oxide. The area at the bottom is a layer of fine silver that is used for bondin due to the inability to braze to an oxide rich surface. The copper carrier is usually E.T. copper. Depending on the method of manufacture this can either be annealed or work hardene

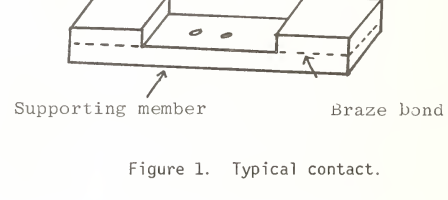

Figure 1. Typical contact.

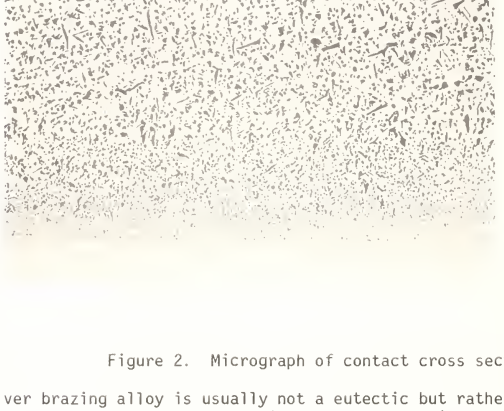

Figure 2. Micrograph of contact cross section.

The silver brazing alloy is usually not a eutectic but rather a copper rich alloy. S manufacturers also use alloys that contain low level constituents such as tin, cadmium, phosphorous, and zinc.

The contacts are bonded to the carriers in several ways. One way is to place the cor on the carrier with a preform of braze alloy and a suitable flux. This assembly is then heated in a furnace to effect the braze. While assembly of the components is the same, different sources of heat such as acetylene torches, induction heaters, and resistance wel may be employed depending upon the materials involved.

However, a rather new and innovative method involves the brazing of the material in trip form. Copper, silver-cadmium oxide, and solder in strip form are brought together and eated so as to form a continuously bonded composite material which is later blanked into ndividual contacts.

A typical bond specification might be that the minimum bond area will be 75 percent of he total surface area of the contact and that no single void shall be larger than 10 percent f the contact surface area. This degree of bond may be necessary to insure both good lectrical conduction as well as adequate heat dissipation. Control of edge disbond is also mportant. An edge disbond is defined as a void opening onto the side of the contact assembly t the braze joint. Excessive edge disbond can cause contact curling due to electrical arc rosion.

3. The Ultrasonic System

Prior to the use of ultrasonics, evaluation of contact bonds was for the most part estructive. Microsections and peel tests were employed to determine the bond quality; owever, with the advent of ever increasing silver prices, the destructive form of testing ad become less than desirable. Also due to the redesign of old line devices, the need arose or a nondestructive evaluation technique that could be used to inspect a larger sampling ize. Various NDE techniques were tried before settling on ultrasonics.

The ultrasonic immersion system we use at Cutler-Hammer operates in both the A- and -scan modes. The tank and recorder are large enough to allow us to 100 percent scan large rders of contacts when the need arises. (Recorder size is 76 cm by 91.5 cm.) The bridge will ndex in the X direction in increments of 25.4 μm to 2.537 cm. The ultrasonic instrument is TekTran Immerscope II, B frame. The A-scan consists of a 50 mHz scope coupled to a very lexible timer. The PR10 Pulser receiver has both wide band and tuned positions along with a ery linear attenuator. The flaw gate is extremely fast on the start of the first delay better than 50 ns).

The transducers used are ceramic, with a focal length of 1.27 cm. The typical focal pot size is between 0.25 mm and 0.36 mm. Transducers of longer focal length are used only hen necessary due to their increased focal spot size. The system consisting of electronics, ecorder, and transducer is capable of recording two 0.25 mm flat bottom holes separated by heir own diameter.

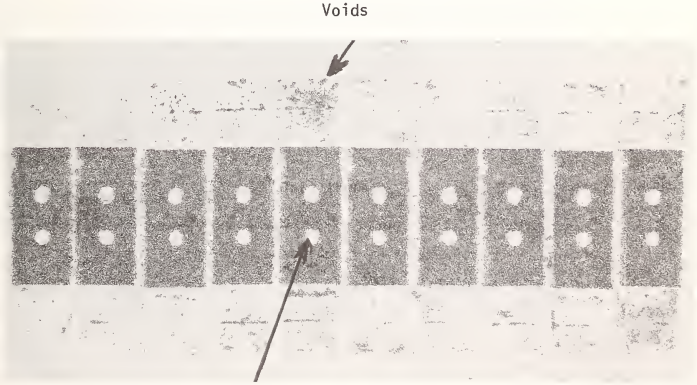

Figure 3. Typical C-scan of received contacts.

Test pieces are actual brazed contacts that have flat bottom holes drilled to the braze bond interface. Three hole sizes are drilled in each test piece (0.38 mm, 0.76 mm, and 1.14 mm). The use of three test holes helps to insure system linearity while also giving a bench mark for evaluating defect size of the C-scan. Figure 3 shows a typical C-scan print from a lot of received contacts. The scan is in the positive mode. (Black being indications above the gate level.)

4. Typical Defect

Typical defects found are illustrated in figures 4 through 7. Discrete voids in the bond caused by trapped gas are shown in figure 4. These will show on the A-scan presentation as a strong signal whose height will be proportional to the defect size. The voids will also be clearly defined on the C-scan, thus allowing easy estimation of the percentage of bond.

Distribution of voids is of great importance. Excessive voids that are concentrated in one area of the bond can result in localized overheating during operation. This could cause the contact to crack and a section to break away. The contact surface area is thus reduced while the contactor current remains constant. The end result is excessive heat that could melt the braze bond and cause a potential failure of the contactor involved.

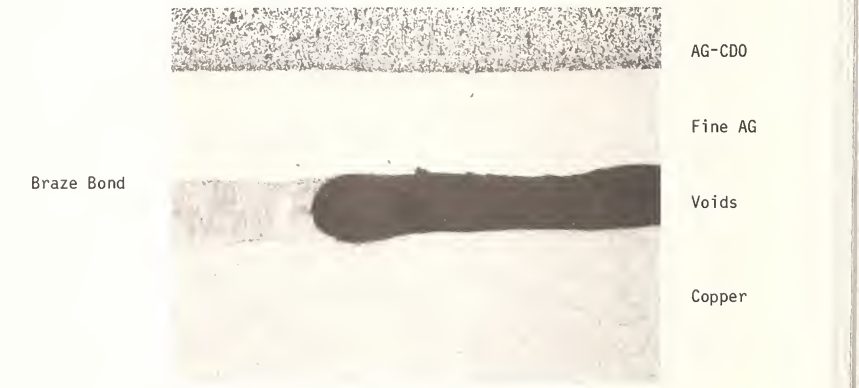

Figure 4. Contact defect.

A condition that is more difficult to interpret is shown in figure 5. Small porosity caused by excessive gas formation will appear on the C-scan as one large void. Depending on the concentration of the porosity, the A-scan signal will also appear to be inflated in amplitude. However, when the transducer is traversed across the contacts, the condition becomes obvious due to the rapid rising and falling of the defect signal above the gate trigger level.

The porosity is considered excessive when the voids are separated by less than their own diameter. However, voids less than 0.38 mm diameter are not considered when estimating the percentage of bond.

A condition where the defects do not occur in the bond but rather at the interface between the fine silver and the silver-cadmium oxide is shown in figure 6. Here we see a buildup of cadmium oxide at this interface which will cause enough of an impedance mismatch to reflect a signal that is over the gate level. On an A-scan presentation the defect can appear to be close packed porosity in the bond, but careful observation of the signal position in time will reveal the true location of the defect. This condition will result in a very weak interface between the fine silver and the silver-cadmium oxide, thus increasing the probability of curling from arc erosion.

An example of segregation of one of the constituents of the brazing alloy is shown in figure 7. In this case, it was probably tin. The layer that was formed is thin and consis

f very small particles but still constitutes an interface which will give a return signal hat will print out as a void. This layer could also result in a very weak interface at the ine silver-bond junction.

Figure 5. Contact defect.

Figure 6. Contact defect.

Figure 7. Contact defect.

5. Conclusions

The use of ultrasonics coupled with the intelligent application of metallographic techniques has greatly increased both the quality and understanding of brazed contact assemblies However, with the ever rising cost of materials and the push toward reduction in material usage, a far greater understanding of braze bond characteristics will be required to insure quality and reliability in the future.

The author would like to acknowledge the work done by our Corporate research staff that led to the writing of this paper. Special thanks is also given to Mr. Robert Hayes and Mr. Michael Campbell whose assistance and comments were most valuable to the completion of this paper.

ational Bureau of Standards Special Publication 596, Ultrasonic Materials Characterization, . Berger and M. Linzer, eds., Proceedings of the First International Symposium on Ultrasonic laterials Characterization held at NBS, Gaithersburg, Md., June 7-9, 1978. Issued ovember, 1980.

ULTRASONIC INTERACTIONS WITH THIN AIR LAYERS IN SOLIDS

Steven C. Gustafson

University of Dayton Research Institute
Dayton, OH 45469

Several investigators have observed that ultrasonic transmission through thin (submicron) air layers in solids may be orders of magnitude larger than the transmission predicted from Newton's and Hooke's laws and from boundary conditions which require the continuity of displacement and stress at layer interfaces. Nonlinear effects in the air layers or interaction effects between adjoining solid surfaces have been suggested as explanations for this phenomenon; these explanations generally imply that harmonics of an incident ultrasonic frequency will be generated in a thin air layer. Measurements designed to detect these harmonics were made for ultrasonic transmission through thin air layers formed between fused silica optical flats. Variations in layer thickness sufficient to change the amplitude of a broad band (approximately 5 to 15 MHz) transmitted ultrasonic pulse by more than a factor of 50 did not change the shape of the pulse. This result indicates that harmonic generation effects are not significant for the experimental conditions employed.

In the course of this work, it was found that stable half-plane air layers could be formed between fused silica optical flats so that the layers joined areas of optical contact at approximately straight-line boundaries. Ultrasonic reflection measurements were made near the edges of these half-plane layers, which appear to form easily measured simulations of ideal half-plane cracks. Such cracks are infinitely thin and, in the limiting cases, either "weak" with stress-free interfaces or "rigid" with displacement-free interfaces; in these cases exact theoretical results are available for elastic wave scattering and diffraction. These results could not be directly applied due to the many unknown characteristics of the half-plane layers and the ultrasonic transducer; however, Fresnel diffraction plots were made for comparison with the experimental data.

1. Introduction

Two types of ultrasonic measurements were made in this work: transmission measurements esigned to detect harmonic generation effects in thin air layers formed between fused silica ptical flats, and reflection measurements designed to investigate scattering and diffraction ffects near the edges of these layers. In both cases similar experimental arrangements were sed. The optical flats were 1.9 cm thick and were flat on one side to within 0.054 μm over heir 7.6 cm diameter. A support fixture was provided with six "fingers" to apply pressure to he edges of the flats so that the shape of the thin air layer between them could be adjusted see fig. 1).

The ultrasonic transducers were broadband PZT longitudinal wave transducers (Panametrics 112 or V113) with center frequencies near 10 MHz and with active element diameters of .64 cm. Salol (phenyl salicylate) was used to bond the transducers to the optical flats or the transmission experiments; due to the transparency of the flats, the quality and lignment of the bonding could be easily assessed. Kodak lens cleaner (a water-based etergent solution) was used with manual pressure to couple the transducers to the flats or the reflection measurements. This couplant provided adequate reproducibility when

the transducer was removed and repositioned, and it appeared to be superior in this respect t various oils and gels. The transducers were driven by a Panametrics 5052 PR pulser-receiver adjusted for its maximum pulse output of about 380 V. For the transmission measurements, the signal from the receiving transducer was amplified by a broadband amplifier prior to display on an oscilloscope. For the reflection measurements, the time-domain signal from the pulser-receiver was digitized and Fourier transformed by a minicomputer system, and frequency spectra were graphed on an associated plotter.

Figure 1. Apparatus for the investigation of ultrasonic interactions with thin air layers between fused silica optical flats

To form thin air layers between optical flats, the flats were first carefully cleaned using separate lens papers wetted with (in sequence) Kodak lens cleaner, acetone, alcohol, a ether. After brushing with an anti-static brush to remove stray dust particles, the flats were quickly placed in contact. Manual pressure at an edge was usually sufficient to initia optical contact (i.e., molecular contact between gases adsorbed on the fused silica surfaces A small region of optical contact would generally spread across the entire surface within a few minutes, and in this condition the flats would be rigidly bonded and could be separated safely only by rapid cooling of the exposed faces with liquid nitrogen. However, the spread of optical contact could be controlled or stopped by applying pressure to the edges of the flats using the support fixture fingers. For the transmission measurements, the fingers wer adjusted so that regions of optical contact surrounded a roughly circular thin air layer. F the reflection measurements, the fingers were adjusted so that a region of optical contact with an approximately straight boundary was formed near the center of the flats. It was fou that this half-plane layer could be held stable indefinitely and that after a few hours the layer would remain stable (i.e., the region of optical contact would not spread or retreat) when all pressure from the support fixture fingers was removed.

The thickness profiles of the air layers were measured using optical interference fringes. Under diffuse monochromatic illumination, dark bands were visible in the thin layers, and the distance between successive bands corresponded to a change in air-layer separation of one-half of one optical wavelength or 0.27 μm. Thus, thickness profiles were determined (to within at least one-quarter fringe or 0.07 μm) by counting fringes as a function of distance from a region of optical contact.

2. Nonlinear Effects in Thin Air Layers

An expression for the fraction T of incident longitudinal ultrasonic wave intensity transmitted at a frequency f through a layer of thickness ℓ, (at normal incidence and withou media attenuation) may be derived from Newton's and Hooke's laws and from boundary condition which require the continuity of displacement and stress at layer interfaces:

$$T = \left[1 + \frac{1}{4}\left(R - \frac{1}{R}\right)^2 \sin^2 k\ell\right]^{-1} ,$$

here $R = \rho c/\rho_o c_o$ is the ratio of acoustic impedances of the layer and the surrounding medium, $= 2\pi f/c$ is the acoustic wave vector, and ρ and ρ_o and c and c_o are, respectively, the ensities and longitudinal wave velocities in the layer and in the surrounding medium. umerous investigators have experimentally verified this or equivalent expressions; however, or the case of thin (submicron) air layers in solids, ultrasonic transmission several orders f magnitude larger than the transmission predicted by the above expression has been observed 1][1].

Suggested explanations for this anomaly have included nonlinear effects in the air layers r interaction effects between adjoining solid surfaces. Specifically, the leading nonlinear erm in the wave equation is nearly three orders of magnitude larger (in magnitude), relative o the linear terms, for air than for solids such as fused silica. Thus, an air layer in used silica may be considered to be a nonlinear layer in a linear medium, and if the layer is ery thin (so that transmission at the fundamental frequency is relatively large), then armonic generation may be observed [2]. An essentially equivalent view is that the isplacement amplitude of an ultrasonic wave in air may be comparable to the layer thickness or practical ultrasonic frequencies and intensities (e.g., 0.35 μm at 10 MHz and 10 W/cm^2), o that half-wave rectified "amplitude" transmission may begin to occur. Air layer hicknesses on the order of 0.1 μm are comparable to the mean free path of air molecules, and n this case molecular collisions with the layer interfaces (which are more frequent than ntermolecular collisions) lead to an effective increase in pressure and acoustic velocity and onsequently to an increase in ultrasonic transmission at the incident frequency. For still maller thicknesses, the layer may be considered to be a loosely bonded solid interface at hich special boundary conditions apply.

Figure 2 shows some transmitted ultrasonic pulses which were measured for layer hicknesses from about 0.14 μm to 0.65 μm. Although amplitude changes of more than a factor f 50 were observed, there were no significant changes in the shape of the transmitted pulses. his result indicates that harmonic generation effects were not significant for the xperimental conditions employed. Since these conditions were typical of the conditions used n ultrasonic nondestructive testing for fine cracks and debonds, it appears that ignificantly higher ultrasonic frequencies or intensities must be employed to observe armonic generation effects and to use these effects for the possible high resolution haracterization of thin-layer defects [2].

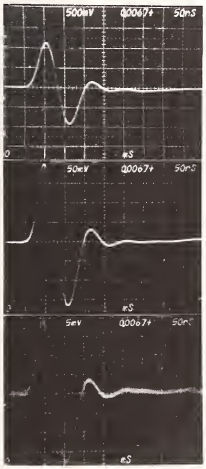

Figure 2. Transmitted pulses for different layer thicknesses: the layer thicknesses, from top to bottom, are 0.14 ± 0.07 μm, 0.38 ± 0.07 μm, and 0.65 ± 0.07 μm. The horizontal scales are 50 ns per division and the vertical scales are the indicated mV per division, beginning at 6.7 μs.

Figures in brackets indicate the literature references at the end of this paper.

3. Scattering Near Thin Air Layer Edges

The half-plane air layers on which reflection measurements were made appear to simulate ideal half-plane cracks. Ideal cracks are infinitely thin and, in the limiting cases, either "weak" with stress-free interfaces or "rigid" with displacement-free interfaces [3]. However, certain geometrical and physical characteristics of actual layers and transducers indicate that the measured scattering will differ from the scattering predicted for ideal half-plane cracks. The air layers have finite thickness and a wedge-shaped thickness profile: interference fringe measurements gave a wedge slope of 0.39 ± 0.07 μm/cm distance from the layer edge (where optical contact began). The layer may be intermediate between the weak and the rigid limiting cases, and this characteristic may change as thickness increases from the layer edge. The transducer has a finite size; thus the beam pattern is not uniform, some ultrasonic intensity is contained in lobes which are not directed perpendicular to the layer, and various mode conversion effects involving transverse or surface waves (for example) may occur.

Exact theoretical results are available for elastic wave scattering and diffraction by the surfaces and edges of ideal weak or rigid half-plane cracks [3]. Due to the layer and transducer characteristics discussed above, these results are not directly applicable. However, an attempt was made to determine the correlation between Fresnel diffraction theory and the reflection measurements. Fresnel diffraction for a semi-infinite reflecting surface is usually expressed in terms of a diffraction parameter $w = 2x/(\lambda d)^{\frac{1}{2}}$, where x is the distance from the edge of the surface to the projection of the transceiver on the plane of the surface, d is the length of this projection, and λ is the wavelength. If x is positive over the reflecting surface, then the ratio of the reflected intensity to the reflected intensity as x approaches infinity is:

$$\frac{I}{I_o} = \frac{1}{2}\left\{\left[\frac{1}{2} + \int_0^w \cos\left(\frac{\pi}{2}s^2\right) ds\right]^2 + \left[\frac{1}{2} + \int_0^w \sin\left(\frac{\pi}{2}s^2\right) ds\right]^2\right\}.$$

This ratio, which is expressed in terms of well-tabulated Fresnel integrals, is 0.25 at w = 0 and reaches a maximum at approximately w = 1.2 (i.e., over the surface); for larger w the ratio oscillates with increasing frequency and decreasing amplitude.

Typical frequency spectra for ultrasonic reflection near thin air layer edges are shown in figures 3, 4, and 5. Reproducible results of this type were obtained with two different transducers; of course, the gross features of the frequency spectra are caused by the transducer frequency response. Thus, the spectra were normalized to the spectrum at w = 0 (i.e., to the spectrum where the transducer axis intersected the layer edge), and the intensity (proportional to the square of the magnitude) at w = 0 was set equal to 0.25. Fresnel plots of the normalized intensities versus the diffraction parameter are shown in figures 6 and 7. Fresnel diffraction appears to be a more appropriate model for the higher frequencies, where the layer is presumably more highly reflecting.

This work was supported by AFML Contract F33615-76-C-5137. The assistance of Dr. J. Moyzis and Mr. K. Shimmin of AFML and of Mr. G. Mescher of UDRI is gratefully acknowledged.

References

[1] Szilard, J., Ultrasound penetration through very thin gas layers embedded in solid bodies, Proc. 4th Int. Conf. NDT, 159, London (1963).

[2] Gustafson, S. C., Ultrasonic transmission through a nonlinear layer in a linear medium, IEEE Ultrasonics Symposium Proceedings, 58 (1977).

[3] Kraut, E. A., Review of theories of scattering of elastic waves by cracks, IEEE Trans. Sonics Ultrasonics, SU-23, 162 (1976).

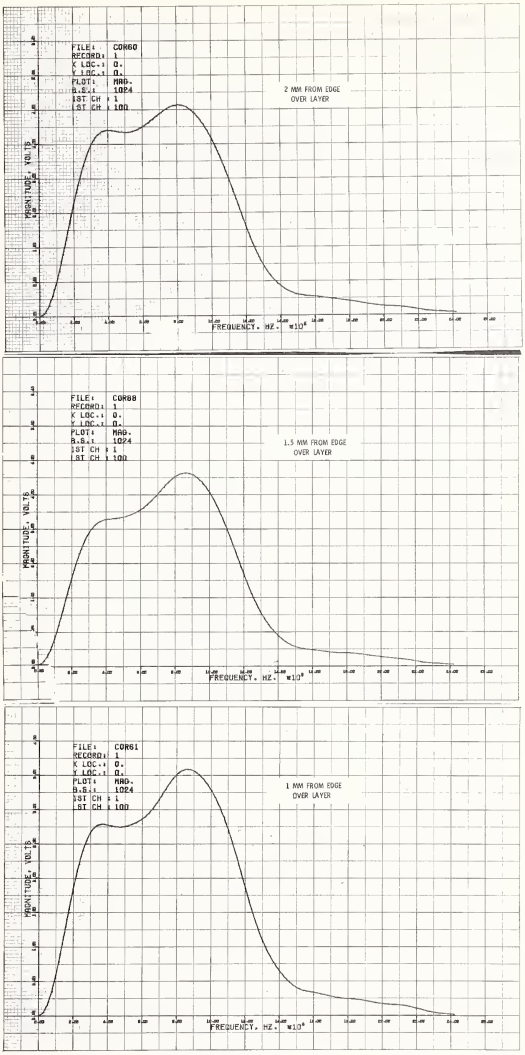

Figure 3. Frequency spectra for reflection near layer edges. Horizontal scales are 2 MHz per division; vertical scales, from top to bottom, are 0.80 V, 0.80 V, and 0.50 V (relative magnitude) per labeled division.

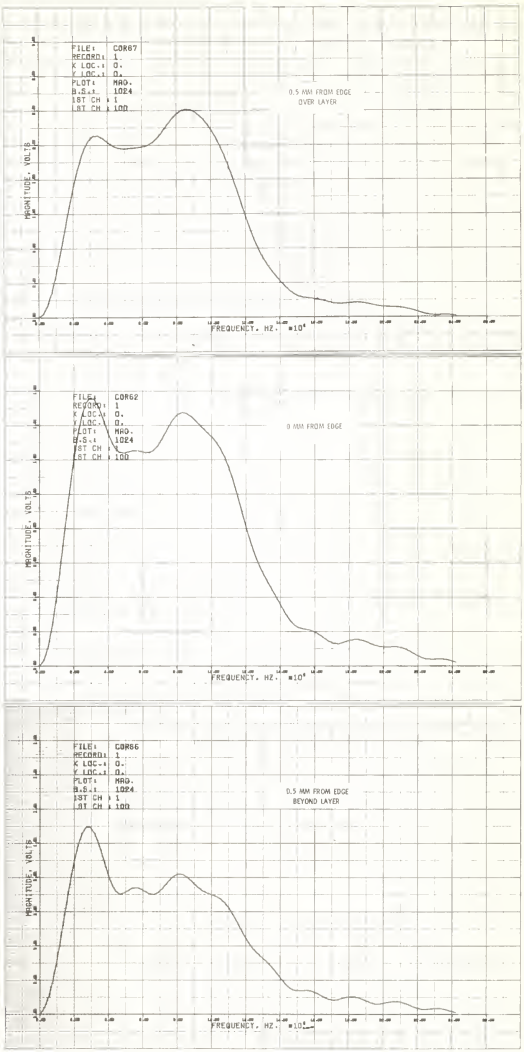

Figure 4. Frequency spectra for reflection near layer edges. Horizontal scales are 2 MHz per division; vertical scales, from top to bottom, are 0.40 V, 0.20 V, and 0.20 V (relative magnitude) per labeled division.

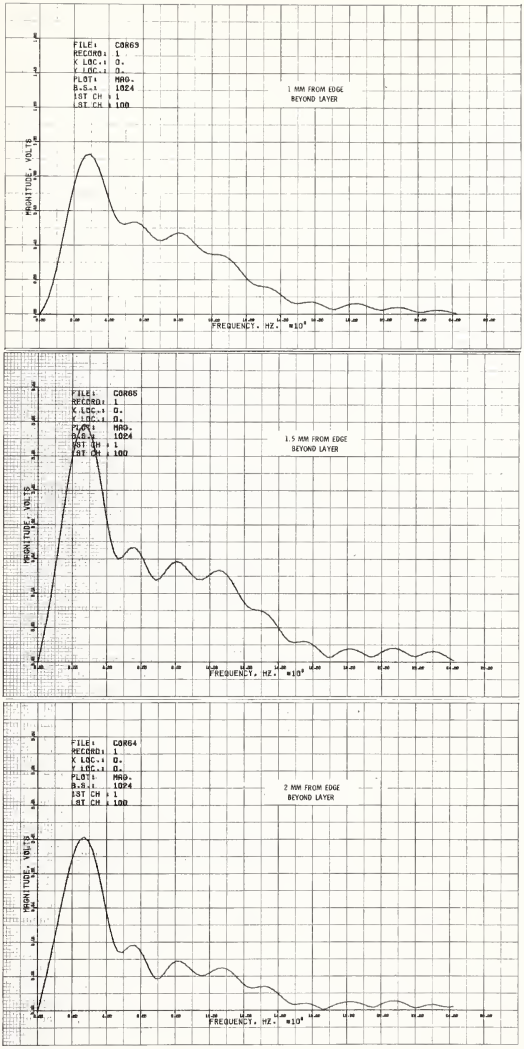

Figure 5. Frequency spectra for reflection near layer edges. Horizontal scales are 2 MHz per division; vertical scales, from top to bottom, are 0.20 V, 0.08 V, and 0.08 V (relative magnitude) per labeled division.

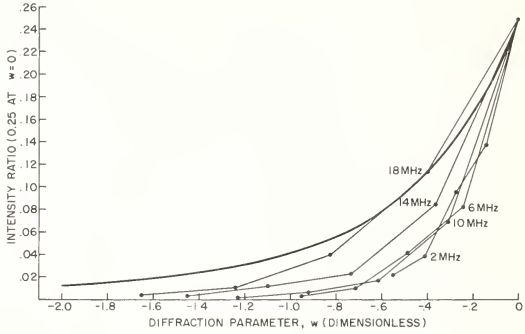

Figure 6. Fresnel plot for diffraction beyond the layer (negative w). The smooth curve is the theoretical result for an ideal half-plane total reflector; the line segments connect experimental points for different frequencies.

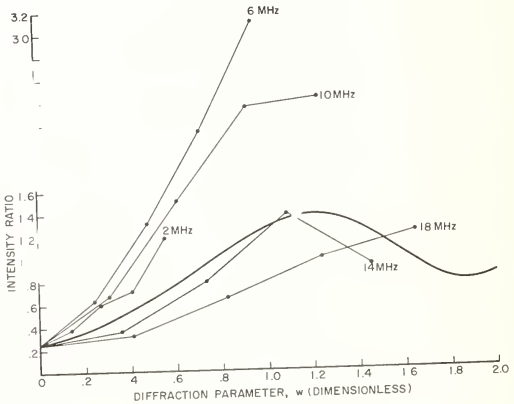

Figure 7. Fresnel plot for diffraction over the layer (positive w). The smooth curve is the theoretical result for an ideal half-plane total reflector; the line segments connect experimental points for different frequencies.

National Bureau of Standards Special Publication 596, Ultrasonic Materials Characterization, H. Berger and M. Linzer, eds., Proceedings of the First International Symposium on Ultrasonic Materials Characterization held at NBS, Gaithersburg, Md., June 7-9, 1978. Issued November, 1980.

GENERALIZED ULTRASONIC IMPEDIOGRAPHY

Jean P. Lefebvre

C.N.R.S. - Laboratoire de Mécanique et d'Acoustique - 31, chemin

and

Joseph Aiguier

13274 Marseille cedex 2
FRANCE

We propose a general method of investigating stratified media: acoustic impedography. Transforming the Pekeris equation, which describes acoustic propagation in an inhomogeneous medium, into a Schroedinger one, we apply the Gelfand-Levitan procedure to solve this inverse scattering problem of quantum mechanics and so recover the scattering potential from the impulse response in reflection. This scattering potential may then be used to compute the acoustic impedance profile.

1. Introduction

Classical ultrasonic echography is a qualitative investigation method of biological edia. It uses narrow-band ultrasonic pressure wave-trains produced by a directional trans- ucer, reflected by the various layers of the medium and collected by the same transducer hich converts the acoustic pressure into an electric signal. Only amplitude information is sed. It leads (when no multiple reflection occurs) to the reflection power of the layers at a iven travel-time (the latter being interpreted as a depth coordinate). A new step, reached y Wright [1][1] and later described by Jones [2], is the quantitative one. It is based upon he use of broad-band pulses, which allows one to obtain the impulse response (by deconvolution) f the medium in reflection. For weakly varying media, this impulse response is shown to be elated to the acoustic impedance profile by a simple analytical expression. This simple xpression is then inverted to recover the acoustic impedance profile from the measure of the mpulse response. The generalization of the method for any type of media requires a complete eformulation of the problem in terms of the inverse problem. This is the aim of this paper for more details and bibliography, see Lefebvre [3]).

Following Ware-Aki [4], we reduce the initial problem, which is here an acoustical one, o a quantum mechanics problem, by transforming the Pekeris equation [5] governing acoustic ropagation, into a Schroedinger one. This allows us to use, without any change, an algorithm f inverse quantum scattering, (the Gelfand-Levitan one), and recover the scattering potential rom the impulse response. The impedance profile is then computed from this potential.

2. The Propagation Equation and Its Transformation into a Schroedinger One

Neglecting absorption, motion, transverse waves, one may equate (in the ultrasonic omain) biological media to static, inhomogeneous fluids. Moreover, for improving lateral esolution, one generally uses highly directional transducers, probing the biological layers ith plane waves at normal incidence. The one dimensional Pekeris equation [5] may thus be sed:

$$-\frac{\partial^2 \psi}{(\partial t^2)} + \rho\, c^2 \frac{\partial}{\partial x}\,\frac{\lambda}{\rho}\,\frac{\partial \psi}{\partial x} = 0 \qquad (1)$$

[1] Figures in brackets indicate the literature references at the end of this paper.

where t is the time, x the space coordinate, ρ the density, c the sound speed, Ψ the scalar potential, ($p^A = \partial\Psi/\partial t$ the acoustic pressure, $N^A = -\lambda/\rho\ \partial\Psi/\partial x$ the acoustic velocity)

A Liouville transformation (similar to the one used by Ware-Aki [4]) leads to a Schroedinger equation.

The first step of this transformation is the introduction of a travel-time ξ:

$$\xi = \frac{x}{c_0} \quad ; \ x \leq 0$$

$$\xi = \int_0^x \frac{dx'}{c(x')} \quad ; \ x > 0 \tag{2}$$

The medium is assumed to be homogeneous in the left half space $x \leq 0$ (where $c = c_0$ and $\rho = \rho_0$ and the transducer is placed at $x = 0$, probing the right half-space $x > 0$ where the medium is heterogeneous (fig. 1).

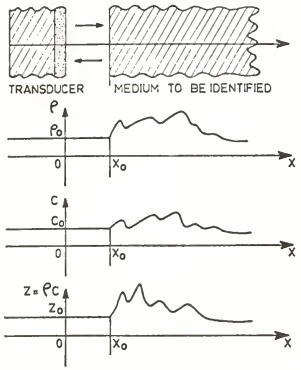

Figure 1. Schematic illustration of the problem.

Generally, the homogeneous space is water or any coupling medium which insures ultrasoni penetration in the biological structure.

The second step of the transformation is the function change $\hat{\Psi} = \eta/\eta_0\ \Psi$ in which $\eta = Z^{-1}$ $Z^{-1/2}$, $Z = \rho c$ being the acoustic impedance (so that $\Psi = \hat{\Psi}$, in the left homogeneous half space where the impulse response will be measured). Equation (1) thus becomes:

$$-\frac{\partial^2\hat{\Psi}}{\partial t^2} + \frac{\partial^2\hat{\Psi}}{\partial \xi^2} - V(\xi)\hat{\Psi} = 0, \tag{3}$$

with

$$V(\xi) = -\frac{\lambda}{2}\frac{dq}{d\xi} + \frac{\lambda}{4}g^2 \tag{4}$$

where

$$g(\xi) = \frac{d}{d\xi}\log Z$$

Finally, a time Fourier transform leads to the one dimensional Schroedinger equation:

$$\frac{\partial^2 \Psi}{\partial \xi^2} + (4\pi^2 \nu^2 - V(\xi))\, \hat{\Psi} = 0 \qquad (5)$$

where, ν is the frequency, $\hat{\Psi}(\xi,\nu)$ the Fourier transform of $\hat{\Psi}(\xi,t)$ and $V(\xi)$ the scattering potential.

3. The Inverse Problem: Identification of the Impedance Profile

The problem is now an inverse-scattering problem, which is the recovery of the scattering potential $V(\xi)$ from the impulse response in reflection $H(t)$.

3.1. General procedure for impediography

The first step is a deconvolution procedure to recover the impulse response in reflection of the medium $H(t)$ from the back-scattered field.

The second step is the use of an inverse quantum scattering algorithm to recover the scattering potential $V(\xi)$; with the Gelfand-Levitan method [6], $V(\xi)$ is given by $K(\xi,t)$, the solution of the Gelfand-Levitan integral equation:

$$K(\xi,t) = -H(t+\xi) - \int_{-\infty}^{\xi} K(\xi,t)\, H(t+\tau)\, d\tau, \qquad (6)$$

for $t \leq \xi$,

with

$$V(\xi) = 2 \frac{d}{d\xi} K(\xi,\xi) \qquad (6)$$

The third step is the recovery of the impedance profile $Z(\xi)$ by solving (4).

3.2. First iteration: the Wright formula

We show that our method is a generalization of the Wright one: A perturbation method leads to the first iteration:

$$V^{(\lambda)}(\xi) = -2 \frac{d}{d\xi} H(2\xi) , \qquad (7)$$

so

$$g^{(\lambda)}(\xi) = 4\, H(2\xi) , \qquad (8)$$

and

$$\left[\text{Log} \frac{Z(\xi)}{Z_o} \right]^{(\lambda)} = 2 \int_0^{2\xi} H(t)\, dt \qquad (9)$$

This is just the Wright formula [1], which is the basis of the impediography technique described by Jones [2]. It already gives good results for very weakly varying media (detection of one percent acoustic impedance changes (see Jones [1]). Figure 2 shows one of our first results by using this simplified procedure (in collaboration with A. Herment[2]).

3.3. Full algorithm

Our present endeavor concerns the development of an experimental verification of the simplified procedure (eq. (9)) (wide-band transducers, digitization, deconvolution, and other numerical problems).

It is hoped that the full Gelfand-Levitan algorithm may be used to solve the general problems of any type of gradient, even when multiple reflections occur. One may show that this is theoretically possible, provided that the Born approximation for the direct problem is still valid (a sufficient condition [6]), which is probably the case for all biological media.

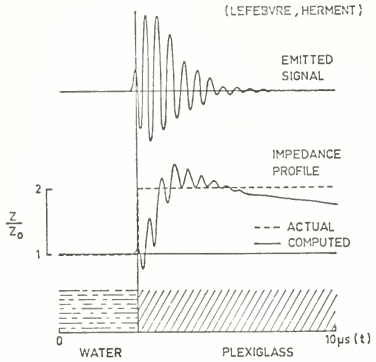

Figure 2. Performance of the first iterate.

References

[1] Wright, H., J. Acoust. Soc. Amer, 53, 1356-1359 (1973); see also Wright, H. A. and Miles P. R., Ocean 73, Abstracts, IEEE Int. Conf. on Engineering in the Ocean Environment (1973).

[2] Jones, J. P., Abstracts, 19th Annual Conference of the American Institute of Ultrasound in Medicine, Seattle, Washington (1974).

[2] Wright, H. A. and Miles, P. R., Ocean 73, IEEE International Conference on Engineering i the Ocean Environment (1973).

[3] Lefebvre, J. P., Acustica, 40, (1978).

[4] Ware, J. A. and Aki, K., J. Acoust. Soc. Amer., 45, 911-921 (1968).

[5] Pekeris, L. L., Geol. Soc. Amer. Memoir, 27 (1948).

[6] Chadan, K. and Sabatier, P. S., Inverse Problems in Quantum Scattering Theory (Springer 1977).

[2]From the "Centre d'Etude des Techniques Chirurgicales" (C.N.R.S.), Hospital Broussais, Paris.

National Bureau of Standards Special Publication 596, Ultrasonic Materials Characterization, H. Berger and M. Linzer, eds., Proceedings of the First International Symposium on Ultrasonic Materials Characterization held at NBS, Gaithersburg, Md., June 7-9, 1978. Issued November, 1980.

LASER PROBE DETECTION OF STONELEY WAVE INTERACTIONS WITH MATERIAL BOUNDARY DEFECTS

Richard O. Claus[1]

Department of Electrical Engineering
Virginia Polytechnic Institute and State University
Blacksburg, VA 24061

Within the past year, measurements of ultrasonic elastic waves on the boundaries between pairs of solids, obtained both indirectly by inferring boundary wave velocities from external surface acoustic wave (SAW) measurements and directly using an interferometric laser scanning system to probe boundaries between transparent solids, have been reported. Additional optical measurements and theoretical analysis of these Stoneley boundary waves have indicated that they may be generated on a wide range of material interfaces using several SAW and bulk wave mode conversion techniques. This current work suggests that a characterization of boundary defects may be obtained from the optical probe data.

1. Introduction

Stoneley waves are generalized surface elastic waves that may propagate along the boundaries between suitable pairs of solids. Recently, the first experimental measurements of Stoneley waves other than those generated by seismic disturbances have been reported. Lee and Corbly observed the waves indirectly by noting variations in SAW propagation on a substrate after the SAW had been converted into Stoneley waves on the boundary between the substrate surface [1][2]. Additional measurements using a differential interferometric laser probe system were reported by the author and C. H. Palmer [2,3]. Although the optical nature of the interferometric technique restricts its use to the probing of boundaries for which at least one of the boundary materials is transparent, it allows the direct detection of boundary surface particles motion induced by Stoneley waves.

Preliminary experiments performed using both direct and indirect methods suggest that Stoneley waves may be used in nondestructive evaluation to indicate the quality of certain adhesive bonding layers or the existence of boundary surface defects. The effects of boundary layers and surface defects upon obtained optical measurements is discussed here. Anticipated experimental work is indicated.

2. Theory

Stoneley first considered the problem of the propagation of an elastic wave on a boundary between solids in 1924 [4]. By assuming the continuity of stress and particle displacement across the plane interface between two elastic isotropic solid half-spaces, he derived an equation from which the speed of the boundary wave may be calculated as a function of the material constants of the two media.

This basic geometry is shown in figure 1. The material constants of the two media are the rigidity moduli μ_1 and μ_2, the Lamé constants λ_1 and λ_2, and the densities ρ_1 and

[1]This material is partially based upon work supported by the National Science Foundation under Grant No. ENG-7805773.

[2]Figures in brackets indicate the literature references at the end of the paper.

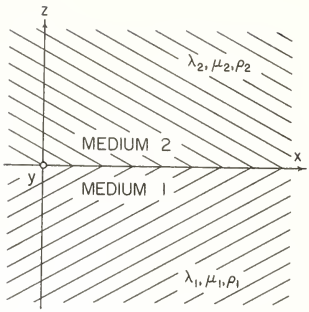

Figure 1. Assumed Stoneley wave boundary geometry.

ρ_2, respectively. Particle displacements in the medium for which $z > 0$ are u_1, v_1, and w_1, parallel to the x, y, and z coordinate axes, and u_2, v_2, and w_2 in the medium defined by $z < 0$. Stoneley demonstrated that particle motion associated with wave propagation in the positive z direction along the boundary has components u_1, w_1 and u_2, w_2 on either side of the boundary; that is, the motion is confined to the x-z plane. In comparison with Rayleigh waves, the amplitude of Stonely wave particle motion at the boundary decreases rapidly with distance into each of the two solids.

Stoneley assumed motion and stress continuity at the boundary, or

$$\begin{aligned} u_1 &= u_2 \\ v_1 &= v_2 \\ w_1 &= w_2 \end{aligned} \tag{1}$$

$$\mu_1 \left(\frac{\partial u_1}{\partial z} + \frac{\partial w_1}{\partial x} \right) = \mu_2 \left(\frac{\partial u_2}{\partial z} + \frac{\partial w_2}{\partial x} \right)$$

$$\mu_1 \left(\frac{\partial v_1}{\partial z} + \frac{\partial w_1}{\partial y} \right) = \mu_2 \left(\frac{\partial v_2}{\partial z} + \frac{\partial w_2}{\partial y} \right) \tag{2}$$

$$\lambda_1 \Delta + 2\mu \frac{\partial w_1}{\partial z} = \lambda_1 \Delta_2 + 2\mu \frac{\partial w_2}{\partial z} \quad .$$

Experimentally, these assumptions require that there be no slippage between the two surfaces and no air gaps along the interface.

The solution using these boundary conditions indicates that the desired elastic wave has the speed, c, where

$$c^4[(\rho_1 - \rho_2)^2 - (\rho_1 M_2 + \rho_2 M_1)(\rho_1 N_2 + \rho_2 N_1)]$$
$$+ 2Pc^2(\rho_1 M_2 N_2 - \rho_2 M_1 N_1 - \rho_1 + \rho_2) \qquad (3)$$
$$+ P^2(M_1 N_1 - 1)(M_2 N_2 - 1) = 0,$$

where $M_1 \equiv (1 - c^2/\alpha_1^2)^{\frac{1}{2}}$, $M_2 \equiv (1 - c^2/\alpha_2^2)^{\frac{1}{2}}$, $N_1 \equiv (1 - c^2/\beta_1^2)^{\frac{1}{2}}$, $N_2 \equiv (1 - c^2/\beta_1^2)^{\frac{1}{2}}$,

$_2 \equiv (1 - c^2/\beta_2^2)^{\frac{1}{2}}$, and $P \equiv 2(\rho_1\beta_1^2 - \rho_2\beta_2)$; finally α_1 and α_2 are the compressional wave peeds in the two media, and β_1 and β_2 are the shear wave speeds.

By analyzing several specific examples, Stoneley indicated that this equation may ave a real root for c if the condition

$$\frac{\rho_1}{\rho_2} = \frac{\lambda_1}{\lambda_2} = \frac{\mu_1}{\mu_2} \qquad (4)$$

s approximately satisfied. A detailed general treatment of the range of existence was ade by Sezawa and Kanai [5] and Scholte, who re-evaluated their treatment graphically 6]. More recently, Owen [7] calculated thirty-one pairs of possible media and Lim and lusgrave extended the Stoneley wave theory to include anisotropic materials [8]. Recent omputer calculations have additionally suggested pairs which include at least one trans- arent material and thus can be studied using the direct optical probe technique. Al- hough thirty-one such pairs have been identified so far, none include two transparent edia.

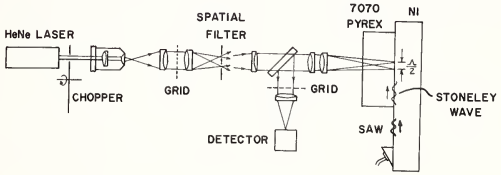

Figure 2. Differential interferometric optical system for boundary wave detection.

3. Experiment

The boundary between nickel and Corning 7070 pyrex glass was one of those suggested y recent calculations. Figure 2 shows one arrangement used to generate and detect Stone- ey waves on the boundary between these media. Using an 8-MHz x-cut quartz crystal trans- ucer mounted on a Rayleigh-angle water wedge, SAW were produced on the free pyrex surface. t the pyrex-nickel junction, these SAW were partially converted into Stoneley waves, par- ially reflected as SAW back to the wedge transducer, and partially mode-converted into aves in the bulk of both the nickel and pyrex and on the external nickel surface as shown n figure 3. All of these waves except those within the nickel have been measured optic- lly.

The operation of the interferometric optical system used in the detection and measure- ent of the waves has been fully described elsewhere [9,10]. Two differential coherent probe eams are focused on the surface of a material to measure SAW or within the bulk to measure ulk waves. For Stoneley waves, the beams were focused on the interface as shown in figure 2.

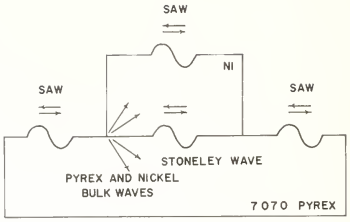

Figure 3. Mode conversion between incident pyrex SAW at left and Stoneley wave on pyrex-nickel boundary.

The two beams are adjusted to be half an acoustic wavelength apart so that either the changes of the refractive index within a medium or the sinusoidal displacement of the surface cause a differential change in optical path length between the two beams and hence a shifting of the interference fringes detected by a Ronchi grid. The interferometer is absolutely calibrated and amplitudes of the acoustic waves can thus be exactly described in terms of optical path changes. For SAW on glass, for example, wave amplitudes as small as 6×10^{-4} Å (6×10^{-14} m) can be detected.

By mechanically translating the sample shown in figure 2 and effectively shifting the beam focus point from the free pyrex surface to the pyrex-nickel boundary, the scan in ifgure 4 was obtained. The vertical mark near the left center of the scan indicates a gain change as noted on the SAW and Stoneley wave scales. Considerable conversion loss is noted. The measured Stoneley wavelength labeled varies from the predicted value by less than two percent.

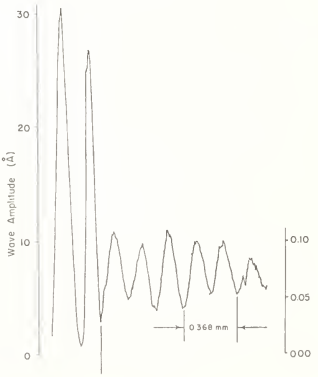

Figure 4. Continuous scan of SAW on 7070 pyrex surface (left) and Stoneley wave on 7070 pyrex-nickel boundary (right). Vertical mark indicates front edge of nickel sample and division between wave types; note gain change.

Stoneley waves similarly generated by SAW conversion were measured on three other predicted media pair boundaries. The wavelengths of all of these waves were different and individually they varied randomly from theoretical data by ±2 percent. Stoneley waves generated by the internal phase matching of compressional nickel waves had comparable wavelengths and no conversion efficiency increase was noted [11]. Attempts were made to similarly generate boundary waves between materials for which Stoneley wave propagation was theoretically not possible. Specifically, pairs such as pyrex and brass that lie just outside Scholte's graphical existence region were investigated. No boundary waves were detected on such pairs.

4. Results

Several experimental difficulties encountered in the generation of Stoneley waves suggest their use for boundary defect detection. First, several techniques were used to bond the individual materials together to form the desired plane boundary. Typical sample surface preparation included machine and hand polishing using successively finer grades of aluminum oxide, optical pastes, and jewelers' rouge. Initially, boundaries were formed by ringing together two such optically polished surfaces. Although waves of the anticipated wavelength were detected on the resulting boundary, their amplitudes were no larger than 0.01 Å and they were detected only near the front edge of the nickel block. Selective boundary attenuation in this case is most probably caused by local separation of the two surfaces. Despite polishing, surface irregularities of ±50 Å certainly must exist and large local surface defects would cause rapid Stoneley wave attenuation. As anticipated, Stoneley wave amplitudes increased with finer and finer surface polishing. Within the bulk of the pyrex and in the vicinity of attenuation, large particle motions due to internal compressional and shear waves were detected indicating that defect-induced mode conversion may allow defect characterization.

To obtain a closer approximation to the theoretical boundary conditions, the two polished materials were clamped using two C-clamps. Negligible increases in detected Stoneley wave amplitude were obtained for spaces due to boundary conditions and wave speed is small [3].

Finally, several bonding materials, including phenyl salicylate, epoxy, Canada balsam, optical cement, and superglue, were used to join the surfaces and fill in any defect gaps. Under pressure, most of the bonding material was forced from between the surfaces. Stoneley wave amplitudes as large as 0.1 Å have been measured as such glued boundaries. Current theoretical work suggests that if the thickness of the bonding layer is much less than wavelength, as is probably the case here, the effect upon wave velocity is small.

One possible defect in an adhesive bonding layer is simply a local lack of bonding material. Experimentally, such local bond defects were generated randomly by uneven pressure and uneven distribution of adhesive prior to surface contact. Measured Stoneley waves were detected and no Stoneley waves were found to propagate across such a region. Although these local adhesive layer voids were clearly visible through the pyrex, they would not be visible on a boundary between opaque samples. Optical measurements suggest that Stoneley waves may be used to qualitatively indicate the integrity of such bonds.

5. Conclusion

From the results of preliminary Stoneley wave measurements, potential use in the quantitative characterization of surface boundary and adhesive bond defects is suggested. Considerable additional measurements are required in this area, specifically point density and strain measurements in the volume surrounding the defect on both sides of the boundary. For these studies, Stoneley wave media pairs consisting of two transparent solids are clearly required.

References

[1] Lee, D. A. and Colby, D. M., Use of interface waves for nondestructive inspection, IEEE Trans. SU.-24 206-212 (1977).

[2] Claus, R. O. and Palmer, C. H., Direct measurements of ultrasonic Stoneley waves, Appl. Phys. Lett., 31, 547-548 (1977).

[3] Claus, R. O. and Palmer, C. H., Direct measurements of acoustic boundary waves, 1978 Acoust. Soc. of Amer. Meeting, Providence, RI (May 1978).

[4] Stoneley, R., Elastic waves at the surface of separation of two solids, Proc. Roy. Soc. Lond., 106, 416-428 (1924).

[5] Sezawa, K. and Kanai, K., The range of existence of Stoneley waves and some related problems, Bull. Tokyo (Imperial) Univ. Earthquake Res. Inst., 17, 1-8 (1939).

[6] Scholte, J. G., The range of existence of Rayleigh and Stoneley waves, Proc. Ned. Akad. von. Wet, 49, 120-126 (1946).

[7] Owen, T. E., Surface wave phenomena in ultrasonics, Prog. Appl. Mat. Res., 6, 69-87 (1964).

[8] Lim, T. C. and Musgrave, M. J. P., Stoneley waves in anisotropic media, Nature, 225, 372 (1970).

[9] Palmer, C. H., Ultrasonic surface wave detection by otpical interferometry, J. Acoust. Soc. Amer., 53, 948-949 (1973).

[10] Palmer, C. H., Claus, R. O., and Fick, S. E., Ultrasonic wave measurement by differential interferometry, Appl. Opt., 16, 1849-1856 (1977).

[11] Claus, R. O., Ultrasonic Stoneley wave measurements, in Proc. IEEE Region 3 Conf. (Atlanta, GA) (April 1978).

National Bureau of Standards Special Publication 596, Ultrasonic Materials Characterization, H. Berger and M. Linzer, eds., Proceedings of the First International Symposium on Ultrasonic Materials Characterization held at NBS, Gaithersburg, Md., June 7-9, 1978. Issued November, 1980.

MATHEMATICAL THEORIES OF THE DIFFRACTION OF ELASTIC WAVES

Yih-Hsing Pao

Department of Theoretical and Applied Mechanics
Cornell University
Ithaca, NY 14853

All analyses and interpretation of backscattered or sidescattered signals in ultrasonic nondestructive evaluation of materials are based on the theory of diffraction of elastic waves, and the solutions for boundary value problems of waves in a solid with cracks. This paper surveys three mathematical theories and analyses of the solutions, namely, the method of integral equation, the method of transition matrix, and the geometric theory of diffraction.

The first two methods are based on an integral representation theorem of Huygens' principle for elastic waves. The first method determines the unknown secondary sources on the surface of a scatterer by solving a vectorial integral equation, and the second one relates the scattered waves to the incident waves by eliminating the unknown surface sources common to both waves. The third method is based on the asymptotic theory for waves at high frequencies and Fermat's principle, and it makes use of exact solution of diffraction for simpler problems. The problem of the diffraction of two-dimensional elastic waves (compressional or shear wave) by a long crack of finite width is used to illustrate and to compare all three methods.

1. Introduction

In this paper, we review three mathematical methods for analyzing the diffraction of elastic waves by a crack in a solid, namely: the method of integral equation, the geometric theory of diffraction, and the method of transition matrix. Although the first two methods had been applied many years ago to study the diffraction of acoustic or optical waves (scalar waves) by a thin strip or disk in fluid, or the complementary problem of a long slit or circular aperture in a screen, they are being developed only recently to analyze the diffraction of elastic waves (vector waves with two speeds). The history of the method of transition matrix is comparatively short and it has not yet been fully tested, even for the diffraction of acoustic waves by a thin disk.

Only waves with harmonic time dependence (monochromatic waves) are considered. The diffracted waves are usually expressed in terms of vector displacement field from which stresses, velocities, or energy cross sections can be calculated. These results when expressed as a function of the frequencies of the incident wave are called steady-state response function. It has shown in reference [1][1] that the power spectra of a scattered pulse equals the products of the frequency spectra of the incident pulse and the steady-state response function. Hence the determination of the steady-state response function over a wide range of frequencies by any one of the aforementioned methods provides a theoretical basis for the ultrasonic spectral analysis of diffracted pulses.

Both the method of integral equation and the method of transition matrix are based on an integral representation of the scattered elastic waves. This integral representation along with some preliminaries of the theory of elasto dynamics are summarized in the next section.

[1]Figures in brackets indicate the literature references at the end of this paper.

It is followed by three sections, each discussing one of the three methods. Pertinent literatures are cited in each section. At the end, we compare all three methods and discuss various features of each method.

2. Integral Representation of Scattered Elastic Waves

We consider a steady state displacement field $\underset{\sim}{u}(\underset{\sim}{x})\exp(-i\omega t)$. The exponential time function with the circular frequency ω is omitted throughout the paper. The stress tensor $\underset{\sim}{\tau}$ is related to $\underset{\sim}{u}$ by Hooke's law for isotropic solids,

$$\underset{\sim}{\tau} = \lambda \underset{\sim}{I}(\nabla\cdot\underset{\sim}{u}) + \mu(\nabla\underset{\sim}{u} + \underset{\sim}{u}\nabla)$$

$$= \lambda \underset{\sim}{I}(\nabla\cdot\underset{\sim}{u}) + 2\mu\nabla\underset{\sim}{u} + \mu\underset{\sim}{I}\times(\nabla\times\underset{\sim}{u}) \qquad (2.1)$$

where λ and μ are Lame's constants, and μ is also called the shear modulus. The traction $\underset{\sim}{t}$ on a surface with a unit vecter normal $\underset{\sim}{n}$ is the normal component of $\underset{\sim}{\tau}$,

$$\underset{\sim}{t} = \underset{\sim}{n}\cdot\underset{\sim}{\tau} = (\lambda\underset{\sim}{n}\,\mathrm{div} + 2\mu\underset{\sim}{n}\cdot\mathrm{grad} + \mu\underset{\sim}{n}\times\mathrm{curl})\,\underset{\sim}{u} \quad . \qquad (2.2)$$

The elastic medium is excited either by an incident wave $\underset{\sim}{u}^i(\underset{\sim}{x})\exp(-i\omega t)$, or a source of body force $\rho\underset{\sim}{f}(\underset{\sim}{x})\exp(-i\omega t)$. The incident wave impinges on an elastic inclusion of volume V which is enclosed by a surface S (fig. 1). The total wave field $\underset{\sim}{u}(\underset{\sim}{x})$ in the medium with the inclusion can be represented by the following integral [2],

$$\int_S [\underset{\sim}{u}(\underset{\sim}{x}')\cdot\underset{\sim}{n}'\cdot\underset{\sim}{\Sigma}(\underset{\sim}{x}|\underset{\sim}{x}') - \underset{\sim}{t}(\underset{\sim}{x}')\cdot\underset{\sim}{G}(\underset{\sim}{x}|\underset{\sim}{x}')]dS'$$

$$+\int_V \rho\underset{\sim}{f}(\underset{\sim}{x}')\cdot\underset{\sim}{G}(\underset{\sim}{x}|\underset{\sim}{x}')dV' + \underset{\sim}{u}^i(\underset{\sim}{x}) = \varepsilon\underset{\sim}{u}(\underset{\sim}{x}) \quad . \qquad (2.3)$$

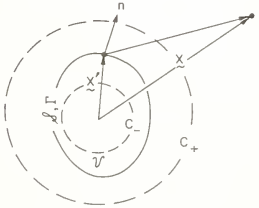

Figure 1. Scattering by a body of volume V and surface S (or a cylindrical surface of circumference Γ).

On the right-hand side of the above, the symbol ε has the value 1, 1/2, or 0 depending on the location of the observation point $\underset{\sim}{x}$,

$$\varepsilon = \begin{cases} 1 & \underset{\sim}{x} \text{ outside S} \\ 1/2 & \underset{\sim}{x} \text{ on S} \\ 0 & \underset{\sim}{x} \text{ inside S} \quad . \end{cases} \qquad (2.4)$$

In the surface integral, $\underset{\sim}{u}(\underset{\sim}{x})$ and $\underset{\sim}{t}(\underset{\sim}{x})$ are the displacement and traction respectively on the surface S due to the total wave field, $\underset{\sim}{G}(\underset{\sim}{x}\,\underset{\sim}{x}')$ and $\underset{\sim}{\Sigma}(\underset{\sim}{x}\,\underset{\sim}{x})$ are the Green's displacement tenso and Green's stress tensors respectively. The component $G_{ij}(\underset{\sim}{x}\,\underset{\sim}{x}')$ represents the displacemen component at the field point $\underset{\sim}{x}$ in the direction of x_j-axis due to a concentrated force appli

t the source point $\underset{\sim}{x}'$ in the direction of x_i-axis; and $\Sigma_{ijk}(\underset{\sim}{x}\ \underset{\sim}{x}')$ is related to G_{ij} as τ_{ij} is elated to u_i in eq. (2.1)

$$\Sigma_{ijk} = \lambda\delta_{ij}\partial_m G_{mk} + \mu(\partial_i G_{jk} + \partial_j G_{ik}) \quad . \tag{2.5}$$

oth $\underset{\sim}{G}$ and $\underset{\sim}{\Sigma}$ are known for an infinite, isotropic medium [2]. The scattered wave in the edium outside the inclusion is then given by

$$\underset{\sim}{u}^s(\underset{\sim}{x}) = \underset{\sim}{u}(\underset{\sim}{x}) - \underset{\sim}{u}^i(\underset{\sim}{x}) \qquad \underset{\sim}{x} \text{ outside } S \quad . \tag{2.6}$$

Equation (2.3) is analogous to the Helmholtz formula which is the foundation of a mathematical theory of Huygens' principle for scalar waves [3]. The corresponding formula for lastic waves was given by Kupradze in the early 1950's [4].

Defining a vector differential operator $\underset{\sim}{T}$,

$$\underset{\sim}{T} \equiv \underset{\sim}{n}\cdot(\lambda\underset{\sim}{I}\ \text{div} + 2\mu\ \text{grad} + \mu\underset{\sim}{I} \times \text{curl}) \tag{2.7}$$

e can then express $\underset{\sim}{t}$ in eq. (2.2) as

$$\underset{\sim}{t} = \underset{\sim}{T}(\underset{\sim}{u}) = (\lambda\underset{\sim}{n}\text{div} + 2\mu\underset{\sim}{n}\cdot\text{grad} + \mu\underset{\sim}{n} \times \text{curl})\underset{\sim}{u}(\underset{\sim}{x}) \tag{2.8}$$

nd $\underset{\sim}{n}\cdot\underset{\sim}{\Sigma}$ in eq. (2.5) as $\underset{\sim}{T}(\underset{\sim}{G})$,

$$\underset{\sim}{n}\cdot\underset{\sim}{\Sigma} = \underset{\sim}{T}(\underset{\sim}{G}) = (\lambda\underset{\sim}{n}\text{div} + 2\mu\underset{\sim}{n}\cdot\text{grad} + \mu\underset{\sim}{n} \times \text{curl})\underset{\sim}{G}(\underset{\sim}{x}\ \underset{\sim}{x}') \quad . \tag{2.9}$$

ne surface integral in eq. (2.3) can thus be written in a symmetric form,

$$\int_S\{\underset{\sim}{u}(\underset{\sim}{x}')\cdot\underset{\sim}{T}'[\underset{\sim}{G}(\underset{\sim}{x}|\underset{\sim}{x}')] - \underset{\sim}{T}'[\underset{\sim}{u}(\underset{\sim}{x}')]\cdot\underset{\sim}{G}(\underset{\sim}{x}|\underset{\sim}{x}')\}dS' + \underset{\sim}{u}^i(\underset{\sim}{x}) = \varepsilon\underset{\sim}{u}(\underset{\sim}{x}) \quad . \tag{2.10}$$

ne prime over $\underset{\sim}{T}$ means differentation with respect to the $\underset{\sim}{x}'$ coordinates. This form of ntegral representation will be convenient in later applications.

2.1. Surface scattering and volume scattering

When the material properties of the inclusion are entirely different from those of the rrounding solid, the surface S defines a surface of discontinuity for the material constants , μ, and mass density ρ). In the absence of a body force ($\underset{\sim}{f} = 0$), the total wave outside S n be calculated from the surface integral in eq. (2.3) provided the surface sources $\underset{\sim}{u}(\underset{\sim}{x}')$ d $\underset{\sim}{t}(\underset{\sim}{x}')$ are known. The determination of these surface sources constitutes the solution of e problem of <u>surface scattering</u>.

On the other hand, when the mass density $\rho_I(\underset{\sim}{x})$ and elastic moduli $\underset{\sim}{C}_1(\underset{\sim}{x})$ of the inclusion dergo a gradual change from the boundary to the interior of the inclusion, and are continuous at the surface S, the scattering effect of this inhomogeneity is equivalent to a distribution of body force, $\rho\underset{\sim}{f}^e$, over the volume V inside S, and [2]

$$\rho f_j^a(\underset{\sim}{x}) = \partial_k\{\Delta C_{jk\ell m}(\underset{\sim}{x})[\partial_\ell u_m(\underset{\sim}{x})]\} + \Delta\rho(\underset{\sim}{x})\omega^2 u_j(\underset{\sim}{x}) \qquad \underset{\sim}{x} \text{ in } V \tag{2.11}$$

where

$$\Delta\rho(\underset{\sim}{x}) = \rho_I(\underset{\sim}{x})-\rho$$

$$\Delta\underset{\sim}{C}(\underset{\sim}{x}) = \underset{\sim}{C}_1(\underset{\sim}{x})-\underset{\sim}{C} \tag{2.12}$$

and

$$C_{ijk\ell} = \lambda\delta_{ij}\delta_{k\ell} + \mu(\delta_{ik}\delta_{j\ell} + \delta_{i\ell}\delta_{jk}) \quad .$$

The ρ and $\underset{\sim}{C}$ are respectively the constant density and moduli of the surrounding medium, and $\partial_k \equiv \partial/\partial x_k$ etc. The wave scattered by this inclusion is given by the volume integral of eq. (2.3) with the equivalent body force,

$$u_j^s(\underset{\sim}{x}) = \rho S_V f_k^e(\underset{\sim}{x}')G_{kj}(\underset{\sim}{x}|\underset{\sim}{x}')dV' \quad . \tag{2.13}$$

The G_{kj} is the Green's displacement tensor of the surrounding medium.

If, in addition, the change of ρ and $\underset{\sim}{C}$ is abrupt at the bounding surface S, the above volume integral should be modified to the following form [5],

$$u_j^s(\underset{\sim}{x}) = S_V\{\omega^2\Delta\rho(\underset{\sim}{x}')u_k(\underset{\sim}{x}')G_{kj}(\underset{\sim}{x}|\underset{\sim}{x}') - \Delta C_{ik\ell m}(\underset{\sim}{x}')[\partial'_\ell u_m(\underset{\sim}{x}')][\partial'_k G_{ij}(\underset{\sim}{x}|\underset{\sim}{x}')]\}dV' \quad . \tag{2.14}$$

In either form, the volume integral in the previous two equations contains the displacement $u_k(x')$ and displacement gradient $\partial'_\ell u_m(\underset{\sim}{x}')$ as the sources which are unknown functions inside the volume V. The determination of these unknown sources constitute the solution of the problem of volume scattering.

One method to determine the unknown volume source functions is by iteration. In the first iteration, the $\underset{\sim}{u}$ inside the inhomogeneous region can be approximated by the incident wave field $\underset{\sim}{u}^i$. This is known as the Born approximation [6]. When $\Delta\rho(\underset{\sim}{x})$ and $\Delta\underset{\sim}{C}(\underset{\sim}{x})$ are large and abrupt, a better first iteration is obtained by letting $u_k(\underset{\sim}{x}')$ and $\partial'_\ell u_m(\underset{\sim}{x}')$ be the same as the corresponding statical displacements and strains. This is the low frequency approximation [5,6].

It was shown that the volume integral of eq. (2.14) can be reduced to the surface integral of eq. (2.10) [2]. Thus these two formulations are completely equivalent when there is a discontinuity of the material constants of the bounding surface S. For the remaining part of this article, we consider only the surface scattering.

2.2. Two-dimensional problems of surface scattering

To illustrate the methods which have been developed to solve the problem of surface scattering, we consider the two-dimensional problems of elastic waves known as the antiplane strain and plane strain. They are defined as follows [7]:

Antiplane Strain (SH Wave):

$$u_1 = u_2 = 0, \quad u_3 = u_3(x_1, x_2) \tag{2.15}$$

Plain Strain (P or SV - wave):

$$u_1 = u_1(x_1, x_2), \quad u_2 = u_2(x_1, x_2), \quad u_3 = 0 \quad . \tag{2.16}$$

The problem of antiplane strain is particularly simple since u_3 satisfies a scalar ave equation

$$\mu\nabla_1^2 u_3 = -\rho\omega^2 u_3 \tag{2.17}$$

here $\nabla_1 = \partial^2/\partial x_1^2 + \partial^2/\partial x^2$ is the two dimensional Laplacian operator. The wave speed is iven by $c_2 = \sqrt{(\mu/\rho)}$, the shear wave speed. The problem is completely analogous to the two imensional acoustic waves in air (scalar waves).

For plane strain conditions $\underset{\sim}{u}(u_1,u_2,0)$ satisfies the two-dimensional vector equation

$$(\lambda+\mu)\nabla_1\nabla_1\cdot\underset{\sim}{u} + \mu\nabla^2\underset{\sim}{u} = -\rho\omega^2\underset{\sim}{u} \quad . \tag{2.18}$$

he disturbance propogates with two speeds, $c_p = \sqrt{(\lambda+2\mu)/\rho}$ for the P-wave, and $c_s = \sqrt{\mu/\rho}$ or the S-wave.

The two-dimensional problems of surface scattering occur when the inclusion is a prismatic ylinder of infinite length, and when both the material properties and the incident wave are onstant along the axis of the cylinder.

Let the S in eq. (2.10) be the surface of the cylinder, its generator being parallel to he x_3-axis. Let Γ be the circumference of the cylinder and dS be the differential arc ength along the curve Γ (fig. 2). Equation (2.10) is thus reduced to

$$\varepsilon\underset{\sim}{u}(\underset{\sim}{x}) = \underset{\sim}{u}^i(\underset{\sim}{x}) + S_\Gamma\{\underset{\sim}{u}(\underset{\sim}{x}')\cdot\underset{\sim}{T}'[\underset{\sim}{G}(\underset{\sim}{x}|\underset{\sim}{x}')] - \underset{\sim}{T}'[\underset{\sim}{u}(\underset{\sim}{x}')]\cdot\underset{\sim}{G}(\underset{\sim}{x}|\underset{\sim}{x}')\}ds' \quad . \tag{2.19}$$

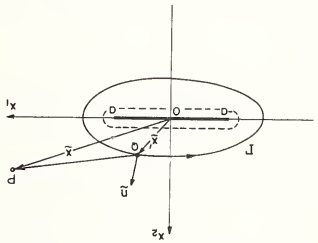

Figure 2. A cylindrical obstacle with circumference Γ, and a thin strip of width 2a.

e Green's displacement tensor for two dimensional waves is,

$$G_{mn}(\underset{\sim}{x}|\underset{\sim}{x}') = \frac{1}{4\pi\rho\omega^2}\{k_s^2 g_s(\underset{\sim}{x}|\underset{\sim}{x}')\delta_{mn} - \partial_m\partial_n[g_p(\underset{\sim}{x}|\underset{\sim}{x}') - g_s(\underset{\sim}{x}|\underset{\sim}{x}')]\} \tag{2.20}$$

ere

$$k_s = \omega/c_s \quad , \quad k_p = \omega/c_p$$

$$g_s(\underset{\sim}{x}|\underset{\sim}{x}') = i\pi H_o^{(1)}(k_s|\underset{\sim}{x} - \underset{\sim}{x}'|)$$

$$g_p(\underset{\sim}{x}|\underset{\sim}{x}') = i\pi H_o^{(1)}(k_p|\underset{\sim}{x} - \underset{\sim}{x}'|) \tag{2.21}$$

$$|\underset{\sim}{x} - \underset{\sim}{x}'| = [(x_1-x_1')^2 + (x_2-x_2')^2]^{1/2} \quad .$$

The $H_0^{(1)}$ is the Hankel function of the first kind.

When the boundary is free of stresses, i.e.

$$\underset{\sim}{t}(\underset{\sim}{x}') \equiv \underset{\sim}{T}'[\underset{\sim}{u}(\underset{\sim}{x}')] = 0 \qquad \underset{\sim}{x}' \text{ on } \Gamma \quad . \tag{2.22}$$

The scattered waves outside Γ are given by

$$\underset{\sim}{u}^s(\underset{\sim}{x}) = S_\Gamma \underset{\sim}{u}(\underset{\sim}{x}')\cdot\underset{\sim}{T}'[\underset{\sim}{G}(\underset{\sim}{x}\ \underset{\sim}{x}')]ds' \qquad \underset{\sim}{x} \text{ outside } \Gamma \quad . \tag{2.23}$$

The problem is now reduced to the determination of the unknown surface displacement $\underset{\sim}{u}(\underset{\sim}{x}')$ at the boundary Γ.

In the next two sections, we discuss two approaches, the method of integral equations and the method of transition matrix, which can be effectively applied to calculate the scattered wave field. A third method known as the geometric theory of diffraction will be discussed in section 5. In the interest of application to nondestructive testing of materials, we consider the scattering of elastic waves by a long and thin crack of width 2a; its cross section on the x_1-x_2 plane is shown in figure 2. The incident wave is a plane wave, its direction of propagation being perpendicular to the edge of the crack. The problem is then either antiplane strain, or plane strain, depending on the polarization of the incident wave.

3. The Method of Integral Equation

The mathematical solution for the scattering of scalar waves by a long strip of finite width was first formulated by Rayleigh in 1897 in terms of an integral equation [8]. The integral equation and various approximate solutions are discussed in the review article by Bouwkamp [9] and in the book by Hönl, Maue and Westpfahl [10]. Detailed solutions for the scattering of SH waves by either a rigid strip or a ribbon-shaped crack are given in referen [11] (section 4.4).

As for the scattering of two dimensional elastic waves $\underset{\sim}{u}(u_1,u_2,0)$ by a crack of finite width, there have been numerous investigations [12,13,14,15]. The solutions are usually for mulated in coupled integral equations for displacement potentials ϕ and ψ where $\underset{\sim}{u} = \nabla\phi + \nabla x($ Numerical results produced are mainly for wave field near the tips of the crack [13,14,15]. At far field, an asymptotic solution for the displacement field was given in reference [12]. The book edited by Sih contains solutions of diffracted waves near the crack [16].

A general formulation of a vector integral equation for the boundary value problems of elastic waves was presented by Kupradze [4]. His formulation begins with the integral formula like that in eq. (2.23). By letting $\underset{\sim}{x}$ approach $\underset{\sim}{x}'$ in eq. (2.23) and treating properly the singularities of the derivatives of Green's function, one obtains immediately the integral equation for the unknown surface displacement $\underset{\sim}{u}(\underset{\sim}{x}')$ on a stress free boundary Γ.

This general vector formulation was applied by Tan to study the diffraction by a rigid strip and a crack [17]. Let the path Γ in eq. (2.23) be composed of two straight lines and two semicircles centered at $x_1=\pm a$ as shown in figure 2. Along this path, $\underset{\sim}{n}'=\pm\underset{\sim}{e}_2$ depending on whether the path is above or below the x_1-axis, and $\underset{\sim}{e}_2$ is a unit vector in the direct of x_2-axis. It was shown by Tan that the part of integration along the two semicircular paths with radius σ vanishes provided that as $\sigma \to 0$, the displacement is of the order of $\sqrt{\sigma}$. Hence eq. (2.23) can be written as

$$\varepsilon\underset{\sim}{u}(\underset{\sim}{x}) = \underset{\sim}{u}^i(\underset{\sim}{x}) + \int_{-a}^{a} \underset{\sim}{U}(x_1')\cdot T_2'[\underset{\sim}{G}(\underset{\sim}{x}\ \underset{\sim}{x}')]dx_1' \tag{3.1}$$

where as a special case of eq. (2.7),

$$T_2 \equiv \lambda\underset{\sim}{e}_2 \text{div} + 2\mu\underset{\sim}{e}_2\cdot\text{grad} + \mu\underset{\sim}{e}_2 \times \text{curl} \tag{3.2}$$

and $\underset{\sim}{U}$ is the jump of the displacement $\underset{\sim}{U}$ across the crack,

$$\underset{\sim}{U}(x_1) = \underset{\sim}{u}(x_1, +0) - \underset{\sim}{u}(x_1, -0) \quad , \tag{3.3}$$

By letting $\underset{\sim}{x}$ in eq. (3.1) approach the source coordinate $\underset{\sim}{x}'$, we obtain a vector integral equation for the unknown function $\underset{\sim}{U}(x_1')$,

$$\frac{1}{2}\,\underset{\sim}{u}(\underset{\sim}{x}) - \underset{\sim}{u}^i(\underset{\sim}{x}) = \int_{-a}^{a} \underset{\sim}{U}(x_1')\, T_2'[\underset{\sim}{G}(\underset{\sim}{x}|\underset{\sim}{x}')]dx_1', \qquad \underset{\sim}{x} = (x_1', 0). \tag{3.4}$$

The previous equation is a Fredholm integral equation of second kind since $\underset{\sim}{u}(\underset{\sim}{x})$ on the left hand side is also an unknown function. It can be transformed into a Fredholm integral equation of first kind if one applies the vector differential operator $\underset{\sim}{T}$ to both sides of eq. (2.19), and obtains the following formula,

$$\varepsilon\underset{\sim}{t}(\underset{\sim}{x}) = \underset{\sim}{t}^i(\underset{\sim}{x}) + \underset{\sim}{T}\int_\Gamma \{\underset{\sim}{u}(\underset{\sim}{x}')\cdot\underset{\sim}{T}'[\underset{\sim}{G}(\underset{\sim}{x}|\underset{\sim}{x}')] - \underset{\sim}{T}'[\underset{\sim}{u}(\underset{\sim}{x}')]\cdot\underset{\sim}{G}(\underset{\sim}{x}|\underset{\sim}{x}')\}ds' \quad . \tag{3.5}$$

Note that the operator $\underset{\sim}{T}$ differentiates with respect to the $\underset{\sim}{x}$ coordinates; and $\underset{\sim}{T}'$ with respect to the $\underset{\sim}{x}'$ coordinates. By letting $\underset{\sim}{x}$ approach $\underset{\sim}{x}'$ and noting that $\underset{\sim}{t} = \underset{\sim}{T}(\underset{\sim}{u})$ vanishes on the surface Γ, we obtain another integral equation for the unknown function $\underset{\sim}{U}(x_1)$,

$$-\underset{\sim}{t}^i(\underset{\sim}{x}) = \int_{-a}^{a} \underset{\sim}{U}(x_1')\cdot T_2 T_2'[\underset{\sim}{G}(\underset{\sim}{x}|\underset{\sim}{x}')]dx_1', \qquad \underset{\sim}{x}=(x_1',0) \quad . \tag{3.6}$$

The $\underset{\sim}{t}^i(\underset{\sim}{x})$ which is the traction generated by the incident wave is a known function. At the surface of the crack, $-a \le x_1 \le a$, the two components of $\underset{\sim}{t}^i$ are the shearing stress τ_{22}^i and normal stress τ_{22}^i. They both are continuous at $x_2 = 0$.

Integral equation like that in eq. (3.6) can only be solved numerically. The following methods are commonly used:

(1) Finite Difference - The integral is replaced by a finite sum of N intervals with unknown variables $\underset{\sim}{U}_i$. Care should be exericised in treating the singular point $x_i = x_i$ at which the Green's function $\underset{\sim}{G}$ may become infinite [11].

(2) Finite Element - Again the region of integration is divided into intervals called linear elements, and within each element the unknown function $\underset{\sim}{U}$ is represented by a linear, quadratic or other elementary functions of $\underset{\sim}{x}'$ with undetermined coefficients. The integration is then carried out within each element, resulting in a system of equations for the undetermined coefficients [18].

(3) Method of Moments [19] - The unknown function $\underset{\sim}{U}$ is expanded in an infinite series of basis functions with unknown coefficients. If the basis functions form a complete orthogonal set within the interval $-a \le x_1' \le a$, these coefficients can be determined by the Hilbert-Schmidt process [11]. Otherwise, the series is truncated into a finite sum and the unknown coefficients are determined by solving a system of linear algebraic equations. This method was used first by Rayleigh for the solution of diffraction of light waves by a slit [8].

Adopting the third approach, Tan [17] assumed an expansion of the following form for the unknown vector function in eq. (3.6),

$$U_j(x_1) = \sum_{n=1}^{n} \{A_{jn}\sin(2\pi n x_1/a) + B_{jn}\cos[(2n-1)\pi x_1/a]\} \qquad j=1,2 \quad .$$

He then solved for the unknown coefficients A_{jn}, B_{jn} numerically and calculated the total scattering cross section as a function of $\omega a/c_p$ and the angular distribution of the scattering intensity. Results of the latter are comparable to those obtained by Harumi [20] who used the method of eigenfunctions where the unknown scattered waves are expanded in series of Mathieu functions.

For cracks with finite length as well as finite width, the scattered waves depend on all three coordinates (x_1, x_2, x_3). Instead of eq. (2.21) the three dimensional Green's function should be used, and the scattered waves are represented by a surface integral. The problem is considerably simplified if the crack surface is circular (penny-shaped crack) and the incident wave symmetric about the axis perpendicular to the crack surface. The scattering of elastic waves by a penny-shaped crack has been analyzed by several authors, using the method of integral equations [21,22,23].

4. The Method of Transition Matrix

Instead of solving the integral equations like eq. (3.4) and (3.6), the scattered wave field can be determined directly by the method of transition matrix. The method was first developed by Waterman in 1968 for the scattering of acoustic (scalar) waves [24], and electromagnetic waves [25], and later extended to the scattering of elastic waves by Pao and Varatharajulu [26], and Waterman [27]. The former based on their derivations on the integral formula eq. (2.10), and the latter started from a different integral formula which involves $\underset{\sim}{u}$, div $\underset{\sim}{u}$, and curl $\underset{\sim}{u}$ as the unknown source functions inside the surface integral [28].

4.1. Transition matrix and the integral representation formula

Consider again the scattering of waves by a long cylinder of arbitrary cross section as discussed in the previous section. According to eq. (2.10), the wave fields inside and outside the cylindrical surface bounded by a curve Γ are respectively

$$S_\Gamma\{\underset{\sim}{u}'\cdot\underset{\sim}{T}'[\underset{\sim}{G}(\underset{\sim}{x}|\underset{\sim}{x}')] - \underset{\sim}{t}'\cdot\underset{\sim}{G}(\underset{\sim}{x}|\underset{\sim}{x}')\}ds' = -\underset{\sim}{u}^i(\underset{\sim}{x}) \quad \underset{\sim}{x} \text{ inside } \Gamma \tag{4.1}$$

$$S_\Gamma\{\underset{\sim}{u}'\cdot\underset{\sim}{T}'[\underset{\sim}{G}(\underset{\sim}{x}|\underset{\sim}{x}')] - \underset{\sim}{t}'\cdot\underset{\sim}{G}(\underset{\sim}{x}|\underset{\sim}{x}')\}ds' = -\underset{\sim}{u}^i(\underset{\sim}{x}) \quad \underset{\sim}{x} \text{ inside } \Gamma \quad . \tag{4.2}$$

In the above, we have used abbreviated notations $\underset{\sim}{u}' = \underset{\sim}{u}(\underset{\sim}{x}')$ and $\underset{\sim}{t}' = \underset{\sim}{t}(\underset{\sim}{x}') = \underset{\sim}{T}'[\underset{\sim}{u}(\underset{\sim}{x}')]$. If the stresses vanish on the bounding curve Γ, eq. (4.2) is identical to eq. (2.23).

The method of transition matrix proceeds as follows [26]: Select two sets of basis functions, common to cylinders of all shapes, and expand the given incident wave $\underset{\sim}{u}^i$ and the unknown scattered waves $\underset{\sim}{u}^s$ in a series of these basis functions. For two dimensional problems of elasto-dynamics, the basis functions are

$$(\psi^\nu)_m^\sigma \quad \text{and} \quad (\hat{\psi}^\nu)_m^\sigma \quad , \qquad , \ \sigma = 1,\ 2;\ m = 0,1,\ldots\infty \tag{4.3}$$

where [28]

$$(\underset{\sim}{\psi}^1)_m^\sigma = \sqrt{\varepsilon_m}\ \nabla[H_m(k_p r)\begin{pmatrix}\cos\\ \sin\end{pmatrix} m\theta] \quad , \qquad k_p = \frac{\omega}{c_p}$$

$$(\underset{\sim}{\psi}^2)_m^\sigma = \sqrt{\varepsilon_m}\ \nabla\times[\underset{\sim}{e}_3 H_m(k_s r)\begin{pmatrix}\cos\\ \sin\end{pmatrix} m\theta], \qquad k_s = \frac{\omega}{c_s} \quad . \tag{4.4}$$

The $H_m(kr)$ is the Hankel function of the first kind and ε_m=1 when m=0, and ε_m=2 when m > 0. The sin mθ is used when σ = 1, and cos mθ is used when σ = 2. The $\hat{\underset{\sim}{\psi}}$ is the regular part of and for real kr it is obtained from the above expressions by replacing $H_m(kr)$ with $J_m(kr)$, the Bissel function of the first kind. The series representations for $\underset{\sim}{u}^i$ and $\underset{\sim}{u}^s$ are then given by

$$\underset{\sim}{u}^{i}(\underset{\sim}{x}) = \sum_{m}\sum_{\sigma}\sum[a^{\sigma}_{\nu m}(\underset{\sim}{\hat{\psi}}^{\nu})^{\sigma}_{m}(\underset{\sim}{x})] \equiv \sum_{\nu} a_{\nu}\,\underset{\sim}{\hat{\psi}}^{\nu}(\underset{\sim}{x}) \tag{4.5}$$

$$\underset{\sim}{u}^{s}(\underset{\sim}{x}) = \sum_{\nu}\sum_{m}\sum_{\sigma}\sum[c^{\sigma}_{\nu m}(\underset{\sim}{\hat{\psi}}^{\nu})^{\sigma}_{m}(\underset{\sim}{x})] \equiv \sum_{\nu} c_{\nu}\,\underset{\sim}{\hat{\psi}}^{\nu}(\underset{\sim}{x}) \quad . \tag{4.6}$$

or convenience, the triple sum is represented by a single summation symbol Σ and one index . y applying additional theorems the Green's tensor $\underset{\sim}{G}(\underset{\sim}{x}|\underset{\sim}{x}')$ can also be expanded into a series f products of these basis functions, one involving $\underset{\sim}{x}$ coordinates and the other involving x' oordinates.

For stress-free boundary, $\underset{\sim}{t}'$ vanishes in eq. (4.1) and (4.2). The unknown surface isplacement $\underset{\sim}{u}'$ in them is expanded also into a series of regular basis functions with unknown oefficients $\tilde{f}^{\sigma}_{\nu m}$,

$$\underset{\sim}{u}(\underset{\sim}{x}') = \sum_{\nu}\sum_{m}\sum_{\sigma}\sum\ [(f^{\sigma}_{\nu m}(\underset{\sim}{\hat{\psi}}^{\nu})^{\sigma}_{m}(\underset{\sim}{x}')] \equiv \sum_{\nu} f_{\nu}\underset{\sim}{\hat{\psi}}^{\nu}(\underset{\sim}{x}') \qquad \underset{\sim}{x}' \text{ on } \Gamma \quad . \tag{4.7}$$

ubstituting all three series together with those for $\underset{\sim}{T}'[\underset{\sim}{G}(\underset{\sim}{x}|\underset{\sim}{x}')]$ into the equations for $\underset{\sim}{u}^{i}$ nd $\underset{\sim}{u}^{s}$, multiplying eq. (4.1) with another basis function $(\underset{\sim}{\hat{\psi}}^{\omega})^{\lambda}_{n}(\underset{\sim}{x})$ and integrating $\underset{\sim}{x}$ oordinate over an inscribing circle c_- inside Γ, and multiplying eq. (4.2) and $(\underset{\sim}{\psi}^{\omega})^{\lambda}_{n}$ and integrating $\underset{\sim}{x}$ variables over a circumscribing circle C+ and Γ (fig. 1), one then btains

$$\sum_{\omega} f_{\omega} Q^{\nu\omega} = -ia_{\nu} \tag{4.8}$$

$$\sum_{\omega} f_{\omega} \hat{Q}^{\nu\omega} = -ic_{\nu} \tag{4.9}$$

ere

$$Q^{\nu\omega} = \frac{1}{\gamma}\int_{\Gamma} \underset{\sim}{T}'[\underset{\sim}{\psi}(\underset{\sim}{x}')]\cdot\underset{\sim}{\hat{\psi}}^{\omega}(\underset{\sim}{x}')ds' \tag{4.10}$$

ere $\gamma = 4\mu k_s^2$ is a constant; and $\hat{Q}^{\nu\omega}$ is the regular part of $Q^{\nu\omega}$. In the previous derivations, e has been made of the orthogonality conditions for $\underset{\sim}{\psi}(\underset{\sim}{x})$ and $\underset{\sim}{\hat{\psi}}(\underset{\sim}{x})$ when integrated over a rcular curve in the $\underset{\sim}{x}$ coordinates.

It is seen that each element of the Q-matrix is composed of a line integral of the pre- lected basis functions $\underset{\sim}{\hat{\psi}}^{\omega}$, or $\underset{\sim}{\psi}^{\omega}$, together with its derivatives. When Γ is a circle, this ne integral can be evaluated in closed form. Otherwise, it can be evaluated numerically. us the pair of equations in the above relate the unknown scattering coefficients c_ν to e unknown f_ω, which in turn are related to the given incident coefficients a_ν. Eliminating from these equations would yield a relation between c_ν and a_ν.

In matrix notation, eqs. (4.8) and (4.9) can be expressed as

$$\underset{\sim}{Q}\,\underset{\sim}{f} = +\,i\,\underset{\sim}{a} \tag{4.11}$$

$$\underset{\sim}{\hat{Q}}\,\underset{\sim}{f} = i\,\underset{\sim}{c} \quad . \tag{4.12}$$

nce, defining the inverse of $\underset{\sim}{Q}$ by $\underset{\sim}{Q}^{-1}$, we find

$$\underset{\sim}{c} = -(\underset{\sim}{\hat{Q}}\,\underset{\sim}{Q}^{-1})\,\underset{\sim}{a} = \underset{\sim}{T}\,\underset{\sim}{a} \tag{4.13}$$

where

$$\underset{\sim}{T} \equiv -\hat{\underset{\sim}{Q}}\,\underset{\sim}{Q}^{-1} \quad .$$

The T matrix is called the transition matrix and for elastic waves, it is symmetric. This completes the deriving of transition matrix from the integral representation formula of elastic waves.

In expanded form, eq. (4.13) reads

$$\begin{pmatrix} (c_1)^{\sigma}_{m} \\ \\ (c_2)^{\sigma}_{m} \end{pmatrix} = \begin{pmatrix} (T^{11})^{\sigma\mu}_{mn} & (T^{12})^{\sigma\mu}_{mn} \\ \\ (T^{21})^{\sigma\mu}_{mn} & (T^{22})^{\sigma\mu}_{mn} \end{pmatrix} \begin{pmatrix} (a_1)^{\mu}_{n} \\ \\ (a_2)^{\mu}_{n} \end{pmatrix} \tag{4.15}$$

and eq. (4.10) carries six indices.

$$(Q^{\nu\omega})^{\sigma\mu}_{mn} = \frac{1}{\gamma} \int_{\Gamma} \underset{\sim}{T}'[(\underset{\sim}{\psi}^{\nu})^{\sigma}_{m}(\underset{\sim}{x}')]\cdot(\underset{\sim}{\hat{\psi}}^{\omega})^{\mu}_{n}(\underset{\sim}{x}')\, ds' \qquad m,n=0,1,\ldots\infty \quad . \tag{4.16}$$

4.2. Transition matrix and Betti's identity

Conceptually, the key point in the original development of the transition matrix is to recognize that the wave field inside a boundary and that outside are related to the same unknown surface sources $\underset{\sim}{u}(\underset{\sim}{x}')$ and $\underset{\sim}{T}'[\underset{\sim}{u}(\underset{\sim}{x}')]$. These relations can explicitly be determined by making use of the integral representation eq. (2.10), for both interior region and exterior region. Mathematically, the key step is the derivation of eqs. (4.8) and (4.9) from eqs. (4 and (4.2). This step is tedious and difficult as it involves the operation with two coordi $\underset{\sim}{x}$ and $\underset{\sim}{x}'$. Recently, a different concept and simpler mathematical derivation of the transit matrix were presented by Waterman [29] based on a conservation law and by Pao [30] on the b of Betti's identity.

The Betti's third identity of elasto-dynamics can be stated as follows [4]: Given two vector displacement fields $\underset{\sim}{u}$ and $\underset{\sim}{v}$ and the corresponding stress fields $\underset{\sim}{\tau}(\underset{\sim}{u})$ and $\underset{\sim}{\tau}(\underset{\sim}{v})$. If b $\underset{\sim}{u}$, $\underset{\sim}{v}$, and $\underset{\sim}{\tau}(\underset{\sim}{u})$ and $\underset{\sim}{\tau}(\underset{\sim}{v})$ are continuous within a volume V which is bounded by a closed surfa S, then

$$\int_S [\underset{\sim}{T}(\underset{\sim}{u})\cdot\underset{\sim}{v} - \underset{\sim}{T}(\underset{\sim}{v})\cdot\underset{\sim}{u}]dS = \int_V [\Delta^{*}\underset{\sim}{u}\cdot\underset{\sim}{v} - \Delta^{*}\underset{\sim}{v}\cdot\underset{\sim}{u}]dV \tag{4.17}$$

where

$$\Delta^{*}\underset{\sim}{u} = \nabla\cdot\underset{\sim}{\tau}(\underset{\sim}{u}) = [(\lambda + \mu)\,\mathrm{grad}\,\mathrm{div} + \mu\nabla^2]\underset{\sim}{u} \tag{4.18}$$

and, as defined in eq. (2.8),

$$\underset{\sim}{T}(\underset{\sim}{u}) = \underset{\sim}{n}\cdot\underset{\sim}{\tau}(\underset{\sim}{u}) = \underset{\sim}{t}(\underset{\sim}{u}) \quad .$$

If both $\underset{\sim}{u}$ and $\underset{\sim}{v}$ satisfy the equation of motion with the same circular frequency

$$\Delta^{*}\underset{\sim}{u} = -\rho\omega^2\underset{\sim}{u} \quad , \qquad \Delta^{*}\underset{\sim}{v} = -\rho\omega^2\underset{\sim}{v} \quad , \tag{4.19}$$

then the volume integral in eq. (4.17) vanishes. Hence, we have

$$\int_S [\underset{\sim}{T}(\underset{\sim}{u})\cdot\underset{\sim}{v} - \underset{\sim}{T}(\underset{\sim}{v})\cdot\underset{\sim}{u}]dS = 0 \tag{4.20}$$

provided $\underset{\sim}{u}$, $\underset{\sim}{v}$, $\underset{\sim}{\tau}(\underset{\sim}{u})$ and $\underset{\sim}{\tau}(\underset{\sim}{v})$ are continuous within the volume bounded by the surface S. T result is a special form of the reciprocity theorem, and can be viewed as an orthogonality condition for two arbitrary functions $\underset{\sim}{u}$ and $\underset{\sim}{v}$ [30]. Note that eq. (2.18) is the two dimen sional version of eq. (4.19).

Applying eq. (4.20) to a cylindrical region bounded by the curve Γ and the circumscribing cle C_+ of unspecified radius, one then obtains two line integrals, one over Γ and one over (fig. 1),

$$\int_{\Gamma}[\underset{\sim}{t}_+\cdot\underset{\sim}{v} - \underset{\sim}{T}(\underset{\sim}{v})\cdot\underset{\sim}{u}_+]ds = \int_{C+}[\underset{\sim}{T}(\underset{\sim}{u})\cdot\underset{\sim}{v}-\underset{\sim}{T}(\underset{\sim}{v})\cdot\underset{\sim}{u}]dS \quad . \tag{4.21}$$

e $\underset{\sim}{t}_+$ and $\underset{\sim}{u}_+$ are respectively the surface traction and surface displacement on Γ approaching om the outside. Let $\underset{\sim}{v}$ be the basis function $\underset{\sim}{\psi}^{\nu}$ in eq. (4.4) and $\underset{\sim}{u} = \underset{\sim}{u}^i + \underset{\sim}{u}^s$ be represented the series in eq. (4.5) and (4.6). For a traction free surface, $\underset{\sim}{t}_+ = 0$ in the previous uation and $\underset{\sim}{u}_+$ can be represented by the series in eq. (4.7). By substituting all three ies in eq. (4.21), and applying orthogonality conditions to the integral over C_+, one ains directly eq. (4.8) [30].

Similarly, by setting $\underset{\sim}{v}$ in eq. (4.20) equal to $\underset{\sim}{\psi}^{\nu}$, one can derive directly eq. (4.9). e remaining steps of the derivation are the same as those in the previous subsection.

The method of transition matrix has just been applied to calculate the scattering of ne waves by an elliptical cylinder [31]. The calculations are carried out for a cavity well as an elastic inclusion in a different elastic material. Differential cross sections e shown for $k_p a$ up to 4 where a is the semimajor axis of the ellipse and for a/b as high 4, where b is the semiminor axis.

The calculations of the T-matrix involves the inversion of an infinite matrix; the size the truncated matrix becomes very large when the aspect ratio a/b or the normalized fre- ncy ka is large. The case of a crack is the limiting case when $a/b \to \infty$ and so far, no erical results based on this method has been reported.

5. The Geometric Theory of Diffraction

When the wave length of an incident wave is very short in comparison with a characteris- dimension of a scatterer, say the width of a crack, a different method of analysis known the geometric theory of diffraction can be applied. The theory is an extension of the ssical theory of geometric optics [32] which neglects the effect of wave length and assumes t light travels along certain curves, called rays. At the interface of two media, the in- ent ray is bent into a reflected ray and a refracted ray. The intensity, polarization, phase of the light along each ray can then be determined from the law of conservation of ht intensity, and Snell's laws of reflection and refraction.

In the 1950s, Keller [33,34] modified the geometric optics by introducing new rays, led diffracted rays. These new rays account for the appearance of light in shadow zones a scatterer. The theory was applied by him [35] to analyze the diffraction of scalar es and electromagnetic waves by an aperture, the geometry of which is the same as that wn in figure 2. He derived formulas for the wave reflected by the screen and that dif- cted by the edge of the screen, and calculated the angular distribution of amplitude and scattering cross section over a wide range of frequencies. The results are accurate for elengths as large as the aperture dimension.

This geometric theory of diffraction of scalar waves was extended to elastic waves by ende in his Ph.D. thesis in 1963 [36]. The thesis, however, has not been published. The lowing discussion is based on the chapter III of the thesis, and Keller's original papers.

When an incident ray representing a compressional wave (P-wave) hits a plane surface, it reflected as two rays, the reflected P-ray and the reflected S-ray (fig. 3A). However, n the incident P-ray hits an edge of the plane, it produces two families of diffracted s. The infinitely many rays of each family lie on the surface of a cone having as axis tangent to the edge at the point of diffraction. The half-vertex angle of the cone of fraction formed by the P-rays equals the angle between the incident P-ray and the axis the edge; and that formed by the S-rays is larger than the incident angle and is deter- ed by Snell's law for elastic waves (fig. 3B):

$$\frac{\cos\theta_p}{c_p} = \frac{\cos\theta_s}{c_s} \tag{5.1}$$

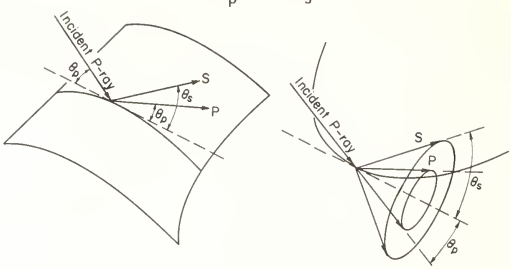

Figure 3. (A) Incident and reflected rays; (B) cones of scattered rays.

When the incident ray is perpendicular to the edge, both half-angles are $\pi/2$ and both cones of diffraction degenerate to a plane orthogonal to the edge.

From a source point P to an observation point Q, the direction of the diffracted ray i determined on the basis of an extended Fermat's principle for edge diffraction: an edge-diffracted ray from P to Q is a curve which has stationary optical length among all curves from P to Q with one point on the edge.

Let $\underset{\sim}{A}\exp[i\omega(s_o/c_p - t)]$ be the incident P-ray at the point of diffraction where $\underset{\sim}{A}$ is th amplitude and s_o is the distance along the incident ray. The vector displacements for the diffracted scattered P-ray, and S-ray are given by

$$\underset{\sim}{u}^d_p = e^{ik_p s_1}[s_1(1 + \frac{s_1}{\rho_1})]^{-1/2}\ \underset{\sim}{D}_p \underset{\sim}{A} e^{ik_p s_o} \tag{5.2}$$

$$\underset{\sim}{u}^d_s = e^{ik_s s_2}[s_2(1 + \frac{s_2}{\rho_2})]^{-1/2}\ \underset{\sim}{D}_s \underset{\sim}{A} e^{ik_p s_o} \tag{5.3}$$

where $k_p = \omega/c_p$ and $k_s = \omega/c_s$, and the time factor $\exp(i\omega t)$ is omitted. In the previous formulas, s_1 and s_2 are the principal radii of curvature of the diffracted wave fronts, or equivalently the distance along the diffracted rays from the points of diffraction to the servation point; ρ_1 and ρ_2 are the distances along the rays from the edge to the other cau tics (the edge is also a caustic) for each family of diffracted rays. For a straight edge ρ_1 is the radius of curvature at the point of diffraction of the curve formed by the inter section of the incident wave front and the plane which contains the incident ray and the edge, and

$$\rho_2 \sin\theta_p \tan\theta_p = \rho_1 \sin\theta_s \tan\theta_s \quad . \tag{5.4}$$

The coefficients $\underset{\sim}{D}_p$ and $\underset{\sim}{D}_s$ in eqs. (5.2) and (5.3) are matrices which relate the diffracted waves to the incident waves. These diffraction matrices only depend upon the dire tions of incidence and diffraction, the wave numbers k_p and k_s, and the geometrical and physical properties of the media at the point of diffraction. They are determined by sol n

ertain simpler "canonical problems" in which only the local geometrical and physical roperties enter. The canonical problem for a crack is the diffraction of P-waves by a raction free half-plane in an infinite medium, which was solved by Maue [37] with the aid of he Wiener-Hopf technique. This and other two dimensional canonical problems are considered n the thesis by Resende. When the incident P-wave is at an arbitrary angle to the half-plane rack, the problem is a three dimensional one and the canonical problem has only been solved ecently [38].

Based on the geometrical theory of diffraction, Rosende solved the problem of the diffraction of a plane compressional wave by a long crack with finite width, and many other roblems. Assume an incident compressional wave propagate at an angle θ_o with the plane of he crack as shown in figure 4. The longitudinal displacement along the direction of propagation is

$$u^i = e^{ik_p(x_1\cos\theta_o + x_2\sin\theta_o)} \quad . \tag{5.5}$$

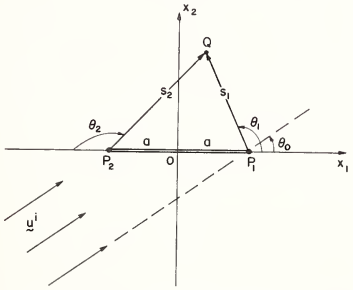

Figure 4. Scattered rays at the edges of a thin crack.

e two points of diffraction on the edges of the crack are $P_1(+a,0)$ and $P_2(-a,0)$, and the int of observation Q is at a distance s_1, angle θ_1 from P_1, and at S_2, θ_2 from P_2. The indent ray is equal to $\exp(ik_p a \cos\theta_o)$ at the point of diffraction P_1, and equal to $p(-ik_p a \cos\theta_o)$ at the point P_2. Let the longitudinal displacement along the diffracted y be denoted by u_s(P-wave), and the transverse displacement in the direction perpendicular the ray by u_θ(S-wave). Since the radii ρ_1 and ρ_2 are infinite, we obtain from eqs. (5.2) d (5.3) that displacements along the ray length s_1 diffracted by P_1 are given by [36]

$$u_{s1}(s_1,\theta_1) = e^{ik_p s_1}\sqrt{1/s_1}\ D_p(\theta_1)e^{ik_p a\cos\theta_o} \tag{5.6}$$

$$u_{\theta 1}(s_1,\theta_1) = e^{ik_s s_1}\sqrt{1/s_1}\ D_s(\theta_1)e^{ik_p a\cos\theta_o} \tag{5.7}$$

d fields diffracted by P_2 along the ray length s_2 are given by

$$u_{s2}(s_2,\theta_2) = e^{ik_p s_2}\sqrt{1/s_2}\ D_p(\theta_2)e^{-ik_p a\cos\theta_o} \tag{5.8}$$

$$u_{\theta 2}(s_2,\theta_2) = e^{ik_s s_2}\sqrt{1/s_2}\ D_s(\theta_2)e^{-ik_p a\cos\theta_o} \quad . \tag{5.9}$$

e cartesian components of the resultant diffracted wave at Q are given by

$$u_1^d(x,y) = u_{s1}\cos\theta_1 + u_{\theta 1}\sin\theta_1 - u_{s2}\cos\theta_2 - u_{\theta 2}\sin\theta_2 \tag{5.10}$$

$$u_2^d(x,y) = u_{s1}\sin\theta_1 - u_{\theta 1}\cos\theta_1 + u_{s2}\sin\theta_2 - u_{\theta 2}\cos\theta_2 \quad . \tag{5.11}$$

The diffraction coefficient $D_p(\theta)$ is given by eq. (15.9) of reference [36], and $D_s(\theta)$ by eq. (15.15) and (15.19) of reference [36]. They are also given in the review article by Achen et al. [39].

So far we have considered only the primary diffraction, that is, the diffraction of the incident wave by each edge. When the waves diffracted by the first edge (+a,o) reaches the second edge (-a,o), it is diffracted again. This process is repeated continuously and is known as the secondary diffraction, which is also discussed in references [36] and [39]. The primarily diffracted field contains the factor $1/\sqrt{\omega}$ and the doubly diffracted field contains the factor $1/\omega$. In general, each time a ray is diffracted by an edge, the corresponding field is reduced by the factor $1/\sqrt{\omega}$.

6. Discussion

In previous sections, we have presented only the analytical aspect of each method. To obtain numerical results from any one of these methods is another task. For the two dimensional problem of diffraction of elastic waves by a crack, results from the solutions of the integral equation have been obtained by Tan [17] and Achenbach, Gautesen and McMaken [39]. The last named three authors also produced numerical results based on the geometric diffraction theory, and the results at high frequencies ($ka \gg 1$) agree very well with the integral equation solution when the secondary diffraction is taken into consideration. Numerical results for a crack based on the method of transition matrix are not yet available.

The theory of geometric diffraction appears to be the easiest to apply if the diffractio coefficients such as $D_p(\theta)$ and $D_s(\theta)$ in eqs. (5.8) - (5.11) are known for a given problem. However the determination of these coefficients depends on the solution for a "canonical problem", and the canonical problems for elastic waves are usually very difficult to solve. Furthermore, whenever the wave field variable is changed, say, from displacement vector $\underset{\sim}{u}$ to stress tensor $\underset{\sim}{\tau}$, a different set of diffraction coefficients must be used. It becomes very inconvenient when this method is applied to calculate tensorial field. As for the accuracy of this method, it has produced accurate results for frequencies as low as $ka = \omega a/c = 2$ in the case of diffraction of acoustic waves. The same limit seems to be valid for the case of elastic waves [39].

To solve an integral equation like that in eq. (3.6) by numerical methods is no longer a difficult task when a large digital computer is readily available. As shown in reference [39], integral equations for certain problems with symmetry can be solved with great precision. However, the solution of each integral equation depends on the incident wave ($\underset{\sim}{t}^i$ in eq. (3.6)), and a new solution must be sought each time the incident wave is changed, either in direction or in magnitude.

The method of transition matrix as outlined in section 4 has the advantage in that the T matrix in eq. (4.14) is independent of the incident wave. The main difficulty in this method is the finding of $\underset{\sim}{Q}^{-1}$, which involves the inversion of an infinite matrix with complex elements. In reference [31], the algorithm developed by Waterman [40] was adopted to calcul diffraction by an elliptical cylinder embedded in a solid. It was found that the matrix inversion became very expensive in computer time when results for large values of ka ($= \omega a/c$ were to be calculated. A general comparison of this method with others when applied to the diffraction of acoustic (scalar) waves by bodies with smooth boundary was reported by Bolome and Wirgin [41].

To conclude this survey, we show in figure 5 an example of differential scattering cros section for the diffraction of SH-waves by a crack of width 2a. The example is taken from a recent report by Weaver and Pao [42]. The problem is mathematically the same as the diffraction of acoustic waves by a weak strip (Neumann's boundary condition on both sides of the strip), or the complementary problem of diffraction of light as a scalar wave by an aper ture. Experimental results of diffraction of acoustic waves by a strip were reported recent by Adler [43].

Analytic solution for this problem has been obtained for low frequencies by solving the scalar version of the integral equation (3.6) [9]. Based on this solution the energy which is proportional to the square of the wave amplitude of the diffracted wave in the direction of $\theta_1 = 38°$ (fig. 4) is calculated and shown in figure 5 in dotted lines. The incident wave is perpendicular to the surface of the crack ($\theta_0 = 90°$ in fig. 4). Numerical solution of the integral equation for higher frequencies is not available. At high frequencies, the analytic solution based on the geometric theory of diffraction can be applied [35]. The calculated energy is shown in dashed lines in figure 5.

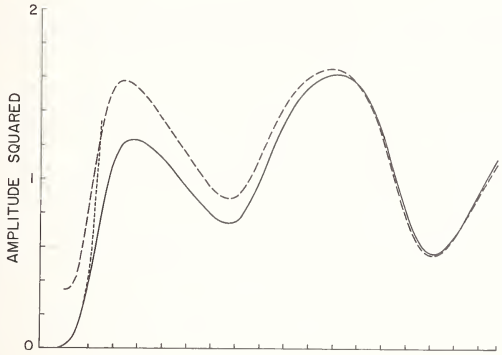

Figure 5. Differential scattering cross sections ($\theta_1 = 38°$; $\theta_0 = 90°$): Dotted lines - low frequency solution of integral equation [9]; dashed lines - geometric theory of diffraction [35]; solid line - transition matrix [42].

A solution based on the method of transition matrix for this problem has been obtained [42] and the result is shown in solid line in figure 5. The result is obtained for a wide range of frequencies ($0 \leq ka < 10$). It agrees exactly with that based on the solution of integral equation at low frequencies, and agrees closely with that based on the geometric theory at high frequencies.

Even in the case of scalar waves, we believe this is perhaps the only example which has been tested by all three methods. Since one sample does not represent the whole, we shall refrain from drawing any conclusion at this stage.

The author acknowledges the support of this research provided by the National Science Foundation through a grant to the College of Engineering (Grant No. ENG77-09222), and a grant to the Materials Science Center of Cornell University.

References

[1] Pao, Y. H. and Mow, C. C., Theory of normal modes and ultrasonic spectral analysis of the scattering of waves in solids, J. Acous. Soc. Amer. 59, 1046 (1976).

[2] Pao, Y. H. and Varatharajulu, V., Huygens' principle, radiation conditions, and integral formulas for the scattering of elastic waves" J. Acous. Soc. Amer. 59, 1361 (1976).

[3] Baker, B. B. and Copson, E. T., The Mathematical Theory of Huygens' Principle (1st ed. 1939, Oxford University Press, London, 1950).

[4] Kupradze, V. D., Dynamical problems in elasticity, in Progress in Solid Mechanics, vol. III, I. N. Sheddon and R. Hill, eds. (North-Holland Publishing Company, N.Y., 1963).

[5] Mal, A. K. and Knopoff, L., Elastic wave velocities in two-component systems, J. Inst. Appl. Math., 3, 376 (1967).

[6] Gubernatis, J. E., Domany, E., Krumhansl, J. A., and Huberman, M., The Born approximation in the theory of the scattering of elastic waves by flaws, J. Appl. Phys. 48, 2812, (1977).

[7] Achenbach, J. D., Wave Propagation in Elastic Solids (North-Holland Publishing Company, New York, 1973).

[8] Rayleigh, L., On the passage of waves through apertures in plane screens, and allied problems, Philisophical Magazine, 43 259, (1897); Scientific Papers, 4, 283 (Cambridge University Press, 1903).

[9] Bouwkamp, C. J., Diffraction theory, Reports on Progress in Physics, 17, 35 (1954).

[10] Hönl, H., Maue, A. W., and Westpfahl, K., Theorie der beugung, in Handbuch der Physics, Band, 25/1, S. Flugge, ed. (Springer Verlag, Berlin, 1961).

[11] Pao, Y. H., and Mow, C. C., Diffraction of Elastic Waves and Dynamic Stress Concentration (Crane and Russak, New York, 1973).

[12] Ang, D. D. and Knopoff, L., Diffraction of vector elastic waves by a finite crack, Proceedings of the National Academy of Sciences, 52, 1075 (1964).

[13] Sih, G. C. and Loeber, J. F., Waves propagation in an elastic solid with a line of discontinuity or finite crack, Quarterly Appl. Math., 27, 193 (1969).

[14] Mal, A. K., Interaction of elastic waves with a Griffith crack, Int'l. J. Eng. Sci., 8, 763 (1970).

[15] Chang, S. J., Diffraction of plane dilational waves by a finite crack, Quarterly J. Mech. and Appl. Math., 24, 423 (1971).

[16] Sih, G. C., Elastodynamic crack problems, Mechanics of Fracture, 4 (Noordhoff International Publishing, Leyden, 1977).

[17] Tan, T. H., Diffraction Theory for Time Harmonic Elastic Waves, Ph.D. Thesis, Technische Hogeschool Delft, Netherlands, (1975); Appl. Sci. Res., 31, 363 (1975); 32, 97 (1976); 33 75 (1977), and 89 (1977).

[18] Hess, J. L., Higher order numerical solution of the integral equation for the two-dimensional Neumann problem Comp. Meth. Appl. Mech. and Eng., 2, 1 (1973).

[19] Harrington, R. F., Field Computation by Moment Methods (Macmillan, New York, 1968).

[20] Harumi, K., Scattering of plane waves by a cavity ribbon in a solid, J. Appl. Phys., 33, 3588 (1962).

[21] Mal, A. K., Diffraction of elastic waves by a penny-shaped crack, Quarterly Appl. Math., 26, 231 (1968).

[22] Mal, A. K., Interaction of elastic wave with a penny-shaped crack, Int. J. Eng. Sci., 8, 381 (1970).

[23] Sih, G. C. and Loeber, J. F., Normal compression and radial shear waves scattering at a penny-shaped crack in an elastic solid, J. Acous. Soc. Amer., 46, 711 (1960).

[24] Waterman, P. C., Matrix theory of elastic wave scattering, J. Acous. Soc. Amer., 60, 567 (1976).

[25] Waterman, P. C., Symmetry, unitarity and geometry in electromagnetic scattering, Physical Review D, 3, 825 (1971).

6] Varatharajulu, V. and Pao, Y. H., Scattering Matrix for Elastic Waves, I. Theory, J. Acous. Soc. Amer., 60, 556 (1976).

7] Waterman, P. C., Matrix theory of elastic wave scattering, J. Acous. Soc. Amer., 60, 567 (1976).

8] Morse, P. M. and Feshbach, H., Methods of Theoretical Physics (McGraw-Hill Book Company, New York, 1953).

9] Waterman, P. C., Matrix theory of elastic wave scattering. II. A new conservation law, J. Acous. Soc. Amer., 63, 1320 (1978).

0] Pao, Y. H., Betti's identity and transition matrix for elastic waves, J. Acous. Soc. Amer. (1978).

1] Varadan, V. V., Scattering matrix for elastic waves, II. Application to elliptic cylinders, J. Acous. Soc. Amer., 63, 1014 (1978).

2] Born, M. and Wolf, E., Principles of Optics (Pergamon Press, New York, Fifth Ed., 1975).

3] Keller, J. B., A geometrical theory of diffraction, in Proc. Symposium on the Calculus of Variations and its Applications, p. 27 (McGraw-Hill Book Co., 1958).

4] Levy, B. R. and Keller, J. B., Diffraction by a smooth object, Comm. Pure and Appl. Math., 12, 159 (1959).

5] Keller, J. B., Diffraction by an aperture, J. Appl. Phys., 28, 426 (1957).

5] Resende, E., Propagation, Reflection and Diffraction of Elastic Waves, Ph.D. Thesis, New York University, (1963).

7] Maue, A. W., Die Beugung elastischer Wellen an der Halbebene, Zeitschrift für Angewandte Mathematick und Mechanik, B. 33, S. 1 (1953).

8] Achenbach, J. D. and Gautesen, A. K., Geometrical theory of diffraction for three-D elastodynamics, J. Acous. Soc. Amer., 61, 413 (1977).

] Achenbach, J. D., Gautesen, A. K., and McMaken, H., Application of elastodynamic ray theory to diffraction by cracks, in IUTAM Symposium on Modern Problems in Elastic Wave Propagation, J. Miklowitz and J. Achenbach, eds. (Wiley and Interscience, New York, 1978).

] Waterman, P. C., Numerical solution of electromagnetic scattering problems, Computer Techniques for Electromagnetics, R. Mittra, ed., 7, 97 (1973).

] Bolomey, J. C. and Wirgin, A., Numerical comparison of the Green's function and the Waterman and Rayleigh theories of scattering from a cylinder and arbitrary cross-section, Proceedings of IEE, 121, (1974).

] Weaver, R. L. and Pao, Y. H., The transition matrix for acoustic waves scattered by a ribbon-shaped crack (in preparation).

] Adler, L. and Lewis, D. K., Diffraction model for ultrasonic frequency analysis and flow characterization, Materials Evaluation, 35, 51 (1977).

ational Bureau of Standards Special Publication 596, Ultrasonic Materials Characterization,
. Berger and M. Linzer, eds., Proceedings of the First International Symposium on Ultrasonic
aterials Characterization held at NBS, Gaithersburg, Md., June 7-9, 1978. Issued
ovember, 1980.

CHARACTERIZATION OF DYNAMIC SHEAR MODULUS IN INHOMOGENEOUS MEDIA USING ULTRASONIC WAVES

Vijay K. Varadan and Vasundara V. Varadan

The Ohio State University
Department of Engineering Mechanics
155 West Woodruff Avenue
Columbus, OH 43210

An inhomogeneous medium containing two linear, elastic phases is still dispersive due to geometric dispersion of waves propagating in such a medium. Results are presently available for the static (low frequency) values of the moduli using self-consistent methods. The model that we will study is a two-dimensional one, namely, a medium containing a random array of infinitely long cylinders of different material. Shear (SH-) waves are assumed to propagate normal to the axis of the cylinders. The wave undergoes multiple scattering between the cylinders and the effective wave number in the medium is complex. An ensemble average of the displacement field will be performed for a random distribution of the scatterers and expressions will be obtained for the average stress and displacement field which are related by the average elastic modulus. The scattering properties of each scatterer will be characterized by the T-matrix which depends on the geometry and nature of the scatterer. The real and imaginary parts of the complex shear modulus are obtained as a function of frequency.

1. Introduction

An inhomogeneous medium containing two linear elastic phases is known to have a complex, frequency dependent propagation constant due to the geometric dispersion of waves by the inhomogeneities. Microscopic as well as continuum theories have been proposed to study the dispersion relation for elastic waves in such a medium. A major advantage of the microscopic theory is that it provides a theoretical framework to discuss in detail the nature and distribution of the inhomogeneities that can be modelled in various approximate ways by adapting the many developments that have taken place in statistical mechanics and physics. In particular, we cite the work of Domany, Gubernatis and Krumhansl [1][1], Korringa [2] and Kröner [3] who have used self-consistent theories and integral equation methods to study the average elastic properties of polycrystalline materials. In references [1-3], the authors have discussed the similarity of the microscopic theory to the multiple scattering formalism of quantum mechanical scattering phenomena. In the continuum approach, such as the effective stiffness theory proposed by Sun, Achenbach and Herrmann [4], the transition from the discrete to the continuous medium is achieved by introducing continuous fields for gross displacements and local deformation. In the microscopic theory, this is achieved by statistical averaging procedures. The aim in both theories is to obtain expressions for the average properties of the continuum in terms of parameters characterizing the size and nature of the inhomogeneities and the frequency of the disturbance propagating in the material.

In this paper, we present a microscopic formalism using the concept of a T-matrix for single scatterers. The idea is not new and has been used extensively in the physics literature. The difference is that the T-matrix we introduce is defined in a special basis namely eigenfunctions of the wave equation. While this immediately leads to an efflorescence of superscripts and subscripts and departs from the neat formalism of integral operators, it

[1] Figures in brackets indicate the literature references at the end of this paper.

also has some advantages. All the theorems that have been developed for the translation and rotation of the eigenfunctions can be incorporated with great advantage and more importantly it provides a convenient set of equations for numerical computations. The dispersion relations that we derive differ from those obtained in reference [4] in that our equations admit complex roots leading to frequency dependent attenuation and velocities for elastic waves.

In order to introduce the concept of an average frequency dependent elastic stiffness tensor, we follow the work of Bedeaux and Mazur [5] who have given a completely rigorous statistical theory for the wave vector and frequency dependent dielectric tensor of a nonpolar fluid of spherically symmetric molecules. Our formalism bears a strong resemblance to what Bedeaux and Mazur [5] call the molecular theories of light scattering and the refractive index where spatial correlations between the molecules are neglected. In the Rayleigh limit we recover a Clausius-Mosotti type formula for the average shear modulus; for higher frequencies we have plotted numerical values of the complex shear modulus as a function of frequency for SH-waves propagating in a medium reinforced with fibers of elliptical cross section.

2. Frequency Dependent Shear Modulus

The model problem that we consider is a linear elastic material containing a random distribution of N infinitely long parallel cylindrical inclusions. The cylinders are assumed to be of arbitrary cross section and are randomly oriented in the plane normal to the axis of the cylinders (the z-axis, see fig. 1). In figure 1, 0_i and 0_j denote the centers of the i-th and j-th inclusions which are referred to a Cartesian coordinate system as shown. The angle of orientation of the j-th inclusion is denoted by α_j. The elastic properties of the inclusions are given by the shear modulus μ_1 and the density ρ_1, while those of the surrounding medium are given by μ and ρ.

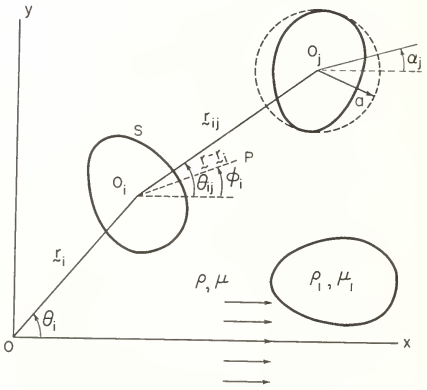

Figure 1. Random distribution and orientation of parallel cylinders.

The basic formalism using the concept of T-matrix and statistical averaging has already been given in references [6,7], and we present only the main features here. Plane harmonic shear waves of frequency ω, wave number k and velocity c_s are incident along the x-axis, and the waves are assumed to be polarized along the axis of the cylinders (SH- waves). In this case the displacement w is parallel to the z-axis and the elastic wave equation reduces to the scalar Helmholtz equation.

The total anti-plane displacement at any point in the medium outside the inclusions is the sum of the incident displacement field and the fields scattered by all the inclusions. This may be written as

$$w(\underline{r}) = w^o(\underline{r}) + \sum_{j=1}^{N} w_j^s(\underline{r} - \underline{r}_j) \tag{1}$$

where $w^o(\underline{r})$ is the incident displacement field and w_j^s is the field scattered by the j-th scatterer to the point of observation $\underline{r}$.

The displacement field that excites or is incident on the i-th scatterer w_i^e is, however, given by

$$w_i^e(\underline{r}) = w^o(\underline{r}) + \sum_{j\neq i}^{N} w_j^s(\underline{r} - \underline{r}_j) \quad ; \quad a < |r - r_i| < 2a \tag{2}$$

where $\underline{r}$ is a point in the vicinity of the i-th scatterer and $\underline{r}_i$ and $\underline{r}_j$ are the position of the i-th and j-th scatterers, respectively. In eq. (2), "a" is the largest dimension of the cross section of the cylinder. In writing the above equation, we have neglected self-polarization effects.

We now expand the exciting and scattered fields in terms of cylindrical basis functions, ψ_n and $Re\psi_n$:

$$w_i^e(\underline{r}) = \sum_{n=-\infty}^{\infty} a_n^i \, Re\psi_n(\underline{r} - \underline{r}_i) \tag{3}$$

$$w_j^s(\underline{r}) = \sum_{n=-\infty}^{\infty} b_n^j \, \psi_n(\underline{r} - \underline{r}_j) \tag{4}$$

where

$$\psi_n = H_n(k|\underline{r} - \underline{r}_i|)\, e^{in\phi_i}$$

$$Re\psi_n = J_n(k|\underline{r} - \underline{r}_i|)\, e^{in\phi_i} \tag{5}$$

In eq. (5), $(|\underline{r} - \underline{r}_i|, \phi_i)$ are plane polar coordinates centered at the i-th scatterer and ϕ_i is the angle that $\underline{r} - \underline{r}_i$ makes with the x-axis.

The coefficients a_n^i and b_n^j are both unknown and one of them can be eliminated by expressing b_n^j in terms of a_n^j and the T-matrix of the j-th scatterer [6,7]. Thus

$$b_n^j = \sum_m T_{nm}^j \, a_m^j \tag{6}$$

Substituting eqs. (3), (4), (5) and (6) in eq. (2), and using the orthogonality of the wavefunctions, we obtain a set of coupled equations for the unknown exciting field coefficients, which is now a function of the orientation angle α_j, the T-matrix (which is a function of the geometry and material properties of each scatterer), and the exact distribution of the inhomogeneities in the medium. We have

$$a_n^i = i^n e^{i\underline{k}\cdot\underline{r}_i} + \sum_{j\neq i}^{N}\sum_{\ell}\sum_{m}(-1)^{n+\ell} e^{i(m-\ell)\alpha_j} T_{\ell m}^j a_m^j \times \psi_{\ell-n}(\underline{r}_i - \underline{r}_j) \tag{7}$$

To cast eq. (7) in a more symmetric form, we define a new propagator between points $\underline{r}_i$ and $\underline{r}_j$ given by

$$\begin{aligned} \phi_n(\underline{r}_i - \underline{r}_j) &= \psi_n(\underline{r}_i - \underline{r}_j) \quad ; \quad \underline{r}_i - \underline{r}_j > 2a \\ &= 0 \quad ; \quad \underline{r}_i - \underline{r}_j < 2a \quad . \end{aligned} \tag{8}$$

Substituting eq. (8) in eq. (7) we obtain

$$a_n^i = i^n e^{i\underline{k}\cdot\underline{r}_i} + \sum_{j\neq i}^{N}\sum_{\ell}\sum_{m}(-1)^{n+\ell} e^{i(m-\ell)\alpha_j} T_{\ell m}^j a_m^j \times \phi_{\ell-n}(\underline{r}_i - \underline{r}_j) \tag{9}$$

Equation (9) is the exact multiple scattering series for the exciting field coefficients. is seen that the first term in eq. (9) is the incident field coefficient a_n^0 in the absence other scatterers. Thus, the iteration of eq. (9) in terms of a_n^0 yields a Born type series for the exciting field. Equation (9) is analogous to the expression for the polarization field in a dielectric medium as given in reference [5], where the T-matrix is analogous to the polarizability and $\phi_m(\underline{r} - \underline{r}_j)$ describes the propagation from point j to i.

The next step is to average over an ensemble of configurations of the positions of the scatterers. The ensemble averaging is fully described in reference [7]. For simplicity, w assume that the scatterers are randomly distributed and oriented and non-overlapping, and make the same approximations for the pair distribution function as in reference [7].

After performing the ensemble average on eq. (9), we assume that the average wave in the effective medium travels as a plane wave with complex wave number K in the direction of incidence; thus this is the coherent wave in the medium. We may write

$$\langle a_n^i \rangle_i = i^n X_n e^{i\underline{k}\cdot\underline{r}_i} \tag{10}$$

where $\langle\ \rangle_i$ denotes an average over the position of all but the i-th scatterer and X_n is the amplitude of the wave. From eqs. (9) and (10), we get a set of coupled equations for the X_n

$$X_n = \frac{2\pi n_o}{k^2 - K^2} \sum_{m} T_{mm} X_m JH_{m-n} \quad . \tag{11}$$

In eq. (11), n_o is the number density of scatterers and JH_{m-n} is an integral involving the pair distribution given by

$$JH_n = 2ka\ J_n(2Ka)\ H_n'(2ka) - 2Ka\ H_n(2ka)\ J_n'(2Ka) \qquad (12)$$

For a non-trivial solution of eq. (10) we require that the determinant of the coefficients of X_n should vanish. This yields an equation for the effective wave number K in terms of the T-matrix of the scatterer. The effective wave number K now is complex and frequency dependent.

Bedeaux and Mazur [5] have obtained expressions for the average dielectric tensor in the medium and Varatharajulu (Varadan) and Vezzetti [8] have shown that for a given statistical model the zeros of the propagator in this model medium yield the average dielectric tensor defined by Bedeaux and Mazur [5]. Extending this discussion to elastic wave propagation, we obtain an expression for the average shear modulus in the medium. The shear stress τ_{rz} is related to the displacement by Hooke's law:

$$\tau_{rz} = \mu(\partial w/\partial r) \qquad (13)$$

The average shear modulus is then given by

$$\langle\mu\rangle = \langle\tau_{rz}\rangle\ /\ \langle\partial w/\partial r\rangle \quad . \qquad (14)$$

The dispersion equation obtained from eq. (11) may be written in the following form

$$K - f(k,T) = 0 \quad . \qquad (15)$$

Defining an average shear modulus $\langle\mu\rangle = \omega^2\langle\rho\rangle K^2$ where $\langle\rho\rangle = c\rho_1 + (1 - c)\rho$ is the average density, we find the effective shear modulus of the composite medium as given by

$$\langle\mu\rangle\ /\mu = (\langle\rho\rangle\ /\rho)\ (k/K)^2 \quad , \qquad (16)$$

where c is the concentration of inclusions. From eqs. (15) and (16), we note that if K is complex and frequency dependent, then $\langle\mu\rangle$ is also complex and frequency dependent. In the Rayleigh or low frequency limit, one can obtain closed form expressions for the effective shear modulus. For higher frequencies, the effective shear modulus can be computed only numerically. Here we show some model calculations for Boron-Aluminum composities in which the fibers are assumed to be elliptical in cross section. In the low-frequency limit, it is sufficient to keep only lower order terms in the expansion of the fields. After some manipulation, we obtain an expression for the effective shear modulus for randomly distributed and oriented eliptical fibers, keeping only the leading terms, and is given by

$$\frac{\langle\mu\rangle}{\mu} = \frac{1 - c_1 T_{11}}{1 + c_1 T_{11}} \quad , \qquad (17)$$

where

$$T_{11} = \frac{1}{4}\,\frac{(1 - m^2)(1 + \frac{b}{a})^2}{(\frac{b}{a} + m)\ (m\,\frac{b}{a} + 1)} \quad , \qquad (18)$$

and $c_1 = \pi abn_0$ is the concentration of elliptical fibers. In eq. (18), $m = \mu_1/\mu$ and a and b are the semi-major and minor axes of the elliptical fibers, respectively. The results given by (17) agree with those obtained by other methods. By taking the limit of $b/a \to 0$ and setting $m = 0$, we obtain the effective shear modulus of a medium containing a random distribution of cracks with random orientation. The result is of the following form:

$$\langle\mu\rangle\ /\mu = (1 - \pi a^2 n_0/4)/(1 + \pi a^2 n_0/4) \quad , \qquad (19)$$

where 2a is the length of a crack and n_0 is its number density.

Equation (17) is exactly similar to the Clausius-Mosotti formula for the refractive index in a medium of point particles whose polarizability is T and whose number density is n_0. Thus eq. (16) is a generalization of this formula that allows the polarizability described by T to be dispersive whereas in the Rayleigh limit, the polarizability is independent of frequency.

For higher frequencies, we keep higher order terms in the expansion of fields as done in references [6,7] and the resulting effective shear moduli are computed numerically. In references [6,7] we have found the values of K as a function of frequency for a medium containing parallel fibers of elliptic cross section that are aligned at arbitrary angles with respect to the direction of coherent wave propagation. In this paper, we have averaged over all orientations of the ellipse by integrating over all possible orientation angles. From the dispersion relation thus obtained we have calculated the complex shear modulus of the average medium using eq. (16).

Figures 2-5 are plots of the real and imaginary parts of the shear modulus as a function of ka for two different values of the concentration of fibers namely 0.5 and 0.7. The density ratio ρ_1/ρ and the shear modulus ratio μ_1/μ are taken as 0.93 and 6.46, respectively. Each set of plots is for two values of the aspect ratio b/a of the elliptic fibers. The imaginary part of the shear modulus is negative since we expect damping of a propagating wave due to geometric dispersion. There is an appreciable difference between the average shear modulus for different aspect ratios at a given concentration. This may merit some consideration in the design and manufacture of fiber reinforced composites. The model as presented here can be improved by including the effects of correlations between the fibers.

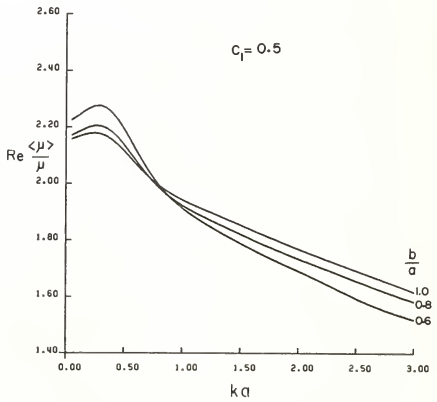

Figure 2. Real part of the average shear modulus as a function of ka for concentration c_1 = 0.5.

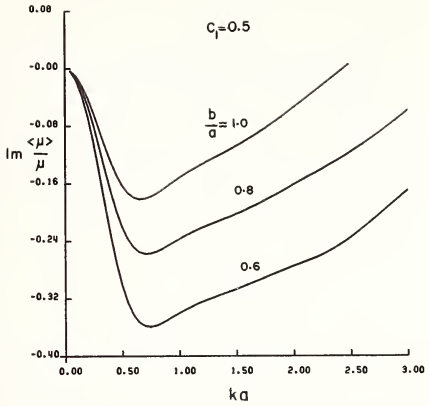

Figure 3. Imaginary part of the average shear modulus as a function of ka for concentration $c_1 = 0.5$.

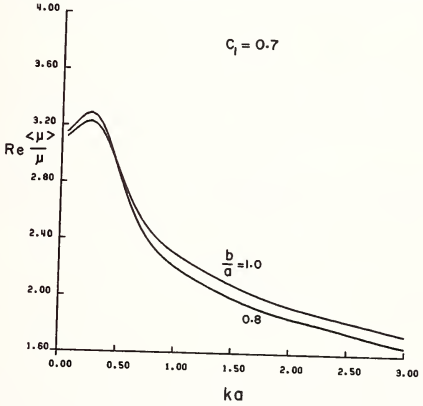

Figure 4. Real part of the average shear modulus as a function of ka for concentration $c_1 = 0.7$.

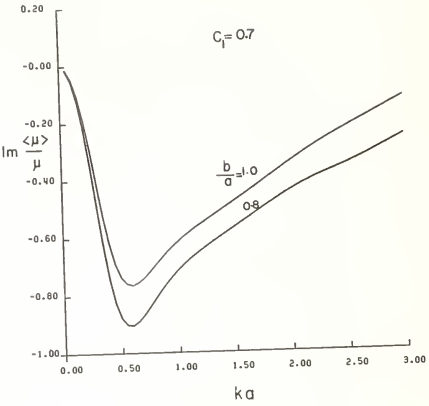

Figure 5. Imaginary part of the average shear modulus as a function of ka for concentration $c_1 = 0.7$.

Computer resources were provided by the Instruction and Research Computer Center of The Ohio State University.

References

[1] Domany, E., Gubernatis, J. E., and Krumhansl, J. A., The elasticity of polycrystals and rocks, Materials Science Center Report, Cornell University, New York (1974).

[2] Korringa, J., Theory of elastic constants of heterogeneous media, J. Math. Phys., 4, 509 (1973).

[3] Kröner, E., Elastic moduli of perfectly disordered composite materials, J. Mech. Phys. Solids, 15, 319 (1967).

[4] Sun, C. T., Achenbach, J. D., and Herrmann, G., Continuum theory for a laminated medium, J. Appl. Mech., 38, 477 (1971).

[5] Bedeaux, D., and Mazur, P., On the critical behavior of the dielectric constant for a nonpolar fluid, Physica, 67, 23 (1973).

[6] Varadan, V. K., Varadan, V. V., and Pao, Y. H., Multiple scattering of elastic waves by cylinders of arbitrary cross section · I-SH-waves, J. Acoust. Soc. Amer. (in press).

[7] Varadan, V. K., and Varadan, V. V., Frequency dependence of elastic (SH-) wave velocity and attenuation in anisotropic two phase media, Int. J. Wave Motion (in press).

[8] Varatharajulu (Varadan), V. V., and Vezzetti, D. J., Approach of the statistical theory of light scattering to the phenomenological theory, J. Math. Phys., 17, 232 (1976).

ational Bureau of Standards Special Publication 596, Ultrasonic Materials Characterization, . Berger and M. Linzer, eds., Proceedings of the First International Symposium on Ultrasonic laterials Characterization held at NBS, Gaithersburg, Md., June 7-9, 1978. Issued lovember, 1980.

CRACK IDENTIFICATION AND CHARACTERIZATION IN LONG WAVELENGTH ELASTIC WAVE SCATTERING

J. E. Gubernatis

Theoretical Division
University of California
Los Alamos Scientific Laboratory
Los Alamos, NM 87545

and

E. Domany

Department of Physics
University of Washington
Seattle, WA 98195

We discuss apparent characteristic features of Rayleigh scattering of elastic waves from cracks. Interpreting these features, we suggest a procedure that in some experimental situations may be useful to distinguish generally-shaped cracks from volume defects and to determine for elliptically-shaped cracks the orientation, shape, and size.

1. Introduction

Cracks can cause significant changes in the mechanical behavior of materials, the most ramatic change being the possibility of fracture. Nondestructive detection of cracks, specially cracks critical to fracture, often utilizes ultrasonic techniques in which an lastic wave propagates through the material and is scattered by the crack. From features of he scattering, the detection and characterization of the crack is attempted. Clearly, in hese important experiments the dominant physical process to be understood is the scattering f the elastic wave by a single crack. In this respect, a simple model problem is that of an lliptical or circular "soft" crack embedded in an infinite, homogeneous isotropic medium.

Recently, several investigators [1-5][1] independently considered theoretical studies of his problem for the limiting case when the wavelength of the elastic wave is considerably arger than the crack. In this quasi-static (Rayleigh) limit, the exact form of the scattered ields can be obtained.

In this paper we continue the spirit, but extend the analysis, of these investigations. ur approach is to start with a volume integral formulation of the scattering [8,9] for which everal useful approximations exist [9-12]. The approximation used here is identical to the uasi-static result derived by Datta [3]. Our purpose is to illustrate in the context of this pproximation apparent characteristic features of elastic wave scattering from cracks, to interpret these results and to discuss experimental procedures that may be useful for their detection and characterization.

More explicitly, we first identify scattering signatures which distinguish cracks of general shape from volume defects (voids and inclusions). Then, we specialize our study to lliptical cracks and propose scattering signatures which allow the determination of the crack rientation, size, and shape. Also the applicability of measuring these signatures in ealistic nondestructive testing situations is assessed.

[1] Figures in brackets indicate the literature references at the end of this paper.

2. Basic Equations

The basic scattering picture is depicted in figure 1. An arbitrarily shaped cavity wit a surface S bounding a region R is embedded in an infinite, homogeneous, elastically isotrop medium. The incident power is directed along the positive z-axis and is monochromatic with angular frequency ω. The unit vector $\hat{r}$ determines the direction of observation of the scattered power relative to some suitably chosen Cartesian coordinate system.

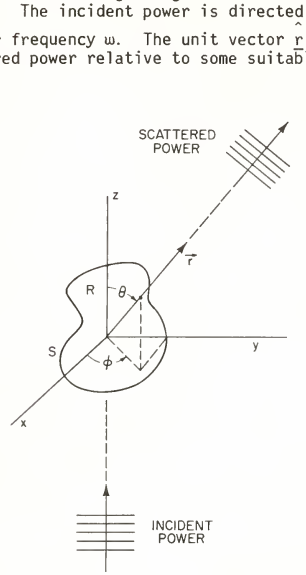

Figure 1. A typical scattering geometry. For purposes of illustration the incident power is along the positive z-axis.

The scattering effectiveness of this cavity is measured by the differential cross secti which is essentially the time average of the fraction of incident power scattered into a particular direction. For incident power associated with a displacement field (omitting exp (-iωt))

$$u_i^0 = a_i e^{i\underline{\alpha}^0 \cdot \underline{r}} + b_i e^{i\underline{\beta}^0 \cdot \underline{r}} \tag{1}$$

where α and β are the wavenumbers of the longitudinal and transverse made with a_i and b_i, th corresponding vector polarization amplitudes, and $\underline{\alpha}^0 = \alpha\hat{\underline{a}}$ and $\underline{\beta}^0 = \beta\hat{\underline{a}}$, the incident wave-vectors. The differential cross section is found [8] to be given by

$$\frac{dP(\omega)}{d\Omega} = \frac{\alpha(\lambda+2\mu)\ |A_i|^2 + \beta\mu|B_i|^2}{\alpha(\lambda+2\mu)\ |a_i|^2 + \beta\mu\ |b_i|2} \tag{2}$$

with λ and μ the Lamé parameters of the medium hosting the cavity, dΩ a differential element of solid angle, and A_i and B_i the vector amplitudes of the displacement field associated wit the scattered (far-field) power:

$$u_i^0 \sim A_i \frac{e^{i\alpha r}}{r} + B_i \frac{e^{i\beta r}}{r} . \tag{3}$$

The scattered amplitudes are related to a quantity called the f-vector [8]

$$A_i = \hat{r}_i \hat{r}_j f_j(\underline{\alpha}) \tag{4a}$$

nd

$$B_i = (\delta_{ij} - \hat{r}_i \hat{r}_j) f_j(\underline{\beta}) \tag{4b}$$

here summation over repeated indices is implied (as throughout the rest of the paper), $\hat{r}$ is he unit vector in the scattered (observation) direction, and $\underline{\alpha} = \alpha\hat{r}$ and $\underline{\beta} = \beta\hat{r}$. For a void he explicit form of the f-vector is

$$f_i(\underline{k}) = \frac{-K^2}{4\pi\rho\omega^2} \left[\rho\omega^2 \int_R dV u_i e^{-i\underline{k}\cdot\underline{r}} + ikC_{ijk\ell}\hat{r}_j \int_R dV \varepsilon_{k\ell} e^{-i\underline{k}\cdot\underline{r}} \right] \tag{5}$$

here $C_{ijk\ell} = \lambda\delta_{ij}\delta_{k\ell} + \mu(\delta_{i\ell}\delta_{jk} + \delta_{ik}\delta_{j\ell})$.

One of our objectives is to apply eq. (5) to the long wave scattering from a crack. To ndicate the nature of our approximation, we write

$$f_i(\underline{k}) \equiv f_i \left[u_i e^{-i\underline{k}\cdot\underline{r}} \; ; \; \varepsilon_{k\ell} e^{-i\underline{k}\cdot\underline{r}} \right] \tag{6}$$

o symbolize that in eq. (5) there are two independent integrations, one with $u_i \exp(-i\underline{k}\cdot\underline{r})$ n the integrand and the other with $\varepsilon_{k\ell}\exp(-i\underline{k}\cdot\underline{r})$; that is,

$$f_i[x_i; y_k] = \frac{k^2}{4\pi\rho\omega^2} \left[\rho\omega^2 \int_R dV x_i + ikC_{ijk\ell}\hat{r}_j \int_R dV y_{k\ell} \right] . \tag{7}$$

specific choice of these fields will produce the exact $f_i(\underline{k})$. Our approximation is based on ubstituting known fields for x_i and $y_{k\ell}$, and as choices for these fields, we consider first a tatic problem of a cavity embedded in a medium that has a uniform stress σ^0_{ij} as $R \to \infty$. The esulting strain field can be written as

$$\varepsilon^{\sigma}_{ij} = e^0_{ij} + \int_R dV \, G^{(0)}_{ijk\ell} \, C_{k\ell mn} \, \varepsilon^{\sigma}_{mn} \tag{8}$$

here e^0_{ij} is the strain field associated with σ^0_{ij} in the defect-free medium, $G^{(0)}_{ijk\ell}$ is the tatic Green's function [13,14] and $\varepsilon^{\sigma}_{ij}$ is a fictitious field defined in the cavity. For llipsoidal cavities $\varepsilon^{\sigma}_{ij}$ was calculated by Eshelby [7]. It is exactly this static field used approximate solution. Returning now to the scattering problem, we note that for an ncident wave of the form

$$u^0_i = u^{\sigma}_i e^{i\underline{k}^0\cdot\underline{r}} \tag{9}$$

he associated strain field is

$$\varepsilon^0_{ij} = e^0_{ij} e^{i\underline{k}^0\cdot\underline{r}}$$

here

$$e^0_{ij} = i\left(u^{\sigma}_i k^0_j + u^{\sigma}_k k^0_i\right)\Big/2 \; . \tag{10}$$

th e^0_{ij} as a static, uniform strain, the tensor $\varepsilon^{\sigma}_{ij}$ (associated with the corresponding static oblem) is defined. When f^{QS}_i is used in eq. (4), the approximation

$$f_i^{QS} = f_i \left[u_i^\sigma \; ; \; \varepsilon_{k\ell}^\sigma \right] \tag{11}$$

can be shown [3,11,12] to produce the scattered amplitudes exactly to the leading order in ω (which is ω^2). Equation (10) is called the quasi-static approximation [11]; it gives the Rayleigh limit to the scattering.

For ellipsoidal cavities, the ε_{ij}^σ needed in eqs. (8) and (11) is given by Eshelby; furthermore, ε_{ij}^σ is itself a uniform (constant) strain. For an ellipsoid, eq. (5) becomes

$$f_i^{QS}(\underline{k}) = \frac{-Vk^2}{4\pi\rho\omega^2} \left[\rho\omega^2 u_i^\sigma + ikC_{ijk\ell} \hat{r}_j \varepsilon_{k\ell}^\sigma \right] \tag{12}$$

where V is the volume of the cavity. ε_{ij}^σ is related to e_{ij}^0 by

$$\varepsilon_{ij}^\sigma = [(I-S)^{-1}]_{ijk\ell} \, e_{k\ell}^0 \equiv \Gamma_{ijk\ell} \, e_{k\ell}^0$$

where I is the identity fourth rank tensor and the fourth rank tensor S is calculated by Eshelby [7].

To obtain results for an elliptical crack, we first consider an ellipsoid with principal axes a > b > c, and then take the following limits:

$$\lim_{c\to 0} V = 0$$

$$\lim_{c\to 0} V\Gamma_{ijk\ell} \equiv \gamma_{ijk\ell} \, .$$

More explicitly, if a and b are along the x- and y- directions, we find

$$\gamma_{3311} = \gamma_{3322} = \frac{4\pi a^3}{3} \frac{2(1-\nu)\kappa_1^2}{E(\kappa)(1-2\nu)} \tag{13a}$$

$$\gamma_{3333} = \frac{1-\nu}{\nu} \gamma_{3311} \tag{13b}$$

$$\gamma_{2323} = \frac{2\pi a^3 \kappa_1^2}{3} \left[\frac{E(\kappa)}{1-\nu} - \frac{\kappa_1^2 [F(\kappa)-E(\kappa)]}{\kappa^2(1-\nu)} \right]^{-1} \tag{13c}$$

$$\gamma_{1313} = \frac{2\pi a^3 \kappa_1^2}{3} \left[E(\kappa) + \frac{\kappa_1^2 [F(\kappa)-E(\kappa)]}{\kappa^2(1-\nu)} \right]^{-1} \tag{13d}$$

where ν is Poisson's ratio [$\nu=\gamma/2(\gamma+\mu)$] and $F(\kappa)$ and $E(\kappa)$ are complete elliptic integrals of the first and second kind with $\kappa = (1 - b^2/a^2)^{\frac{1}{2}}$ and $\kappa_1^2 = 1 - \kappa^2$. The corresponding expressions for a circular crack of radius a are

$$\gamma_{3311} = \gamma_{3322} = \frac{16a^3}{3} \frac{\nu(1-\nu)}{1-2\nu} \tag{14a}$$

$$\gamma_{3333} = \frac{(1-\nu)}{\nu} \gamma_{3311} \tag{14b}$$

$$\gamma_{2323} = \gamma_{1313} = \frac{8a^3}{3} \frac{(1-\nu)}{(2-\nu)} \quad . \tag{14c}$$

or both elliptical and circular cracks $\gamma_{ijk\ell} = \gamma_{jik\ell} = \gamma_{ij\ell k}$. Terms that cannot be obtained rom eq. (13) by these interchanges of indices are zero. We note that $\gamma_{ijk\ell}$, and hence the cattered fields, are proportional to $4\pi a^3/3$, the volume of the smallest sphere that can ncircle the crack independent of b. We note that

$$\gamma_{3311}/\gamma_{1313} + \gamma_{3311}/\gamma_{2323} = 2(2 - \nu)/(1 - 2\nu) \tag{15}$$

nd hence that only two of the $\gamma_{ijk\ell}$ are independent.

3. Results

In this section, we address the problem of flaw characterization in two stages. First, everal features are found that distinguish cracks from volume defects, including one valid or arbitrarily-shaped (not necessarily planar) cracks. Second, for the special case of lliptical cracks, we discuss procedures for determining crack orientation, size, and shape. he applicability of these procedures to realistic nondestructive testing situations is also ssessed.

4. Crack Identification

In the quasi-static limit the f-vector for scattering from a cavity has form [1]

$$f_i = VP u_i^{\sigma} + Q_{ij} \hat{r}_j \tag{16}$$

here

$$P = - k^2/4\pi \tag{17a}$$

nd

$$Q_{ij} = \frac{-ik^3}{4\pi\rho\omega^2} C_{ijk\ell} \int_R d\underline{r}\, \varepsilon_{k\ell}^{\sigma}(\underline{r}) \quad . \tag{17b}$$

lternately, Q_{ij} can be obtained using the surface integral formulation of the problem. With crack regarded as the limiting case of the volume $V \to 0$,

ith

$$f_i = Q_{ij}^{*} \hat{r}_j$$

$$Q_{ij}^{*} = \lim_{V \to 0} Q_{ij} \, .$$

ut as seen from eq. (17b) the tensor Q_{ij}, and hence Q_{ij}^{*}, depends only on the incident ield and not on the scattered direction $\underline{r}$. Thus, from (4a) the magnitude of the ongitudinal field is

$$A_i \hat{r}_i = f_i \hat{r}_i = Q_{ij}^{*} \hat{r}_i \hat{r}_j$$

which is invariant under the replacement of $\hat{r}$ by $-\hat{r}$. Physically, for any incident direction this means the scattering in any two diametrically opposite directions is identical (fig. 2). This general result is valid only for cracks since the first term in eq. (16) is nonzero for all cavities (and more generally for all inclusions). Consequently, if the measured scattered fields are equal at any two diametrically opposite points, the defect must be a crack. A similar analysis can be made for the amplitude of the transverse scattered fields with the identical conclusion.

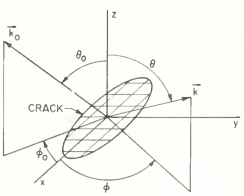

Figure 2. The coordinate system defining the incident angles θ_0 and ϕ_0 and the scattered angles θ and ϕ relative to the crack orientation.

Considering the special case of elliptical cracks, we can find other scattering signatures of cracks. Below we give for an incident longitudinal plane wave the Rayleigh limit scattered amplitudes and explicitly illustrate these signatures. In our equations, $\gamma^{(0)} = \gamma_{3311}$, $\gamma^{(1)} = \gamma_{1313}$ and $\gamma^{(2)} = \gamma_{2323}$; the incident direction $\hat{a}$ is characterized by the angles θ_0 and ϕ_0; and the scattered direction $\hat{r}$, by θ and ϕ. All angles are defined in a coordinate system fixed by the principal axes of the crack and by $\hat{n}$, and the semi-major axis a and semi-minor axis b are in the x- and y- directions while $\hat{n}$ is in the z-direction (fig. 3).

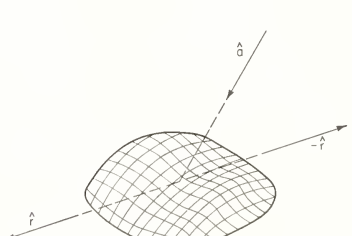

Figure 3. An invariance property of Rayleigh scattering from cracks. For an incident direction $\hat{a}$ the scattering in the direction $\hat{r}$ is equal to the scattering in the direction $-\hat{r}$.

For a longitudinal wave incident in an arbitrary direction,

$$\underline{0}^{\sigma} = \cos\phi_0 \sin\theta_0 \hat{\underline{x}} + \sin\phi_0 \sin\theta_0 \hat{\underline{y}} + \cos\theta_0 \hat{\underline{z}}$$

and

$$\underline{\alpha}^{0} = \alpha\, \hat{\underline{u}}^{\sigma} ,$$

the scattered longitudinal (L) and transverse (T) displacement fields are

$$A_i = \hat{r}_i \frac{\alpha 2}{4\pi} \frac{\nu}{1-\nu} \left\{ \gamma^{(0)} \left[1 + \frac{(1-2\nu)}{\nu} \cos^2 \theta \right] \right. \tag{18a}$$

$$\times \left[1 + \frac{(1-2\nu)}{\nu} \cos^2 \theta_0 \right] + \frac{(1-2\nu)}{2} \left[\gamma^{(1)} \cos \phi \cos \phi_0 \right.$$

$$\left. \left. + \gamma^{(2)} \sin \phi \sin \phi_0 \right] \sin 2\theta \sin 2\theta_0 \right\}$$

$$B_i = \frac{\alpha\beta}{4\pi} \left(\hat{\theta}_i \left\{ -\gamma^{(0)} \left[1 + \frac{(1-2\nu)}{\nu} \cos^2 \theta_0 \sin \right] 2\theta \right. \right. \tag{18b}$$

$$\left. + \sin 2\theta_0 \cos 2\theta \left[\gamma^{(1)} \cos \phi \cos \phi_0 + \gamma^{(2)} \sin \phi \sin \phi_0 \right] \right\}$$

$$\left. - \hat{\phi}_i \sin 2\theta_0 \cos \theta \left[\gamma^{(1)} \sin \phi \cos \phi_0 - \gamma^{(2)} \cos \phi \sin \phi_0 \right] \right)$$

where $\hat{\theta}$ and $\hat{\phi}$ are unit vectors in the θ and ϕ directions. By inspecting these equations, we found three additional crack identifiers: One, if both the incident and scattered directions are anywhere in the crack plane ($\theta = \theta_0 = 90°$), then the magnitudes of the scattered fields, and hence the cross sections, are constants:

$$A = \alpha^2 \nu \gamma^{(0)}/4\pi(1-\nu) \quad . \tag{19a}$$

$$B = 0 \quad . \tag{19b}$$

Thus, the plane of the crack is a "plane of constant scattering". Furthermore, the existence of such a plane is a special property of elliptical cracks and is useful not only to distinguish these from volume defects, but also to determine the crack plane orientation, $\hat{n}$. (See below.)

Two, for normal incidence and for incidence along the crack edge ($\theta_0 = 0°$ and $90°$), the angular distribution of scattered L waves (and similarly for scattered T waves) is identical and also independent of ϕ_0 and ϕ, that is,

$$A \propto 1 + \frac{(1-2\nu)}{\nu} \cos^2 \theta \tag{20a}$$

$$B \propto |\sin 2\theta| \tag{20b}$$

Three, as seen from eq. (20), the scattering for normal incidence has a twofold symmetry about $\theta = 90°$ (i.e., the crack plane). This feature is also absent in the scattering from volume defects. (From eq. (4) and eq. (12) it can be demonstrated that the ρ contribution gives rise to an additional $\cos\theta$ dependence for L waves and a $\sin\theta$ dependence for T waves.)

Thus, to leading order in ω, the scattered power has a higher symmetry than the scatterer; furthermore, there are simple, measurable, qualitative features of the scattering that not only distinguish an elliptical crack from volume defects, but also determine the crack plane orientation.

5. Crack Characterization

Maintaining our specialization to elliptical cracks, we now discuss features that characterize the crack. This characterization consists of the determination of the orientation, size, and shape.

Our first task is to determine the orientation of the crack plane. For elliptical cracks this task can be accomplished concurrently with the task of differentiating cracks from ellipsoidal defects. For example, the plane of constant scattering is coincident with the crack plane.

The more difficult task is to determine the orientation within this plane of the crack major axis. Knowing the crack plane allows us to specify θ and θ_0 in (16). To complete the specification of the crack orientation one must utilize the ϕ-dependence of the scattering. By inspecting eq. (18) one sees that the relative magnitude of the ϕ-dependent terms is maximized when $\theta = \theta_0 = 45°$. In that case, for a pulse-echo experiment ($\phi = \phi_0$), the scattered longitudinal amplitude is, for example,

$$A_i \hat{r}_i = p + q \cos^2 \phi \tag{21a}$$

where

$$p = \frac{\alpha^2}{16\pi(1-\nu)} \left[2\nu\gamma^{(0)} + (1 - 2\nu)\gamma^{(2)} \right] \tag{21b}$$

$$q = \frac{\alpha^2}{16\pi(1-\nu)} (1-2\nu) [\gamma^{(1)} - \gamma^{(2)}] \quad . \tag{21c}$$

Since p, q > 0, the maxima of the backscattered power (at $\phi = 0°$ or $180°$) locate the direction of the major axis. However, the ϕ dependence is proportional to $\gamma^{(1)} - \gamma^{(2)}$, which (fig. 4) may be too small to measure for all b/a ratios. Consequently, the orientation of the major axis may be hard to determine experimentally. Physically, in the Rayleigh limit, scattering by an elliptical crack is similar to scattering by a circular crack.

This discussion bears directly on the last task characterizing the crack, the determination of a and b/a. In principle, knowledge of any two of $[\gamma^{(0)}, \gamma^{(1)}, \gamma^{(2)}]$ is sufficient to uniquely determine a and b/a. However, figures 4 and 5 reveal that $\gamma^{(1)} - \gamma^{(2)}$ and p/(p+q), the ratio of the minimum to maximum value of eq. (21a), depend very weakly on b/a; as such, experimental determination of b/a may be difficult. For example, from figure 5, the value of b/a would be determined by exact measurement of p/(p+q). Then, with figure 4, knowledge of $\gamma^{(0)}$ determines a. However, from figure 5 one sees that the variation from b/a = 0 (needle-shaped crack) to b/a = 1 (circular crack) results at best in a 10 percent change in p/(p+q). Thus, it seems that the Rayleigh limit cannot be used effectively to determine b/a (or the orientation of the crack major axis). One can, though, estimate the crack length, a, provided some assumption concerning the range of b/a values is taken. If $x_0 < b/a < 1$ and a specific value $\gamma^{(0)}$ is obtained from measurement then

$$[\gamma^{(0)}/\gamma^{(0)}(1)]^{1/3} < a < [\gamma^{(0)}/\gamma^{(0)}(x_0)]^{1/3} \tag{22}$$

where

$$\gamma^{(0)}(x) = \gamma^{(0)}(b/a).$$

A similar analysis with the same conclusions can be made for incident shear waves. We discuss this elsewhere [15].

6. Conclusions

In contrast to long wavelength scattering of acoustic or quantum mechanical waves, which are isotropic with little information about the scatterer, the scattering of elastic waves, in

ıddition to an isotropic component, possesses dipolar and quadrapolar components with mportant information about the scatterer [1]. We examined the angular content for the cattering from cracks and, after examining this content, identified features that may be ıseful in crack characterization experiments.

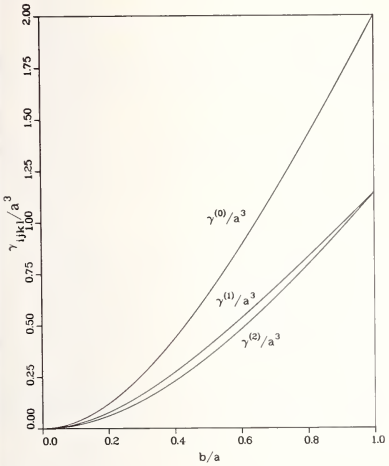

Figure 4. Curves of $\gamma^{(0)}$, $\gamma^{(1)}$, and $\gamma^{(2)}$ as a function of b/a. The $\gamma^{(0)}$, $\gamma^{(1)}$, and $\gamma^{(2)}$ have units of volume with the unit of length the same as a and b. $\nu = 1/4$.

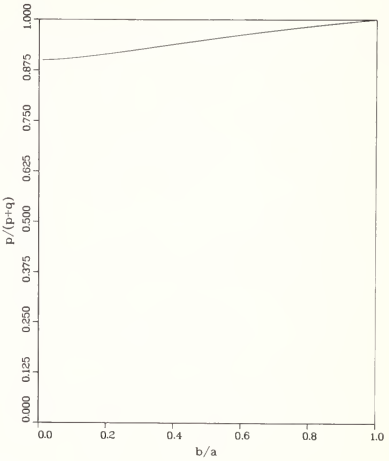

Figure 5. A measure of the sensitivity of the scattering from an elliptical crack to its shape, b/a. $\nu = 1/4$.

With great generality, we found that for any angle of incidence the Rayleigh scattering rom any crack, in contrast to the scattering from volume defects, is identical in any two liametrically opposite directions. This feature identifies the defect as a crack, but does ıot characterize the crack as to its size, shape and orientation. Additional identifying eatures, as well as a characterizing procedure, were specified for an elliptical crack. In his case, we found that it is in principle possible to characterize the crack uniquely. In ıractice, because of certain shape insensitive parameters, we believe the crack may appear ircular, and possibly the best one can do is to measure the crack plane orientation and ounds for the crack length a.

This work received support from the Center for Advanced Nondestructive Evaluation Science Center, Rockwell International). One of us (J. E. Gubernatis) also received support rom the United States Department of Energy.

References

[1] Gubernatis, J. E., Krumhansl, J. A., and Thomson, R. M., Interpretation of elastic wave scattering theory for analysis and design of flaw characterization experiments: the long wavelength limit, Los Alamos Scientific Laboratory Report LA-UR-76-2546, submitted to J. Appl. Phys.

[2] Domany, E., Krumhansl, J. A., and Teitel, S., Quasi-static approximation to the scatteri of elastic waves by a circular crack, J. Appl. Phys., 49, 2599 (1977).

[3] Datta, S. K., Diffraction of plane elastic waves by ellipsoidal inclusions, J. Acoustic. Soc. Am., 61, 1432 (1977).

[4] Kohn, W. and Rice, J. R., Scattering of long wavelength elastic waves from localized defects in solids, submitted to J. Appl. Phys.

[5] Budiansky, B. and Rice, J. R., On the estimation of a crack fracture parameter by long wavelength scattering, unpublished.

[6] Kraut, E. A., Review of theories of scattering of elastic waves by cracks, IEEE Trans. Sonics Ultrason., SU-23, 162 (1976).

[7] Eshelby, J. D., The determination of the elastic field of an ellipsoidal inclusion and related problems, Proc. Roy. Soc. London, 271, 376 (1957).

[8] Gubernatis, J. E., Domany, E., and Krumhansl, J. A., Formal aspects of the theory of the scattering of ultrasound by flaws in materials, J. Appl. Phys., 48, 2804 (1977).

[9] Gubernatis, J. E., Domany, E., Krumhansl, J. A., and Huberman, M., Theory of the scattering of ultrasound by flaws, in 1975 Ultrasonics Symposium Proceedings, J. deKlerk ed., p. 107 (IEEE, New York, 1975).

[10] Gubernatis, J. E., Domany, E., Huberman, M., and Krumhansl, J. A., The fundamental theor of elastic wave scattering by defects in elastic materials: integral equation methods for application to ultrasonic flaw detection, Materials Science Center Report 2654, (Cornell University, 1975).

[11] Gubernatis, J. E., Long wave approximations for the scattering of elastic waves from flaws, Los Alamos Scientific Laboratory Report LA-UR-77-2900, submitted to J. Appl. Phys

[12] Gubernatis, J. E., The scattering of long wavelength elastic waves from ellipsoidal voi and inclusions, unpublished.

[13] Gubernatis, J. E., Domany, E., and Krumhansl, J. A., The elasticity of polycrystals and rocks, J. Geo. Res., 80, 4851 (1975).

[14] Gubernatis, J. E. and Domany, Macroscopic engineering properties of polycrystalline materials: elastic properties, J. Appl. Phys., 46, 1875 (1975).

[15] Gubernatis, J. E. and Domany, E., Rayleigh scattering of elastic waves from cracks, unpublished.

National Bureau of Standards Special Publication 596, Ultrasonic Materials Characterization, H. Berger and M. Linzer, eds., Proceedings of the First International Symposium on Ultrasonic Materials Characterization held at NBS, Gaithersburg, Md., June 7-9, 1978. Issued November, 1980.

A NEW METHOD FOR CALCULATING ELASTIC WAVE SCATTERING BY A FLAW

William M. Visscher

Theoretical Division, Los Alamos Scientific Laboratory
P. O. Box 1663
Los Alamos, NM 87545

The displacement vector is expanded in orthogonal functions which satisfy the equations of motion for the elastic medium. The coefficients in the expansion are determined by the requirement that the square of the deviance from the boundary conditions, integrated over the surface of the flaw, be a minimum. This leads to a set of linear equations for the coefficients. A program has been written which computes direct and mode-converted scattering from axially symmetric rigid obstacles and voids. Examples are exhibited, including direct and mode-converted scattering from spheres, oblate and prolate spheroids, cones, and pillboxes, with ka varying from .01 to 10, and aspect ratios up to 7. It is concluded that this is an efficient and practical method for calculating elastic-wave scattering.

1. Introduction

In order to display the simplicity of the method we propose, we will describe its application to a special case, and remark later about potential generalizations. The special case is the computation of elastic wave scattering from a flaw, either a void or an immovable rigid inclusion in a homogeneous isotropic medium. Illustrated in figure 1 is the geometry, showing a conical flaw. The method is easiest to apply to axially symmetric shapes such as this, although there is no restriction in principle to figures of revolution.

As shown in figure 1, we will use spherical coordinates with the origin inside the flaw (usually at the centroid). The physical situation is that a plane wave with wave vector k_0 (polar angles θ_0, ϕ_0) is incident, and is scattered, giving rise to asymptotically spherical outgoing waves with wave number k at an angle of observation θ, ϕ.

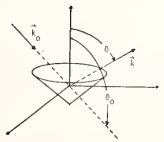

Figure 1. The origin of the spherical coordinate system is inside the flaw. The incoming wavevector $\vec{k}_0$ is directed in the (θ_0, ϕ_0) direction; the outgoing wavevector $\vec{k}$ in the (θ, ϕ) direction.

In section 2 we will state the principles and write down the equations on which the method is based. In section 3 is recorded the forms of the basis functions and the boundary conditions which the displacement vector must satisfy. Section 4 exhibits formulae for total and differential cross sections, both direct and mode-converted. Section 5 contains some practical computational considerations, and section 6 consists of a selection of examples of calculated cross sections for voids and rigid inclusions of spheres, oblate and prolate spheroids with aspect ratios up to 7, pillboxes and cones, for values of ka from .01 to 10. Finally, section 7 includes a discussion of generalization to unsymmetric shapes, multiple flaws, elastic inclusions, inclusions within inclusions, and ultrasonic lens design.

2. Equations for Elastic Waves

If $\vec{S}(r,\theta,\phi)$ is the vector displacement of a point which was at r,θ,ϕ in the undisturbed system (i.e. when there is no incident wave), then

$$\rho\ddot{\vec{S}} = (\lambda + \mu)\,\vec{\nabla}(\vec{\nabla}\cdot\vec{S}) + \mu\,\nabla^2\vec{S} \tag{1}$$

in a homogeneous isotropic elastic medium with density ρ and Lamé constants λ,μ. We denote the set of solutions of eq. (1) with $\ddot{S} = -\omega^2\,\vec{S}$ by $\vec{S}_{p\ell m} = \vec{S}_k$; they will be exhibited in section 3.

The physics of the scattering situation dictates that we seek a solution of eq. (1) of the form

$$\vec{S} = \vec{S}_{in}(\theta_0,\phi_0) + \sum_k a_k\,S_k \tag{2}$$

where $\vec{S}_{in}$ is the incoming plane wave along the direction θ_o, ϕ_o, and $\vec{S}_k$ is an asymptotically spherical outgoing wave specified by indices $k = p,\ell,m$ which will designate polarizations and angular eigenvalues.

The complex coefficients a_k in eq. (2) are determined by requiring that the appropriate boundary conditions on the surface Σ of the defect be satisfied. For the rigid inclusion these are simply that

$$\vec{S} = 0 \text{ on } \Sigma \quad . \tag{3a}$$

For the void defect they are the 3 components of stress across the surface vanish (or, in the case of the elastic inclusion, be continuous). These conditions will be given in detail in the next section; for the present they will be denoted as

$$\Theta\,\vec{S} = 0 \text{ on } \Sigma \quad , \tag{3b}$$

where Θ is a matrix which is a function of position on Σ, and is a first-order differential operator.

Now, if eqs. (3a) or (3b) are to be satisfied, then

$$I\{\vec{S}\} = \int_\Sigma d\sigma|\vec{S}|^2 \tag{4a}$$

or

$$I\{\vec{S}\} = \int_\Sigma d\sigma|\Theta\vec{S}|^2 \tag{4b}$$

(where σ is an arbitrary positive measure on Σ) must vanish. But in practical calculations the set $\{k\}$ in eq. (2) is finite, which renders it impossible to exactly satisfy eq. (4).

Our prescription is to choose the a_k's so that $I\{\vec{S}\}$ is as small as it can be within whatever constraints are imposed on the set $\{k\}$ in eq. 2; generally a maximum value of $\ell = \ell_{max}$ is dictated by computer time or memory limitations. Specifically, we require $I\{\vec{S}\}$ to be a minimum with respect to variations in the a's;

$$\frac{\partial I\{\vec{S}\}}{\partial a_k^*} = 0 \quad , \quad k \text{ in } \{k\} \quad . \tag{5}$$

quation (5) is a set of linear equations in a_k, viz.

$$\sum_{k'} B_{kk'} a_{k'} + C_k = 0 \quad , \tag{6}$$

here

$$B_{kk'} = \int_\Sigma d\sigma \, \vec{S}_k^* \cdot \vec{S}_{k'} \quad , \tag{7}$$

$$C_k = \int_\Sigma d\sigma \, \vec{S}_k^* \cdot \vec{S}_{in} \quad , \tag{8}$$

or the rigid boundary conditions, and the S's are simply replaced by θS's in the case of he void. We will always take dσ to be simply the element of surface area on Σ.

The bulk of the labor involved in the calculation of scattering is the evaluation of he surface integrals in (7) and (8), which for all shapes except spheres must be performed numerically. For elastic waves, which have three polarizations, and for a prescribed ℓ_{max}, there are $3(1 + 3 + 5 + \ldots + 2\ell_{max} + 1) = 3(\ell_{max} + 1)^2$ members of the set k}, and this is the rank of the hermitian matrix B if the surface Σ has no symmetries.

If, however, we restrict Σ to be a surface of revolution, with the axis of symmetry hosen to be the z-axis, then clearly

$$B_{kk'} = B_{p\ell m, p'\ell' m'} = \delta_{mm'} B_{p\ell m, p'\ell' m} \quad , \tag{9}$$

significant simplification (B becomes diagonal in ℓ as well if Σ is a sphere).

The numerical calculation then proceeds by choosing $\vec{S}_{in}$ and Σ and ℓ_{max}, calculating he matrix $B_{kk'}$, and the vector C_k, finding the inverse $B^{-1}{}_{kk'}$, obtaining

$$a_k = -B^{-1}{}_{kk'} C_{k'} \quad . \tag{10}$$

hese are the partial-wave amplitudes, from which differential and total cross sections re readily obtainable, as outlined in section 4.

3. Basis Functions and Boundary Conditions

Following Ying and Truell [1][1] we write

$$\vec{S} = \vec{\nabla} \psi + \vec{r} \times \vec{\nabla} \psi + \vec{\nabla} \times (\vec{r} \times \vec{\nabla})\xi \quad , \tag{11}$$

$$p = 1 \qquad p = 2 \qquad p = 3$$

here φ, ψ, and ξ are scalar functions and we have specified the polarization index p. p = 1 eans longitudinal polarization, p = 2 and 3 are the two orthogonal transverse polariza- ions.

Equation (11), substituted into eq. (1), gives, with time dependence assumed harmonic,

$$-\omega^2 \phi = (\lambda + 2\mu)\nabla^2 \phi \tag{12a}$$

$$-\omega^2 \psi = \mu \nabla^2 \psi \tag{12b}$$

$$-\omega^2 \xi = \mu \nabla^2 \xi \quad . \tag{12c}$$

[1] Figures in brackets indicate the literature references at the end of this paper.

In the usual way, we separate eq. (12) in spherical polar coordinates, and define our basis functions

$$\vec{S}_{1\ell m} = k_L^{-1} \vec{\nabla} \phi_\ell^m(k_L r,\theta,\phi) \tag{13a}$$

$$\vec{S}_{2\ell m} = \vec{r} \times \vec{\nabla} \phi_\ell^m(k_T r,\theta,\phi) \tag{13b}$$

$$\vec{S}_{3\ell m} = k_T^{-1} \vec{\nabla} \times (\vec{r} \times \vec{\nabla}) \phi_\ell^m(k_T r,\theta,\phi) \tag{13c}$$

where

$$\phi_\ell^m(kr,\theta,\phi) = Y_\ell^m(\theta,\phi)\, h_\ell^{(1)}(kr), \tag{14}$$

$$h_\ell^{(1)} = j_\ell + iy_\ell$$

and

$$k_L^2 = \omega^2/(\lambda + 2\mu) \tag{15a}$$

$$k_T^2 = \omega^2/\mu \tag{15b}$$

The incident wave $\vec{S}_{in}$ is taken to be a longitudinally polarized plane wave:

$$\vec{S}_{in} = k_L^{-1} \vec{\nabla} e^{i\vec{k_o} \cdot \vec{r}}$$

(notice that $\vec{k}_o$ can be in any direction, but $k_o^2 = k_L^2$) and the surface Σ is parameterized by the equation

$$r = f(\theta) \quad , \tag{17}$$

where $f(\theta)$ is a single-valued function of its argument (this restricts Σ to be "star-shaped").

The boundary conditions on Σ which $\vec{S}$ must satisfy are, for the case of the rigid immovable obstacle, simply that it vanish. For the void, the boundary conditions are that all three components of stress across Σ must vanish. These relations are most easily expressed in a cartesian coordinate system which has two of its axes in Σ, the third normal to Σ. Figure 2 shows the geometry; since Σ has axial symmetry, the unit vector $\hat{\phi}$ can always be taken to be one of these cartesian axes. The others are

$$\hat{n} = (f^2 + f'^2)^{-\frac{1}{2}}(f, -f', 0) \tag{18a}$$

$$\hat{P} = (f^2 + f'^2)^{-\frac{1}{2}}(f', f, 0), \tag{18b}$$

$$\hat{\phi} = (0, 0, 1) \tag{18c}$$

where $f' = df/d\theta$, and the vectors on the right-hand-side are expressed in terms of their spherical polar components (V_r, V_θ, V_ϕ).

The stress tensor σ is, in cartesian coordinates $i = 1, 2, 3$;

$$\sigma_{ij} = \mu(S_{i,j} + S_{j,i}) + \lambda\delta_{ij} \vec{\nabla} \cdot \vec{S} \quad , \tag{19}$$

where $S_{i,j} = \partial S_i/\partial x_j$. The void boundary conditions are then

$$\sigma_{nn} = 0 \tag{20a}$$

$$\sigma_{np} = 0 \tag{20b}$$

$$\sigma_{n\phi} = 0 \tag{20c}$$

which must be transformed back into spherical coordinates in order to be useful. The set $\hat{n}$, $\hat{p}$, $\hat{\phi}$ forms a right-handed cartesian system of axes. It is different for each point on Σ.

Figure 2. The right-handed cartesian coordinate systems $\hat{n}$ (normal to Σ), $\hat{p}$ (coplanar with z-axis and tangent plane to Σ), and $\hat{\phi}$ (same as spherical coordinate unit vector) are defined for each point in Σ.

Equations (20) become, in spherical coordinates,

$$\sigma_{nn} = 2\mu \; S_{n,n} + \lambda \vec{\nabla} \cdot \vec{S}$$

$$= 2\mu \left\{ S_{r,r} - \sin^2 \xi \left(S_{r,r} - S_{\theta,\theta} - \frac{S_r}{r} \right) \right. \tag{21a}$$

$$\left. - \tfrac{1}{2} \sin 2\xi \left(S_{r,\theta} + S_{\theta,r} - \frac{S_\theta}{r} \right) \right\} - k_\ell^2 \, \phi$$

$$\sigma_{np} = \mu \left(S_{n,p} + S_{p,n} \right) \tag{21b}$$

$$= \mu \left\{ \sin 2\xi \left(S_{r,r} - S_{\theta,\theta} - \frac{S_r}{r} \right) + \cos 2\xi \left(S_{r,\theta} + S_{\theta,r} - \frac{S_\theta}{r} \right) \right\}$$

$$\sigma_{n\phi} = \mu (S_{n,\phi} + S_{\phi,n})$$

$$= \mu \left\{ \cos \xi \, (S_{\phi,r} + S_{r,\phi}) - \sin \xi \, (S_{\phi,\theta} + S_{\theta,\phi}) \right. \tag{21c}$$

$$\left. - \frac{S_\phi}{r \sin \theta} \sin (\theta - \xi) \right\} ,$$

where

$$\tan \xi = f'/f \tag{22}$$

and $\theta - \xi$ is the angle between the polar axis $\hat{z}$ and $\hat{n}$, the normal to Σ. In eq. (21)

$$A_{,r} = \frac{\partial A}{\partial r}$$

$$A_{,\theta} = \frac{1}{r} \frac{\partial A}{\partial \theta} \tag{23}$$

$$A_{,\phi} = \frac{1}{r \sin \theta} \frac{\partial A}{\partial \phi}$$

Equations (21), with eqs. (20), specify in elaborate detail just what the operator Θ in (3b) is. The detail in which one must indulge before a computer program can be written is even more excruciating, involving multiple derivatives of Bessel functions and spherical harmonics.

4. Scattered Power

One must be quite sure that all the details are exactly right, because wrong phase factors, for instance, in a partial wave expansion, cannot be squared away, unless the same mistake is made in each term. Special care must be used in power calculations, because, as usual, we have been treating the displacement $\vec{S}$ as if it were a complex quantity, whereas we really always want its real part. This indefinition causes no trouble as long as we are interested only in quantities linear in $\vec{S}$. But the power is quadratic, so we must proceed cautiously.

The power flow per unit area is

$$\vec{P} = \text{Re}\ \sigma\ \ \text{Re}\ \dot{\vec{S}} \quad . \tag{24}$$

After taking a time-average this becomes

$$\vec{P} = \tfrac{1}{2}\ \text{Re}\ \sigma^* \dot{\vec{S}} \quad , \tag{25}$$

where complex conjugation is devoted by the asterisk. The cross section is defined, as usual, to be the asymptotic outgoing power per unit solid angle divided by the incident power flux. The latter is

$$\begin{aligned} \vec{P}_{in} &= \tfrac{1}{2}\ \text{Re}\ \sigma_{in}{}^* \dot{\vec{S}}_{in} \\ &= \tfrac{1}{2}\ \vec{k}_o\ \omega(2\mu + \lambda) \quad , \end{aligned} \tag{26}$$

where the second step used eq. (16). (We remark that eq. (26) has dimensions power flux/length [2]. This is because our $\vec{S}$ has been dimensionless, and one should therefore multiply our powers by the square of a displacement amplitude to get dimensionally correct powers.)

At large distances from the scatterer, the scattered power flows radially outward. The amount passing through solid angle $d\Omega$ is

$$r^2 d\Omega\ P_r = \frac{r^2 d\Omega}{2}\ \text{Re}\ \left(\sigma^*_{out}\ \dot{\vec{S}}_{out}\right) r \quad , \tag{27}$$

where $\vec{S}_{out}$ is the second term in (2), and σ_{out} is the stress tensor formed from it.

After using eqs. (13), (14), and (21) and inserting the asymptotic form

$$h_\ell^{(1)}(\rho) \sim \frac{1}{\rho}\ e^{i[\rho-(\ell+1)\pi/2]} \tag{28}$$

for the spherical Bessel functions, one gets for the cross section for scattering into the longitudinal (p = 1) mode

$$d\sigma_L/d\Omega = k_L^{-2}\ \Big|\sum_{\ell,m}\ i^{\ell}\ Y_\ell^m(\theta,\phi)\ a_{1\ell m}\Big|^2 \quad , \tag{29}$$

which, when integrated over angles, gives a total longitudinal cross section

$$\sigma_L = k_L^{-2} \Big|\sum_{\ell,m} a_{1\ell m}\Big|^2 \quad . \tag{30}$$

As is customary [1], we introduce the normalized dimensionless cross-section

$$\gamma_L = \sigma_L/\pi a^2 = \Big|\sum_{\ell,m}\Big|\ a_{1\ell m}\ \Big|^2/\pi(k_L a)^2 \tag{31}$$

where a is some characteristic dimension of the flaw (naturally the radius in the case of the sphere).

Similarly, using the asymptotic forms for the outgoing transverse waves eqs. (13b) and (13c), one gets for the mode-converted cross section

$$d\sigma_T/d\Omega = k_L k_T^{-3} \left\{ \left| \sum_{\ell,m} i^{-\ell} \; a_{2\ell m} \; m \; Y_\ell^m / \sin\theta + a_{3\ell m} \; Y_\ell'^m \right|^2 \right.$$
$$\left. + \left| \sum_{\ell,m} i^{-\ell} \left(a_{2\ell m} Y_\ell'^m + a_{3\ell m} \; m \; Y_\ell^m / \sin\theta \right) \right| \right\}^2 \qquad (32)$$

where $Y_\ell'^m(\theta,\phi) = \dfrac{\partial Y_\ell^m(\theta,\phi)}{\partial\theta}$, and from which, using the fact that

$$\int d\Omega \left[Y_\ell^{m*} Y_{\ell'}^{\;m} \; m^2/\sin^2\theta + Y_\ell'^{m*} Y_{\ell'}'^m \right] = \ell(\ell+1)\delta_{\ell\ell'} \qquad (33)$$

one can obtain

$$\sigma_T = k_L k_T^{-3} \sum_{\ell,m} \ell(\ell+1) \left\{ |a_{2\ell m}|^2 + |a_{3\ell m}|^2 \right\} \; . \qquad (34)$$

With

$$\gamma_T = \sigma_T/\pi a^2 \quad , \qquad (35)$$

this completes the collection of formulae we need at present.

5. Practical Considerations and Results

We have written a Fortran program, EWS3D (Elastic Wave Scattering in 3 Dimensions), which computes cross sections for axially symmetric voids and obstacles. Some computationally significant observations follow.

The incident plane longitudinal wave can be expanded into orthogonal functions in the defect coordinate system;

$$\vec{S}_{in} = k_L^{-1} \vec{\nabla} e^{i\vec{k}_o\cdot\vec{r}} = 4\pi \sum_{\ell',m'} i^{\ell'} Y_{\ell'}^{m'*}(\theta_o, \phi_o) k_L^{-1} \vec{\eta}_{\ell'}^{m'}(k_L r, \theta, \phi) \qquad (36)$$

where θ_o, ϕ_o are the polar and azimuthal angles of the incoming wave vector $\vec{k}_o$, and $\eta_{\ell'}^{m'} = Y_{\ell'}^{m'} j_{\ell'}(k_L r)$. Without any loss of generality for axially symmetric defects, we will always take $\phi_o = 0$.

As was remarked above, the B matrix (7) is diagonal in m. And it is clear from eq. (36) that the $p\ell m$ component of the C vector will contain contributions only from $m' = m$. This is the mathematical statement of the physically obvious remark that for an axially symmetric scatterer m is a good quantum number.

The computational significance of this fact is that B has a block-diagonal structure (one block for each m) and therefore each m may be treated independently, greatly reducing computing time, programming complexity, and computer memory requirements. The rank of the diagonal block of B which must be inverted for given m and ℓ_{max} is $3(\ell_{max} - m + 1)$: this is to be compared with $3(\ell_{max} + 1)^2$, the rank of the B matrix which would need to be inverted as a whole if the flaw had no symmetries.

The calculation, therefore, proceeds by finding $a_{p\ell m}$ first for $m = 0$ ($p = 1,2,3$; $\ell = 0, 1, \ldots \ell_{max}$) then for $m = 1,2\ldots$ up to $m = \ell_{max}$, for which only $\ell = \ell_{max}$ is needed. Negative m's need not be computed separately; their amplitudes are related to those for positive m's in the following way:

$$a_{p\ell -m} = -(-1)^{p+m} \; a_{p\ell m} \quad . \qquad (37)$$

This can be directly verified by examining the structure of the B matrix and the C vector:

$$B_{p\ell-m,p'\ell'-m} = (-1)^{p-p'} B_{p\ell m,p'\ell' m} \qquad (38a)$$

$$C_{p\ell-m} = -(-1)^{p+m} C_{p\ell m} \quad , \qquad (38b)$$

which can be established from the definitions of B and C, eqs. (13), (21), and the property of the spherical harmonics

$$Y_{\ell}^{-m}(\theta,\phi) = (-1)^{m} Y_{\ell}^{m*}(\theta,\phi) \quad . \qquad (39)$$

Equations (37) and (38) are true for both the void and rigid boundary conditions.

Another fortuitous circumstance is that once the necessary surface integrals have been calculated and stored, very little additional computation is required to generate cross sections for any flaw orientation. This is because B is independent of $\vec{k}_o$, and C depends on $\vec{k}_o$ in a very simple way.

6. Examples

The input parameters of EWS3D are λ and μ, the Lamé constants; $k_L a$, where a is the radius of the largest circular cross section of the flaw; a type index which is 0 or 1 depending on whether void or immovable obstacle boundary conditions are used; H, which is negative, zero, or positive depending on whether the object is a cone, a spheroid, or a pillbox, and whose magnitude is the height of the cone or pillbox in units of a; AR, the aspect ratio is the quotient of the height by the largest diameter (it is larger than 1 for prolate spheroids, less than 1 for oblate ones); ℓ_{max} is the cutoff in ℓ, and $n_{\ell eg}$ is the number of points used in the interval $-1 < \cos\theta < 1$ for the numerical integrations in the calculation of matrix elements of B and C, which are done by Gauss-Legendre quadrature.

Figures 3a and 3b show scattering from a spherical void, with ka = .1. This is well into the domain in which the Rayleigh limit reigns, and the cross sections shown here agree with that limit, which is discussed in reference [1].

Figure 4a illustrates scattering from a spherical void, with ka = 1 and $\ell_{max} = 2$. Figure 4b is the cross section for ka = 1 and $\ell_{max} = 4$. Taking $\ell_{max} = 6$ yields curves which are indistinguishable from figure 4b.

Figures 5a and 5b show the cross sections for scattering from a rigid immovable sphere, with ka = 1. The similarity to the case of the void is apparently superficial; the ratio of forward scattering to scattering at 90° is much different.

Figure 6 is included as an exercise for the reader who wishes to test his agility in visualization of angular transformations. This is the same situation as shown in figure 5a, but the incoming wave has $\theta_o = 45°$. Forward scattering then has $\theta = 45°$, $\phi = 0$; backward scattering has $\theta = 135°$, $\phi = 180°$.

Figures 7a, 7b, and 7c show the cross section for a spherical void with ka = 10 and ℓ_{max} = 10, 12, and 14 respectively. Convergence has effectively occurred at $\ell_{max} = 12$.

Figures 8a and 8b have ka = 10, $\ell_{max} = 14$ and $\theta = 90°$ for a void sphere. Figure 8a shows weak diffraction rings also in the backward direction.

Figures 9a and 9b are examples of scattering from a prolate spheroid, with aspect ratio of 7. It should be remembered that ka = 1 here means that kb = 7 (b = semi-major axis).

Figures 10a and 10b picture the cross section for scattering from an oblate spheroidal void with aspect ratio 1/7 and ka = 5. Notice the specular reflection peak in figure 10b.

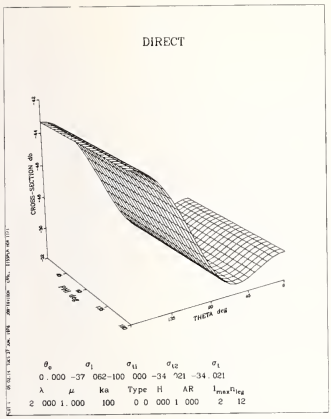

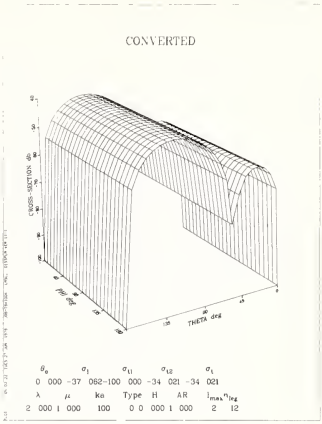

Figure 3. Direct (a) and mode-converted (b) scattering at ka = .1 from a spherical void. Normalized total cross sections are printed in db; a zero cross section is taken to be -100 db. Forward and backward mode-converted cross sections are zero by symmetry considerations.

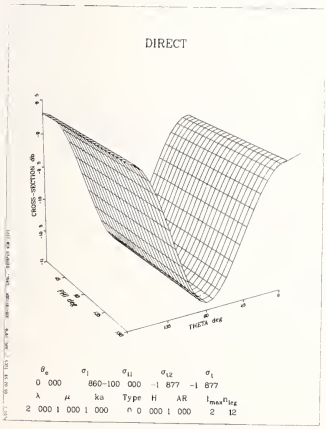

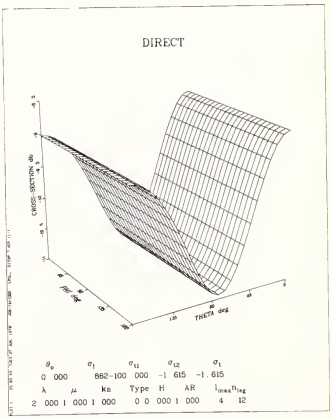

Figure 4. Scattering from a spherical void for ka = 1. (a) has $\ell_{max} = 2$; (b) has $\ell_{max} = 4$. Taking $\ell_{max} = 6$ causes no change from (b).

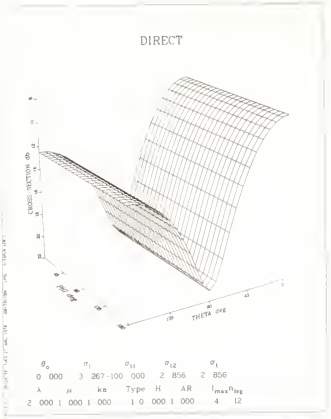

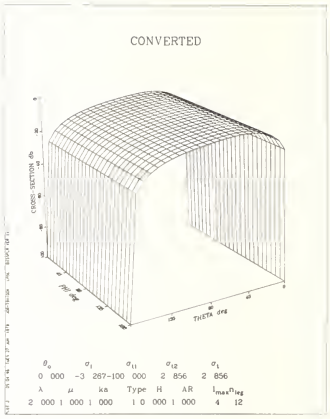

Figure 5. Scattering from a rigid immovable spherical obstruction for ka = 1; (a) is proportional to longitudinal scattered power; (b) to transverse.

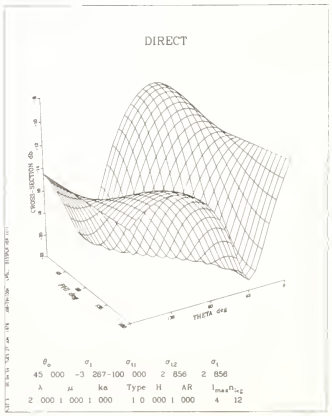

Figure 6. Same as figure 5a, but for θ_o = 45°.

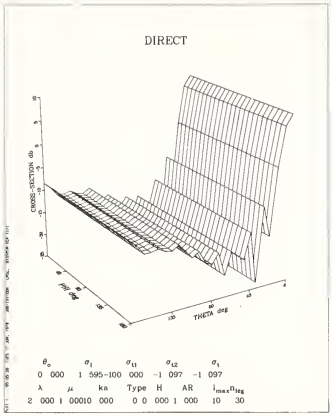

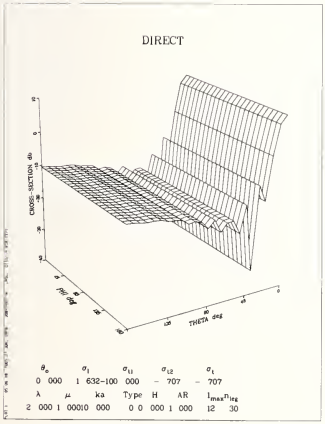

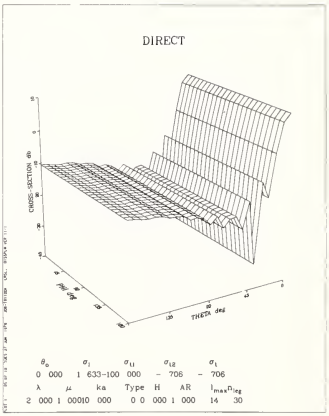

igure 7. Direct scattering at ka = 10 fom a void sphere. (a), (b), and (c) have ℓ_{max} = 10, 12, and 14 respectively to illustrate convergence. Notice that (a) has a different scale (-25 to +10 db) from (b) and (c) (-40 to +10 db).

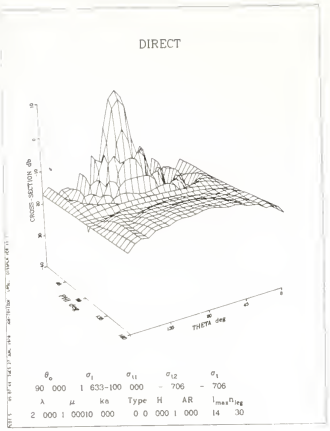

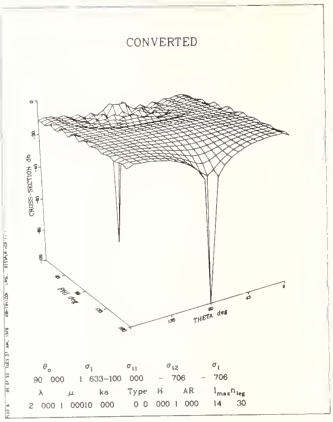

Figure 8. Direct (a) and mode-converted (b) scattering from a spherical void, for ka = 10 with $\theta_o = 90°$. The forward scattering peak (in a) or dip (in b) is surrounded by diffraction rings. The ripples in σ_t for $\Theta = 0$ and π are attributable to the fact that for $\ell = 1$ m = 1, and p = 2 or 3 $\tilde{S}_{p\ell m}$ is indeterminate at $\Theta = 0$ and π. The ripples are lessened by increasing $n_{\ell eg}$.

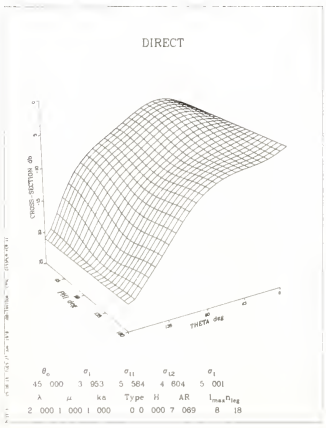

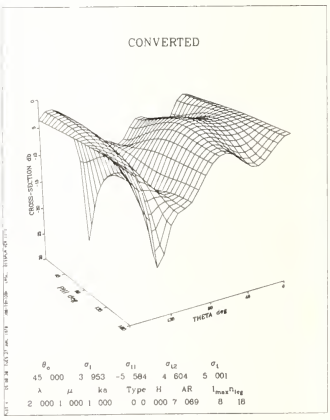

Figure 9. Scattering of an incoming wave at $\theta_o = 45°$ by a prolate spheroid with length 7 times its diameter. ka = 1; a is still the radius.

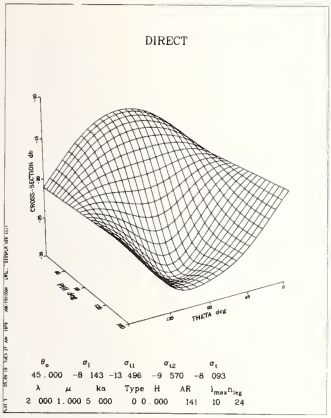

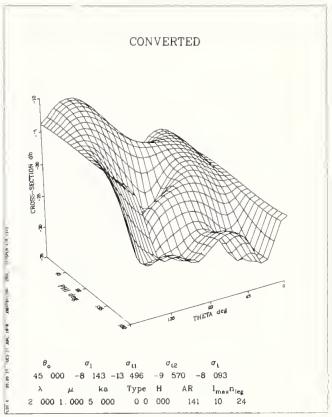

gure 10. Cross section for Θ_o = 45°, ka = 5 for an oblate spheroid whose diameter is 7 times its height.

Figures 11a and 11b show scattering from a pillbox with aspect ratio 1/2 and ka = 5, r ℓ_{max} = 8 and 14. It is clear that for a given ka, a higher ℓ_{max} is required for surces with less than spherical symmetry. Figure 11c has ka = 10, showing forward scatterg with diffraction rings, and a specular reflection peak.

Figures 12a, 12b, 12c, and 12d are examples of scattering from a cone with aspect tio 1/2, ka = 5 and ℓ_{max} = 12; higher ℓ_{max} gives no perceptible change.

The graphs shown in figures 3-12 were produced by the graphics package DISSPLA: the mputing was done on a CDC 6600. Little attempt has been made to optimize the program; e CP time per case, which consists of calculating scattered power in three polarizations to 25 x 25 = 625 directions for each of five incident directions, is approximately (ℓ_{max} eg/5) seconds, plus 9 seconds per plot.

$n_{\ell eg}$ should be scaled with ℓ_{max}; little is gained in accuracy by making $n_{\ell eg} >$ ℓ_{max}. For a sphere $\ell_{max} \approx 1.2$ ka is enough; for a cone one needs $\ell_{max} \gtrsim 2$ ka for sual convergence.

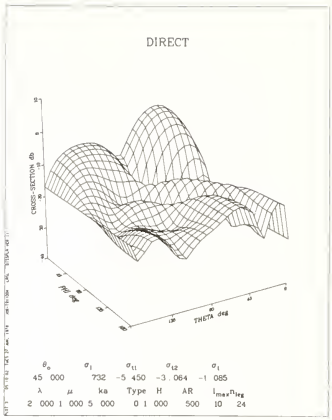

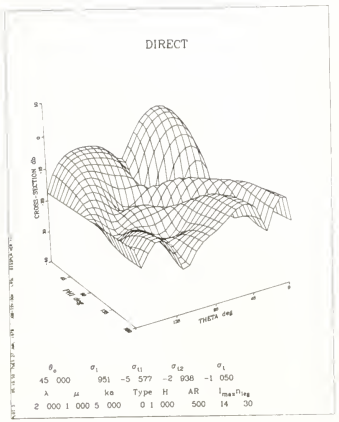

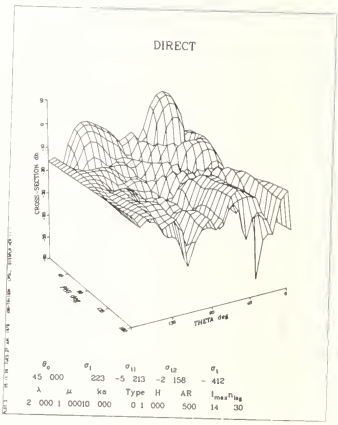

Figure 11. Scattering from a pillbox of a wave incident at 45° with ka = 5 for ℓ_{max} = 10 (a) and ℓ_{max} = 14 (b). The forward and specular peaks are evident, and are more dramatic in (c), which has ka = 10.

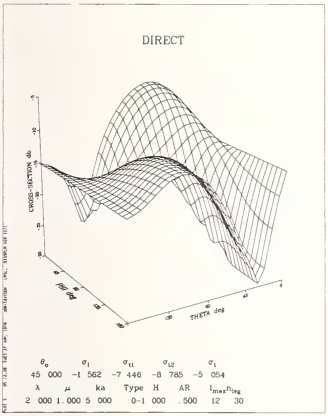

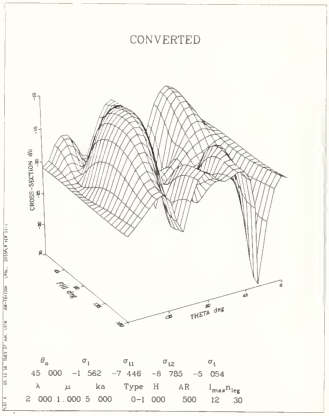

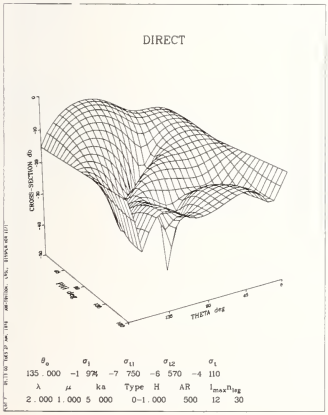

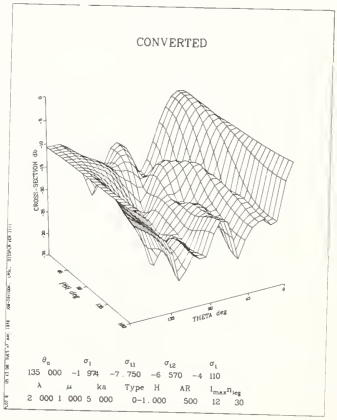

gure 12. Scattering from a cone whose flat surface faces up, as in figure 1, for ka = 5. (a) and (b) have $\theta_o = 45°$; (c) and (d) have $\theta_o = 135°$.

7. Generalizations

Extension to unsymmetric flaws will be straightforward but time consuming, because the surface integrals will then be really two-dimensional, and B will no longer be diagonal in m. Computation times and capacities will be multiplied manyfold, but some problem undoubtedly exists which will justify the effort.

Only minor revision of the existing EWS3D program is necessary to compute scattering from an elastic inclusion. In this case, the displacement inside will be expanded

$$\vec{s}^{(i)} = \sum_{p\ell m} a^{(i)}_{p\ell m} \vec{s}^{(i)}_{p\ell m} \quad , \tag{40}$$

as well as the displacement outside

$$\vec{s}^{(0)} = \vec{s}_{in} + \sum_{p\ell m} a^{(0)}_{p\ell m} \vec{s}^{(0)}_{p\ell m} \quad . \tag{41}$$

Whereas $\vec{s}^{(0)}_{p\ell m}$ contains $h^{(1)}_{\ell}(kr)$, $\vec{s}^{(i)}_{p\ell m}$, because it must be regular at the origin, will contain $j_{\ell}(kr)$. Both continuity in displacement across Σ and continuity in stress must now be involved, and the functional to be minimized will be a linear combination of (4a) and (4b) with S replaced by $\vec{s}^{(i)} - \vec{s}^{(0)}$ in (4a) and appropriate modification made in (4b). There will now be two sets of amplitudes $a^{(i)}_{p\ell m}$ and $a^{(0)}_{p\ell m}$, for which linear inhomogeneous equations can be derived as before.

This process can be continued as many times as one pleases to treat flaws within flaws, e.g., thick walled bubbles.

EWS3D can be used for ultrasonic lens design by looking at the scattered wave at finite distance from the flaw (lens) rather than only at its asymptotic form. One might also wish to have something other than a plane wave incident.

Scattering of incident transverse polarized waves can be treated by replacing eq. (36) with whatever transverse wave is appropriate to the physical problem under consideration.

Scattering by two spherical voids Σ_1 and Σ_2 would be interesting and not difficult to calculate by modification of EWS3D, because axial symmetry is maintained. $I\{\vec{S}\}$ will no longer be in integral over a single surface Σ, but the sum of integrals over Σ_1 and Σ_2. Computational difficulties will be worsened if the distance between the spheres is large compared to k^{-1}, because then large values of ℓ will contribute.

References

[1] Ying, C. F. and Truell, Rohn, J. Appl. Phys., 27, 1086-1097 (1956).

ational Bureau of Standards Special Publication 596, Ultrasonic Materials Characterization,
. Berger and M. Linzer, eds., Proceedings of the First International Symposium on Ultrasonic
aterials Characterization held at NBS, Gaithersburg, Md., June 7-9, 1978. Issued
ovember, 1980.

LOW FREQUENCY BEHAVIOR OF AMPLITUDE AND PHASE SHIFT IN ELASTIC WAVE SCATTERING

John M. Richardson

Rockwell International, Science Center
1049 Camino Dos Rios
Thousand Oaks, CA 91360

The problem of the scattering of elastic waves is treated in the low-frequency regime by a systematic expansion in powers of the frequency in the domain of the scatterer. The zeroth and first degree scattering amplitudes vanish if the scatterer is localized in all directions. The second degree scattering amplitude corresponds to the Rayleigh regime. In general, the third and higher degree scattering amplitudes are non-vanishing. However, in the case where the scatterer has inversion symmetry about the origin, it has been shown that the third degree scattering amplitude vanishes. This conclusion is valid for the most general anisotropic elastic scatter possessing the above inversion symmetry. The scattering amplitude is actually a second rank tensor and it is to be emphasized that the above result applies to any element or linear combination of elements. This general result implies that the frequency derivative of the phase shift approaches zero at least quadratically as the frequency goes to zero. In other words, at sufficiently low frequency the effective scattering center of a scatterer with inversion symmetry is its geometrical center. This result can be used in the processing of experimental scattering data to determine the position of the geometrical center of a sufficiently symmetric scatterer.

1. Introduction

In a previous publication [1][1], henceforth called Paper I, we investigated the effect of atterer symmetry on the low frequency behavior of the scattering of elastic waves. ecifically, it was proved that if the scatterer possesses inversion symmetry about the igin, then the third degree term in the frequency expansion of the scattering amplitude nishes identically for all transducer configurations. Furthermore, this result does not ply to any higher degree terms.

One purpose of the present paper is to explore the consequences of this result in terms the behavior of the amplitude (i.e., the absolute value of the scattering amplitude) and ase shift at low frequencies. A second purpose is the application of this result in the ocessing of experimental scattering data--in particular, the determination of the position the geometrical center of a scatterer known a priori to have inversion symmetry.

In Section 2, we present notational preliminaries and a mathematical statement of the oblem. In Section 3, a discussion is given to the consequences of inversion symmetry and e verification of these consequences using the exact theory of scattering from a spherical clusion involving locally isotropic material. Finally, in Section 4 the main result is plied to the interpretation of experimental scattering data.

2. Preliminaries and Problem Statement

We consider a general scattering problem in an elastic medium where an incident plane ve of given polarization propagates in the direction $\hat{e}^i$ toward an inhomogeneity confined to e scatterer domain $\mathcal{D}_s$ as shown in figure 1. The amplitude of a specified polarization

[1] Figures in brackets indicate the literature references at the end of this paper.

component of the scattered wave in the far field is observed in the direction $\vec{e}^s$. The host medium (i.e., the medium external to the scatterer domain $\mathcal{D}_s$) is assumed to be homogeneous and isotropic with a uniform density ρ and a uniform isotropic elastic constant tensor given by

$$C_{\alpha\beta\gamma\delta} = \lambda\delta_{\alpha\beta}\delta_{\gamma\delta} + \mu(\delta_{\alpha\gamma}\delta_{\beta\delta} + \delta_{\alpha\delta}\delta_{\beta\gamma}) \tag{1}$$

where λ and μ are the Lamé constants. The Greek indices α, β... label the cartesian coordinate directions and each index takes the values 1, 2, 3. In the scatterer domain $\mathcal{D}_s$ we assume inhomogeneous anisotropic properties with the nonuniform density $\rho + \delta\rho(\vec{r})$ and nonuniform elastic constant tensor $C_{\alpha\beta\gamma\delta} + \delta C_{\alpha\beta\gamma\delta}(\vec{r})$ where $\vec{r} = (x,y,z)$ is the position vector.

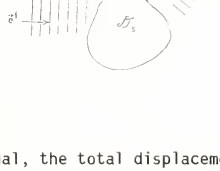

Figure 1. Scattering geometry.

As usual, the total displacement field $\vec{u} = \vec{u}(\vec{r},\omega)$ at the frequency [2] ω is assumed to b decomposed into an incident field $\vec{u}^i$ and a scattered field $\vec{u}^s$, i.e.,

$$\vec{u} = \vec{u}^i + \vec{u}^s \ . \tag{2}$$

We assume that the incident field is composed of a plane wave of polarization $\vec{a}$ propagating i the incident direction $\vec{e}^i$, namely

$$\vec{u}^i = [\vec{e}^i\vec{e}^i \exp(ik_\ell \vec{e}^i\cdot\vec{r}) + (\overleftrightarrow{1} - \vec{e}^i\vec{e}^i) \exp(ik_t \vec{e}^i\cdot\vec{r})]\cdot\vec{a} \tag{3}$$

The part of the scattered wave propagating in the direction $\vec{e}^s$ in the far field is given by

$$\vec{u}^s \underset{r \text{ large}}{\sim} r^{-1}[\vec{e}^s\vec{e}^s \exp(ik_\ell r) + (\overleftrightarrow{1} - \vec{e}^s\vec{e}^s) \exp(ik_t r)]\cdot\overleftrightarrow{A}(\vec{e}^s,\vec{e}^i;\omega)\cdot\vec{a} \tag{4}$$

where $\overleftrightarrow{A}(\vec{e}^s,\vec{e}^i;\omega)$ is the so-called scattering amplitude sensor. In (3) and (4) $\overleftrightarrow{1}$ is the unit tensor and k_ℓ and k_t are the wave numbers for longitudinal and transverse waves, respectively The latter are defined by

$$k_\ell = \omega/c_\ell \ , \tag{4}$$

$$k_t = \omega/c_t \ , \tag{5}$$

where c_ℓ and c_t, the longitudinal and transverse propagation velocities in the host medium, are given by

$$c_\ell^2 = (\lambda + 2\mu)/\rho \ , \tag{6}$$

$$c_t^2 = \mu/\rho \ . \tag{7}$$

he scattering amplitude tensor satisfies the reality condition

$$\overleftrightarrow{A}(\vec{e}^s,\vec{e}^i;-\omega) = \overleftrightarrow{A}^*(\vec{e}^s,\vec{e}^i;\omega) \tag{8}$$

here, as usual, the asterisk denotes the complex conjugate.

If the scatterer is localized (in all spatial directions), the scattering amplitude ensor can be expanded in a power series in the frequency ω, namely

$$\overleftrightarrow{A}(\vec{e}^s,\vec{e}^i;\omega) = \sum_{n=0}^{\infty} \overleftrightarrow{A}_n(\vec{e}^s,\vec{e}^i)\,\omega^n \quad . \tag{9}$$

he spatial localization implies the vanishing of the 0th and 1st degree terms, i.e.,

$$\overleftrightarrow{A}_0 = \overleftrightarrow{A}_1 = 0 \text{ for all } \vec{e}^i \text{ and } \vec{e}^s \ . \tag{10}$$

he reality condition (8) implies that $\overleftrightarrow{A}_n$ is real if n is even and $\overleftrightarrow{A}$ is imaginary if n is dd. The leading term $A_2\omega^2$ corresponds to the Rayleigh regime which has been investigated by ubernatis et al. [3].

It is useful to consider the scalar projections of $\overleftrightarrow{A}$ associated with specified olarizations of the incident wave and specified polarization components of the scattered ave. In general, we can write

$$\vec{b}\cdot\vec{u}_{s_{r \text{ large}}} \to r^{-1}\,\vec{b}\cdot[\vec{e}^s\vec{e}^s \exp(ik_\ell r) + (\overleftrightarrow{1}-\vec{e}^s\vec{e}^s)\exp(ik_t r)]\cdot\overleftrightarrow{A}\cdot\vec{a} \tag{11}$$

here $\vec{b}$ is an arbitrary unit vector. If $\vec{b} = \vec{e}^s$ we obtain

$$\vec{b}\cdot\vec{u}_{s_{r \text{ large}}} \to r^{-1}\exp(ik_\ell r)\vec{b}\cdot\overleftrightarrow{A}\cdot\vec{a} \tag{12}$$

d, on the other hand, if $\vec{b} \perp \vec{e}^s$ we obtain

$$\vec{b}\cdot\vec{u}_{s_{r \text{ large}}} \to r^{-1}\exp(ik_t r)\vec{b}\cdot\overleftrightarrow{A}\cdot\vec{a} \ . \tag{13}$$

e description of the scattering from one polarization to another is indicated by the scheme:

Longitudinal to longitudinal: $\vec{a} = \vec{e}^i$, $\vec{b} = \vec{e}^s$

Longitudinal to transverse: $\vec{a} = \vec{e}^i$, $\vec{b} \perp \vec{e}^s$ (14)

Transverse to longitudinal: $\vec{a} \perp \vec{e}^i$, $\vec{b} = \vec{e}^s$

Transverse to transverse: $\vec{a} \perp \vec{e}^i$, $\vec{b} \perp \vec{e}^s$.

It will be convenient in the subsequent analysis to denote an arbitrary scalar projection of $\overleftrightarrow{A}$ by the symbol B in accordance with the expression

$$\vec{b} \cdot \overleftrightarrow{A} \cdot \vec{a} = B = B\,(\vec{e}^{s},\vec{b},\vec{e}^{i},\vec{a};\omega) \ . \tag{15}$$

The phase shift γ associated with a given scalar projection is defined by

$$\gamma = \gamma(\vec{e}^{s},\vec{b};\ \vec{e}^{i},\vec{a};\omega) = \mathrm{Arg}B \ . \tag{16}$$

The phase shift still involves an arbitrary integral multiple of 2π. To remove this ambiguity, we introduce the convention

$$0 \leqslant \lim_{\omega\to 0} \gamma(\vec{e}^{s},\vec{b};\ \vec{e}^{i},\vec{a};\omega) < 2\pi \ , \tag{17}$$

that is, the phase shift for any scattering process in the Rayleigh limit is defined to be nonnegative and less than 2π. The conventions can be extended to higher frequency by the requirement of continuity [4], i.e., $B(\vec{e}^{s},\vec{b};\ \vec{e}^{i},\vec{a};\ \omega)$ is a continuous function of ω.

3. Consequences of Inversion Symmetry

The results presented so far are completely general for the case of any spatially localized scatterer in a homogeneous isotropic host medium. Here, we turn to the consideration of the restrictions imposed by the assumption that the scatterer possesses inversion symmetry.

In Paper I, it was proved that if the scatterer has inversion symmetry with respect to the origin ($\vec{r} = 0$), i.e.,

$$\delta\rho(\vec{r}) = \delta\rho(-\vec{r}) \tag{18}$$

$$\delta C_{\alpha\beta\gamma\delta}(\vec{r}) = \delta C_{\alpha\beta\gamma\delta}(-\vec{r}) \ , \tag{19}$$

it then follows that

$$\overleftrightarrow{A}_3 \equiv 0 \text{ for all } \vec{e}^{i} \text{ and } \vec{e}^{s} \ . \tag{20}$$

It is to be emphasized that inversion symmetry does not imply that any $\overleftrightarrow{A}_n = 0$ for all $\vec{e}^{i}$ and $\vec{e}^{s}$ when $n>3$. No results are yet available in relation to the converse theorem, i.e., that $\overleftrightarrow{A}_3 = 0$ for all $\vec{e}^{i}$ and $\vec{e}^{s}$ implies inversion symmetry.

The scalar projection $\vec{b}\cdot\overleftrightarrow{A}\cdot\vec{a} \equiv B$ can, of course, be expanded in the power series

$$B = \sum_{n\ \mathrm{even}} B_n\omega^n + i\sum_{n\ \mathrm{odd}} B_n\omega^n \tag{21}$$

corresponding to (9). It clearly follows from (10) that $B_0 = B_1 = 0_1$. For convenience, we have expressed the coefficients in (21) in such a form that the reality condition (8) implies that $B_n = B_n(\vec{e}^{s},\vec{b};\vec{e}^{i},\vec{a})$ is real for all n.

If the scatterer does not possess inversion symmetry, we obtain

$$|B| = |B_2|\,\omega^2\,[1+(B_2^{-1}B_4+1/2\,B_2^{-2}B_3^2)\,\omega^2+O(\omega^4)] \tag{22}$$

$$\gamma = \mathrm{Arg}B_2 + B_2^{-1}B_3\omega + O(\omega^3) \tag{23}$$

s $|B|$ is proportional to ω^2 as $\omega\to 0$, as one would expect, and involves only even powers of ω general. According to the convention (17) the phase shift in the Rayleigh limit is given

$$\lim_{\omega\to 0}\gamma = \mathrm{Arg}B_2 = \begin{cases} 0 & B_2>0 \\ \pi & B_2<0 \end{cases} \tag{24}$$

ce B_2 is real. For $\omega>0$, $\gamma - \lim_{\omega\to 0}\gamma$ is proportional to ω unless $B_3 = 0$. The time delay n the scattering of a monochromatic wave (relative to the delay in scattering from a point the origin) is given by

$$\tau = \partial\gamma/\partial\omega = B_2^{-1}B_3 + O(\omega^2)\ . \tag{25}$$

arly, in the case of a given set of values of $\vec{e}^{\,i},\vec{a},\vec{e}^{\,s}$ and $\vec{b}$ the delay τ could be made to ish by shifting the origin. However, there is at the present time no proof available that ingle shift of the origin can make τ vanish in the limit $\omega\to 0$ for all values of $\vec{e}^{\,i},\vec{a},\vec{e}^{\,s}$ and n the case of a scatterer not possessing inversion symmetry with respect to some center. e we have assumed that $\vec{a}$ and $\vec{b}$ are parallel or perpendicular to $\vec{e}^{\,i}$ and $\vec{e}^{\,s}$, respectively, furthermore this assumption is maintained in the subsequent discussion.

If the scatterer has inversion symmetry about the origin it follows, of course, from (20) t

$$B_3 = 0 \text{ for all } \vec{e}^{\,i},\vec{a},\vec{e}^{\,s},\vec{b} \tag{26}$$

, as before, this statement cannot be applied to any B_n with $n>3$. The results (22),) and (24) are now replaced by

$$|B| = |B_2|\omega^2(1 + B_2^{-1}B_4\omega^2) \tag{27}$$

$$\gamma = \mathrm{Arg}B_2 + B_2^{-1}B_5\omega^3 + O(\omega^5) \tag{28}$$

$$\tau = \partial\gamma/\partial\omega = 3B_2^{-1}B_5\omega^2 + O(\omega^4) \tag{29}$$

$$\partial\tau/\partial\omega = \partial^2\gamma/\partial\omega^2 = 6B_2^{-1}B_5\omega + O(\omega^3)\ . \tag{30}$$

t s to be noted that $|B|$ is qualitatively the same as before. Also, the phase shift γ in f limit $\omega\to 0$ is the same as before. However, now the quantity $\gamma - \lim_{\omega\to 0}\gamma$ is proportional to

ω^3 and it is noteworthy that the corresponding coefficient is proportional to B_5 (i.e., the frequency expansion of $\vec{A}$ must be carried to the 5th power before a deviation of the phase shift from its zero frequency value is produced). The most interesting feature of these results is that the time delay τ, given by (29), approaches 0 quadratically in ω as $\omega \to 0$. This means that in the Rayleigh limit the effective center of scattering is the origin in the case of any scatterer possessing inversion symmetry about this origin and moreover that this effective center approaches the origin quadratically with respect to frequency.

In figures 2 and 3 we present an exact [5] computational example of the low frequency behavior of $|B|$ and γ = ArgB for the case of longitudinal-to-longitudinal backscatter from a B_4C spherical inclusion in a SiC matrix. It was assumed that both substances exist in the form of macroscopically isotropic uniform aggregates. The radius of the sphere is denoted b a and the quantities c_ℓ and k_ℓ are defined by (6) and (4), respectively. These results, of course, verify the theoretical results (27) and (28) for the low frequency behavior of $|B|$ a γ. It is particularly noteworthy that the theoretical expression for γ, neglecting terms of the fifth and higher degrees, gives a close fit to the computational result in figure 3 even up to $\omega a/c_\ell = k_\ell a \sim 0.5$.

4. Application to the Interpretation of Experimental Phase Shift Data

Here, we show how the results of the last section can be applied in an experimental situation to the determination of the position of the geometrical center of a scatterer with inversion symmetry.

We assume that the scatterer in the experimental situation possesses inversion symmetry about some point $\vec{r}_0$ (or at least a sufficiently good approximation to such symmetry). As is usual, the point $\vec{r}_0$ is not known with precision a priori. As we have stated, our purpose he is to apply the results of the last section to the determination of $\vec{r}_0$. Here, we consider only longitudinal-to-longitudinal scattering, i.e., the incident wave is longitudinally polarized and only the longitudinal component of the scattered wave is observed. The extension of the treatment to other polarizations is obvious.

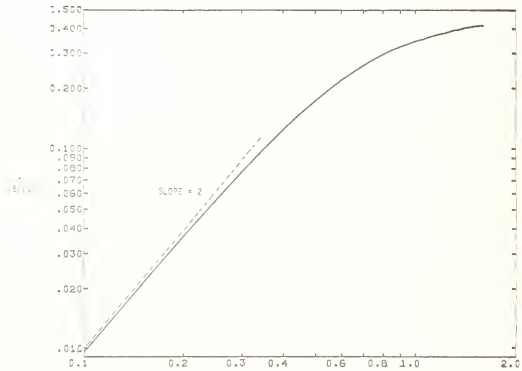

Figure 2. Magnitude of scattering amplitude vs. ka - $\ell \to \ell$ backscatter from spherical B_4C inclusion in SiC matrix.

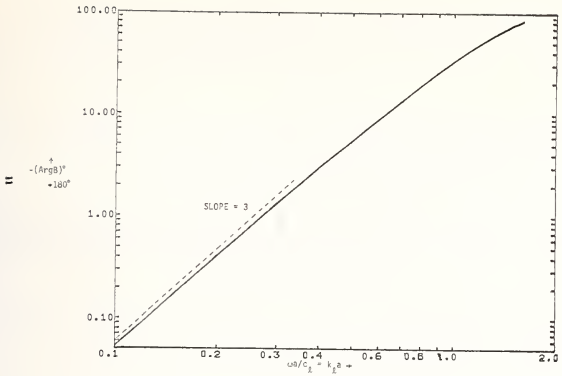

Figure 3. Phase shift vs. ka - $\ell \to \ell$ backscatter from spherical B_4C inclusion in SiC matrix.

Let us denote the experimentally determined phase shift, using $\vec{r} = 0$ as the origin, by γ' the theoretical phase shift, using $\vec{r} = \vec{r}_0$ as the origin, by γ. It is easy to show that, de from experimental error,

$$\gamma' = \gamma + \frac{\omega}{c_\ell} (\vec{e}^s - \vec{e}^i) \cdot \vec{r}_0 \ . \tag{31}$$

hence

$$\frac{\partial \gamma'}{\partial \omega} = \frac{\partial \gamma}{\partial \omega} + \frac{1}{c_\ell} (\vec{e}^s - \vec{e}^i) \cdot \vec{r}_0 \ . \tag{32}$$

ng a result of the last section, namely $\lim_{\omega \to 0} \partial\gamma/\partial\omega = 0$, we obtain

$$\lim_{\omega \to 0} \frac{\partial \gamma'}{\partial \omega} = \frac{1}{c_\ell} (\vec{e}^s - \vec{e}^i) \cdot \vec{r}_0 \ . \tag{33}$$

we perform three scattering experiments characterized by a linearly independent set of tors $\vec{e}^s - \vec{e}^i$, we then can determine the position $\vec{r}_0$ of the center of symmetry.

Of course, it is not possible in an experimental situation to take the limit $\omega \to 0$. A ctical procedure would be to fit an expression of the form (23), i.e.,

$$\gamma' = \mathrm{Arg}B_2 + \gamma_1 \omega + \gamma_3 \omega^3 \tag{34}$$

the experimental phase shift data in an accessible range of frequency not too far above the Rayleigh regime. The 0th degree term $\mathrm{Arg}B_2$ is 0 or π and the correct choice of these alternative values may be known a priori. The adjustable coefficients γ_1 and γ_2 can be calculated by a standard least square procedure. Clearly the value of γ_1 is the quantity of interest. The specific example given in figure 3 gives some idea of how high we can take the upper limit of the accessible range of frequency without encountering significant deviations

between (34) and experimental data. It is clear in this example that the neglected term i.e. $O(\omega^5)$, does not contribute significantly below $k_\ell a = \omega a/c_\ell \sim 0.4$.

References

[1] Richardson, J. M., Scattering of elastic waves from symmetric inhomogeneities at low frequencies, to be submitted to J. Appl. Phys.

[2] It is assumed implicitly that the time factor is exp(-iωt).

[3] Gubernatis, J. E., Krumhansl, J. A., and Thomson, R. M., Interpretation of elastic wave scattering theory for analysis and design of flaw characterization experiments: I. Long wavelength limit. Los Alamos Scientific Laboratory Report, LA UR-76 - 2546 (1976).

[4] This convention becomes inapplicable if there is a zero of B on the real ω-axis (or, as a practical matter, near this axis). In such a case it may be useful to consider continuity with respect to $\vec{a}$ and/or $\vec{b}$.

[5] That is, the computational results are exact except for the truncation of an infinite series and the inevitable round-off error.

tional Bureau of Standards Special Publication 596, Ultrasonic Materials Characterization,
Berger and M. Linzer, eds., Proceedings of the First International Symposium on Ultrasonic
terials Characterization held at NBS, Gaithersburg, Md., June 7-9, 1978. Issued
vember, 1980.

A NOTE ON NONDESTRUCTIVE DETECTION OF VOIDS BY A HIGH FREQUENCY INVERSION TECHNIQUE[1]

Jack K. Cohen and Norman Bleistein

Department of Mathematics
University of Denver
Denver, CO 80202

A direct approach is described for the solution of the inverse problem for the nondestructive detection of scatterers of high contrast, such as voids or strongly reflecting inclusions.

When a wave (e.g., acoustic, elastic, electromagnetic) propogates through a medium, the ve is deformed by irregularities in that medium. The deformation of the probing wave is aracteristic of the irregularity. This is the basis of a method for nondestructive aluation of solid materials. A known high frequency probing wave is introduced into the dium. The wave scattered by the irregularity is observed. The nature of the irregularity to be inferred from the nature of the scattered wave.

The type of problem we have described here is called an inverse problem. The rresponding direct problem would be to find the scattered wave given the "incident wave" robe) and the irregularities of the medium. Inverse problems are often attacked directly; i.e., one solves the direct problems for prescribed irregularities, seeking an regularity for which the scattered wave most nearly approximates the data.

In contrast, we are engaged in research on direct solutions of the inverse problem. An verse method for nondestructive detection of scatterers of high contrast, such as voids or rongly reflecting inclusions, will be described here. This method is known by the acronym FFIS, which stands for Physical Optics Far Field Inverse Scattering. In this method, the ase and range normalized far field scattering amplitude is shown to be directly portional to the Fourier transform of the characteristic function of the scatterer. The aracteristic function is equal to unity inside the region occupied by the scatterer and is ro outside. Thus, knowledge of this function provides a description of the scatterer. wever, for bandlimited data, it is easier to reproduce a directional derivative of the aracteristic function. These ideas were developed in a series of papers [1,2,3,4,5][2].

The specific application discussed here is to describe flaws contained in a sphere. servations of backscatter acoustic signals are made on the surface of the sphere. The llowing formula may be derived for the radial derivative of the characteristic function ee [2]):

$$R\hat{x} \cdot \nabla\gamma(\underline{x}) = A \int_{\Omega} d\Omega \; \hat{x} \cdot \hat{x}_o \, \frac{\partial V}{\partial t}\left(\hat{x}_o, \, 2(x_o - \underline{x} \cdot \hat{x}_o)/c\right).$$

is research was partially sponsored by the Center for Advanced Nondestructive Evaluation erated by the Science Center, Rockwell International, for the Defense Advanced Research ject Agency and the Air Force Materials Laboratory under Contract No. F33615-74-5180 and tially supported by Department of Energy under Contract No. EY-76-F-02-2482.

gures in brackets indicate the literature references at the end of this paper.

Here, R is the unknown reflection coefficient, γ is the unknown characteristic function, $(\hat{})$ denotes unit vector, A is a known constant which depends on the source configuration, V is the range normalized impulse response in the direction $\hat{x}_o$ at time $t = 2(x_o - \underline{x} \cdot \hat{x}_o)/c$, x_o is the radius of the observation sphere and the integration domain Ω is the unit sphere with variable $\hat{x}_o$.

Thus, implementation of the POFFIS result requires an integration over the directions of observation of the scattered data. A computer implementation of this result for "pitch-catch" or backscatter type probing has been developed. This program incorporates such real world constraints as data being bandlimited and aspect angle limited.

The output of the program is both numerical and graphical, displaying the scatterer through a series of two dimensional "slices" depicting its boundaries in various planes. The program has been tested on synthetic data with frequencies on the order of 10^7 Hz, while varying other of the natural dimensionless parameters of the problem.

In the figures here, the radial derivative is plotted in a longitudinal slice through the center at a set of sample latitudes. The derivative is plotted normal in the radial line at each latitude. (see fig. 1.)

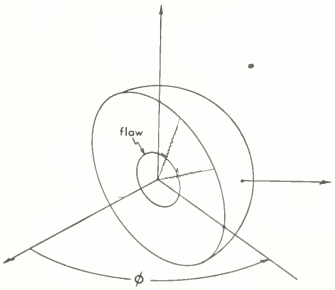

Figure 1. Longitude of tabulated derivative.

To test the method, synthetic backscattered data from a spherical void of 400 μm was used. The value of the dimensionless parameters "ka" was about seven. Tests were run with one hundredth observations and two hundred observations around the surface of the observatic sphere. Output of the type in figure 1 is plotted for a slice at longitude 0° for several latitudes. Figure 2 shows the result for 100 observations; figure 3 shows the result for 2(observations. The 400 μm circle is shown in each figure and excellent agreement is demonstrated.

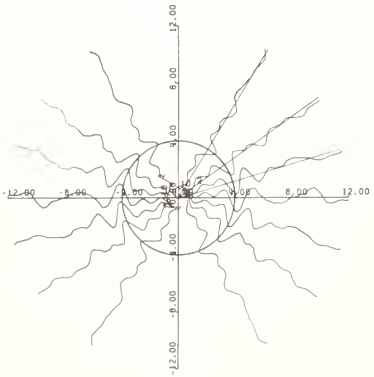

Figure 2. Model: 400 μm circle. Longitudinal 0°, M1=7.

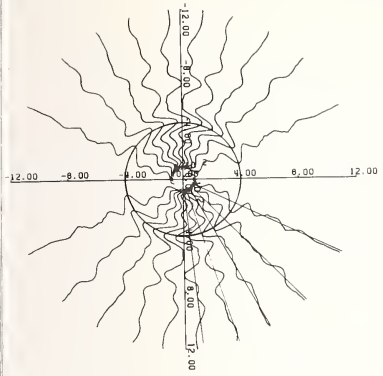

Figure 3. Model: 400 μm circle. Longitudinal 0°, Ml=10.

References

1] Bojarski, N. N., Three dimensional electromagnetic short pulse inverse scattering, Syracuse University Research Corporation, Syracuse, New York, NTIS #AD-845 126 (1967).

2] Bleistein, N., Physical optics far field inverse scattering in the time domain, J. Acous. Soc. Amer., 60, 1249-1255 (1976).

3] Mager, R. D. and Bleistein, N., An approach to the limited aperature problem of physical optics farfield inverse scattering, IEEE Trans. Ant. and Prop. (in press).

4] Armstrong, J., An Analysis of the Aperture Limited Fourier Inversion of Characteristic Function, Thesis, in preparation (1977).

5] Bleistein, N. and Cohen, J. K., Application of a new inverse method to nondestructive evaluation, Denver Research Institute Report #MS-R-7716 (1977).

tional Bureau of Standards Special Publication 596, Ultrasonic Materials Characterization,
Berger and M. Linzer, eds., Proceedings of the First International Symposium on Ultrasonic
terials Characterization held at NBS, Gaithersburg, Md., June 7-9, 1978. Issued
vember, 1980.

MOTION PICTURE OF THE COMPUTER SIMULATION OF ELASTIC WAVES GENERATED BY TRANSDUCERS

Kasaburo Harumi

Faculty of Technology
Department of Mathematics and Physics
Faculty of Technology
Gunma University
Tenjincho 1-5
Kiryu, Gunma, Japan

and

Tetsuo Saito and Toshiaki Fujimori

Shimizu Construction Co., Ltd.
Research Laboratory
Echujima 3-4
Kotoku, Tokyo, Japan

A motion picture of the computer simulation of elastic waves in a half space of iron is represented. By the use of the finite difference method, the displacement vector diagrams of elastic waves are pictured for the problems of radiation from a normal pressure transducer and reflection by a rigid ribbon. The mechanism for the generation of transverse waves and surface waves is shown in the diagrams.

1. Introduction

Recently, numerical experiments by computer have been widely used in various fields 2][1]. In a previous paper [3], we reported on an analysis of the nearfield of elastic es generated by a transducer. Thereafter, we investigated computer simulation of elastic es [4,5]. Numerical experiments were found to have the following advantages over conven- nal laboratory experiments:

1) all information at each point in a solid at any time is available;

2) there is no difficulty in changing the experimental conditions, even in cases which are impossible to achieve in the laboratory;

3) it is very easy to see the details of the motion, if we take small enough mesh sizes and carefully investigate the displacement diagrams for each time;

4) and the mechanism of elastic wave propagation in a solid can be easily understood from items 1) and 3).

For these reasons, illustrating the results of numerical experiments in a diagram is a y effective means of understanding elastic wave propagation in a solid. In particular, development of numerical experiments can make possible the analysis of sound fields when oretical approaches are too difficult. Numerical experiments can thus be considered to be uated between theory and experiment. As an example of such a numerical experiment, a film ut the sound field near the source and the wave scattering by an obstacle has been pro- ed. This work should lead to a better understanding of elastic wave propagation and uld improve our understanding of ultrasonic testing.

gures in brackets indicate the literature references at the end of this paper.

2. Fundamental Equations and Finite Difference Approximation

The fundamental equations of elastic waves for the displacement, u, are given by:

$$\frac{\partial^2 u}{\partial t^2} = (\lambda+2\mu)\ \mathrm{grad}(\mathrm{div}\ u) + \mathrm{rot}\ \mathrm{rot}\ u \tag{1}$$

where ρ is the density, and λ and μ are the Lame's constants.

For simplicity of the analysis, we consider the two dimensional fundamental equations rectangular x-y coordinates,

$$\frac{\partial^2 u}{\partial t^2} = v_L^2 \frac{\partial^2 u}{\partial x^2} + (v_L^2 - v_T^2)\frac{\partial^2 v}{\partial x \partial y} + v_T^2 \frac{\partial^2 u}{\partial y^2}$$

$$\frac{\partial^2 v}{\partial t^2} = v_T^2 \frac{\partial^2 v}{\partial x^2} + (v_L^2 - v_T^2)\frac{\partial^2 u}{\partial x \partial y} + v_L^2 \frac{\partial^2 v}{\partial y^2} \tag{2}$$

where u and v are the displacements in the x and y directions, and the velocities v_L and v_T of longitudinal and transverse waves are given by

$$v_L^2 = \frac{\lambda+2\mu}{\rho}\ , \qquad v_T^2 = \frac{\mu}{\rho}\ .$$

Boundary conditions on the surface (y = 0) are given as follows when the normal stress T_{yy} is applied on the ribbon source,

$$\begin{aligned} T_{yy} &= (v_T^2 - v_T^2)\frac{\partial u}{\partial x} + v_T^2 \frac{\partial v}{\partial y} = 0 \qquad (\ |x| > a) \\ &= f(t)\ (\ |x| < a,\ t>0) \\ T_{xy} &= \frac{\partial u}{\partial y} + \frac{\partial v}{\partial x} = 0 \quad . \end{aligned} \tag{3}$$

By the use of the centered finite difference method, eqs. (2) and (3) are written as follows:

$$\begin{aligned} u(x,y,t+k) = {} & 2u(x,y,t) - u(x,y,t-k) + (v_L k/h)^2 [u(x+h,y,t) - \\ & 2u(x,y,t) + u(x-h,y,t)] + (v_L^2 - v_T^2)/4(k/h)^2 \\ & [v(x+h,y+h,t) - v(x+h,y-h,t) - v(x-h,y+h,t) + \\ & v(x-h,y-h,t)] + (v_T\ k/h)^2 [u(x,y+h,t) - 2u(x,y,t) \\ & + u(x,y-h,t)] \end{aligned} \tag{4}$$

$$V(x,y,t+k) = 2v(x,y,t) - v(x,y,t-k) + (v_T k/h)^2[v(x+h,y,t) - 2v(x,y,t) + v(x,y-h,t)] + (v_L^2 - v_T^2)/4\cdot(k/h)^2 [u(x+h,y+h,t) - u(x-h,y+h,t) - u(x+h,y-h,t) + u(x-h,y-h,t)] + (v_L k/h)^2[v(x,y+h,t) - 2v(x,y,t) + v(x,y-h,t)]$$

$$(v_L^2 - 2v_T^2)[u(x+h,0,T) - u(x-h,0,t)]/2h + v_L^2[v(x,h,t)-v(x,-h,t)]/2h = 0 \quad (x > a)$$

$$= f(t) \quad (x < a) \qquad (5)$$

$$[u(x,h,t) - u(x,-h,t)]/2h + [v(x+h,0,t) - v(x-h,0,t)]/2h = 0$$

At first, we take the displacements u = v = 0, and obtain the value of displacements for ach time step from eqs. (4) and (5). By the symmetry of the displacements with respect to he y axis, we use the relations v(-h,y,t) = v(h,y,t) and u(-h,y,t) = -u(h,y,t).

Erom the stability condition of the finite difference method, we may determine the ratio f the mesh size k in the time domain to the mesh size h in space as follows [6,7]:

$$\frac{v_L^2 k^2}{h^2} = (1 + (v_S/v_L)^2)^{-1} \quad . \qquad (6)$$

Since we assume the medium is steel, the velocity ratio of transverse to longitudinal aves is taken as 0.55. Therefore, the stability condition (6) gives the criterion $v_L^2 k^2/h^2$ 0.75. Consequently, once we select a mesh size k in the time domain the mesh size h in pace is determined accordingly, or vice versa.

3. Numerical Calculations

The numerical calculation is made in two dimensions using rectangular x-y coordinates. he force function f(ε) is assumed to be sinusoidal with a period of 2π. We select the mesh ize in time domain k to be one-twelfth of the period, i.e., k = π/6. The mesh size in space omain, h, is determined by stability consideration derived in the previous section. An nfinitely long ribbon source with width 2a = 17h is assumed. If the wavelength, λ_L, of the ongitudinal wave is chosen to satisfy the relation, $2\pi a/\lambda_L = k_L a = 5$, where k_L is the wave-umber of the longitudinal wave, then in terms of physical parameters for a 1 MHz transducer nd in iron we have:

$$v_L \simeq 6 \text{ mm}/\mu\text{s},$$

$$\lambda_L \simeq 6 \text{ mm}, \; k_L = \frac{\pi}{3} \text{ mm}^{-1},$$

$$k \simeq 1/12 \; \mu\text{s},$$

$$h \simeq \frac{(6)\cdot(1/12)}{\sqrt{0.75}} = 1/\sqrt{3} \text{ mm},$$

and $2a = 17h \simeq 10$ mm.

By the use of finite difference method we obtained the displacement vectors at every point for a fixed time t, and they are illustrated with COM (computer output microfilm). A motion picture is then made with pictures of the displacement vector fields corresponding to a sequence of time t.

4. Explanation of Picture and Analysis of Elastic Waves

The film is composed of five parts. In each case the sequence number n in time space (t = nk) is denoted at the upper right corner. The displacement vectors for every lattice point are displayed in the vector diagrams, and as the diagram is symmetric with respect to the y axis, only the right quarter space is represented. The solid line denoted by SOURCE shows the transducer, and the characters C.L. at the upper left corner denote the center lin The vectors with dot marks are the vectors for transverse waves, and are enlarged by 1.8 times the longitudinal wave vectors. The surface wave vectors are distinguished by asterisk

1) Continuous sinusoidal normal stress applied on the source.

1-A vector diagram of displacements of elastic waves transmitted from the transducer (Film No. 1).

The vector diagram at the moment t = 102k is shown in figure 1. Here, vectors near the center line with the vector parallel to the center line denote the main part of the longitudinal wave. The main part of the transverse wave TM is distinguished by the vectors with dots; they have the vector component perpendicular to the direction of propagation. We can also observe the side of transverse wave TS, which is predicted by the directivity pattern o radiation from a small transducer in figure 2 [8]. As the speed of a longitudinal wave is faster than the speed of a transverse wave, the main part of the transverse waves overlap into the longitudinal waves. When two waves overlap, the main part of the transverse wave diminishes, but the longitudinal waves past the transverse waves appear again.

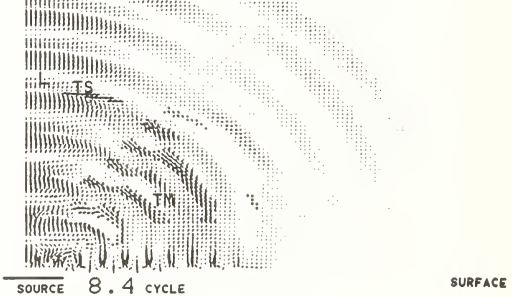

Figure 1. Vector diagram for case 1-A. L is the longitudinal wave, TM is the main part of the transverse wave, TS is the side lobe of the transverse wave.

1-B Vector diagram near the source (46 x 38h).

In order to see the details of the motion of elastic waves, we enlarge the small region ear the source, $0 < x < 46h$ and $0 < y < 38h$, (fig. 3). In this picture, we can see the echanism of generation of transverse waves. In the first place, positive pressure is applied r a half cycle, which produces the displacement vectors with positive y components near the

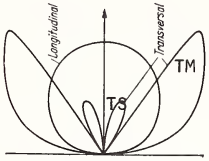

Figure 2. Directivity pattern of a small transducer.

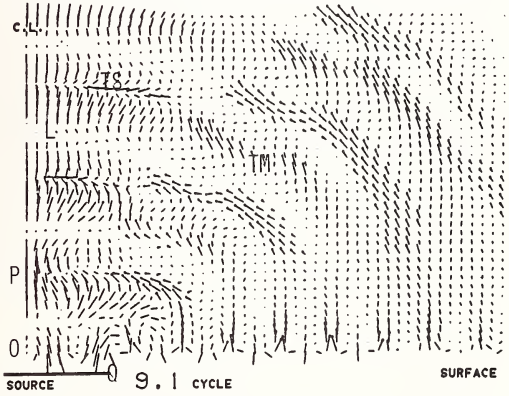

Figure 3. Vector diagram near the source for case 1-B. T is the commencement of the transverse wave, S is the surface wave, TM is the main part of the transverse wave, and TS is the side lobe of the transverse wave. The triangular region OPQ is the domain in which there exists no transverse wave.

urce. After the half cycle ($n \geq 7$), a negative normal force is applied until one cycle anspires ($n = 12$), which produces the displacement vectors with negative x and y components shown in the appended figures. These vectors with negative x or y components form the arc and become the transverse waves T [5]. The diminishing and reappearing of the main part the transverse waves are the same as in 1-A. The elliptic motion of displacement of rface wave S should be pointed out. In this case, the near field distance is given by $= a^2/\lambda_L = 7h$, and within the near field distance, we find a very complex behavior of dis-

acements. Because of alternative production of the longitudinal wave and the transverse

wave with arc-shaped vectors, and of the influence of the surface wave as well, we find a very complex behavior of displacements witnin the near field distance. As is pointed out in the former paper [3], we cannot observe the transverse waves in the triangular region OPQ in figure 3, because the transverse waves grow up from the arc-shaped vectors outside this region. We may observe the elliptic motion of displacements near the center line which is caused by the interaction of the longitudinal and transverse waves in the side lobe TS ($5h \leq x < 10h$, $20h \leq y < 30h$) in figure 3.

1-C Lattice representation near the source ($46h \geq x \geq 38h$).

The deformation of an elastic body near the source is shown in figure 4. First, a positive pressure is applied to the source, and the body is compressed and shrunk. After a half cycle, a negative pulling force is applied, and the body is stretched and expanded. When this process is repeated, the longitudinal waves propagate with both compressed and expanded parts, as shown in figure 4. The deformations of the transverse waves are very complicated, but we can see the shearing motion of the transverse waves. We also recognize clearly the deformation of the surface that is quite similar to that of the water surface wave.

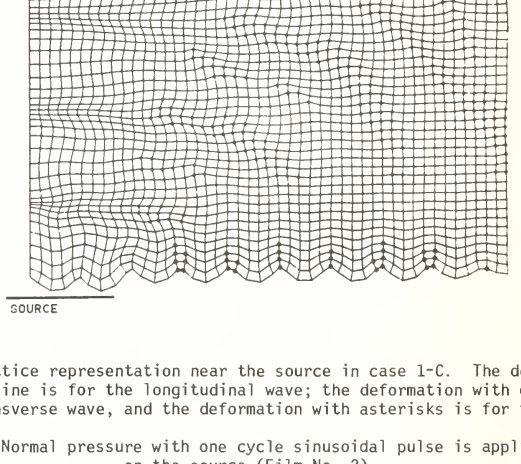

Figure 4. Lattice representation near the source in case 1-C. The deformation near the center line is for the longitudinal wave; the deformation with dot marks is for the transverse wave, and the deformation with asterisks is for the surface wave.

2) Normal pressure with one cycle sinusoidal pulse is applied on the source (Film No. 2).

At first the normal pressure with one cycle sinusoidal pulse is applied to the source, and after one cycle, no pressure is applied. The vector diagram at the moment $t = 115k$ is shown in figure 5. In this case, the transverse wave propagates with a speed equal to half the velocity of that of the longitudinal wave. In this case, the transverse wave obviously appears in front of the source.

3) Normal pressure with four cycle sinusoidal burst is applied to the source (Film No. 3).

At first, the normal pressure with four cycle sinusoidal burst is applied to the source and after four cycles no pressure is applied. The diagrams are the same as those for the

ontinuous wave (case 1) until the time step t = 48k, but after this period, the longitudinal ave propagates faster than the transverse wave, and the two waves separate from each other s shown in figure 6. After the two waves have separated, the side lobe of the transverse ave TS is observed in front of the source.

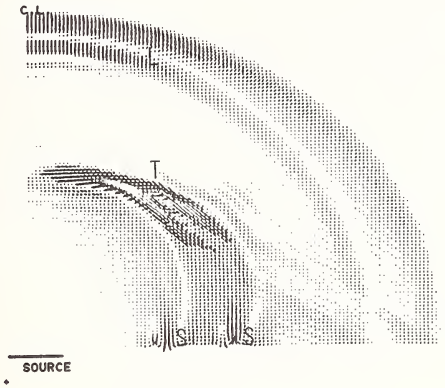

Figure 5. Vector diagram of displacements in case 2. L is the longitudinal wave, T is the transverse wave and S is the surface wave.

Figure 6. Vector diagram of displacements in case 3. TM is the main part of the transverse wave and TS is the side lobe of the transverse wave.

4) Reflection of the longitudinal wave by a rigid ribbon normally placed on the center line (Film No. 4).

A rigid ribbon of width 2d = 17h, whose displacement is assumed to be zero on its surface, is placed normally on the center line at y = 43h and $-8.5h \leq x \leq 8.5h$. The longitudinal wave of Film No. 2 is scattered by the rigid ribbon, and the reflected longitudinal wave RL and reflected transverse wave RT are shown in figure 7. The directivity patterns for the two scattered waves are shown in figure 8 [9], where the broken line denotes the transverse wave. This curve has maxima and minimum at A, B, C, and D. The ratio of maxima and minimum of this curve at A, B, C, and D is given by 2.7:2.0:4.0:3.0, whereas the ratio of maxima and minimum of the transverse wave vectors at A, B, C, and D in figure 7 is given by 0.8:0.6:1.2:1.0. These two ratios show very good agreement. However, the values $k_L d$ are given by $k_L d = 5$ in figure 7 and $k_L d = 4$ in figure 8, where d is the half width of the ribbon. The result in figure 8 is obtained from theory, and the ratio of strength of longitudinal and transverse wave varies according to the distance from the ribbon; therefore, it is rather difficult to get the strength ratio of the two waves. But it is rather easy to obtain the absolute value of each wave in figure 7. The details of the mechanism of scattered wave are explained in the film.

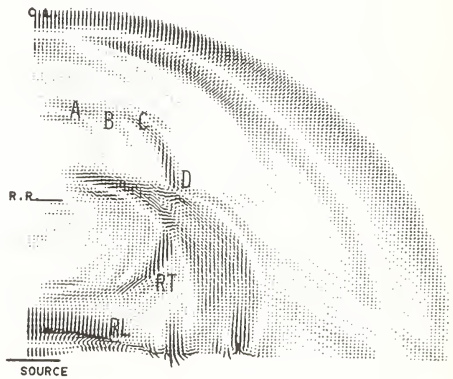

Figure 7. Vector diagram of displacements of the reflection of the longitudinal wave by a rigid ribbon in case 4. RL is the reflected longitudinal wave and RT is the reflected transverse wave. A, B, C, and D are the maxima and minimum of the transverse wave which correspond to A, B, C, and D in figure 8.

5) Reflection of the longitudinal wave by a rigid ribbon placed in parallel on the center line. (Film No. 5).

A rigid ribbon is placed in parallel on the center line at x = 0 and $38h \leq y \leq 48h$. The longitudinal wave of Film No. 2 (one cycle sinusoidal pulse) is scattered by the ribbon, and the reflected longitudinal wave RL and transverse wave RT are shown in figure 9 (t = 101k); in this figure, we may see the very weak reflected longitudinal wave just reaching the surface. Waves are scattered near the ribbon so as to remove the displacement on the surface of ribbon; the scattered longitudinal wave is produced mainly at the tip of the ribbon. The other scattered wave is produced on the whole surface so as to remove the displacement on the

whole surface of ribbon. Therefore, we observe the strong scattered wave near the side face of the ribbon. When the scattered wave propagates in the direction normal to the ribbon surface, as the displacement of scattered wave has negative y components, the displacement of the scattered wave is perpendicular to the direction of propagation. Hence, the strong scattered wave becomes a transverse wave. This strong transverse wave has maximum displacement at A in figure 9, which corresponds to the maximum of the scattered transverse wave A in figure 10 [10].

The ratio of the two maxima A and B of the transverse wave vectors is given by 2.5:1.0 in figure 10, and the ratio of two maxima of the broken line at A and B in figure 10 is given by 3.6:1.2. The values $k_L d$ are given by $k_L d = 3$ in figure 9 and $k_L d = 1$ in figure 10.

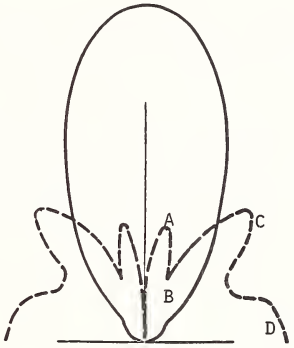

Figure 8. Directivity pattern of the scattered wave for the incident longitudinal wave. Broken lines is for the transverse wave, and A, B, C, and D are the maxima and minimum of the transverse wave.

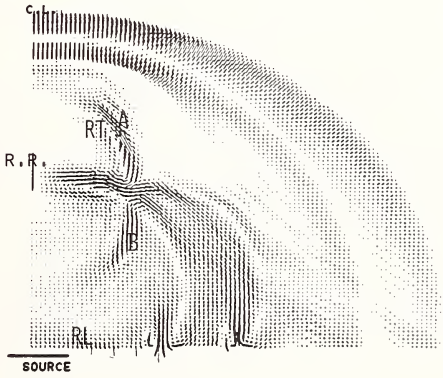

Figure 9. Vector diagram of displacements of the reflection of the longitudinal wave by a rigid ribbon in case 5. RL is the reflected longitudinal wave, and RT is the reflected transverse wave. A and B are the two maxima of the reflected transverse wave.

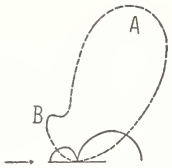

Figure 10. Directivity pattern of the scattered wave by a rigid ribbon placed in parallel with the propagation direction. The broken line is for the transverse wave.

5. Conclusion

The results of numerical experiments on elastic waves show that the motion of elastic waves in solids, which is impossible to see by conventional experiments, is easily observed by computer simulation. We can especially observe the movement dynamically by using movie film. The dynamic motion of the waves is often misunderstood if it is observed statically. Moreover, the theoretically difficult problems such as one-cycle transient stress wave problems and four-cycle stress wave problems may be analyzed easily. By observing the film repeatedly, the following observations may be made:

1) we can observe the displacements of the side lobes of the transverse wave in front of the source, which undergo elliptic motions due to the interaction with longitudinal waves;

2) in the case of continuous sinusoidal excitation, the transverse waves repeatedly appear and disappear by overlapping with the longitudinal waves;

3) the mechanism of the generation of the transverse wave has been determined as shown in the Appendix and in the previous paper [5];

4) in the case of reflections, it is easy to obtain the strength of each wave by the numerical experiment rather than by theory;

5) the movement of each point at each time is obtained from the diagram and the film, which facilitates the analysis of mechanisms to a great extent.

As described above, it becomes obvious that the numerical experiment is quite effective for the analysis and understanding of the mechanisms of elastic wave propagation. Furthermore, not much cost is required for the numerical experiment compared with that in a laboratory experiment, so that it will be a promising field for the study of elastic wave behavior in regions not covered by theory and experiment.

The authors express their hearty gratitude to Mr. Y. Kobayashi for his advice and help in producing the film and Miss K. Hoshi and Miss K. Kamiyama for their help during this work. Part of the computation was carried out by means of the HITAC 8800 in Tokyo University.

References

[1] Alterman, Z. and Karal, F. C., Jr., Bull. Seismol. Soc. Amer., 58, 367 (1968).

[2] Alterman, Z. S. and Lowenthal, D., Geophys. J. Royal Astron. Soc., 20, 101-126 (1970).

[3] Harumi, K., Suzuki, F., and Sato, Y., J. Acoust. Soc. Amer., 53, 660-664 (1973).

[4] Harumi, K., Saito, T., and Habuka, Y., Graphic display of the computer simulation of elastic wave No. 1, in Report of the Meeting of Ultrasonic Testing in Japan 2623, in Japanese (1977).

[5] Harumi, K., Saito, T., Kobayashi, M., and Habuka, Y., Graphic display of the computer simulation of elastic wave No. 2, Mechanism of Generation of Transverse Wave and Surface Wave, in Report of the Meeting of Ultrasonic Testing in Japan 2632, in Japanese (1977).

[6] Mitchell, A. R., Computational Methods in Partial Differential Equations, p. 34 (John Wiley, New York, NY, 1969).

[7] Harumi, K. and Toda, Y., Improvement of Stability Condition by the Use of Physical Meaning, Topics in Numerical Analysis III (Elsevier Publ. Co., 1977).

[8] Roderick, R. L., The radiation pattern from a rotationally symmetric stress source on a semi infinite solid, Metals Research Report Brown University 1950. Referenced by J. and H. Krautkramer, Ultrasonic Testing of Materials, p. 69 (Springer-Verlag Berlin, 1977).

[9] Harumi, K., Scattering of plane waves by a rigid ribbon in a solid, Appl. Phys., 32, 1494 (1961).

10] Ibid., p. 1495.

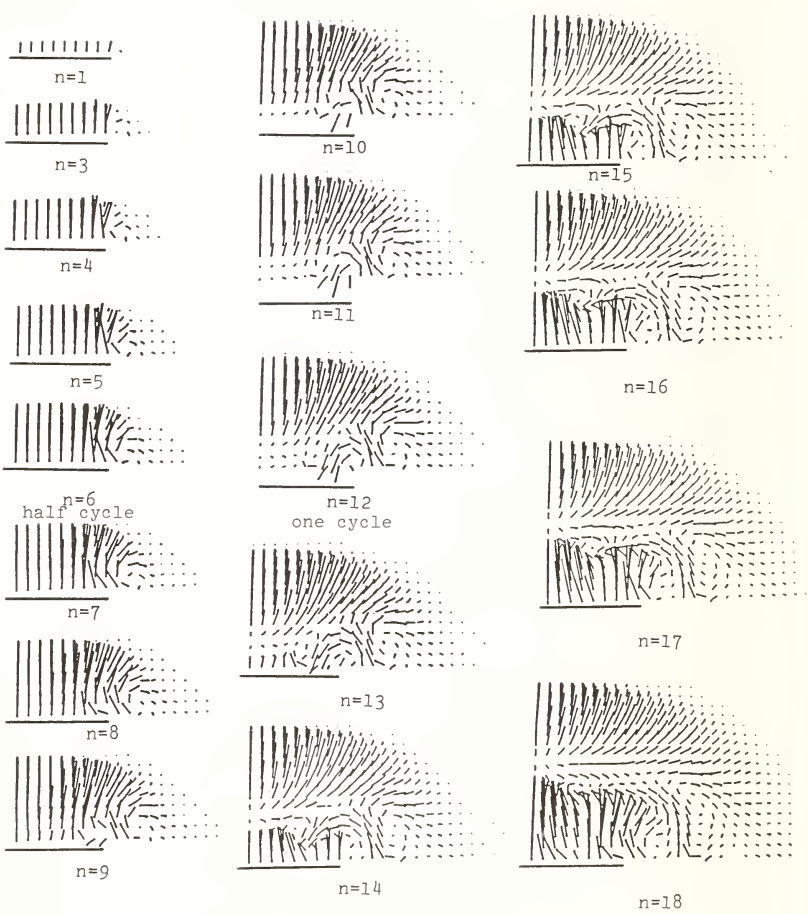

Vector diagrams of displacements near the source. They are shown from the beginning of normally-applied sinusoidal stress to one and a half cycles; n denotes the lattice number in time space, and $t = nk$, where $k = \pi/6$; A denotes the arc-shaped vectors which grow into the transverse wave T; S is the surface wave vector.

National Bureau of Standards Special Publication 596, Ultrasonic Materials Characterization, H. Berger and M. Linzer, eds., Proceedings of the First International Symposium on Ultrasonic Materials Characterization held at NBS, Gaithersburg, Md., June 7-9, 1978. Issued November, 1980.

ULTRASONIC CHARACTERIZATION OF AUSTENITIC WELDS[1]

L. Adler, K. V. Cook and D. W. Fitting

Metals and Ceramics Division
Oak Ridge National Laboratory
Oak Ridge, TN 37830

Nondestructive evaluation of austenitic stainless steel weld metal is a very difficult problem. Mechanical anisotropy appears to be a major contribution and is caused by preferred local orientation of elongated subgrains and preferred crystallographic orientation. The result of this anisotropy is the directional dependence of the ultrasonic velocities (shear and longitudinal) and ultrasonic attenuation. The directional dependence of these ultrasonic parameters causes large errors in locating and sizing flaws in welds. Initial studies [1][2] were carried out in a type 308 stainless steel electroslag weld to characterize this anisotropy. The apparent symmetry in the macrostructure of the electroslag weld leads us to expect orthotropic symmetry in elastic constants. A technique was developed to measure variations in velocity and attenuation with direction. The velocity data compared favorably to theoretical calculations using this orthotropic model. From the velocity data all elastic constants and engineering constants for this weld were determined. Studies of other types of welds showed that orthotropic symmetry is typical of austenitic welds. Data will be presented to show how anisotropy affects defect location and sizing in welds.

1. Introduction

The inspection of austenitic steels with welded or cast structures using ultrasonic echniques is often of limited value. Inspectability can vary on apparently identical pecimens; therefore, we initiated some basic studies in an attempt to correlate theoretical nd experimental results for nondestructive testing. This paper describes some of the work lone at Oak Ridge National Laboratory to gain an understanding of the basic weld structure and ts effects on ultrasonic inspectability and flaw characterization.

In austenitic stainless steels, grain growth is easy in the [001] direction and, consequently, when randomly oriented grains in base material begin to grow into fused metal, ompetitive growth processes favor crystals oriented in the [001] direction, parallel to the olidification direction (fig. 1). The microstructure within a short distance from the fusion ine consists predominantly of elongated grains having the favorable growth orientations and aving boundaries and subboundaries parallel to the local solidification direction. These actors produce mechanical anisotropy in the stress-strain relationship. Consequently, both elocity and attenuation of the ultrasonic wave through such material will be direction dependent. The objective of this paper is (a) to model the anisotropy for welds, (b) to test he model by ultrasonic techniques, and (c) to show how proper weld characterization can lead o better ultrasonic inspectability.

[1]Research sponsored by the Division of Reactor Research and Technology, U.S. Department of Energy, under contract W-7405-eng-26 with Union Carbide Corporation.

[2]Figures in brackets indicate the literature references at the end of this paper.

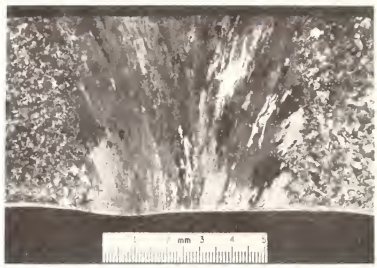

Figure 1. Macrograph of cross section cut in a plane normal to the hypothetical 2-axis of figure 2.

2. Theory

2.1. Ultrasonic wave propagation in anisotropic solids with orthotropic symmetry

The apparent symmetry in the macrostructure of an austenitic stainless steel weld suggested the assumption of orthotropic symmetry for the stress-strain relationship. The general relation of stress to strain in matrix notation is

$$\{\sigma\} = [C]\,\{\varepsilon\} \tag{1}$$

where $\{\sigma\}$ is the stress matrix, $\{\varepsilon\}$ is the strain matrix and $[C]$ is the elastic stiffness matrix. For a material with orthotropic symmetry there are nine independent terms in $[C]$:

$$[C] = \begin{bmatrix} C_{11} & C_{12} & C_{13} & 0 & 0 & 0 \\ C_{12} & C_{22} & C_{23} & 0 & 0 & 0 \\ C_{13} & C_{23} & C_{33} & 0 & 0 & 0 \\ 0 & 0 & 0 & C_{44} & 0 & 0 \\ 0 & 0 & 0 & 0 & C_{55} & 0 \\ 0 & 0 & 0 & 0 & 0 & C_{66} \end{bmatrix} \tag{2}$$

The relationship between the elastic stiffness constants and the velocity of the ultrasonic wave is expressed by the Christoffel relation:

$$\begin{vmatrix} \lambda_{11} - \rho V^2 & \lambda_{12} & \lambda_{13} \\ \lambda_{12} & \lambda_{22} - \rho V^2 & \lambda_{23} \\ \lambda_{13} & \lambda_{23} & \lambda_{33} - \rho V^2 \end{vmatrix} = 0 \ , \tag{3}$$

where, for a material with orthotropic symmetry

$$\lambda_{11} = \ell^2 C_{11} + m^2 C_{66} + n^2 C_{55}$$
$$\lambda_{12} = \ell m (C_{12} + C_{66})$$
$$\lambda_{13} = n\ell (C_{13} + C_{55})$$
$$\lambda_{22} = \ell^2 C_{66} + m^2 C_{22} + n^2 C_{44} \qquad (4)$$
$$\lambda_{23} = mn (C_{44} + C_{23})$$
$$\lambda_{33} = \ell^2 C_{55} + m^2 C_{44} + n^2 C_{33}$$

where ℓ, m and n are direction cosines of the propagation direction and ρ is the density of the material. The coordinate system attached to the weld is defined as shown in figure 2. Elements of the elastic stiffness matrix are calculated from measurement of sound velocity in a number of specified directions by application of the following relations:

Table 1. Relationships between elastic stiffness and ultrasonic propagation velocity.

Propagation Direction	Elastic Stiffness Relations[a]
1 axis	$C_{11} = \rho V_{11}^2, C_{66} = \rho V_{12}^2, C_{55} = \rho V_{13}^2$
2 axis	$C_{22} = \rho V_{22}^2, C_{66} = \rho V_{21}^2, C_{44} = \rho V_{23}^2$
3 axis	$C_{33} = \rho V_{33}^2, C_{55} = \rho V_{31}^2, C_{44} = \rho V_{32}^2$
1' axis (Rotation around 3)	$C_{12} = \ell^{-1} m^{-1} [(\ell^2 C_{11} + m^2 C_{66} - \rho V_{11}'^2)(\ell^2 C_{66} + m^2 C_{22} - \rho V_{11}'^2)]^{1/2} - C_{66}$
2' axis (Rotation around 1)	$C_{23} = m^{-1} n^{-1} [(m^2 C_{22} + n^2 C_{44} - \rho V_{22}'^2)(m^2 C_{44} + n^2 C_{33} - \rho V_{22}'^2)]^{1/2} - C_{44}$
3' axis (Rotation around 2)	$C_{13} = n^{-1} \ell^{-1} [(n^2 C_{11} + \ell^2 C_{55} - \rho V_{33}'^2)(n^2 C_{55} + \ell^2 C_{33} - \rho V_{33}'^2)]^{1/2} - C_{55}$

[a]The first subscript on V indicates the direction of propagation and the second subscript indicates the polarization; e.g., V_{31} represents shear velocity propagating in the 3-direction and polarized along the 1-direction. Once the elastic constants are calculated from the relations above, the last three equations can be solved to calculate the variations of the velocities as a function of orientation.

3. Experimental System

An apparatus developed to measure variation of velocity with direction in structured materials is illustrated in figure 3. A cylindrical sample (mounted on a goniometer) is slowly rotated about its axis. Ultrasound is transmitted through the sample on a fixed-distance path from transmitter to receiver. The signal transmitted through the sample is displayed on an oscilloscope, and the variation of velocity is measured by noting the time shift of the ultrasonic waveform. The system is aligned using an aluminum reference cylinder. This technique is capable of detecting velocity variations on the order of 1 percent.

Three cylindrical samples and a cubical sample (fig. 4) are machined from the weld. The three cylinders are selected such that their axes lie along the coordinate axes. The cylinders are used for measurement of the velocity changes with orientation. By rotating each sample about its axis, continuous data may be obtained for longitudinal velocity as a function of orientation in the three orthogonal planes. For example, by rotating the sample about its 2-axis one can obtain not only V_{11} and V_{33}, but also V_{33}' (see table 1) which is required for calculation of the elastic constants. A cube is also fabricated from the weld. Contact longitudinal and shear velocity measurements made on this sample are necessary to convert the relative velocities determined from the cylindrical samples to absolute velocities.

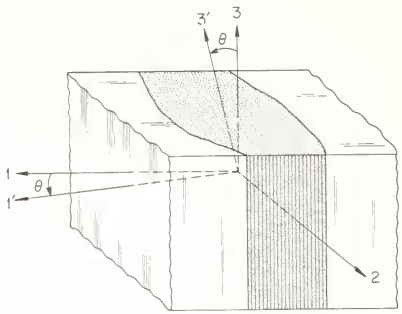

Figure 2. Idealized electroslag weld with coordinate axes. Also shown is a positive rotation around the 2 axis.

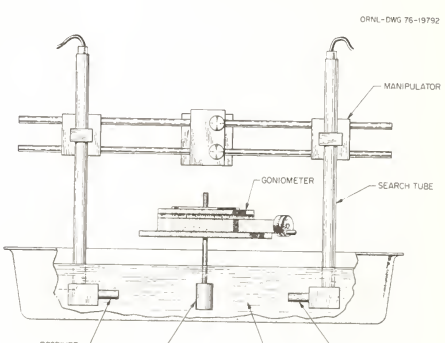

Figure 3. Apparatus for measurement of longitudinal velocity variations in a cylindrical sample.

4. Experimental Results

Two different types of weld material were available: (1) an electroslag single-pass wel of 308 stainless steel and (2) an Inconel 82 multipass weld (47 passes). Plots of theoretical and experimental velocity data for these two welds are given in figures 5 and 6. Figure shows only the planes demonstrating anisotropy. The longitudinal data illustrated are obtain by through-transmission directly across the diameter of the sample. Shear-wave data were obtained from the cubical specimen. The solid curve is theoretical and is obtained by solving the last three equations from Table 1 for the primed velocities. Dots denote experimental results.

Experimental data are also presented in figures 7 and 8 for the variation of attenuation with orientation for the two welds. Again, plots for the single-pass weld do not include the plane of isotropy.

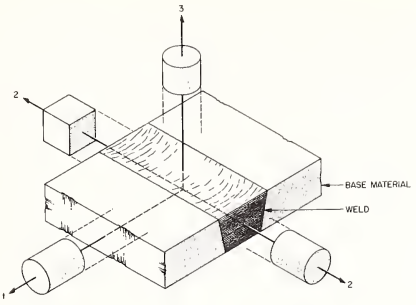

Figure 4. Sample selection for ultrasonic studies from a section of weld.

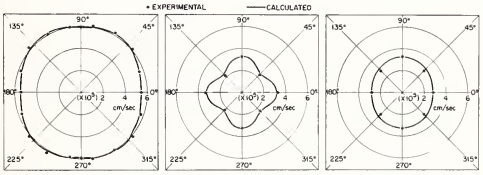

(a)

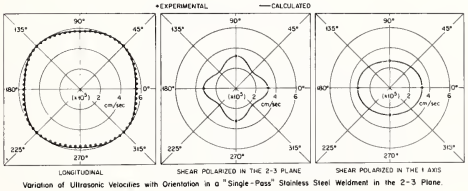

(b)

Figure 5. Anisotropic variation of velocity in type 308 stainless steel weld metal. The solid curves are calculated from the Christoffel relations for the assumed orthotropic symmetry. Points are experimental. (a) In the 1-3 plane. (b) In the 2-3 plane.

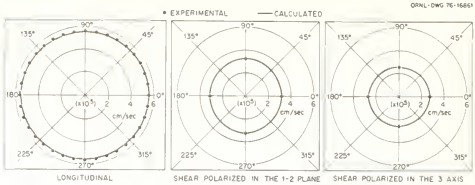

Variation of Ultrasonic Velocities with Orientation in a "Multi-Pass" I-82 Weldment in the 1-2 Plane.

(a)

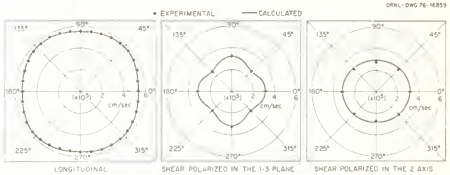

Variation of Ultrasonic Velocities with Orientation in a "Multi-Pass" I-82 Weldment in the 1-3 Plane

(b)

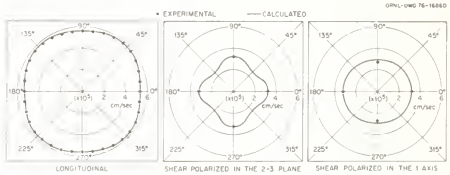

Variation of Ultrasonic Velocities with Orientation in a "Multi-Pass" I-82 Weldment in the 2-3 Plane.

(c)

Figure 6. Variation of ultrasonic velocities with orientation in a multipass Inconel 82 weldment. The solid curves are calculated from the Christoffel relations for the assumed orthotropic symmetry. Points are experimental. (a) In 1-2 plane. (b) In 1-3 plane. (c) In 2-3 plane.

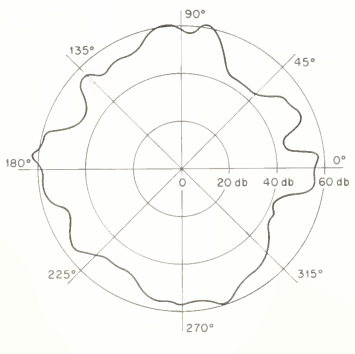

(a)

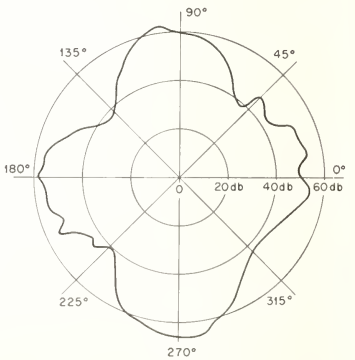

(b)

Figure 7. Variation of relative ultrasonic longitudinal wave attenuation with orientation in a single-pass stainless steel weld. (a) In the 1-3 plane. (b) In the 2-3 plane.

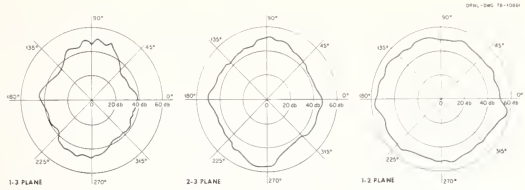

(a) (b) (c)

Figure 8. Variation of relative ultrasonic longitudinal wave attenuation with orientation in a multipass I-82 weld. (a) In the 1-3 plane. (b) In the 2-3 plane. (c) In the 1-2 plane.

5. Effect of Anisotropy on Sizing Defects

It has been shown before that spectra of ultrasonic waves diffracted by defects can be used for size estimation [2,3]. Figure 9 demonstrates the error which could be made in predicting the amplitude spectra of an ultrasonic shear wave diffracted from a disc-shaped flaw if mechanical isotropy were assumed, when instead the material was anisotropic. The spectrum for the highest velocity shown is the true diffracted amplitude distribution when account is taken of anisotropy; that is, the distribution that would be measured. The spectrum in the foreground of the plot is that predicted from the assumption of an isotropic material. The figure dramatically demonstrates the absolute necessity of correcting for velocity variation within the weld. The greatest error results with a 45° diffracted shear wave, because of the large variations in velocity with orientation. It is ironic that this is the most commonly used angle for testing welds. It is possible to misjudge both size and location for a defect in weld by as much as 40 percent unless the correct procedure is followed.

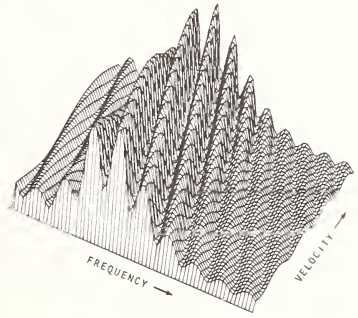

Figure 9. Effect of anisotropy on the amplitude spectrum of a 45° diffracted shear wave in stainless steel weld metal.

6. Summary

Mechanical anisotropy of austenitic stainless steel weld metal causes serious problems with conventional ultrasonic testing methods. A thorough characterization of these welds permits considerable improvement to be made in methods of defect location and sizing.

Analysis of the weld structure leads to the assumption of orthotropic symmetry in elastic constants. This assumption permitted the elements of the stiffness matrix to be determined from only a small number of ultrasonic velocity measurements. The elastic and engineering constants were determined for a single-pass weld of type 308 stainless steel and an Inconel 82 multipass weld. A technique developed to measure variations in velocity and attenuation with direction gave data that compared favorably to theoretical calculations using the orthotropic model.

The effects of anisotropy on sizing defects using ultrasonic frequency analysis was presented. It was found that weld characterization, with calculation of the elastic constants and acoustic velocity, permits corrections to be made which improve sizing accuracy.

The authors wish to thank R. A. Cunningham, Jr. and H. T. Murrin, Jr., for their mechanical design and fabrication contributions. We thank W. E. Deeds and W. A. Simpson for reviewing this paper. We are indebted to J. H. Bratten and other Graphic Arts personnel for their contributions. We also thank Jan Renfro of the Metals and Ceramics Division Reports Office for the typing and preparation of the paper.

References

[1] Dewey, B. R., Adler, L., King, R. T., and Cook, K. V., Measurements of anisotropic elastic constants of type 308 stainless steel electroslag welds, Experimental Mechanics, 17, 420-426 (1977).

[2] Adler, L. and Whaley, H. L., Interference effect in a multifrequency ultrasonic pulse echo and its application to flaw characterization. J. Acous. Soc. Amer., 51, 881-887.

[3] Adler, L. and Lewis, D. K., Diffraction model for ultrasonic frequency analysis and flaw characterization, Materials Evaluation, 35, 51-56 (1977).

National Bureau of Standards Special Publication 596, Ultrasonic Materials Characterization, H. Berger and M. Linzer, eds., Proceedings of the First International Symposium on Ultrasonic Materials Characterization held at NBS, Gaithersburg, Md., June 7-9, 1978. Issued November, 1980.

AUSTENITIC STAINLESS STEEL CASTING INSPECTION POTENTIAL

Joseph L. Rose and Alexander J. Rogovsky

Drexel University
32nd and Chestnut Streets
Philadelphia, PA 19104

and

Peter Wieser

Steel Founder's Society of America
Rocky River, OH 44116

Ultrasonic inspection of stainless steel castings represents one of the most difficult and unsolved problems in nondestructive testing due primarily to the tremendous scattering and absorption of ultrasound by the grain structure. A study has been conducted to determine the variation of ultrasonic attenuation on heat treated and nonheat treated specimens of austenitic stainless steel castings (CN7M) using both immersion and contact pulse-echo techniques at frequencies 1.0, 2.25, 3.5, 5.0, and 10.0 MHz. Measurements showed significant variation in ultrasonic attenuation from one location to another in each specimen. Variation of ultrasonic attenuation depends on frequency and has a range of up to 10-15 dB/cm for the 25.4 mm (one inch) thick material examined. Heat treatment of the specimens did not change the range of attenuation variation. However, some change in the location of maximum and minimum attenuation areas were observed. Ultrasonic wave velocity differences at locations with various attentuation have also been indicated. Careful observation of the micrographs allows us to conclude that there is no significant variation of dendritic structure between heat treated and non-heat treated specimens. The microstructural differences have also been correlated with ultrasonic signal response.

It has been indicated that the ultrasonic attenuation values essentially depend on the grain sizes and the number of grain boundaries. For locations with minimum attenuation, the principal direction of dendrites is oriented in the plane of the ultrasonic wave propagation. For the maximum attenuation location, the principal direction of dendrites appears to be out of the plane of ultrasonic wave propagation.

The potential values and procedures of ultrasonic inspection for austenitic stainless steel castings are discussed. Sample ultrasonic test results and attenuation versus frequency curves are included in the paper along with typical micrographs showing the dendritic type structure, characteristic of the austenitic stainless steel materials.

1. Introduction

Ultrasonic inspection of austenitic stainless steel castings (ASSC) is one of the most difficult and still unsolved problems in NDT due to a complicated microstructure affecting the acoustical properties of these alloys. In spite of such difficulties, the problem has been attracting the attention of many researchers and engineers because of the excellent service features and anticorrosion strength of austenitic stainless steel structures [1-16][1].

[1]Figures in brackets indicate the literature references at the end of this paper.

These materials are routinely employed in the nuclear, chemical, transportation, and other industries of great practical importance. Many NDT techniques are not efficient for the volumetric testing of ASSC structures during in-service and pre-service inspection.

Ultrasonic evaluation, by far, seems to be the most logical inspection candidate, but attempts to apply conventional ultrasonic techniques have not yet been successful. Current research is, therefore, oriented toward a better explanation of physical effects encountered with the ultrasonic testing of ASSC, and the development of new techniques that may overcome these hampering effects.

2. Microstructure and Acoustical Properties of Austenitic Stainless Steel Castings

Stainless steel casting alloys are iron, chromium, and nickel alloys, with high content of chromium (17-30 percent) and nickel (8-30.5 percent) [17]. These alloys also contain small amounts of such elements as carbon, silicon, phosphorous, sulphur, and in some cases molybdenum, columbium, copper, selanium. ASSC alloys do not have a transformation during cooling in the solid state and their austenitic matrix structure does not change noticeably during heat treatment [3]. The austenitic matrix consists of austenitic dendrites, the dimensions of which can reach several millimeters. A second phase, ferrite, may be present, primarily in chromium predominant Fe-Cr-Ni alloys, such as alloys CF-8, CF-8M. Carbides are undesirable for optimum corrosion resistance in low carbon (less than 0.08 percent C) alloys and are eliminated by a solution heat treatment, followed by rapid cooling. Sharply outlined columnar dendritic microstructure with ASSC alloys have high acoustical anisotropy which causes variation of acoustical properties in different directions and locations within these materials [3]. Anisotropy of some stainless steels was also investigated by Holmes [1], Matsomata and Kumura [12], Pelsener and Louis [2], Kupperman, Reiman, and Fiore [7,9,11,14,16], and Adler et al. [15].

Because of the variation of elastic constants for different directions of the crystalline structure of ASSC, the velocity of ultrasound propagation also varies in these directions. For example, measurements performed by Kupperman et al. [9] in type 308 SS weld metal determined variations of the longitudinal wave velocity within 5.23-6.57 $\cdot 10^5$ cm/s and transverse velocity within 2.9-4.04 $\times 10^5$ cm/s. Maximum value of the longitudinal wave velocity relates to direction at 45° from the dendrite axis. Recent research by Adler et al. [15] showed 10-12 percent changes of longitudinal wave velocity and 15-30 percent changes in transverse wave velocity. Velocity changes for transverse waves strongly depend on the type of polarization of the transverse wave. Some investigators [2,7] determined a so-called guide effect when preferred orientation of dendrites distorts straight propagation of ultrasound. As a result of orientation dependent ultrasound velocity and the wave guide effect, an ambiguity in the determination of defect locations takes place.

The large grain size and high anisotropy of ASSC cause a strong scattering of ultrasound on the boundaries of grains, the dimensions of which rather often exceed the ultrasonic wave lengths. Because of the intensive scattering, useful ultrasonic signals are attenuated and many spurious signals, so-called structural noise (or "grass"), are generated. These spurious signals, when reaching the receiver at the same instant, interfere with one another and can either amplify or attenuate one another. Resultant spurious pulses can have such amplitudes and shapes that it is difficult to discriminate structural noise and signals from flaws. Because of very similar spectral and amplitude characteristics of noise and reflections from flaws, conventional methods of improving the signal/noise ratio by averaging and correlation techniques are not sufficient, and improvement of this ratio requires implementation of specific techniques and the development of new original test procedures.

Various and sometimes enormous ultrasound attenuation manifests itself as one of the main hampering factors for ASSC inspection. To date, however, it was not clear as to why the attenuation varies so significantly from one area to another in one flawless specimen. Experimental study of this important ultrasonic attenuation characteristic and its correlation with microstructural analysis has been conducted, and is presented in the following section of this paper.

3. Experimental Study of the Correlation Between Ultrasonic Attenuation and Microstructure of ASSC

Emphasis in this study was placed on examining the ultrasonic wave response through a 5.4 mm thick CN7M type cast stainless steel plate which was first divided into two halves ith dimensions 76.2 mm x 152.4 mm x 25.4 mm. One section was heat treated and the second ne, after preliminary investigation, was also divided into two sections (#1 and #2, fig. 1), ne of which (#1) was heat treated later, too.

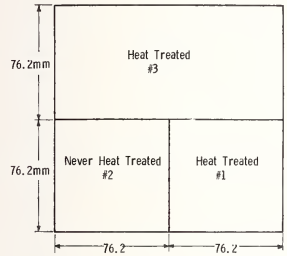

Figure 1. Lay up of the 25.4 mm thick, 152.4 x 152.4 mm^2 CN7M steel block.

A preliminary investigation was carried out on sections 76.2 mm x 152.4 mm using ltrasonic echo-pulse immersion techniques at frequency 2.25 MHz. A sample histogram of the back wall echo (BWE) amplitudes measured on specimen #3, is depicted in figure 2. This istogram illustrates the wide range (up to 24 dB) of BWE amplitude due to the attenuation ariation. As a result of these measurements, areas of interest of the highest and the lowest attenuation were determined.

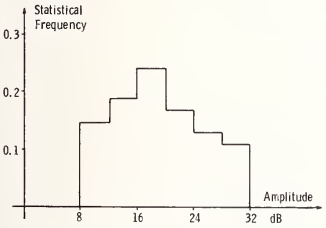

Figure 2. Histogram of back wall echo amplitudes on CN7M specimen.

Further experiments were conducted using contact echo-pulse technique at a frequency range of ultrasonic transducers from 1 MHz to 10 MHz. The specimens were milled to improve acoustical coupling during the contact testing and also to eliminate variations of echo-amplitudes due to the scattering from the rough surfaces. On each of the specimens, (fig. 3) three locations were selected for analysis, one for maximum ultrasonic signal response, one for minimum ultrasonic response, and one for approximately intermediate ultrasonic signal response. These three characteristic locations were chosen on each specimen in order to perform the following microstructural analysis and correlation between ultrasonic measurements and micrographs of appropriate sections. When measuring the echo amplitudes of the ultrasonic signals, some variations of the order of 3 to 5 mm in the location of the maximum and minimum attenuation response were found at different frequencies. In the case of locations where attenuation was minimal, the attenuation coefficient, α, could be calculated knowing the amplitudes A_1, A_2 of the first and second back wall reflections, thickness of a specimen d at that location and considering the divergence of the ultrasonic beam at the second reflection in comparison with the first reflection:

$$\alpha_{min} = \frac{A_2 - A_1 - \Delta G}{2d} \quad (1)$$

where ΔG is a quantity taking into account the divergence of the ultrasonic beam. ΔG can be determined by means of the BEW curve of the DGS diagram for any particular transducer and material thickness. (For d = 1", ΔG = 0.5 dB).

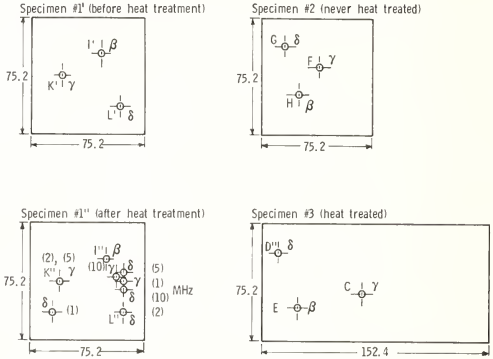

Figure 3. Location of spots with maximum (δ), minimum (γ), and average (β) attenuation on specimens #1, 2, 3.

A similar computation cannot be carried out for locations of very high attenuation since the information regarding the second echo amplitude was not available. The following formula was, therefore, used to compute the maximum and intermediate attenuation:

$$\alpha_{max,\ int} = \alpha_{min} + \frac{A_1 - A_{1min}}{2d} \quad (2)$$

where A_{1min} is the back wall echo amplitude at the spot with the minimum attenuation. Figure 4 shows the attenuation coefficient variation versus frequency for maximum (G, D) and minimum (F, K) attenuation locations. The maximum attenuation versus frequency curves are quite similar for different specimens. Figure 5 also shows the attenuation coefficient versus frequency curve for the specimen #1 before and after heat treatment. The specimen was heat treated by heating to 2035 °F (1112 °C), holding at temperature for 5.5 hours and quenching in circulating water. It is interesting to note that for the case of location L, attenuation decreased by 5 dB/cm at 10 MHz after heat treatment. The change in attenuation was less at lower frequencies. A change in the location of maximum attenuation upon heat treatment may be explained by possible changes in the microstructures because of the solution of carbide particles and slight grain boundary movement during heat treatment. Nine sections, C, D, E, F, G, H, I, K, and L were cut out from specimens, polished and etched for microstructural analysis using several techniques. The first etching technique employed a Glycerol, HCl, and HNO3 etch; the second one employed a chromic acid electrolytic etch for grain boundaries; the third, a special etch that is used for dendrite analysis.

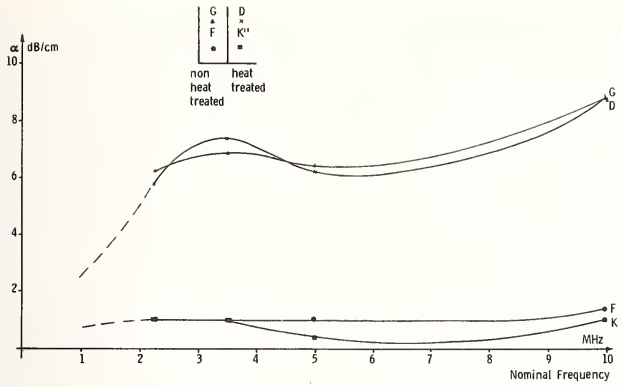

Figure 4. Variation of maximum and minimum attenuation vs. frequency.

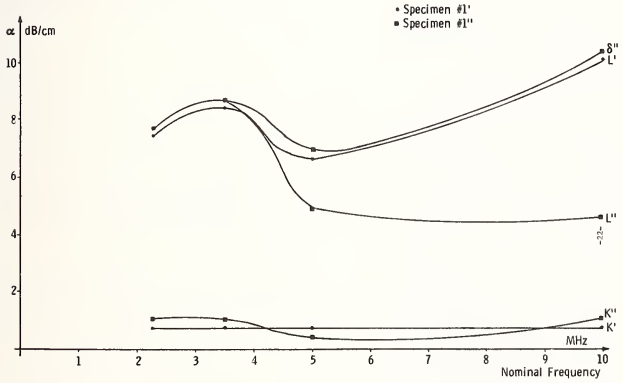

Figure 5. Correlation of attenuation on specimen #1 before heat treatment (#1') and after heat treatment (#1").

A preliminary analysis of 80 photomicrographs, taken using the first technique, revealed a difference in microstructure for specimens of various attenuation characteristics. These data suggested that variations in ultrasonic attenuation depend mainly on the relative orientation of the ultrasonic beam and the direction of columnar dendritic growth.

Special emphasis was placed on the microstructure of sections C, D, K, and F which were found the most characteristic (table 1). The analysis of the microstructure of these specimens has revealed the information that follows.

Table 1

Specimen	Condition	Attenuation (dB/cm at 5 MHz)
G	AS cast	High - 6.5
D	Heat treated	High - 6.2
F	AS cast	Low - 1.0
K	Heat treated	Low - 0.4

The difference in the ultrasonic attenuation behavior is a result of different grain sizes or the number of grain boundaries. The larger the number of grain boundaries, the greater the attenuation. Attention is called to figure 6 which shows the dendritic structure of the two low attenuation specimens etched with the special etch to bring out the dendrites. The dendrites in both specimens are in only two columnar grains. One grain, in the F specimen has the dendrite orientation parallel to the beam and one at an angle in three dimensions that appears to be about 45° to the beam direction. The spines of the dendrites in K specimen are both at 45° to the beam. This causes a considerable disparity in dendrite direction but both specimens have low attenuation, the lowest attenuation is for the K specimen with two 45° directions.

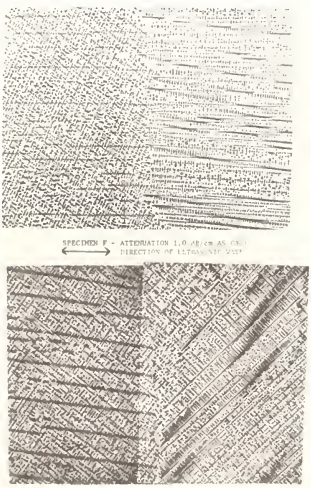

Figure 6. Low attenuation specimens, dendrite etch 6X.

The high attenuation specimens shown in figure 7 contain several grains with different dendrite orientation in each grain. Specimen G has nine grains showing; these grains are also delineated by the electrolytic chromic acid etch shown in figure 8. Specimen D in figure 7 also shows nine grains on the face of the specimen.

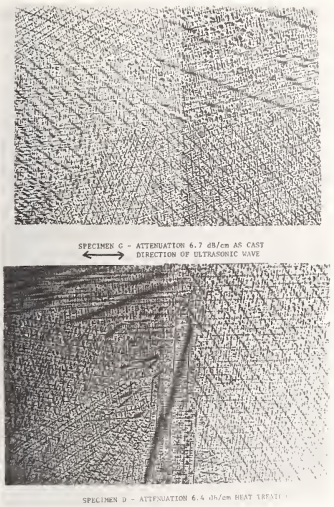

Figure 7. High attenuation specimens, dendrite etch 6X.

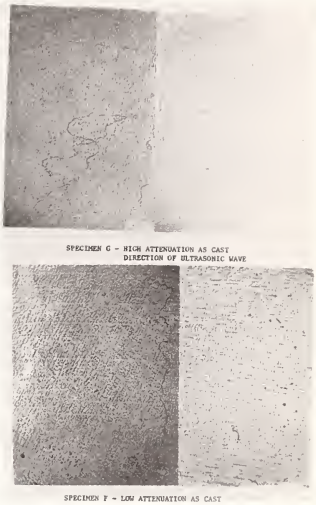

Figure 8.

Some movement of the grain boundaries did occur during heat treatment. While these are no longer coincident with the dendrites, they are of the same relative magnitude. The electrolytic chromic acid etch only works for identifying grain boundaries when these contain carbides. Accordingly, it is fine in the as-cast condition as shown for F and G in figure 8, but did not work for the heat treated specimens. While some wandering of grain boundaries does occur, it was not considerable on the specimens examined, and the effect of heat treatment on attenuation was also small.

4. Potential of ASSC Inspection

The research on ultrasonic attenuation and its correlation with microstructural analysis of the ASSC specimens as well as results of other investigators reveal extremely severe hampering conditions for ultrasonic inspection. The situation is poor, but not absolutely hopeless.

Effects of the severe ultrasonic attenuation, possible deflection of the ultrasonic beam, and velocity dispersion make the problem of a flaw size determination and/or classification almost impossible even if flaw detection is possible. But in some cases, careful analysis of the statistical distributions of such material parameters as attenuation, using averaging for the determination of a reference signal and attenuation can provide a relative estimation of the flaw sizes in ASSC. Sample measurements of flat bottom holes with diameter 1.98 mm (5/64 in) using this procedure and flaw detector USL-35 have determined flaw size with accuracy ±20 percent.

Investigation of the acoustical properties of ASSC is carried out along with the research and development of new techniques capable of improving the signal/noise ratio and/or overcoming the affects of different instabilities on the distorting ultrasonic signals. A general solution technique is outlined below followed by the special recommendations based on our current research.

Application of broad band transducers allows us to decrease interference effects contributing to noise development. Narrow beam transducers also have the potential for improving the signal/noise ratio because the interrogative beam is narrower, fewer reflections and interboundary transformations of ultrasonic waves on dendritic structure occur. A narrow beam is being achieved by using focused and double (pitch-catch) transducers. Principles of broad band and narrow beam transducers have been recently realized by Sattler, Hacker, and Birchak in the design of special transducers for centrifugal cast stainless steel piping with thickness 2.4 in (6.1 cm) [13]. Application of this transducer has improved testing and provided detection of 3/16 in (4.8 mm) side drilled hole on the 3/4 thickness depth in accordance with ASME code. Variation of the focusing point can expand the materials thickness test range. Measurement of the ultrasonic attenuation of different spots of ASSC specimen using various frequencies allows us to choose the optimal frequency of the inspection and brings additional important information for flaw location and evaluation.

Results of the attenuation measurement can also serve as a baseline for periodical in-service inspection of critical ASSC parts and structures. Although conventional averaging techniques of ultrasonic signals at a fixed location of material cannot improve signal/noise ratio, signal averaging accompanied with transducer displacement can provide information about material thickness and even flaw location. In reference [5], it was shown that this technique should be accomplished by operator memorizing and comparing flaw reflection and noise patterns. The pattern memorization and comparison can be conducted more efficiently by computer assisted NDE. Application of pattern recognition techniques for ASSC inspection problem is rather promising. Mucciardi et al. [18] implemented such an approach for 304 stainless steel inspection for base metal as well as for weldments.

Combination of the use of longitudinal and horizontally polarized shear waves, more preferable because of lesser attenuation with controlled ultrasonic beam focusing, can provide multiple features for pattern recognition processing. Various probabilistic pattern recognition techniques considered by Rose [19] can determine statistical differences between structure noise and real flaws like cracks, shrinkages, and other discontinuities in castings. Such techniques mentioned in reference [5] as frequency variation, multifrequency testing, variation of the probe pattern width can also be combined with pattern recognition.

5. Conclusions

Ultrasonic inspection of austenitic stainless steel castings is strongly hampered by the effect of microstructure on acoustical properties of these alloys. The most essential of these phenomena are a high noise level, variation in the velocity of the ultrasonic propagation and attenuation, deflection and distortion of the ultrasonic beam due to anisotropy of dendritic structure and large dimensions of grains.

Ultrasonic attenuation varied significantly from one location to another in the ASSC. Variation of ultrasonic attenuation depends on frequency and has a range of up to 10-15 dB/cm for 25.4 mm (one inch) thick specimens.

Heat treatment of the ASSC specimen did not change the maximum values of attenuation. There were found, however, some changes in the location of maximum and minimum attenuation areas.

The difference in the ultrasonic attenuation behavior is a result of different grain sizes and the number of grain boundaries. The larger the number of grain boundaries, the greater is the attenuation. The attenuation is also essentially affected by the relative orientation of the ultrasonic beam and the plane of the dendritic column growth.

There is no significant variation of dendritic structure between heat treated and non-heat treated specimens, although some minor movement of the grain boundaries did occur.

In spite of many hampering effects, implementation of some specific and new techniques can improve potential of ASSC inspection. These techniques include an application of: broad band and narrow beam transducers, double (pitch-catch) probes, longitudinal and horizontally polarized shear waves instead of conventional vertically polarized shear waves, measurement

of ultrasonic attenuation for the choice of the optimum frequency providing valuable information for flaw detection and a baseline for further periodical inspection, averaging procedures for determination of statistical means of the attenuation and reference signal, enhancing signal/noise ratio by means of signal accumulation when moving the transducer, and pattern recognition using different probabilistic approaches, frequency and wave mode variation.

6. Nomenclature

δ - maximum attenuation recording location

β - average attenuation recording location

γ - minimum attenuation recording location

C, D, E, F, G, H, I, K, L - sections containing micrograph information

α - ultrasonic attenuation (db/cm)

A_1, A_2 - attenuator reading, corresponding to amplitude of the 1st, 2nd back reflections (dB)

ΔG - quantity taking into account the divergence of the ultrasonic beam

d - thickness of material (cm)

We would like to thank Professor John F. Wallace of Case Western Reserve University and graduate student Robert Zajko of Drexel University for the microstructural analysis of the CN7M steel specimens.

References

[1] Holmes, E., Ultrasonic behavior in austenitic stainless steel, Appl. Material Research, 181-184 (1963).

[2] Pelsener, J. P. and Louis, G., Ultrasonic testing of austenitic steel castings and welds, British J. NDT, 107-113 (1974).

[3] Lavender, J. D., Ultrasonic Testing of Steel Castings, Steel Founder's Society of America (1976).

[4] Kupperman, D. S., Fiore, N. F., and Reimann, K. J., Ultrasonic investigation of welds in cast stainless steel, in Proc. 8th World Conf. NDT, Cannes, France (Sept. 1976).

[5] Ermolov, J. N. and Pilin, B. P., Ultrasonic inspection of materials with coarse grain anisotropic structures, NDT International, 275-280 (1976).

[6] Silber, F. A. and Ganglbayer, O., Contribution to ultrasonic testing of austenitic steel welds, in Proc. 8th World Conf. NDT, Cannes, France (Sept. 1976).

[7] Jotchev, B. and Pawlowski, Z., Effect of material acoustic anisotropy on the shape of ultrasonic wave beam, in Proc. 8th World Conf. NDT, Cannes, France (Sept. 1976).

[8] Mech, S. J. and Michaels, T. E., Development of ultrasonic examination methods for austenitic stainless steel weld inspection, Materials Evaluation, 35, 81-86 (1977).

[9] Kupperman, D. S. and Reimann, K. J., Effect of shear wave polarization on defect detection in stainless steel weld metal, Ultrasonics, 16, 21-27 (1978).

[10] Yoneyama, H., Shibata, S., and Kishijami, M., Ultrasonic testing of austenitic stainless steel welds false indications and the cause of their occurrence, NDT International, 3-8 (1978).

[11] Kupperman, D. S. and Reiman, K. J., Acoustic properties of stainless steel weld metal, presented at the 2nd International Conference on Nondestructive Evaluation in the Nuclear Industry, Salt Lake City (Feb. 1978).

[12] Matsumoto, S. and Kumura, K., The relationship between grain size and ultrasonic attenuation coefficient in austenitic stainless steel and iron, Trans. Natl. Res. Inst. for Metals, 14, 155-164 (1972).

[13] Hacker, M. G. and Sattler, F. J., Ultrasonic inspection of centrifugal cast stainless steel, presented at the National Spring ASTM Conference, New Orleans (April 1978).

[14] Kupperman, D. S. and Reimann, K. J., Stainless steel weld inspection with horizontally polarized shear waves, presented at the National Spring Conference, New Orleans (April 1978).

[15] Cook, K. V., Simpson, W. A., Adler, L., and Lewis, D. K., Flaw location and characterization in anisotropic materials by ultrasonic spectral analsyis, presented at the National Spring ANST Conference, New Orleans (April 1978).

[16] Kupperman, D. S., Reiman, K. J., and Fiore, N. F., Role of microstructure in ultrasonic inspectability at austenitic stainless steel welds, Materials Evaluation, 36, 70-74 (1978).

[17] Handbook of Stainless Steels, McGraw-Hill Book Co., pp. 10-1 to 10-9 (1977).

[18] Mucciardi, A. N., Chang, J. K., and Lawrie, W. E., Development of Adaptive Learning Networks for Pipe Inspection, Task 1, Adaptronics, Inc., McLean, Virginia (Oct. 1976).

[19] Rose, J. L., A 23 flaw sorting study in ultrasonics and pattern recognition, Materials Evaluation, 35, 87-92 (1977).

National Bureau of Standards Special Publication 596, Ultrasonic Materials Characterization, H. Berger and M. Linzer, eds., Proceedings of the First International Symposium on Ultrasonic Materials Characterization held at NBS, Gaithersburg, Md., June 7-9, 1978. Issued November, 1980.

IMPROVEMENT OF SIGNAL-TO-NOISE RATIO FOR THE ULTRASONIC TESTING OF COARSE GRAINED MATERIALS BY SIGNAL AVERAGING TECHNIQUES

S. Kraus and K. Goebbels

Institut für Zerstörungsfreie Prüfverfahren
Universität, Geb. 37, D-6600 Saarbrücken 11
Federal Republic of Germany

Flaw detection with ultrasound is limited by attenuation and diffraction, by noise from scattering processes at grain boundaries ("grass"), and by electronic noise. For coarse grained materials like castings and austenitic welds, scattering restricts the detectability of flaws. Methods to improve the signal-to-noise ratio (SNR) have to take into account that the noise signal is the sum of the scattering processes at all grain boundaries in the sound beam, depending on grain size, wavelength and elastic anisotropy, beam diameter, and pulse length. While short pulses and focusing probes reduce, both axially and laterally, the volume wherein scattering will be excited, averaging techniques make the scattering signals into incoherent, stochastic ones: 1) Variation of position of the probe by about one grain diameter leads to a variation in the scattering signal amplitude but leaves unchanged, in a first approximation, the defect signal. 2) In the same way, variation of the angle of incidence by about 1° changes the scattering indication, while keeping the flaw signal constant. 3) Variation of the ultrasonic frequency by about 0.1 MHz, especially for broadband transducers, modifies the noise amplitude, but not the reflector signal.

In each case the sum over several digitized A-scans (e.g., 256) reduces drastically the scattering signals and enhances the SNR. The measurement techniques are outlined and examples are given especially for austenitic welds.

1. Introduction

Ultrasonic inspection of fine grained steels and ferritic welds normally shows no problems with the signal-to-noise (SNR). For coarse grained materials like castings and austenitic welds, flaw signals often are accompanied by "grass"-indications (ultrasonic scattering) reducing the SNR; for example: 1) The austenitic grain size of ASTM 4 results, for 2 MHz shear waves, in an average scattering amplitude corresponding to a circular disk of 4 mm diameter, oriented perpendicular to the sound beam. Single noise indications range from 10 to 15 dB higher. 2) For the inspection of pressure vessels with austenitic cladding from the ferritic side with 2 MHz shear waves, scattering signals excited in the cladding are higher than the amplitude from a 3 mm diameter flat bottom hole (FBH) in the cladding, in the interface, or in the base material near the interface (figs. 1 and 2).

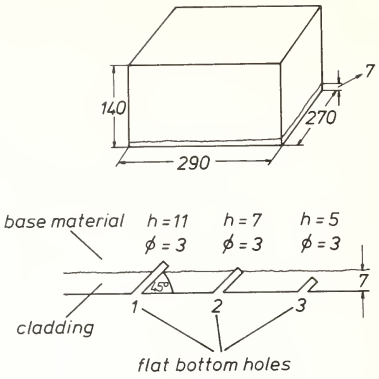

Figure 1. Cladded test block with different flat bottom holes in the cladding interface zone.

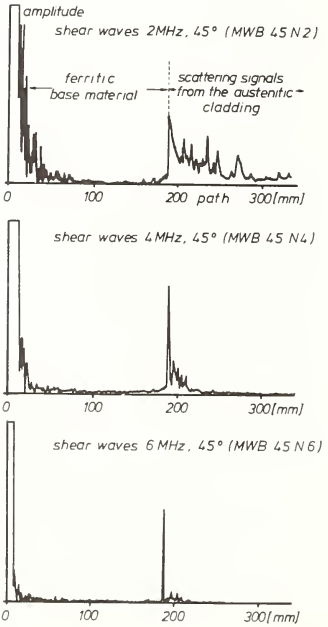

Figure 2. Detection of a flat bottom hole (3 mm diameter) in the cladding interface of a test block, with the frequency varied from 2 MHz to 6 MHz.

These limits of detectability are caused by ultrasonic scattering. Scattering signals are the result of the superposition of the reflections at all grain boundaries in the sound beam for a given time of flight. The mean scattered intensity is proportional to the mean grain volume (Rayleigh scattering) or to the mean grain size (stochastic scattering), the two being predominant in ultrasonic insoection between 1 and 10 MHz. The mean scattered intensity is proportional to the elastic anisotropy, which is of particular importance for austenitic steels and welds. For these reasons scattering signals are coherent with flaw signals and methods to improve the SNR have to take this into account.

Before describing averaging techniques some other methods are reviewed. 1) The mean backscattering amplitude $A_S(x)$ measured in the pulse-echo technique as a function of sound path x is proportional to the square root of the pulse length [1][1]:

$$A_S(x) = A_0 \, (\alpha_S \Delta)^{1/2} \, e^{-\alpha x} \, , \qquad (1)$$

where A_0 is the amplitude excited in the surface of the material under test, α_S is the scattering coefficient, Δ the pulse length and α the attenuation coefficient (the sum of α_S and the absorption coefficient α_A). The amplitude of the signal reflected from the backwall is given by

$$A(x) = A_0 \, e^{-\alpha x} \, , \qquad (2)$$

disregarding beam diffraction in eqs. (1) and (2). Therefore, the SNR is proportional to [2]

$$SNR \sim A(x)/A_S(x) = (\alpha_S \Delta)^{-1/2} \sim \Delta^{-1/2} \, .$$

Going from Δ 10 wavelengths (λ), to Δ λ then improves the SNR by about 10 dB, the reason being axial reduction of the volume wherein scattering can be excited [3]. 2) To reduce this volume laterally higher frequencies, for the same probe dimensions, or focused beams can be used. The flat bottom holes of 3 mm diameter in the test object of figure 1 could not be detected with an 8 x 9 mm^2, 2 MHz shear wave probe (fig. 2, top). With 4 and 6 MHz shear waves, all the FBH were detected. Figure 2 (middle and lower) shows the result for the FBH in the interface. Figure 3 shows the result for the three FBH obtained with a 2 MHz shear wave focusing probe (5 mm focus diameter at the depth of the FBH). If the defect type does not correspond to a FBH but more to a side drilled hole, the improvement in SNR by use of higher frequencies cannot be obtained in the same manner (because geometrical reflection and directivity pattern determine the improvement for the FBH). Therefore, in this case other techniques like signal averaging methods have to be used.

2. Signal-Averaging Techniques

For a given position of the probe, the high-frequency backscattering signal as function of time of flight of function of sound path is the result of the reflections at all the grain boundaries in the sound beam. The amplitude modulated signal has a frequency spectrum quite similar to that of the transmitting pulse and, therefore, it is coherent with the signal obtained by reflection at a real defect. To make this noise signal into an incoherent, stochastic one, it is necessary to vary the interference result while keeping the flaw signal constant, at least in the first approximation, in both amplitude and time delay. Then, summing several A-scans (with this assumption), a signal is obtained with reduced scattering amplitudes relative to the reflector amplitude. The techniques used electronically are described below. The important assumption is that the mean grain size d_G of the structure where scattering is excited is smaller than the diameter d_R of the reflector or flaw.

[1]Figures in brackets indicate the literature references at the end of this paper.

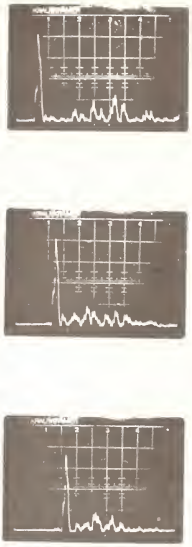

Figure 3. Detection of three flat bottom holes (3 mm diameter) in the base material, the interface and in the cladding of a test block using a focused probe.

3. Spatial Averaging

The variation of the position of the probe by about one grain diameter changes the resulting scattering signal but leaves unchanged the reflector signal ($d_R >> d_G$). Figure 4 shows this for eight A-scans and the backwall echo, measured with 10 MHz longitudinal waves. Variation of the probe position by 0.3 mm corresponds to about one grain diameter (ASTM 1). The scattering amplitudes change drastically while the backwall echo remains constant and therefore, the sum over these A-scans improves the SNR. This is demonstrated in figure 5. With increasing number of averaging processes the scattering signals are reduced, finally to the curve corresponding to eq. (1), while the backwall echoes are resolved better and better. For a real defect, the variation of the probe position depends on the dynamic echo curve of the flaw. Figure 6 gives an example for a slag inclusion in an austenitic weld and compares the normal A-scan to the averaging result over 256 A-scans. The reflector amplitude corresponds to a 1 mm diameter side drilled hole (SDH).

4. Directional Averaging

In a similar manner, changing the position of the scattering volume for a fixed probe position, the variation of the angle of incidence leads to an improvement in the SNR. In this case, it is sufficient to vary the angle by about 1° to obtain a totally changed scattering signal while the reflector signal remains constant or varies only slightly. For the averaging process, summing up different A-scans, for which the angle of incidence (45°) is varied by ±3° (in the material under test), the amplitude-locus curve has to be taken into account. Figure 7 represents the comparison between the normal A-scan and the averaged result from 1024 A-scans. The reflector in the root of the weld (thickness of the specimen: 60 mm) was a 3 mm SDH.

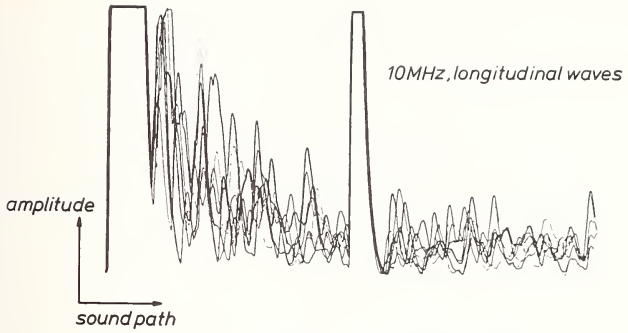

Figure 4. Scattering signals and backwall echo for eight A-scans from different positions on a coarse grained austenitic steel block (30 mm thickness).

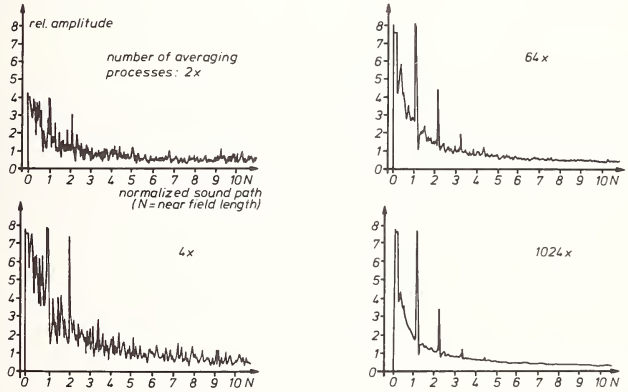

Figure 5. Backwall echoes obtained by 2, 4, 64, and 1024 averages. Specimen: austenitic steel, 30 mm thickness, grain size ASTM 1. Frequency: 10 MHz longitudinal waves.

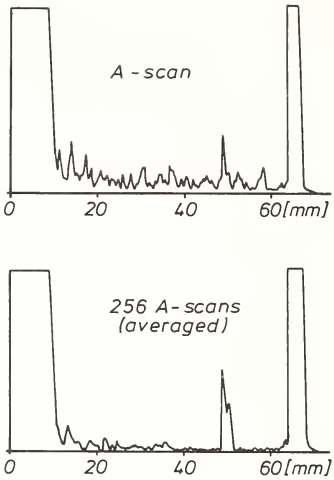

Figure 6. Spatial averaging: slag inclusion in an austenitic weld (f = 5 MHz, 63 mm thickness).

5. Frequency Averaging

A third averaging process can be made by changing the frequency of the pulse electronically for fixed probe position and fixed angle of incidence. Small bandwidth transducers are not very suitable because these need a long burst to change the frequency spectrum by a small amount. However, for broadband transducers excited with short pulses, a frequency change of about 0.1 MHz changes the scattering signal drastically while the flaw signal remains practically constant. This is demonstrated in figure 8 for a 5 MHz broadband probe, where the single A-scan is shown above and the result of 1024 averages is shown in the lower part. The frequency was swept from 3.7 to 5.3 MHz. The reflector was the same as in figure 7 (3 mm SDH).

6. Analog and Digital Averaging Processes

An important distinction is to be made between analog and digital averaging. By the analog technique [4], while changing probe position, angle of incidence, or frequency, a small gate (e.g., 1 μs duration) is driven slowly through the time signal and the mean amplitude in the gate is registered, for example on an x-t-recorder. This requires totally constant coupling between probe and test piece during the recording process: variations in A_o, excited in the surface of the material (see eq. (1)), by fluctuations of coupling are reflected directly into the registered curve. The digital technique [1] consists in summing up each digitized A-scan. In this case, fluctuations in the coupling influence the resulting curve generally, but not locally. Therefore, the digital technique, although more expensive, is preferred. The time needed for digital averaging is a function of the number of A-scans used and, more important, the velocity of the signal-averaging equipment. Today, an adding rate of at least 1 μs/address is standard (resulting in 1 s for 1000 averaging processes over 1000 addresses each time). An instrument with much greater averaging speed has been developed [5].

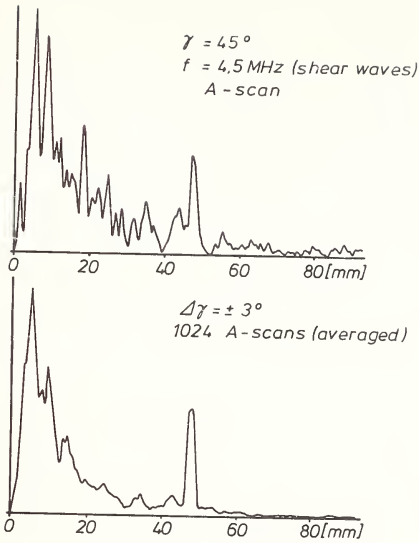

Figure 7. Directional averaging: side drilled hole (3 mm diameter) in an austenitic weld (f = 4.5 MHz, 60 mm thickness).

7. Averaging Over High-Frequency and Rectified Signals

A second important distinction concerns averaging over high-frequency (rf) and rectified signals. The results presented in the figures 5-8 and in figure 9 (right side) were obtained by averaging over rectified signals. Therefore, only amplitudes above zero are added together and the final curve for the scattering signal corresponds to eq. (1). In the same way the averaging process can be executed with high-frequency signals. Then, because of phase shifts in the scattering signals, positive and negative amplitudes are added together. The result is a scattering signal going to zero with increasing number of averaging processes while the reflector signal is kept constant (fig. 9, left side). Therefore, with high-frequency averaging the SNR can be much better than for averaging over rectified signals. However, this advantage only exists if the phase shifts for the reflector signal do not exceed some tenths of the wavelength. For greater shifts, the result for the reflector amplitude is the same as that for the scattering; it will go to zero. For this reason, and taking into consideration the condition of the material surfaces in practical applications, we prefer averaging over rectified signals.

8. Linear and Exponential Averaging

Let us also consider the adding process. For the examples given here, each A-scan is added with the same weighting factor (1). Another development, known as exponential averaging [3], calls for adding single A-scans with a varying weighting factor, whereas previous signals are attenuated relative to signals coming in at the actual testing time. This can be of advantage for automatic testing equipment with linear movement of the probe, because it is not necessary to wait for the result of the averaging process; instead, after each A-scan, a result is displayed, and there is real-time feedback. With increasing speed of averaging, this advantage vanishes; the accuracy of the linear averaging process will then be preferred, because of its higher accuracy.

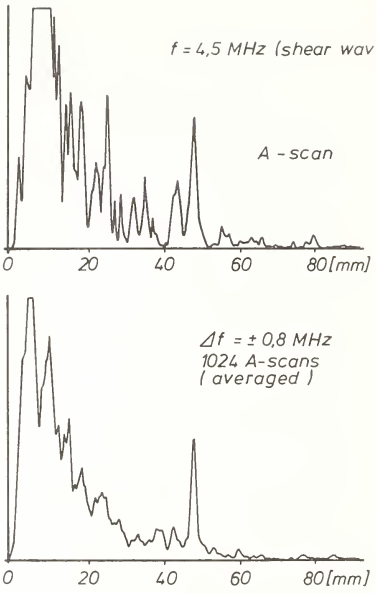

Figure 8. Frequency averaging: side drilled hole (3 mm diameter) in an austenitic weld (f = 4.5 MHz, 60 mm thickness).

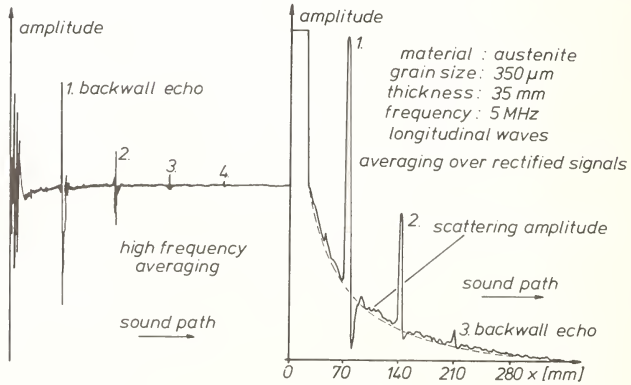

Figure 9. Averaging over rf and rectified signals.

9. Discussion

Different signal averaging techniques are discussed to improve the SNR when scattering is present, as in castings and austenitic welds. At present, objective and reproducible data are obtained by the use of the linear averaging process over rectified and digitized signals. The examples given here show that it is not only possible to improve the SNR by some 5, 10 or 15 dB, but also to locate defects, which cannot be detected in a single A-scan. The averaging process over some hundred or thousand A-scans can be executed during a time less than 1 s and therefore, it will be of interest to combine a normal ultrasonic inspection device with a small averaging unit, containing only an analog-to-digital converter, the averaging circuit, a data store and an additional display. Further development of the averaging technique should exploit the advantages of electronically controlled phased arrays.

The work described was executed with financial support of the Bundesministerium für Forschung und Technologie (reactor safety research program). The authors are grateful for this support.

References

[1] Goebbels, K. and Höller, P., Quantitative determination of grain size and detection of inhomogeneities in steel by ultrasonic backscattering measurements, this volume.

[2] Ermolov, I. N. and Pilin, B. P., Ultrasonic inspection of materials with coarse grain anisotropic structures, NDT International, 9, 275 (1976).

[3] Goebbels, K., Kraus, S., and von Klot, R., Signalanhebung bei der Ultraschall-Prüfung grobkörniger Werkstoffe. Seminar ZfP in der Kernreaktortechnik, IzfP, Saarbrücken (March 1978).

[4] Koppelmann, J., Ultraschallmeßeinrichtung für Härtetiefenmessungen an Stahlwalzen, Materialprüfung, 14, 156 (1972).

[5] Linzer, M., Dietz, D., and Parks, S. I., Development of High-Sensitivity Ultrasonic Techniques for In-Service Inspection of Nuclear Reactors, Annual Report NUREG/CR-0460, U.S. Nuclear Regulatory Commission, Washington, DC (1978).

National Bureau of Standards Special Publication 596, Ultrasonic Materials Characterization, H. Berger and M. Linzer, eds., Proceedings of the First International Symposium on Ultrasonic Materials Characterization held at NBS, Gaithersburg, Md., June 7-9, 1978. Issued November, 1980.

AUSTENITIC STAINLESS STEEL WELD INSPECTION

S. J. Mech, J. S. Emmons, and T. E. Michaels

P. O. Box 1970
Hanford Engineering Development Laboratory
Richland, WA 99352

This paper describes analytical techniques applied to ultrasonic waveforms obtained from inspection of austenitic stainless steel welds. Experimental results obtained from a variety of geometric and defect reflectors are presented. Specifically, frequency analysis parameters, such as simple moments of the power spectrum, cross-correlation techniques, and adaptive learning network analysis, all represent improvements over conventional time domain analysis of ultrasonic waveforms. Results for each of these methods are presented, and the overall inspection difficulties of austenitic stainless steel welds are discussed.

1. Introduction

This paper reports on progress in remote ultrasonic pre-service and in-service inspection of piping welds in liquid-metal-cooled reactors. Specifically, the paper discusses roblems and possible solutions involved in inspecting weldments in Schedule 40 austenitic tainless steel piping.

Problems associated with ultrasonic inspection of austenitic stainless steel welds have reviously been well documented [1][1]. Serious efforts are being made to understand the tructures contributing to the attenuative and beam-scattering properties of austenitic eldments that obscure rejectable defects [2,3].

In light-water reactor coolant lines, areas with a high probability of developing tress-corrosion cracks can be predicted and monitored with some accuracy. This is not rue of liquid-metal-cooled reactors, however, because the preferred locations of defect ormation in these environments are not yet known. The challenge for in-service ultrasonic nspection, therefore, is to develop an inspection system that will allow the entire volume f the weld to be inspected in a liquid-metal-cooled reactor.

While a variety of inspection techniques is available to inspect welds pre-service, adiation and temperature preclude the use of many of these techniques after the first power ycle. Ultrasonic inspection appears to be the most viable of the possible solutions.

One problem with using ultrasonic techniques for in-service inspection, however, is hat an ultrasonic scanner would have to be repositioned to within 0.127 cm (±0.05 in) of ts former position relative to a weld in order to achieve meaningful comparisons between he scanner's assessment of the weld's pre-service condition and its in-service condition, r condition at the time of inspection.

Since such close repositioning is clearly not obtainable manually, especially on iping that will move slightly during the lifetime of the reactor, an alternate plan was

[1] Figures in brackets indicate the literature references at the end of this paper.

developed to record baseline data during pre-service inspection and use the recorded data to reposition the scanner during subsequent in-service inspection. Given enough pre-service data about the surface and internal characteristics of a given specimen, it was felt a computer could reposition the scanner more repeatably relative to a point on the weld than manual repositioning could.

The remainder of this paper will report on this and related work. We will also discuss methods of improving upon pre-service inspection data analysis, and ways to use pre-service data for maximum benefit during in-service inspection.

The data included in this paper were acquired using conventional ultrasonic pulser-receiver electronics, commercially-available transducers, digitally-controlled scanning mechanisms, and a high-speed transient digitizer. A minicomputer was employed for data acquisition and archival data storage, scanner control and data analysis.

2. Experimental Procedure

An "as-received" 20.3 cm (8 in) Schedule 40 stainless steel piping weld sample with electro-discharge machined (EDM) notches on the inside diameter (as shown in fig. 1) was examined with a single circumferential scan of 500 equally-spaced angular positions. The transducer was a wideband (80 percent bandwidth), 3 MHz transducer containing dual elements with approximately 10 degree cross-beam focus in a 60 degree longitudinal mode. Inspection data were stored as digital records of the original ungated RF waveform obtained at each point of examination. During the analysis phase of this project, these original waveforms would be used to evaluate the analytical method being considered.

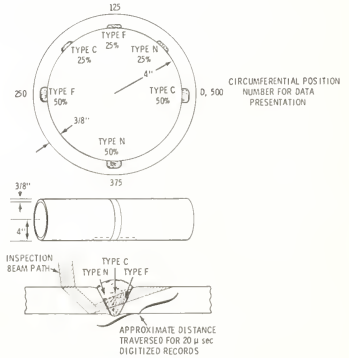

Figure 1. Inspection beam path and notch locations.

Subsequent to the initial pipe section examination, a sector of a 25.4 cm (10 in) diameter, 1.016 cm (0.4 in) wall, stainless steel pipe weldment was prepared, with two reflector that remained unchanged between successive scans, and one reflector enlarged in 0.038 cm

(0.015 in) increments between scans, as shown in figure 2. In this examination, the transducer was a dual element 4 MHz unit, operating in a pitch-catch mode, and set to generate a 45 degree shear wave. The 0.076 cm (0.03 in) wavelength used compares with 0.178 cm (0.07 in) for the refracted longitudinal 3 MHz previously used, and was selected to give sufficient sensitivity to detect the 0.038 cm (0.015 in) changes in notch depth. The effective diameter of the inspection beam at the focal point was estimated to be 0.1016 cm (0.04 in). This focal point was mechanically adjusted to a depth of 0.127 cm (0.04 in) by employing the 0.254 cm (0.1 in) deep stationary notch as a reference target.

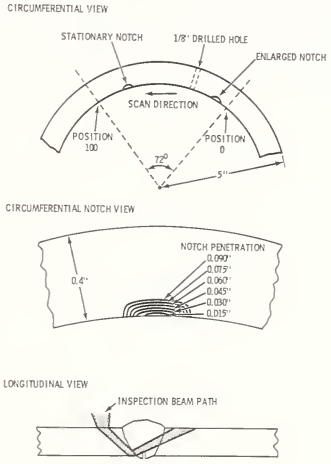

Figure 2. "Growing Notch" test specimen geometry.

Between scans, the pipe section was removed from the scanner, the "growing" EDM notch was enlarged, and the sample reinserted into the scanner. Data obtained on successive scans were digitally recorded on magnetic discs for later retrieval and analysis.

To demonstrate the practicality of this method of detecting small changes in reflectors, it was necessary to devise a technique that would permit the remote scanning mechanism to be removed and reinstalled without unreasonable mechanical tolerances, yet produce effective scan replication within 0.127 cm (0.05 in). The last test addressed this problem.

The configuration for this test consisted of a pipe section with a pattern of fiducial marks approximately 5.08 cm (2 in) apart, as shown in figure 3. These marks become reference points for realignment of the scanning unit during in-service inspection. During the initial scan, the surface was profiled with an additional small focused transducer, servo-controlled normal to the pipe surface. The position of these surface marks was catalogued, together with the ultrasonic examination data. On three successive tests, the pipe specimen was physically repositioned several inches away from its last position, then relocated by the

profiling transducer. Once the surface and the reference marks were relocated, the positional data relative to the reference marks was stored, along with the ultrasonic scan data. Later this data was employed to reposition all of the data scans such that these later scans were mechanically reproduced within 0.127 cm (0.05 in) at the focal point.

Figure 3. Pipe section profile results. Note these surface marks are drilled and punched indents.

3. Data Analysis Techniques

Digitized time domain waveforms (RF) were processed by three computational methods: amplitude detection, cross correlation, and transformation to the frequency domain using a fast Fourier transform (FFT) algorithm. Simple moments of the power spectral density of the frequency domain information were calculated as:

$$M_K(i) = \sum_{j=1}^{i} J^K p_j,$$

where i is the frequency index and P_j is the discrete analog of the power spectral density,

$$p(\omega) = (A_\omega^2 + B_\omega^2)^{1/2} \quad .$$

These techniques and their results, as applied to the pipe section shown in figure 1, are more fully described in reference [4], while the results are summarized in figure 4.

The data resulting from the aforementioned techniques were employed as input vectors for an adaptive learning network (ALN) model [5]. Twenty of the 500 examination points were used for training the model, while another 20 were used for testing it. The remaining 460 points of the 500-point data set were subjected to the model created by the network, with the results as illustrated in figure 5.

Two techniques, single- and multiple-pass, were used to analyze the growing notch test series data. Each technique was based on a different premise. Single-pass techniques assume no archival data, and reflect the pre-service inspection situation. Multiple-pass techniques assume archival data are available, such as in the in-service inspection situation. The single-pass technique employed both the amplitude detection method and the second moment of the power spectral density, M_2, which proved to be the most successful single-pass indicator of rejectable defects. Results of these analyses are shown in figure 6.

Multiple-pass techniques were developed utilizing prior (baseline) data to enhance those features that change between examinations, while suppressing those that are unchanging. This would be a simple model of a defect that developed after the baseline examination. The first multiple-pass technique cross-correlated a baseline waveform with a corresponding waveform taken during a subsequent examination. These waveforms were then aligned in time,

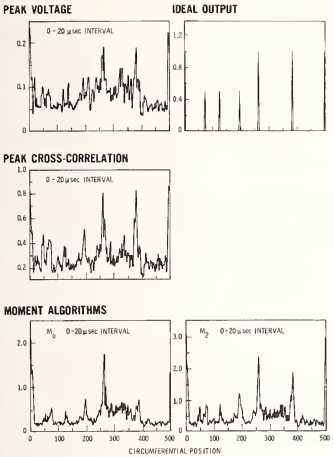

Figure 4. Peak Voltage, total power M_0, and moment M_2 for 60° refracted longitudinal inspection.

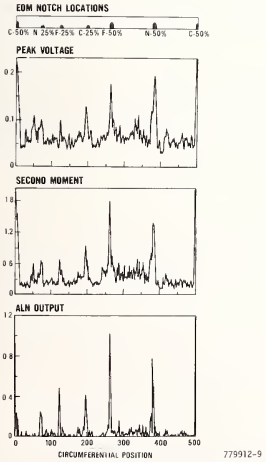

Figure 5. Comparison of peak voltage, second moment, and ALN.

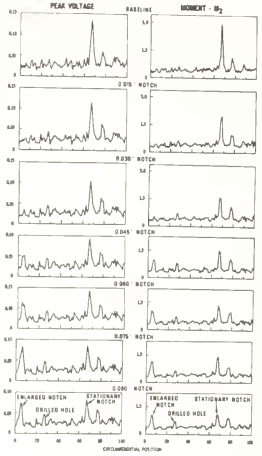

Figure 6. Peak voltage and moment results.

as indicated by this cross-correlation. The resulting waveform differences, indicated as E_1, are illustrated in figures 7 and 8.

The second of the multiple-pass techniques not only minimized the time skew error, E_1, but also scaled the amplitude of the baseline data to produce a least-squared error in amplitude. The resulting error, E_2 was then both time- and amplitude-corrected before the waveforms were subtracted.

Profile data were taken during the baseline examination to accurately catalog the location of the reference marks and the profile of the local surface. During subsequent examination, these data were used to determine the mechanical alignment changes that would permit analysis of waveforms obtained during different scans. Once the mechanical alignments are made, any or all of the previously-mentioned techniques are viable.

4. Results and Discussion

Digital time-domain records of wideband, ungated ultrasonic waveforms can be processed to produce outputs similar to conventional ultrasonic testing (UT) techniques. Synthetically, one can gate and/or band-limit the signal. Similarily, modified A-scans, B-scans and C-scans can be produced.

Processes such as the second moment algorithm, M_2, the best signal analysis process which we have found to date, can be used with significant improvement over conventional techniques. Further, multiple data sets can be generated from a set of single scan records and analyzed as a composite in a process such as regression analysis, producing results superior to any of the individual data sets.

Techniques have been developed that capitalize on the fact that detailed historical information exists for the entire volume being examined. The time-domain algorithms that generate the waveform differences, E_2, utilize prior information to minimize both the time skew and sensitivity changes caused by a change in acoustic path length. Simple waveform subtraction clearly reveals the small changes in the presence of large stationary reflections.

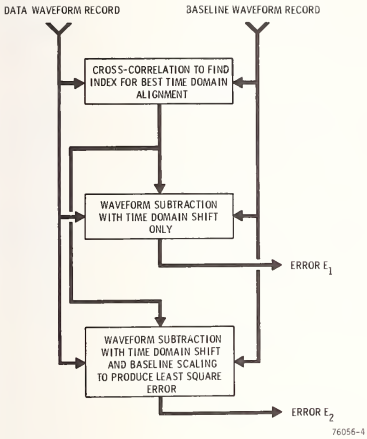

Figure 7. Numerical analysis differencing schemes.

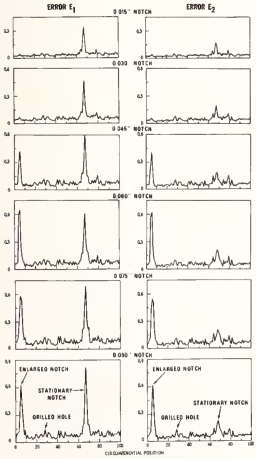

Figure 8. Results of differencing algorithms.

The analysis technique, E_2 as shown in figure 8, demonstrates the ability to detect a 0.038 cm (0.015 in) change in defect depth. The resulting defect indicator is significantly larger than the stationary background, even though the background contains a stationary defect of approximately twice the depth. The enlarging notch is detected between 0.076 cm (0.03 in) and 0.114 cm (0.045 in) depth because of the size and location of the focal point, as previously described. Similarly, at depths greater than 0.114 cm (0.045 in) the indicator shows no significant improvement because the entire inspection beam is intercepted by only the shallowest portion of the notch.

For data generated after the baseline inspection to be useable in the manner just described, absolute mechanical repeatability on the order of 0.127 cm (0.05 in) must be realized at the focal point. This, obviously, is an unreasonable requirement to place on a mechanical system over the life span of a reactor. Utilization of fiducial marks, historical profile data, and coordinate transformation permit this requirement to be met.

Providing the mechanical scanning system has better than 0.0127 cm (0.005 in) reproducibility and 0.0025 cm (0.001 in) resolution within the surface defined by a set of reference marks, waveform replication can be expected, as shown in figure 9. It is worth noting that the magnitude of the resulting waveform differences between successive scans relative to a single waveform is of the same order of magnitude as the data obtained during the growing notch series. Thus, the alignment and differencing scheme, E_2, if used here, should be sufficient to resolve the same 5-10 percent change in defect size determined earlier.

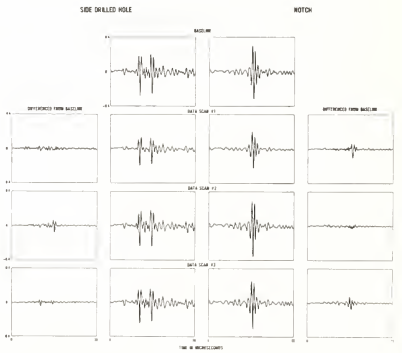

Figure 9. Scan waveforms and differences from baseline for side-drilled hole and notch signals.

5. Conclusions

Analytical techniques have been developed and demonstrated that improve on conventional UT pre-service and in-service inspection processes. Utilization of frequency domain information, specifically the second-moment algorithm, produces a better single process defect indicator than time-domain information. Combinations of both time and frequency domain information in an adaptive learning network produced results superior to any single process.

Multiple-pass analytical techniques, utilizing detailed archival records of ultrasonic waveforms have been shown to be useful in detecting small changes in the presence of large stationary signals. These techniques could be applied during in-service inspection by utilizing the baseline data.

Reference marks and local profile data have been utilized to demonstrate that UT in-service examination may be performed with the accuracies mandated by the analysis techniques.

References

[1] Caussin, P., Ultrasonic testing of austenitic stainless steel structures, Association Vincotte, B-1640 (Rhode-Saint-Genese, Belgigue, Sept. 1976).

[2] Tomlinson, J. R., Wagg, A. R., and Whittle, M. J., Ultrasonic inspection of austenitic welds, presented at 2nd International Conference on Nondestrutive Evaluation in the Nuclear Industry (Salt Lake City, UT, Feb. 13, 1978).

[3] Kupperman, D. S., Reimann, K. J., and Fiore, N. F., Role of microstructure in ultrasonic inspectability of austenitic stainless steel welds, Materials Evaluation, 36, [5] (1978).

[4] Mech, S. J. and Michaels, T. E., Development of ultrasonic examination methods for austenitic stainless steel weld inspection, Materials Evaluation, 35, [7] (1977).

[5] Mech, S. J., Michaels, T. E., Emmons, J. S., and Sugiyama, M. M., Development of ultrasonic examination methods for austenitic stainless steel weld inspection, presented at ASNT Fall Conference (Detroit, MI, Oct. 1977).

National Bureau of Standards Special Publication 596, Ultrasonic Materials Characterization, H. Berger and M. Linzer, eds., Proceedings of the First International Symposium on Ultrasonic Materials Characterization held at NBS, Gaithersburg, Md., June 7-9, 1978. Issued November, 1980.

APPLICATION OF ADAPTIVE LEARNING NETWORKS TO ULTRASONIC SIGNAL PROCESSING: DETECTING CRACKS IN STAINLESS STEEL PIPE WELDS[1]

Ramesh Shankar and Anthony N. Mucciardi

Adaptronics, Inc.
Westgate Research Park
7700 Old Springhouse Road
McLean, VA 22102

Unambiguous discrimination has been achieved between cracks and geometrical (benign) reflectors in sample welded sections on 304 Stainless Steel (SS) pipe using nonlinear signal processing of ultrasonic pulse echoes via the Adaptive Learning Network (ALN) methodology.

Two sizes of stainless steel pipes were considered--nominal 4 in (10.16 cm) and 10 in (25.4 cm), Schedule 80. Circular welds were fabricated on three sections of a 10 in (25.4 cm) pipe and on one section of a 4 in (10.16 cm) pipe. Cracks were induced intentionally during the welding process; these cracks were distributed uniformly around the welds. A mechanical scanning system, using a single transducer in the pulse-echo mode, was designed. The system enabled accurate transducer positioning in both the circumferential and axial direction (to within 0.01° and 0.001 in (25.4 μm), respectively.

The ALN classifier was synthesized from signal parameters related to spectral shifts in an ensemble of pulse-echo waveforms collected around the vicinity of a defect region. The waveform ensemble was obtained by angulating the transducer over ±11°, in increments of 5.5°, around the nominal normal to the assumed crack plane. The ALN classifier discriminated unambiguously between cracks and benign geometrical reflectors.

Current work includes implementation of the ALN classifier into a ruggedized and portable microprocessor-based UT pipe inspection system.

1. Introduction

Development of fast, automatic, and reliable means for ultrasonic (UT) inspection of welds in austenitic stainless steel (SS) pipes is an important objective for the nuclear power industry. In this paper, results of a study are presented in which use of the Adaptive Learning Network (ALN) methodology enabled automatic and unambiguous discrimination between cracks and other geometrical reflectors in sample circular weld sections on 304SS Schedule 80 pipes.

[1]This work was supported by the Electric Power Research Institute (EPRI), Palo Alto, California, under EPRI Research Contract RP-770-1.

Reliable discrimination between pulse echoes from cracks and from benign geometrical reflectors is complicated by the attenuative property of stainless steel and by the apparent resemblance of the two signal classes. In addition, due to the high ratio of occurrence of geometrical reflectors to cracks--sometimes as high as 1,000 to 1--the need exists for an automatic and fast inspection scheme to scan pipe sections quickly, filter out responses due to geometrical reflectors, and identify and characterize crack locations.

This program was directed to:

1) collecting pulse-echo data using a transducer scanning apparatus and inferring automatically via an ALN the circumferential and axial locations;

2) collecting an ensemble of pulse-echo data at each suspected location by angulating the transducer; and

3) classifying the ensemble pulse-echo data using an ALN modeled to discriminate between geometrical reflectors and cracks.

These three aspects of the program are presented in flow chart form in figure 1. The first aspect, location of suspicious regions via a preliminary ALN classifier, was termed "Scan Logic 1" (SL1). The second aspect, angulation of transducer and collection of ensemble pulse-echo data, was termed "Scan Logic 2" (SL2). The third aspect was to classify the SL2 pulse-echo data into a crack or a nondefect class. A fourth aspect--performing destructive tests, verifying crack locations, and, if necessary, retraining the ALN classifiers--was not considered; however, these tests are crucial in determining actual crack locations and will be performed at a future date. It must be emphasized that only a partial characterization of the cracks in the weld samples was available; that is, cracks were assumed to be at those locations where they were intentionally initiated during the welding process.

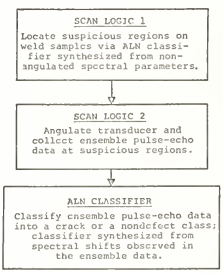

Figure 1. Illustration of decision logic.

2. Ultrasonic Data Processing and Parameterization

A data window of 256 points was extracted from the 2,048-point sampled ultrasonic pulse-echo signal captured by the transient digital recorder. Since the sampling rate was 20 MHz, this window represented a total time duration of 12.8 μs and in terms of distance, it permitted 3.88 cm of the weld section to be examined. (Assuming a shear-wave velocity of 3.03×10^5 cm/s in stainless steel, the total distance traveled is

$3.03 \times 10^5 \times 12.8 \times 10^{-6} = 3.88$ cm). This data window was found to be sufficiently long to inspect the entire weld crown section or the weld root section, but not both. It was necessary, therefore, to move the transducer to two axial positions for a given circumferential position on the pipe. In the first axial position, the beam was aligned to the top half of the weldment--the "top scan"--and in the second axial position--the "bottom scan"--the beam was aligned to the bottom half of the weldment.

Weld regions suspected of containing cracks from the SL1 analysis were more exhaustively inspected by angulating the transducer. Ultrasound data were collected with the transducer aligned such that it was as near to normal incidence to the crack plane as possible (0° position) and at ±5.5° and ±11° off 0°. Each defect region was thus characterized by an ensemble of 5 pulse-echo waveforms.

Fifteen parameters were computed from the pulse-echo signal spectrum at 0°. These parameters included fractional power in three bands descriptive of low, mid, and high frequency, higher order moments of the normalized spectrum, frequencies at which 25, 50, and 90 percent in total power were attained, and frequency value at peak power spectral response.

At each of the other four scanning angle positions, the following parameters were computed:

1) location in frequency of the largest peak in the spectrum;

2) change in parametric values with respect to their values at 0°.

A total of 80 parameters was computed from the ensemble of pulse-echo waveforms. Most of these parameters were sensitive to change in energy content and/or shifts in frequency with respect to the nominal 0° position. Significantly, parameters independent of pulse-echo amplitude were excluded; providing thus a self-normalizing capability to the classifier.

3. Classifier Synthesis and Performance

An ALN classifier to discriminate between cracks and benign reflectors was synthesized from the 80-parameter input vector defined for each observation. The model was trained to map parameter inputs from cracks onto +1 and inputs from nondefects onto -1. A schematic of the designed ALN classifier appears in figure 2. It consists of a 21-element network which uses as its inputs 22 of the candidate 80 parameters. The model realizes an incomplete 16th order multinomial in these 22 inputs. The inputs selected by the model are:

0° Scan Angle: Six parameters selected. These were x_1, normalized power in the 0-1 MHz band; x_5, ratio of powers in the 2-4 MHz and 1-2 MHz bands; x_7, frequency at which 50 percent of the total power is achieved; x_9, frequency of largest peak in power spectrum; and x_{11} and x_{12}, respectively, the frequency and magnitude of second largest peak in spectrum.

-11° Scan Angle: Five parameters selected. [Recall that these and subsequent parameters (except the spectral parameters) relate to the change in the nominal parameter values from those obtained at 0° scan angle.] The parameters were x_{19}, shift in second moment of the normalized power spectrum; x_{24}, shift in frequency of largest peak; x_{27}, shift in magnitude of second largest spectral peak; x_{28}, frequency of largest peak in spectrum; x_{29}, shift in carrier frequency.

-5.5° Scan Angle: Four parameters selected. These were x_{33} and x_{34}, shifts in 1-2 and 2-4 MHz bands, respectively, of power spectrum; and x_{43}, shift in magnitude of second largest peak in spectrum.

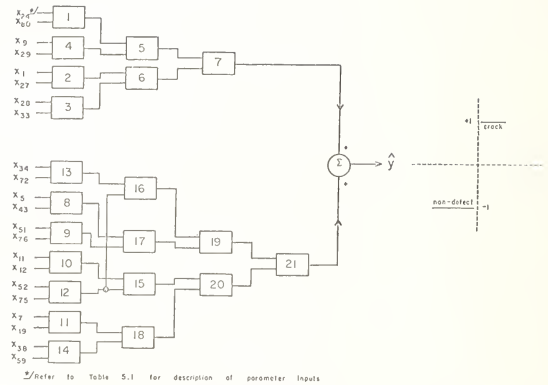

y/Refer to Table 5.1 for description of parameter inputs

ALEM	W0	W1	W2	W3	W4	W5
1	+.1986A5E+01	+.27981BE+01	-.6539A6E+01	-.5809B6E+01	-.1721AFE+01	+.2524A6E+01
2	+.1591B7E+01	+.1A1C8FE+03	+.1F36AE+07	+.2108DFE+04	+.3704A1E+04	+.4731BE+07
3	+.1187B7E+01	+.21C4A7E+01	+.1B2F3FE+01	+.92A25E+07	+.21AF3E-04	+.1781EE+07
4	-.5411B7E+02	+.3B1D3E+02	+.11C47E+03	+.C0D37E+07	+.1444A1E+07	+.1B9B5E+02
5	+.1B4A4E+02	+.3A83EE+09	+.1157CFE+01	+.4A5A5E+09	+.1983A1E+09	+.2395CE+00
6	+.6A4A1E+01	+.1D3E1E+01	+.7B91EE+00	+.1728A1E+08	+.5514A1E-01	+.B1267E+01
7	+.A3A3AE-01	+.A701A7E+00	+.F.F7A7E+00	+.FA3DDE+01		
8	+.A2151E+03	+.8777AE+00	+.1B1755E+07	+.2A79.0+07	+.A47931E+10	+.2A773E+07
9	+.2A51A7E+03	+.A1A71F+01	+.1C1A9E+07	+.1E7A9E+01	+.2F751E+01	+.2AA8FE+05
10	+.5397C7E+01	+.5A7110+01	+.1A1E1F+07	+.1E2787+07	+.1121.0+01	+.1B562E+02
11	+.5D7C4E+03	+.5A1A3F+02	+.F1C7.8F+03	+.C7D2A7E+08	+.1E7C4E+07	+.2A751E+08
12	+.B7C4A1E+02	+.1A17.0+03	+.1F7F5E+01	+.1D1F7+07	+.A7.6E+10	+.515A3E+07
13	+.1B7A4E+09	+.2F7F2F+00	+.A*****E+05	+.9D5A7+01	+.1E*****E+01	+.1C52DE+01
14	+.7A51F+08	+.1A32C+00	+.1E7.6E+01	+.1E5A5E+05	+.1E7C3E+07	+.4A7A7E+03
15	+.7A7A7E+01	+.1B1A7F+01	+.1C1A9E+07	+.2F7A7E+01	+.2F7A7E+01	+.B57A8E+08
16	+.B7A5A7E+02	+.1A7D3F+01	+.7C7A5E+01	+.1A91A7E+01	+.1E7C1A7E+01	+.3A1DAE+01
17	+.1A9A2E-01	+.2A7.9F+09	+.A5A7A7E+03	+.1A5A3E+01	+.1E5A3E+01	+.1C5D2E+08
18	+.1F7A7E+09	+.A31A8E+09	+.7A67A7E+03	+.1E3A7E+01	+.1E*****E+01	+.2F7A62L+00
19	+.9185A7E-01	+.A9D3A7E+09	+.2A61A7E+03	+.2F7D7A+01		
20	+.1A7A7E-01	+.5A1A7E+03	+.7A7.7E+05	+.A7D3F+10		
21	+.7B7A1E+01	+.B7D1A7E+03	+.1F7A7E+05	+.1D5A7E+00		

Figure 2. Schematic of designed adaptive learning network (ALN) crack-classifier.

+5.5° Scan Angle: Three parameters selected. These were x_{51}, shift in second moment of power spectrum; x_{52}, shift in ratio of powers in 2-4 and 1-2 MHz bands; and x_{59}, shift in magnitude of largest peak in spectrum.

+11° Scan Angle: Four parameters selected. These were x_{72}, shift in frequency of largest peak in power spectrum; x_{75}, shift in magnitude of second largest peak; x_{76}, frequency value of largest peak in spectrum; x_{80}, sum (over all scan angles) of frequency shifts at 25, 50, and 90 percent total power.

Although parameters selected from the different scan angles exhibited an approximate symmetry (for example, frequency of largest peak in spectrum selected for ±11° scan angle, and shift in magnitude of second largest peak in spectrum for ±5.5° scan angle), perfect symmetry was not achieved for the following reasons:

1) The "0°" scan angle was not necessarily the true position of normal incidence to the crack; rather it was the angle found by visual means and, consequently, should be interpreted as the closest to the achievable normal incidence.

2) Cracks may not be planar; so, identical signal responses (and hence parameters) will not be observed even at equal angular positions about true normal incidence.

The classifier discriminated unambiguously between all the cracks and nondefects including, significantly, six observations withheld from the design stage of the classifier. A polar plot is shown in figure 3 of the actual crack locations in the four sample welds and the ALN-inferred positions.

4. Summary

Unambiguous discrimination has been achieved, using the ALN methodology, between cracks and other geometrical reflectors for sample welded sections of 304SS pipes. It was demonstrated that by using nonlinear signal processing via ALN's, discrimination between different reflector classes in the 304SS environment can be performed accurately and reliably.

Six of the 22 parameters selected by the ALN classifier were from the power spectrum at the transducer nominal 0° position, and the remaining 16 were from shifts in the parameters observed at the various scanning angles from the values of these parameters at 0°. It was shown that a crack, when examined ultrasonically from different angles with respect to its nominal plane, displays characteristic shifts in the ensemble pulse-echo spectra. These shifts are not, of course, obvious visually, but are manifest in the frequency distribution. It was also demonstrated that by nonlinearly combining, via the ALN methodology, parameters related to the observed shifts, accurate and reliable discrimination between reflector classes is achieved. Parameters sensitive to the reflected signal amplitude were purposely excluded from the 80-parameter input set used to synthesize the classifier. Amplitude is a prime discriminant used in current industry practice, but is prone to wide variations due to instrument settings and/or to anisotropy of local grain structure. A self-normalizing capability was, thus, obtained in the designed classifier.

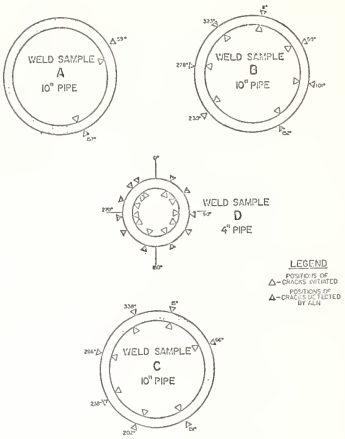

FIGURE 3: COMPARISON OF ACTUAL CRACK LOCATIONS AND ALN INFERRED LOCATIONS IN FOUR WELD SAMPLES

Figure 3: Comparison of actual crack locations and ALN inferred locations in four weld samples.

References

[1] Shankar, R., Mucciardi, A. N., Cleveland, D., Lawrie, W. E., and Reeves, H. L., Adaptive nonlinear signal processing for characterization of ultrasonic NED waveforms; task 2: measurement of subsurface fatigue crack size, Adaptronics, Inc. Final Report under Contract No. F33615-74-C-5122, AFML-TR-76-44 (April 1976).

[2] Mucciardi, A. N., Shankar, R., and Buckley, M. J., Applications of adaptive learning networks to nondestructive evaluation technology, NAECON '75 Record, pp. 460-469 (May 1975).

[3] Shankar, R., Mucciardi, A. N., Lawrie, W. E., and Stein, R. N., Development of adaptive learning networks for pipe inspection, Adaptronics, Inc. Final Report under EPRI Contract No. RP-770-1.

National Bureau of Standards Special Publication 596, Ultrasonic Materials Characterization, H. Berger and M. Linzer, eds., Proceedings of the First International Symposium on Ultrasonic Materials Characterization held at NBS, Gaithersburg, Md., June 7-9, 1978. Issued November, 1980.

USE OF A COMPACT ULTRASONIC DELAY LINE FOR THE CALIBRATION OF A PULSE ECHO INSTRUMENT

Morio Onoe and Hiroaki Yamada

Institute of Industrial Science
University of Tokyo
22-1, Roppongi 7 Chome, Minato-Ku
Tokyo 106, JAPAN

For quantitative characterization of material properties and defects, it is important to calibrate the characteristics of an ultrasonic pulse echo instrument. Test blocks usually used for this purpose are heavy and bulky. Furthermore, they check only the overall sensitivity of the combination of a search unit and a pulser/receiver.

This paper presents a simple method for calibrating an ultrasonic pulse echo instrument. An ultrasonic delay line for the PAL television system is utilized. The delay line is compact, light, and inexpensive, yet it has a low insertion loss, a wide frequency bandwidth, and good stability against temperature change and aging.

With the present method, the sensitivity, linearity, dynamic range, and time base of a pulser/receiver can be easily calibrated. At the same time, if desired, the sensitivity of a search unit on a test block can be calibrated.

Another use of the delay line for the simulation of a search unit is discussed. It makes possible the calibration of a pulser/receiver without the use of any particular search unit.

1. Introduction

For quantitative characterization of material properties and defects, it is important to calibrate the characteristics of an ultrasonic pulse echo instrument, which consists of a search unit and pulser/receiver. A widely adopted practice is the use of ultrasonic reference blocks specified by ASTM, IIW, AWS, etc. Blocks are made of such material as aluminum, steel, titanium, plastic, etc. Artificial defects such as flat bottom holes, side drilled holes, notches, and step wedges, are usually provided in blocks.

For the calibration of a pulse echo instrument, a search unit is positioned on a surface of a block so as to obtain on a display of the instrument a maximum of an echo reflected from an artificial defect. The sensitivity of the instrument is calibrated by adjusting the gain, so that the echo yields a desired amplitude. The sensitivity thus calibrated is an overall characteristic of the combination of the search unit and the pulser/receiver.

Reference blocks are heavy and bulky. Special care is required to prevent rust and wear. A good ultrasonic coupling between the search unit and the block, and a careful manipulation of the search unit are essential in order to obtain reproducible results. These requirements are not easily met, especially in on-line test instruments.

Sometimes, it is desirable to check the performance of components of an instrument. The receiver including a display can be calibrated by purely electrical means, although such auxiliary test instruments as a signal generator and an attenuator are required. The calibration of a pulser is not so easy, because most pulsers operate properly only when a search unit is connected.

This paper presents a simple method for calibrating an ultrasonic pulse echo instrument. An ultrasonic delay line for the PAL television system is utilized instead of reference blocks. The delay line is compact, light, and inexpensive, yet it has a low insertion loss, wide frequency bandwidth, and good stability against temperature change and aging.

Two methods for utilizing the delay line are presented. The first method is named the shunt method. A high impedance element is connected in series with the delay line. Then the combined unit is inserted in parallel with the output terminal of the pulser/receiver with the search unit is attached.

The second method is named the simulation method. A parallel and series connection of capacitors with the delay line yields a resultant input impedance, which closely simulate the input impedance of a search unit is attached to the pulser/receiver. Hence, the calibration can be done without using any particular transducer.

The paper starts with an analysis of the conventional calibration method using reference blocks. Then follows a brief description of PAL delay lines. Next both shunt and simulation methods using delay lines are analyzed and their experimental results are presented.

2. Analysis of Conventional Calibration Method Reference Blocks

The arrangements of a pulser/receiver, search units, and a reference block in the conventional calibration method are shown in figure 1, for the twin or TR mode, and figure 2 for the single mode, respectively.

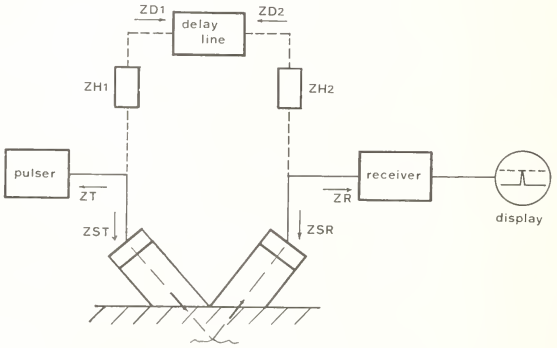

Figure 1. Block diagram of an ultrasonic instrument in the twin mode.

The operation of the twin mode is expressed by equivalent circuits shown in figure 3. The following notations are used in the figure:

- I1: Current source of the pulser
- ZT: Internal output impedance of the pulser
- ZR: Input impedance of the receiver
- ZST: Input impedance of the search unit
- ZSR: Output impedance of the search unit
- YR: Transfer admittance (short circuit output current/input voltage) of the search unit placed on a reference block
- V1: Voltage due to the transmitting pulse at the input of the receiver
- V2: Voltage due to the reflecting echo at the input of the receiver

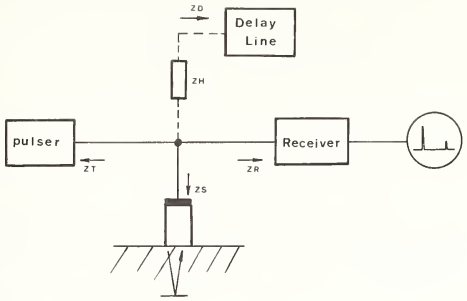

Figure 2. Block diagram of an ultrasonic instrument in the single mode.

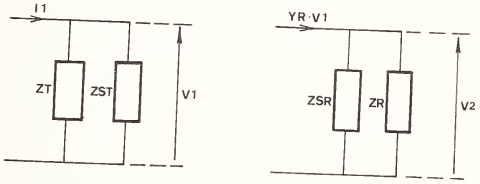

Figure 3. Equivalent circuits for the conventional calibration method in the twin mode.

It can be seen that:

$$V1 = ZK1 \cdot I1 \quad , \tag{1}$$

$$V2 = ZK2 \cdot YR \cdot V1 \quad . \tag{2}$$

Where

$$Zk1 = \frac{ZT \cdot ZST}{ZT + ZST} \quad , \tag{3}$$

$$ZK2 = \frac{ZR \cdot ZSR}{ZR + ZSR} \quad . \tag{4}$$

In the case of the single mode, eqs. (1) and (2) still holds, if ZK1 and ZK2 are replaced by the following ZK.

$$ZK = \frac{ZT \cdot ZR \cdot ZS}{ZT \cdot ZR + ZR \cdot ZS + ZS \cdot ZT} \quad , \tag{5}$$

where ZS is the impedance of the search unit.

First the gain of receiver is adjusted by means of a calibrated attenuator, so that the echo amplitude of the display reaches a specific level. The linear gain value is read as A1. Then the search unit is placed on a test piece. When a defect echo is found, the gain is adjusted until its amplitude on the display reaches again the same level. Let the gain and the transfer admittance of the search unit in this case be A2 and YX, respectively. Then the following equation is obtained from eq. (2).

$$A1 \cdot YR \cdot ZK2 \cdot V1 = A2 \cdot YX \cdot ZK2 \cdot V1 \quad . \tag{6}$$

Hence,

$$\frac{A1}{A2} = \frac{YX}{YR} \quad . \tag{7}$$

The dB value of the ratio in the left side of the equation is simply the difference of dB readings of the attenuator between two measurements. The right side is a quantitative measure of the defect in terms of YR. A simple method for measuring the transfer admittance has been presented elsewhere [1,2][1].

In order to obtain an accurate calibration, it is essential to keep the coupling between the search unit and the reference block or the test piece constant. Individual variations of the pulser/receiver and the search unit have little effect. This is a definite advantage. On the other hand, it is difficult to detect malfunctions of each component of the instrument.

3. PAL Delay Lines

In a number of European countries including Germany and the United Kingdom, the color television system called PAL is used instead of the NTSC system. PAL stands for Phase Alternation Line, which means the phase of the color subcarrier is reversed for every horizontal scan line. In a receiver, an ultrasonic delay line is used to recover color signal components by adding and subtracting the delayed and undelayed signals [3].

Specifications for a PAL delay line are very severe, because extremely accurate phase delay must be maintained over a range of temperature and for a long time. The delay line consists of a glass plate and two piezoelectric ceramic transducers mounted on the sides of the plate as shown in figure 4. The ultrasonic shear wave launched from the input transducer reflects five times at the sides before reaching the output transducer in order to reduce the size of the delay medium.

(a)

(b)

Figure 4. PAL delay lines (courtesy of Kinsekisha Laboratory Ltd.).

[1]Figures indicated in brackets indicate the literature references at the end of this paper.

Typical performance is shown in table 1. Data listed above the horizontal line in table are applicable to most PAL delay lines, whereas data below the line are applicable only to the model shown in figure 4.

Table 1. Performance of PAL delay line.

Normal Frequency	4.43 MHz
Bandwidth	±1 MHz
Insertion Loss	8±3 dB
Delay	63.943 μs
Phase Delay Variation	±5 ns
Spurious	3rd time > 21 dB others > 26 dB
Temperature Range	0 - 60 °C
Dimensions	42 x 47 x 6 mm
Weight	15 g
Input Admittance--- ∿ 300 ohms shunted by 170 pF	
Terminating Resistance	270 ohms

Thanks to a large volume of production in television industry, a delay line of such high performance is available at the price of only a few dollars. The delay line yields delayed output pulses at every odd multiple of the basic delay time (about 63.9 μs) in the twin mode and at every even multiple in the single mode. The amplitude and the delay time are well defined and stable against temperature change and aging. These features can be utilized for the calibration of ultrasonic pulse echo instruments. It can be used in the frequency range from 3 to 5 MHz without modification. For operation at 2 MHz, only the replacement of ceramic transducers is required to obtain a satisfactory result.

4. Shunt Method

The use of a delay line in the shunt method for the twin mode is shown by dotted lines in figure 1. High impedance elements, ZS1 and ZS2, are connected in series with the input and output terminals of a delay line. Then it is connected between the output of a pulser and the input of a receiver in parallel with the search unit.

Its operation can be expressed by equivalent circuits shown in figure 5. It can be seen that:

$$V3 = \frac{ZD1 \cdot V1}{ZH1 + ZD1} = \frac{ZD1}{ZH1} \cdot V1 \qquad (8)$$

$$V4 = \frac{ZD2 \cdot ZK2}{ZH1 + ZD2 + ZK2} \cdot YD \cdot V3$$

$$= \frac{ZD1}{ZH1} \cdot \frac{ZD2}{ZH2} \cdot ZK2 \cdot YD \cdot V1 \qquad (9)$$

where

ZD1, ZD2: Input and output impedances of the delay line, respectively. Usually both are the same, namely ZD.
V3: Voltage due to the transmitting pulse at the input of the delay line
V4: Voltage of delayed output at the input of the receiver
YD: Transfer admittance of the delay line.

The approximation is valid under the condition:

$$ZH1, ZH2 >> ZD1, ZD2, ZK1, ZK2 , \qquad (10)$$

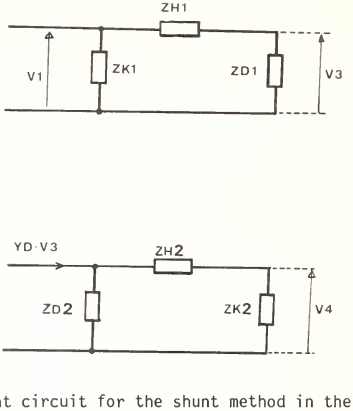

Figure 5. Equivalent circuit for the shunt method in the twin mode.

which is easily satisfied in practice. Under this condition, connecting and disconnecting the delay line can be carried out at will without interfering in the operation of the search unit. An adjustment of the gain of the receiver yields the echo amplitude of the specified level on the display, as in the case of the conventional calibration. The linear gain value is read as A3. Then the following equation is obtained instead of eq. (7).

$$\frac{A3}{A2} = \frac{V2}{V4} = \frac{ZH1}{ZD1} \cdot \frac{ZH2}{ZD2} \cdot \frac{YX}{YD} \tag{11}$$

Since the first two terms at the right side are constant, YX is calibrated in terms of YD.

In the case of the single mode, the delay line is connected, as shown by dotted line in figure 2. Equation (11) still holds, if the following substitutions are made:

$$ZH1 = ZH2 = ZH \tag{12}$$

$$ZD1 = ZD2 = ZD \tag{13}$$

One important difference between the shunt method and the conventional calibration method should be noted. In eq. (2), YR depends on the coupling, the position and characteristics of search units and hence its value is not stable. On the other hand, all the terms in eq. (9), including YD, are independent of the characteristics of the search units except its input and output impedances and are very stable. Hence the gain reading A3 is a good quantitative measure of the performance of the pulser/receiver. A calibration is achieved without using reference blocks. This feature is conveniently used in on-line systems where the use of reference blocks is troublesome. Once the pulser/receiver has been calibrated, then the calibration of search units can be made based on eq. (11).

The linearity and the dynamic range of the pulser/receiver can be calibrated by changing the value of the high impedance element, ZH. Since the delay time of the delay line is very stable, the time base of the display can be accurately calibrated. A time controlled gain or the depth compensation of the receiver can also be calibrated by utilizing multiple reflection echoes in the delay line.

In the following, a few experimental results will be described. The delay line works satisfactorily at 4 and 5 MHz. It yields enough output even at 2 MHz. The output of most

ılsers, however, contains a considerable amount of harmonics, which distort the output aveform of the delay line. The replacement of ceramic transducers as mentioned in Section 3 olves this problem.

The delay time of 128 μs in the single mode corresponds to the one-way distance of 20 cm n steel for shear wave. In the angle beam testing, a shorter delay is preferable. The delay ime in the single mode can be halved by connecting both the input and the output transducers n parallel. Figure 6 shows the output waveforms on the display in this case.

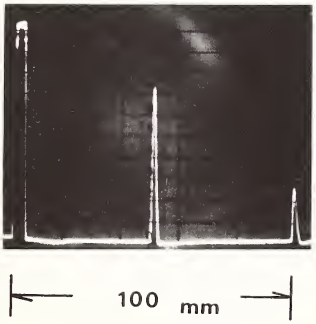

Figure 6. Output waveforms of the delay line.

Figure 7 shows the transfer admittance of the delay line with the series high impedance element (capacitance) as a function of capacitance value. A search unit, 5Q20N (5 MHz, quartz, 20 mm diameter, normal probe), and reference blocks, STB-G (Japanese Industrial Standard Z 2344) are used. The reference of 0 dB is the echo reflected from a flat bottom hole of 2 mm at the distance of 15 cm. The levels of echoes reflected from holes of 4 and 5.6 mm are also marked. It can be seen that the output of the delay line can be easily controlled over a wide range by the series capacitance. Various delay line units are now in practical use. Figure 8 shows typical examples: (a) is a variable type, (b) and (c) are fixed types.

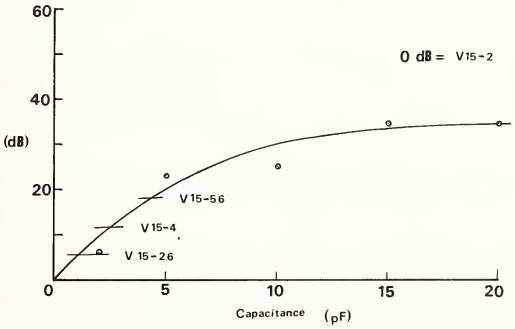

Figure 7. Transfer admittance of the delay line with the series capacitance.

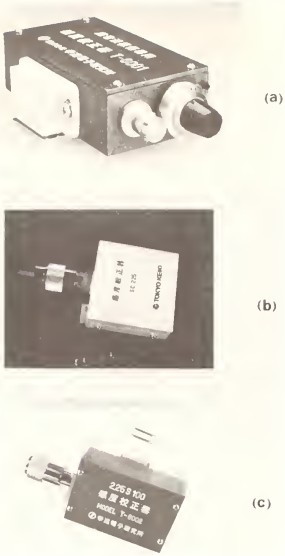

Figure 8. Ultrasonic calibrators using delay lines (courtesy of Tokyo Keiki Co. and Teitsu Denshi Co.).

5. Simulation Method

Most pulsers operate properly only when a search unit is connected. Hence the complete specification of a pulser should include the specification of the input impedance of the search unit to be used during the test of the pulser. The input impedance of search units varies widely. It is difficult to standardize or manufacture search units to a close specification. In this section, the simulation of a search unit by a delay line is described.

The input impedance of a delay line as well as a search unit can be reasonably approximated by the series resonant circuit shunted by a capacitance as shown in figure 9. The impedance values, however, are different. When the impedance value of the delay line is lower than that of the search unit, a convenient method for transforming the impedance level is the use of series and parallel capacitances as shown by dotted lines in figure 9. The trimming of impedance can be done easily by the adjustment of capacitances.

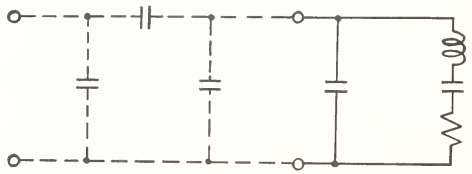

Figure 9. Equivalent circuit for input impedance of a delay or a search unit.

Figure 10 shows the transformed impedance simulating a 5Q20N search unit. Its transfer admittance is also plotted. With this simulation method, a pulser/receiver can be calibrated without using any particular search unit.

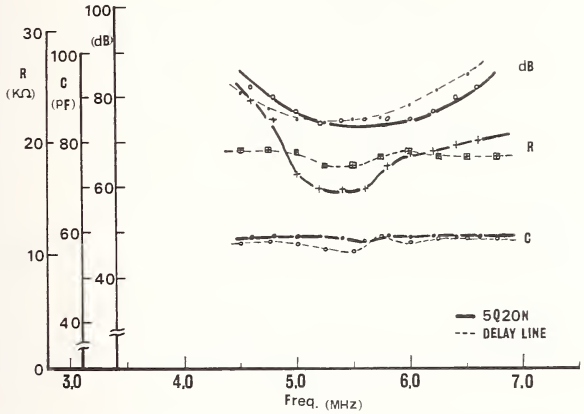

Figure 10. Input impedance and transfer admittance of a calibrator simulating a 5Q20N search unit.

6. Conclusion

Two methods for utilizing a PAL delay line for the calibration of an ultrasonic pulse echo instrument are presented. Performances of a pulser/receiver and search units can be separately calibrated. The delay line is light, compact, stable and inexpensive. It can be built into each instrument. In the shunt method, a high impedance element is inserted in series without affecting the operation of search units. In the simulation method, the input impedance of a search unit is simulated by transforming the impedance of a delay line. A pulser/receiver can be calibrated without using any particular search unit.

The authors would like to thank Dr. T. Shimada of Kinsekisha Laboratory Ltd. for providing delay lines and Dr. E. Yamamoto of Tokyo Keiki Co. and Mr. H. Nishiumi of Teitsu Denshi Co. for their cooperation during the development of the calibrators.

References

[1] Onoe, M., A method for measuring short circuit response product of a transducer in the reciprocity calibration, in Reports of 1968 Fall Meeting of Acoust. Soc. Japan, 3 - 1 - 2 (in Japanese).

[2] Onoe, M., A simple method for measuring transfer admittance of ultrasonic transducer, in Abstracts, 3rd Intern. Symp. on Ultrasonic Imaging and Tissue Characterization, National Bureau of Standards, Washington, D.C. (1978).

[3] Backers, F. T., A delay line for PAL colour television receivers, Philips. Tech. Rev., 29, 243-251 (1968).

National Bureau of Standards Special Publication 596, Ultrasonic Materials Characterization, H. Berger and M. Linzer, eds., Proceedings of the First International Symposium on Ultrasonic Materials Characterization held at NBS, Gaithersburg, Md., June 7-9, 1978. Issued November, 1980.

NEW AND IMPROVED ASTM TYPE ULTRASONIC STANDARD REFERENCE BLOCKS

Don L. Conn

Research Center
Armco Steel Corporation
703 Curtis Street
Middletown, OH 45043

This paper describes the development of diffusion bonded ultrasonic reference standards (blocks) of the ASTM type which offer many advantages over standards containing conventional drilled flat bottom holes.

These advantages include: (1) Diffusion bonded blocks contain perfectly flat and dimensionally accurate sonically reflecting areas. (2) The reflecting areas are truly perpendicular to the sound beam. (3) Diffusion bonded blocks can be fabricated from many materials. (4) Such blocks can be interrogated from either end resulting in two sound travel distances per block. (5) Diffusion bonded reference standards can be fabricated containing either naturally occurring or simulated defects.

1. Introduction

The need for standard reference blocks to aid the reproducibility of ultrasonic test results was recognized very early in the history of nondestructive testing. According to Panian and Van Valkenburg, Alcoa, Sperry, Grumman and other companies developed several different types of standards as early as the late 1940s to assist in ultrasonic system setup and calibration [1][1]. Due to a lack of standardization these reference blocks were composed of a myriad of materials of every size and shape each containing one or more man made discontinuities to serve as the necessary sonic reflector. The popularity of each type was the province of the material supplier or the customer and total agreement between the two parties was rare.

In 1951, Subcommittee VI of ASTM Committee E07 undertook the development of practical reference standards for ultrasonic inspection and in 1958 issued the Tentative Recommended Practice for Fabricating and Checking Aluminum Alloy Ultrasonic Standard Reference Blocks (E127-58T) [2]. The success of this work is underscored by the fact that after 20 years the same procedure, albeit with some modifications, is being used to manufacture and test aluminum standard blocks. ASTM standard reference blocks remain the one commonly accepted method of demonstrating ultrasonic test system calibration and performance.

The longevity of the acceptance of ASTM blocks as the industrial standard is not to be construed to mean that either the described fabricating procedure or the resulting reference standards are without fault. For example, for several years numerous reports were received throughout industry of non-uniform test results from supposedly identical inspection systems.

[1]Figures in brackets indicate the literature references at the end of this paper.

As material acceptance limits became more stringent and test sensitivity increased, increasing variability was noted in the test results. Nondestructive testing operators began to note that the system calibration changed with any change of instruments, cables, transducers, and even sets of ASTM reference blocks. It was quite apparent that ultrasonic testing was far short of a quantitative science.

In 1974 the National Bureau of Standards launched a study into the ultrasonic test variability that could be attributed primarily to ASTM reference blocks. Sushinsky, Eitzen, et al. issued a report in April, 1977 that detailed normal variations in ASTM block response of 20 to 40 percent and an outlying variation of almost 700 percent [3]. The investigators attributed the observed variation to several factors (primarily metallurgy); however, it is certain that reflector size and flatness contributed heavily. For obvious cost reasons however, it was not feasible to metallographically section a large number of blocks and investigate the accuracy of the fabrication process. As an outgrowth of this investigation NBS now offers a calibration service for ASTM E-127 type reference blocks.

Also during the early 1970s the ARMCO Steel Corporation Research Center was actively involved in a comprehensive internal cleanliness investigation in which methods for nondestructively detecting and evaluating micro inclusions were explored. After many nondestructive and destructive tests it became apparent that the response received by an ultrasonic test system used to rate inclusion concentrations was modified due to inclusion type. Hence, another investigation was begun into the measurement of the acoustic properties of the inclusion types associated with steel products. In an attempt to fabricate steel samples containing discrete inclusions of known size, composition, and orientation the diffusion bonding technique was explored and refined. The application of this refined technique to the manufacture of ASTM type ultrasonic reference standards containing air backed voids was a natural outgrowth of this work.

2. ASTM E-127-75 Reference Block Fabrication Procedure

Figure 1 is an engineering drawing depicting the construction and tolerances necessary to meet the Recommended Practice ASTM E-127-75 which governs the fabrication of aluminum reference standards. The manufacturing technique and tolerances for steel blocks

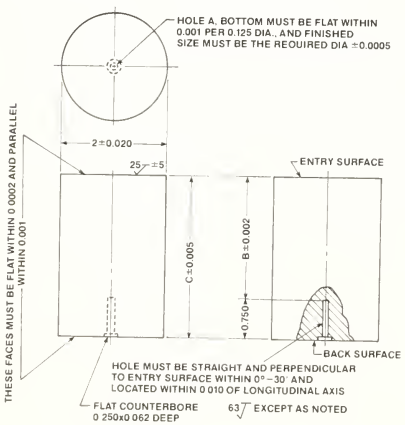

Figure 1. ASTM E-127 ultrasonic standard reference block. All dimensions are in inches (1 in = 25.4 mm).

are quite similar and are outlined in another ASTM document [4]. Upon reference to figure 1 it becomes apparent that a good machinist with good equipment working with easily machined material can indeed fabricate high quality flat bottom holes to a depth of 1.905 mm (0.750 in) as long as the drill size is large. When that same machinist attempts to drill flat bottom holes of 1/64, 2/64, or even 3/64 inches in diameter to a depth of 1.905 mm (0.750 in) while maintaining a straight hole whose bottom is precisely parallel to the sound beam entry surface, then the task becomes much more formidable[2]. It is almost a certainty that judicious "polishing" of the hole bottom has been used on several occasions to obtain the proper ultrasonic response from selected blocks.

3. Diffusion Bonding Method

The diffusion bonding process has been used by several research and commercial concerns as a method of material joining for many years [5]. Applications of the technique are far ranging, encompassing the glass, plastics, metals and other fields. Particularly in metals the process yields a bond of high mechanical strength that is difficult to detect metallurgically. This type of bond, illustrated in figure 2 also reflects very little incident ultrasonic energy and is normally invisible sonically at frequencies to 15 MHz and beyond. This characteristic has led to the selection of this bonding method for the manufacture of ultrasonic reference standards [6].

Figure 2. Photomicrograph of a typical diffusion bond in steel.

4. Diffusion Bonding as Applied to ASTM Type Blocks

When the diffusion bonding process is applied to the manufacture of ASTM Type ultrasonic reference standards some interesting advantages surface. As can be seen from figure 3 a cylinder of the prospective standard block material is sectioned. A hole of the selected flat bottom hole size is drilled through the center of the center slice or wafer, all mating surfaces ground, then the cylinder is reassembled and diffusion bonded using heat and pressure. The result is a cylindrical standard block containing a cylindrical void with truly perpendicular ends at a selected location along the length of the cylinder. A series of blocks having the wafer at the same relative position in each block but with increasing cylindrical void diameters forms the well known area amplitude block set. The unique advantage here is that not only are the reflecting ends of the cylindrical void of a known exact size and truly perpendicular to the sound beam but the block set can be inspected from either end yielding two discrete sound travel distances or calibration points per block.

[2]The conversion of flat bottom hole sizes from the English to the metric system has led to controversy among the nondestructive testing specification writers. Metric equivalent drill sizes are not readily available among the smaller hole sizes and the precise relationship between the hole sizes can be lost through substitution. For that reason the common 1/64 inch increment hole sizes will be referred to in this paper; 1/64 in is approximately 0.4 mm.

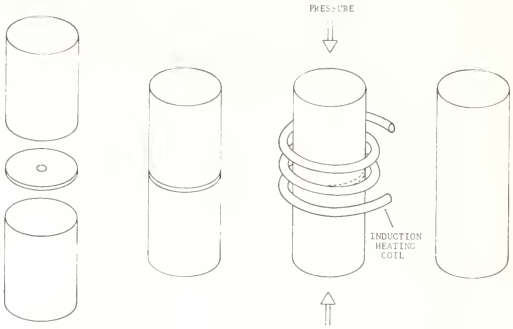

Figure 3. Fabrication of diffusion bonded reference block.

A series of blocks having identical holes in the center of each wafer but fabricated in such a manner that the wafer position is at a different location in each block as sketched in figure 4 yields what are commonly designated as distance amplitude (DA) blocks. Not only can the blocks be again inspected from either end reducing by one-half the number of blocks needed to obtain a DA curve but the uniform overall length of the block set reduces the amount of search tube manipulation required.

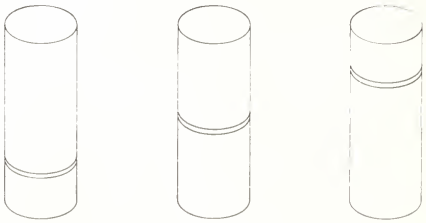

Figure 4. Diffusion bonded blocks with different water positions.

5. Diffusion Bonded Area Amplitude Blocks

When a set of diffusion bonded area amplitude blocks were ultrasonically examined per ASTM E48-75 and the data plotted on the Area Amplitude Response Curve for 4340 Steel Reference Blocks, the results were as shown in figure 5. To further explore the performance of the diffusion bonded blocks a much more stringent evaluation was conducted. In this case the response from the equivalent number 8 block was adjusted to match the system

vertical limit. The system gain was increased for each of the remaining blocks to obtain the same reference response on the instrument screen[3]. The increased gain required for each remaining diffusion bonded block was recorded and compared to theory. The same procedure was used to measure the response from the best set of 4340 steel reference blocks available and the results listed in table 1. The results indicate very good agreement between the commercial blocks, the diffusion bonded blocks and theory in all cases except the equivalent Number 1 hole in the diffusion bonded blocks. The response is 6 dB higher than the theory predicts. The probable cause involves "walking" or wandering of the drill through the wafer resulting in an oversized hole. Subsequent sectioning and polishing failed to corroborate this hypothesis due to the inadvertent removal of the 1/64 in diameter cylindrical void while sectioning the block. Photomicrographs of the cylindrical voids representing equivalent number 2 and number 3 holes are shown in figure 6. With proper care similar dimensional accuracy and end flatness should also be obtained with the void equivalent to the number 1 hole. At the present time three additional sets of diffusion bonded area amplitude blocks are being fabricated in order to substantiate this preliminary data.

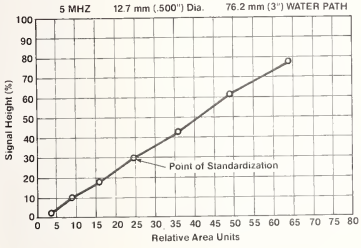

Figure 5A. Area amplitude curve from best available 4340 steel reference blocks plotted as shown in ASTM E428.

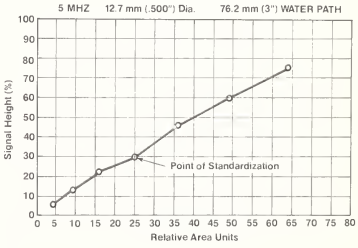

Figure 5B. Area amplitude curve from diffusion bonded blocks plotted per ASTM E428.

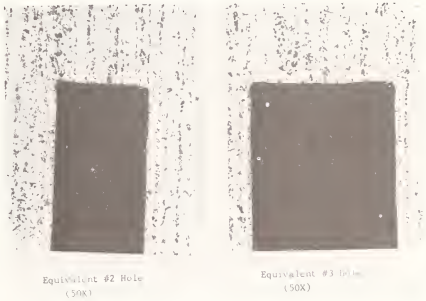

Figure 6. Photomicrographs of diffusion bonded voids representing the equivalent reflecting areas of 2/64 in and 3/64 in flat bottom holes.

[3]The measurements were made immersed with an Automation Industries S-80 Reflectoscope and a 5 MHz, 3/8 in (9.5 mm) diameter ceramic transducer. The water path distance was 3 in (7.6 cm). The attenuator was checked over a range of ± 12 dB and was found to be within ±1 dB. It was assumed that for the 36 dB range of the measurements similar accuracy or at least high repeatability would be maintained.

Table 1. This table lists the results obtained from the examination of the best available 4340 steel reference area amplitude standards and the ARMCO diffusion bonded area amplitude standards compared with calculated results obtained from the literature. Note that the difference of ±1 dB from the calculated value holds for all but the #1 diffusion bonded block. (see text)

dB RELATIONSHIPS BETWEEN FLAT BOTTOM HOLE SIZES

FBH SIZE	CALCULATED DIFFERENCE (APPROXIMATE)	MEASURED DIFFERENCE 4340 BLOCKS	MEASURED DIFFERENCE DIFFUSION BONDED BLOCKS
#8	40	40	40
#7	42 > 2dB	43 > 3dB	42 > 2dB
#6	45 > 3dB	47 > 4dB	44 > 2dB
#5	48 > 3dB	49 > 2dB	46 > 2dB
26 / 4B	52 > 4dB	36 / 4B 53 > 4dB	28 / 4B 51 > 5dB
#4	57 > 5dB	58 > 5dB	55 > 4dB
#3	64 > 7dB	65 > 7dB	62 > 7dB
#2	76 > 12dB	76 > 11dB	68 > 6dB
#1			

6. Diffusion Bonded Distance Amplitude Blocks

A set of diffusion bonded distance amplitude blocks were ultrasonically examined and the resulting data plotted on the ASTM E428-75 Distance Amplitude Response Curve for 4340 steel reference blocks. The results shown in figure 7 indicate good agreement with the results from the best available type 4130 distance amplitude blocks. Again, additional sets of diffusion bonded distance amplitude blocks are being fabricated for substantiation.

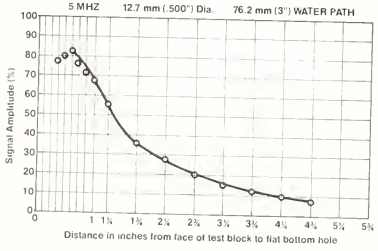

Figure 7A. Distance amplitude curve from best available 4130 steel reference blocks plotted as shown in ASTM E428.

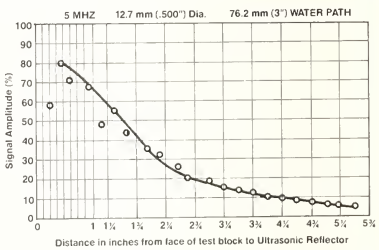

Figure 7B. Distance amplitude curve from diffusion bonded blocks plotted per ASTM E428.

7. Extension of the Diffusion Bonded Method

The advantages inherent in the diffusion bonded method of ASTM type standard fabrication can be successfully utilized for the manufacture of other standards types. Consider for example the test standardization problem associated wih the ultrasonic inspection of round bars. The normal procedure involves either spiraling the bars through a small self-sealing ultrasonic immersion tank containing a fixed position ultrasonic transducer or rotating the bar in a large ultrasonic tank and traversing the ultrasonic transducer along the length of the bar. In either case the transducer scans a spiral path along the bar length. Many customer specifications require dynamic calibration of the ultrasonic test system at production scanning speeds in order to demonstrate adequate system defect

alarm response and to prove that the scan path affords sufficient inspection coverage. This requirement can only be met by fabricating a rotatable standard complete with the specified flat bottom holes drilled to the proper depths. In addition the standard must be of sufficient length to contact the drive rollers so that the standard can be rotated beneath the ultrasonic transducer "at production scanning speeds." The difficulty with this requirement lies in the method used to fabricate the standard. As shown in figure 8 the flat bottom holes drilled to mid-thickness and beyond, when rotated 90°, become side drilled holes which markedly interfere with the desired response of the ultrasonic test system. This undesirable response effectively prohibits the use of such standards to calibrate the system at "production scanning speeds."

If the standard is constructed in the manner shown in figure 9 utilizing the diffusion bonding method however, the reflecting areas become thin discs rather than the elongated cylinders that result from the drilling operation. It is now possible to rotate the bar and calibrate the test system at "production scanning speeds" without spurious signals from unwanted reflecting areas. Again it is interesting to note that when the disc shaped voids are bonded at 1/4 and 1/2 the thickness of the bar a true 3 point calibration results. (The disc located at 1/4 thickness appears at the 3/4 thickness position when the bar is rotated 180°.)

Many other types of ultrasonic reference blocks can be readily fabricated using the diffusion bonding technique. Reference blocks have been manufactured containing oxide, silicate, and sulfide inclusions of various sizes. Silicon discs varying in thickness from 100 to 1000 Å (10 to 100 nm) have been successfully bonded inside steel matrices to determine the effects of inclusion thickness on ultrasonic detectability. Fatigue cracks, porosity, or other naturally occurring defect types can probably be sealed in a myriad of materials via the diffusion bonding technique. The possibilities are limitless.

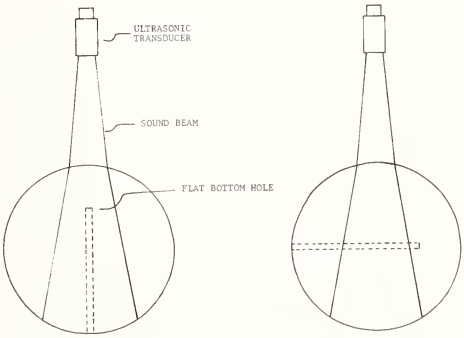

Figure 8. Conventional rotatable standard containing F.B.H.'s

8. Summary

The primary emphasis of this paper has been on the diffusion bonding technique as an improved method of manufacture of ASTM type ultrasonic reference standards. The advantages include better control of the size, geometry, and orientation of the reflecting area than is possible using conventional fabrication techniques. The utility of the diffusion bonded area amplitude blocks is doubled due to the attainment of two sound travel distances per block. The number of necessary diffusion bonded distance amplitude blocks is halved due to the same duality of sound travels. In addition the uniform height of the DA blocks reduces set up time.

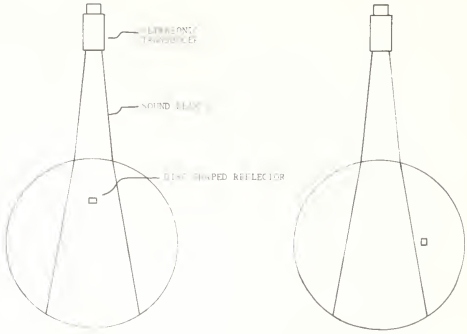

Figure 9. Diffusion bonded rotatable standard with disc shaped reflectors.

Finally the extension of the diffusion bonded fabrication method to other ultrasonic standards types is described and the advantages enumerated.

References

[1] Panian, F. C. and Van Valkenburg, H. E., Development of ASTM standard reference blocks for ultrasonic inspection, in Proceedings of American Society for Testing Materials, Vol. 59 (Philadelphia, 1959).

[2] Anon., Tentative recommended practice for fabricating and checking aluminum alloy ultrasonic standard reference blocks, ASTM Designation E127-58T, 1958 Book of ASTM Standards, Part 3 (American Society for Testing Materials, Philadelphia, 1958).

[3] Sushinsky, G. F., Eitzen, D. G., et al., Improved ultrasonic standard reference blocks, Report No. AFML-TR-77-40 (Air Force Material Laboratory, Wright-Patterson AFB, Ohio, April, 1977).

[4] Anon., Standard recommended practice for fabrication and control of steel reference blocks used in ultrasonic inspection, ASTM Designation E428-71, 1976 Annual Book of ASTM Standards, Part II (American Society for Testing Materials, Philadelphia, 1976).

[5] Anon., Diffusion welding, Welding Handbook, Sixth Edition on Welding, Cutting, and Related Process, Chapter 52, Section 3B (American Welding Society, New York, 1971).

[6] Paton, N. E., Ultrasonic samples using diffusion bonding techniques, in Proceedings of the ARPA/AFML Review of Quantitative NDE, Report No. AFML-TR-75-212, (Air Force Materials Laboratory, Rockwell International Science Center, Thousand Oaks, CA., January 1976).

National Bureau of Standards Special Publication 596, Ultrasonic Materials Characterization, H. Berger and M. Linzer, eds., Proceedings of the First International Symposium on Ultrasonic Materials Characterization held at NBS, Gaithersburg, Md., June 7-9, 1978. Issued November, 1980.

PERFORMANCE DIFFERENCES IN QUARTZ ULTRASONIC SEARCH UNITS

G. J. Posakony

Battelle-Northwest
Richland, WA 99532

The sound field propagating from an ultrasonic search unit is influenced by many factors including the basic design, manufacturing procedure and operational conditions. This paper discusses the differences in performance measured from well characterized quartz search units manufactured to fulfill the sound field requirements established for the evaluation of ultrasonic reference blocks in accordance with ASTM E127. Measurements show that the sound beam landmark position, such as the near-far field transition, are shifted substantially when the ground electrode and the positive electrode are of different size. Search units with electrodes of equal size are compared with those which have electrodes of unequal size. Comparisons are also made describing the difference in sound field resulting from continuous wave, burst continuous wave and pulsed excitation. While some differences would be expected and are explainable, recognition of these differences is essential to the selection and acceptance of the design that can produce the desired sound field pattern.

1. Introduction

Under current practice ultrasonic test blocks are the basis for establishing system sensitivity and hence inspection accept/reject criteria for most ultrasonic examinations. There are reports [1][1] of wide differences in the quality and reproducibility of ultrasonic test blocks used by industry. Reports describe differences in the unit to unit response of search units, test instrumentation and the test blocks. In this text, a limited experimental study was performed in an attempt to identify and document differences in typical quartz search units used in the calibration of ultrasonic test blocks in accordance with ASTM E127-75 [2]. The experiment includes an evaluation of the transmitted and pulse echo responses obtained from well-characterized quartz ultrasonic search units. The experiment includes an evaluation of both continuous wave and pulsed excitation of search units, and describes the measured differences under a variety of test conditions. The results strongly indicate the need for selection of specific designs for the ultrasonic search units that are to be used to qualify the ultrasonic test blocks used by industry. The results further indicate the need to establish a better theoretical base for the operation and performance of narrow-band and broad-band pulse echo test systems.

2. Background

Most inspection accept/reject criteria for materials requiring ultrasonic examination are based on a comparison of the amplitude of the echo response reflected from a flaw within a part with the response obtained from a machined defect in a test "reference" block. Flat bottomed holes (FBH), EDM notches and side drilled holes are typical machined defects used as reference reflectors to adjust the sensitivity of the ultrasonic flaw detection instrument. ASTM E127-75 "Standard Recommended Practice for Fabricating and Checking Aluminum Alloy

[1]Figures in brackets indicate the literature references at the end of this paper.

Ultrasonic Standard Reference Blocks", provides a detailed description for the fabrication and evaluation of flat bottomed hole test blocks. Qualification of the various test blocks designed to meet E127 is established by demonstrating that the ultrasonic amplitude response from the reflectors in a test block set satisfy accepted distance amplitude or area amplitude curves.

ASTM is continually updating and refining its recommended practices. A committee of E7-06-02 "Aluminum Reference Blocks" is reviewing E127 to develop an improved procedure for calibration of test blocks. Of particular interest to this author is the ultrasonic response of the 5 MHz, 3/8 in (9.5 mm) diameter search unit presently recommended. A sketch of the response curve from search units acceptable under E127 is shown in figure 1. This type of response is obtained by profiling the on-axis pulse echo response of the search unit using a 1/2 in (12.7 mm) diameter steel ball in water as the target and recording the amplitude observed on the display of a flaw detector instrument. The dotted line shows the theoretical tone burst pulse echo response from a ball target for a 5 MHz, 3/8 in (9.5 mm) search unit. The comparison shows that the theoretical on-axis response particularly at the near-far field transition falls short of the profile described in the Recommended Practice. The curve in the far field, however, is reasonably close to the theoretical predictions.

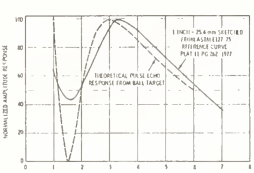

Figure 1. Comparison of ASTM E127-75 [1] response curve and theoretical prediction.

The search unit response curve carries significant importance as the amplitude response from the reflectors in the test blocks is directly dependent on the character of the sound beam of the evaluation search unit. Historically [3], the sound beam profile curves in E127 were developed empirically from large numbers of measurements recorded from the response of the 1/2 in (12.7 mm) diameter ball target in water using commercial ultrasonic flaw detectors employing "nominal" 3/8 in diameter, 5 MHz quartz search units. Variations in unit to unit performance of the search units resulting from the manufacturing procedures or operational use, directly effects the test sensitivity used for a given test and can result in substantial differences in test results between vendors and users. Availability of reliable and reproducible search units with calculable and tractable performance characteristics is a key link in improving the reliability and credibility of ultrasonic testing. While the differences in the theoretical and recommended curves do not show a major difference, the fact that the near-far field transition peak (Y_0+) is beyond the theoretical peak requires investigation. Further, obtaining search units that meet ASTM E127 requirements has been increasingly difficult.

3. Experimental Study

In an attempt to determine the reason for the difference between the theoretically predicted curve for the 3/8 in (9.5 mm) diameter, 5 MHz search unit and the curve shown in ASTM E127 (fig. 1), a series of commercially available 5 MHz search units were studied. Units were obtained on an "on loan" basis for the experiment from both manufacturers and users. Two different engineering designs were evaluated, namely, (1) a 1/2 in (12.7 mm) diameter quartz element with a 3/8 in (9.5 mm) positive electrode and a 1/2 in (12.7 mm) negative or ground electrode with a wrap around configuration, and (2) a 3/8 in (9.5 mm) quartz element with full electrodes on positive and negative sides. The two designs are shown in figure 2.

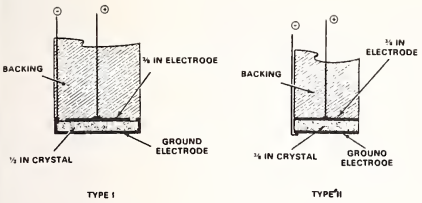

Figure 2. Two designs used to fabricate ultrasonic search units.

The experiment performed was to evaluate the sound beam pattern from the two designs when these units were driven with continuous wave, tone burst and pulse excitations. The objective of the experiment was to determine the influence, if any, resulting from the different excitations and use the data to make recommendations concerning the manufacturing design that could most reliably satisfy present ASTM requirements. Specific goals were:

1) Establish that a piezoelectric element which was mounted on a backing member and which had both edge and back clamping could meet the theoretical prediction for plane piston radiators.

2) Determine if tone burst excitations of the search unit would differ from continuous wave.

3) Evaluate the difference between pulse excitation, tone burst excitation, and continuous wave excitation (center frequency of pulse excitation at 5 MHz).

The theoretical on-axis pressure response for a 3/8 in (9.5 mm) plane piston radiator is based on the equation:

$$P = 2\,Po\,\sin\left[\left(\frac{\pi}{\lambda}\right)\left(\sqrt{a^2 + x^2} - x\right)\right]$$

where: Po is radiation pressure at search unit face

a is radius of search unit

x is on-axis distance from the search unit.

For the experiment it was assumed that the response for both designs of search units would be approximately the same. A modified Tektronix constant voltage generator was used for both the continuous and tone burst excitation. A Sperry Reflectoscope Model 771 with 10N pulser-receiver was used for the pulse excitation phase of the experiment. The on-axis profiles were developed by carefully plotting the cross section profiles using a microprobe hydrophone and reconstructing the on-axis profiles from these data.

The experimental apparatus is shown in figure 3. The system consists of a large water tank mounted on a heavy-duty lathe bed. The search unit is mounted in an x-y-θ manipulator and the initial positioning of the search unit is determined from the pulse echo response off a steel plate test target mounted perpendicular to the axis of the lathe bed. This assures that the sound field is projecting in a known path along the axis of the tank. Once the search unit has been positioned the reflector plate is removed and the microprobe hydrophone is lowered to an appropriate depth and the field response at specific locations is mapped.

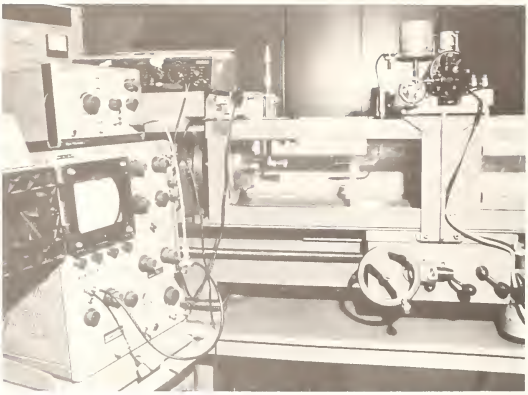

Figure 3. Experimental test apparatus.

The hydrophone used in the experiments (see fig. 4) contains a 0.01 in (0.25 mm) 10 MHz piezoelectric element mounted on a small wire and fabricated into a small diameter steel tube. The hydrophone is broadbanded to cover a broad frequency spectrum (e.g., 0.5 to 10 MHz). Continuous wave, tone burst and pulsed excitations applied to the ultrasonic search unit generates the ultrasonic beams. The output of the hydrophone, which measures the pressure distribution, is amplified, processed and recorded to provide cross section sound field plots at various distances from the transmitting search unit.

Figure 4. Ultrasonic microprobe hydrophone.

A typical profile recorded from the experimental system is shown in figure 5 (plot #43). This is a plot of a 5 MHz, 3/8 in diameter (9.5 mm) with equal front and back electrodes (Type 2). The plot clearly demonstrates that under continuous wave excitation a mounted quartz crystal with both edge and back clamping will produce a field pattern as predicted by plane piston theory. The peak response at a2/λ (3 in - 76 mm) has a pressure twice that of the energy at the search unit face. The landmark locations $a^2/4\lambda$, $a^2/3\lambda$, $a^2/2\lambda$, a^2/λ, and $2a^2/\lambda$ are at the correct locations (i.e., 0.75 in, 1 in, 1.5 in, 3 in, 6 in) and have the correct pressure distributions. Figure 5 demonstrates that the analytical and experimental values are the same for continuous wave excitation. These types of profiles are used throughout the experiment in developing the on-axis profiles as shown later in the text, and in establishing the performance differences for various types of excitation. While experiments

were performed on continuous wave, tone burst continuous wave, and pulse excitations, no differences were found between the continuous wave and tone burst field patterns providing the tone burst contained a minimum of 10 cycles at the fundamental or test frequency. Consequently, the text compares only the continuous wave with the pulsed excitation.

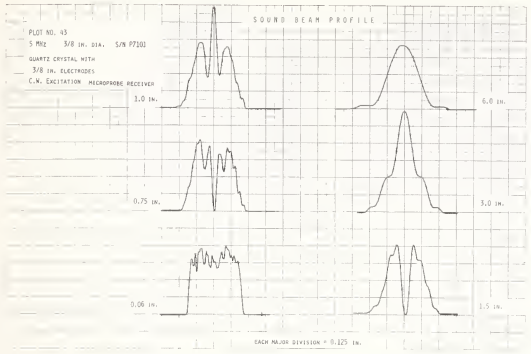

Figure 5. Cross axis sound field plots at selected locations.

4. Experimental Results

Initial efforts to generate the on-axis profiles of the various search units by moving the carriage containing the hydrophone along the axis of the lathe were unsuccessful. The mechanical alignment proved extremely critical and measurements were not reliably repeatable. To insure the validity of the data the approach of measuring the cross axis profile and reconstructing the on-axis profile from these data was chosen. As the objective of the experiment was to determine the performance differences under various excitation conditions, plots were made of:

1) Type 1 search unit design comparing the theoretical pressure pattern with the measured pressure patterns.

2) Type 2 design comparing the theoretical pressure pattern with the measured pressure pattern. The microprobe hydrophone was used for obtaining these data for 'a' and 'b'.

3) The pulse echo response from a 1/2 in (1.27 mm) ball target comparing the response from the Type 1 and Type 2 search unit designs with that of the ASTM E127-75 search unit plot.

To verify that the frequency response of the continuous wave and pulsed excitation were in fact at 5 MHz a spectrum analysis of the search unit-microprobe response was measured. Figure 6 shows the measured plots. Figure 6a is the response measured for the continuous wave while 6b is the response from the Sperry Reflectoscope. While the output of the Reflectoscope was a few kHz below the 5 MHz center frequency, this is not considered to be a major contributor to the differences noted in the field plots.

The response of the Type 1 search unit under cw and pulsed excitation conditions is shown in figure 7. The Type 1 search unit is a 1/2 in (12.7 mm) diameter quartz transducer blank with a 3/8 in (9.5 mm) diameter positive electrode. The ground electrode is wrapped around so that both the positive and ground wires egress from the rear surface of the assembly. The measured plot of the continuous wave excitation shows the first null in the near field and the near-far field transition ($a^2/2\lambda$ and a^2/λ) to extend beyond the theoretical limit by approximately 30 percent. The pressure pattern in the far field is not greatly different from the theoretical prediction. Interestingly enough, when the same

search unit was pulsed excited using the Sperry Reflectoscope, the peak response was shortened from the continuous wave measurement and approximated the peak response predicted by theory. Figures 8 and 9 contain the profile data from which the curve on figure 7 was established.

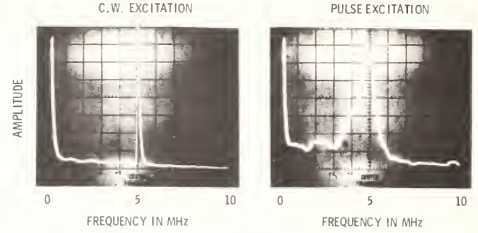

Figure 6. Analysis of excitation spectrum.

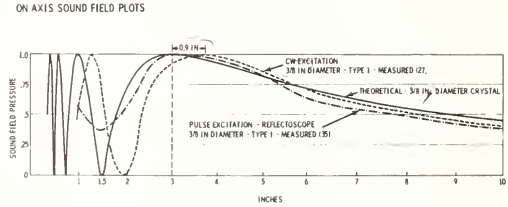

Figure 7. Distance amplitude on-axis plots type I search unit.

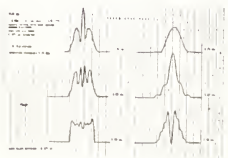

Figure 8. Profile from continuous wave excitation.

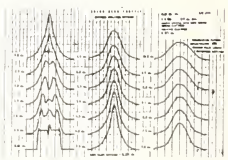

Figure 9. Profile from pulsed wave excitation.

Figures 10, 11, and 12 show the response from the Type 2 search unit design. In this design the quartz transducer is 3/8 in (9.5 mm) and has equally sized front and back electrodes. The continuous wave response closely approximates theory, however, the pulsed response shows a foreshortening in both the first null and peak response. Furthermore, the far-field pressure pattern falls significantly below the desired curve. Figures 10 and 11 show the cross sectioned profiles used to establish these curves.

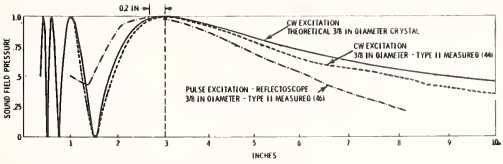

Figure 10. Distance amplitude on-axis sound field plots; type 2 search unit.

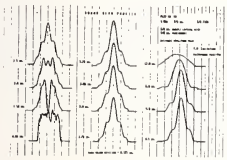

Figure 11. Profile from continuous wave excitation.

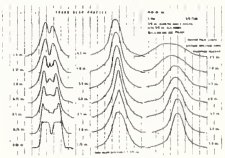

Figure 12. Profile from pulsed wave excitation.

The pulse echo responses shown in figures 13, 14, and 15 were made by removing the microprobe from the text fixture and replacing it with a 1/2 in (12.7 mm) diameter steel ball target. The echo returning from the ball target was gated and input to a peak detector. The output of the peak detector was used to drive the x-y recorder and profiles were made of the responses. Figure 13 is the on-axis summation of the profile recording shown in figures 14 and 15. In this experiment neither the Type 1 nor the Type 2 search units exactly matched the ASTM E127-75 reference curve. The ASTM document has sufficient latitude to allow use of the Type 1 search unit as recorded in figure 13; however, the Type 2 search unit would not be acceptable. The pressure and pulse echo curves have been extremely helpful in determining some of the differences that can occur in search unit performance of even the well-characterized quartz-type search units.

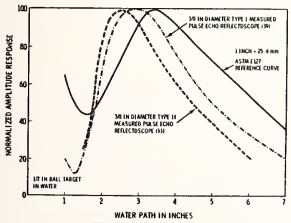

Figure 13. Distance amplitude on-axis profile from pulse echo tests.

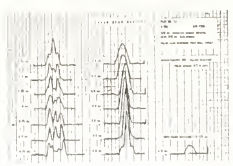

Figure 14. Profile from type 1 search unit.

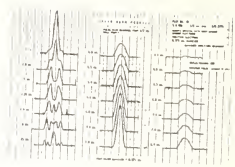

Figure 15. Profile from type 2 search unit.

5. Experimental Conclusions

While the experiment was a limited study, it provides some conclusions that must be considered if reliable and reproducible test results are to be achieved. Certainly further theoretical and experimental work must be performed; however, conclusions that can be reached at this time are as follows:

1) An ultrasonic search unit consisting of a piezoelectric transducer mounted on a backing and assembled into a housing can produce a field pattern that matches the theoretical prediction providing the element is excited by continuous wave or tone-burst continuous wave excitation.

2) Plane wave theory based on piston displacement does not accurately predict the radiation pattern generated from pulse or broadband excitation.

3) The design of the search unit, particularly as it applies to the relationship between the size of the ground and positive electrodes has a substantial influence on the sound beam generated by the search unit. Units designed with a positive electrode smaller than the ground electrode develop both electric and acoustic field fringing which make the apparent aperture of the search unit larger than the size of the positive electrode.

4) Careful attention must be given to the design and performance of the search units used in calibrating the ultrasonic reference blocks which become the basis for accepting, rejecting and sizing of defects. Reproducible performance is necessary if we are to reduce the variability in interpretation of test results. Variations in the far field pressure profile dramatically influence the amplitude of the echo response from an ultrasonic test block with a net result of incorrect adjustment of sensitivities or distance amplitude correction electronics which can result in establishing an inaccurate accept/reject criteria.

6. Significance of Experiment

The experimental results shown in the test are alarming. The ultrasonic calibration block is used as the basis for establishing sensitivity of a test instrument and as the means for establishing accept/reject criteria for ultrasonic inspections. The search unit used for calibrating the reference blocks is one of the critical items in determining the quality, acceptability, and reproducibility of test blocks used by industry. The manufacturers of ultrasonic search units have a responsibility in providing units which are reliable and reproducible; however, since no basic guideline exists other than the on-axis and cross-axis profiles described in E127, manufacturers may provide a variety of search units utilizing different designs which "apparently" satisfy the ASTM requirements. The National Bureau of Standards has an intensive program [4] designed to identify the response differences in ultrasonic test blocks and to make recommendations for means for reducing the error bounds associated with ultrasonic materials inspection. Further efforts by NBS, industry and other research organizations can substantially aid in increasing the reliability of ultrasonic

testing and help gain greater credibility for the test results achieved in nondestructive evaluation. It is evident that if search unit performance can be "standardized" much of the ambiguity as well as the unit to unit performance differences would be reduced. By the same token, variations such as those shown in figure 13 can lead to gross misinterpretation of test results and inject further mystery into an already complicated testing procedure.

References

[1] Eitzen, D. G., et al., Improved Ultrasonic Standard Reference Blocks, Progress Report No. 2 - Report No. NBSIR-76-984. National Bureau of Standards, Washington, DC.

[2] Anon, Standard Recommended Practice for Fabricating and Checking Aluminum Alloy Ultrasonic Standard Reference Blocks E127-75, in 1977 Book of ASTM Standards Part II (Am. Soc. Test. Mat., Philadelphia, 1977).

[3] Panian, F. C. and Van Valkenburg, H. E., Development of ASTM Standard Reference Blocks for Ultrasonic Inspection Proceedings, Vol. 59, American Society for Testing Materials (Philadelphia, PA, 1959).

[4] Chwirut, D. J., Sushinsky, G. F., and Eitzen, D. G., Procedures for the Calibration of ASTM E127 Type Ultrasonic Reference Blocks, NBS Tech Note 924, National Bureau of Standards, Washington, DC.

National Bureau of Standards Special Publication 596, Ultrasonic Materials Characterization, H. Berger and M. Linzer, eds., Proceedings of the First International Symposium on Ultrasonic Materials Characterization held at NBS, Gaithersburg, Md., June 7-9, 1978. Issued November, 1980.

CHARACTERIZATION OF PROBES USED FOR PERIODIC INSPECTION

F. H. Dijkstra

Röntgen Technische Dienst b.v. R & D Department
Delftweg 144, Rotterdam
The Netherlands

Reproducibility of ultrasonic data is essential, particularly in the field of periodic inspection. This fact, together with the special requirements for the inspection techniques used by R.T.D. (e.g., in Germany: the RSK - Rules) make good methods for characterization of the ultrasonic search units necessary. The calibration reflectors to be used for the inspection are relatively small, and the tandem technique for the detection of perpendicular flaws in thick walled components is prescribed. The requirements are explained by means of an example of a multi-probe system normally used for the inspection of nuclear components. Some of the most important methods for characterization of the probes are introduced:

1) Eddy sonic sensor to establish the angle beam characteristics in steel; 2) recording of the probe's properties by means of real scale test blocks, including the signal-to-noise ratio on clad; 3) D.G.S.-curves of probes for inspection of austenitic structures; 4) beam sections in water and steel by isosonography; and 5) frequency and bandwidth determination.

1. Introduction

Reproducibility of ultrasonic data is important in periodic inspection. In the past few years, this fact has led to an increasing mechanization of inspection, in order to minimize inaccuracies caused by manual scanning. However, other factors may affect the reproducibility, e.g., 1) calibration; 2) equipment properties and quality; and 3) tolerances of probe parameters.

In this presentation the last mentioned factor is discussed. Some methods are described, which although not yet perfect, help to make better probe reproducibility possible. The aim is to express the transducer parameters in absolute values (quantification). For instance, the well-known and valuable system, schlieren optics, is very suitable for investigation of sound beam behavior, but not for its quantification. In the last few years, much attention has been paid to methods in order to make this quantification possible.

For pre-service and in-service inspections (PSI and ISI) of nuclear pressure vessels the ASME Code and its alternative versions are used. In Germany the directives of the Reactor Safety Committee (RSK)[1] are applied [1][2], with regard to the following requirements:

1) for pre-service inspection: 100 percent volumetric inspection of the entire vessel wall; 2) perpendicular incidence of the sound beam with respect to the expected flaws, by means of appropriate probe angle choice; 3) above 100 mm wall thickness, the tandem technique should be applied; 4) for perpendicular reflectors, e.g., in the tandem technique, the registration level is 6 dB below a 10 mm diameter flat bottom hole; and 5) for flaws which have to be found using reflection by flaw tips and facets (inclined incidence) a registration level of a 3 mm diameter flat bottom hole has to be used.

[1]Reaktorsicherheitskommission.
[2]Figures in brackets indicate the literature references at the end of this paper.

Figure 1 shows an ultrasonic transducer, specially developed for mechanized inspections, which can be performed up to 30 meters under water [2], and a special probe holder. A number of these probes and holders can be used to build up a multiple probe system, of which an example is shown in figure 2. This system, called "TET-System" (Tandem-Echo-Transmission), incorporates the following techniques: 1) impulse echo technique (single probe technique), both sides; 2) tandem technique; 3) longitudinal angle probe (type SEL) with separate transmitter and receiver for the upper zone (clad); 4) normal beam probe; and 5) pitch and catch (transmission) technique.

Figure 1. Probe and holder for mechanized inspection.

The system shown uses 32 gates for 11 zones. The probe configuration depends on the requirements; figure 3 shows another possible arrangement.

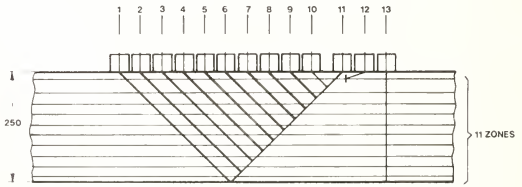

Figure 2. Principle of multi-probe system with combined techniques.

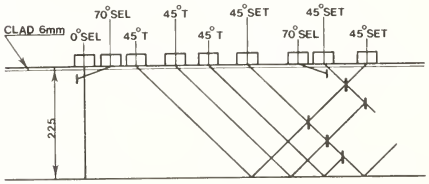

Figure 3. Example of a multiple probe system for a reactor vessel wall with thickness 225 mm.

2. The Eddy Sonic Sensor (ESS) for the Determination of Directional Characteristics of Angle Probes.

Especially when used for long sound paths (e.g., up to 450 mm) the directional characteristics of the probe are important: 1) the transmitting sound field of the probe used as a transmitter in tandem technique or pitch and catch; 2) the receiving sound field, for the use in such techniques as a receiver; and 3) the characteristics of a transceiver probe (both transmitter and receiver).

These data are used as a starting point for the composition of multiple probe systems (zone dimensions, scanning pattern, etc.) and for studying the reproducibility of probe fabrication.

In the BAM (Bundesanstalt für Materialprüfung) in Berlin, a technique for the determination of directional properties of transducers has been developed [3]: this is used in Europe as a standard method. Figure 4 shows a block diagram of the equipment. The probe, operated as a transmitter, is coupled acoustically to a calibration block with a 100 mm radius and a width of, e.g., 50 mm. The radius is scanned by an eddy sonic sensor (ESS). The energy received by the ESS controls the Y-movement of an X-Y-plotter, after having passed a preamplifier and the amplifier and monitor of an ultrasonic instrument, which also makes the signal visible on its CRT (Cathode Ray Tube). The X-movement of the plotter is controlled by the probe position signal. Using an appropriate calibration of the X- and Y-axis, a curve as shown in figure 5 can be obtained.

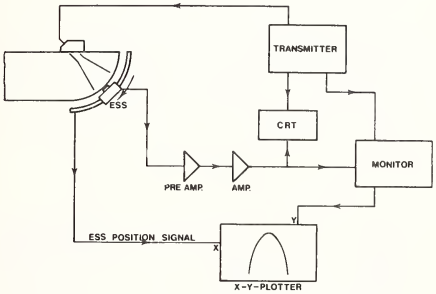

Figure 4. ESS block diagram.

It should be realized that this beam plot only represents the directional characteristics of the probe as a transmitter. According to Wüstenberg [3] the receiving characteristics are identical, which can be checked by using the inverted process of figure 4, the ESS being operated as a transmitter [3]. The directional characteristic of a probe used as a transceiver is obtained by multiplication of those in the transmitting and the receiving operations. This can be illustrated by a measurement as is shown in figures 6 and 7. Figure 6 shows the results of a transverse scan of a transmitted beam (distance 40 mm) by an ESS. The curves represent the transmitted energy as a function of the probe displacement. Figure 7 shows a scan on a 2 mm flat circular reflector, the same probe (2.25 MHz, 1.27 mm diameter) being operated as a transceiver at the same distance. It can be seen that the curve width is reduced. At each point in the beam section the amplitude reduction with respect to the maximum on the beam axis is the square of that in figure 6, which corresponds with theory. (The measured deviation is approximately 2 dB, due to the dimensions of ESS and reflector.) A small reflector was chosen in order to minimize the influence of the directional characteristics of the reflecting area. In this way, it is shown that the impulse echo beam width can be derived from the ESS-curve. In other words, ESS beam characterization gives useful

information about the directional properties of the probe under ideal circumstances, with minimized influences of, e.g., test block dimensions, sound attenuation, acoustic coupling, and probe handling.

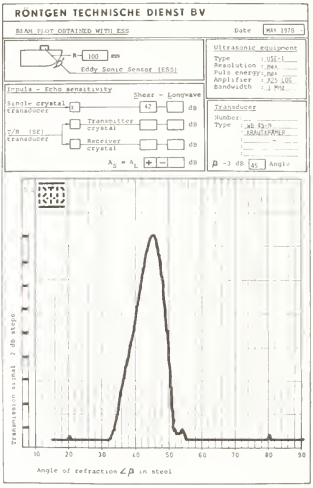

Figure 5. Beam characteristics data sheet.

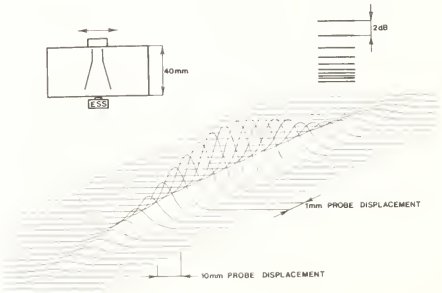

Figure 6. Sound beam scan with ESS. Distance: 40 mm. Probe: 2.25 MHz, 1/2 in (1.27 cm) diameter.

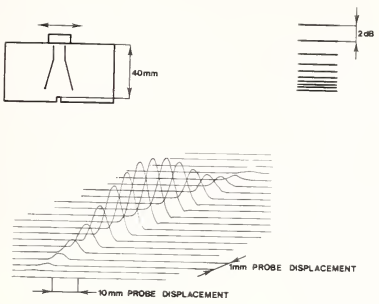

Figure 7. Scan on 2 mm Ø target. Distance: 40 mm. Probe: 2.25 MHz, 1/2 in (1.27 cm) diameter.

The principle of the ESS is shown in figure 8. Particles of the calibration block surface, brought into oscillation by the probe under measurement, move within the magnetic field of the sensor. Consequently, eddy currents are set up in the object material and a voltage is induced in the coil. This voltage signal is proportional to the sound pressure. The left hand sensor in figure 8 is for shear waves, the right hand one for compressional waves.

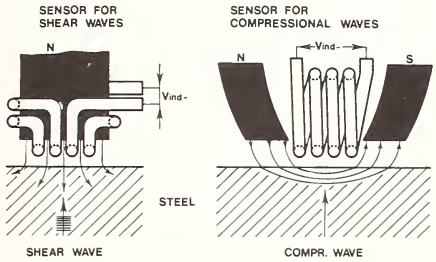

Figure 8. Principle of eddy sonic sensor.

The observations which follow are made in relation to the curve shown in figure 5. At the left hand side (vertical axis) the amplitude scale in 2 dB steps is indicated (linear, by application of a logarithmic amplifier).

In slots in the calibration block radius at the positions 20° and 80°, a coil was positioned fed by a H.F. sine wave signal. The ESS picks this signal up in its movement along the radius, and in this way the record shows a small peak at 20° and 80°. These peaks can be used by the customer for a check on the correct equipment calibration during the ESS measurement. The interpretation of the angle at the curve top is difficult, especially for probes with large angles of incidence. Therefore, it was agreed to use the center of the curve at

the -3 dB level, which is equal to the -6 dB level for impulse echo operation. The curve in figure 5 was derived for a Krautkrämer WB 45-N transducer. A comparison of the probe angle measurements with an ESS and by means of the normal procedure (calibration block) almost always shows differences. These can be caused by complex influences such as calibration block geometry and the sound attenuation in the material in combination with the crystal dimensions.

The ESS beam plot is used as an official document (probe fingerprint). It can be a great help in monitoring tolerances in probe fabrication, but can also be used to determine wear, sensitivity reduction or defects of probes after use. Figures 9 and 10 show the equipment used for the ESS measurements.

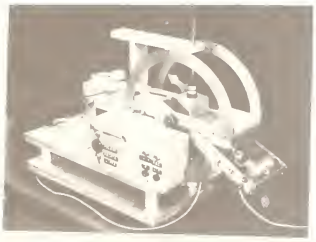

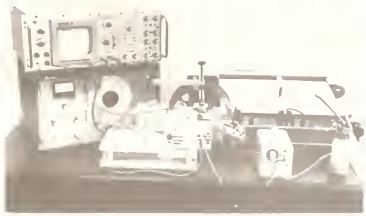

Figures 9 and 10. ESS equipment.

3. Determination of Probe Parameters

Authorities, especially the T.U.V.[3] in the Federal Republic of Germany, increasingly require the application of real scale test and reference blocks for probe parameter determination and for calibration of multiple probe systems. These blocks have to be fabricated out of representative materials; e.g., in the case of nuclear components, the original clad layer and surface condition have to be used, and they should contain the prescribed calibration reflectors for optimum reflection by a completely mounted probe system. The application of such real scale calibration, test and reference blocks has already been usual in R.T.D. for many years.

Besides their use on site for calibration of probe systems, the following transducer properties have to be determined in the laboratory preceding an inspection: 1) sensitivity in finding the prescribed test reflectors, and sensitivity reserve; 2) beam widths, both in impulse echo and in tandem and pitch and catch technique, in longitudinal and transverse direction; and 3) signal-to-noise (S/N) ratio at all distances used during the inspection, and also on original clad if available.

The probes are moved over the block surface mechanically; both probes and block are under water in an immersion tank in order to obtain optimal coupling conditions. The results (echo envelopes) are recorded by means of an X-Y-plotter, using standard sheets (fig. 11), which are used as an official document. In addition, the sheets are used as a basis for programming the computerized data handling unit in on-site inspection, and for correct interpretation of the results during the on- and off-line evaluation.

[3]Technischer Überwachungsverein.

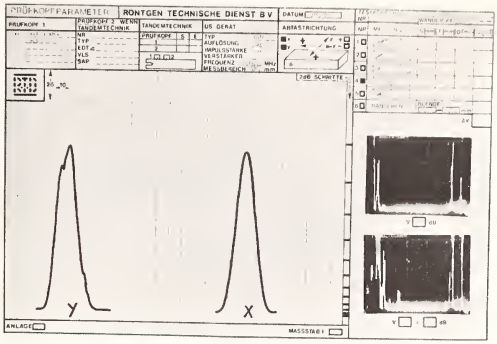

Figure 11. Probe parameters data sheet.

Except the above probe parameters, the forward/backward (F/B) ratio has become of nterest, playing an important part in the S/N ratio in the tandem inspection of the upper ones (fig. 12). Due to unwanted reflections inside the transmitting probe, a backward shear ave beam can occur, generating signals in the receiver which can lead to misinterpretations. he F/B ratio is expressed in a number (dB) and can be determined by turning the transmitting robe through 180°, when positioned on a 250 mm thick test block in the transmission position. he reduction of the energy received by the second probe is the F/B ratio. At this time, a ew immersion tank with an extremely precise probe manipulation unit for fast and accurate etermination of probe parameters is being built at R.T.D.

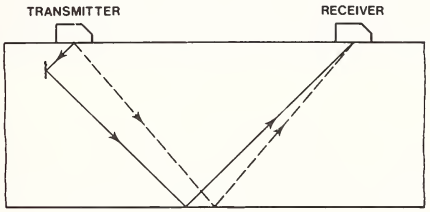

Figure 12. Influence of F/B ratio in tandem technique.

4. DGS Curves of Longitudinal Angle Probes for the Inspection of Austenitic Structures

The inspection of austenitic welds presents problems due to noise signals from nisotropic and coarse grained weld material. It is therefore important to concentrate the ltrasonic energy on a relatively small spot. The material thickness is divided into a number f zones: a special transducer with an appropriate focal distance is necessary for each zone.

For this purpose, longitudinal angle probes with separate transmitter and receiver (SEL robes) are fabricated by R.T.D.; these have a crystal tilt angle for optimum S/N ratio in a

special zone. The focal curve of such probes is extremely important for the S/N ratio and flaw detectability at any chosen depth; this curve does not meet the "distance law" as laid down in, e.g., the DGS (AVG) diagrams[4]. In addition, the high sound attenuation in the material under test shifts the focus towards the probe index point. Therefore, the focal curve has to be measured for each probe type and material individually. This is usually done in the following manner. The starting point is a reference block of a material which as closely as possible corresponds to the material under test (e.g., austenitic steel, inconel); the block contains a number of side drilled holes, with diameters $\geq 0.7\ \lambda$ (λ = wave length). An advantage of this reflector type is its independence of inaccuracies in the incidence angle; the echo amplitude as a function of the distance is measured; and although the universal AVG-diagram cannot be applied for SEL type probes, it is possible to calculate the focal curves for other reflector types (e.g., flat bottom holes, back wall) with the above curve as a starting point, but only for corresponding distances [4].

Figure 13 shows an example of a DGS-diagram obtained in this way for a probe, type 60° MSEL 4, focal length approximately 15 mm (= 7.5 mm depth). The curve for 2 mm cylindrical hole was measured; the other curves were calculated.

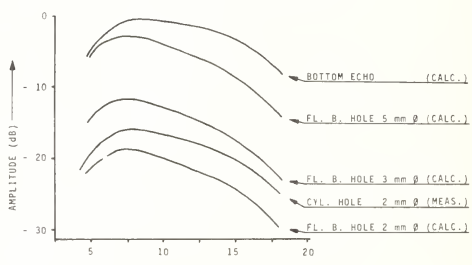

Figure 13. DGS curves of TR/R probe measured and calculated for austenitic steel.

Many checks with different probes and test-pieces showed that, in practice, accuracy of such diagrams of ± 4 dB is easily obtainable. Therefore, perpendicular incidence on the flat reflectors during the measurements was absolutely necessary.

5. Isosonography

A very useful instrument in the study of ultrasonic beams and the determination of probe properties is the isosonograph. It makes use of a fluid (e.g., water) as a sound propagation medium. The principle is shown in figure 14. The transducer, in this case a normal beam type, is mounted in an immersion tank. A ball reflector brought into a vertical oscillation, can make a slow movement either along the probe axis (longitudinal beam section) or perpendicular (cross section) at a certain distance. The probe, operated as a transceiver, receives the reflected energy. The amplitude as a function of the reflector movement is recorded by means of a facsimile recording system [5]. The "flying spot" of a helix type electrode, synchronized in its rotation to the reflector movement, draws grey lines on electrosensitive paper. One line across the paper corresponds with a single reflector movement ("television type" recording). The paper advance is equal to the slow reflector movement along or perpendicular to the beam axis. The grey tones depend on the amplitude, which is divided in a number of steps by a quantizer. The maximum intensity corresponds with the highest amplitude, although the lowest amplitude can also be associated with a higher intensity, in order to see the beam contour more clearly. An interpretation of the amplitude can be carried out, but only within certain limits. Figure 15 shows an isosonograph. Figure 16 is a typical isosonogram (2.25 MHz probe, 25.4 mm diameter). The longitudinal scan can be seen at the left hand side, a number of cross scans at the right side.

[4]DGS = Distance-Gain-Size
AVG = Abstand-Verstärkung-Grösse (Krautkrämer)

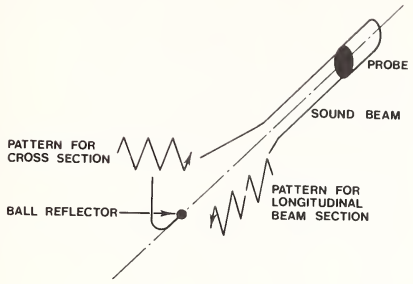

Figure 14. Principle of isosonograph medium: water.

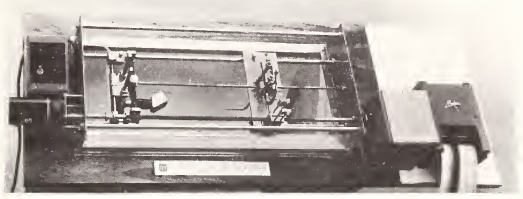

Figure 15. Isosonograph.

Although the generation of transverse waves in water is impossible, an impression (e.g., uniformity, side lobes) of the behavior of angle probes can be obtained by isosonography. Compressional waves generated in water can thus be used. A comparison with the shear wave beam in steel is possible by taking the following factors into account: difference in sound velocity (steel 3230 m/s, water 1480 m/s); difference in projected crystal height, caused by different refraction index; and lower attenuation in water.

A comparison using focused probes (curved crystals or lenses) is impossible, because the curvature calculations use the refraction index; the beam in water is thus highly distorted.

For this reason, an attempt was made to obtain isosonograms in steel, using the principle of figure 17. Only the transmitted beam is measured by this method. So far, very good and reproducible results with focused probes (45°, shear waves) have been obtained.

Isosonography can be used to obtain an impression of beam behavior (near field estimation, focused probes, side lobes, etc.). As a probe fingerprinting method, it is only used on a limited scale.

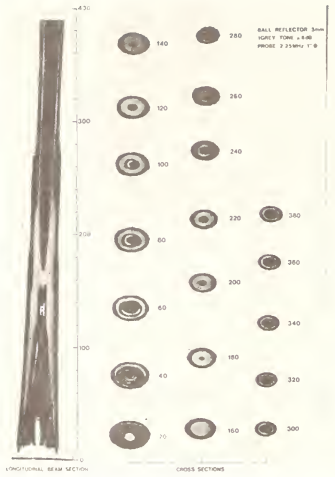

Figure 16. Isosonogram.

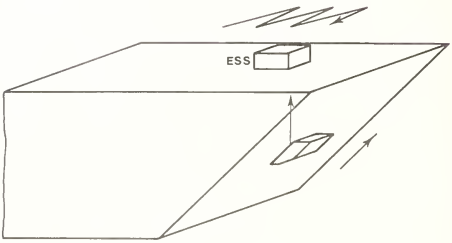

Figure 17. Isosonography in steel block.

6. Determination of Probe Frequency and Bandwidth

The accuracy of AVG diagrams, the behavior of calibration reflectors, the beam shape have direct relations to the probe frequency. In addition, the bandwidth is important in connection with the obtainable signal-to-noise ratio in inspecting austenitic structures, although the influence is not yet fully understood.

The accurate determination of the probe frequency and bandwidth with the aid of a transmitting unit, a gate, a spectrum analyzer and an oscilloscope, as is often attempted, is difficult. The following reasons can be mentioned: the pulse strength has an influence on the echo shape and the spectrum; deviations are introduced by the noncontinuous character of the signal; the reflector shape and nonperpendicular incidence have their influences; and the gate generator (which opens and closes the amplifier input in order to select the relevant echo) influences the accuracy. In Europe a number of those concerned have agreed on the use

of certain equipment for this purpose. By this means, the results are more comparable. For example, the transmitter unit, has a standard pulse strength (100 V at 50 ohms) and a standard rise time (10 ns). However, deviations and incomparability still exist, as long as the measuring procedure is not strictly defined.

7. Closing Remarks and Recommendations

The determination of directional angle probe characteristics by an ESS supplies useful information about the probe under restricted conditions. This probe characterization method has proved to be useful in transducer fingerprinting. However, the determination of probe parameters by means of reflectors in the original material under "on-site conditions" is still indispensable. The exact angle of incidence, especially at long distances, the S/N ratio, beamwidth and sensitivity should be derived from such measurements.

The tolerances in angle of incidence required (in many cases ± 1°) presently are such that an accurate determination method like the ESS is necessary. However, the relationship to real circumstances should be taken into account.

Because the ESS has become valuable for probe fingerprinting, the following points are recommended for further investigation. The influence of the amplifier frequency characteristics; the influence of the frequency response of the ESS itself; and the influence of the transmitting pulse. The value of an ESS curve as an official document would be increased by these investigations.

A standard method for determination of probe frequency and bandwidth should be agreed upon. Some probe users already specify these probe parameters (e.g., frequency 1 MHz ± 10 percent, bandwidth 300 kHz).

Even if good methods for probe characterization are used and probe tolerances are carefully monitored, the inspection quality also depends on other factors, such as frequency characteristics of amplifiers; pulse strength with respect to possible distortion of signals; suppression of spurious signals by adequate cable and equipment screening; and impedance matching of equipment/cables/transducers. It is remarkable that, although many people know how necessary impedance matching of their home stereo units is for optimum results, this aspect receives insufficient attention in ultrasonic inspection.

References

[1] Institut für Reaktorsicherheit der Tüv E.V., Geschäftsstelle Reaktor-Sicherheitskommission: RSK-Leitlinien für Druckwasser/Siedewasserreaktoren, last issue.

[2] de Raad, J. A. and Engl, G., A continental viewpoint of NDT techniques, in Proc. 10th Symposium NDE, San Antonio, TX (April 23-25, 1975).

[3] Wüstenberg, H., Untersuchungen zum Schallfeld von Winkelprüfkopfen für die Materialprüfung mit Ultraschall (Thesis) Berlin (1972).

[4] Wüstenberg, H. and Mundry, E., Properties of cylindrical boreholes as reference defects in ultrasonic inspection, Nondestructive Testing (August 1971).

[5] de Raad, J. A., Ultrasonic and Other NDE Methods for Tube Joints Used in Heat Exchangers, R.T.D. Technical Monograph No. A-2670.

National Bureau of Standards Special Publication 596, Ultrasonic Materials Characterization, H. Berger and M. Linzer, eds., Proceedings of the First International Symposium on Ultrasonic Materials Characterization held at NBS, Gaithersburg, Md., June 7-9, 1978. Issued November, 1980.

PROPOSAL OF A CHARACTERIZATION SHEET FOR ULTRASONIC TRANSDUCERS

Elie E. Borloo and Pierre Jehenson

Commission of the European Communities
Joint Research Centre
Department of Physical and Natural Sciences
Materials Division - Nondestructive Testing Laboratories
Ispra, ITALY

No recommended practice has yet been established for the characterization of ultrasonic transducers. Those manufacturers who intend to certify the quality of their products have produced their own certification sheets for this purpose. The characterized parameters and the corresponding measurement techniques are not always the same from one manufacturer to another; this situation means that comparison of characteristics is often difficult and sometimes impossible. In this paper, the authors make a proposal for a characterization sheet which is designed in such a way that the measurement data are clearly defined for each parameter and can easily be revised.

1. Introduction

Users of ultrasonic equipment are now aware that in order to perform reproducible and quantitative ultrasonic tests, it is absolutely necessary to characterize the equipment. The equipment includes the ultrasonic transducer, the ultrasonic instrument and the connection cable.

Manufacturers of ultrasonic equipment have been furnishing data sheets with their instruments or transducers but these are often inadequate. We address this problem, but only in regard to transducer characterization.

The data sheets used by the different manufacturers and laboratories differ considerably. We think that there is an urgent need to set up, preferably on an international basis, a recommended practice on the characterization procedure for ultrasonic transducers. This requires that those parameters which are considered to be important, and the measurement methods, should be defined. In this way, results from different origins may be compared.

2. Characteristics of Transducers

The characteristics of transducers can be subdivided into three groups:

1. beam characteristics;
2. electrical characteristics; and
3. mechanical characteristics (design parameters).

The main parameters of the beam are:

1. distribution of the axial pressure as a function of distance;
2. diameter of the beam, as a function of the axial distance;
3. symmetry of the beam; or

4. eccentricity of the beam;

5. divergence angle;

6. near field distance;

7. squint angle;

8. angle of incidence;

9. exit point of the beam (for angle transducers); and

10. characteristics of the focal zone (for focused transducers).

The main electrical parameters of the transducer are:

1. center frequency;

2. frequency spectrum;

3. transfer function;

4. bandwidth;

5. damping factor;

6. sensitivity;

7. resolution;

8. noise level;

9. emitted ultrasonic power;

10. electrical impedance; and

11. matching coil.

Among the mechanical parameters we consider:

1. characteristics of the piezoelectric material itself;

2. metalization of the piezoelectric material;

3. connections;

4. bonding between the various internal components;

5. acoustic lens or wearface;

6. damping material;

7. housing and connector; and

8. protection against environment.

The characterization of transducers should be possible not only by extremely specialized and well-equipped laboratories but also by unspecialized people and normal NDT laboratories. For instance, methods using reference blocks rather than electronic equipment should be retained. This does not, however, prevent the use of specialized electronic measurements of some parameters which are very important for manufacturers and for laboratories dealing with optimization of ultrasonic techniques.

3. Ultrasonic Transducer Characterization Sheet

In this paper, we do not describe the measurement methods of the different parameters, but simply illustrate the "Ultrasonic Transducer Characterization Sheet" we use in our laboratories. This document was drawn up taking into account all the existing characterization sheets known to us.

In the upper part of figure 1, the transducer description is reported on the basis of the data given by the manufacturer. In the lower part the different characterization possibilities are listed. Several methods for sound beam profiling (A) are considered and discussed here. Forms for all are available but we include in this report only one. Form A1 (fig. 2) is the document relating to sound beam profiling by means of Schlieren imaging. Two pictures are taken one at zero degrees and the other at 90 degrees. In order to allow reproducible measurement to be carried out, we suggest that the manufacturers should put an angular reference mark on all the transducers that have a circular shape.

Form A2 (not shown) is the document relating to sound beam profiling by the point-by-point method. This characterization is particularly suitable for strongly focused immersion transducers. The data to be furnished includes: an oscillogram of the reflected wave from a ball giving information on the frequency and the damping factor of the transducer, an axial scan, from which the focal distance and the length of the focal zone can be measured, two cross sections of the beam at 0 degrees and at 90 degrees at the last axial maximum. From these pictures, the beam diameter at focal distance can be measured and the symmetry of the beam can be observed.

Form A3 (not shown) is the document relating to sound beam profiling giving quantitative information on the ultrasonic beam by axial and cross section plots. The different grey-scale levels are calibrated; axial sections and cross sections can easily be obtained. This characterization method is particularly suitable for immersion transducers, whether focused or not.

Form A4 (not shown) provides a quantitative cross section plot of a line focused transducer. This document only contains information relating to the focal section of such a transducer.

Form B1 (fig. 3) is the document giving pulse wave form (real time) and spectrum analysis information. The pulse waveform indicates the frequency and bandwidth of the transducer; the frequency spectrum shows the center frequency, the bandwidth and the harmonic content. The frequency axis must be wide enough to cover the frequency range, up to at least 3 times the center frequency.

Form C1 (fig. 4) is an example of a distance-amplitude plot. This can be made either by immersion or in contact when using reference blocks.

Form D1 (fig. 5) shows the impedance and phase behavior of the transducer relative to the frequency. This measurement also reveals whether or not there is an adaptation network in the transducer housing.

Form E1 (fig. 6) is the document used in our laboratory for the characterization of transducers by liquid crystals. This method is very economical for checking the homogeneity of the emission from flat transducers. In this example, the liquid crystals are applied on the front face of the transducer. The visualization of cross sections at any distance in the beam is also possible and a technique to make images of longitudinal sections of the beam is under development.

The characterization sheets as proposed here, have the great advantage that at any future time forms for other characterization techniques can easily be added and unneeded ones can be rejected. For example, there is presently no form relating to the beam characteristics of angle transducers. In fact, this document is now in preparation; it awaits the operation of a transducer characterization bench using an electrodynamic detector system.

On all the sheets, the data relative to the instrument settings should always be given in clear values to allow measurements to be repeated with other instrumentation and to ensure reproducible results.

These characterization sheets have been set up in collaboration with different Italian industries and particularly with the "Instituto di Ricerca BREDA". Our next aim is to define the measurement methods for the different parameters. These methods will have to be reported on the back of each corresponding characterization sheet.

The purpose of this proposal for characterization sheets is to initiate a discussion in this important field and comments and suggestions will be greatly welcomed. Information on data sheets mentioned but not shown (A2,A3,A4) is available from the author.

COMMISSION OF THE EUROPEAN COMMUNITIES JOINT RESEARCH CENTRE - ISPRA ESTABLISHMENT DEPARTMENT OF PHYSICAL AND NATURAL SCIENCES MATERIALS DIVISION *NON-DESTRUCTIVE TESTING LABORATORIES*	ORDER DATE:	FORM: GEN.
	Sheet No	of ..... sheets

ULTRASONIC TRANSDUCER CERTIFICATION FORM

Manufacturer data:

Manufecturer: ..... Type: ..... Production data .....

Frequency: ..... Seriel Nr. .....

Element size: ..... Contact ☐; Immersion ☐

Element material: ..... Wear face material: .....

Test angle: ..... Housing: ..... Connector: .....

Angle wedge fixed ☐; interchangeable ☐ specific ☐ type .....

Lens configuration: flat ☐; y_o^* distance in water: .....

point focus ☐; focal distance in water: .....

line focus ☐; focal distance in water: .....

Tuning coil: yes ☐; no ☐; in housing ☐; in cable ☐

Damping characteristics: low ☐; medium ☐; high ☐; Q factor: .....

Attached cable type ..... length .....

Maximum environmental conditions: pressure ..... temperature .....

Remarks: .....

.....

.....

.....

- sound beam profiling (Form A)
- real time and spectrum analysis (Form B)
- distance - amplitude plot (Form C)
- impedance and phase plot (Form D)
- liquid crystals anelysis (Form E)

Remarks: .....

.....

.....

Address: J.R.C. Ispra - 21020, Varese - Italy
Tel. (0332) 780131 - Telex: 38042 - 38058

CUSTOMER:	DEPARTMENT MANAGER:	FINAL DATE:

4-7 :

COMMISSION OF THE EUROPEAN COMMUNITIES JOINT RESEARCH CENTRE - ISPRA ESTABLISHMENT DEPARTMENT OF PHYSICAL AND NATURAL SCIENCES MATERIALS DIVISION *NON-DESTRUCTIVE TESTING LABORATORIES*	ORDER DATE: Sheet No	FORM: A1 of ... ... sheets

SOUND BEAM PROFILING

SCHLIEREN IMAGE (qualitative information)

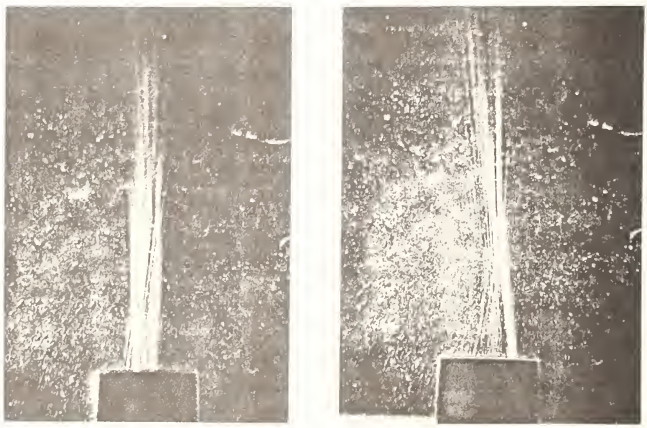

Scale 1

0 degrees 90 degrees

Generator Data: continuous sine wave: ..... MHz
amplitude measured on transducer: ..... volts

Transducer data: type: ..... ; frequency: .....
crystal dimensions: ..... (effective)
serial number .....

Remarks: .....
.....
.....

CUSTOMER:	OPERATOR.	FINAL DATE:

COMMISSION OF THE EUROPEAN COMMUNITIES
JOINT RESEARCH CENTRE - ISPRA ESTABLISHMENT
DEPARTMENT OF PHYSICAL AND NATURAL SCIENCES
MATERIALS DIVISION
NON-DESTRUCTIVE TESTING LABORATORIES

ORDER DATE: 16/11/1977

FORM: D1

Sheet No ..... of ..... sheet

REAL TIME AND SPECTRUM ANALYSIS

Generator data: .....

.....

.....

Damping: 50 ohms - P.R.F.: ...1000..... Hz

Type of test: immersion ☒ contact ☐

Reflector: flat ....X..... block .....

Selected echo: interface ☒
backwall ☐

REAL TIME

X axis:....1..... mμ sec/div.

Y axis:...100.... mV/div.

intermediate amplif...1..... db eff.

gated time base width ..10.....Xμ sec.

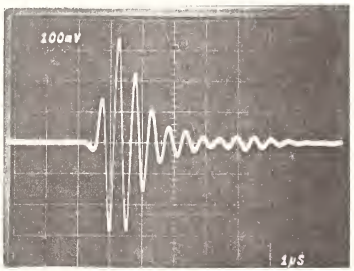

FREQUENCY SPECTRUM

Instrument data:

input atten: 10... db; bandwidth 30 kHz

X axis scan width 10.. MHz

center frequency: ....5..... MHz

Y axis: zero reference level: ..36.. dbm

.....10..... db/div.

Measured data:

central frequency: 1.15 MHz

bandwidth at:

- 3 db: 1.66 to 1.91 MHz; Δf: 0.25 MHz; Q: 7..
- 6 db: 1.51 to 2.04 MHz; Δf: 0.53 MHz; Q: 3.

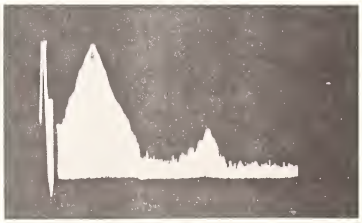

Transducer data: type: b6 0002 ; frequency ....2..... MHz; Serial No. .....0002.....

Remarks: .....

.....

.....

CUSTOMER: INT.

OPERATOR: LAGINI

FINAL DATE: 16/1/1978

4-78

COMMISSION OF THE EUROPEAN COMMUNITIES
JOINT RESEARCH CENTRE - ISPRA ESTABLISHMENT
DEPARTMENT OF PHYSICAL AND NATURAL SCIENCES
MATERIALS DIVISION
NON-DESTRUCTIVE TESTING LABORATORIES

ORDER DATE:

FORM: C1

Sheet No ..... of ..... sheets

DISTANCE – AMPLITUDE PLOT

Generator Data: .....

.....

.....

Damping: 50 ohms

Type of test: immersion ☐ contact ☐

Reflector:.....mm diam. ..... ball

flat ..... block .....

Selected echo: interface ☐
backwall ☐

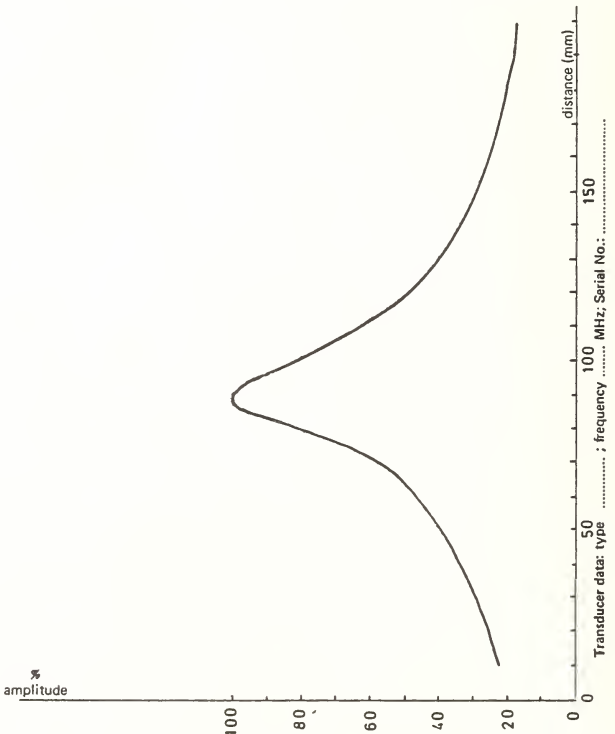

CUSTOMER:	OPERATOR:	FINAL DATE:

4-78

COMMISSION OF THE EUROPEAN COMMUNITIES
JOINT RESEARCH CENTRE - ISPRA ESTABLISHMENT
DEPARTMENT OF PHYSICAL AND NATURAL SCIENCES
MATERIALS DIVISION
NON-DESTRUCTIVE TESTING LABORATORIES

ORDER DATE: 19/1/1978

FORM: D1

Sheet No ..... of ..... sheets

IMPEDANCE AND PHASE PLOT

Instrumentation data: .....

.....

.....

.....

Measurement data: .....

.....

.....

.....

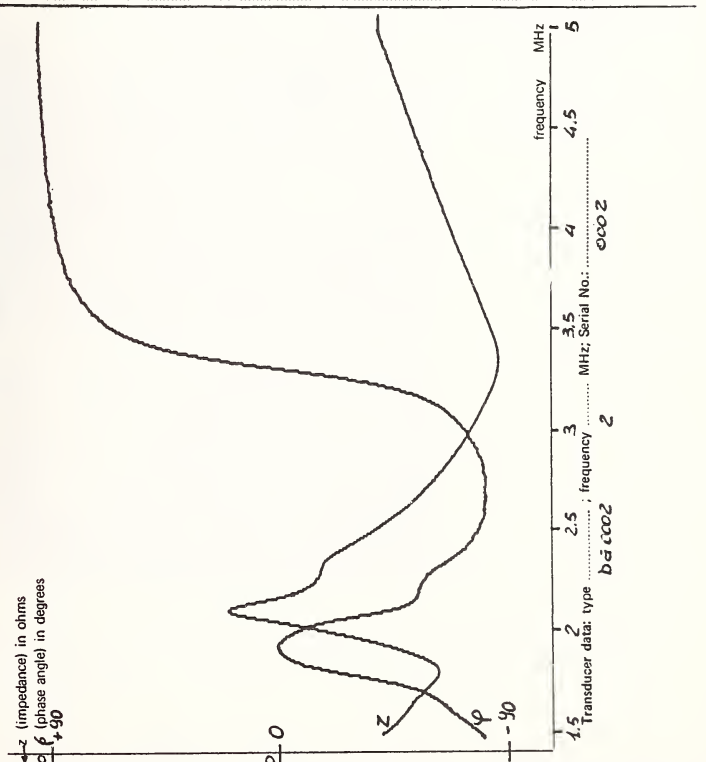

CUSTOMER: INT.

OPERATOR: LAGHI

FINAL DATE: 16/1/1978

COMMISSION OF THE EUROPEAN COMMUNITIES
JOINT RESEARCH CENTRE - ISPRA ESTABLISHMENT
DEPARTMENT OF PHYSICAL AND NATURAL SCIENCES
MATERIALS DIVISION
NON-DESTRUCTIVE TESTING LABORATORIES

ORDER DATE: 15-11-77 | FORM: E1

Sheet No ..... of ..... sheet

LIQUID CRYSTALS ANALYSIS

Generator data: C.W. sine ....20..... Volts p/p - 50 ohms
Amplifier: .....NO.....

Applied cw swept between:

1.. MHz and ..5.... MHz

Most uniform beam emission

obtained at 1.47 MHz

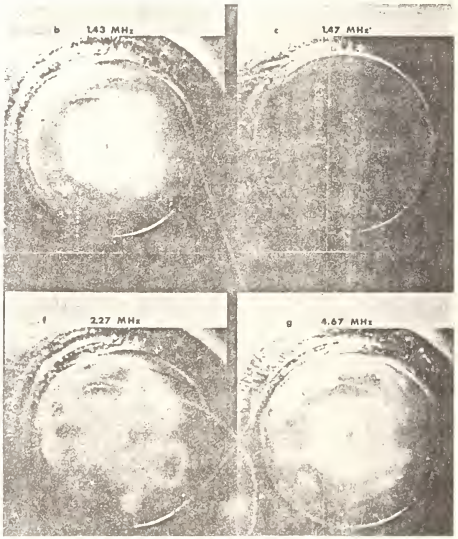

Transducer data: Type M.T..... ; Frequency ..1.5..... MHz; Serial No. ....7.22.....

Remarks: .....

CUSTOMER:	OPERATOR: R. DENIS	FINAL DATE:
UNIV. BOLOGNA		18-1-1978

4-78

National Bureau of Standards Special Publication 596, Ultrasonic Materials Characterization, H. Berger and M. Linzer, eds., Proceedings of the First International Symposium on Ultrasonic Materials Characterization held at NBS, Gaithersburg, Md., June 7-9, 1978. Issued November, 1980.

THE MEASUREMENT AND GENERATION OF ULTRASOUND BY LASERS

C. Harvey Palmer

Department of Electrical Engineering
Johns Hopkins University
Baltimore, MD 21218

This paper is intended as an introduction to the section on laser generation and detection of ultrasound. Because of the special importance of ultrasonic waves in materials characterization, it is essential to have a variety of transducers to perform the wide range of tasks required. Lasers can be used both to generate and to measure ultrasonic waves, and they have important advantages. For example, they are noncontact and thus do not disturb the waves to be measured; furthermore, they can provide accurate, quantitative measurements of local amplitudes and phases because they can be absolutely calibrated. The possibility of generation of ultrasonic pulses by lasers suggests several applications.

1. Introduction

This paper is designed to provide some perspective for the following papers on laser generation and detection of ultrasound. As the very title of the Symposium, Ultrasonic Materials Characterization, suggests, ultrasonic testing of materials occupies a central position in nondestructive evaluation. Acoustic wave pulses are used to make thickness measurements, to locate flaws, to detect changes in microstructure, and to determine the various elastic moduli of a material.

Since various kinds of transducers, such as piezoelectric and electromagnetic-acoustic (EMAT), already exist, one may question the need for optical methods. But optical methods have significant advantages which make them a most useful addition to the existing transducers, both for the generation and for the measurement of ultrasound.

Optical measuring methods are already widely used, and their advantages well documented. They are noncontact and thus do not disturb the waves being measured; they can be absolutely calibrated and hence can yield accurate, quantitative data; they can be highly local and can measure sound fields adjacent to a structure, boundary, or defect; they can be used within transparent media and thus can directly measure reflections or transmission of both shear and dilatational waves as well as internally generated acoustic emission transients.

Optical generation of acoustic waves is still in its infancy so that its full potential is not known. Nevertheless, the ability to generate ultrashort elastic pulses on the surface of a material or within transparent materials in a highly localized, known region, and without contact is clearly an important advantage.

After a brief summary of measuring methods, this paper will review some of the literature on the generation of ultrasound by light, and then suggest possible applications of the technique.

2. Optical Measuring Methods

A variety of optical techniques have been successfully used to measure (as well as to visualize) acoustic wave fields. (Excellent review articles have been written by Whitman and Korpel [1][1], White [2], and Stegeman [3].) Some of these techniques are well adapted to surface acoustic waves (SAW), others to bulk waves within transparent media. The knife-edge technique, Adler et al. [4], for example, is used for SAW. It depends upon the deviation of

a laser beam produced by the tilting surface of a specimen as an acoustic wave passes under the focused light. This technique is highly localized (though the laser beam can be electrically or mechanically scanned so as to visualize the sound fields over a region of the surface). Optical heterodyning has been used by Massey [5] and by Whitman, et al. [6] to study surface waves and surface vibrations.

Bulk waves can be detected by the Bragg effect. Techniques based on the Bragg diffraction of light by a sound wave have been developed by Korpel, et al. [7], Auth and Mayer [8], Ippen [9], and others. If the optical beam is directed transversely to the direction of the sound waves and is sufficiently wide to encompass a number of acoustic wavelengths, the sound wave acts like an optical diffraction grating. When the sound wave moves in only one direction (SWR=1), the spectral orders of the light (except for the zeroth order) are frequency shifted. When the sound wave moves in both directions (SWR large), spectra are still formed, and each order has more than one optical frequency. This technique, while well developed and well understood theoretically, does not yield local information about the sound waves. If the light beam diameter is smaller than the wavelength of the sound, the light beam is deviated by the acoustically induced local density changes. The paper in this section by Djordjevic and Green describes such small beam techniques.

Optical interferometry provides a very versatile technique for both surface and bulk acoustic measurements. The central problem has been that for high sensitivity it is necessary to maintain a round trip optical path difference of $\lambda/4$ between the two beams. Several new types of interferometer have been developed to overcome this difficulty. The swept-path interferometer of Mezrich, et al. [10] uses a moving reference mirror so that at one instant in each cycle of the motion the phase is correct and the maximum signal value is recorded. The quadrature-dual interferometer employed by Vilkomerson [11] produces two out-of-phase optical beams; the optical signals are electronically squared, added, and the square root taken. The sensitivity is then independent of the optical path difference (though phase information is lost). It is also possible to stabilize the optical path by piezoelectrically driving the reference mirror. Such interferometers have been built by Palmer and Green [12], by Jette, et al. [13] by Bondarenko, et al. [14], and others. Still another method to minimize the path difference problem is the differential interferometer of Palmer, et al. [15].

A new optical technique, based on Doppler frequency shifting by sound induced particle motion will be described in a forthcoming article by Fick and Palmer [16]. The method determines directly the particle motion of any desired point within a suitable transparent solid.

3. Generation of Ultrasound by Lasers

The extremely high power densities available with pulsed lasers suggests the possibility of generating short ultrasonic pulses for the characterization of materials. White [17] has given a comprehensive treatment of the theory of generation of sound by transient heating. He shows that the conversion efficiency of light power to sound power is directly proportional to the incident peak optical power absorbed, and inversely proportional to the acoustic frequency. White points out that, for good efficiency, it is desirable to have the heat absorbed in a thin constrained film, rather than in a film with a free boundary.

Brienza and DeMaria [18] demonstrated the generation of sound in a free metal film deposited on crystals such as $LiNbO_3$, quartz, and sapphire. The crystals provide a delay medium through which the generated sound can propogate. A thin layer of CdS was evaporated on the far end of the quartz or sapphire crystals to provide a piezoelectric receiving transducer. The $LiNbO_3$ was more satisfactory because it is both a delay medium and a piezoelectric material so that no CdS layer was needed. Also the thin CdS layer had a very narrow bandwidth whereas the $LiNbO_3$ device had a broad bandwidth. The light source was a Q-spoiled Nd-glass mode-locked laser which delivered 10^{-12} to 10^{-11} second pulses, evenly spaced by the round trip time of the laser, corresponding to 200 MHz. The generated sound waves exhibited discrete, harmonically related frequencies, unlike the continuous spectrum produced by a shock wave.

[1] Figures in brackets indicate the literature references at the end of this paper.

Cachier [19] also used thin film absorbers and was able to generate shear waves as well as dilatational waves. Kubota and Nakatani [20] produced intense dilatational acoustic pulses in transparent media and both shear and dilatational waves in opaque materials. Their samples acted as resonant cavities. They concluded from their experiment that low frequency sound waves might be produced by the radiation pressure of the light pulses.

Very recently, Bondarenko, et al. [14], employed a Q-switched ruby laser to generate short acoustic pulses on one surface of a metal specimen. They used a controlled-path interferometer, somewhat similar to that of Palmer and Green [12], to detect waves transmitted to the other surface. The Russian interferometer had a bandwidth of 5 kHz to 150 MHz, and a threshold sensitivity of 10^{-9}m (10 Å), which could detect multiple reflections of the acoustic pulses in specimens and could locate simulated flaws. The paper of Gutfeld, which follows, is an expansion of earlier work from the same laboratory [21] in which the thin heat absorbing film was backed by a dielectric plate to provide the constraint suggested by White [17].

4. Some Applications

The successful generation of ultrasound by lasers will make possible the nondestructive evaluation of materials without contact either by the transmitting or the receiving transducer. (Although the EMAT is also noncontact, it is a "local" transducer.) In addition, laser generated short ultrasonic pulses could be used to simulate acoustic emission transients by generating surface or buried seismic pulses with more nearly ideal characteristics than are now obtained by the method of Breckenridge, et al. [22] who use breaking glass capillaries or by Hsu, et al. [23] who use breaking pencil lead. An interesting possibility is the efficient generation of Stoneley waves between two appropriate media, one of which is transparent. (It has already been demonstrated that Stoneley waves can be detected optically [24].) Stoneley waves can be used for NDE of laminates, as suggested by Lee and Corbly [26]. Finally, laser generated acoustic pulses have medical applications as explained in the paper of Rocha, Griffen, and Thomas in this session.

References

[1] Whitman, R. L. and Korpel, A., Appl. Opt., 8, 1567 (1969).

[2] White, R. M., Proc. IEEE, 58, 1238 (1970).

[3] Stegeman, G. I., IEEE Trans. Sonics Ultrason. SU-23, 33 (1976).

[4] Adler, R., Korpel, A., and Desmares, P., IEEE Trans. Sonics Ultrason. SU-15, 157 (1968).

[5] Massey, G. A., Proc. IEEE, 56, 2157 (1968).

[6] Whitman, R., Laub, L. J., and Bates, W., IEEE Trans. Sonics Ultrason. SU-15, 186 (1968).

[7] Korpel, A., Laub, L. J., and Sievering, H. C., Appl. Phys. Lett., 10, 295 (1967).

[8] Auth, D. C. and Mayer, W. G., J. Appl. Phys., 38, 5138 (1967).

[9] Ippen, E. P., Proc. IEEE (Letters), 55, 248 (1967).

[10] Mezrich, R., Vilkomerson, D., and Etzold, K., Appl. Opt., 15, 1499 (1976).

[11] Vilkomerson, D., Appl. Phys. Lett., 29, 183 (1976).

[12] Palmer, C. H. and Green, R. E., Appl. Opt., 16, 2333 (1977); Mater. Eval., 35, 107 (October 1977).

[13] Jette, A. N., Morris, M. S., Murphy, J. C., and Parker, J. G., Mater. Eval., 35, 90 (October 1977).

[14] Bondarenko, A. N., Drobot, Y. B., and Kruglov, S. V., All-Union Scientific-Research Institute of Physicotechnical and Radio-Engineering Measurements, Khabarovsk. Translated from Defektoskopiya, No. 6, p. 85 (November-December 1976).

[15] Palmer, C. H., Claus, R. O., and Fick, S. E., Appl. Opt., 16, 1849 (1977).

[16] Fick, S. E. and Palmer, C. H., Appl. Opt. (to be published).

[17] White, R. M., J. Appl. Phys., 34, 3559 (1963).

[18] Brienza, M. J. and DeMaria, A. J., Appl. Phys. Lett., 11, 44 (1967).

[19] Cachier, G., J. Acoust. Soc. Amer., 49, 975 (1971).

[20] Kubota, K. and Nakatani, Y., Jap. J. Appl. Phys., 12, 888 (1973).

[21] Gutfeld, R. J. and Melcher, R. L., Appl. Phys. Lett., 30, 257 (1977).

[22] Brechenridge, F. R., Tschiegg, C. E., and Greenspan, M., J. Acoust. Soc. Amer., 57, 626 (1975).

[23] Hsu, N. N., Simmons, J. A., and Hardy, S. C., Mater. Eval., 35, 100 (October 1977).

[24] Claus, R. O. and Palmer, C. H., Appl. Phys. Lett., 31, 547 (1977).

[25] Lee, D. A. and Corbly, D. M., IEEE Trans. Sonics Ultrason. SU-24, 206 (1977).

National Bureau of Standards Special Publication 596, Ultrasonic Materials Characterization, H. Berger and M. Linzer, eds., Proceedings of the First International Symposium on Ultrasonic Materials Characterization held at NBS, Gaithersburg, Md., June 7-9, 1978. Issued November, 1980.

THERMOELASTICALLY GENERATED MHz WAVES FROM METALLIC THIN FILM-LIQUID INTERFACES

R. J. von Gutfeld

IBM Thomas J. Watson Research Center
P. O. Box 218
Yorktown Heights, NY 10598

The thermoelastic generation of MHz elastic waves from a three layer structure consisting of a transparent substrate and an evaporated thin metallic film in contact with a liquid is described. Pulsed laser light, incident on the film through the substrate produces expansions which result in a propagating strain wave. The amplitude of the wave is determined mainly by the linear thermal expansion coefficient of the liquid based on measurements as a function of film thickness and thermal expansion coefficients of various liquids. These data are compared to calculated results which take into account both the thermal and elastic parameters of all three media. Some practical applications for waves generated in this manner are discussed in relation to nondestructive testing.

1. Introduction

Several recent papers have described the use of repetitively pulsed lasers to generate MHz elastic waves from constrained metal surfaces [1-3][1]. The application of these waves for detection of several kinds of artifically produced flaws in a variety of samples has also been demonstrated with detection at 20 MHz. The advantage of clamping was originally pointed out by White who showed, in a single medium analysis, the effect on the propagating strain amplitude as a result of changes in the boundary conditions [4]. In the present work we study some simple multilayered structures for the purpose of enhancing the strain amplitude generated in clamped thin films. We have also analyzed the results based on an extension of White's theory as it applies to three media. The present structure consists of a transparent substrate with an evaporated metallic film on one surface. This film is also in contact with a liquid rather than a second solid as was described in the previous references [1-4]. This three medium layered structure has the advantage of requiring no bonding agents thereby making the experimental results reliably reproducible and the analysis more straightforward. The present analysis takes into account the thermal and elastic parameters of all three media, thereby permitting a direct comparison with the data. A detailed derivation and discussion of the theory as it applies here will be presented elsewhere [5].

2. Experimental Arrangement and Data

The experimental setup is shown in figure 1. A nitrogen pumped dye laser (5 ns pulse width) is the thermal excitation source. The light was focused onto the ends of a multifiber incoherent light pipe. The output of the light pipe was directed with a spot size of ~ 2 mm diameter onto the transparent substrate with optical absorption occurring at the metallic film/substrate interface. The substrates were 1/8 in (3 mm) thick, 1 in (2.54 cm) diameter pyrex wafers with optically polished faces. The metallic films (molybdenum) were e-beam evaporated onto one face of the pyrex substrate to thicknesses ranging from 550-4000 Å (55-400 nm). The free film surface was in contact with the liquid under test via a small cell into which substrate and film were mounted. A Mylar[2] polyethylene terephthalate

[1] Figures in brackets indicate the literature references at the end of this paper.
[2] Dupont Registered Trademark.

membrane maintained separation between the liquid under test and the water which contained the pickup transducer. The Mylar presents a fairly good acoustic match for the two liquids on either side, thereby minimizing acoustic reflections for the generated elastic waves. The frequencies of the elastic waves investigated were 2.25 and 20 MHz using standard Panametrics transducer/receivers centered at those frequencies with a bandwidth of ± 25 percent to the half maximum. The waves detected by these transducers were amplified by 40 db for the 2.25 MHz detector, 20 db for the 20 MHz detector, processed by a boxcar integrator and plotted on a chart recorder.

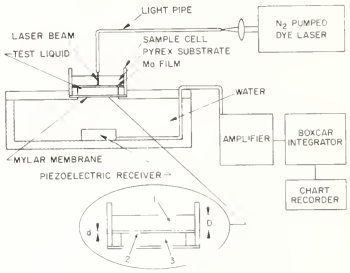

Figure 1. Experimental arrangement showing laser incident on sample at pyrex-Mo interface. A cell in which the test liquid is contained maintains contact between the liquid and the film. The elastic wave is generated at the film-liquid interface and passes through the Mylar membrane to the water and piezoelectric receiver. The insert shows the three media comprising the structure, (1) the transparent substrate of thickness D, (2) the absorbing film of thickness d, and (3) the liquid in contact with the lower film surface.

In figures 2 and 3 we present data for four sample thicknesses in conjunction with four different liquids measured at 2.25 and 20 MHz respectively. The linear thermal expansion coefficients of the substances under investigation are given in table 1. In addition, the density and acoustic velocity of all the liquids and the Mylar membrane are tabulated. These are used to calculate the strain amplitude, ε_1, in the first liquid from the measured value in the water, ε_3. These strains are simply related by,

$$\varepsilon_3 = T_{12}T_{23}\varepsilon_1 \ , \tag{1}$$

where T_{ij} is the strain transmission coefficient from medium i to j, related to the acoustic impedance, Z_i and the acoustic velocity, v_i by,

$$T_{ij} = \frac{2z_i}{z_i+z_j}\,\frac{v_i}{v_j} \ . \tag{2}$$

For example, in our experiment with pyrex-Mo-acetone as the three layers, T_{12} is the transmission coefficient for an elastic wave propagating from acetone to Mylar and T_{23} is the coefficient for propagation from Mylar to water. The data of figures 2 and 3 are proportional to the strain amplitude, ε_1, obtained by applying eq. (1) to the experimentally obtained receiver voltages proportional to ε_3.

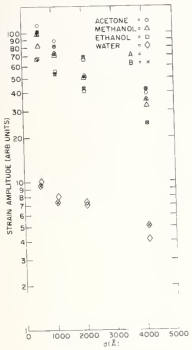

Figure 2. Strain amplitude for two sets of four samples of varying Mo film thicknesses; dots denote set A and crosses set B. The data were taken at 2.25 MHz in conjunction with acetone, methanol, ethanol and water as the interface liquids.

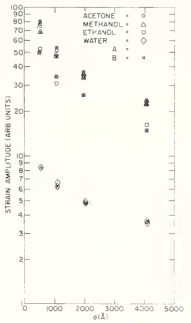

Figure 3. Same as figure 2 but for detection at 20 MHz.

Table 1

Expansion coefficient, β, density, ρ, and acoustic velocity v of materials described in text.

Substance	β	ρ(gm/cm^3)	v(cm/s)
Mo	5.0×10^{-6}	10.2	5.3×10^{5}
acetone	5.0×10^{-4}	0.79	1.2×10^{5}
methanol	4.0×10^{-4}	0.79	1.1×10^{5}
ethanol	3.7×10^{-4}	0.79	1.2×10^{5}
water	6.9×10^{-5}	1.0	1.5×10^{5}
Mylar	2.0×10^{-5}	1.4	3.0×10^{5}
pyrex	5.0×10^{-7}	2.29	6.5×10^{5}

To obtain maximum strain amplitude, it is evident that a thin metal film in conjunction with a thermally insulating substrate and liquid of high thermal expansion coefficient is required. Thicker metal films tend to produce a lower temperature rise resulting in decreased thermal expansion of the liquid. The ratio of strain amplitudes for the four liquids is approximately that of the ratio of the thermal expansions

coefficients of the liquids for a given film thickness. We find also that the strain obtained from a pyrex-Mo-acetone configuration is approximately 4 to 5 times larger as detected in water in the setup of figure 1 compared to a pyrex-Mo-pyrex configuration, where the strain propagate into and is detected in water. The latter structure is of the type described in references [1,2]. Thus a substantial net gain in strain amplitude has been realized by the use of the metal liquid interface. In our experiments, the thin film acts mainly as the optical absorber which transfers the energy to the highly expanding liquid. In that sense the metal film and liquid behave similarly to a liquid with a high absorption constant. This can be achieved by adding high concentrations of absorbing dyes to the liquid as described by Gournay [6]. However, such dye solutions are quite messy to work with, very wavelength selective and tend to precipitate on cold surfaces.

3. Analysis of Experimental Results

The strain amplitude resulting from harmonic excitation can be obtained for a three medium structure by solving the following coupled equations,

$$\frac{\partial^2 u}{\partial x^2} - \frac{1}{v^2}\,\frac{\partial^2 u}{\partial t^2} = \beta\,\frac{\partial T}{\partial x} \tag{3}$$

$$\frac{\partial T}{\partial t} = \frac{K}{\rho C}\,\frac{\partial^2 T}{\partial x^2} + \frac{P}{\rho C}\ . \tag{4}$$

In the above, u is the particle displacement, β the coefficient of linear thermal expansion, K the thermal conductivity, ρ the density, C the heat capacity per unit mass and P the absorbed power density, here taken to vary harmonically as described in references [1-4]. T is the temperature above ambient. The usual elastic boundary conditions apply at the interfaces, i.e., continuity of normal stress and displacement. The thermal boundary conditions at the interfaces and far from the region of thermal excitation are (see inset of fig. 1),

$$\begin{aligned}
&\text{air-pyrex, } (x=0), && \frac{\partial T}{\partial x} = 0 && \text{(a)}\\
&\text{pyrex-metal film, } (x=D), && K_2\left(\frac{\partial T}{\partial x}\right)_2 - K_1\left(\frac{\partial T}{\partial x}\right)_1 = P && \text{(b)}\\
&\text{metal film-liquid, } (x=D+d), && K_2\left(\frac{\partial T}{\partial x}\right)_2 = K_3\left(\frac{\partial T}{\partial x}\right)_3 && \text{(c)}\\
&\text{Region of detection } (x-D>>d), && T,\ \frac{\partial T}{\partial x} = 0 && \text{(d)}
\end{aligned} \tag{5}$$

where the subscripts 1, 2, and 3 refer to the substrate of thickness D, metal film of thickness d and the liquid in contact with the film respectively. In figure 4, sets of curves are presented showing the strain amplitude as a function of the normalized parameter, τd, with τ defined as,

$$\tau \equiv \sqrt{\frac{2\pi f}{\kappa}}\ , \tag{6}$$

where κ is the thermal diffusivity and f the frequency of the incident harmonic thermal excitation of the film. Physically, τ represents the reciprocal thermal skin depth of the metal film as described in reference [4]. The curves of figure 4 represent the solution of eqs. (3) and (4) together with the boundary conditions of eq. (5). The curves are normalized for a uniform peak power absorption over the surface X=D of 1 w/cm^2 varying at a frequency f. The computer solutions require as additional input data thermal and elastic constants of the three media for which we used standard handbook values [7]. The exception was the thermal conductivity of the metal film for which we somewhat arbitrarily took 1/3 the tabulated value in an attempt to compensate for size effects and additional defect scattering usually present in thin films compared to their respective bulk material. These curves calculated at 20 MHz are frequency independent so long as $\tau >> k$ where k is the acoustic wave number. This

frequency independence does not apply for a harmonically excited, free surface, i.e., the case, D=0. Then the strain is proportional to $f^{\frac{1}{2}}$ when plotted against τd. An absolute comparison between the computed curves and the data requires a detailed calibration of the frequency response of the detectors. We chose instead to make a relative comparison by normalizing the experimental value for the 1000 Å (110 mm) thick film to the computed one and using that normalization factor to plot the remaining data points. Then, as a function of τd our data is nearly frequency independent as seen in figure 4.

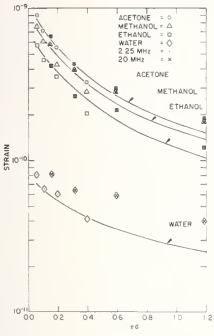

Figure 4. A comparison of theory and experiment. Experimental points were normalized for the 1100 Å (110 nm) thick film to the computer value (solid curve). Except for data with water at 20 MHz, points lie within 20 percent or better of computed values.

4. Concluding Remarks

The good agreement found between the experimental results and the three medium theory over most of the range of parameters investigated led us to try some simple experiments whereby a strain wave can be generated from relatively low power lasers for use in nondestructive testing applications. We illustrate once again such application by scattering elastic waves from small cylinders using here a GaAs diode to generate the waves. The output of the diode was focused onto the light fiber which in turn was used in conjunction with a special cell shown in figure 5. The front window of the cell consists of a thin film of Mo evaporated onto a 5 mil (127 μm) Mylar sheet. The Mo is in contact with a small volume of acetone which is contained by a second Mylar window. Pulses of 100 ns width were used to generate waves with only ∿ 10 W of optical power incident at the Mo-acetone interface. Several aluminum rods were mounted in a water tank from which the elastic waves were scattered and detected at 7.5 MHz via a boxcar integrator and chart recorder, (fig. 6). The displacement in arrival time for the different samples coincides with the path difference of the scattered waves due to the difference in sample diameters. From this simple example, it is apparent that wave reconstruction of scattering objects can in principle be determined using the present technique.

In summary, we have shown some results for generating elastic waves from three layered structures that can be used to obtain MHz waves for a variety of possible applications. An analysis that properly accounts for all the boundary conditions at the interfaces is used to compare to the experimental results. Methods for optimizing the strain amplitude for a given power density are suggested by these results.

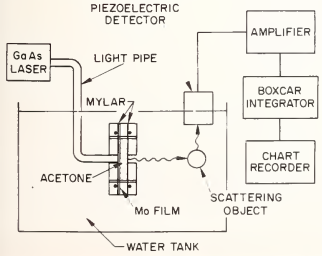

Figure 5. Experimental arrangement for scattering from Al cylinders using GaAs (∿ 10 W incident power) as excitation source on a Mylar-Mo-acetone cell designed for efficient conversion of optical to elastic energy.

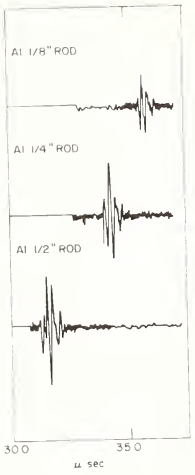

Figure 6. Elastic waves at 7.5 MHz scattered from three different diameter aluminum rods. Traces shown are recorded on a high gain setting of a boxcar integrator starting at a time 33.0, 32.7, and 30.7 μs after initiation of the GaAs laser as shown by noise preceding the arrival of the scattered signal. The difference in the scattered wave arrival time is consistent with the path difference between the generating surface and the detector for concentrically mounted rods of differing diameters.

We have had very useful discussions with H. F. Budd who greatly assisted in the thermal calculations presented. We are also grateful for expert technical assistance from E. E. Tynan.

References

[1] von Gutfeld, R. J. and Melcher, R. L., Appl. Phys. Lett., 30, 257 (1977).

[2] von Gutfeld, R. J. and Melcher, R. L., Mater. Eval., 35, 97 (1977).

[3] von Gutfeld, R. J., 1977 IEEE Ultrasonics Proceedings, J. deKlerk and B. R. McAvoy, eds., p. 397.

[4] White, R. M., J. Appl. Phys., 34, 3559 (1963).

[5] von Gutfeld, R. J. and Budd, H. F., to be published.

[6] Gournay, L. S., J. Acoust. Soc. Amer., 40, 1322 (1966).

[7] Handbook of Chemistry and Physics, 44th ed., Cleveland (Chemical Rubber Publ. Co., 1963).

National Bureau of Standards Special Publication 596, Ultrasonic Materials Characterization, H. Berger and M. Linzer, eds., Proceedings of the First International Symposium on Ultrasonic Materials Characterization held at NBS, Gaithersburg, Md., June 7-9, 1978. Issued November, 1980.

OPTO-ACOUSTIC AND ACOUSTO-ELECTRIC WIDEBAND TRANSDUCERS

H. A. F. Rocha, P. M. Griffen, and C. E. Thomas

General Electric Company
Research and Development Center
Schenectady, NY 12301

1. Introduction

The ultimate limit to longitudinal resolution in an ultrasonic imaging system is set by the attenuation in the material through which the beam travels. The operating frequency is usually chosen as a compromise between a high value for good resolution and a low value for good penetration.

In order to optimize longitudinal resolution we propose to generate short acoustic pulses with a broad frequency spectrum and to detect the resulting echoes with wideband transducers. The primary intended use of this type of system is the visualization of atherosclerotic plaque. However, other applications of this system are considered. Two major problems are discussed: 1) generation of fast acoustic pulses; and 2) detection and amplification of the corresponding echoes without appreciable waveform degradation.

2. Opto-Acoustic Transmitter

An opto-acoustic transmitter was built using a Q-switched neodymium-YAG laser as a generator of sharp optical pulses with a wavelength of 1.06 μm.

The optical pulse waveform is shown in figure 1 and indicates a pulse width less than 15 ns. The measured power output was 30 mJ per pulse, which was decreased by 10 dB when operating in the TEM_{ooo} mode.

Generation of acoustic pulses was produced by absorption of the optical beam. Both solid and dispersed absorbers were employed. The solid absorbers were black anodized surfaces in aluminum and black lacquer coatings on metallic and nonmetallic materials. The other type of absorber used was a suspension of carbon particles in water. Coupling to the absorber was made either through lens-mirror systems or by means of aligned fiber optical couplers.

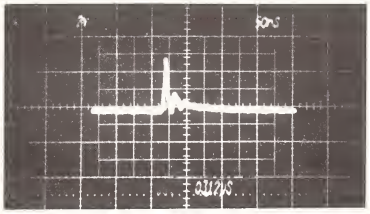

Figure 1. Laser optical pulse.

3. Acousto-Electric Receiver

The initial concept of the receiver evolved from the conventional condenser microphone, but with scaled-down dielectric thickness (fig. 2).

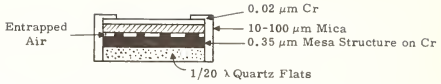

Figure 2. Basic electrostatic receiver.

Mesa structures consisting of suitably etched metal layers deposited on optical flats were successfully fabricated. Many materials and mesa configurations were tried, a typical example being shown in figure 3. On a quartz flat 1 cm diameter, 1 cm thick, optically polished to λ/20, were sputtered successive layers of chromium (200 nm) and gold (350 nm). The gold layer was pattern-etched to obtain an orthogonal set of square mesas 50 μm x 50 μm x 0.35 μm high spaced at 115 μm on centers.

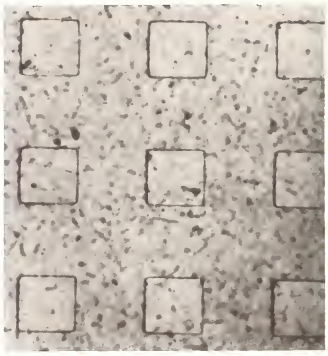

Figure 3. Micrograph of mesa structure.

The best solid dielectric found during this investigation was natural mica, carefully cleaved to about 10 to 25 μm. A unit built under these conditions detected acoustic pulses produced by the Nd-YAG laser and transmitted through 5 cm of aluminum. The waveform is shown in figure 4; the pulse is less than 15 ns wide and shows the typical shape of a step function after passing through a low-pass filter.

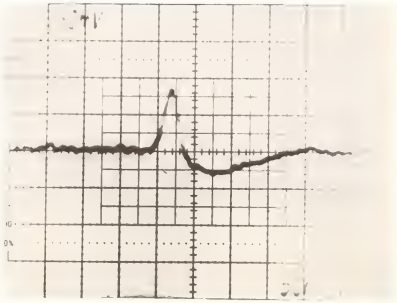

Figure 4. Laser-generated acoustic pulse, detected by an electrostatic transducer.

The main problem associated with the mica-mesa transducer is the repeatability of operation. Identical units using similar substrates showed variations in sensitivity ranging over several decades. A possible reason may be related to the layered nature of mica which introduces additional uncontrollable air gaps in series with the mesa air gap.

4. Transmitter Acoustic Dosage

One of the precautions that must be taken when proposing a new type of transmitting transducer for possible use in a biomedical field is the measurement of the effective dosage. In the acoustic field this problem is particularly acute because of the difficulty of obtaining instantaneous power measurements of short bursts.

Fortunately, a great deal of dosage work has been carried out using lead zirconate-titanate (PZT) transducers and thousands of these units are used every day in medical diagnostic work. Therefore, it was decided not to attempt to make absolute instantaneous acoustic power measurements, but rather to make comparative measurements between the acoustic pulses produced by the laser system and the well-characterized PZT transducers.

Figure 5 shows the test setup used. A conventional PZT transducer was energized by a gated burst with a carrier frequency of 2.25 MHz. A mesa-mica electrostatic receiver operating at a 500 v bias received the acoustic pulse transmitted through a water delay column. The transmitted burst and the received signal are shown in figure 6.

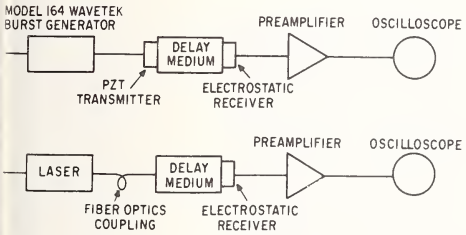

Figure 5. Acoustic dosage measurements.

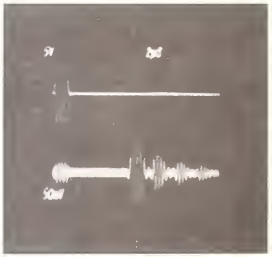

Figure 6. Received pulse-PZT excitation.

The laser was then coupled to the fiber optics unit (without absorber), and its optical output at that power setting was measured by the calorimetric method to be 1.5 mJ per pulse. The absorber was then added to the end of fiber optics coupling and applied in lieu of the PZT transmitter. The corresponding acoustic pulse was detected by the same undisturbed receiver. The receiver output, after 40 dB amplification, is shown in figure 7.

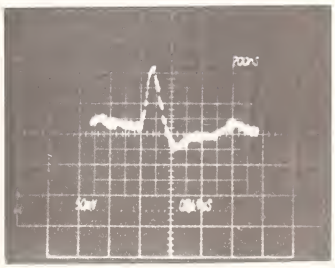

Figure 7. Received pulse-laser excitation.

The comparison of the two tests shows that the amplitude of the acoustic pulse produced by the 1.5 mJ laser pulse is equivalent to the acoustic pulse produced by a PZT transducer excited by a 15 v rms burst. Even a full-strength 30 mJ pulse would produce the equivalent of a 300 v rms pulse excitation to a PZT transducer commonly encountered in commercial equipment

5. Receiver Bandwidth

The test set up shown in figure 8 was used to measure the bandwidth of the mesa-mica electrostatic receiver.

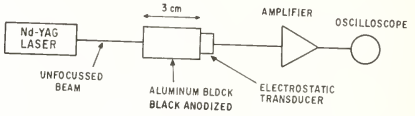

Figure 8. Test set up for measurement of bandwidth.

The received pulse was detected by the electrostatic transducer, amplified, and displaye on the screen of an oscilloscope. The corresponding waveform is shown in figure 9. It shows a rise-time of less than 15 ns, corresponding to a bandwidth exceeding 20 MHz.

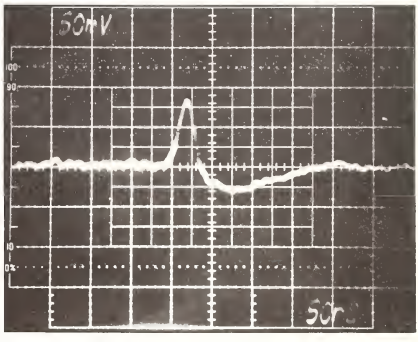

Figure 9. Response of electrostatic transducer.

6. Receiver Sensitivity

The sensitivity of the mesa-mica electrostatic receiver was measured in relation to that of conventional PZT transducers. The corresponding test set ups are shown in figures 10 and 11.

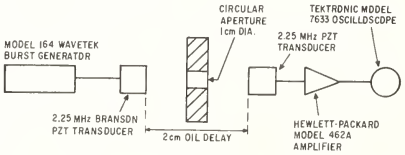

Figure 10. Sensitivity measurement test set up--PZT receiver.

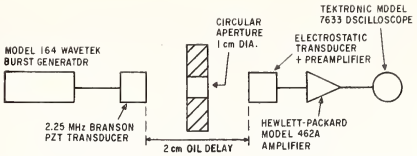

Figure 11. Sensitivity measurement test set up--electrostatic receiver.

Figure 12 shows the transmitted and the received pulses under the test conditions of figure 13.

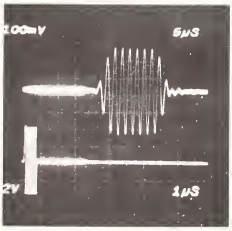

Figure 12. Insertion loss measurement--PZT receiver.

The gain of the 462A amplifier was set at 20 dB. The overall insertion loss is, therefore,

$$\frac{10\ v}{250\ mv} - 20\ dB = 52\ dB.$$

Figure 13 shows the transmitted and the received pulses under the test conditions of figure 11. The solid dielectric is 25 μm mica biased at 900 v. Note that, because of the large bandwidth of the electrostatic receiver, the exciting pulse was made only one cycle wide. The combined gain of the transducer preamplifier and the 462A amplifier was 26 dB. The over all insertion loss is

$$\frac{10\ v}{500\ mv}\ 26\ dB = 52\ dB.$$

The electrostatic transducer showed a sensitivity equivalent to that of PZT.

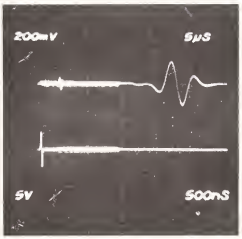

Figure 13. Insertion loss measurement--electrostatic receiver.

7. System Operation

The combination laser transmitter/electrostatic receiver has many advantages over conventional piezoelectric elements. For instance:

1.) A simple lens can be used to change the size of the optical beam falling on the absorber. This is equivalent to having a transmitter with a continuously variable diameter.
2.) Small spot sizes can generate very wide acoustic beams. Beam widths of 160 degrees (at 50 percent points) have been measured in aluminum.
3.) Cylindrical lenses can be used to produce the equivalent of a transducer with a continuously variable shape.
4.) Electro-optic deflectors can produce one- and two-dimensional scanning arrays.

However, the most important application of this system may lie outside the acoustic imaging field. Biological tissues offer varying degrees of attenuation of ultrasonic pulses, the attenuation factor normally increasing with frequency. If a sharp pulse, (with an extended frequency spectrum) is transmitted, the echoes produced by internal reflections will have a different frequency spectrum as a result of the strong attenuation of the high-frequency components. In the time-domain the echoes will present the characteristic shape of a unit function after passing through a low-pass filter. Examination of these waveforms or, better yet, their spectral analysis may lead to the determination of the attenuation factors in vivo, a long-waited goal in the field of macro tissue characterization.

This work was supported by the National Heart, Lung, and Blood Institute under contract NO1-HV-5-2966.

National Bureau of Standards Special Publication 596, Ultrasonic Materials Characterization, H. Berger and M. Linzer, eds., Proceedings of the First International Symposium on Ultrasonic Materials Characterization held at NBS, Gaithersburg, Md., June 7-9, 1978. Issued November, 1980.

POINT DENSITY AND DEFECT CHARACTERIZATION VIA MEASUREMENTS OF ULTRASONIC BULK WAVES

R. O. Claus[1] and C. R. Johnson, Jr.

Department of Electrical Engineering
Virginia Polytechnic Institute and State University
Blacksburg, VA 24061

The qualitative justification of simple physical models of both ultrasonic compressional wave propagation and void defects in transparent isotropic elastic solids is provided by observable correlation between experimental wave measurements obtained using a differential interferometric laser probe technique and theoretically predicted values. Specifically, a significant decrease in successive wave amplitude maxima, not predicted by simple plane or parallel spherical wavefront models, appears in the simulation of a general concentric wavefront model. Local deviations between experimental and theoretical data are due to point defects. Refinements of both wave and defect models are suggested.

1. Introduction

Within the past ten years, several coherent optical methods have been developed to measure ultrasonic compressional and shear waves within transparent media, and ultrasonic surface acoustic waves [1][2]. One of the most versatile of these, a differential interferometric technique with effective two-dimensional spatial resolution, was developed in 1971 independently by Palmer to study elastic wave propagation and by Chartier to detect local defects in magnetic recording surfaces [2,3]. Using Palmer's calibrated SAW detection system, surface waves with maximum particle displacements less than 10^{-3} Å (0.1 pm) have been observed [4]. Measurements of compressional and shear waves within transparent media may be obtained with equivalent sensitivity if consideration of the materials' photoelastic constants is included in the calibration calculations and if a geometrical model for the acoustic wave field is assumed. Such measurements have been reported [4].

Recently, differential interferometry has been applied to the detection of leaky and Stoneley waves on media boundaries [5] and the decay of the components of SAW-induced particle motion with distance below the substrate surface [6]. The complicated theoretical analysis of these measurements has required independent computer modeling and simulation of wave propagation, acousto-optic interactions, and defect effects. Since the consideration of these three problems at the same time leads to cumbersome numerical analysis, simplified models are needed. We consider here the performance of simple compressional wave and defect models in predicting differential interferometric probe data.

2. Differential Interferometry

Differential interferometric probe measurements of compressional waves have been described in detail elsewhere [7]. The basic optical system is shown in figure 1. The input 2 mW HeNe laser beam at the left is mechanically chopped to provide a synchronous detection reference signal, expanded with a microscope objective and lens combination, and passed through the beam splitter H to produce an interference pattern which is focused on the bandpass spatial filter. The filter output is two optical beams of approximately equal intensity. These beams are then focused as indicated on points P and Q separated by half a

[1]This material is partially based upon work supported by the National Science Foundation under Grant No. ENG-7805773.

[2]Figures in brackets indicate the literature references at the end of this paper.

longitudinal wavelength, $\Lambda/2$, within the transparent specimen. Wave-induced changes in material density along the beam paths within the solid produce differential optical path length changes between the two beams. After passing through the specimen, the beams interfe producing a straight line interference pattern which is focused on a Ronchi grid. Light transmitted by the grid is focused on the 0.2 mm^2 active area of a PIN 020A low-noise photodetector. Optical adjustments are required to match the interference fringe pattern spacing and the spatial period of the grid. Detected signal power is proportional to the difference in optical path length between the two beams; therefore, the measured longitudinal wave amplitudes are effectively integrated over the regions of acousto-optic interaction. Scannir within samples is achieved by mechanically translating the specimen with respect to the fixec optical beams.

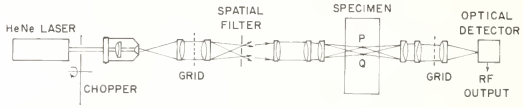

Figure 1. Differential interferometric optical system for the detection of compressional waves in transparent solids.

3. Wave Modeling

For simplicity, standing bulk waves in solids comprised of successive regions of local compression and rarification have in the past been modeled for differential optical analysis by parallel plane wavefronts [7]. For assumed sinusoidal driving signals applied to a compressional mode transducer mounted on a transparent specimen, the induced index of refraction, assuming such plane wavefronts as shown in figure 2, is

$$n(x) = n_o[1 + a \sin(\frac{2\pi}{\Lambda} x)] , \qquad (1)$$

where Λ is the longitudinal wavelength, n_o the unperturbed index of refraction, and a the peak index deviation. At the beam locations, assuming maximum sensitivity, the indices are simply

$$n(x_1) = n_o(1 + a \sin Kx) \qquad (2)$$

$$n(x_2) = n_o(1 - a \cos Kx), \qquad (3)$$

where $K = 2\pi/\Lambda$. The optical detector output signal is then proportional to the absolute value of the relative optical retardation $\Delta R = (\Delta n)d$ given here by

$$\Delta R(x) = 2n_o \, ad \sin Kx . \qquad (4)$$

Since the phase added to the detected signal by the processing electronics is unknown, an arbitrary phase factor is included in the sine argument. Optical measurements predicted by this model are therefore

$$m_1(x,\phi) \propto |\sin(Kx + \phi)|, \; -\frac{\pi}{2} < \phi < \frac{\pi}{2} \quad . \qquad (5)$$

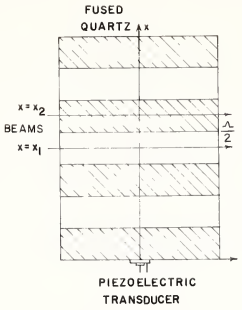

Figure 2. Plane wavefront compressional waves. Regions with densities greater and and less than equilibrium density are indicated by hatched and open areas, respectively. Density along each optical path is constant (after Palmer, reference [7].

Experimentally, 8 MHz compressional waves were generated in a 100 mm cube of fused quartz of less than optical quality using a fundamental mode 12.4 mm x 6.2 mm rectangular x-cut quartz crystal transducer. Due to beam spreading, especially in the direction parallel to the narrow dimension of the transducer, and attenuation, an expected decrease in compressional wave amplitude was noted with increasing distance from the transducer. As shown in figure 3, such a decrease is not predicted by a plane wave model simulations [8].

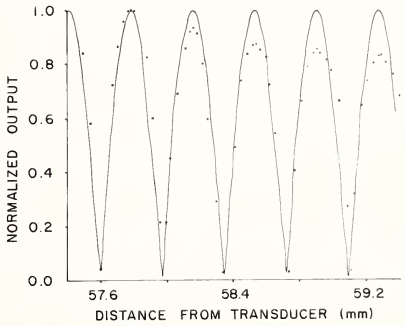

Figure 3. Compressional wave in fused quartz. Peak amplitudes of experimental data, indicated by solid circles, decay; amplitudes of data calculated using plane wave model, with $\phi = -0.4$ for best fit, remain constant.

By increasing the complexity of the numerical evaluation algorithms slightly, a more realistic model may be considered. If surfaces of constant acoustic phase are modeled as parallel spheres of radius r, the index of refraction in a geometry similar to that shown in figure 2 is

$$n(x,y) = n_o[1 + a \sin(\frac{2\pi}{\Lambda} x + \sqrt{r^2 - y^2} + \sqrt{r^2 - Y^2})] \quad (6)$$

where Y is half the width of the specimen [9]. The anticipated system output signal for a scanned wave using this index model is

$$m_2(x,r,\phi) \propto \left| \int_0^Y \sin(Kx + \sqrt{r^2 - y^2} + \sqrt{r^2 - Y^2} + \phi) dy \right| , \quad (7)$$

where again the arbitrary phase ϕ has been included. The limits of integration represent transversal of half of the 100 mm fused quartz cube, which is sufficient due to the model's symmetry.

The implicit relationship between the density at one location (x,y) on the line of measurement and m_2 indicates the increased complexity of density inferral arising from a marginal increase in model complexity. To obtain point density predictions from a calibrated complex model such as (7), r and ϕ need to be varied to obtain the best match to the data record. Simulations using (7), however, also predict no amplitude decay with distance. The resulting indistinguishability of the two density models from normalized measurements along lines perpendicular to the medium illustrates the identifiability problem [10]. This uncertainty could be resolved by comparing the differing predictions of the two models for skewed lines of measurement.

Due to beam spreading, compressional acoustic wavefronts do not retain their spatial characteristics with increasing distance from the transducer. For acoustic wavefronts concentric with the x-y coordinate origin in figure 2, the retardation as a function of x becomes

$$R(x) = n_o d + 2n_o a \int_0^Y \sin(K \sqrt{x^2 + y^2}) dy . \quad (8)$$

Such a concentric wavefront model may be further generalized by assuming an arbitrary effective origin for the center of curvature on the x axis. If the distance between that origin and the x-y coordinate origin is designated by z, the predicted system measurement is

$$m_3(x,z,\phi) \propto \left| \int_0^Y \sin(K \sqrt{(z+x)^2 + y^2} + \phi) dy - \int_0^Y \sin(K \sqrt{(z+x-\frac{\Lambda}{2})^2 + y^2} + \phi) dy \right| \quad (9)$$

Simulation of (9) demonstrates both the retention of the periodic scallop and localized decay, as indicated in table 1. For the purpose of simulating differential interferometric measurements in other applications, this may be the simplest model and the easiest to implement numerically.

Table 1. Relative maxima for concentric wavefront model.

D (mm)[a]	P[b]	N[c]
57.66	6.92	1.00
57.93	6.67	0.96
58.30	6.46	0.93
58.67	6.42	0.92
67.25	7.63	1.00
67.65	7.46	0.97
68.00	7.31	0.96
68.40	7.00	0.92
68.75	6.96	0.91
80.32	8.30	1.00
80.69	8.16	0.98
81.07	7.97	0.96
81.44	7.78	0.94
81.81	7.62	0.92

[a]Distance from optical beam in medium to arbitrary origin of concentric compressional waves.

[b]Predicted measurements for numerical step-size of 0.25 mm across 50 mm optical path.

[c]Normalized measurements for listed decaying portions of predicted wave.

Simulation of (9) suggests the consideration of a model combining a relatively flat central lobe with nonplanar and in general nonparallel edge structure as shown in figure 4. Recent point probe Doppler measurements indicate also that the amplitude of the longitudinal wave along a plane of constant phase is not constant; rather, it decays from a maximal central region value to amplitudes comparable to edge effect reflected waves at the side boundaries [11]. A general model must therefore consider both the position of the acoustic field wavefronts in space and the amplitude variations along field lines of constant phase. If s represents the field amplitude shape factor [12], anticipated optical measurements are

$$m_4 = \left|\sin(Kx + \phi)\right| + \left(1 - \frac{\ell}{2d}\right)\left|\int_0^Y \sin\left[sK\sqrt{(z+x)^2+y^2} + \phi\right]dy - \int_0^Y \sin\left[sK\sqrt{(z+x-\frac{\Lambda}{2})^2 + y^2} + \phi\right]dy\right| . \qquad (10)$$

This measurement retains spatial periodicity and predicts necessary maxima decay with distance. The performance of this model for several physically realizable shape factors, for example, an exponentially decaying amplitude along successively broadening wavefronts characterized by corridor width and diffraction spread angle requires a large amount of numerical evaluation due to its realistic complexity.

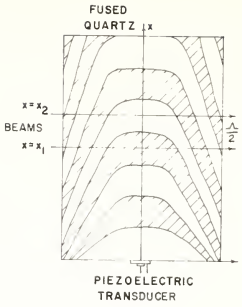

Figure 4. Corridor model of compressional waves [12].

4. Defect Effects

Defects have been considered both experimentally and numerically [13,14]. For work in transparent glass-type media, defects may be reasonably modeled as spheres since they are usually bubbles trapped during cooling. Such defects affect differential interferometric measurements in two ways. First, the index of refraction of the gases trapped in bubble defects is different from that of the transparent host material so the bubble will induce a change in the relative retardation between the two focused laser beams. Since the beams have finite Gaussian cross sections, the volume of the bubble and that of the beams must be convolved to determine the total effect on the output signal [15].

Experimentally, bubble defects in glasses may be easily observed by optical scattering. A scan of a compressional wave field which contains a bubble defect is shown in figure 5, in which the irregularity on the side of one of the scallops is caused by the defect. Simulated convolution data is also shown in figure 5. Since the differential interferometric system is not calibrated in terms of index of refraction, defect size is known only qualitatively. Due to the optical interaction, small perturbations expected due to the second effect, namely acoustic wave scattering and reflection, are masked. The integrating property of the probe technique helps to further obscure these effects.

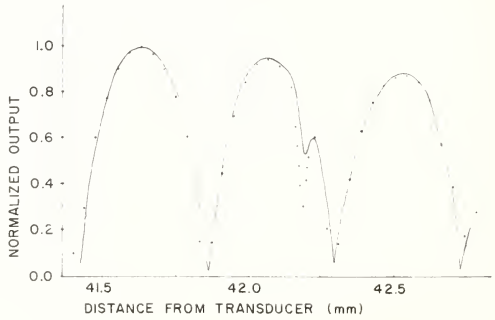

Figure 5. Optical scan of compressional wave in 7070 pyrex with bubble defect. Experimental data is indicated by solid circles; data calculated assuming circular bubble and Gaussian optical beam profiles by solid line.

5. Conclusion

We have considered several simple models of compressional wave and defect detection via differential interferometric optical measurements. Both models can be extended with a corresponding increase in simulation complexity. Applications in the modeling of acoustic boundary waves and the Goos-Hänchen effect, and the prediction of interior wave behavior from external SAW measurements could follow.

References

[1] Whitman, R. L. and Korpel, A., Optical probing of surface waves and surface wave devices, IEEE Trans. Sonics Ultrason., SU-23, 33-63 (1976).

[2] Palmer, C. H., Ultrasonic surface wave detection in optical interferometry, J. Acoust. Soc. Amer., 53, 948-949 (1973).

[3] Chartier, M., Laser interferometric equipment for vibration and distance to surface of floating heads measurements for mass memory magnetic disks, Technical Report, Laboratoire Central de Rencherches Thomson-CSF, Orsay, France (Nov. 1971).

[4] Palmer, C. H., Claus, R. O., and Fick, S. E., Ultrasonic wave measurement by differential interferometry, Appl. Opt., 16, 1849-1856 (1977).

[5] Claus, R. O. and Palmer, C. H., Direct measurements of ultrasonic Stoneley waves, Appl. Phys. Lett., 31, 547-548 (1977).

[6] Claus, R. O. and Palmer, C. H., New applications of differential interferometry in ultrasonics, Proc. Annual Meeting Opt. Soc. Amer., (Toronto, Canada, Oct. 1977).

[7] Palmer, C. H., South, H. M., and Mak, T. H., Optical interferometry for measurement of Rayleigh and distortional waves, Ultrasonics, 12, 106-108 (1974).

[8] Claus, R. O. and Johnson, Jr., C. R., Optical measurements of material density, Part I: Model development, Proc. 1978 CISS, The Johns Hopkins University (Baltimore, MD, March 1978).

[9] Johnson, Jr., C. R. and Claus, R. O., Optical measurements of material density, Part II: Model justification, Proc. 1978 CISS, The Johns Hopkins University (Baltimore, MD, March 1978).

[10] Tse, E., A quantitative measure of identifiability, IEEE Trans. Sys. Man. and Cybernetics, SMC-8, 1-8 (1978).

[11] Fick, S. E., personal communication.

[12] Claus, R. O. and Johnson, Jr., C. R., Acoustic wave density modeling in optically transparent solids, Proc. Ninth Annual Pittsburgh Conf. on Modeling and Simulation (Pittsburgh, PA, April 1978).

[13] Sachse, W., The scattering of elastic pulses and the nondestructive evaluation of materials, Materials Evaluation, 35, 83-106 (1977).

[14] Shankar, R. and McDonough, R. N., Ultrasonic measurement of defects in metals using cepstral processing, Proc. Intl. Conf. on Acoustics, Speech, and Signal Proc., pp. 533-537 (Tulsa, OK, April 1978).

[15] Claus, R. O., Optical measurements of ultrasonic Stoneley waves, Ph.D. dissertation, The Johns Hopkins University, (March 1977).

National Bureau of Standards Special Publication 596, Ultrasonic Materials Characterization, H. Berger and M. Linzer, eds., Proceedings of the First International Symposium on Ultrasonic Materials Characterization held at NBS, Gaithersburg, Md., June 7-9, 1978. Issued November, 1980.

VISUALIZATION OF ULTRASONIC BULK WAVES IN SOLIDS WITH AN INTERNAL LIGHT PROBE

B. Boro Djordjevic and Robert E. Green, Jr.

The Johns Hopkins University
Department of Mechanics and Materials Science
Baltimore, MD 21218

Traditional ultrasonic measurement methods for characterizing materials rely on piezoelectric transducers acoustically coupled to the specimen's surface. The extension of such surface observations to the actual behavior of ultrasonic bulk waves requires theoretical assumptions and approximations. Because of new, stringent requirements on ultrasonic measurements, there is a need for better understanding and documentation of ultrasonic bulk wave propagation in solids. For this purpose, the measurement of ultrasonic bulk waves by a light probe in transparent solids provides critical comparison between internal and surface observations. The bulk wave measurements by an internal light probe indicated that pulsed ultrasonic waves exhibited interactions and changes not resolvable by surface-mounted piezoelectric transducers.

1. Introduction

The use of surface-mounted piezoelectric transducers for generation and detection of ultrasonic waves is convenient, simple, and sensitive. However, with the advancement of ultrasonic nondestructive test methods, it is desirable to internally measure ultrasonic bulk waves experimentally for direct comparison with the surface observations. This is especially desirable for calibration of transducers with regard to the beam profile and frequency response.

Common optical techniques such as birefringence or Schlieren allow the direct observation of the acoustic field inside a transparent solid. These methods, although very useful, are only capable of imaging ultrasonically-disturbed regions of solids and contain no ultrasonic waveform information. However, to critically evaluate the accuracy of surface mounted sensors, the internal light probe should resolve the ultrasonic waveforms. For this purpose, an internal optical probe is being developed which is capable of resolving the waveform of ultrasonic pulses in transparent solids. The system used in the present work is based on light diffraction produced by longitudinal ultrasonic waves.

The interaction of light and sound can generally be grouped into the two distinct types as schematically shown in figure 1. The ultrasonic disturbance can be illuminated by a light beam whose diameter is larger than the ultrasonic wavelength. Raman and Nath [1][1] were the first to analyze this case by using similar analysis as used with optical diffraction gratings. Under wide beam illumination, an ultrasonic wave acts as an optical phase grating diffracting the light with the angles and intensities of diffraction determined by the wavelength components of the ultrasonic wave. To be able to completely specify the shape of the ultrasonic pulses, measurements should be performed on all components of the diffraction pattern which is experimentally difficult, if not impossible.

The case of an illuminating light beam diameter smaller than the acoustical wavelength reduces the diffraction of light to a single order whose diffraction angle is dependent on local stress as seen by the traversing light beam. Because the diffraction is thus a function only of the localized stress in the small section of the specimen traversed by the

[1]Figures in brackets indicate the literature references at the end of this paper.

ultrasonic pulse, it is possible to measure the variation of the stress inside the transparent solid due to the ultrasonic wave.

The general diffraction of the light by ultrasound has been observed by many authors [2-9] and a summary and general theory has been given in papers by Bhatia and Noble, [10] and Klein and Cook [11].

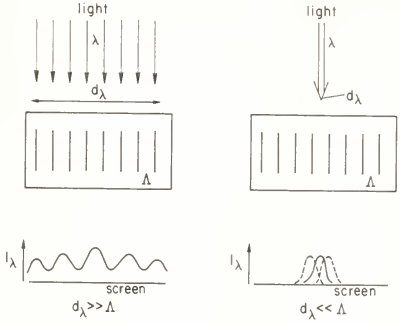

Figure 1. Two distinct types of light diffraction by ultrasonic waves in solids.

2. Optical System

The optical system used in the present work for measuring the traveling ultrasonic pulses is shown schematically in figure 2. The narrow light beam traverses the transparent test block parallel to the plane wave fronts generated by a commercial ultrasonic transducer. The incident He-Ne laser light beam diameter is reduced so that it is smaller than the shortest ultrasonic wavelength observed. As the light traverses the test block, the periodic variation in stress produces a corresponding variation in index of refraction causing the periodic angular variations of the diffracted outgoing light beam. Thus the angular displacement of the outgoing light beam is due to the integrated effect of the diffraction across the optical path length in the specimen and is a function of frequency, amplitude and effective diameter of the ultrasonic wavefront. The angular displacement of the diffracted beam is measured by

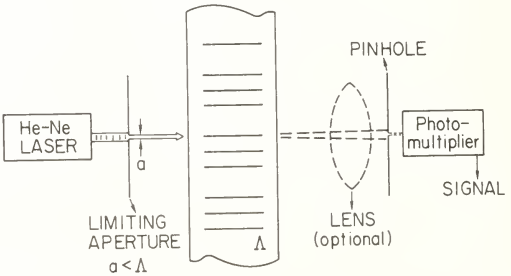

Figure 2. Optical system used for narrow beam light probing of ultrasonic pulses in solids.

a pinhole-photomultiplier assembly. The change in the localized light intensity at the pinhole due to the diffracted beam motion across the pinhole is detected as a time-varying current output of the photomultiplier. The signal is then electronically processed and recorded as a function of time on an oscilloscope or a transient recorder. As shown, the apparatus is sensitive only to planar longitudinal stress waves. However, the light probe can be used throughout the test block, traversing ultrasonic pulses from different directions, making possible useful determination of the ultrasonic bulk waveforms.

3. Experimental Procedure and Results

The light probe measurements were performed on an optically polished rectangular fused quartz block with 5 cm square sides and 15.2 cm length. The commercial piezoelectric transducer was placed on the block so that the ultrasonic pulse traversed a 5 cm section. The light beam traversed the other 5 cm section parallel to the transducer surface and normal to the face of the block. The quartz block was positionable so that the beam could be moved to any location. The signal was recorded simultaneously on a dual channel oscilloscope with the top trace showing the piezoelectric transducer output and the bottom trace showing the output from the light probe.

Figure 3 was obtained with a 1 MHz Aerotech Gamma rectangular transducer acoustically coupled to the specimen with stopcock grease. The optical beam was positioned 2 mm below the surface of the specimen face on which the transducer was mounted and directly beneath the center of the transducer. The electrical burst applied to the transducer shown on the top trace in figure 3 generated an ultrasonic signal which was first detected by the optical sensor. The optically-measured ultrasonic waveform is evidently different from the applied electrical signal as can be seen by comparing the initial pulses from the two traces. However, upon the first reflection the ultrasonic signal measured by both sensors is very similar in shape with the optical signal shifted slightly to the right due to the delay caused by physical separation of the probes. At this location, the optical probe sensed only the outgoing wave reflected from the top surface in contact with the transducer. There is no evidence of stress variations by the earlier incoming ultrasonic pulses due to reflections from the bottom. Figure 4 was recorded under the same conditions except that the optical sensor was positioned in the middle of the test specimen between the ultrasound reflecting surfaces. The time sequence of the ultrasonic pulse detection from left to right in figure 4 is as follows: the first waveform of the top trace shows the initial electrical pulse applied to the transducer; the first waveform of the bottom trace is due to the downward

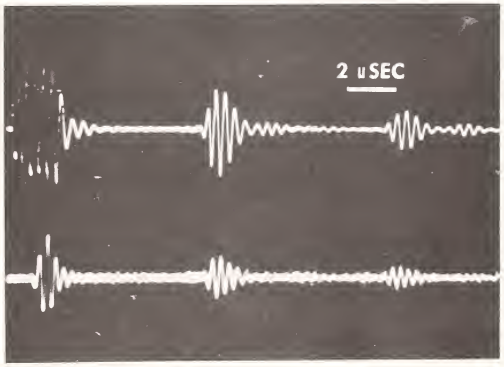

Figure 3. Ultrasonic signal observed from 1 MHz Aerotech Gamma transducer (top trace) and by light probe centered 2 mm below the transducer.

moving (away from transducer) ultrasonic pulse located in the middle of the specimen as sensed by the light probe; the second waveform of the bottom trace is due to the phase-shifted upward-moving ultrasonic pulse in the middle of the specimen; the second waveform on the top trace is the first reflection measured by piezoelectric transducers, etc. The waveforms of both sensors are comparable. The light probe measures the ultrasonic pulse propagation in both directions and shows the phase shifts upon reflections.

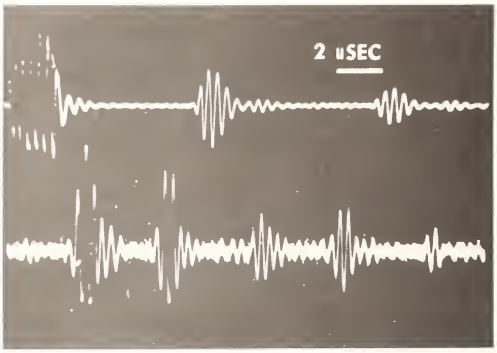

Figure 4. Ultrasonic signal observed from 1 MHz Aerotech Gamma transducer (top trace) and by light probe centered halfway down from the transducer (bottom trace).

The signal observed by the light probe in figures 3 and 4 shows the expected and commonly assumed mode of ultrasonic bulk wave propagation through the test specimen. However, it is equally possible to have a case of ultrasonic waves which do not propagate as expected from surface piezoelectric transducer indications as illustrated in figure 5. The light beam was placed 1/3 of the way down directly beneath a 2-1/4 MHz Aerotech Gamma transducer which was driven by a longer pulse width. The optical probe measurements show increasingly longer and more intense train of overlapping ultrasonic pulses due to spreading of the wave packet to the point where the single ultrasonic pulse interacts with itself in a nonlinear manner. This is not resolved by the surface-mounted piezoelectric sensor which indicates the presence of a single reflecting pulse. The only hint of a possible problem by the piezoelectric sensor is the geometrical distortion of the second reflection wave packet envelope. The extent of bulk wave degeneration and interaction was, however, readily observed by the light probe, which indicated that by the time of detection of the second reflection from the top surface there exists a region with a continuous train of overlapping ultrasonic pulses, generated by the single ultrasonic pulse. With the light probe halfway down and displaced 2 cm to the right of the centerline of the 1 MHz transducer the optical probe demonstrates the ultrasonic beam spread as indicated in figure 6. There is no ultrasonic field present at this location immediately after the initial pulse, but at later times the ultrasonic intensity builds up to a detectable level due to beam spreading during sequential reflections of the pulse. Similarly, it was observed that many transducers exhibit nodal lines and nonuniform intensity of the ultrasonic beam profile. Also it was observed that each ultrasonic pulse interacts with itself during reflection with an increase in the degeneration of the original signal as the ultrasonic intensity and pulse length were increased.

4. Conclusions

Bulk ultrasonic waveform changes can be studied using the present optical system and additional information is obtainable on possible limits and accuracy of the surface ultrasonic measurements as well as on the performance of different piezoelectric transducers. The

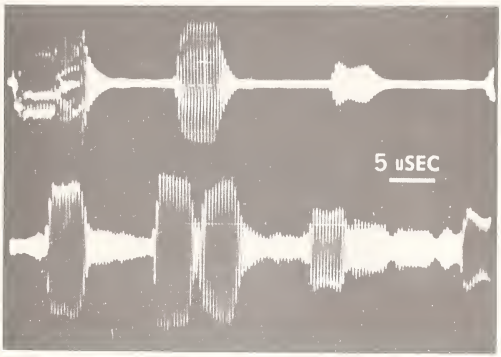

Figure 5. Ultrasonic signal observed from 2-1/4 MHz Aerotech Gamma transducer (top trace) and by light probe 1/3 of the way down from the transducer (bottom trace).

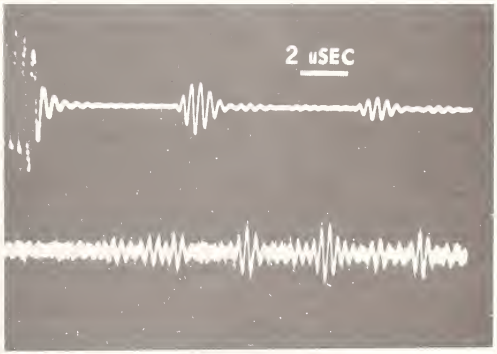

Figure 6. Ultrasonic signal observed from 1 MHz Aerotech Gamma transducer (top trace) and by light probe halfway down from the transducer and 2 cm on the side from the centerline of the transducer (bottom trace).

internal light probe observations can be made to agree with the surface-mounted piezoelectric transducers. However, the possible presence of nodal lines, nonlinear interactions, waveform spread and waveform change of ultrasonic pulses indicated by light probe measurements emphasize the existence of serious limitations and sources of problems in practical ultrasonic measurements. It is in this direction that additional work is necessary for full understanding of ultrasonic bulk wave propagation and interaction modes. Such work should aid in better definition of the effect the transducer load and surface boundaries have on ultrasound propagation as well as the actual behavior of the ultrasonic bulk waves interacting with the structural defects in real, finite solids.

The same optical system can also be used for relative transducer calibration by measuring the frequency and ultrasonic beam radiation profile inside transparent solids from surface mounted ultrasonic transducers.

This work was supported in part by the U. S. Army Research Office. A special note of thanks in this regard is due Dr. George Mayer. Thanks are due to Mrs. Corinne Harness for her skill and patience in typing this manuscript.

References

[1] Raman, C. V. and Nath, N. S. N., The diffraction of light by high frequency sound waves, Part I - Proc. Indian Academy of Sci., 2, 406-412 (1935), Part II - Proc. Indian Academy of Sci., 2, 413-420 (1935), Part III - Proc. Indian Academy of Sci., 3, 75-84 (1936), Part IV - Proc. Indian Academy of Sci., 3, 119-125 (1936), Part V - Proc. Indian Academy of Sci. 3, 459-465 (1936).

[2] Zankel, K. L. and Hiedemann, E. A., Diffraction of a narrow beam of light by ultrasonic waves, IRE Trans. Ultrasonic Eng., 71-75 (1960).

[3] Hargrove, L. E., "Successive diffraction theory for diffraction of light by ultrasonic waves of arbitrary waveform, J. Acoustic Soc. Amer., 36, 323-326 (1964).

[4] Hiedemann, E. A. and Zankel, K. L., "The study of ultrasonic waveform by optical methods, Acustica, 11, 213-223 (1961).

[5] Zitter, R. N., Ultrasonic diffraction of light by short acoustic pulses, J. Acoust. Soc. Amer., 43, 864-870 (1968).

[6] Nomoto, O. and Negishi, K., Diffraction of light by ultrasonic waves of finite amplitude, Acustica, 15, 223-235 (1965).

[7] Cook, B. D., Determination of ultrasonic waveforms by optical methods, IEEE Trans. Sonics Ultrasonics, 89-94 (1964).

[8] Shutilov, V. A., Angles and character of the deflection of a light beam in ultrasonic field," Soviet-Physics Acoustic, 12, [2], 205-210 (1966).

[9] Liu, J. M. and Green, Jr., R. E., Optical probing ultrasonic diffraction in single crystal sodium chloride, J. Acoustical Soc. Amer., 53, 468-478 (1973).

[10] Bhatia, A. B. and Noble, W. J., Diffraction of light by ultrasonic waves, I. - General Theory. Proc. Phys. Soc. (London) A220, 358-367 (1953). II. - Approximate expressions for the intensities and comparison with experiment. Proc. Phys. Soc. (London) A220, 368-383 (1953).

[11] Klein, W. R. and Cook, B. D., Unified approach to ultrasonic light diffraction, IEEE Trans. Sonic Ultrasonics, 123-134 (1967).

National Bureau of Standards Special Publication 596, Ultrasonic Materials Characterization, H. Berger and M. Linzer, eds., Proceedings of the First International Symposium on Ultrasonic Materials Characterization held at NBS, Gaithersburg, Md., June 7-9, 1978. Issued November, 1980.

LIGHT DIFFRACTION BY ULTRASONIC BEAMS HAVING PHASE DIFFERENCE δ

O. Leroy

Katholieke Universiteit
Leuven Campus Kortrijk
Kortrijk, Belgium

and

P. Kwiek and A. Sliwinski

Uniwersytet Gdanski
Gdansk, POLAND

The theoretical analysis of the diffraction of light by two partially overlapped ultrasonic beams showing a phase-difference δ is considered. Symmetry properties of the diffraction pattern are independent of the degree of superposition of the two beams. The intensities, however, depend on this feature, so that purely adjacent beams can be used to compute the ultrasonic pressure of each beam. In the case of two beams, oscillating at a fundamental frequency and at a second harmonic, we find

$$\sin (2\pi \mu_2 L_1/\lambda) = (I_2 - I_1) / I_1 \quad ,$$

where I_1 and I_2 are intensities measured when there is a phase-difference $\delta = \pi/2$ and $\delta = 0$ respectively, and μ_2 is the pressure of the second beam. We found a relation independent of the Raman-Nath parameter ρ. Experiments in the Raman-Nath region were performed and the cosinusoidal relation between the first order intensity of the diffracted lightwave and δ was followed exactly. The sinusoidal dependence of μ_2 on the intensities was also confirmed experimentally.

1. Introduction

Diffraction of light by superposed ultrasonic beams has been extensively studied in the past, while the problem of the diffraction of light by adjacent ultrasonic beams has not received an equivalent theoretical treatment. Several experiments were performed but no theory at that time could give a satisfactory explanation. Zankel [1][1] suggested an experiment to measure ultrasonic pressure, where he considered adjacent ultrasonic beams having a phase-difference π. In order to verify his experiment theoretically, he assumed that adjacent and superposed ultrasonic beams diffract an incident light beam in the same way. In order to evaluate this assumption theoretically, we considered [2] two partially overlapped ultrasonic beams at two harmonics of the same fundamental tone, with a phase-difference δ. The symmetry properties of the diffraction pattern were the same for the case of adjacent and superposed ultrasonic beams. For $\rho < 1$ (Raman-Nath region $\rho = \lambda^2/(\mu_0 \mu_1 \lambda^{*2})$) we found also that the expressions for the intensities were the same, which also confirms the experiment and the assumption of Zankel. For $\rho > 1$ we found totally different expressions for the intensities [3,4]. In this paper, two adjacent ultrasonic beams are considered, a fundamental tone and its second harmonic with a phase-difference δ. From the general formula for the intensities of the diffracted light waves we deduce a simple relation between the ratio of the pressure of the ultrasonic beams and the measured intensities. Experiments were performed by Kwiek et al., [5] and showed that there was a good agreement with theory.

[1]Figures in brackets indicate the literature references at the end of this paper.

2. The Set of Difference-Differential Equations

We consider an incident beam of light with frequency ν and wavelength λ, perpendicular to the direction of propagation of two adjacent ultrasonic waves, having respectively width L_1, frequency ν_1^* wavelength λ_1^* and width L_2, frequency ν_2^*, wavelength λ_2^* as in figure 1.

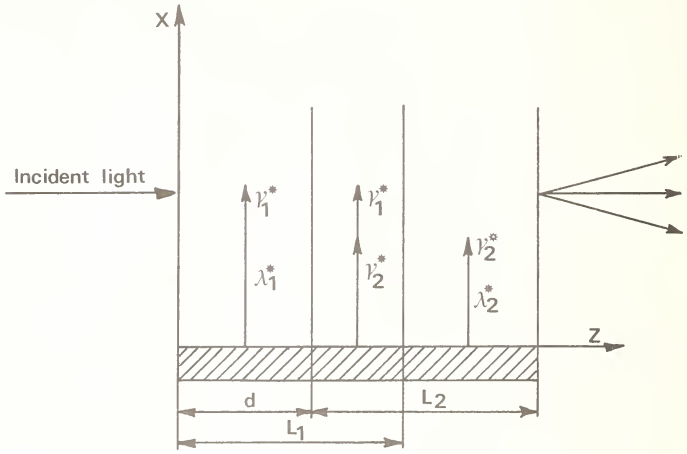

Figure 1. Geometry of the problem of the diffraction of light by two parallel partly superimposed, partly adjacent ultrasonic beams.

The refractive index is assumed to be

$$\mu(x,t) = \mu_0 + \mu_1 [H(z) - H(z-L_1)] \sin 2\pi (\overset{*}{\nu}_1 t - x/\lambda_1^* + \Delta_1)$$
$$+ \mu_2[H(z-d) - H(z-d-L_2)] \sin 2\pi (\overset{*}{\nu}_2 t - x/\lambda_2^* + \Delta_2) \qquad (1)$$

where

μ_0 = refractive index of the undisturbed medium,
μ_1 and μ_2 = maximum variation of the refractive index of the disturbed medium,
$H(z)$ = unit function, defined by : $H(z) = 1$ for $z > 0$ and $H(z) = 0$ for $z < 0$.

The set of difference-differential equations was deduced [3] and can be summarized as follows. Writing the electric field in the form

$$E(x,z,t) = \text{esp}(2\pi i\, t)\ \phi\ (x,z,t) \quad , \qquad (2)$$

and substituting this expression in the Maxwell equations, we find

$$\Delta\phi + (2\pi/\lambda)^2\ \mu\ (x,t)\ \phi = 0, \qquad (3)$$

which is a partial differential equation in the unknown function $\phi(x,z,t)$. Taking into account the periodicity of $\mu(x,t)$ in the variables x and t, we develop ϕ in a double Fourier series,

$$\phi(x,z,t) = \sum_{n=-\infty}^{+\infty} f_n(z) \exp(2\pi i n x/\Lambda) \exp(-2\pi i n N t) \qquad (4)$$

with

$$\Lambda = n_1\lambda_1^* = n_2\lambda_2^*;\ \nu_1^* = n_1^* N,\quad {}^*_2 = n_2 N \quad . \tag{5}$$

This expression is substituted into eq. (3). Neglecting terms in μ_1^2, μ_2^2, and $\mu_1\mu_2$ with respect to terms in μ_1 and μ_2, equating the coefficients of

$$\exp(2\pi i n x/\Lambda)\ \exp(-2\pi i n N t) \quad , \tag{6}$$

and putting

$$f_n(z) = \phi_n(z)\ \exp(-2\pi i \mu_0 z/\Lambda) \quad , \tag{7}$$

we find the system of differential equations for the amplitudes of the diffracted lightwaves:

$$\begin{aligned} &2\,\frac{d\,\phi_n}{d_\zeta} - [H(\zeta) - H(\zeta-\zeta_1)](\phi_{n-n_1} - \phi_{n+n_1}) \\ &-\alpha\ H(\zeta-d_1)\ [\phi_{n-n_2}\ \exp(-i\delta) - \phi_{n+n_2}\ \exp(i\delta)] = i\rho n^2 \phi_n \quad . \end{aligned} \tag{8}$$

where

$\phi_n(\zeta)$ = amplitude of the diffracted lightbeam of the n^{th} order,

$$\zeta = 2\pi\ \mu_1\ z/\lambda;\ \zeta_1 = 2\pi\ \mu_1\ L_1/\lambda;\ d_1 = 2\pi\ \mu_1\ d/\lambda \quad , \tag{9}$$

$$\rho_1 = \lambda^2/(\mu_0\ \mu_1\ \Lambda^2);\ \delta = (n_1\ \delta_2 - n_2\ \delta_1)/n_1 \quad , \tag{10}$$

$$\delta_i = 2\pi\ \Delta_i;\ \alpha = \mu_2/\mu_1 \quad . \tag{11}$$

3. Intensity-Distributions

A necessary and sufficient condition to have a symmetrical diffraction pattern, is [2]

$$\delta = \frac{n_1 - n_2}{n_1} \cdot \frac{\pi}{2} + p \cdot \frac{\pi}{n_1}\ ,\ p = m\ n_1 - \ell\ n_2 \quad , \tag{12}$$

where m and ℓ are arbitrary integers.

We remark that this property is independent of ρ and of the degree of superposition of the two beams. The same expression was found by O. Leroy [6] in the case of pure superposed ultrasonic beams.

For ρ very small, and $d = L_1$, thus purely adjacent (i.e., nonoverlapping), and $L_1 = L_2$, the amplitude for the diffracted lightwave of the order r was given by O. Leroy [4]:

$$\psi_r(2\zeta_1) = \sum_{q=-\infty}^{+\infty} J_{r-ng}(\zeta_1)\ J_q\ (\alpha\ \zeta_1)\ \exp\ (-iq\delta) \quad . \tag{13}$$

This is the identical expression for the amplitude of the diffracted lightwave caused by two superposed ultrasonic beams of width L_1, while we consider a total width of $L_1 + L_1$.

Calculating

$$I_r = \psi_r\ (2\zeta_1)\ \psi_r^*\ (2\zeta_1) \quad , \tag{14}$$

we find a general expression for the intensities as a function of α and δ. In the special case of n = 2, we find

$$\psi_1(2\zeta)\cdot\psi_1^*(2\zeta) = [J_1(\zeta_1)\, J_0(\alpha\,\zeta_1) - \cos\delta\, J_1^2\,(\alpha\,\zeta_1)]^2 + J_1^4\,(\alpha\,\zeta_1)\,\sin^2\delta \quad , \tag{15}$$

in which Bessel functions of higher order than 1 have been dropped. If $\alpha\,\zeta_1 < 0.5$ we have

$$J_0\,(\alpha\,\zeta_1) \cong 1 \text{ and } 2J_1\,(\alpha\,\zeta_1) \cong \sin\alpha\,\zeta_1 \tag{16}$$

and the intensities of the first orders are given by

$$I_{\pm1}\,(2\zeta_1) = J_{\pm1}^2\,(\zeta_1)[1 \mp \cos\delta\,\sin\alpha\,\zeta_1] \tag{17}$$

in which $J_{\pm1}^2\,(\zeta_1)$ is a good approximation, in the Raman-Nath region, $\rho < 1$, for the intensities of the first diffraction orders caused by the first ultrasonic beam. Thus

$$I_{\pm1}\,(2\zeta_1) = I_{\pm1}\,(\zeta_1)\,(1 \mp \cos\delta\,\sin\alpha\,\zeta_1) \quad , \tag{18}$$

is valid for $\rho < 1$ and $\alpha\,\zeta_1 < 0.5$, in the case of superimposed ultrasonic beams as well as in the case of adjacent ultrasonic beam.

We remark that for $\delta = \frac{\pi}{2}$

$$I_{\pm1}\,(2\zeta_1) = I_{\pm1}\,(\zeta_1) = I_1 \quad . \tag{19}$$

Thus the second beam has no influence on this diffraction order. For $\delta = 0$

$$I_{\pm1}\,(2\zeta_1) = I_{\pm1}\,(\zeta_1)\cdot(1 \mp \sin\alpha\,\zeta_1) \quad . \tag{20}$$

Putting $I_{-1}\,(2\zeta_1)$ for $\delta = 0$ equal to I_2 we find

$$\sin\alpha\,\zeta_1 = \frac{I_2 - I_1}{I_1} \quad , \tag{21}$$

or

$$\sin\frac{2\pi\,\mu_2\,L_1}{\lambda} = \frac{I_2 - I_1}{I_1} \quad , \tag{22}$$

from which we can easily calculate μ_2, the pressure of the second ultrasonic wave. Thus only the intensities of the 1st order of the diffracted lightwave are responsible for calculations of μ_2.

Equation (8) was also integrated for $\rho > 1$ by O. Leroy [4], using the NOA-method, and an identical expression, eq. (18) was found. Thus either within or outside the Raman-Nath region we obtain eq. (22), although the method of integrating the eq. (8) is totally different. A generalization of this method to any μ_n can be performed.

4. Experimental Verifications

In the case of $0.1 < \rho < 0.2$, experiments have been performed by Kwiek et al., [5], and, as can be seen in figure 6, good agreement was found with the theoretical prediction. The phase-difference δ between the two beams have an essential influence on the intensity distribution of diffracted light. For the orders ±1, the spectrum is a cosinusoidal function of δ. Also the parameter α in $\sin\alpha\,\zeta_1$ which determines the amplitude changes in the intensity for a certain δ is represented. The region $\rho > 1$ was not experimentally tested.

5. Remarks

The diffraction of light by two adjacent ultrasonic waves, the fundamental tone and its second harmonic, was also studied by F. Poleunis and O. Leroy [7]. By applying the method

of the separation of the variables, they derived a symmetrical diffraction. The intensities of the first orders are independent of the second harmonic, a result which we find for $\delta = \pi/2$. As these authors did not consider a phase-difference δ, they found a mean value of $I_{\pm 1}$ and I_{-1}, and of course, did not find any effect of δ in the diffraction pattern. The same problem was studied by ourselves (unpublished results), taking into account explicitly that the diffracted lightbeams of the first order enter the second ultrasonic region under the Bragg-angles, but considering no phase-difference; the same mean value was found for $I_{\pm 1}$. A result which is not in agreement with the symmetry-properties was also found. The mathematical model has to include the phase-difference δ; otherwise the problem is treated in the implicit supposition that the phase-difference has no influence. So we indeed find mean values for the intensities of the diffracted lightwaves.

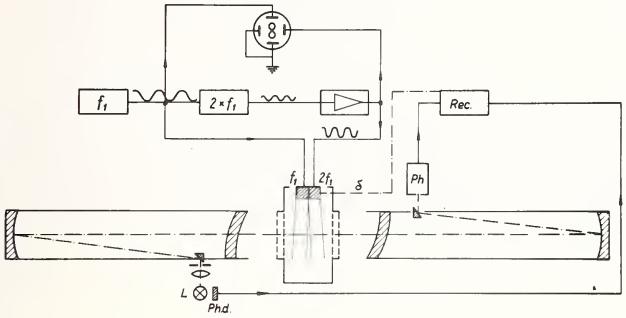

Figure 2. The experimental setup for verification of the theory of light by two adjacent ultrasonic beams. f_1 is the H.F. generator of frequency f_1 = 1 MHz, 2 x f_1 is the harmonic generator to f_2 = 2 MHz, f_1, $2f_1$ are the ultrasonic transducers, 18 is the phase control oscilloscope, δ is the phase-difference which could be changed mechanically with an accuracy of 0.015 wavelength (for 1 MHz in water), L is the monochromatic light source, and Phd is the optical feedback preventing light source fluctuations.

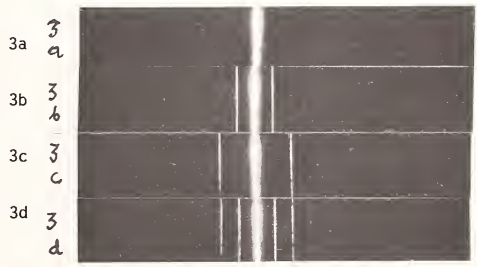

Figure 3. Photos of diffraction spectra for: a) without ultrasonic beams, b) only for the first ultrasonic beam (1 MHz), c) only for the second ultrasonic beam (2 MHz), and d) for the simultaneous operation of both beams.

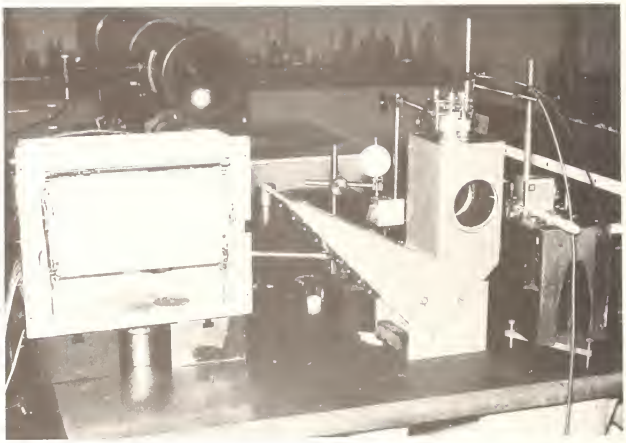

Figure 4. Photo of the experimental arrangement. Special triangular vessel in which reflection of ultrasonic are reduced below 45 dB.

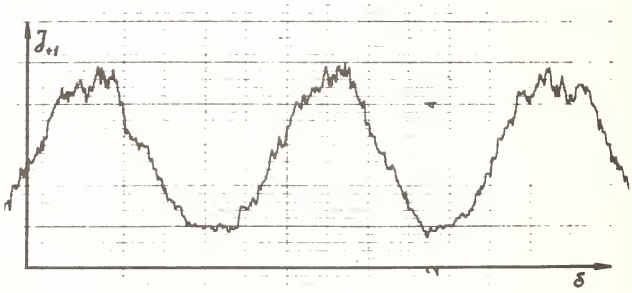

Figure 5. Original recording of the light beam intensity after passing through two ultrasonic beams of frequencies 1 and 2 MHz in the first order $|J_{+1}|$ versus the phase difference $|\delta|$.

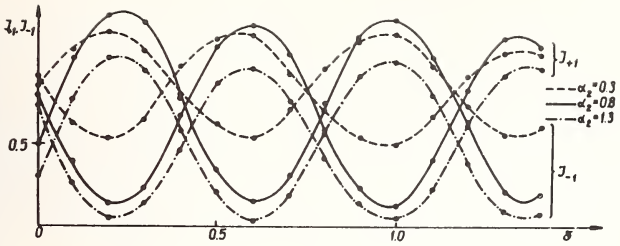

Figure 6. Dependence of light intensity in the ±1 orders diffracted by two adjacent ultrasonic beams | of 1 and 2 MHz | in water versus phase-difference δ for various α.

6. Conclusions

In studying the diffraction of light by adjacent ultrasonic waves, the phase-difference plays an important role, and can be used in measuring the ultrasonic pressure μ_2, where

$$\mu_2 = \frac{\lambda}{2\pi L_1} \arcsin \frac{I_2 - I_1}{I_1} \quad .$$

References

[1] Zankel, K. L., Diffraction of light by two ultrasonic waves of the same frequency, J. Acoust. Soc. Amer., 32, 706-713 (1960).

[2] Leroy, O., General symmetry properties of the diffraction pattern in the diffraction of light by parallel adjacent ultrasonic beams, J. Sound Vibration, 26, 389-393 (1973).

[3] Leroy, O., Diffraction of light by two parallel adjacent ultrasonic waves, having the same wavelengths, J. Sound Vibration, 32, 241-249 (1974).

[4] Leroy, O., Diffraction of light by two adjacent parallel ultrasonic beams, Acustica, 29, 303-309 (1973).

[5] Kwiek, P., Leroy, O., and Sliwinski, A., On the verification of the theory of ultrasonic light-diffraction by adjacent ultrasonics, Acoustics Letters, 1, 130-133 (1977).

[6] Leroy, O. and Mertens, R., Diffraction of light by two superposed ultrasonic waves, having arbitrary frequencies. General symmetry properties; method of solutions by series expansion, Proceedings Indian Academy Sciences, 68, 296-313 (1968).

[7] Poleunis, F. and Leroy, O., The diffraction of light by two adjacent parallel ultrasonic waves, one being a fundamental tone and the other its second harmonic, J. Sound Vibration, 58, 509-515 (1978).

☆ U. S. GOVERNMENT PRINTING OFFICE · 1980 340-997/289

NBS-114A (REV. 2-8C)

U.S. DEPT. OF COMM. BIBLIOGRAPHIC DATA SHEET (See instructions)	1. PUBLICATION OR REPORT NO. NBS SP 596	2. Performing Organ. Report No.	3. Publication Date November 1980

4. TITLE AND SUBTITLE

Ultrasonic Materials Characterization

5. AUTHOR(S)

Harold Berger and Melvin Linzer, Co-Editors

6. PERFORMING ORGANIZATION (If joint or other than NBS, see instructions)

NATIONAL BUREAU OF STANDARDS
DEPARTMENT OF COMMERCE
WASHINGTON, D.C. 20234

7. Contract/Grant No.

8. Type of Report & Period Covere

Final

9. SPONSORING ORGANIZATION NAME AND COMPLETE ADDRESS (Street, City, State, ZIP)

Same as above.

10. SUPPLEMENTARY NOTES

Library of Congress Catalog Card Number: 80-600148

☐ Document describes a computer program; SF-185, FIPS Software Summary, is attached.

11. ABSTRACT (A 200-word or less factual summary of most significant information. If document includes a significant bibliography or literature survey, mention it here)

Nondestructive testing has traditionally involved a search for flaws in materials or structures; it has long been appreciated that voids, cracks, inclusions, and similar flaws can lead to failure. Obviously, once a flaw has been detected, it is natural to consider methods that will give more information. What is the flaw size, type, location, or orientation? This information is necessary if a realistic assessment of the influence of the flaw on performance is to be made. In addition, it is now more widely recognized that parameters such as hardness, grain size, bonding, and residual stress can also have a strong influence on material performance The use of ultrasonic nondestructive testing to characterize materials both in terms of properties and flaws is the subject of this volume. Therefore, this volume is about nondestructive characterization of parameters that influence the performance of materials.

12. KEY WORDS (Six to twelve entries; alphabetical order; capitalize only proper names; and separate key words by semicolons)

Attenuation; defect characterization; flaws; materials characterization; nondestructive testing; residual stress; ultrasonics; and velocity.

13. AVAILABILITY

[X] Unlimited

☐ For Official Distribution. Do Not Release to NTIS

[X] Order From Superintendent of Documents, U.S. Government Printing Office, Washington, D.C. 20402.

☐ Order From National Technical Information Service (NTIS), Springfield, VA. 22161

14. NO. OF PRINTED PAGES

644

15. Price

$11.00

USCOMM-DC 6043-P8

NBS TECHNICAL PUBLICATIONS

PERIODICALS

JOURNAL OF RESEARCH—The Journal of Research of the National Bureau of Standards reports NBS research and development in those disciplines of the physical and engineering sciences in which the Bureau is active. These include physics, chemistry, engineering, mathematics, and computer sciences. Papers cover a broad range of subjects, with major emphasis on measurement methodology and the basic technology underlying standardization. Also included from time to time are survey articles on topics closely related to the Bureau's technical and scientific programs. As a special service to subscribers each issue contains complete citations to all recent Bureau publications in both NBS and non-NBS media. Issued six times a year. Annual subscription: domestic $13; foreign $16.25. Single copy, $3 domestic; $3.75 foreign.

NOTE: The Journal was formerly published in two sections: Section A "Physics and Chemistry" and Section B "Mathematical Sciences."

DIMENSIONS/NBS—This monthly magazine is published to inform scientists, engineers, business and industry leaders, teachers, students, and consumers of the latest advances in science and technology, with primary emphasis on work at NBS. The magazine highlights and reviews such issues as energy research, fire protection, building technology, metric conversion, pollution abatement, health and safety, and consumer product performance. In addition, it reports the results of Bureau programs in measurement standards and techniques, properties of matter and materials, engineering standards and services, instrumentation, and automatic data processing. Annual subscription: domestic $11; foreign $13.75.

NONPERIODICALS

Monographs—Major contributions to the technical literature on various subjects related to the Bureau's scientific and technical activities.

Handbooks—Recommended codes of engineering and industrial practice (including safety codes) developed in cooperation with interested industries, professional organizations, and regulatory bodies.

Special Publications—Include proceedings of conferences sponsored by NBS, NBS annual reports, and other special publications appropriate to this grouping such as wall charts, pocket cards, and bibliographies.

Applied Mathematics Series—Mathematical tables, manuals, and studies of special interest to physicists, engineers, chemists, biologists, mathematicians, computer programmers, and others engaged in scientific and technical work.

National Standard Reference Data Series—Provides quantitative data on the physical and chemical properties of materials, compiled from the world's literature and critically evaluated. Developed under a worldwide program coordinated by NBS under the authority of the National Standard Data Act (Public Law 90-396).

NOTE: The principal publication outlet for the foregoing data is the Journal of Physical and Chemical Reference Data (JPCRD) published quarterly for NBS by the American Chemical Society (ACS) and the American Institute of Physics (AIP). Subscriptions, reprints, and supplements available from ACS, 1155 Sixteenth St., NW, Washington, DC 20056.

Building Science Series—Disseminates technical information developed at the Bureau on building materials, components, systems, and whole structures. The series presents research results, test methods, and performance criteria related to the structural and environmental functions and the durability and safety characteristics of building elements and systems.

Technical Notes—Studies or reports which are complete in themselves but restrictive in their treatment of a subject. Analogous to monographs but not so comprehensive in scope or definitive in treatment of the subject area. Often serve as a vehicle for final reports of work performed at NBS under the sponsorship of other government agencies.

Voluntary Product Standards—Developed under procedures published by the Department of Commerce in Part 10, Title 15, of the Code of Federal Regulations. The standards establish nationally recognized requirements for products, and provide all concerned interests with a basis for common understanding of the characteristics of the products. NBS administers this program as a supplement to the activities of the private sector standardizing organizations.

Consumer Information Series—Practical information, based on NBS research and experience, covering areas of interest to the consumer. Easily understandable language and illustrations provide useful background knowledge for shopping in today's technological marketplace.

Order the **above** *NBS publications from: Superintendent of Documents, Government Printing Office, Washington, DC 20402.*

Order the **following** *NBS publications—FIPS and NBSIR's—from the National Technical Information Services, Springfield, VA 22161.*

Federal Information Processing Standards Publications (FIPS PUB)—Publications in this series collectively constitute the Federal Information Processing Standards Register. The Register serves as the official source of information in the Federal Government regarding standards issued by NBS pursuant to the Federal Property and Administrative Services Act of 1949 as amended, Public Law 89-306 (79 Stat. 1127), and as implemented by Executive Order 11717 (38 FR 12315, dated May 11, 1973) and Part 6 of Title 15 CFR (Code of Federal Regulations).

NBS Interagency Reports (NBSIR)—A special series of interim or final reports on work performed by NBS for outside sponsors (both government and non-government). In general, initial distribution is handled by the sponsor; public distribution is by the National Technical Information Services, Springfield, VA 22161, in paper copy or microfiche form.

BIBLIOGRAPHIC SUBSCRIPTION SERVICES

The following current-awareness and literature-survey bibliographies are issued periodically by the Bureau:

Cryogenic Data Center Current Awareness Service. A literature survey issued biweekly. Annual subscription: domestic $35; foreign $45.

Liquefied Natural Gas. A literature survey issued quarterly. Annual subscription: $30.

Superconducting Devices and Materials. A literature survey issued quarterly. Annual subscription: $45. Please send subscription orders and remittances for the preceding bibliographic services to the National Bureau of Standards, Cryogenic Data Center (736) Boulder, CO 80303.